

### **INTER - International Network on Timber Engineering Research**

2014 the International Network on Timber Engineering Research (INTER) was founded.

#### **Scope**

Presentation, discussion and documentation of research results in timber engineering and development of application rules for timber design codes or standards related to timber engineering.

#### **Approach**

Annual meetings in different countries/places hosted by meeting participants

Presentation and discussion of papers

Peer review of the abstracts before the meeting and of the papers during the meeting

Decision of the acceptance of the abstracts before the meeting by a well-defined review process

Decision of the acceptance of the papers for the proceedings during the meeting

Publication of the papers and the discussion in proceedings

#### **Rules**

All decisions including the appointment of the chairperson or the location of annual meetings are made by the participants attending a meeting.

#### **Membership**

Persons contributing to or being interested in research related to timber engineering.

INTER PROCEEDINGS MEETING FIFTY-SEVEN 2024



**MEETING FIFTY-SEVEN**

**PADOVA, ITALY**

**AUGUST 2024**

---

# INTER

---

International Network on Timber Engineering Research

# Proceedings

Meeting 57

26 - 29 August 2024

Padova, Italy

Edited by Rainer Görlacher

Timber Scientific Publishing  
KIT Holzbau und Baukonstruktion  
Karlsruhe, Germany  
2024



**Publisher:**

Timber Scientific Publishing  
KIT Holzbau und Baukonstruktion  
Reinhard-Baumeister-Platz 1  
76131 Karlsruhe  
Germany  
2024

ISSN 2199-9740

## Table of Contents

1	List of Participants	1
2	Minutes of the Meeting	5
3	INTER Papers, Padova 2024	27
57 - 2 - 1	Lateral Torsional Buckling of Glulam Beam-Columns: Axial Compression and Bending Verification - J Töpler, U Kuhlmann, J Schänzlin	31
57 - 5 - 1	Derivation of Visual Grading Assignments for Turkish Red Pine and Scots Pine Graded in Accordance with Turkish Standard TS 1265- 2012 - F Kurul, M Özdemir, T Yılmaz, M Arslan, S Ermiş, T Dündar	51
57 - 6 - 1	Strength Grading of Saturated Softwood Foundation Piles - G Pagella, G Ravenshorst, M Mirra, J-W van de Kuilen	71
57 - 7 - 1	Fatigue Behaviour of in Tension Axially-Loaded Self-Tapping Screws - R Brandner	91
57 - 7 - 2	On Stiffness and Strength of Glued-in Rods and Threaded Rods Parallel to the Grain - C Binck, A Frangi	111
57 - 7 - 3	Embedment Strength of Glued-in Rods and Dowels Oriented Parallel to Grain - S Aicher, K Simon	131
57 - 7 - 4	A Proposal for the Stiffness of Steel-Timber Dowel-Type Connections - L Buchholz, U Kuhlmann, J Gauß	149
57 - 7 - 5	Design Proposal for the Final Slip Modulus of Dowel-Type Timber Connections Based on the Beam-on-Foundation (BoF) Approach - R Lemaître, M Schweigler, E Binder, E Sauvignat, J-F Bocquet	165
57 - 7 - 6	Parametrization of the Non-Linear Behaviour of Timber Joints with Self-Tapping Screws - D Caprio, R Jockwer, A Ringhofer	183
57 - 7 - 7	The Effective Timber Thickness for Brittle Failure Assessment of Dowel-Type Connections - C D Aquino, M Schweigler, L Rodrigues, R Lemaître, J-F Bocquet, J M Branco, T K Bader	203

57 - 7 - 8	Brittle Failure Modes of Connections with Dowel-Type Fasteners Loaded Parallel to the Grain: A Comparison Between Eurocode 5 and CSA O86 - J M Cabrero, N L Rodriguez, T Tannert, A Salenikovich, Y H Chui	223
57 - 7 - 9	Design Brittle Failure Capacities of Connections with Dowel-Type Fasteners Laterally Loaded Parallel to Grain and Reinforced - R Lemaître, D Lathuillière, J-F Bocquet	241
57 - 7 - 10	Reinforcements for Compression Perpendicular to Grain of CLT Elements with Fully Threaded Screws: Experimental Validation of the Design Model- R Maderebner, T Stieb, L Rathiens, R Tomasi	243
57 - 12 - 1	Punching-Shear Resistance of Point-Supported CLT Panels - H Ganjali, T Tannert, Md Shahnewaz, C Dickof, M Popovski	259
57 - 12 - 2	Comparison of Calculation Methods for Application on Veneer-Reinforced Timber with Standard Lamella - N Kainz, P Aondio, M Danzer, S Winter	279
57 - 12 - 3	Strength and Stiffness of Adhesively Bonded Timber-Steel Composite Beams - S Aurand, P Haase, J Boretzki, M Albiez, P Dietsch, T Ummenhofer	299
57 - 15 - 1	OSB Sheathed Timber-Framed Shear Walls with Optimized Performance for Horizontal Loading - N Manser, R Steiger, M Geiser, A Frangi	317
57 - 15 - 2	Proposal for an Analytical Model of Light Timber-Framed Shear Walls with additional Cladding - L Rauber, B Hoffmeister	335
57 - 15 - 3	Seismic Performance of Braced Timber Frames - M Popovski, Z Chen	353
57 - 15 - 4	Investigation on the Performance of Platform-Type Coupled-Panel CLT Shear Walls under Seismic Conditions - J Chen, F Lam, M Li, M Popovski	373
57 - 15 - 5	Investigating the In-Plane Rigid Diaphragm Conditions of Cross Laminated Timber Floors for Seismic Design - G D'Arenzo, V Nicolussi, P Rigo, L Pozza, A Polastri, D Casagrande	393
57 - 15 - 6	Design Implications for Cross-Laminated Timber Shear Walls Connected to Perpendicular Walls - G D'Arenzo, E M Ruggeri, J Hummel, M Fossetti, W Seim	411

57 - 16 - 1	Structural Means for Fire-Safe Green Façade Design on Multi Storey Buildings - T Engel, S Winter	431
57 - 20 - 1	Comfort Assessment of Timber Floor Vibrations - M Felicita, R Roijackers, R Cojocaru, G Ravenshorst	445
4	INTER Notes, Padova 2024	463
Note 1	Beech LVL and Moisture – a Known Challenge C Sandhaas	465
Note 2	Withdrawal Capacity of Coated Ring Shanked Nails - A Ceylan, Z C Girgin	469
Note 3	An Ecologic Lightweight Suggestion for the Concrete Layer of CLT-Composite Floors - Z C Girgin	473
Note 4	Structural Design Method for CLT Drift Pinned Joint - S Nakashima	477
5	Peer Review of Papers for the INTER Proceedings	481
6	Meeting and List of CIB-W18 and INTER Papers	483



# 1 List of participants

## AUSTRIA

R Brandner	Graz University of Technology
U Hübner	Association of the Austrian Wood Industries, Wien
T Stieb	University of Innsbruck
R Tabelander	University of Innsbruck

## CANADA

J Chen	University of British Columbia, Vancouver
G Doudak	University of Ottawa, Gatineau
H Ganjali	University of Northern British Columbia, Prince George
F Lam	University of British Columbia, Vancouver
M Popowski	FPIInnovations, Vancouver
A Salenikovich	Université Laval, Quebec
T Tannert	University of Northern British Columbia, Prince George

## DENMARK

G D'Arenzo	Aarhus University
------------	-------------------

## ESTONIA

A Just	Tallinn University of Technology
J L Vihmann	Tallinn University of Technology

## FRANCE

R Lemaitre	CERIB, Epernon
------------	----------------

## GERMANY

S Aicher	MPA University of Stuttgart
S Aurand	Karlsruhe Institute of Technology (KIT)
H J Blaß	Karlsruhe Institute of Technology (KIT)
L Buchholz	University of Stuttgart
P Dietsch	Karlsruhe Institute of Technology (KIT)
T Ehrhart	University of Stuttgart
T Engel	Technical University of Munich (TUM)
R Görlacher	Karlsruhe Institute of Technology (KIT)
P Grönquist	University of Stuttgart
R Jockwer	TU Dresden
N Kainz	Technical University of Munich (TUM)
M Kazmiruk	University of Stuttgart
J-D Kleefeldt	University of Stuttgart

U Kuhlmann	University of Stuttgart
L Rauber	RWTH Aachen University
C Sandhaas	Karlsruhe Institute of Technology (KIT)
W Seim	University of Kassel
O A Sisman	Eurotec GmbH, Hagen
C Tapia Camu	MPA University of Stuttgart
J Töpler	Biberach University of Applied Sciences
M Westermayr	Adolf Würth GmbH & Co. KG, Künzelsau
S Winter	Technical University of Munich (TUM)

#### ITALY

D Casagrande	University of Trento
M Fragiacomò	University of L'Aquila
L Marchi	University of Padova
V Nicolussi	Università di Bologna
P Pichler	StructureCraft Builders Inc., Trento
A Polastri	CNR - IBE, San Michele all'Adige
L Pozza	Università di Bologna
P Rigo	Università di Bologna
R Scotta	University of Padova
P Vinco da Sesso	StructureCraft Builders Inc., Trento

#### JAPAN

S Nakashima	Building Research Institute, Tsukuba
-------------	--------------------------------------

#### LIECHTENSTEIN

M Fehr	Hilti Corporation, Schaan
M Pagliarin	Hilti Corporation, Schaan

#### NEW ZEALAND

D Moroder	PTL Structural & Fire, Christchurch
-----------	-------------------------------------

#### NORWAY

H Stamatopoulos	Norwegian University of Science and Technology, Trondheim
R Tomasi	Norwegian University of Life Science, Ås

#### PORTUGAL

C Dapieve Aquino	University of Minho
------------------	---------------------

#### SPAIN

J M Cabrero	Universidad de Navarra, Pamplona
-------------	----------------------------------

## SWEDEN

E Binder	Linnaeus University, Vaxjö
D Caprio	Chalmers University of Technology
H Danielsson	Lund University
M Schweigler	Linnaeus University, Vaxjö
E Serrano	Lund University

## SWITZERLAND

C Binck	ETH Zürich
M Felicita	ETH Zürich/EMPA Dübendorf
A Frangi	ETH Zürich
N Manser	ETH Zürich/EMPA Dübendorf
P Palma	EMPA, Dübendorf

## THE NETHERLANDS

M Mirra	Delft University of Technology
G Pagella	Delft University of Technology
R Roijackers	Lüning Ingenieurs in Houtconstructies, Arnhem
J W Van de Kuilen	Delft University of Technology / TU Munich

## TURKEY

A Ceccotti	Boğaziçi University, Istanbul
T Dundar	Istanbul University-Cerrahpaşa
Z C Girgin	Yildiz Technical University
M Ozdemir	Marmara Forestry Research Institute

## USA

M O Amini	American Wood Council, Leesburg
B Yeh	APA - The Engineered Wood Association, Tacoma





# 2 Minutes of the Meeting

by F Lam, Canada

## CHAIRMAN'S INTRODUCTION

P Dietsch opened the INTER 2024 meeting and welcomed the delegates to beautiful Padua. INTER 2024 is the 11<sup>th</sup> meeting of the International Network on Timber Engineering Research. In total, our group, formerly named CIB W-18, had 57 meetings in 51 years.

INTER 2024 is hosted by our Italian friends, led by Roberto Scotta from University of Padova. The Chair thanked the organization team of Roberto Scotta, Daniele Casagrande, Luca Marchi, Michele Mirra, Giorgio Pagella, Andrea Polastri Luca Pozza and Cristina Puntel.

P Dietsch thanked Frank Lam, who has been a member of INTER for 30 years, most of the time not only as a participant but also serving the INTER community in his role. The Chair thanked Rainer Görlacher for preparation of proceedings, organization of reviews, provision of papers, and support for the organizers and participants.

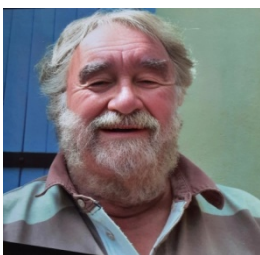
INTER 2024 is the 5<sup>th</sup> meeting in Italy, after meetings in Florence in 1986, Venice in 2001, Florence in 2006 and Alghero in 2011.

R Scotta welcomed the group to Padova and provided logistic information on the venue and the meeting.

INTER continues the tradition of yearly meetings to discuss research results related to timber structures with the aim of transferring them into practical applications, meaning codes and standards. INTER is an independent body with strong links to standardization, hence the Chair welcomed all colleagues who are also representing standardization committees.

INTER 2024 has 73 participants from 18 countries with a high participation from outside Europe indicating a strong interest in the work of the group worldwide.

P Dietsch announced the passing of two very influential colleagues last year.



Ron Marsh



Jürgen Ehlbeck

P Dietsch provided the following obituary for Ron Marsh. Ron Marsh worked as Engineer for Arup for his whole life. He joined Arup already in 1959 as design engineer. At Arup he became a specialist in timber design. In this role he attended about 20 meetings of CIB W-18, the last in Florence 2006 on the invitation of Ario Ceccotti. Ron Marsh worked at many Arup offices, for example in Iraq in his early years and Japan towards the end of his career, a task for which he even learned Japanese.

P Dietsch did not have the chance to meet Ron in person but commented that those that knew him speak warmly about his lively character, and open, embracing personality making him a person that everybody liked to have around. After his retirement he moved to France to the region of St. Emilion with his wife in 2003 where they lived since then. Ron Marsh died on July 1st 2024 at the age of 88.

Ario Ceccotti provided the following additional information on the obituary for Ron Marsh (1936-2024).

As a Civil Engineer, Ron was definitively attracted by timber. Very good friend of Dr. John Sunley, one of the Founders of CIB-W18, he was a specialist in design with timber, helping many parts of the Arup firm with his knowledge and experience. He was actively attending the CIB-W18 meetings. His first CIB-W18 meeting was in 1973, the second meeting of the Group. His strict contact with the Arup works around the world gave him a special inclination to spot concrete follow-ups of the works presented during the CIB meetings, always trying to find the link from theory to practice. His friendship with Hans Larsen, Jan Kuipers, and Jürgen Ehlbeck, is a pillar of the history of the Group.

P Dietsch provided the following obituary for Jürgen Ehlbeck. Jürgen Ehlbeck, born in Hamburg in 1930, studied and worked at the University of Karlsruhe under Prof. Möhler before being appointed Möhler's successor in 1981 as the Chair of Timber Structures and Building Construction at the University Karlsruhe. Mechanical connections were his primary focus. But under his leadership, timber construction research also transitioned from deterministic approaches to probability-based approaches. Ehlbeck was deeply committed to technology transfer, being a key member in the development of the German code DIN 1052 and shaping the first generation of Eurocode 5. CIB-W18, now INTER, was especially important to him. He participated in 30 meetings of CIB-W18 but was one of the first Professors of his generation that let his staff members present their results instead of him presenting the results achieved at his institute. Ehlbeck died on September 21, 2023 just before reaching the age of 93.

P Dietsch asked for a minute of silence in memory of Ron Marsh and Jürgen Ehlbeck.

26 papers were accepted for this meeting with 24 final submittals. These papers were chosen from 40 submitted abstracts with an acceptance rate of 2/3. The papers were selected based on a review process of the abstracts with 4 acceptance criteria (state of the art, originality, assumed content and relation to standards or codes).

In total, 14 long-time members of this group acted as reviewers, each abstract was reviewed by at least 6 reviewers. P Dietsch thanked all reviewers as well as all authors of abstracts and papers.

Papers to be presented at INTER meetings shall be submitted at least one month before the meeting to enable all participants to read the papers beforehand. Papers must be presented and defended by one of the authors. The presentations are limited to a maximum of 20 minutes each in order to allow time for meaningful discussions after each presentation. The presenters were asked to relate the presentations to the objective of translating research results into design rules. All presenters were asked to conclude their presentation with a clear statement concerning the impact of their results on existing applications or future developments in codes and standards.

In INTER meetings, the delegates have the right to decide on the acceptance of the papers for the proceedings. All authors are invited to amend their papers according to the comments and recommendations of the experts in this group before final submittal for the proceedings. The proceedings will be produced by Rainer Görlacher in Karlsruhe. Finalized papers must be sent to Rainer Görlacher at the latest end of September this year.

The following 11 topics will be covered in this meeting:

(2) – timber columns	- 1 paper
(5) – stress grading	- 1 paper
(6) – stresses for solid timber	- 1 paper
(7) – joints and fasteners	- 11 papers
(12) – laminated members	- 3 papers
(15) – structural stability	- 6 papers
(16) – fire	- 1 paper
(20) – serviceability	- 1 paper

There would be a possibility to present notes towards the end of the technical session. The presentation of notes is strictly limited to 10 minutes without discussion.

## INFORMATION FROM OTHER ORGANIZATIONS

European standardization. The Eurocode revision is in its final stage. S Winter provided an update on the work of SC 5. The time frame for last Eurocodes to be published is Sept 30, 2027. Date of withdrawal of 1<sup>st</sup> generation of Eurocodes is March 30, 2028. Formal vote on EN 1995 1-1 is intended to be held by May 26, 2025. There was discussion on balance between comprehensiveness versus simplicity / more exact versus conservatism. WCTE 2025 will have a focus session on Eurocode 5 and S Winter encouraged participants to contribute.

The European work on product standards in CEN/TC 124 is still slowed down. The main work item here is the so-called CPR Acquis process. U Huebner gave a short breakdown on the process and status. The call for additional products to join the process ended in August 2024. Wood based panels are currently excluded and dated references are required.

G Doudak gave an update on Canadian CSA O86 code on Engineering Design in Wood with new design information on CLT, self-tapping screws, mechanically laminated timber and a new clause on lateral torsional buckling.

D Moroder gave an update on New Zealand codes and standards work where they will be looking at European and Canadian design provisions for connections. They will also coordinate with Australian colleagues on standards updates and revisions.

BJ Yeh and M Amini provided updates on US codes and standards. The PRG320 CLT product standard will be updated. European species for inclusion in CLT production in N.A. will be considered. US NDS targets changes in 2027 at a 6-year code cycle. CLT system including shear walls and rocking wall systems as well as horizontal diaphragms are topics of importance.

P Dietsch commented that INTER is a working commission, not a conference. Good quality papers are the foundation of this group but its reinforcement is the discussion process. The Chair encouraged participants to speak out to continue the tradition of lively discussions in the quest for even higher quality results.

## TIMBER COLUMNS

57 - 2 - 1 Lateral Torsional Buckling of Glulam Beam-Columns: Axial Compression and Bending Verification - J Töpler, U Kuhlmann, J Schänzlin

Presented by J Töpler

G Doudak received clarification on how non-elastic deformation was detected in the compression zone during testing. He commented that application of larger axial load would have been interesting.

O Sisman commented that stiffness of the beam column depended on connection stiffness and application of load over an area can offer some restriction to lateral buckling. He commented that the proposed design formula would be too complicated. J Töpler said this should not be an issue.

JW van de Kuilen commented that there was past work on this topic. He asked how sure would the numerical model verified from a different test condition be transferred to this study. JW van de Kuilen and J Töpler discussed that loading should be fine and compression strength test data of different species would have been nice to have but there was no certainty if full scale moment rotation test data was available. J Töpler agreed that such data would increase the validity of the FEM but was quite comfortable the validity of the FEM.

P Dietsch commented that a combination of shear and torsional shear was observed but that the stress interaction was superficially covered and the approach from H Kreuzinger on this topic was available and the authors should check this approach. J Töpler agreed.

The proposed  $k_{pl,c}$   $k_{pl,m}$  factors could be challenged as code proposal because  $k_{pl,m}$  jumped from 1 to 6. J Töpler said as experimental data was limited, he did not want to be specific. He stated that  $k_{pl,c} = 1$  for softwood and a different factor for beech should be okay. P Dietsch suggested that the interaction between torsional stresses and shear stresses from shear force should be clarified in paper.

A Frangi commended the work but suggested to look into past work in more detail.

## STRESS GRADING

57 - 5 - 1 Derivation of Visual Grading Assignments for Turkish Red Pine and Scots Pine Graded in Accordance with Turkish Standard TS 1265- 2012 - F Kurul, M Özdemir, T Yılmaz, M Arslan, S Ermiş, T Dündar

Presented by T Dündar

F Lam received confirmation that grade quality index rules were not available in the European grading system.

A Ceccotti commented that there were lots of works presented in the CIB forum on strength grading in the past and this topic is of importance.

## STRESSES FOR SOLID TIMBER

57 - 6 - 1 Strength Grading of Saturated Softwood Foundation Piles - G Pagella,  
G Ravenshorst, M Mirra, J-W van de Kuilen

Presented by G Pagella

There was a question whether one would consider a system factor in design. J W van de Kuilen said there is a system factor of 1.1 which could be considered.

O Sisman commented that as B and C grades are quite close, one should consider reducing the number of grades.

S Aicher commented that B and C grades differentiation was a bit superficial and different KR might be needed.

P Dietsch asked if moisture profile of the timber was considered to verify that the piles are saturated over the full cross-section before tetsing. G Pagella said piles were submerged for months and no consideration of moisture profile was taken. Small specimen moisture tests indicated small changes even after one hour.

S Aicher stated that the strength at tip of the pile should be considered rather than the strength along the length of the pile, and one should consider which part of the log diameter would not be important. G Pagella said if we only look at the tip KR will not be considered. Other data on the topic could support the findings but relying on data from existing buildings in other parts of Europe would be important but difficult.

## TIMBER JOINTS AND FASTENERS

57 - 7 - 1 Fatigue Behaviour of in Tension Axially-Loaded Self-Tapping Screws -  
R Brandner

Presented by R Brandner

P Dietsch received confirmation that up to 10000 load cycles could be considered as low cycle fatigue. P Dietsch inquired on the potential influence of the hardening and forming processes of the screws on their fatigue behaviour. R Brandner said that the screws had the same hardening process. They discussed that the tensile failure mode was not expected at these percentages of failures and discussed potential effects. It was agreed that a solution would be needed for code and standard implementation.

P Vinco da Sessa asked if there are any studies planned to consider the influence of moisture exposure and climatic conditions. R Brandner agreed that this area is important but did not have an answer yet. It was agreed that without technical evidence one would need to be very conservative.

C Sandhaas commented about the process of fixing the screws using steel fixtures in fatigue tests as friction activated from the steel plate could influence the results. C Sandhaas also commented about the necessity to consider the fact that a connection always includes numerous screws.

A Frangi commented that as connections with multiple screws were not considered, can the results be trusted. R Brandner responded that one can trust the results. The tensile failure results were low but withdrawal failure information are okay.

U Kuhlmann commented that the boundary between low and high cycle fatigue of 10000 cycles is just a number. Toughness of the steel is an important factor and is covered in EN 1993-1-10. It is a question of choice of steel. Also hardness treatment from cold forming would decrease the toughness. It is also well known that manufacturers of screws produce screws with high hardness.

U Huebner discussed if this item could be covered in a product standard, differentiating between normal (quasi-static) and special applications (seismic, fatigue). P Dietsch mentioned that this would be challenging to control in practice.

#### 57 - 7 - 2 On Stiffness and Strength of Glued-in Rods and Threaded Rods Parallel to the Grain - C Binck, A Frangi

Presented by C Binck

E Serrano asked how was the stiffness of the joint measured. C Binck responded that deformation between end of timber and the sleeve of the GIR was measured.

D Moroder questioned how the bond quality in manufacturing be controlled in the chosen sequence of installation.

H Stamatopoulos and C Binck discussed parallel to grain application versus small angle application which can potentially reduce the influence of shrinkage cracks. H Stamatopoulos received clarification of whether a camera system was used from one or both sides of the specimen.

P Vinco da Sessa commented on possible tolerance issues during manufacturing of the GIR and not to consider the full length as embedment length due to the increased splitting potential.

S Aicher commented that too much recommendations are given based on testing of only one product from a single manufacturer. Typical construction practice would use a larger hole to ease production which would influence performance of the connection. He emphasized that one should not provide a proposal based on a single producer. A Frangi responded that one did not observe bond line failure and stiffness of the connection could be achieved easily. Therefore the results should be



applicable to other producers. S Aicher said results from testing with one mm oversized holes cannot be generalized to other situations.

R Jockwer questioned measurement of stiffness for different unbonded lengths. C Binck responded if the 5 cm unbonded length was neglected, stiffness would be 5% higher. Stiffness values for different unbonded length could be corrected but was not done in the original version of the paper.

C Sandhaas received confirmation that the measurement differences across the specimen width were so small that taking an average was acceptable.

S Winter discussed failure mode versus capacity in slide 75 and received explanation that in some cases yield point of the rod was close to shear failure load.

### 57 - 7 - 3 Embedment Strength of Glued-in Rods and Dowels Oriented Parallel to Grain - S Aicher, K Simon

Presented by S Aicher

A Salenikovich asked about the limits to use in terms of deformation to establish the resistance. S Aicher responded that maximum value at 5 mm seemed to make sense in most cases. In situations where reinforcements were involved, loads associated with much smaller deformations would be reasonable. One should keep in mind that the design equation from EC5 is very conservative. A Salenikovich suggested that potential splitting failures might be the reason of setting the conservative EC5 approach.

R Jockwer and H Blass commented and discussed the origin of EC5 provisions that could be based on embedment tests from the UK.

U Hübner commented that the current project team for EC5 studied embedment strength including density correction, 75%CI on characteristic strength and embedment tests for hardwood. They could not reach past values with today's analysis. He mentioned that their own and Gehris' back calculations also showed inconsistencies with EC5 provisions.

### 57 - 7 - 4 A Proposal for the Stiffness of Steel-Timber Dowel-Type Connections - L Buchholz, U Kuhlmann, J Gauß

Presented by L Buchholz

A Salenikovich commented that how stiffness was determined needed to be considered carefully when combining data from different projects. L Buchholz described how the testing was established which was similar to other cases.

H Blass questioned whether the approach of estimating the maximum load for stiffness estimation was used in all cases especially for the reinforced connections as there seemed to large differences from C Sandhaas' results on beech. L Buchholz responded that this could be due to difference in manufacturers. L Buchholz also confirmed that the evaluation of the effect of number of fasteners was also done with databases from others.

A Frangi commented he could share more ETH data (Gehri, Wydler) on the topic.

P Dietsch discussed with U Hübner if there would be room to consider this issue in the code. They agreed that more discussion would be needed as all kinds of connections would need to be considered and influence of number of dowels also play a role.

A Frangi commented that the paper should show equations for the +- 50% band.

57 - 7 - 5 Design Proposal for the Final Slip Modulus of Dowel-Type Timber Connections Based on the Beam-on-Foundation (BoF) Approach - R Lemaître, M Schweigler, E Binder, E Sauvignet, J-F Bocquet

Presented by R Lemaitre

A Frangi asked if experimental data was available to check the approach. R Lemaître responded not yet but they will have information from long term tests.

M Fragiaco stated that test data from other organizations exist to benchmark the results. He commented about the use of viscoelastic spring versus localized effects. R Lemaître said that elastic springs were used. M Fragiaco questioned why EC5 are higher. Some of these springs should be outside the elastic range. M Fragiaco stated that test data for model verification would be needed.

H Stamatopoulos commented that experimental data should be used to back calculate the spring parameters and changing local properties of the springs could ameliorate the results. Currently  $K_{SLS,fin}$  seems a fictitious number.

D Moroder and R Lemaître discussed difficulties in finding  $k'_{def}$  values in EC5.

J Töpler and JW van de Kuilen discussed  $k_{def}$  factors established from past papers. J Töpler asked if primary and secondary creep was considered and mentioned that the reduction of stiffness could be an approach. P Dietsch suggested further clarification in the paper on this issue would be needed.

57 - 7 - 6 Parametrization of the Non-Linear Behaviour of Timber Joints with Self-Tapping Screws - D Caprio, R Jockwer, A Ringhofer

Presented by D Caprio

A Frangi questioned how the experimental data from different sources was put together. D Caprio stated in some cases there was high variability. A Frangi stated that rationale to justify ignoring some cases would be needed.

M Fragiacommo commented that what is needed by designers are reliable formulae. Equations to get the non-linearity are not needed. He asked if there is a plan to do research to receive analytical predictions of the behaviour. He further commented that an analytical way to predict the stiffness was also missing.

A Salenikovich mentioned that he could contribute data to the database.

D Moroder received clarifications about comparison with test data, higher coefficient of variation with high stiffness and envelope of the curves were provided.

C Tapia Camu commented that some of the parameters in the model do not have physical meaning and questioned how these were treated in the correlation matrix.

P Dietsch suggested that further clarifications as well as editorial work on the paper would be needed.

57 - 7 - 7 The Effective Timber Thickness for Brittle Failure Assessment of Dowel-Type Connections - C D Aquino, M Schweigler, L Rodrigues, R Lemaître, J-F Bocquet, J M Branco, T K Bader

Presented by C D Aquino

P Dietsch commented that the current EC5 model seemed to be not far from results of the paper.

T Tannert received confirmation which version of the proposed standard was compared. C D Aquino stated that the enquiry version was used but the changed proposal still represents an upper bound.

A Frangi commented that the upper limit cannot be accepted as design approach.

P Palma commented that based on experiments performed, the coefficient of variation should be higher.

T Ehrhart pointed out a couple of typo and illustration issues.

57 - 7 - 8 Brittle Failure Modes of Connections with Dowel-Type Fasteners Loaded Parallel to the Grain: A Comparison Between Eurocode 5 and CSA O86 - J M Cabrero, N L Rodriguez, T Tannert, A Salenikovitch, Y H Chui

Presented by J M Cabrero

C Sandhaas commented that since the presented approach would be intended as the main model for EC5 one should carefully scrutinize the approach. The model would only be as good as its validation. C Sandhaas questioned how the experimental data was evaluated to calibrate the proposed model as in most resources either necessary information is missing or the evaluation was done on different levels of deformation. She questioned that the failure modes stated in the paper could be properly differentiated from the information in the original reports. C Sandhaas pointed out a range of issues including the use of reinforced connections to validate the approach, how splitting was considered, about factors such as the  $k_t$ -factor being fiddle factors, why some data were culled and how mixed failure types between beginning fastener yielding and brittle failure were treated. C Sandhaas received confirmation that there was no model verification.

P Dietsch commented that a collaborative approach would be needed.

H Blass questioned the robustness of the approach to achieve desired safety for all cases. He has little trust in some of the used references. He stated that an upper bound should not be introduced but a lower bound should be used in Eurocode 5.

T Tannert said that the Canadian code was set based on 30 tests or so. Here 400 data points were considered with relatively comparable design models.

U Hübner commented about the project team and working group contributing to this work and urged for collaboration.

H Blass commented that some tests were not appropriate and collaboration on this basis would not make sense.

57 - 7 - 9 Design Brittle Failure Capacities of Connections with Dowel-Type Fasteners Laterally Loaded Parallel to Grain and Reinforced - R Lemaître, D Lathuillière, J-F Bocquet

Presented by R Lemaître

A Frangi commented that we do not want to design for brittle failures so reinforcements would be needed to improve ductility. A Frangi asked how effective were the reinforcements to change the failure mode. R Lemaître stated that

reinforcement could improve the reliability of the connection through improvement of the shear strength and also help control the splitting failure mode.

JM Cabrero commented that this work aimed to establish the brittle failure capacity. JM Cabrero received confirmation that the simple model in EC5 for stiffness predictions was compared with the complex model in the paper.

A Salenikovich received confirmation that the load displacement curves actually indicated brittle failure. They discussed brittle failure preceded by yielding failure of the connector and how to deal with this issue in design where some design properties of the steel elements were set at the mean level.

H Blass commented that the characteristic values have hidden adjustment factors.

D Moroder questioned about the frequency of splitting failure mode.

R Jockwer received confirmation of the detail of the reinforcement pattern before and behind the dowel. They discussed the mechanics of the distribution of force between the dowels in relationship to the stiffness of the connection in different shear plane.

P Dietsch commented in some test cases the use of too many screws could have led to splitting failures. Also the paper had many proposals which were not included in the presentation which made face-to-face discussion and evaluation of these cases difficult. P Dietsch questioned what happened if only the first dowel was reinforced and asked if there was experimental/technical evidence to support these cases.

R Lemaître said experimental data from the tests for the Lisbon pavilion was available for support.

P Dietsch said naming of symbols in the paper needed more work for clarity.

P Dietsch commented that a  $k$  factor for tension was 1.5 in EC5 but it was changed to 1.0 here. R Lemaître said it could be for conservatism. P Dietsch suggested reworking the paper to clean up issues.

57 - 7 - 10 Reinforcements for Compression Perpendicular to Grain of CLT Elements  
Owith Fully Threaded Screws: Experimental Validation of the Design  
Model - R Maderebner, T Stieb, L Rathiens, R Tomasi

Presented by R Tomasi

P Dietsch received clarification that the screw tip distance was at least  $0.1t_{CLT}$  but recommended to discuss the results of the underlying Master thesis in the community. P Dietsch commented that failure mode  $a_2$  is related to horizontal elongation of the wood which for CLT is hindered by the orthogonal arrangement. A comparison to the results of the unreinforced situation would have been helpful. Finally the Torx tests fixed the screw head against rotation which might not be

realistic and lead to overestimation of results compared to practical situations, where screw heads could feature small horizontal movement.

F Lam inquired about distance requirements and long-term effects in these situations.

## LAMINATED MEMBERS

57 - 12 - 1 Punching-Shear Resistance of Point-Supported CLT Panels - H Ganjali, T Tannert, Md Shahnewaz, C Dickof, M Popovski

Presented by H Ganjali

P Dietsch commented that experimental work indicated premature delamination failure of some specimens. These results should be culled. P Dietsch questioned the claim that shear analogy method being cumbersome and asked whether the transformed section method can take into account the other issues offered by shear analogy method. H Ganjali claimed that the middle layer showed similar longitudinal shear stresses between the two methods. P Dietsch stated that the rolling shear stresses in the inner cross layers are more important than the longitudinal shear stresses in the middle layer. H Ganjali agreed.

H Blass questioned the use of transformed section method. He asked where was the consideration of the shear modulus as the transformed section method was based on bending stresses only. As  $G_{RS}/G_{long}$  was not considered the results are inappropriate. T Tannert suggested that the transformed section approach allowed longitudinal shear stress distributions to be calculated even though the rolling shear stresses were not accurate. P Dietsch stated that differences in the shear stiffness must be considered.

R Brandner stated that short spans were tested in a past work (last year INTER meeting) on the topic and it should be cited. T Tannert responded that in long span floors rolling shear and punching shear failures would not be a problem. P Dietsch mentioned that the work of Bogensberger should be taken into account.

JW van de Kuilen stated that the creep factor seemed high and received confirmation that the loading was based on 55% of the fifth percentile of the short-term capacity.

J Töpler and H Ganjali discussed how to consider the influence of the rotational stiffness (clamping situation) at the support which would be related to the span under consideration.

S Aicher questioned the statement attributing the difference in results to uncertainties from different manufacturers. The high variability in rolling shear

strength would more likely to be the cause. H Ganjali said statistical work not reported supported the claim.

57 - 12 - 2 Comparison of Calculation Methods for Application on Veneer- Reinforced Timber with Standard Lamella - N Kainz, P Aondio, M Danzer, S Winter  
Presented by N Kainz

U Kuhlmann mentioned the necessity to vary the span to change the ratio between bending and shear stresses.

W Seim stated that comparisons between model and test results should be based on deformations and not stresses. He commented more detailed information on shell elements was missing in the paper. JW van de Kuilen agreed with W Seim's comments.

S Aicher stated the paper missed analytical results for engineers. He echoed the comment that one cannot measure stresses which would be obtained via strain measurements with knowledge of the elasticity constants. These issues should be addressed in the final paper submission.

J Töpler and N Kainz discussed model uncertainties. J Töpler mentioned the WG11 procedures to verify the model.

P Dietsch stated the results would depend on  $E_{90}$  which would be dependent on annual ring orientation; hence, using polar approach might be more appropriate. N Kainz responded that he would not expect not much effect. P Dietsch stated a lot of the cited reference are in German language. One should consider giving English reference and expand the reference list.

C Tapia Camu commented that one advantage of this veneer reinforcement method would be the reinforcement against stress concentration for holes etc. He questioned the use of such simplified models as they would render worse results compared to a solid model.

57 - 12 - 3 Strength and Stiffness of Adhesively Bonded Timber-Steel Composite Beams - S Aurand, P Haase, J Boretzki, M Albiez, P Dietsch, T Ummenhofer  
Presented by S Aurand

R Brandner commented that he would not recommend changing the partial safety actor and that the Eurocode has a system effect approach. S Aurand responded that

this was not considered in this study. P Dietsch added that the system effect approach might work.

G Doudak received confirmation that only one geometry was considered in the experiment and residual load capacity was available in the vertical case after the first load drop off.

U Hübner commented about the relationship between mechanical performance, cost and ecological assessment of European products. Reuse of beams might not be easy as 1:1 replacement because every building would be slightly different.

A Frangi suggested some optimization should be performed in terms of arrangement.

T Ehrhart discussed about shrinkage. S Aurand responded that this should not be critical because the steel could take up the load. T Ehrhart commented about the shear stress calculations in relation to the location of the failure plane.

S Winter commented about the partial safety factor. System effect approach might be preferred and fire protection of the steel should work. He discussed moisture change effect in the vertical reinforced beam needing tests with varying climatic conditions. He received confirmation that comparisons at the mean level were made.

W Seim stated that he is not sure about standardization with these hybrid materials of timber and steel with such long bonding length. He commented about vertical reinforcement case with using 4 timber parts rather than 2 timber parts.

F Lam commented that the stressed volume effect in shear might need to be considered.

## **STRUCTURAL STABILITY**

57 - 15 - 1 OSB Sheathed Timber-Framed Shear Walls with Optimized Performance for Horizontal Loading - N Manser, R Steiger, M Geiser, A Frangi

Presented by N Manser

F Lam received clarification that the objective is to establish the shear strength capacity of the OSB panel as this failure mode cannot be avoided in design of the timber frame shear wall.

H Blass asked as the shear strength of OSB is of interest why not just test the shear strength of the OSB. N Manser said that was also done. H Blass asked whether the tested OSB/3 is representative. N Manser said the producers do not control shear strength of the OSB; therefore, this is a problem.

R Jockwer and N Manser discussed the differences in failure modes of OSB in full scale wall tests versus panel tests. Also the factors in EC5 may be an issue.



S Winter commented that the full-scale tests indicated tensile failure mode of the OSB and not the shear failure of OSB so evaluation of the tension strength of OSB panels should be considered. N Manser said that although tensile failure of OSB existed, the limit for nailed connection is clearly shown in the test. S Winter commented that more realistic design might lead to more deformation leading to differences in observed behaviour.

G Doudak asked about differences in failure mode in two side sheathed versus one side sheathed wall. N Manser said they are similar. G Doudak asked if there are more staples on top versus the bottom. N Manser said they are the same.

A Salenikovich commented that some of the factors are not available in the Canadian code and asked about the background of the reduction factors. N Manser said that the background was not available. They further discussed the loading configurations and the influence of hold downs on lateral resistance.

#### 57 - 15 - 2 Proposal for an Analytical Model of Light Timber-Framed Shear Walls with additional Cladding - L Rauber, B Hoffmeister

Presented by L Rauber

G Doudak received clarification on the difference in the ductility ratio between the cases with and without cladding. Also the influence of difference in failure mode on added capacity from both sheathing types.

P Dietsch commented on the formulation of conclusions needing to clarify the failure of fasteners versus influence of cladding. Extra capacity from additional number of fasteners versus contribution of cladding was not clear in the paper and presentation.

M Fragiacommo commented that the overstrength factor did not seem right and the delay of brittle failure via the use of staples. L Rauber and M Fragiacommo discussed the load path between connections, OSB sheathing and cladding.

C Sandhaas commented on the load set up in relation to the vertical loading.

R Tomasi also commented that full anchorage was provided without vertical load.

R Jockwer asked about the error if only EYM was used. L Rauber responded that there was no issue if EYM was used.

H Blass discussed the load transfer mechanism and change in failure mode in the fasteners when cladding was introduced.

F Lam commented there was large volume of work on stucco cladded light wood frame shear wall from UBC and CUREE project in the 2000's. Although the contribution of stucco is clear, it was not included in NA code because of difficulties

in quality control of onsite applied stucco. Also in N.A. staples are not considered in shear wall designs.

D Casagrande commented on spacing requirements of staples as related to fire resistance issues.

A Ceccotti received clarification that ISO21581 was followed. He mentioned that between ISO and European rules, implications on seismic design are different. He commented that dynamic response of cladded structures should be considered as seismic mass would increase and period would decrease.

57 - 15 - 3 Seismic Performance of Braced Timber Frames - M Popovski, Z Chen  
Presented by M Popovski

F Lam received confirmation that the GLT brace was C grade columns per recommendations of designers participating in the project. F Lam also received confirmation that the observed brittle failure occurred at high deformation after yielding of the fasteners.

P Dietsch asked as positive effects of reinforcement were observed why not make the reinforcements a requirement. M Popovski responded that yes this will be considered. T Tannert said Canadian standards do not provide design guidance on reinforcements but this needs to be developed. M Popovski responded that they will work on this.

M Fragiaco commented on the 30% difference between ductile and non ductile cases. He questioned the Q factors for the unreinforced connections. M Popovski will coordinate for procedures for the reinforced connections.

A Ceccotti asked why use ASTM standards for cyclic testing. M Popovski said that ASTM standard B is related to the European approach. A Ceccotti asked how collapse was decided. M Popovski said that European approach consider 80% post peak load; however, in this study a lower load was considered.

G Doudak and M Popovski discussed Q factor in Eurocode versus RdRo in Canadian code. In this study Rd was referenced. They also discussed using larger spacing and end distances for seismic to guard against splitting failures. M Popovski reaffirmed that the splitting was caused by large deformations. M Popovski also confirmed that that building period calculated from code equations were compared with period of archetype but yielded little difference.

O Sisman commented that dowels will fail less.

H Blass commented that information on the reinforcement cases is given in ETAs and received clarification that the moisture content of the connections were 11.8 to

14.5%. He discussed moisture content of GLT in practice with higher moisture contents more issues with reinforcement could arise.

C Binck received clarification of the periods of the four and seven stories buildings.

57 - 15 - 4 Investigation on the Performance of Platform-Type Coupled-Panel CLT Shear Walls under Seismic Conditions - J Chen, F Lam, M Li, M Popovski

Presented by J Chen

D Casagrande commented that similar approaches were taken in Eurocode and discussed the interactive behaviour of the hold downs and vertical joints. He asked for suggestions to make this less challenging. J Chen responded that commercial hold downs can work and the process could be simplified without considering hierarchy of yielding sequence. D Casagrande said if hold downs yielded much earlier then this might not work.

G Doudak received clarifications that two screws per connection were tested and inquired about the method for applying the results to computer model. He received confirmation that gamma-analytical was assumed to be 1 and discussed about this assumption. Also he received confirmation that the uplift in analysis showed 55 mm of displacement of the hold down which can be achieved as shown in experimental results.

H Ganjali asked about the performance of hold downs under biaxial loading. F. Lam responded that UBC test data on commercial hold downs and angle brackets for CLT systems were published in journals. The results showed hold down capacities were not influenced by biaxial loading while angle brackets capacities were.

57 - 15 - 5 Investigating the In-Plane Rigid Diaphragm Conditions of Cross Laminated Timber Floors for Seismic Design - G D'Arenzo, V Nicolussi, P Rigo, L Pozza, A Polastri, D Casagrande

Presented by G D'Arenzo

F Lam commented about complications in research on in-plane stiffness of CLT diaphragms including diaphragm aspect ratio, openings, supporting beams acting as tension ties, irregular diaphragm shape, and contribution of topping.

D Moroder received confirmation that different floor constructions and spacing of the fasteners were studied. He questioned how to define the stiffness of diaphragms in practice and how to quantify the influence of walls above the diaphragm.

G D'Arenzo agreed that these issues are complicated and confirmed that a maximum

value in each story was calculated. D Moroder received confirmation that the analytical equations were used to estimate diaphragm stiffness.

G Doudak received confirmation that only one direction of the diaphragm was studied. G Doudak asked about the ratio of stiffness between wall and floor and received clarification of the value of  $k$  for single story structures. Also the diaphragm was considered rigid if  $k_{\text{floor}}/k_{\text{wall}} < 1$ .

A Frangi and G D'Arenzo discussed whether the diaphragm can be easily reached for conventional design of connections. A Frangi asked whether a differentiation between multi-storey and single-storey was necessary.

A Ceccotti and G D'Arenzo discussed where the two real cases were loaded. Also typical CLT building floors would usually be semi-rigid, whereas the results in this study showed closer to rigid diaphragm behaviour.

57 - 15 - 6 Design Implications for Cross-Laminated Timber Shear Walls Connected to Perpendicular Walls - G D'Arenzo, E M Ruggeri, J Hummel, M Fossetti, W Seim

Presented by G D'Arenzo

F Lam commented that J Brown PhD thesis from University of Canterbury studied the contribution of end walls on CLT working as shear core and the work should be cited. G D'Arenzo responded that he was aware of the work but the work is different.

D Casagrande discussed the importance of hold down design in order to achieve optimal ductility, indicating the possibility of inverting loading direction. G D'Arenzo agreed that this would be an important and good approach. D Casagrande further commented that a nonuniform application of vertical loads could influence the assumed rocking behaviour.

A Ceccotti agreed that studying 3D effect would be important especially for tall buildings.

M Fragiaco commented that B Dujic's paper from ~ 10 years ago already addressed some of these issues including a long perpendicular wall with hold downs. Influence of perpendicular walls in tubular systems for taller building would be important. He commented that simplified approaches would be needed to make these situations applicable. Finally tubular systems would need floor stiffness to ensure system behaviour.

D Moroder discussed asymmetrical response and questioned the use of screws in connections as bolts are sometimes preferred.

G Doudak and G D'Arenzo discussed diaphragm actions.

P Dietsch commented that the 1<sup>st</sup> and 2<sup>nd</sup> conclusion should be reconsidered based on comments from discussions on past research.

## **FIRE**

57 - 16 - 1 Structural Means for Fire-Safe Green Façade Design on Multi-Storey Buildings - T Engel, S Winter

Presented by T Engel

R Lemaitre asked about the effect of wind. T Engel mentioned that the issue of wind would be challenging to implement in testing requirements.

P. Vinco da Sesso commented that the difference between dried and living plant seemed to be limited.

S Aicher commented about the importance of risk associated with the mass of the wood, the mass of wood in the dried state as fuel load is important. Also burning of the leaves seemed to promote fire growth.

P Dietsch questioned that the distance of 50 cm was not supported and suggested that the author add information in the final paper.

T Ehrhart and T Engel agreed that the influence of wind may change the fire spread characteristics of such fires. T Ehrhart agreed that fire load considerations are important.

P Palma asked about the possibility of external fire leading to compartment fire. T Engel said this is possible but not likely unless open windows are available.

A Frangi commented that testing in an outdoor environment might not be appropriate as comparability with other tests are limited and stated that no consensus is given on European level for façade tests.

## **SERVICEABILITY**

57 - 20 - 1 Comfort Assessment of Timber Floor Vibrations - M Felicita, R Roijackers, R Cojocar, G Ravenshorst

Presented by M Felicita

F Lam asked, how was the continuity between adjacent panels considered? Also, the boundary conditions suggest the floors were supported by walls and what about floors supported by beams? M Felicita responded that pin-pin connectors were used to connect adjacent panels in the model. Results were not sensitive to the type of

connection. The beam supported case was not studied and can be considered in future.

P. Vinco da Sesso commented that concrete topped CLT floors are commonly used and pinned connections between adjacent panels may not be appropriate. M Felicita responded that model results indicated low impact whether pin connections or other fasteners were considered.

A Frangi and M Felicita discussed about the fact that the simplified method assumed resonance occurred whereas the advanced model had factors that considered low probability occurrence of resonance, discussing which one is more suitable for codes. E Serrano and M Felicita discussed details of the difference between the simplified and advanced model.

P Dietsch asked whether the CLT layup was adapted to the different sizes and spans of floors. M Felicita said this was not done. P Dietsch asked whether there are plans to consider the influence of non-load bearing walls. M Felicita agreed that this is an important topic and will be studied in future.

E Serrano asked whether point loads were applied in the FEM. M Felicita said that the model did not consider modelling loading from a walker but only consider the dynamic properties of the floor.

D Casagrande questioned the ratios between longitudinal versus transverse properties. M Felicita responded that manufacturer's publication data was used.

## **NOTES**

Four notes were presented.

## **ANY OTHER BUSINESS**

D Moroder invited the participants to attend the 5th International Conference on Timber Bridges in Rotorua NZ June 29 to July 2, 2025.

The Chair commented that some papers did not follow the scope of this working group as agreed by the group and indicated on the website. Members are encouraged to self-interpret the scope and contact the Chair if they see issues. It could be discussed if the review score on the item "relation to standards or codes" could be given more weight in case of marginal differences in scores between abstracts. The Chair asked for feedback until the next INTER meeting.

## VENUE AND PROGRAMME FOR NEXT MEETING

Turkish Colleagues invited the participants to attend INTER 2025 Istanbul Turkey Aug 24 to 28 2025

Upcoming possible future venues are

Oslo, Norway, Western Canada, Eastern Canada, New Zealand

## CLOSE

The Chair thanked the participants, the authors, and the presenters for contributing to INTER 2024. The Chair noted that 1/3 of the presenters were women.

The Chair thanked Frank Lam for his continued support to CIBW18 and INTER over the years.

The Chair thanked Rainer Görlacher for his support in between the INTER meetings and for organizing the INTER proceedings. R Görlacher after 35 years of service to the group announced that he will step down from his role.

The Chair thanked the host again for organizing and hosting INTER 2024.

R Scotta also expressed thanks to the team for their effort.

### 3 INTER Papers, Padova 2024

- 57 - 2 - 1 Lateral Torsional Buckling of Glulam Beam-Columns: Axial Compression and Bending Verification - J Töpler, U Kuhlmann, J Schänzlin
- 57 - 5 - 1 Derivation of Visual Grading Assignments for Turkish Red Pine and Scots Pine Graded in Accordance with Turkish Standard TS 1265- 2012 - F Kurul, M Özdemir, T Yılmaz, M Arslan, S Ermiş, T Dündar
- 57 - 6 - 1 Strength Grading of Saturated Softwood Foundation Piles - G Pagella, G Ravenshorst, M Mirra, J-W van de Kuilen
- 57 - 7 - 1 Fatigue Behaviour of in Tension Axially-Loaded Self-Tapping Screws - R Brandner
- 57 - 7 - 2 On Stiffness and Strength of Glued-in Rods and Threaded Rods Parallel to the Grain - C Binck, A Frangi
- 57 - 7 - 3 Embedment Strength of Glued-in Rods and Dowels Oriented Parallel to Grain - S Aicher, K Simon
- 57 - 7 - 4 A Proposal for the Stiffness of Steel-Timber Dowel-Type Connections - L Buchholz, U Kuhlmann, J Gauß
- 57 - 7 - 5 Design Proposal for the Final Slip Modulus of Dowel-Type Timber Connections Based on the Beam-on-Foundation (BoF) Approach - R Lemaître, M Schweigler, E Binder, E Sauvignat, J-F Bocquet
- 57 - 7 - 6 Parametrization of the Non-Linear Behaviour of Timber Joints with Self-Tapping Screws - D Caprio, R Jockwer, A Ringhofer
- 57 - 7 - 7 The Effective Timber Thickness for Brittle Failure Assessment of Dowel-Type Connections - C D Aquino, M Schweigler, L Rodrigues, R Lemaître, J-F Bocquet, J M Branco, T K Bader
- 57 - 7 - 8 Brittle Failure Modes of Connections with Dowel-Type Fasteners Loaded Parallel to the Grain: A Comparison Between Eurocode 5 and CSA O86 - J M Cabrero, N L Rodriguez, T Tannert, A Salenikovich, Y H Chui
- 57 - 7 - 9 Design Brittle Failure Capacities of Connections with Dowel-Type Fasteners Laterally Loaded Parallel to Grain and Reinforced - R Lemaître, D Lathuillière, J-F Bocquet
- 57 - 7 - 10 Reinforcements for Compression Perpendicular to Grain of CLT Elements with Fully Threaded Screws: Experimental Validation of the Design Model- R Maderebner, T Stieb, L Rathiens, R Tomasi



- 57 - 12 - 1 Punching-Shear Resistance of Point-Supported CLT Panels - H Ganjali, T Tannert, Md Shahnewaz, C Dickof, M Popovski
- 57 - 12 - 2 Comparison of Calculation Methods for Application on Veneer-Reinforced Timber with Standard Lamella - N Kainz, P Aondio, M Danzer, S Winter
- 57 - 12 - 3 Strength and Stiffness of Adhesively Bonded Timber-Steel Composite Beams - S Aurand, P Haase, J Boretzki, M Albiez, P Dietsch, T Ummenhofer
- 57 - 15 - 1 OSB Sheathed Timber-Framed Shear Walls with Optimized Performance for Horizontal Loading - N Manser, R Steiger, M Geiser, A Frangi
- 57 - 15 - 2 Proposal for an Analytical Model of Light Timber-Framed Shear Walls with additional Cladding - L Rauber, B Hoffmeister
- 57 - 15 - 3 Seismic Performance of Braced Timber Frames - M Popovski, Z Chen
- 57 - 15 - 4 Investigation on the Performance of Platform-Type Coupled-Panel CLT Shear Walls under Seismic Conditions - J Chen, F Lam, M Li, M Popovski
- 57 - 15 - 5 Investigating the In-Plane Rigid Diaphragm Conditions of Cross Laminated Timber Floors for Seismic Design - G D'Arenzo, V Nicolussi, P Rigo, L Pozza, A Polastri, D Casagrande
- 57 - 15 - 6 Design Implications for Cross-Laminated Timber Shear Walls Connected to Perpendicular Walls - G D'Arenzo, E M Ruggeri, J Hummel, M Fossetti, W Seim
- 57 - 16 - 1 Structural Means for Fire-Safe Green Façade Design on Multi Storey Buildings - T Engel, S Winter
- 57 - 20 - 1 Comfort Assessment of Timber Floor Vibrations - M Felicita, R Roijackers, R Cojocar, G Ravenshorst





# Lateral torsional buckling of glulam beam-columns: Axial compression and bending verification

Janusch Töpler, Institute for Timber Design, Biberach University of Applied Sciences, Germany

Ulrike Kuhlmann, Institute of Structural Design, University of Stuttgart, Germany

Jörg Schänzlin, Institute for Timber Design, Biberach University of Applied Sciences, Germany

## 1 Introduction

Lateral torsional buckling (LTB) and subsequent member failure is a realistic risk for glulam (GL) beam-columns and represents a complex 3-dimensional mechanical behaviour, see Figure 1. Beam-columns can be designed according to EN 1995-1-1 (2004) and prEN 1995-1-1 (2024) by the simplified  $k_c$ - $k_m$ -method or by calculation of internal forces according to 2<sup>nd</sup> order theory (T2O; subscript 2 in equations), see Figure 2. The current drawbacks of the  $k_c$ - $k_m$ -method are: (i) the main part of the design equation of the  $k_m$ -method is a pure regression model that is not fully considering all relevant parameters; (ii) the mechanical background of the exponent 2 of the bending component of the

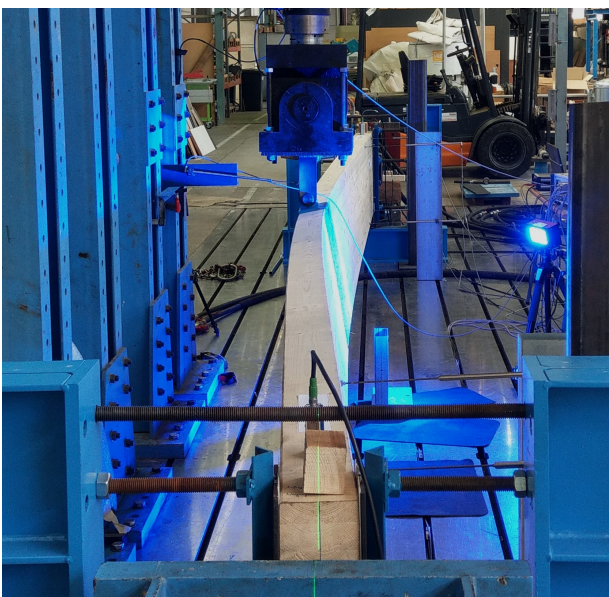


Figure 1. Lateral torsional buckling of a GL 24h beam-column with  $600 \cdot 120 \cdot 8000 \text{ mm}^3$ .

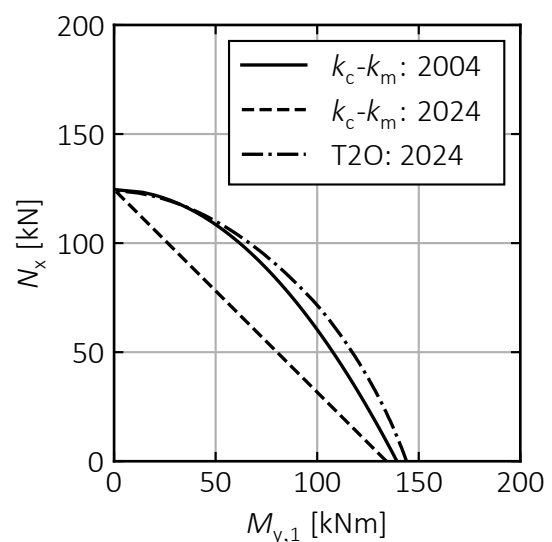


Figure 2. Load-bearing capacity of a GL 24h beam-column with  $600 \cdot 120 \cdot 8000 \text{ mm}^3$ ;  $k_c$ - $k_m$ -method and design with T2O calculations from EN 1995-1-1 (2004) and prEN 1995-1-1 (2024).

$N_x$ - $M_{y,1}$ -interaction in EN 1995-1-1 (2004) was unclear during its revision and therefore a conservative linear interaction was reintroduced; (iii) the inconsistent imperfection assumptions discussed by *Töpler & Kuhlmann* (2023); and (iv) there were no results of LTB tests on GL beam-columns for validating the design equations.

This paper discusses the analytical background of the nonlinear  $N_x$ - $M_{y,1}$ -interaction of the  $k_c$ - $k_m$ -method and a mechanical derivation of new equations for the  $k_m$ -method. The results of 16 full-scale LTB tests on GL beam-columns are presented, which served as validation for a numerical model. An extensive numerical parameter study was conducted to investigate the influence of different loading scenarios, cross-sectional dimensions, and material grades on the  $N_x$ - $M_{y,1}$ -interaction of timber beam-columns. The findings are compared with current design rules and literature. Finally, a proposal for a modification of the  $k_c$ - $k_m$ -method and the design with internal forces according to T2O is presented, which increases reliability and allows for a more economic design.

The design for bending and axial compression is addressed in this article. A detailed report on the investigations is given by *Töpler & Kuhlmann* (2024) and *Töpler* (2025).

## 2 Design methods in Eurocode 5

### 2.1 Methods according to EN 1995-1-1 (2004)

In case of a geometrically nonlinear calculation of internal forces, e.g., by T2O, the LTB design with bending and compression can be carried out using Equations (1) and (2).

$$\left(\frac{\sigma_{c,0,d}}{f_{c,0,d}}\right)^2 + \frac{\sigma_{m,y,d}}{f_{m,y,d}} + k_{red} \cdot \frac{\sigma_{m,z,d}}{f_{m,z,d}} \leq 1.0 \quad (1)$$

$$\left(\frac{\sigma_{c,0,d}}{f_{c,0,d}}\right)^2 + k_{red} \cdot \frac{\sigma_{m,y,d}}{f_{m,y,d}} + \frac{\sigma_{m,z,d}}{f_{m,z,d}} \leq 1.0 \quad (2)$$

For rectangular cross-sections, the size effect on the bending strength at biaxial bending can be taken into account with  $k_{red} = 0.7$ , according to *Buchanan et al.* (1985) and *van der Put* (1991). The positive influence of compressive plasticizing on the cross-sectional resistance is taken into account by the exponent 2 at the compressive force component, which was derived by *Blaß* (1987), *Buchanan et al.* (1985), and *Zahn* (1986).

In case of a geometrically linear calculation of internal forces, by 1<sup>st</sup> order theory (T1O; subscript 1 in equations), the LTB design can be conducted with Equation (3).

$$\frac{\sigma_{c,0,d}}{k_{c,z} f_{c,0,d}} + \left(\frac{\sigma_{m,y,d}}{k_m f_{m,y,d}}\right)^2 \leq 1.0 \quad (3)$$

$k_{c,z}$  is based on the investigations by *Blaß* (1987), where the effects of geometrical bow imperfections, structural imperfections, and materially nonlinear behaviour (compressive

plasticizing in grain direction) are covered by  $\beta_c$ . The exponent 2 corresponds to the nonlinear interaction of  $N_{z,crit}$  and  $M_{y,crit}$  when determining the critical load, as suggested by *Leicester* (1988a) and discussed in Section 3.3.  $k_m$  can be calculated for  $0.75 < \lambda_{m,rel} \leq 1.4$  as proposed by *Heimeshoff* (1986) with Equation (4).

$$k_m = 1.56 - 0.75 \lambda_{m,rel} \quad (4)$$

Equation (4) is a regression model without mechanical background, which only partially covers the influence of the height-to-width ratio, material properties, and imperfections.

## 2.2 Methods according to prEN 1995-1-1 (2024)

In case of a geometrically nonlinear calculation of internal forces, e.g., by T2O, the LTB design with bending and compression can be carried out using Equations (1) and (2).

In case of a geometrically linear calculation of internal forces, by T1O, some modifications were made compared to EN 1995-1-1 (2004). As the mechanical background of the exponent 2 in Equation (3) was unclear during the revision of Eurocode 5, the linear  $N_x$ - $M_{y,1}$ -interaction from, e.g., DIN 1052 (2004) was reintroduced, see Equation (5).

$$\frac{\sigma_{c,0,d}}{k_{c,z} f_{c,0,d}} + \frac{\sigma_{m,y,d}}{k_m f_{m,y,d}} \leq 1.0 \quad (5)$$

Equation (5) is significantly more conservative than Equation (3), see Figure 2. The  $k_c$ -method remained unchanged, but Equation (6) for calculating  $\beta_c$  was introduced.

$$\beta_{c,y/z} = \frac{e_{z/y}}{L} \cdot \pi \cdot \sqrt{\frac{3 E_{0,k}}{f_{c,0,k}}} \cdot \frac{f_{c,0,k}}{f_{m,y/z,k}} \quad (6)$$

where  $e_{y/z}$  is the equivalent bow imperfection,  $L$  is the member length, and  $E_{0,k}$ ,  $f_{c,0,k}$ , and  $f_{m,y/z,k}$  are the characteristic values of the elastic modulus and strengths. Equation (6) was derived from the differential equations for in-plane buckling with linear  $N_x$ - $M_{y,2}$ -interaction, see *Schänzlin et al.* (2022). In contrast to the  $\beta_c$  values given in EN 1995-1-1 (2004), no positive or negative effect of compressive plasticizing in grain direction is taken into account in Equation (6).  $k_m$  can be calculated with Equations (7) and (8).

$$k_m = \frac{1}{\Phi_m + \sqrt{\Phi_m^2 - \lambda_{m,rel}^2}} \quad (7)$$

$$\Phi_m = 0.5 \cdot (1 + \beta_\theta + \beta_m \cdot (\lambda_{m,rel} - 0.55) + \lambda_{m,rel}^2) \quad (8)$$

$\beta_\theta$  and  $\beta_m$  can be determined according to prEN 1995-1-1 (2024) similarly to  $\beta_c$ . Equations (7) and (8) were shaped to resemble the  $k_c$ -method and are still based on a regression model without mechanical background.

### 3 Analytical background

#### 3.1 General

This section contains the analytical background of the interaction equations in EN 1995-1-1 (2004), see Equations (1), (2), and (3), and a mechanically sound analytical derivation of new equations for the  $k_m$ -method. Most was already discussed by other authors, but sometimes in a different or more complex shape, and some so far back in time that they might not be remembered anymore. Further details are given by *Töpler (2025)*.

#### 3.2 Exponent 2 at the compressive force component

A model presented by *van der Put (1991)* is employed in this paper to analytically derive an  $N_x$ - $M_{y,2}$ -interaction relationship that incorporates plasticizing and to validate the exponent 2 in Equations (1) and (2).

For a bilinear elastoplastic material behaviour in grain direction and the stress distribution in Figure 3, the axial compressive force  $N_x$  and the bending moment  $M_{y,2}$  can be calculated with Equations (9) and (10) according to *van der Put (1991)*.

$$N_x = f_{c,0} H B + \frac{f_m - f_{c,0}}{2} \cdot (H - H_{pl}) \cdot B \tag{9}$$

$$M_{y,2} = \frac{f_m - f_{c,0}}{2} \cdot (H - H_{pl}) \cdot \left( \frac{H}{2} - \frac{H - H_{pl}}{3} \right) \cdot B \tag{10}$$

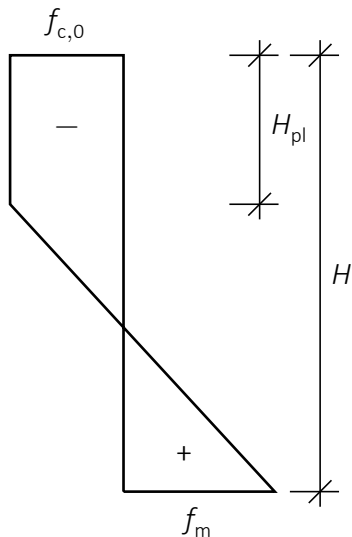


Figure 3. Distribution of stresses in grain direction over the cross-sectional height  $H$  for a combined loading by an axial compressive force  $N_x$  and a bending moment  $M_{y,2}$  with bilinear elastoplastic material behaviour.

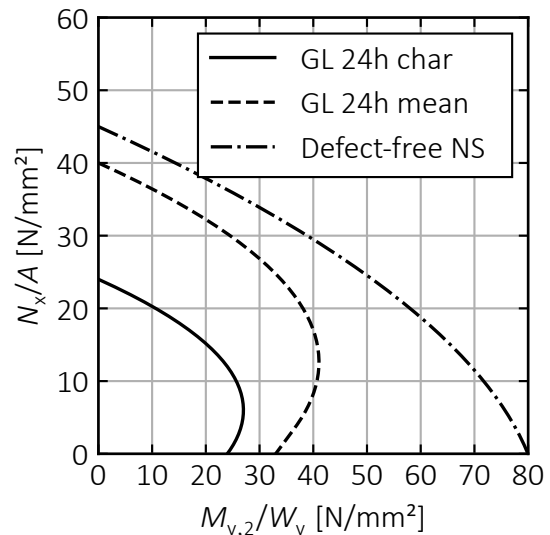


Figure 4. Cross-sectional resistances for a combined loading by an axial compressive force  $N_x$  and a bending moment  $M_{y,2}$  and bilinear elastoplastic material behaviour for three timber materials with different  $f_{c,0}$  and  $f_m$ .

where  $f_{c,0}$  is the compressive strength (only in Section 3.2 with the mechanically correct negative sign),  $f_m$  is the bending strength,  $H$  and  $B$  are the cross-sectional height and width, and  $H_{pl}$  is the height of the plastic area. Solving Equation (9) for  $H_{pl}$  and inserting the result in Equation (10) leads, after some transformations, to the familiar-looking interaction in Equation (11) with Equations (12) and (13).

$$\left(\frac{N_x}{A f_{c,0}}\right)^2 - a \cdot \frac{N_x}{A f_{c,0}} + \frac{M_{y,2}}{W_y f_m} = b \quad (11)$$

$$a = \left( \frac{5 f_{c,0}^2 + 3 f_{c,0} f_m}{f_m^2 - f_{c,0} f_m} - \frac{4 f_{c,0}^2 - f_m^2 + f_{c,0} f_m}{f_m^2 - f_{c,0} f_m} \cdot \frac{N_x}{A f_{c,0}} \right) \quad (12)$$

$$b = \frac{-3 f_{c,0} f_m - f_{c,0}^2}{f_m^2 - f_{c,0} f_m} \quad (13)$$

where  $A$  is the cross-sectional area and  $W_y$  is the elastic section modulus. The interaction equation thus depends on the ratio of  $f_{c,0}/f_m$ .

Table 1 provides the values of  $a$  and  $b$  and the resulting interaction equations, and Figure 4 illustrates three cases. Figure 4 demonstrates the high impact of the  $f_{c,0}/f_m$  ratio on the nonlinearity of the  $N_x$ - $M_{y,2}$ -interaction relationship. For common values of  $f_{c,0,k}$  and  $f_{m,k}$ , the parameters  $a$  and  $b$  become  $a > 0$  and  $b \approx 1$ , see Table 1. Therefore,  $a$  can be neglected on the safe side (greyed out in Table 1). This results in Equation (14) which is identical to Equation (1) from EN 1995-1-1 (2004) and prEN 1995-1-1 (2024), except for the additional  $M_{z,2}$  component in the standards.

$$\left(\frac{N_x}{A f_{c,0}}\right)^2 + \frac{M_{y,2}}{W_y f_m} = 1 \quad (14)$$

This interaction formula is therefore a mechanically sound limit criterion for tensile failure due to combined axial compression and bending, considering compressive plasticizing.

Table 1. Values of  $a$  and  $b$  and interaction equations for different timber materials with the compressive utilisation ratio  $\mu_c = N_x/A f_{c,0}$  and the bending utilisation ratio  $\mu_m = M_{y,2}/W_y f_m$ .

	$f_{c,0}/f_m$ <sup>1</sup> [N/mm <sup>2</sup> ]	$\mu_c = (a, 0.5, 1)$	$b$	Interaction equation
GL 24c char <sup>2</sup>	-21.0 / 24.0	(0.62, 0.31, 0.01)	0.99	$\mu_c^2 - \mu_c(0.62 - 0.61\mu_c) + \mu_m = 0.99$
GL 24h char <sup>2</sup>	-24.0 / 24.0	(1.00, 0.50, 0.00)	1.00	$\mu_c^2 - \mu_c(1.00 - 1.00\mu_c) + \mu_m = 1.00$
GL 30c char <sup>2</sup>	-24.5 / 30.0	(0.44, 0.23, 0.02)	0.98	$\mu_c^2 - \mu_c(0.44 - 0.42\mu_c) + \mu_m = 0.98$
GL75 char <sup>3</sup>	-59.4 / 75.0	(0.36, 0.20, 0.03)	0.97	$\mu_c^2 - \mu_c(0.36 - 0.33\mu_c) + \mu_m = 0.97$
GL 24h mean <sup>4</sup>	-40.0 / 33.0	(1.68, 0.85, 0.02)	0.98	$\mu_c^2 - \mu_c(1.68 - 1.66\mu_c) + \mu_m = 0.98$
Defect-free NS <sup>5</sup>	-45.0 / 80.0	(-0.24, -0.01, 0.22)	0.78	$\mu_c^2 + \mu_c(0.24 - 0.46\mu_c) + \mu_m = 0.78$

<sup>1</sup> If  $-f_{c,0} < f_m$ , the input bending strength for Equations (11) to (13) need to be chosen higher than  $f_m$  for actually reaching the bending resistance  $f_m W_y$  due to the plasticizing.

<sup>2</sup> EN 14080 (2013); <sup>3</sup> ETA-14/0354 (2018); <sup>4</sup> Schilling et al. (2021); <sup>5</sup> Norway spruce (NS) DIN 68364 (2003).



### 3.3 Nonlinear $N_x$ - $M_{y,1}$ -interaction for lateral torsional buckling

*Leicester* (1988a) demonstrated that the  $N_x$ - $M_{y,1}$ -interaction for LTB is nonlinear. The derivation is given below.

For LTB of beam-columns, the critical load is given by Equation (15), see *Hörsting* (2008).

$$\alpha_{c,z} + \alpha_m^2 = 1 \quad (15)$$

where  $\alpha_{c,z} = N_x/N_{z,crit}$ ,  $\alpha_m = M_{y,1}/M_{y,crit}$ ,  $N_{z,crit}$  is the critical compressive load for in-plane buckling around the z axis, and  $M_{y,crit}$  is the critical bending moment for LTB.

Additionally, for very slender beam-columns, the member resistances approach the critical loads and  $k_{c,z} A f_{c,0} \rightarrow N_{z,crit}$  and  $k_m W_y f_m \rightarrow M_{y,crit}$ , where  $k_{c,z}$  and  $k_m$  are the reduction factors from the  $k_c$ - and the  $k_m$ -method,  $A$  is the cross-sectional area,  $W_y$  is the elastic section modulus,  $f_{c,0}$  is the compressive strength, and  $f_m$  is the bending strength. Thus, Equation (15) can be rearranged to Equation (16), which is identical to the  $N_x$ - $M_{y,1}$ -interaction for LTB in EN 1995-1-1 (2004), see Equation (3).

$$\frac{N_x}{k_{c,z} A f_{c,0}} + \left( \frac{M_{y,1}}{k_m W_y f_m} \right)^2 \rightarrow 1 \quad (16)$$

No size effect must be applied to  $f_m$  in this interaction, as it describes the critical load of very slender beam-columns, which is purely stiffness-dependent.

### 3.4 Reduction factor $k_m$ accounting for lateral torsional buckling

*Leicester* (1988b), *Taras* (2010), and *Wilden et al.* (2023) discussed a mechanically sound derivation of the reduction factor  $k_m$  that accounts for LTB. The derivation is given below. For timber construction, the formulation with bow imperfections  $e_y$  instead of twist imperfections  $e_\theta$  in Equation (25) is new.

The differential equations for LTB with a constant bending moment  $M_{y,1}$ , see e.g., *Hörsting* (2008), are the basis of the derivations. By means of the initial functions  $v_2(x) = v_2 \cdot \sin(\pi \cdot x/L)$  and  $\theta_2(x) = \theta_2 \cdot \sin(\pi \cdot x/L)$ , the differential equations can be transformed into Equations (17) and (18), which are valid at midspan.

$$G_0 I_x \theta_2 - M_{y,1} \cdot (v_2 + e_y) = 0 \quad (17)$$

$$\frac{\pi^2}{L^2} E_0 I_z v_2 - M_{y,1} \cdot (\theta_2 + e_\theta) = 0 \quad (18)$$

where  $G_0$  and  $E_0$  are the shear and elastic moduli in grain direction,  $I_x$  and  $I_z$  are the respective moments of inertia,  $v_2$  and  $\theta_2$  are the deformation in y direction and the rotation around the x axis at midspan,  $e_y$  and  $e_\theta$  are the bow imperfection in y direction and the twist imperfection at midspan, and  $L$  is the member length.

The key in the derivation is the assumption that the imperfections are affine to the 1<sup>st</sup> eigenmode,  $e_y = kv_2$  and  $e_\theta = k\theta_2$ , where  $k$  is a scaling factor. Inserting this into Equations (17) and (18) and then inserting Equations (17) in (18) results after a few transformations in Equation (19).

$$\frac{e_y}{e_\theta} = \frac{M_{y,crit}}{N_{z,crit}} \quad (19)$$

A linear  $M_{y,2}$ - $M_{z,2}$ -interaction according to Equation (20) is assumed.

$$\frac{M_{y,2}}{W_y f_m} + \frac{M_{z,2}}{W_z f_m} = 1 \quad (20)$$

$M_{z,2}$  can be calculated with Equation (21) according to prEN 1995-1-1 (2024).

$$M_{z,2} = \frac{\frac{M_{y,1}^2}{G_0 I_x} e_y + M_{y,1} e_\theta}{1 - \alpha_m^2} \quad (21)$$

With the coupled imperfections from Equation (19), Equation (21) can be simplified to Equation (22).

$$M_{z,2} = \frac{\alpha_m N_{z,crit} e_y}{1 - \alpha_m} \quad (22)$$

The common assumption is made that the geometrically nonlinear LTB behaviour does not significantly influence the bending moment around the strong axis, and  $M_{y,2} = M_{y,1}$  applies. Inserting  $M_{y,2}$  and  $M_{z,2}$  in Equation (20) leads to a quadratic equation that can be solved in a similar way to the  $k_c$ -method, which results in Equations (23) to (25).

$$k_m = \frac{1}{\Phi_m + \sqrt{\Phi_m^2 - \lambda_{m,rel}^2}} \quad (23)$$

$$\Phi_m = 0.5 \cdot (1 + \beta_m + \lambda_{m,rel}^2) \quad (24)$$

$$\beta_m = \frac{e_y}{L} \cdot \frac{H}{B} \cdot \frac{\pi}{2} \cdot \sqrt{\frac{E_0}{G_0}} \quad (25)$$

Equations (23) to (25) are similar to the  $k_m$ -method in prEN 1995-1-1 (2024), see Equations (7) and (8), except for the lack of the  $\beta_\theta$  and the  $(\lambda_{m,rel} - 0.55)$  components. The advantage of Equations (23) to (25) is the discussed mechanical background that Equations (4), (7), and (8) are lacking.

## 4 Experiments

### 4.1 General

16 LTB tests with combined axial compression and bending on GL 24h according to EN 14080 (2013) were conducted within the research project IGF 21285 N, see *Töpler & Kuhlmann* (2024). Two parameters were varied: the slenderness ratio  $\lambda_{m,rel}$  by means of the member length and height, and the utilisation ratio  $\mu_c = N_x/N_{x,R}$  of the axial compressive resistance, calculated with the  $k_c$ -method in EN 1995-1-1 (2004), see Table 2. A more detailed description of the LTB tests is given in *Töpler & Kuhlmann* (2023).

Table 2. Test program for lateral torsional buckling of glulam GL 24h beams.

Series number	Number of specimens	Length [mm]	Height x Width [mm <sup>2</sup> ]	$\lambda_{m,rel}$ <sup>1</sup>	$\mu_c$	$N_x$ [kN]
T04 – T05	2	8000	600 x 120	0.94	0.00	0
T06 – T07	2	8000	600 x 120	0.94	0.20	25
T08 – T09	2	8000	600 x 120	0.94	0.40	50
T10 – T11	2	8000	600 x 120	0.94	0.60	75
T12 – T13	2	6000	480 x 120	0.74	0.00	0
T14 – T15	2	6000	480 x 120	0.74	0.20	35
T16 – T17	2	6000	480 x 120	0.74	0.40	70
T18 – T19	2	6000	480 x 120	0.74	0.60	105

<sup>1</sup> Calculated with characteristic material values, taking into account an increase of  $E_{0,05}G_{0,05}$  by a factor of 1.4 according to DIN EN 1995-1-1/NA (2013).

### 4.2 Test setup and execution

At one end of the beams, at the front in Figure 1, the horizontal support was formed by an abutment and a centrally located calotte. At the other end, at the rear in Figure 1, the horizontal load was applied centrally by a cylinder with a yoke joint. Vertical loading, vertical supports, and measuring devices are described in *Töpler & Kuhlmann* (2023).

First, the axial compressive force was applied force-controlled up to the values given in Table 2. Secondly, the vertical force was applied displacement-controlled at midspan.

### 4.3 Results and evaluation

Typical load-deformation curves with the horizontal deformation of the beam axis at midspan  $v$  and the vertical cylinder force  $F_z$  are given in Figure 5. The general load-bearing behaviour is described in *Töpler & Kuhlmann* (2023). As the axial compressive force increased, (i) the peak of the load-deformation curve shifted to the left; (ii) the maximum vertical force  $F_z$  decreased; and (iii) the maximum deformations  $v$  increased.

The experimentally determined load-bearing capacities are plotted in Figure 6, where  $M_{y,1}$  is the bending moment applied by  $F_z$ . Additionally, the characteristic resistances from the  $k_c$ - $k_m$ -method and design with calculations using T20 from EN 1995-1-1 (2004) and DIN EN 1995-1-1/NA (2013), and the results of FE analyses with the same input values are given. The FE model is described in Section 5. The bow imperfection was

chosen to be equal to the horizontal eccentricity of the vertical force. Experimentally, an increase in the compressive force and its utilisation ratio  $\mu_c$  from 0% to 60% reduced the bending load-bearing capacity by about 20%. This confirmed the nonlinearity of the  $N_x$ - $M_{y,1}$ -interaction curve of the  $k_c$ - $k_m$ -method in EN 1995-1-1 (2004), see Equation (3) and was supported by the results of comparative calculations with T2O and FE analyses. The failure behaviour is described in *Töpler & Kuhlmann (2023)*. No influence of the axial compressive force on the failure mode was detected.

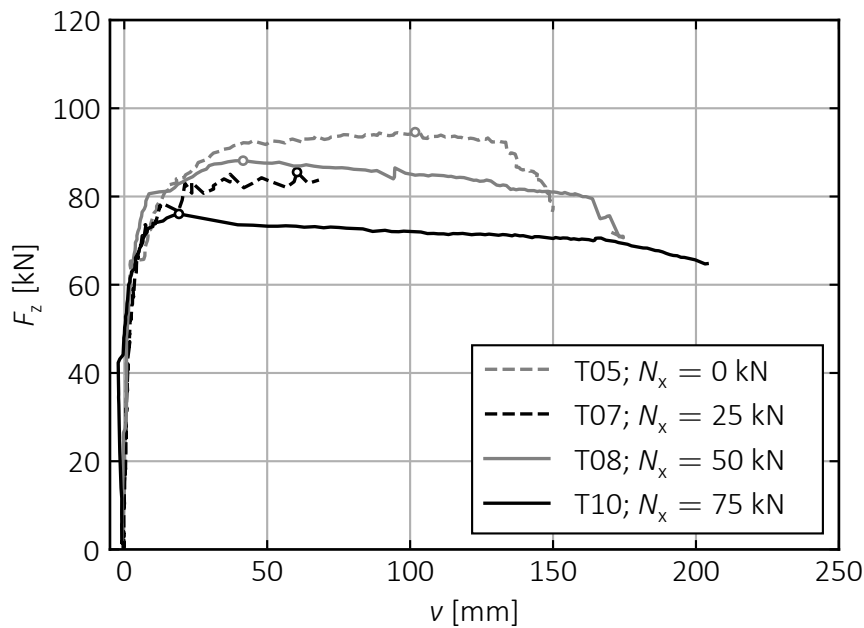
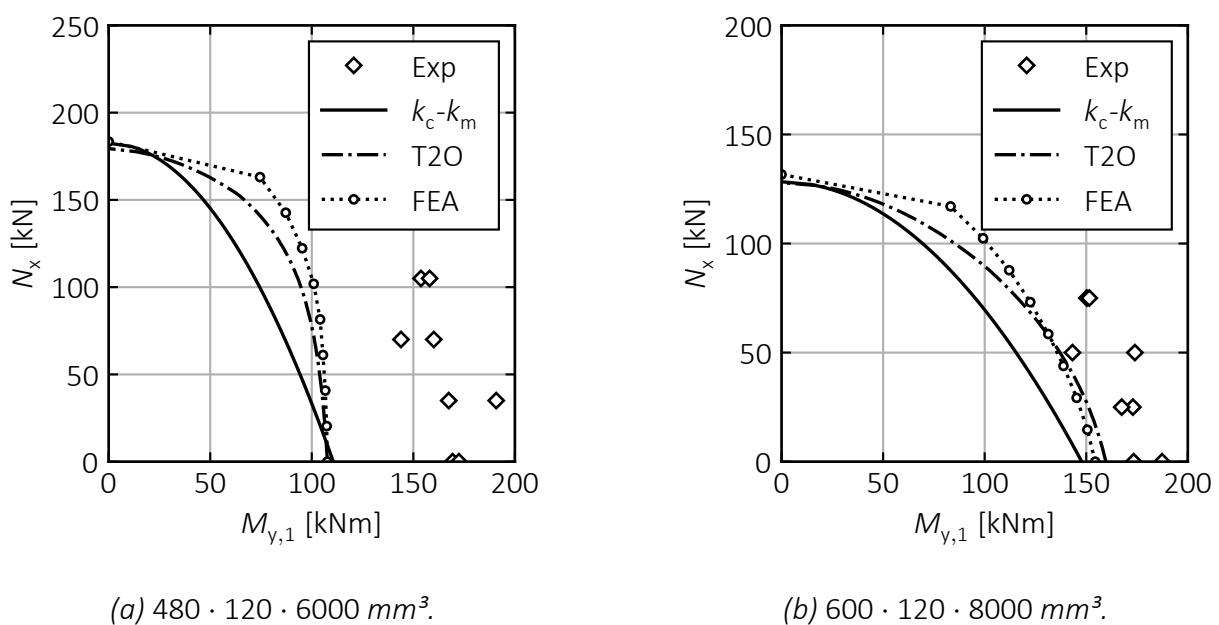


Figure 5. LTB tests T05, T07, T08, and T10 with  $\lambda_{m,rel} = 0.94$ ; vertical force  $F_z$  plotted over the horizontal deformation of the beam axis at midspan  $v$ ; circles mark maximum vertical forces.



(a)  $480 \cdot 120 \cdot 6000 \text{ mm}^3$ .

(b)  $600 \cdot 120 \cdot 8000 \text{ mm}^3$ .

Figure 6. Experimentally (Exp) determined load-bearing capacities; characteristic resistances of the  $k_c$ - $k_m$ -method and design with calculations using T2O according to EN 1995-1-1 (2004) and DIN EN 1995-1-1/NA (2013); and characteristic resistances from FE analyses.

## 5 Numerical simulations

### 5.1 General

The numerical simulations were conducted for an in-depth analyses of the influence of the slenderness, the material, and the loading on the  $N_x$ - $M_{y,1}$ -interaction curves for LTB with combined axial compression and bending. The numerical analyses were conducted with solid elements in Abaqus/CAE 2023. A description of the model and its verification and validation is given in *Töpler & Kuhlmann (2023)* and *Töpler & Kuhlmann (2024)*.

Single-span beams with fork bearings were investigated, loaded by a constant bending moment, by a uniform line load at the upper edge of the beam, or by a concentrated load at midspan at the upper edge of the beam. In addition, the axial compressive force was varied. The axial compressive force was applied first and kept constant. Afterwards, the bending moment was applied. For the constant bending moment, an idealised support in the member axis was modelled. For the uniform line load or the concentrated load, a realistic support at the lower edge of the beam was created.

GL 24h, GL 30c, and GL75 with the nominal material properties and an anisotropic material model with elastoplastic behaviour for compression in grain direction and shear were analysed, see also *Töpler & Kuhlmann (2023)* and *Töpler & Kuhlmann (2024)*. Shear was always neglected as a failure criterion in the evaluation of the FE analyses.

Equivalent bow and twist imperfections at midspan of  $e_y = L/1000$  and  $e_\theta = 0.5 \cdot (e_{\theta, \text{mid}} + e_{\theta, \text{supp}})$  with  $e_{\theta, \text{supp}} = 1/100$  and  $e_{\theta, \text{supp}} = L/1500H$  were assumed according to the investigations in *Töpler & Kuhlmann (2023)*. Cross-sectional height-to-width ratios of 1, 2, 4, 8, 12, and 16 were modelled with a width of 120 mm. The member length was varied between  $2.5H$  and  $25H$  or  $50H$ . This resulted in over 17,000 FE analyses.

### 5.2 Results

#### 5.2.1 Plate bending around the x axis

With an increasing height-to-width ( $H/B$ ) ratio at the same relative slenderness  $\lambda_{m, \text{rel}}$ , the LTB deformation behaviour of the timber beams significantly changed, see Figure 7. At  $H/B = 4$ , no plate bending was observed. At  $H/B = 12$ , a strong plate bending around the x axis occurred, which increased the eigenvalues and the load-bearing capacities by up to 20% compared to calculations with beam theory. The effect was greatest for the constant bending moment. With an increasing  $H/B$  ratio, the ratio of the plate bending stiffness to the buckling stiffness of the compression chord decreases, and the deformation behaviour changes. With regard to this effect, calculations of eigenvalues and load-bearing capacities based on beam theory, e.g., the design equations in EN 1995-1-1 (2004), provide conservative results for beams with large  $H/B$  ratios.

The pronounced plate bending at large  $H/B$  ratios is characteristic of the anisotropic material timber, with its large difference between the elastic moduli in grain direction and perpendicular to the grain, the large  $E_0/E_{90}$  ratio. For isotropic materials such as steel and concrete, the effect can only be observed at significantly higher  $H/B$  ratios.

### 5.2.2 Cross-sectional warping due to shear forces

Figure 8 displays the reduction factors  $k_m$  calculated from the FE results over the relative LTB slenderness  $\lambda_{m,rel}$  for different utilisation ratios of the axial compressive resistance  $\mu_c$  for loading by a constant bending moment and by a concentrated force.  $\lambda_{m,rel}$  was calculated using prEN 1995-1-1 (2024). Beams subjected to shear forces had significantly lower load-bearing capacities for  $L/H < 6$ . See the drop of  $k_m$  at  $L/H < 6$  in Figure 8b in comparison with Figure 8a. This can be explained by the fact that shear stresses due to shear forces led to cross-sectional warping and its obstruction to residual stresses, secondary stresses, in grain direction. The superposition of these secondary stresses with the primary stresses from bending increased in the edge bending stresses and thus reduced the load-bearing capacities, see also *Töpler & Kuhlmann (2022a)*.

The fact that this effect occurred for  $3 < L/H < 6$  is characteristic of timber with its large difference between the elastic and shear moduli in grain direction, the large  $E_0/G_0$  ratio.

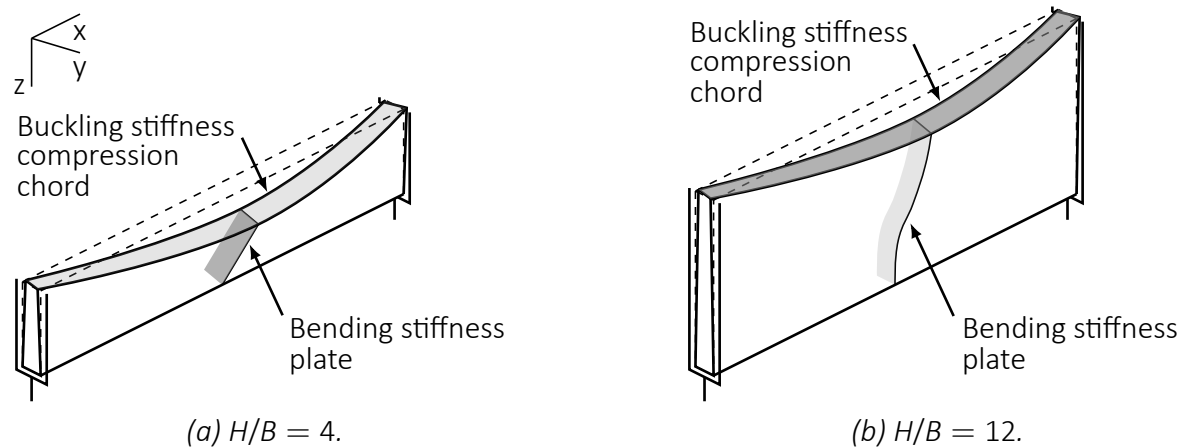


Figure 7. Schematic illustration of lateral torsional buckling deformation behaviours of timber beams.

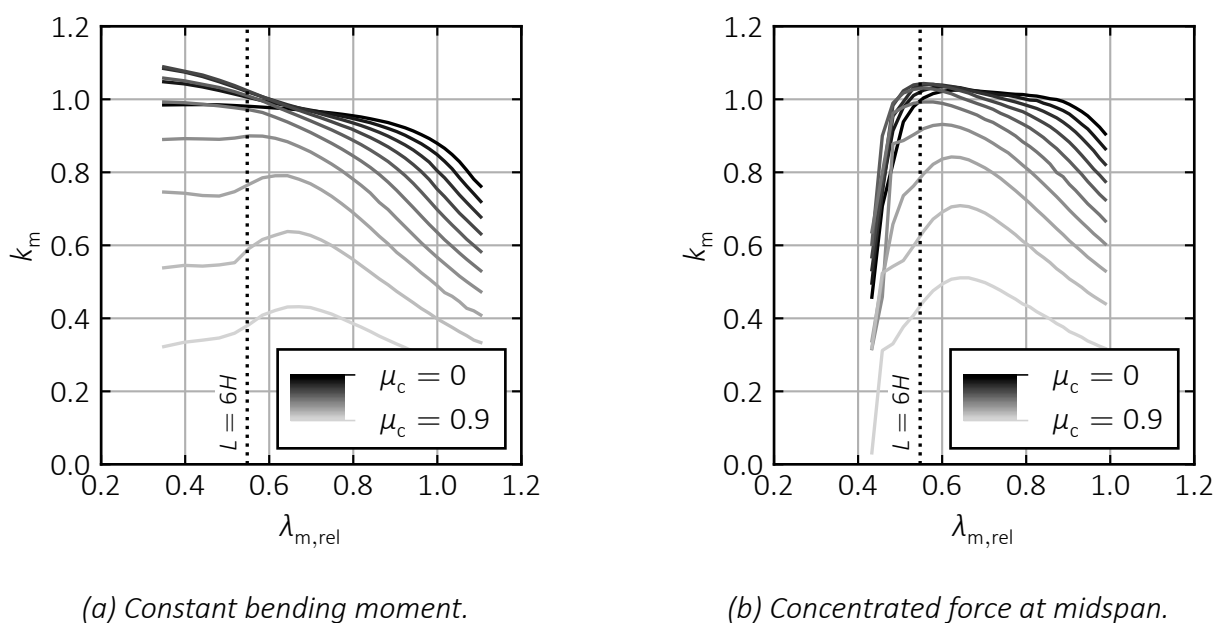


Figure 8. Reduction of the load-bearing capacity  $k_m$  from FE analyses over the relative LTB slenderness  $\lambda_{m,rel}$  according to prEN 1995-1-1 (2024) for different utilisation ratios  $\mu_c$ ; GL 24h and  $H/B = 4$ .

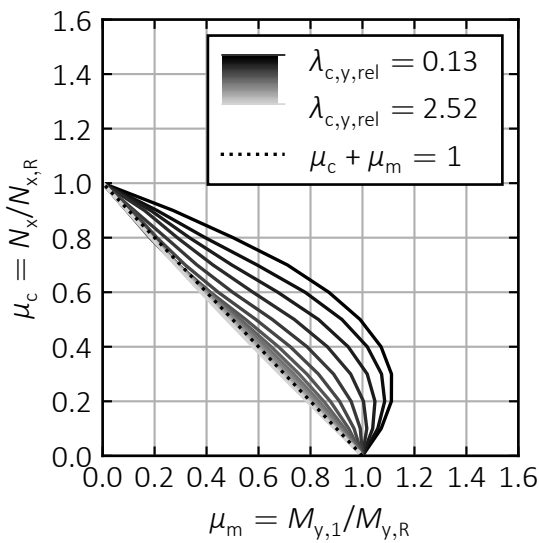
5.2.3  $N_x$ - $M_{y,1}$ -interaction

At  $\lambda_{m,rel} > 0.7$ , the load-bearing capacities, or  $k_m$ , in Figure 8 followed the typical lateral-torsional buckling curves and decreased with increasing slenderness. With increasing compressive load, or  $\mu_c$ ,  $k_m$  decreased nonlinearly, first less, then more.

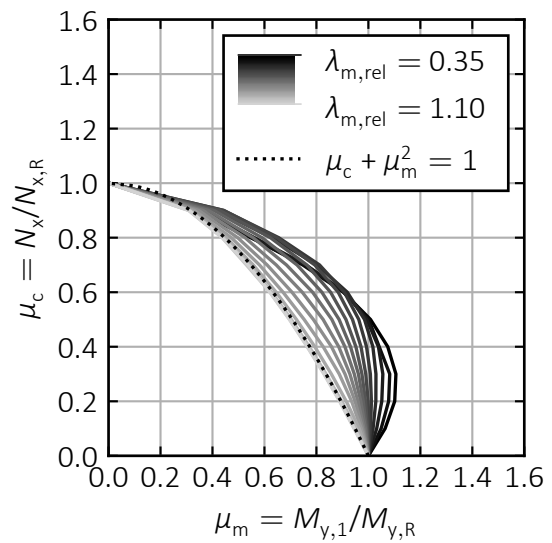
At  $\lambda_{m,rel} < 0.7$ , the influences of (i) shear warping, see Section 5.2.2, (ii) compressive plasticizing in grain direction, and (iii) the nonlinear interaction relationship of the critical load, see Equation (15), were overlapping. For beams subjected to shear forces, the influence of shear warping was decisive, and it significantly reduced the load-bearing capacity, see Figure 8b. For beams subjected to a constant bending moment, no shear warping occurred, see Figure 8a. Plasticizing even increased the bending load-bearing capacity for low compressive forces,  $k_m > 1$ , and decreased  $k_m$  nonlinearly for higher compressive forces, first less, then more. With increasing  $\lambda_{m,rel}$ , the influence of compressive plasticizing decreased, which tended to reduce the load-bearing capacity. This effect was overlapped by the increasing influence of the nonlinear interaction relationship of the critical load with increasing slenderness. Thus, for high utilisation ratios  $\mu_c$ , despite decreasing compressive plasticizing, there was sometimes an increase in bending load-bearing capacity with a peak at  $\lambda_{m,rel} \approx 0.5$  to 0.8.

In-plane buckling occurred for  $H/B = 1$  and LTB for  $H/B \geq 2$ .

Figure 9 presents two typical  $N_x$ - $M_{y,1}$ -interaction diagrams from FE analyses for two  $H/B$  ratios with varying relative in-plane buckling and LTB slendernesses  $\lambda_{c,y,rel}$  and  $\lambda_{m,rel}$ . The relative load-bearing capacities are given as ratios of the bending or compressive load-bearing capacity to the load-bearing capacity for pure bending or pure compression (including stability behaviour). Additionally, for  $H/B = 1$ , the linear interaction is plotted,



(a)  $H/B = 1$  and varying  $\lambda_{c,y,rel}$ .



(b)  $H/B = 4$  and varying  $\lambda_{m,rel}$ .

Figure 9. Relative compressive load-bearing capacity  $N_x/N_{x,R}$  over the relative bending load-bearing capacity  $M_{y,1}/M_{y,R}$  from FE analyses; GL 24h and constant bending moment.

and for  $H/B = 4$ , the limit condition according to Equation (3) is plotted.

For  $H/B = 1$ , a distinctly nonlinear  $N_x$ - $M_{y,1}$ -interaction occurred for  $\lambda_{c,y,rel} \approx 0.3$ , which was caused by compressive plasticizing in grain direction, see Figure 9a. With increasing slenderness, the non-linearity of the  $N_x$ - $M_{y,1}$ -interaction decreased until it was almost linear for  $\lambda_{c,y,rel} = 0.8$  (GL75) to 1.2 (GL 24h). For large slendernesses, the compressive forces were so small that no (significant) plasticizing occurred.

For  $H/B \geq 2$ , the  $N_x$ - $M_{y,1}$ -interaction was always distinctly nonlinear, see Figure 9b. At low slendernesses, the same nonlinear curve as for  $H/B = 1$  occurred as a result of compressive plasticizing. With increasing slenderness, there was a slight increase in non-linearity due to the superposition of the influence of compressive plasticizing and the nonlinear interaction relationship of the critical load, see Equation (15). Subsequently, the nonlinearity decreased and approached the limit value of the critical load from Equation (15), which was reached between  $\lambda_{m,rel} = 0.8$  (GL75) and 0.9 (GL 24h). The load-bearing capacity of slender beams was equal to the critical load.

For significant shear forces, here induced by a concentrated force or a uniform line load, and  $1.0 \leq \lambda_{m,rel} \leq 1.5$ , a reduction in shear stiffness due to shear plasticizing occurred, which reduced the load-bearing capacity by up to 20%. This “shear plasticizing” due to local shear cracks was discussed by *Töpler & Kuhlmann* (2023).

For GL75, due to the high compressive plasticizing, see *Töpler & Kuhlmann* (2022b), larger stiffness reductions occurred than for GL 24h and GL 30c. This effect reduced the non-linearity of the  $N_x$ - $M_{y,1}$ -interaction curve at low slendernesses compared to GL 24h in Figure 9.

## 6 Discussion

For in-plane buckling,  $H/B \approx 1$ , *Blaß* (1987), *Buchanan et al.* (1985), and *Zahn* (1986) reported similar results as the numerical results in Figure 9a, which yielded a linear  $N_x$ - $M_{y,1}$ -interaction for slender members and a nonlinear  $N_x$ - $M_{y,1}$ -interaction for stocky members. This is also reflected in the design procedures according to EN 1995-1-1 (2004) and prEN 1995-1-1 (2024), see Sections 2.1 and 2.2.

For LTB,  $H/B \gtrsim 2$ , the analytical derivations, see Section 3.3, the experimental results, see Section 4.3, and the FE results, see Section 5.2.3, confirmed the non-linearity of the  $N_x$ - $M_{y,1}$ -interaction for stocky and slender members. In addition to the analytical derivation of *Leicester* (1988b), see Section 3.3, *Bell & Eggen* (2001) presented numerical calculation results that produced a similar nonlinear interaction relationship. This is also reflected by the nonlinear Equation (3) from EN 1995-1-1 (2004), but not anymore by the conservative linear Equation (5) from prEN 1995-1-1 (2024).

The authors are not aware of any investigations concerning the influence of the plate bending at LTB of timber beams with large  $H/B$  ratios. Also, cross-sectional warping due to shear has not yet been reported, with the exception of the own investigations in *Töpler & Kuhlmann* (2022a).



## 7 Design proposals

For the  $k_c$ - $k_m$ -method, it is highly recommended to reintroduce the nonlinear  $N_x$ - $M_{y,1}$ -interaction from EN 1995-1-1 (2004), Equation (3), in prEN 1995-1-1 (2024) for an economic design of timber beam-columns.

For considering the material-dependent stiffness reduction due to compressive plasticizing at in-plane buckling and the shear force-dependent stiffness reduction due to shear plasticizing at LTB, it is proposed to introduce the coefficients  $k_{pl,c}$  and  $k_{pl,m}$  and to **modify** the formulas of T2O in prEN 1995-1-1 (2024), see Equations (26) to (28).

$$M_{x,2} = \frac{\pi}{L} \cdot \frac{M_{y,1} k_{pl,m} e_y + \alpha_m^2 G_0 I_x e_\theta}{1 - \alpha_{c,z} - \alpha_m^2} \quad (26)$$

$$M_{y,2} = \frac{N_x k_{pl,c} e_z + M_{y,1} \cdot (1 + \alpha_{c,y} \delta_y)}{1 - \alpha_{c,y}} \quad (27)$$

$$M_{z,2} = \frac{\left( N_x k_{pl,c} + \frac{M_{y,1}^2}{G_0 I_x} \cdot k_{pl,m} \right) \cdot e_y + M_{y,1} e_\theta + M_{z,1} \cdot (1 + \alpha_{c,z} \delta_z)}{1 - \alpha_{c,z} - \alpha_m^2} \quad (28)$$

For the  $k_c$ - and the  $k_m$ -method, it is proposed to include  $k_{pl,c}$  and  $k_{pl,m}$  in the calculation of  $\beta_c$  and  $\beta_m$  by Equations (29) and (30).

$$\beta_{c,y/z} = k_{pl,c} \cdot \frac{e_{z/y}}{L} \cdot \pi \cdot \sqrt{\frac{3E_{0,k}}{f_{c,0,k}}} \cdot \frac{f_{c,0,k}}{f_{m,y/z,k}} \quad (29)$$

$$\beta_m = k_{pl,m} \cdot \frac{e_y}{L} \cdot \frac{H}{B} \cdot \frac{\pi}{2} \cdot \sqrt{\frac{E_{0,k}}{G_{0,k}}} \quad (30)$$

For softwood GL and LVL,  $\beta_c = 0.1$ , and  $\beta_m = 0.01 \cdot k_{pl,m} \cdot H/B$  and for solid timber made of softwood,  $\beta_c = 0.2$  and  $\beta_m = 0.02 \cdot k_{pl,m} \cdot H/B$  may be used.

$k_{pl,c}$  and  $k_{pl,m}$  were determined by curve fitting of Equations (26) to (28) to the FE results, see *Töpler & Kuhlmann* (2024). For softwood,  $k_{pl,c} = 1$  should be assumed. For beech, a value of  $k_{pl,c} \approx 4$  at  $e_{y/z} = L/1000$  is plausible, see *Töpler & Kuhlmann* (2022b). For softwood without significant shear forces,  $k_{pl,m} = 1$  and with significant shear forces,  $k_{pl,m} = 6$  should be assumed. Further research on determining  $k_{pl,c}$  for wood species other than softwood and specifying  $k_{pl,m}$  for shear forces is required.

For the  $k_m$ -method, it is proposed to apply the mechanically derived Equations (23) and (24). Additionally, a limit value can be introduced for design practice, above which  $k_m < 1.0$ , i.e. LTB, should be taken into account, see Equation (31).

$$\Phi_m = 0.5 \cdot (1 + \beta_m \cdot (\lambda_{m,rel} - 0.7) + \lambda_{m,rel}^2) \quad (31)$$

The limit criterion 0.7 was determined based on the point where  $k_m = 0.9$  in calculations using T2O, see *Töpler & Kuhlmann (2024)*.

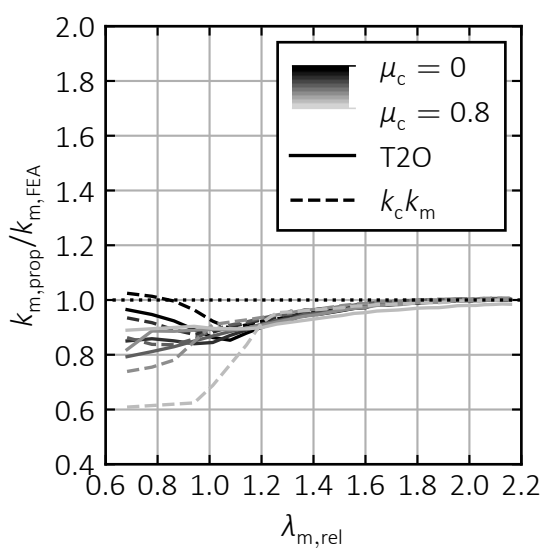
For considering the increase in edge bending stresses due to cross-sectional warping, it is recommended to introduce a respective clause in prEN 1995-1-1 (2024):

*(x) The increase in edge bending stresses due to shear-induced cross-sectional warping should be taken into account for members with significant bending and shear stresses in the same plane and  $L/H < 6$ . This may be done by analyses with membrane theory.*

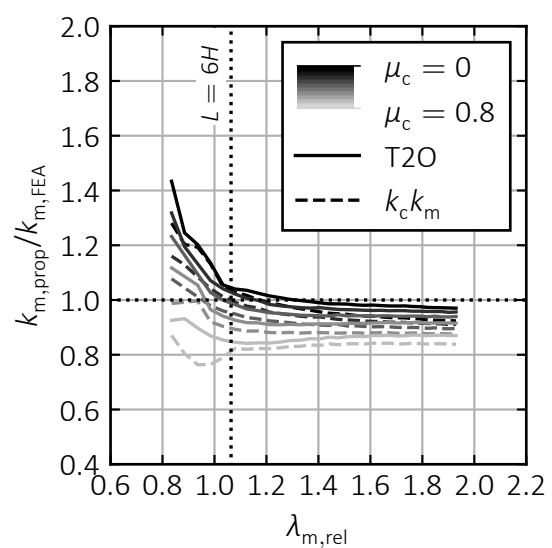
Simplified formulas for considering the increase in bending stress could be determined by further experimental and numerical investigations.

Figures 10a and 10b exemplary present the ratio of the reduction factors by the  $k_c$ - $k_m$ -method and by calculations using T2O with the proposed changes to results from FE analyses,  $k_{m,prop}/k_{m,FEA}$ , over  $\lambda_{m,rel}$  for GL 24h,  $H/B = 8$ , and a constant bending moment or a concentrated force at midspan. For  $\lambda_{m,rel} > 1.2$ , the load-bearing capacities according to the design methods and FE analyses are very similar. Minor deviations for concentrated forces and high  $\mu_c$  result from the general application of  $k_{pl,m}$ , although shear plasticizing decreases with increasing  $\mu_c$ . For  $\lambda_{m,rel} < 1.2$  and constant bending moment, the  $k_c$ - $k_m$ -method is clearly on the safe side at high  $\mu_c$ , as the positive effects of compression plasticizing are not fully considered. For  $\lambda_{m,rel} < 1.2$  and concentrated forces, the importance of the limiting criterion  $L/H \geq 6$  for the application of the beam theory is demonstrated. Both the limit criterion  $L/H \geq 6$  and  $k_{pl,m}$  could be formulated in more detail to take into account the influence of the utilisation ratio  $\mu_c$ .

The proposed modifications of the design procedures in prEN 1995-1-1 (2024) enable a more economical and reliable design of timber beam-columns prone to LTB.



(a) Constant bending moment.



(b) Concentrated force at midspan.

Figure 10. Ratio of the reduction factors by the design proposals in Section 7 to the reduction factors from FE analyses,  $k_{m,prop}/k_{m,FEA}$ , over the relative LTB slenderness  $\lambda_{m,rel}$  for different utilisation ratios  $\mu_c$ ; GL 24h and  $H/B = 8$ .

## 8 Summary and outlook

This paper is based on the investigations described in *Töpler & Kuhlmann (2023)*.

It is demonstrated analytically that the exponent 2 for considering compressive plasticizing in the  $N_x$ - $M_{y,2}$ -interaction equation is on the safe side for common timber materials and that this interaction equation represents tensile failure for combined bending and compression, see Section 3.2. Subsequently, an analytical derivation of the nonlinear  $N_x$ - $M_{y,1}$ -interaction for LTB of slender beam-columns is presented, see Section 3.3. Finally, a mechanical derivation of the  $k_m$ -method is described, see Section 3.4.

The results of 16 LTB tests on glulam beams made of GL 24h are discussed in Section 4, which confirmed the nonlinearity of the  $N_x$ - $M_{y,1}$ -interaction for LTB.

An extensive numerical parameter study covering the reasonable member dimensions, different timber materials, and loading conditions for an in-depth analysis of the  $N_x$ - $M_{y,1}$ -interaction at LTB is described in Section 5. It turned out that plate bending around the x axis at  $H/B = 12$  increased the eigenvalues and the load-bearing capacities by up to 20%, see Section 5.2.1. For beams with  $L/H < 6$  and subjected to shear forces, a pronounced cross-sectional warping due to shear stresses appeared and significantly reduced the load-bearing capacities, see Section 5.2.2. Generally, in-plane buckling occurred for  $H/B = 1$  and LTB for  $H/B \geq 2$ . The FE results confirmed the non-linearity of the  $N_x$ - $M_{y,1}$ -interaction for LTB. For significant shear forces, a reduction in shear stiffness due to shear plasticizing occurred, which reduced the load-bearing capacity by up to 20%. This was in line with the experimental results reported in *Töpler & Kuhlmann (2023)*.

Based on the analytical, experimental, and numerical investigations, design proposals are presented in Section 7 that (i) consider the stiffness reduction due to compressive and shear plasticizing at LTB; (ii) contain mechanically derived equations for the  $k_m$ -method; and (iii) implement a limit criterion to account for the negative effect of shear warping on the edge bending stresses. But foremost, the nonlinear  $N_x$ - $M_{y,1}$ -interaction for LTB from EN 1995-1-1 (2004) was confirmed.

In a subsequent publication, the shear verification for LTB of GL beams will be discussed.

## 9 Acknowledgements

The research project was supported by the German Federal Ministry for Economic Affairs and Climate Action on the basis of a decision of the German Bundestag (IGF project no. 21285 N). This support is gratefully acknowledged. We would like to thank the Forschungs- und Materialprüfanstalt (FMPA) of the Brandenburg University of Technology Cottbus-Senftenberg for conducting the experiments. We would also like to thank Schaffitzel Holzindustrie GmbH + Co. KG for providing the test specimens and Microtec Srl GmbH for providing the sorting data. Many thanks also to the members of the committee accompanying the project for the fruitful discussions and valuable comments.

## 10 References

- Bell, K. & T. E. Eggen (2001). "Stability of timber beams and columns". In: *International Association for Bridge and Structural Engineering (IABSE) Conference*. Lahti, Finland.
- Blaß, H. J. (1987). "Design of timber columns". In: *CIB-W18*. 20-2-2, Dublin, Ireland.
- Buchanan, A. H.; K. C. Johns & B. Madsen (1985). "Column design methods for timber engineering". In: *CIB-W18*. 18-2-1, Beit Oren, Israel.
- DIN 1052 (2004). *Entwurf, Berechnung und Bemessung von Holzbauwerken – Allgemeine Bemessungsregeln und Bemessungsregeln für den Hochbau*. German Institute of Standardization (DIN), Berlin, Germany.
- DIN 68364 (2003). *Kennwerte von Holzarten – Rohdichte, Elastizitätsmodul und Festigkeiten*. German Institute of Standardization (DIN), Berlin, Germany.
- DIN EN 1995-1-1/NA (2013). *Nationaler Anhang – National festgelegte Parameter – Eurocode 5: Bemessung und Konstruktion von Holzbauten – Teil 1-1: Allgemeines – Allgemeine Regeln und Regeln für den Hochbau*. German Institute of Standardization (DIN), Berlin, Germany.
- EN 14080 (2013). *Timber structures - Glued laminated timber and glued solid timber - Requirements*. European Committee for Standardization (CEN), Brussels, Belgium.
- EN 1995-1-1 (2004). *Eurocode 5: Design of timber structures – Part 1-1: General – Common rules and rules for buildings*. European Committee for Standardization (CEN), Brussels, Belgium, with corrections and amendments + AC:2006 and A1:2008.
- ETA-14/0354 (2018). *Beam BauBuche GL75*. Austria Institute of Construction Engineering (OIB), Vienna, Austria.
- Heimeshoff, B. (1986). "Berechnung und Ausführung von Holzbauwerken". In: *Ingenieur-Holzbau 86*. Leinfelden-Echterdingen, Germany.
- Hörsting, O.-P. (2008). "Zum Tragverhalten druck- und biegebeanspruchter Holzbauteile". Dissertation. Technische Universität Carolo-Wilhelmina zu Braunschweig, Braunschweig, Germany. DOI: <https://doi.org/10.24355/dbbs.084-200807140200-0>.
- Leicester, R. H. (1988a). "Beam-column formulae for design codes". In: *CIB-W18*. 21-2-2, Parksville, Vancouver Island, Canada.
- Leicester, R. H. (1988b). "Format for buckling strength". In: *CIB-W18*. 21-2-1, Parksville, Vancouver Island, Canada.
- prEN 1995-1-1 (2024). *Eurocode 5 – Design of timber structures – Part 1-1: General rules and rules for buildings (Version 2a)*. CEN/TC 250/SC 5 N 2077. European Committee for Standardization (CEN): Brussels, Belgium.
- Schänzlin, J.; G. Bosch & P. Hamm (2022). *k<sub>c</sub>-method – consideration of creep deformations*. CEN/TC 250/SC 5/WG 3 N 354.
- Schilling, S.; P. Palma & A. Frangi (2021). "Probabilistic description of the mechanical properties of glued laminated timber made from softwood". In: *Proceedings of the 8<sup>th</sup> meeting of International Network on Timber Engineering Research (INTER)*. 54-12-4, online. DOI: <https://doi.org/10.3929/ethz-b-000505371>.

- Taras, A. (2010). "Contribution to the development of consistent stability design rules for steel members". Dissertation. Graz University of Technology, Graz, Austria. DOI: <https://doi.org/10.3217/1smsn-1bq83>.
- Töpler, J. (2025). "Load-bearing capacity of imperfection-sensitive timber members under combined bending and compression". in preparation. Dissertation. Institute of Structural Design, University of Stuttgart, Germany.
- Töpler, J. & U. Kuhlmann (2022a). "Experimentelle und numerische Untersuchungen von Brettschichtholz aus Buchen-Furnierschichtholz (BauBuche)". In: *Doktorandenkolloquium Holzbau Forschung und Praxis*. Stuttgart, Germany, pp. 131–139. DOI: <http://dx.doi.org/10.18419/opus-12607>.
- Töpler, J. & U. Kuhlmann (2022b). "In-plane buckling of beech LVL columns". In: *Proceedings of the 9<sup>th</sup> meeting of International Network on Timber Engineering Research (INTER)*. 55-2-1, Bad Aibling, Germany. DOI: <http://dx.doi.org/10.18419/opus-12610>.
- Töpler, J. & U. Kuhlmann (2023). "Lateral torsional buckling of glulam beams". In: *Proceedings of the 10<sup>th</sup> meeting of International Network on Timber Engineering Research (INTER)*. 56-12-6, Biel/Bienne, Switzerland. DOI: <http://dx.doi.org/10.18419/opus-13593>.
- Töpler, J. & U. Kuhlmann (2024). *Optimierung des Ersatzstabverfahrens für biegedrillknickgefährdete Bauteile aus Holz unter Momenten-Normalkraft-Belastung*. Research report, IGF No. 21285 N. Institute of Structural Design, University of Stuttgart, Stuttgart, Germany.
- van der Put, T. A. C. M. (1991). "Discussion of failure criterion for combined bending and compression". In: *CIB-W18*. 24-6-1, Oxford, England.
- Wilden, V.; B. Hoffmeister & M. Feldmann (2023). "Ein mechanisch konsistenter Ansatz für den Stabilitätsnachweis für Holztäger unter Druck und Biegung um die starke Achse". In: *Bautechnik 100.Sonderheft Holzbau*, pp. 19–30. DOI: <https://doi.org/10.1002/bate.202200073>.
- Zahn, J. J. (1986). "Design of wood members und combined load". In: *Journal of Structural Engineering* 112.9, pp. 2109–2126. DOI: [https://doi.org/10.1061/\(ASCE\)0733-9445\(1986\)112:9\(2109\)](https://doi.org/10.1061/(ASCE)0733-9445(1986)112:9(2109)).

## DISCUSSION

**The paper was presented by J Töpler**

*G Doudak received clarification on how non-elastic deformation was detected in the compression zone during testing. He commented that application of larger axial load would have been interesting.*

*O Sisman commented that stiffness of the beam column depended on connection stiffness and application of load over an area can offer some restriction to lateral buckling. He commented that the proposed design formula would be too complicated. J Töpler said this should not be an issue.*

*JW van de Kuilen commented that there was past work on this topic. He asked how sure would the numerical model verified from a different test condition be transferred to this study. JW van de Kuilen and J Töpler discussed that loading should be fine and compression strength test data of different species would have been nice to have but there was no certainty if full scale moment rotation test data was available. J Töpler agreed that such data would increase the validity of the FEM but was quite comfortable the validity of the FEM.*

*P Dietsch commented that a combination of shear and torsional shear was observed but that the stress interaction was superficially covered and the approach from H Kreuzinger on this topic was available and the authors should check this approach. J Töpler agreed.*

*The proposed  $k_{pl,c}$   $k_{pl,m}$  factors could be challenged as code proposal because  $k_{pl,m}$  jumped from 1 to 6. J Töpler said as experimental data was limited, he did not want to be specific. He stated that  $k_{pl,c} = 1$  for softwood and a different factor for beech should be okay. P Dietsch suggested that the interaction between torsional stresses and shear stresses from shear force should be clarified in paper.*

*A Frangi commended the work but suggested to look into past work in more detail.*



# Derivation of Visual Grading Assignments for Turkish Red Pine and Scots Pine Graded in Accordance with Turkish Standard TS 1265- 2012

Fatih Kurul, Istanbul University-Cerrahpaşa, Faculty of Forestry

Mehmet Özdemir, General Directorate of Forestry, Marmara Forestry Research Ins.

Tülay Yılmaz, General Directorate of Forestry, Marmara Forestry Research Ins.

Mehmet Arslan, General Directorate of Forestry, Marmara Forestry Research Ins.

Selim Ermiş, General Directorate of Forestry, Marmara Forestry Research Ins.

Türker DüNDAR, Istanbul University-Cerrahpaşa, Faculty of Forestry

Keywords: Visual grading assignment, *Pinus brutia*, *Pinus sylvestris*, Structural timber, TS 1265

## 1 Introduction

Türkiye has a national standard TS 1265 for the visual grading of softwood timber for structural uses since 1973. The visual grades determined according to TS 1265 were the basis for the allowable design stresses to be used in the design of timber structures given in the Turkish building code for timber structure, TS 647 (1979). After adopting TS EN 1995-1-1 (Eurocode 5) in Türkiye in 1996, TS 647 has become obsolete as it was superseded by Eurocode 5. The visual grades of TS 1265 remained unchanged, but no characteristic properties for the different grades have been derived after the transition. Therefore, the most significant obstacle to the construction of wooden structures in Türkiye with local wood species was the unknown strength classes required to design timber structures by Eurocode 5. Consequently, if the grades and species or species combination in TS 1265 have been assigned to a strength class by EN 1912, the local softwood timber visually graded according to TS 1265 can be used for structural purposes in conjunction with Eurocode 5.

In 2019, a comprehensive research project supported by the General Directorate of Forestry was initiated to determine the strength classes of local softwood timber cor-



responding to their visual grades according to TS 1265 (2012). In this project, Turkish red pine (*Pinus brutia*), Anatolian black pine (*Pinus nigra*), Scots pine (*Pinus sylvestris*), fir (*Abies* spp.), spruce (*Picea orientalis*) and cedar (*Cedrus libani*) were studied as they are the most common softwood species of Türkiye. The strength classes of six softwood species derived by this project were submitted to the CEN TC 124/WG2/TG1 committee in 3 reports including two tree species each and with the approval of the committee, they were included in the EN 1912 (2024) standard.

This study aims to present the results of the aforementioned project for two softwood species, Turkish red pine (*Pinus brutia*) and Scots pine (*Pinus sylvestris*). Changes in the strength classes and grading yields were also questioned by increasing the limits for single knots given in the TS 1265 (2012) standard on the basis of the ratio of the knot diameter to the width of the section where the knot is located (KDR).

## 2 Materials and Methods

### 2.1 Sampling Strategy

Türkiye has 22,9 million hectares forestland which is approximately 29% of the total land. Pure coniferous forests cover 48% of the total forestland. An additional 20% of forestland consists of softwood and hardwood mixed stands as well. The most common softwood species are Turkish red pine (*Pinus brutia*), Anatolian black pine (*Pinus nigra*), Scots pine (*Pinus sylvestris*), fir (*Abies* sp.), cedar (*Cedrus* sp.), and spruce (*Picea* sp.) (OGM, 2020). In 2020, OGM produced 10,3 million cubic meters of sawlogs of which 8,5 million cubic meters were softwood species for timber production. Turkish red pine and Scots pine met half of the demand for softwood sawlogs with a production of 3.4 million cubic meters and 770.000 cubic meters, respectively.

Turkish red pine grows especially in the Mediterranean, Aegean and Marmara coastal and back-coast regions, as well as locally in the Black Sea Region as seen in Figure 1. It is commonly used for structural purposes. In order to sampling timber source of Turkish red pine in Türkiye, its main growing areas were first divided into four main regions; Eastern Mediterranean region, Western Mediterranean region, South Aegean region, and North Aegean region. The nine Regional Directorates of Forestry in these regions provided 92% (3.14 million cubic meters) of the annual Turkish red pine sawlog production in 2021. In the next step, nine “Operational Directorates of Forestry” representing the “Regional Directorates” geographically and have the big amount of sawlog sales volume in 2021 were selected, as seen in Figure 1.



Figure 1. Sampling of Turkish red pine stands in Türkiye.

Scots pine forest constitutes 6,4% of total forestland of Türkiye which ranks third place among the softwoods. It grows mostly in Northern part of Türkiye and partly in inner Anatolia as seen in Figure 2. For sampling of timber source of Scots pine in Türkiye, its growing areas were divided into 4 main regions; Eastern Black Sea region, Middle Black Sea region, Western Black Sea region, and Inner Anatolia region. The eight Regional Directorates of Forestry in these regions provided 87% (670.000 cubic meters) of the annual Scots pine sawlog production in 2021. For taking of sawlog samples, eight “Operational Directorates of Forestry” representing the “Regional Directorates” geographically and have the big amount of sawlog sales volume in 2021 were selected (Figure 2).

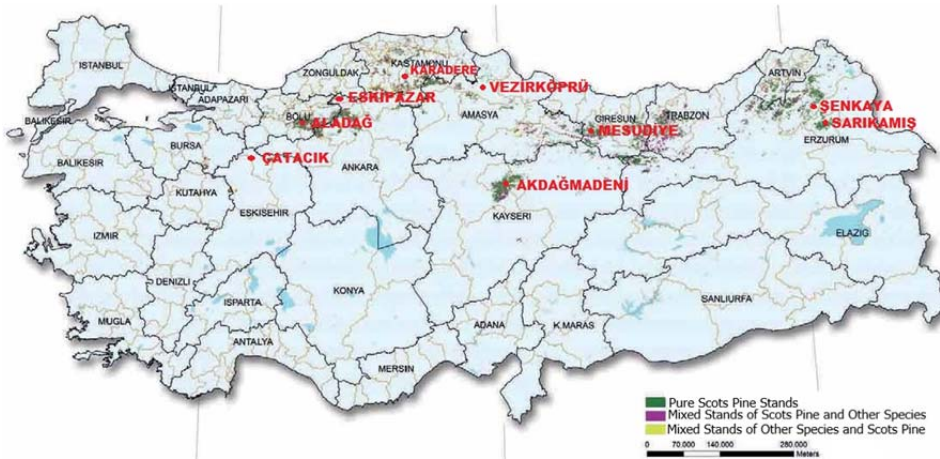


Figure 2. Sampling of Scots pine stands in Türkiye.

Sawlog samples were taken from the log yards of selected operational directorates. Attention was paid to ensure that the selected log samples represented different ages and diameters. The volume of sawlogs to be taken was determined by considering the sales amounts of selected operational directorates as well. A total of 212 cubic metres of Red pine and 220 cubic metres of Scots pine sawlogs of different ages and diameters were supplied from the selected regions.

The logs were sawn into timber in five nominal cross sections which were 50×100 mm, 50×150 mm, 50×200 mm 75×150 mm, and 75×200 mm. During sawing, atten-

tion has been paid to the number of timbers in each cross section sawn from each region was as balanced as possible. Following the sawing, the timber was kiln-dried to a target moisture content of 12%. At the end of the sawing, 2764 and 3179 beams in different cross sections were obtained from Turkish red pine and Scots pine, respectively.

**2.2 Visual Grading of the Timbers According to TS 1265 (2012)**

Türkiye’s national visual grading standard, TS 1265 (2012), gives the definition, classification and specifications, inspections and tests, marketing and control rules for softwood timber manufactured from pine, fir, spruce, and cedar with a rectangular cross section for only structural purposes. Softwood timber are sorted into three classes; Class 1 with high load bearing capacity, Class 2 with moderate load bearing capacity, and Class 3 with low load bearing capacity. Measurements of features other than knots are conducted according to TS EN 1309-3 (2018). The knots are measured according to the guidelines given in the standard. Table 1 gives some of the visual grading rules of the standard. Figure 3 shows the measurement methods of single knots and knot clusters.

*Table 1. Some of the visual grading rules in TS 1265 (2012).*

Characteristics	Grades		
	High Load Bearing Capacity Class 1	Moderate Load Bearing Capacity Class 2	Low Load Bearing Capacity Class 3
<b>Knots</b>			
a) Single knots:			
- In square timber, beams, and whole timber; the ratio of knot diameter to the width of the face on which the knot is visible must be max.	1/5	1/3	1/2
	The narrow diameter is no greater than 50 mm	The narrow diameter is no greater than 70 mm	No limitation
b) Knot cluster:			
- In square timber, beams, and whole timber; the ratio of the sum of knot diameters within the worst 150 mm length to the width of the face on which the knots are visible must be max.	2/5	2/3	3/4
<b>Slope of grain</b>			
a) In case of presence of sur-	Deviation in 1 m-length is not greater than;		
	70 mm	120 mm	200 mm

face fissure;			
b) In case of no surface fissure;	100 mm	200 mm	300 mm
<b><u>Fissures</u></b>			
a) Pith fissures	No limitation	No limitation	No limitation
b) Surface fissures	Not allowed	No greater than 1/5 the length of the piece	No limitation
<b><u>Annual ring width</u></b>			
	Area of the growth ring bigger than 4mm should not be greater than 1/2 of the whole cross section area	No limitation	No limitation
<b><u>Wane</u></b>			
	The sum of wane lengths should not exceed 1/3 of the length of the edge, and the area reduced by wane in any cross section should not exceed 1/8 of the nominal area of that section.	The sum of wane lengths should not exceed 2/3 of the length of the edge, and the area reduced by wane in any cross section should not exceed 1/8 of the nominal area of that section.	Allowed. However, strips must have been cut across the four sides of the round wood with a saw.
<b><u>Crook (Spring)</u></b>			
a) The largest deviation in 2 m-length where the crook is maximum, maximum	5 mm	8 mm	15 mm
b) The rate of largest deviation to lumber length, maximum	1/400	1/250	1/100
<b><u>Twist</u></b>			
		Not allowed	Do not exceed 2 mm in 1 m-length
<b><u>Cup</u></b>			
	1% of timber width	2% of timber width	4% of timber width

Visual grading was conducted in four main steps. In the first step, moisture content and dimensions of the specimens were measured and marked for traceability according to log number that indicates tree species, origins, ages and diameters of the logs. In step two, the top and bottom sides of the specimens for bending testing were selected randomly. Following the selection, the specimens were first examined on the basis of three strength related features; knots, fibre deviations and growth rate (annual ring width). In third step, the biggest defect located in between the loading point was determined based on the four sides of the timber. In order to ensure that the biggest defect is located within the test zone, the loading points were shifted to the right or left along the specimens, which was prepared longer than required for the

test. The “test grade” of the specimen was assigned by considering this biggest defect. If the largest defect could not be located in between the loading points, the second largest defect was taken into account. In this case, the “test grade” and “timber grade” were different from each other. In the fourth step, the “general timber grade” was determined by taking into account all the features listed in TS 1265 (2012). In all specimens, the knot diameter ratio (KDR) of the biggest knots (or knot clusters) located in between the loading points and the mean width of the annual rings in the cross section were measured and recorded. After the visual grading the loading points and the support points were marked on the randomly selected top side of all specimens according to the depth of the board and the location of the defect that determined the “test class”. Then the excess parts remaining at the ends of the specimens were cut.

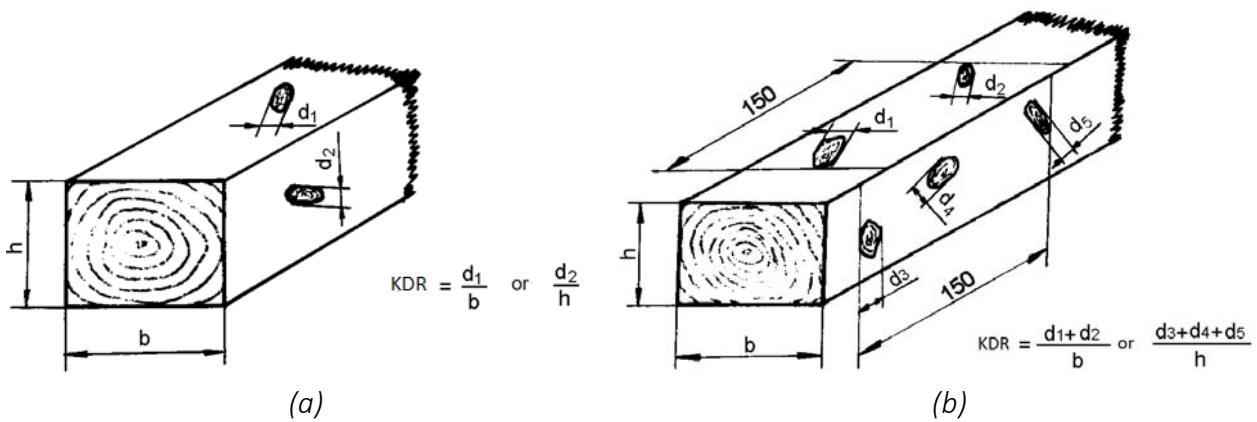


Figure 3. Measurement method of (a) single knots, (b) knot clusters (square timber, beams, whole timber).

For Turkish red pine, total of 2764 boards were graded visually according to TS 1265 (2012) and 1367 of them were selected for testing in bending. In Scots pine, 1500 specimens of 3179 boards graded visually were selected for testing. While making the selection the visual grades, the regions and the cross-section dimensions of the boards were taken into account and it was aimed to have at least 40 specimens in each visual grade in each region. It was also considered that the selected specimens for mechanical tests were distributed as evenly as possible to each cross-section. Although it was aimed to have at least 40 specimens in each cross section from each grade, this number was below 40 in some grades in some regions for Turkish red pine. The main reason of this was that there was not enough number of timbers in these grades in these regions. In Scots pine the number of specimens were more than 40 in all regions. Table 2 shows the distribution of the test specimens into the visual grades.

Table 2. Distribution of the test samples into the visual classes.

	Class 1	Class 2	Class 3	Rejected	Total
Turkish red pine	376	393	402	196	1367
Scots pine	435	436	443	186	1500

### 2.3 Mechanical Testing

The selected specimens were tested in edgewise bending in order to determine the local modulus of elasticity in bending and bending strength in accordance with EN 408+A1 (2014). The density and the moisture content of the specimens were also be determined on defect free pieces with full cross section cut from the specimens after the test. The moisture content of the timber was determined in accordance with EN 13183-1 (2002). The test values for modulus of elasticity parallel to the grain and the density of specimens not tested at the 12% moisture content were adjusted by using the formulas given in EN 384+A2 (2022).

### 2.4 Derivation of Visual Grading Assignments

The method for determining characteristic values of mechanical properties and density which indicate the strength class, for defined populations of visual grades is given in EN 384+A2 (2022).

Before the calculation of characteristic values of strength, stiffness and density of specimens from each region (sub-sample), the specimen numbers of the regions were checked and the possibilities of merging the regions with less than 40 specimens were examined in terms of geographical and ecological characteristics. In Turkish red pine, the number of specimens was below 40 in Isparta, İzmir, and Muğla regions in Grade 1, in Çanakkale in Grade 2, and in Muğla in Grade 3. Thus, the calculations were made by merging the regions of Antalya and Isparta, Denizli and Muğla, and Çanakkale and İzmir. The merged regions are all in close vicinity of each other in geographical and ecological aspect. In Scots pine, the numbers of specimens in all the regions were more than 40. Therefore, no merging was required for Scots pine when calculating the characteristic values.

The bending strength values of the specimens with a depth of nominal 100 mm were adjusted to 150 mm depth by dividing by the factor  $k_h$  as indicated in EN 384+A2 (2022). Since the local bending modulus of elasticity  $E_{m.local}$  were determined in this study, they are used as modulus of elasticity parallel to grain.

After completing the adjustments, the test results were checked whether they were normally or logarithmically normally distributed to calculate the 5-percentile values of bending strength and density. For all regions of both Turkish red pine and Scots pine, the bending strength, modulus of elasticity in bending and density were assumed as logarithmically normally distributed. Thus, the parametric method defined in EN 14358 (2016) was used to calculate the 5-percentile strength value  $f_{05,i}$  and the 5-percentile density value  $\rho_{05,i}$ , and the mean stiffness value of each region (sub-sample). The characteristic values of the bending strength, the modulus of elasticity, and the density for each grade were calculated in accordance with EN 384+A2 (2022). Thus, the strength classes corresponding to the calculated characteristic values in EN 338 (2016) standard were determined.

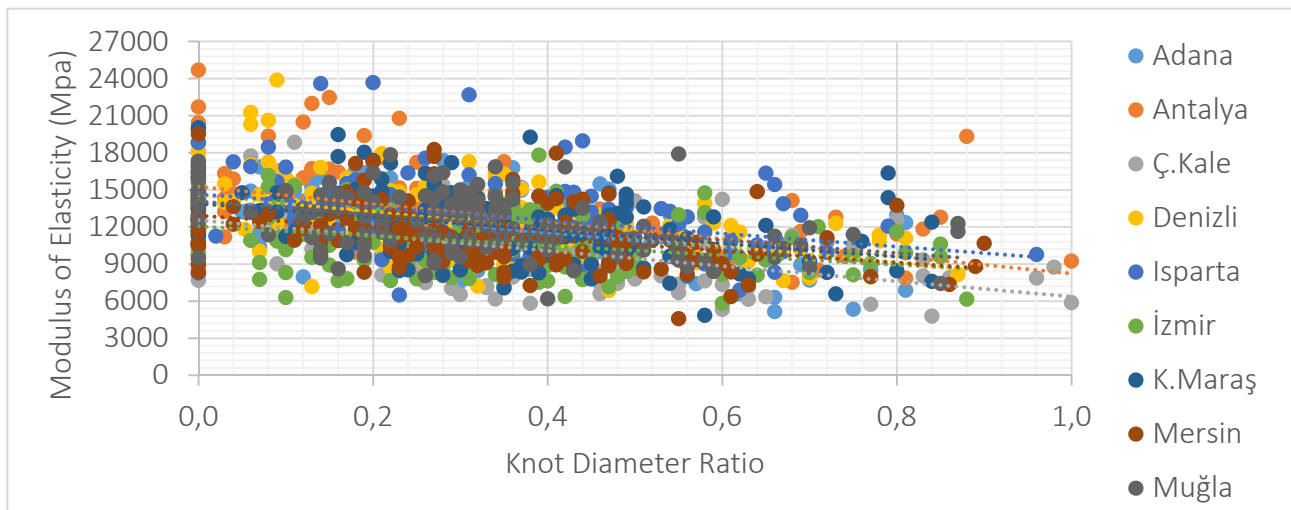
As a trial, the characteristic values were also re-calculated by increasing the limits for single knots given in the TS 1265 (2012) standard on the basis of the knot diameter ratio (KDR). In this calculation, the visual classification composition was reconstructed by increasing the KDR limits from 0.20 to 0.25 for Class 1, from 0.33 to 0.40 for Class 2 and from 0.50 to 0.60 for Class 3. Thus, how changes in KDR ratios affect the characteristic values and visual grading efficiency were analysed.

### 3 Results and Discussions

#### 3.1 Mechanical Test Results

Table 3 and Table 4 show the test results of Turkish red pine and Scots pine specimens according to different regions and visual classes, respectively. As seen from Table 3 and Table 4 the mean MCs of all the specimens vary between 14,3% and 15,8%. The mean values of the local modulus of elasticity in bending and bending strength of the specimens decreased as the visual class decreased for both softwood species as expected.

Figure 4 and Figure 5 show the relationships between the KDR and MoE and bending strength of Turkish red pine and Scots pine, respectively. As seen in Figure 4 and Figure 5, the MoE and bending strength decrease as the KDR values increase as expected. However, the correlations between the KDR and MoE and bending strength were not too strong. In the graphs, the KDR of 0,5 is the limit value for Grade 3 of timber and the points with higher KDR values than 0,5 belong to rejected timber.



	Adana	Antalya	Ç.Kale	Denizli	Isparta	İzmir	K.Maraş	Mersin	Muğla
R <sup>2</sup>	0,24	0,23	0,27	0,23	0,12	0,10	0,16	0,14	0,18



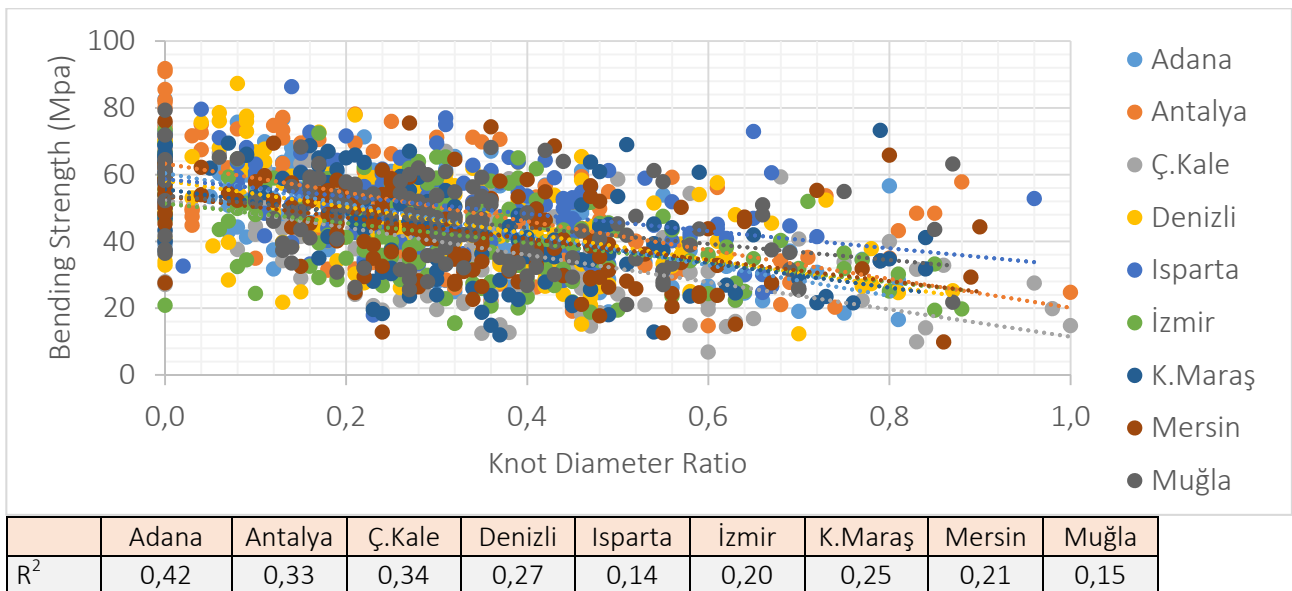


Figure 4. The relationships between the KDR and MoE and bending strength of Turkish red pine.

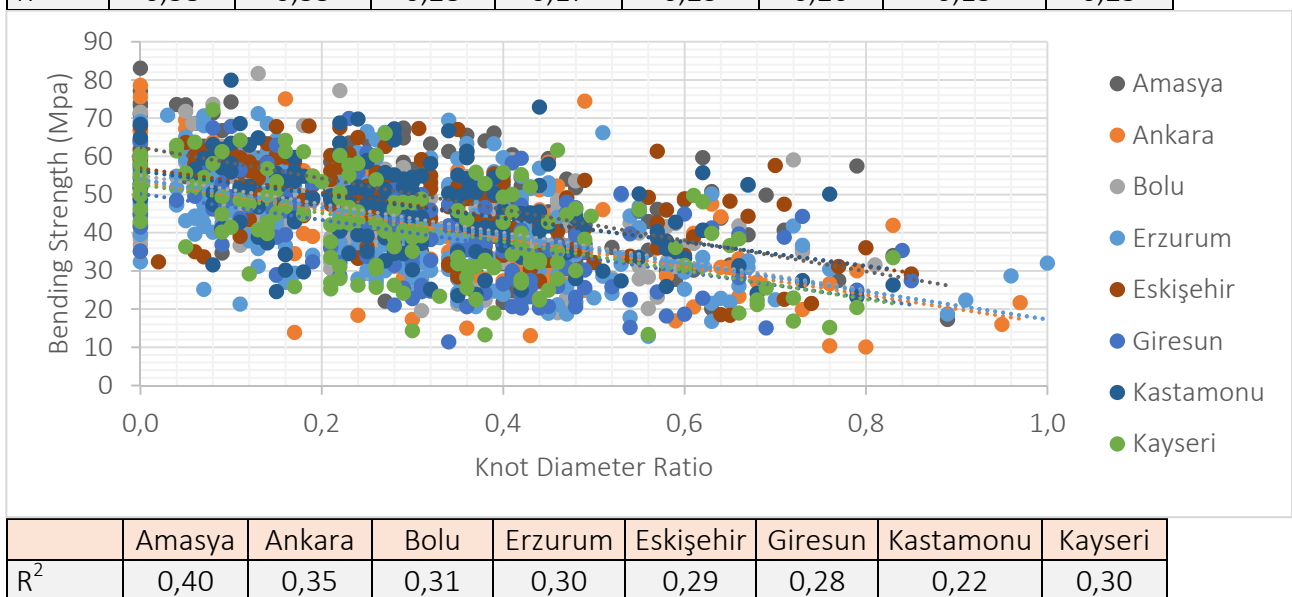
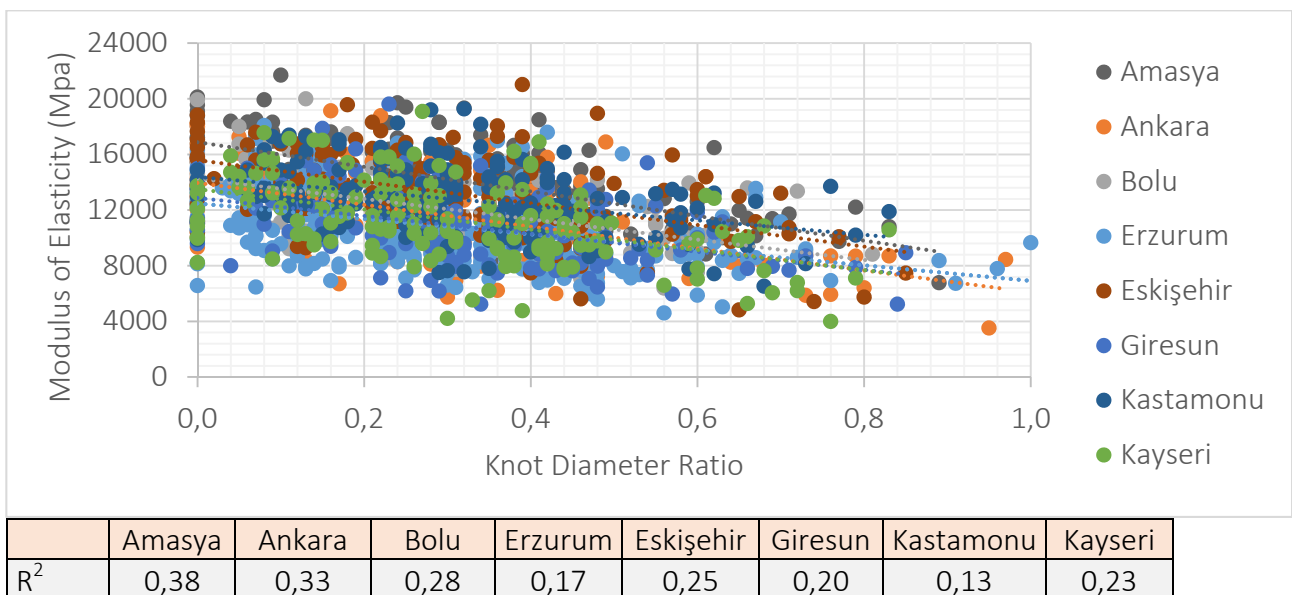


Figure 5. The relationships between the KDR and MoE and bending strength of Scots pine.



Table 3. Test results of Turkish red pine according to the sub-samples and the visual class.

Sub-samples	No of Spec.	MC (%)	Bending S. (MPa)	MoE (MPa)	Density (kg/m <sup>3</sup> )	No of Spec.	MC (%)	Bending S. (MPa)	MoE (MPa)	Density (kg/m <sup>3</sup> )
Adana	49	14,8 (5,5)	56,1 (19,1)	13428 (15,3)	554,5 (12,7)	46	14,9 (7,8)	48,4 (21,7)	12198 (18,2)	558,5 (10,2)
Antalya	47	14,4 (7,0)	65,2 (22,1)	15877 (25,7)	608,1 (10,1)	46	14,7 (7,3)	48,8 (25,3)	12917 (16,4)	597,8 (10,6)
Çanakkale	40	14,3 (6,8)	54,1 (22,3)	12885 (18,0)	562,0 (10,6)	35	14,4 (7,2)	38,9 (31,7)	10623 (22,1)	570,1 (7,1)
Denizli	45	14,4 (5,8)	58,5 (23,4)	14550 (20,5)	569,4 (10,7)	59	14,4 (6,7)	47,2 (22,2)	12552 (17,8)	551,1 (11,7)
Isparta	38	15,7 (7,7)	57,9 (21,1)	14391 (21,4)	590,8 (7,4)	40	15,6 (7,0)	49,8 (24,3)	13086 (19,0)	580,8 (9,4)
Izmir	37	14,4 (5,5)	50,1 (24,5)	12123 (21,2)	567,5 (7,9)	45	14,4 (5,3)	42,5 (30,7)	10497 (19,1)	544,5 (7,8)
K.Maraş	40	14,4 (5,3)	58,2 (16,1)	14028 (17,5)	583,7 (11,6)	40	14,6 (5,9)	42,7 (30,6)	12236 (20,1)	545,7 (9,4)
Mersin	41	14,3 (7,2)	52,8 (17,2)	12624 (18,1)	519,1 (9,4)	41	14,8 (6,8)	43,7 (26,9)	11607 (19,2)	517,5 (9,2)
Muğla	39	14,4 (5,9)	52,4 (21,7)	13306 (16,8)	553,2 (8,3)	41	15,1 (8,6)	45,7 (23,5)	12812 (16,6)	559,9 (8,9)
<b>Total</b>	<b>376</b>	<b>14,6 (6,9)</b>	<b>56,4 (22,1)</b>	<b>13743 (21,4)</b>	<b>567,8 (10,9)</b>	<b>393</b>	<b>14,7 (7,4)</b>	<b>45,5 (26,6)</b>	<b>12097 (19,8)</b>	<b>558,3 (10,3)</b>
Class 3										
Adana	53	15,0 (7,1)	40,2 (25,0)	11799 (16,6)	563,2 (9,4)	21	14,8 (7,5)	31,2 (32,7)	9356 (27,1)	532,8 (8,2)
Antalya	43	14,6 (9,2)	43,5 (28,1)	11976 (16,2)	581,5 (9,7)	20	14,3 (6,6)	38,1 (34,2)	11064 (23,8)	560,1 (8,3)
Çanakkale	46	14,5 (5,7)	34,1 (37,4)	9751 (20,4)	563,7 (10,9)	27	15,0 (6,7)	25,7 (50,0)	8384 (26,8)	524,5 (11,3)
Denizli	47	14,3 (7,3)	38,1 (31,0)	11436 (18,4)	549,4 (10,5)	20	13,9 (3,5)	35,4 (32,3)	10487 (16,4)	542,9 (12,3)
Isparta	48	15,7 (8,0)	47,6 (19,9)	12340 (18,2)	565,8 (6,8)	22	15,8 (7,5)	42,0 (26,5)	11169 (20,9)	555,1 (6,0)
Izmir	45	14,3 (4,9)	38,6 (32,5)	10581 (22,5)	552,6 (7,0)	24	14,4 (5,6)	32,3 (26,6)	9488 (23,8)	537,3 (5,5)
K.Maraş	41	14,6 (6,6)	35,3 (33,5)	11439 (21,1)	540,8 (10,6)	21	14,5 (6,4)	36,6 (42,6)	10131 (28,1)	534,3 (10,3)
Mersin	41	14,7 (6,4)	40,4 (31,7)	11109 (22,3)	516,0 (7,7)	22	14,7 (8,0)	29,8 (42,3)	9137 (22,0)	508,7 (7,6)
Muğla	38	14,6 (5,3)	42,8 (26,4)	11871 (17,8)	542,6 (11,1)	19	14,2 (7,9)	40,4 (31,3)	10579 (20,8)	529,8 (9,6)
<b>Total</b>	<b>402</b>	<b>14,7 (7,4)</b>	<b>40,1 (30,4)</b>	<b>11369 (20,2)</b>	<b>553,7 (9,8)</b>	<b>196</b>	<b>14,6 (7,5)</b>	<b>34,2 (37,8)</b>	<b>9908 (24,8)</b>	<b>535,7 (9,2)</b>

The number in the parenthesis are the coefficient of variation.

Table 4. Test results of Scots pine according to the sub-samples and the visual class.

Sub-samples	No of Spec.	MC (%)	Bending S. (MPa)	MoE (MPa)	Density (kg/m <sup>3</sup> )	No of Spec.	MC (%)	Bending S. (MPa)	MoE (MPa)	Density (kg/m <sup>3</sup> )	
											Class 1
Amasya	55	14,9 (7,0)	60,2 (14,9)	16065 (14,1)	556,5 (8,8)	49	15,1 (6,7)	50,0 (19,5)	14659 (16,5)	527,5 (7,3)	
Ankara	45	14,8 (9,0)	52,3 (23,9)	13647 (19,8)	518,0 (10,0)	44	14,7 (8,1)	42,7 (22,9)	11557 (21,4)	504,4 (8,9)	
Bolu	49	14,7 (6,9)	54,6 (18,6)	14084 (17,6)	536,3 (10,7)	49	14,8 (6,3)	43,3 (22,9)	12158 (15,2)	505,5 (7,6)	
Erzurum	106	14,8 (6,3)	52,4 (18,2)	12264 (18,7)	506,3 (10,2)	98	14,8 (7,2)	42,6 (23,6)	10730 (20,4)	484,8 (10,7)	
Eskişehir	52	15,0 (6,7)	54,1 (16,6)	14700 (15,8)	547,5 (8,7)	52	14,9 (6,9)	49,6 (16,3)	13776 (14,1)	541,4 (10,1)	
Giresun	44	14,8 (6,6)	49,2 (17,9)	12555 (17,2)	514,1 (10,2)	40	14,6 (7,5)	39,3 (25,7)	10813 (25,5)	503,7 (12,0)	
Kastamonu	44	14,9 (7,1)	53,6 (18,2)	13800 (14,3)	520,6 (9,6)	58	14,5 (5,1)	47,6 (22,5)	13183 (20,4)	503,8 (9,3)	
Kayseri	40	15,0 (6,3)	52,0 (18,6)	13022 (17,7)	557,0 (8,4)	46	14,9 (6,5)	41,6 (25,3)	11950 (20,4)	537,3 (10,4)	
<b>Total</b>	<b>435</b>	<b>14,9 (6,9)</b>	<b>53,6 (18,9)</b>	<b>13638 (19,1)</b>	<b>529,1 (10,2)</b>	<b>436</b>	<b>14,8 (6,8)</b>	<b>44,7 (23,4)</b>	<b>12229 (21,9)</b>	<b>509,9 (10,4)</b>	
Class 3 Rejected											
Amasya	54	14,7 (5,5)	45,0 (23,0)	13260 (16,6)	522,0 (9,1)	21	14,6 (7,6)	38,5 (31,8)	11117 (16,9)	510,2 (5,6)	
Ankara	53	14,8 (8,3)	37,4 (31,0)	10807 (23,2)	497,8 (9,6)	22	15,0 (8,5)	28,9 (37,9)	8662 (26,7)	507,3 (11,7)	
Bolu	50	14,7 (6,9)	37,8 (26,9)	10900 (17,4)	488,1 (8,0)	20	14,5 (7,4)	35,6 (22,5)	10352 (19,1)	484,1 (9,0)	
Erzurum	87	14,8 (7,3)	38,5 (30,0)	10263 (25,7)	481,6 (11,1)	39	14,4 (5,4)	32,1 (34,9)	9006 (25,5)	482,0 (9,8)	
Eskişehir	50	15,0 (7,4)	41,8 (28,7)	12428 (28,2)	533,0 (10,4)	21	14,6 (4,8)	38,8 (31,8)	11140 (34,6)	534,1 (12,5)	
Giresun	49	14,6 (5,8)	34,1 (30,5)	9962 (21,5)	472,9 (9,2)	21	14,7 (4,2)	30,4 (38,4)	9043 (26,5)	484,5 (8,5)	
Kastamonu	50	14,7 (6,0)	43,3 (24,8)	12223 (18,5)	483,3 (8,9)	21	14,6 (5,3)	36,9 (25,8)	10951 (19,9)	488,3 (6,4)	
Kayseri	50	14,8 (7,5)	36,1 (29,7)	10402 (24,5)	504,7 (9,6)	21	14,7 (7,0)	30,3 (38,6)	8720 (38,0)	503,6 (9,2)	
<b>Total</b>	<b>443</b>	<b>14,8 (6,9)</b>	<b>39,3 (29,1)</b>	<b>11213 (24,4)</b>	<b>496,8 (10,4)</b>	<b>186</b>	<b>14,6 (6,4)</b>	<b>33,7 (33,6)</b>	<b>9775 (28,0)</b>	<b>497,7 (9,9)</b>	

The number in the parenthesis are the coefficient of variation.

### 3.2 Five-percentile Values

Table 5 shows the calculation of 5-percentile values for Turkish red pine in Class 1, Class 2, and Class 3, respectively. The calculations were made by merging the regions with less than 40 specimens and close to each other in geographic and ecological aspect. Thus, Isparta was merged with Antalya, İzmir was merged with Çanakkale and Muğla was merged with Denizli.

Table 5. The 5-percentile values of Turkish red pine.

Source	No of Spec.	MC (%)	Adj. Bending S. (MPa)*		Adj. MoE*	Adj. Density (kg/m <sup>3</sup> )*	
			Mean	$f_{05,i}$	( $\bar{E}_i$ ) (GPa)	Mean	$P_{0.5,i}$
<b>Class 1</b>							
Adana	49	14,8 (5,5)	55,0 (17,9)	38,4	13,3 (15,3)	554,5 (12,7)	444,8
Antalya-Isparta	85	15,1 (7,7)	61,2 (21,8)	39,1	14,8 (24,5)	600,4 (9,1)	511,4
Ç.Kale-İzmir	77	14,4 (5,5)	50,1 (22,7)	30,9	12,3 (19,7)	564,6 (9,4)	471,4
Denizli-Muğla	84	14,4 (5,9)	54,3 (22,9)	34,3	13,7 (19,4)	561,9 (9,7)	473,6
K.Maraş	40	14,4 (5,3)	56,4 (16,8)	39,6	13,8 (17,5)	583,7 (11,6)	466,7
Mersin	41	14,3 (7,2)	51,3 (17,3)	35,6	12,4 (18,1)	519,1 (9,4)	437,7
<b>Total</b>	<b>376</b>	<b>14,6 (6,9)</b>	<b>56,1 (18,2)</b>		<b>13,7 (19,2)</b>	<b>566,7 (10,9)</b>	
<b>Class 2</b>							
Adana	46	14,9 (7,8)	47,3 (21,5)	30,2	12,0 (18,2)	558,5 (10,2)	461,6
Antalya-Isparta	86	15,2 (7,2)	48,7 (24,3)	29,8	12,8 (17,6)	589,9 (10,1)	495,1
Ç.Kale-İzmir	80	14,4 (6,5)	40,0 (31,0)	20,8	10,3 (20,4)	555,7 (7,8)	482,0
Denizli-Muğla	100	14,8 (7,9)	45,9 (22,9)	28,6	12,5 (17,2)	554,7 (10,6)	460,9
K.Maraş	40	14,6 (5,9)	42,1 (30,2)	21,9	12,0 (20,1)	545,7 (9,4)	457,9
Mersin	41	14,8 (6,8)	43,1 (25,9)	25,8	11,4 (19,2)	517,5 (9,2)	436,5
<b>Total</b>	<b>393</b>	<b>14,7 (7,4)</b>	<b>44,8 (25,7)</b>		<b>11,9 (18,6)</b>	<b>558,3 (9,6)</b>	
<b>Class 3</b>							
Adana	53	15,0 (7,1)	39,4 (24,6)	23,9	11,6 (16,6)	563,2 (9,4)	472,9
Antalya-Isparta	91	15,2 (8,6)	45,2 (23,9)	27,8	12,0 (17,3)	573,2 (8,4)	493,1
Ç.Kale-İzmir	91	14,4 (5,3)	35,3 (34,2)	17,7	9,9 (21,9)	558,2 (9,2)	471,6
Denizli-Muğla	85	14,5 (6,7)	39,6 (29,1)	22,1	11,4 (18,1)	546,3 (10,8)	450,3
K.Maraş	41	14,6 (6,6)	35,1 (33,5)	16,8	11,2 (21,1)	540,8 (10,6)	445,6
Mersin	41	14,7 (6,4)	39,3 (31,2)	21,2	10,9 (22,3)	516,1 (7,7)	446,8
<b>Total</b>	<b>402</b>	<b>14,7 (7,4)</b>	<b>39,4 (29,1)</b>		<b>11,2 (19,3)</b>	<b>553,7 (9,4)</b>	

The number in the parenthesis are the coefficient of variation.

\* Adjusted values based on the moisture contents and/or timber depths

In Scots pine the number of the tested beams from all the regions were more than 40. Therefore, no needs to merge any regions for Scots pine when calculating the characteristic values. Tables 6 shows the 5-percentile values of bending strength and density and mean values of modulus of elasticity of the regions in Class 1, Class 2, and Class 3, respectively.

Table 6. The 5-percentile values of Scots pine.

Source	No of Spec.	MC (%)	Adj. Bending S. (MPa)*		Adj. MoE ( $\bar{E}_i$ ) (GPa)	Adj. Density (kg/m <sup>3</sup> )	
			Mean	$f_{0.5,i}$		Mean	$P_{0.5,i}$
<b>Class 1</b>							
Amasya	55	14,9 (7,0)	59,1 (14,5)	44,6	15,9 (14,1)	556,5 (8,8)	473,8
Ankara	45	14,8 (9,0)	50,5 (22,5)	30,0	13,4 (19,8)	517,9 (10,0)	431,4
Bolu	49	14,7 (6,9)	52,5 (17,1)	38,0	13,9 (17,6)	536,3 (10,7)	439,6
Erzurum	106	14,8 (6,3)	51,6 (18,0)	36,2	12,0 (18,7)	506,3 (10,2)	418,7
Eskişehir	52	15,0 (6,7)	53,1 (16,4)	37,5	14,5 (15,8)	547,5 (8,7)	466,9
Giresun	44	14,8 (6,6)	48,1 (18,4)	33,2	12,4 (17,2)	514,1 (10,2)	426,5
Kastamonu	44	14,9 (7,1)	52,6 (18,2)	35,8	13,7 (14,3)	520,6 (9,6)	436,5
Kayseri	40	15,0 (6,3)	50,9 (18,7)	34,3	12,8 (17,7)	557,0 (8,4)	475,0
<b>Total</b>	<b>435</b>	<b>14,9 (6,9)</b>	<b>52,4 (17,9)</b>		<b>13,4 (17,1)</b>	<b>529,0 (9,7)</b>	
<b>Class 2</b>							
Amasya	49	15,1 (6,7)	49,0 (19,7)	32,1	14,5 (16,5)	527,5 (7,3)	461,0
Ankara	44	14,7 (8,1)	41,8 (22,8)	25,1	11,3 (21,4)	504,4 (8,9)	427,7
Bolu	49	14,8 (6,3)	42,5 (22,6)	26,7	12,0 (15,2)	505,5 (7,6)	437,9
Erzurum	98	14,8 (7,2)	42,0 (24,0)	26,3	10,5 (20,4)	484,8 (10,7)	401,6
Eskişehir	52	14,9 (6,9)	48,8 (16,1)	35,5	13,6 (14,1)	541,4 (10,1)	450,3
Giresun	40	14,6 (7,5)	38,3 (24,5)	23,5	10,5 (25,5)	503,7 (12,0)	408,9
Kastamonu	58	14,5 (5,1)	46,6 (21,9)	30,1	12,9 (20,4)	503,8 (9,3)	425,7
Kayseri	46	14,9 (6,5)	40,9 (25,6)	24,4	11,7 (20,4)	537,3 (10,4)	442,2
<b>Total</b>	<b>436</b>	<b>14,8 (6,8)</b>	<b>43,8 (22,2)</b>		<b>12,0 (19,2)</b>	<b>510,5 (9,6)</b>	
<b>Class 3</b>							
Amasya	54	14,7 (5,5)	44,4 (23,4)	27,4	13,1 (16,6)	522,0 (9,1)	443,4
Ankara	53	14,8 (8,3)	36,7 (29,9)	19,5	10,5 (23,2)	497,8 (9,6)	418,3
Bolu	50	14,7 (6,9)	37,2 (27,1)	21,1	10,7 (17,4)	488,1 (8,0)	420,7
Erzurum	87	14,8 (7,3)	37,8 (28,6)	21,3	9,9 (25,7)	481,6 (11,1)	394,9
Eskişehir	50	15,0 (7,4)	40,9 (26,7)	25,5	12,0 (28,2)	533,0 (10,4)	441,4
Giresun	49	14,6 (5,8)	33,3 (29,7)	18,3	9,7 (21,5)	472,9 (9,2)	398,5
Kastamonu	50	14,7 (6,0)	42,5 (23,8)	26,4	12,0 (18,5)	483,3 (8,9)	410,5
Kayseri	50	14,8 (7,5)	35,5 (30,3)	19,2	10,1 (24,5)	504,7 (9,6)	421,4
<b>Total</b>	<b>443</b>	<b>14,8 (6,9)</b>	<b>38,5 (27,5)</b>		<b>10,9 (22,2)</b>	<b>496,8 (9,6)</b>	

The number in the parenthesis are the coefficient of variation.

\* Adjusted values based on the moisture contents and/or timber depths

### 3.3 Derivation of Characteristic Values and Strength Classes

Following the calculation of the 5-percentile values of the regions, the characteristic values of bending strength, modulus of elasticity and density were derived from the regions in accordance with EN 384+A2 (2022). The characteristic values of bending strength, modulus of elasticity and density of each visual grade and corresponding strength classes in EN 338 (2016) are given in Table 7 for Turkish red pine and in Table 8 for Scots pine.

Table 7. Derivation of characteristic values of visual grades and comparison with the requirement in EN 338 in Turkish red pine.

Grade	Characteristic Bending Strength (MPa)				Characteristic Modulus of Elasticity (GPa)				Characteristic Density (Kg/m <sup>3</sup> )							
	St. Class	$1,2f_{05,i,min}$	$\frac{\sum_{i=1}^{ns} n_i f_{05,i}}{n}$	$k_n$	$f_k$	St. class req.	$1,1\bar{E}_{i,min}$	$\frac{\sum_{i=1}^{ns} n_i \bar{E}_i}{n}$	$k_n$	$E_{0,mean,k}$	St. class req.	$1,1\rho_{05,i,min}$	$\frac{\sum_{i=1}^{ns} n_i \rho_{05,i}}{n}$	$k_n$	$\rho_k$	St. class req.
1	<b>C35</b>	37,1	35,9	1,0	35,9	35,0	14,2	14,2	1,0	14,2	13,0	481,5	473,3	1,0	473,3	390
2	<b>C24</b>	24,9	26,5	1,0	24,9	24,0	12,0	12,5	1,0	12,0	11,0	480,1	469,9	1,0	469,9	350
3	<b>C20</b>	20,2	21,9	1,0	20,2	20,0	11,4	11,7	1,0	11,4	9,5	490,2	466,6	1,0	466,6	330

Table 8. Derivation of characteristic values of visual grades and comparison with the requirement in EN 338 in Scots pine.

Grade	Characteristic Bending Strength (MPa)				Characteristic Modulus of Elasticity (GPa)				Characteristic Density (Kg/m <sup>3</sup> )							
	St. Class	$1,2f_{05,i,min}$	$\frac{\sum_{i=1}^{ns} n_i f_{05,i}}{n}$	$k_n$	$f_k$	St. class req.	$1,1\bar{E}_{i,min}$	$\frac{\sum_{i=1}^{ns} n_i \bar{E}_i}{n}$	$k_n$	$E_{0,mean,k}$	St. class req.	$1,1\rho_{05,i,min}$	$\frac{\sum_{i=1}^{ns} n_i \rho_{05,i}}{n}$	$k_n$	$\rho_k$	St. class req.
1	<b>C35</b>	36,0	36,5	1,0	36,0	35,0	13,9	14,1	1,0	13,9	13,0	460,6	442,9	1,0	442,9	390
2	<b>C27</b>	28,1	28,0	1,0	28,0	27,0	12,1	12,7	1,0	12,1	11,5	441,8	429,0	1,0	429,0	360
3	<b>C20</b>	21,9	22,3	1,0	21,9	20,0	11,3	11,5	1,0	11,3	9,5	434,4	416,9	1,0	416,9	330

As seen in Table 7, when the sub-samples with insufficient number of specimens were combined with another one closest to it, the strength classes of Class 1, Class 2, and Class 3 were found as C35, C24, and C20 respectively. In Scots pine, the strength classes of Class 1, Class 2, and Class 3 were found as C35, C27, and C20 respectively.

Red pine is known as the tree of the Eastern Mediterranean basin and it is called Turkish pine because it has its widest growing areas in Türkiye. In Europe it has a limited distribution in the Mediterranean coastal zone in the Balkans and Italy. For this reason, the strength values of the red pine timber from any country were not assigned in the EN 1912 (2024) standard before.

When *Pinus brutia* compared to the other pine species, *Pinus nigra* and *Pinus sylvestris* can be considered as similar timber sources with similar wood densities. In EN 1912 (2024), ME1 (the best) grade *P. nigra* timber from Spain is assigned as C30. Anatolian black pine timber from Türkiye was assigned as C35 for Class 1, C24 for Class 2, and C18 for Class 3. ST-II grade and S2 grade (can be assumed to be second grade) of *Pinus nigra* timber grown in France and Italy were assigned as C24. MEG grade (third grade) *Pinus nigra* timber from Spain and SS grade (first grade) from UK were assigned as C22. ST-III grade black pine timber from France and ME2 from Spain were assigned as C18. Seco et al. (2004) found the strength class of ME1 timber as C35 and ME2 as C18 in Spanish grade *P. nigra*. The strength classes of Scots pine timber from CNE Europe, Northern Europe, Spain vary between C30 in the best visual grades and C14 in the worst visual grades (EN 1912-2024).

In EN 1912 (2024), S13 and S13K grades Scots pine from CNE Europe and T3 grades from Northern Europe were assigned as C30. ME1 grade from Spain was assigned as C27. S10, S10K and SS grades from CNE Europe and T2 grade from Northern Europe were assigned as C24. MEG grade from Spain was assigned as C22. S7 and S7K from CNE Europe, T1 from Northern Europe, ME2 from Spain were assigned C18. GS grade from CNE Europe was assigned as C16 and T0 from Northern Europe was assigned as C14.

In this study, it can be stated the strength classes of Turkish graded red pine and Scots pine timber were found a bit higher than the same or similar pine species grown in Europe.

Stapel and van de Kuilen (2014a) analyzed the effect of different lumber sizes on the classification results by applying the visual grading rules in DIN 4074-1. They stated that many parameters determine the strength class of wood. Regarding strength, wood quality is primarily expressed in terms of the cross-section of the lumber and the knot and knot cluster used to calculate the knot ratios. They showed that both the cross section and the grading method significantly affect the characteristic strength values of Norway spruce. They suggested alternative, simple grading approaches for boards, explaining the limitations of the applicability of the current standard to specific cross-sections. In another study, Stapel and van de Kuilen

(2014b) showed how some selected national standards affect the classification results. The yields or mechanical properties were lower than the declared values depending on the parameters. The results also show the effectiveness and applicability of different national standards for the strength grading of structural timber from various origins. It also recommends reconsidering the limits for weld areas and cross-sections in the EN 1912 standard.

### 3.4 Characteristic Values with Alternative Knot Diameter Ratios

Table 9 and Table 10 show the characteristic values of bending strength, modulus of elasticity and density of each visual grade and corresponding strength classes derived by increasing KDR limits for Turkish red pine and Scots pine, respectively.

As seen in Table 9, when the knot limits were increased from 0.20 to 0.25 for Class 1, from 0.33 to 0.40 for Class 2 and from 0.50 to 0.60 for Class 3, the strength classes were decreased from C35 to C30 for Class 1, from C24 to C20 for Class 2, and from C20 to C18 for Class 3. Similarly, the strength classes of the first-, second- and third-class timber in Scots pine decreased from C35 to C30, C27 to C22 and C20 to C18, respectively.

Table 9. The characteristic values of Turkish red pine derived by increasing KDR limits.

Visual Grade	Strength Class	Characteristic Bending Strength (MPa)		Characteristic MoE (GPa)		Characteristic Density (Kg/m <sup>3</sup> )	
		$1,2f_{05,i,min}$	$\frac{\sum_{i=1}^{ns} n_i f_{05,i}}{n}$	$1,1\bar{E}_{i,min}$	$\frac{\sum_{i=1}^{ns} n_i \bar{E}_i}{n}$	$1,1\rho_{05,i,min}$	$\frac{\sum_{i=1}^{ns} n_i \rho_{05,i}}{n}$
1	C30	31,4	31,5	13,8	13,9	470,9	475,4
2	C20	21,0	24,5	12,0	12,5	479,3	463,6
3	C18	18,4	20,0	11,3	11,5	468,8	457,7

Table 10. The characteristic values of Scots pine derived by increasing KDR limits.

Visual Grade	Strength Class	Characteristic Bending Strength (MPa)		Characteristic MoE (GPa)		Characteristic Density (Kg/m <sup>3</sup> )	
		$1,2f_{05,i,min}$	$\frac{\sum_{i=1}^{ns} n_i f_{05,i}}{n}$	$1,1\bar{E}_{i,min}$	$\frac{\sum_{i=1}^{ns} n_i \bar{E}_i}{n}$	$1,1\rho_{05,i,min}$	$\frac{\sum_{i=1}^{ns} n_i \rho_{05,i}}{n}$
1	C30	35,0	33,0	13,7	14,0	442,5	430,1
2	C22	22,3	25,2	12,0	12,5	435,6	419,0
3	C18	19,2	21,2	10,8	11,3	424,7	410,5

Although the strength classes decreased with increasing KDR limits, the visual grading yield increased as expected. Table 11 compares the number of timber specimens and yielding in each visual class for both current and trial KDR limits. The highest yield increase is seen in Class 1 timber, while the most dramatic decrease is seen in rejected timber.

Table 11. Comparison of the number of timber specimens and yielding of current and trial KDR limits.

Visual Class	Current KDR (TS 1265)	Trial KDR	Yield (%)
Turkish Red Pine			
Class 1	376	540	+43,6
Class 2	393	412	+4,8
Class 3	402	295	-26,6
Rejected	196	120	-38,7
Scots Pine			
Class 1	435	627	+44,1
Class 2	436	463	+6,2
Class 3	443	313	-29,3
Rejected	186	97	-47,8

## 4 Conclusions

The following conclusions may be drawn from the results of this research:

- In Turkish red pine timber graded in accordance with TS 1265 (2012); the strength classes corresponding to Class 1, Class 2, and Class 3 were found as C35, C24 and C20, respectively.
- In Scots pine timber graded in accordance with TS 1265 (2012); the strength classes corresponding to Class 1, Class 2, and Class 3 were found as C35, C27, and C20, respectively.
- In general, the strength classes of both pine species were slightly higher than the values given in the EN 1912 standard for European grown same or similar pine species.
- When the current knot diameter ratio limits in TS 1265 were increased, the strength classes of Class 1, Class 2 and Class 3 red pine timber were decreased to C30, C20 and C18, respectively. Similarly, the strength classes of Class 1, Class 2 and Class 3 Scots pine timber were decreased to C30, C22 and C18, respectively. However, the visual grading yields improved for both pine species.

## 5 References

EN 338 (2016): Structural timber - Strength classes. CEN.

EN 384+A2 (2022): Structural timber - Determination of characteristic values of mechanical properties and density. CEN.

EN 408+A1 (2014): Timber structures - Structural timber and glued laminated timber - Determination of some physical and mechanical properties. CEN.



- EN 1309-3 (2018): Round and sawn timber-Method of measurement – Part 3: Features and biological degradations. CEN
- EN 1912 (2024): Structural Timber - Strength classes - Assignment of visual grades and species. CEN.
- EN 13183-1 (2012): Moisture content of a piece of sawn timber – Part 1: Determination by oven dry method. CEN.
- EN 14358 (2016): Timber structures - Calculation and verification of characteristic values. CEN.
- Eurocode 5 (2004): Design of timber structures - Part 1-1: General and rules for buildings. CEN. (EN 1995-1-1).
- Fernández-Golfín Seco, J. I., Diez Barra, M. R., Hermoso Prieto, E., & Conde García, M. (2004). Mechanical characterization of timber from Spanish provenances of lario pine according to European standards. *Wood science and technology*, 38, 25-34.
- OGM (2020): Annual Report. General Directorate of Forestry.
- Stapel, P., Van de Kuilen, J.-W.G., (2014a): Influence of cross-section and knot assessment on the strength of visually graded Norway spruce. *European Journal of Wood and Wood Products*, 72(2): p. 213-227.
- Stapel, P., Van de Kuilen J.-W.G., (2014b): Efficiency of visual strength grading of timber with respect to origin, species, cross section, and grading rules: a critical evaluation of the common standards. *Holzforschung*, 68(2): p. 203-216.
- TS 1265 (2012): Sawn timber (Coniferous) - For building construction. Turkish Standard Institution (TSE).
- TS 647 (1979): Building Code for Timber Structures. Turkish Standard Institution (TSE).

DISCUSSION

**The paper was presented by T Dündar**

*F Lam received confirmation that grade quality index rules were not available in the European grading system.*

*A Ceccotti commented that there were lots of works presented in the CIB forum on strength grading in the past and this topic is of importance.*



# Strength grading of saturated softwood foundation piles

Giorgio Pagella<sup>1</sup>, Geert Ravenshorst<sup>1</sup>, Michele Mirra<sup>1</sup>, Jan-Willem van de Kuilen<sup>1,2</sup>

<sup>1</sup> Delft University of Technology, Faculty of Civil Engineering and Geosciences, Biobased Structures and Materials, Delft 2628CN, The Netherlands

<sup>2</sup> Technical University of Munich, School of Engineering and Design, Wood Technology, München 80333, Germany

Keywords: timber foundation piles, saturated softwood, strength grading.

**Abstract.** In the next generation of Eurocode 5 (EC5), verification rules for the design of timber foundation piles will be included, together with provisions to determine the required values of material properties. The values given in the current Dutch National Annex to EC5 [20] are based on historical data, without providing strength parameters along the length of the wooden pile. In order to ensure the reliability of material property values for effective design, a large testing campaign was conducted on spruce piles from the Netherlands and pine piles from Germany, where the compressive strength and stiffness were determined on saturated segments extracted from head, middle-part and tip of the piles. The relationships between the compressive strength and parameters characterized with visual grading were investigated. A correlation analysis was conducted including the historical data from literature of other wood species, to investigate the most influencing visually-determined material properties on the compressive strength. Three possible strength classes for the characteristic compressive strength of spruce and pine piles were proposed in relation to visual grading, along with design values calculated according to the new draft of EC5 (2023). The results of this study contribute to the engineering design of European softwood foundation piles, supporting the integration of reliable design values into future versions of Eurocode 5.

## 1 Introduction and scope of the research

Timber foundation piles were historically adopted under buildings and infrastructures in Europe constructed on weak soils [1],[2]. Presently, mostly concrete foundation piles are used. However, in the context of a new circular construction ecosystem, there is a growing interest in using timber foundation piles as exemplified by The Natural Pavilion in Almere (NL) [3] completely built on timber piles in 2022. To enable engineers to adequately design timber foundation piles, verification rules, reliable material properties and grading specifications are required. These aspects have to be considered alongside the fact that wooden foundation piles used under buildings, bridges and quay walls, remain submerged under the water table for their whole service life, enduring high moisture levels. This makes them insusceptible to fungal decay, allowing for the utilization of timber species across all durability classes [4].

However, submerged timber piles may be susceptible to bacterial decay, proceeding at a very slow rate, allowing the piles to perform their function for centuries before showing a substantial reduction of their load-carrying capacity [1],[5]. In this context, the mechanical properties of saturated wooden foundation piles have not been widely studied in literature, and little or no design guidance can be found in timber design standard Eurocode 5 (EC5) [6]. The first inclusion of compressive strength values for timber piles was reported in the Dutch design code for Timber Structures NEN 6760:1997 [7], with a declared 'dry' characteristic compressive strength value for a single wooden pile  $f_{c,0,k} = 19.8$  MPa at 12% moisture content (MC). This value was derived from a statistical analysis in [8] based on compression tests carried out in [9] for saturated European spruce with small average diameters (ca. 140 mm), and length of 900 mm (length-to-diameter ratio close to 1:6 in accordance with EN 408 [17]). The mentioned characteristic value ( $f_{c,0,k}$ ) was recalculated from dry to wet with the modification factor ( $k_{mod}$ ) from the Dutch code NEN 6760 (1997), aligning it with the design practice, where the verification starts from the material properties at MC = 12%, factoring in climate conditions and load durations using  $k_{mod}$  in the calculation. The value of  $f_{c,0,k} = 19.8$  MPa is also used as a basis for values given in the current Dutch National Annex of EC5 2013 [20], although here design values are directly provided.

Since timber foundation piles are only used in saturated conditions, a new approach is chosen in the new draft of EC5 (2023) [21], where saturated compressive strength values are to be determined for timber piles. Moreover, the given  $k_{mod}$  values are only to be used for load duration effects in new defined service class 4. In the Annex P of the draft EC5 2023, verification rules and specifications are provided for the utilization of these material properties, while Annex Q outlines requirements for timber foundation piles to which Annex P applies. The annex P is partly based on the Dutch grading standard for timber foundation piles NEN 5491 [22].

Currently, the compressive strength and stiffness properties available in literature for saturated round wood [8],[9],[10], are not fully comprehensive for a correct design or assessment of timber piles, since they are based on a limited database, without providing grading boundaries and strength parameters spanning from the head to the tip of the pile. The tip is especially critical as, depending on soil conditions, it corresponds to the critical cross section of the pile during service, primarily due to the high stresses associated with its smaller cross section.

Depending on the requested pile-tip diameter, pile length, design project, and soil stratigraphy, the piles are typically sourced from softwood trees. Timber piles are cut at the lower section of the tree trunk ("butt log"), close to the base [11]. However, the material properties of the piles are susceptible to the growing condition of the trees in the forest [12]. Warmer climates accelerate tree growth, resulting in larger diameter and pile tapering, but lower density [13]. Forest management practices [14],[15], guaranteeing optimal spacing among trees, ensure that trees growing in proximity tend to grow straight and tall, while inadequate spacing can result in wider and less

straight growth. Thus, the selection of the tip from a log can imply different material properties, varying with growing conditions and areas, and required length and tip diameter of the timber piles employed in a foundation.

In order to overcome these knowledge gaps, the objectives of this study are:

- The characterization of the mechanical properties of spruce and pine foundation piles to be used together with the provisions in the new Eurocode 5 (2023).
- An investigation in the correlations between visual grading (according to Annex Q of draft EC5 2023) and compressive strength and stiffness along timber piles, in order to derive possible strength classes for an adequate design of timber piles. The correlations also include literature data on spruce, larch and Douglas Fir piles [9].

## 2 Materials

In order to characterize the mechanical properties of wooden foundation piles, 70 full-scale logs were tested, comprising:

- 38 spruce (*Picea abies*) piles felled in 2019 in a forest in Holterberg (NL);
- 32 pine (*Pinus sylvestris*) piles felled in 2019 in a forest in Nuremberg (DE).

All piles had average length of 14 m, mean head diameter ( $D_{\text{head}}$ ) of 290 mm, and a mean tip diameter ( $D_{\text{tip}}$ ) of 135 mm.

## 3 Characterization of the material and mechanical properties

### 3.1 Compression tests parallel to the grain

The full-scale logs were cut into head, middle, and tip segments with a length of approximately 6 times the smallest diameter of the tapered log sections, according to EN 408 [17]. This was done to investigate the compressive strength profile over the length of the tapered piles. During handling and cutting procedures, until the time of the test, the piles were kept submerged in water to avoid drying and consequent cracking, with average MC higher than 70%, well above fiber saturation point [16]. This was done to recreate the same in-soil conditions where the piles were fully under the water table, in order to obtain comparable mechanical and physical properties during testing. Compression tests were performed to determine the saturated short-term compressive strength ( $f_{c,0,wet}$ ) and static modulus of elasticity ( $E_{c,0,wet}$ ) of the pile segments in direction parallel to the grain. A displacement-controlled test setup was used (Fig. 1), where the pile segments were subjected to an axial load in direction parallel to the grain [23], as in [18],[19]. A hinge, mounted on a steel plate, was placed on top of the specimen to have a uniformly distributed compression load on the pile. Four linear potentiometers were mounted on the segment to measure its deformation

(P-sensors in Fig. 1), along its lateral surface, at 90° from each other, and with a variable length equal to 2/3 of the length of the specimen. The tests were conducted at a displacement rate of 0.02 mm/s until the peak load was reached. After the peak load (reached at approximately 5 minutes [17]), the test continued at a higher speed until the cracks were visible, and to show the post-peak behaviour of the pile [23].  $f_{c,0,wet}$  was derived from the ratio between the maximum force reached in compression and the average cross-sectional area of each specimen.  $E_{c,0,wet}$  was calculated with the stress variation ( $\Delta\sigma$ ) divided by the strain variation ( $\Delta\varepsilon$ ), between 10% and 40% in the slope of the linear elastic portion of the stress-strain curve.

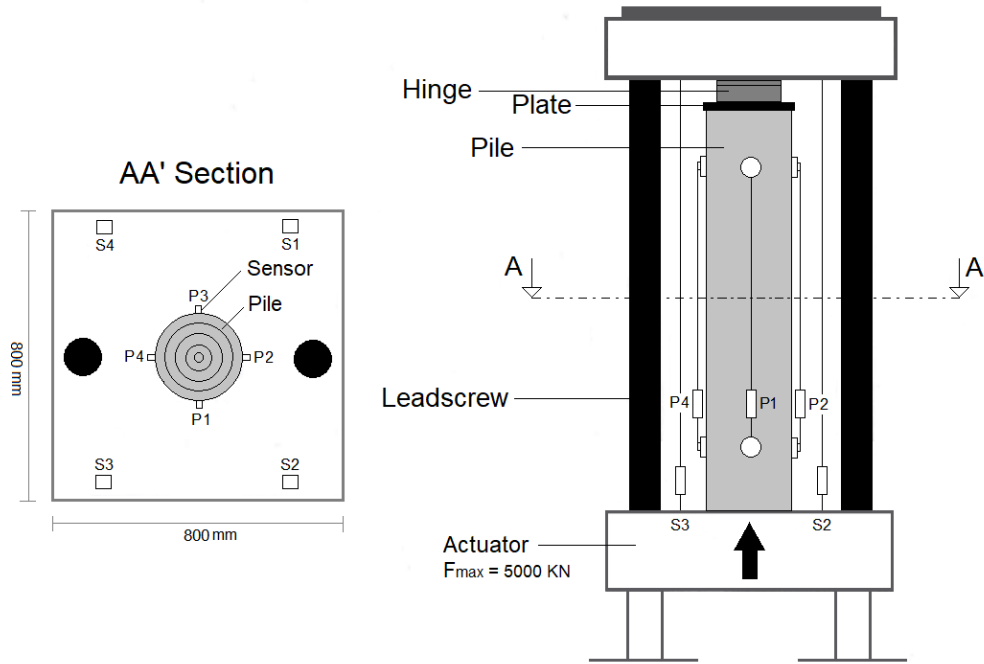


Figure 1: Sensors positioning and set-up for the compression test of pile segments.

### 3.2 Determination of other material properties

The material properties of all pile segments were characterized in order to find their correlations with the saturated compressive strength of the piles. The material properties included:

- Experimentally-determined properties: moisture content ( $MC$ ) and density ( $\rho$ ).
- Visually-graded properties: diameter ( $D$ ), number of annual rings ( $Age$ ), rate of growth ( $RoG$ ), maximum knot-ratio at the failure section ( $KR$ ), slope of the grain ( $SoG$ ) and tapering.

#### 3.2.1 Experimentally-determined properties

$MC$  was determined with the oven-dry method, according to EN 13183 [24], for two 30-mm-thick discs taken from both sides of each selected segment. The global  $MC$  values were related to the full cross-section of the pile. The wet density ( $\rho_{wet}$ ) of each pile segment was calculated from the ratio between its wet mass ( $m_{wet}$ ) and its wet volume ( $V_{wet}$ ) at test  $MC$ , which were both calculated immediately after the calculation

of MC of the discs. In this way MC of the discs could be precisely related to the MC of the pile segment. The dry density  $\rho_{dry}$  (MC = 0%) of each pile segment was also calculated, from the ratio between its dry mass ( $m_{dry}$ ) and its dry volume ( $V_{dry}$ ). The pile segments were not oven-dried due to their large dimensions and number (in total 253 samples, with average length of 1.5 m). Thus,  $V_{dry}$  was calculated from  $V_{wet}$ , assuming an average 12% volumetric shrinkage from green to oven-dry MC for both spruce, pine and fir, according to [16]. In addition to this, the density at MC = 12% ( $\rho_{12}$ ) was calculated, in order to have a standardized value comparable with results in the Standards and literature.  $\rho_{12}$  was determined from the calculated mass  $m_{12}$  (Eq. 1.1) and the volume  $V_{12}$  at MC = 12% (Eq. 1.2). In order to determine  $V_{12}$ , the volumetric shrinkage at MC = 12% was calculated on the basis of the following three assumptions according to [16]: (a) shrinkage starts at the fiber saturation point (MC = 30%); (b) the dimensions of the pile decrease linearly with decreasing MC; (c) variability in volumetric shrinkage can be expressed using a coefficient of variation of approximately COV = 15 %, accounting for wood's intrinsic growth characteristics. Based on this, Equation 1.3 was used to calculate the volume  $V_{12}$  at MC = 12%.

$$\rho_{12} = m_{12} / V_{12} \quad (1.1)$$

$$m_{12} = m_{dry} (1 + u_{ref}) \quad (1.2)$$

$$V_{12} = V_{wet} \cdot (1 - S_0) \cdot (1 - u_{ref} / u_{30}) \quad (1.3)$$

Where:

$u_{30} = 30\%$  moisture content at fiber saturation point (assumed 30% [16])

$u_{ref} = 12\%$  moisture content at 12%.

$S_0 = 12\%$  volumetric shrinkage from green (MC = 30%) to oven-dry (MC = 0%) assumed to be 12% [16] for both pine and spruce.

### 3.2.2 Visually-determined growth characteristics

The visually-determined growth characteristics of the piles can give information on the quality of the material [12],[13],[16]. The diameter of the pile was measured at the pile head and the tip section and classified in sizes [21]. Based on the minimum tip diameter selected for pile, the draft EC5 2023 provides sizes for the piles ranging from 8 – 16, from a minimum diameter of ca. 75 mm (circumference 240 mm, class 8), up to a diameter of 155 mm (circumference of 490 mm, class 16). Age (number of annual rings) was calculated over the radius R, by counting the annual rings (Fig. 2a). RoG was calculated by counting the number of growth rings over the outer 75% of the representative radius of the cross section, in accordance with NEN-EN 1309-3 (2018) [25]. An example is provided in Figure 2, where the pith is eccentric: the length equal to 75% of the radius was divided by the number of growth rings counted, the RoG was expressed in millimeters. KR was measured according to [22], i.e. the ratio between the sum of the knot diameters perpendicular to the longitudinal axis of the log, over a 150 mm length, and the circumference of the log in that section (Fig. 2b). The knots



are wood defects where the fiber deviates, potentially reducing the compressive strength of the pile-segment in the section where they occur [18]. In the present standards [22], KR of round wood has to be less than or equal to 0.5, while the largest knot has to be less than or equal to 50 mm or 1/12 of the circumference. SoG was determined in accordance with [25], (Fig. 2c), where SoG = 1/10 ( $\alpha = 5.7^\circ$ ) is considered as the current highest acceptable value for strength grading according to the draft EC5 2023. However, all SoG values were considered in this study. Finally, the effect of tapering on the mechanical properties was analysed, by measuring the ratio between the difference in diameter of head and tip of the pile segment and its length. A constant taper limited to a maximum of 15 mm/m complies with the grade requirements in [22].

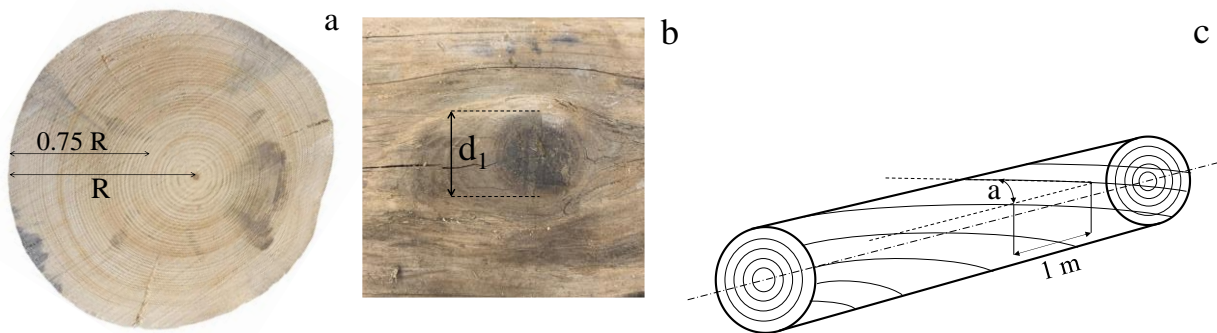


Figure 2: (a) Age over the radius ( $R$ ) and RoG over 0.75 radius for a cross section where the pith is eccentric; (b) diameter ( $d_1$ ) of a knot perpendicular to the longitudinal direction of the log; (c) SoG measurement over a distance of 1 meter.

### 3.2.3 Determination of characteristic values for visual grading

The spruce and pine segments tested in this study were visually graded, defining limits for their saturated characteristic compressive strength values according to the Annex Q and P of the draft EC5 2023. Characteristic values (mean  $E_{c,0,wet}$  and the 5-percentile value of  $f_{c,0,wet}$  and  $\rho_{12}$ ) were determined for spruce and pine piles, according to the parametric calculation in NEN-EN 14358 [26].

The most influencing visually-graded properties on  $f_{c,0,wet}$  were used to calculate one or several Indicating Properties (IPs) by means of multiple linear regression as in Equation 1 [27]. A set of known dependent variables (i.e. a set of values of  $f_{c,0,wet}$ ) and predictor variables (i.e. determined visually-graded properties) were then used to estimate the regression coefficients ( $\beta_m$ ). By choosing predefined limits of the IPs, the pile segment was either assigned to a graded class or rejected. Each  $IP_{SP}$  limit was chosen on the basis of the minimum samples for each grading class ( $\geq 40$ ). The pile's characteristic compressive strength ( $f_{c,0,k,wet}$ ) below the IP limit was calculated with the parametric method in EN 14358 [26]. The calculation is based on Parametric Tolerance Limit (PTL) approach. PTL was defined as the value for which, with a probability of  $\alpha$  (95% confidence level), the  $p\%$  fractile of the underlying population is higher than this value (Eq. 1.5). The approach works with the assumption that the population of data is normally distributed, denoted as  $m_1, m_2, \dots, m_n$ . The  $n$  test values constitute the sample. The saturated characteristic compressive strength of the piles PTL ( $f_{c,0,k,wet}$ ) is expressed

in Equation 1.5. For the calculation, the standard deviation  $S_y$  (Eq. 1.7) was multiplied by a factor  $k(n)$  in Equation 1.8 (the confidence level factor) and subtracted from the mean value  $\bar{y}$  (Eq. 1.6).

$$\hat{y}_j = \hat{\beta}_0 + \hat{\beta}_1 z_{j1} + \hat{\beta}_2 z_{j2} + \dots + \hat{\beta}_m z_{jm} \quad (1.4)$$

$$PTL(f_{c,0,k,wet}) = \bar{y} - k(n) * s_y \quad (1.5)$$

$$\bar{y} = \frac{1}{n} \sum_{i=1}^n m_i \quad (1.6)$$

$$s_y = \sqrt{\frac{1}{n-1} \sum_{i=1}^n (m_i - \bar{y})^2} \quad (1.7)$$

$$k(n) = u_{1-p} + \frac{u_\alpha}{\sqrt{n}} \quad (1.8)$$

Where:

$u_{1-p}$  is the  $(1 - p)$  percentile of the standardised normal distribution function ( $p = 5\%$  was assumed).

$u_\alpha$  is the  $\alpha$ -percentile of the standardised normal distribution function ( $\alpha = 95\%$  was assumed).

## 4 Test results

$f_{c,0,wet}$ ,  $E_{c,0,wet}$  and  $\rho_{12}$  of a total of 253 spruce and pine pile segments, divided in head, middle-part and tip, were characterized in Table 1. No significant difference was found in  $f_{c,0,wet}$ ,  $E_{c,0,wet}$  and  $\rho_{12}$  of spruce heads and middle-parts. For both spruce and pine,  $f_{c,0,wet}$ ,  $E_{c,0,wet}$  and  $\rho_{12}$  show a decreasing trend from the head to the tip, with the tip exhibiting the poorest mechanical properties. The  $f_{c,0,wet}$  values determined along the length of the pile are suitable to be considered for design practice and grading criteria (Paragraph 5.1). In Figure 3, the cumulative distributions of  $f_{c,0,wet}$  of spruce and pine piles are plotted together with  $f_{c,0,wet}$  values from literature: saturated spruce, Douglas fir and larch from Van de Kuilen [8]. While the data available from literature presented in Figure 3 are all softwood piles characterized in fully-saturated conditions, they show a large range of  $f_{c,0,wet}$ , also associated with limited sample sizes in case of Douglas Fir and larch. This highlights the contribution provided by this research, in enlarging the database for the saturated compressive strength of spruce and pine piles. The mechanical properties were defined for spruce and pine segments with diameters ( $D$ ) between 150 mm and 290 mm, assigned to size 13-16 according Annex Q of draft EC5 2023. The correlation analysis was conducted for all the material and mechanical properties at test moisture content ( $MC > 70\%$ ), well above fiber saturation. The correlation matrix was presented both for spruce piles (Tab. 2) and for pine piles (Tab. 3). A strong correlation was found between  $f_{c,0,wet}$  and  $E_{c,0,wet}$  of both spruce and pine. Visually graded parameters such as KR, Age and RoG (Fig. 4) exhibited the highest correlation with  $f_{c,0,wet}$  indicating that factors such as growing conditions and the geographical areas where trees are located can significantly influence Age, RoG, and KR of the piles. Contrarily, diameter (Fig. 4a) and tapering (Fig. 4d) resulted in a very weak correlation with  $f_{c,0,wet}$ . This implies a substantial variability in material properties

even among piles of similar diameter and length, highlighting the contribution of this research in relation to present literature. Finally, all the tested pile segments had SoG < 1:10, higher deviation of grain direction was not measured. This parameter was not included in the correlation analysis. The data of Larch, Douglas fir and spruce characterized in [8] showed highest  $f_{c,0,wet}$  values compared to spruce and pine tested at TU Delft (TUD) for a smaller range of diameter (130-170 mm in Figure 4a) and KR values ranging at 0.2-0.5 (Fig. 4b). The difference in  $f_{c,0,wet}$  could be attributed to a higher quality of the piles in [8], possibly due different growing conditions: higher Age and lower RoG values, even for smaller diameters. Although, this assumption cannot be validated, since age and RoG were not measured in [8].

Table 1: Mean and standard deviation (SD) for saturated stiffness ( $E_{c,0,wet}$ ), compressive strength ( $f_{c,0,wet}$ ) and density ( $\rho_{12}$ ) of spruce and pine segments.

Wood species	Segment	Sample size (No.)	$E_{c,0,wet}$ (MPa)		$f_{c,0,wet}$ (MPa)		$\rho_{12}$ (kg/m <sup>3</sup> )	
			mean	SD	mean	SD	mean	SD
Spruce ( <i>Picea abies</i> )	Head + Middle	81	10500	1300	16.9	2.4	500	44
	Tip	51	8800	1200	14.4	2.1	460	40
Pine ( <i>Pinus sylvestris</i> )	Head	35	11800	1200	21.6	2.4	520	53
	Middle	37	10300	1400	19.1	2.3	490	38
	Tip	49	8600	1100	16.6	2.1	470	37

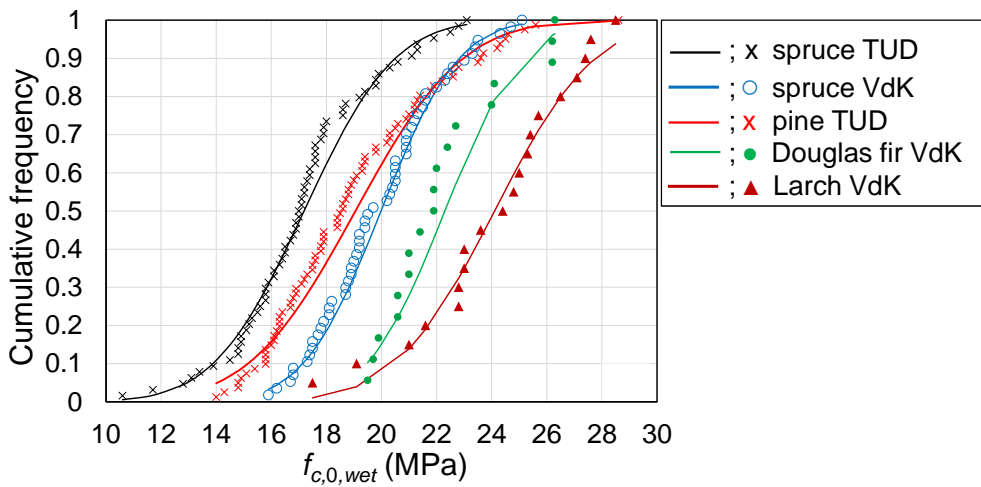


Figure 3: Cumulative distributions of  $f_{c,0,wet}$  for spruce and pine tested at TU Delft (TUD), together with the data from literature: spruce, Douglas fir and larch in Van de Kuilen (VdK) 1994 [8]. The lines show the normal distribution fitted to the data.

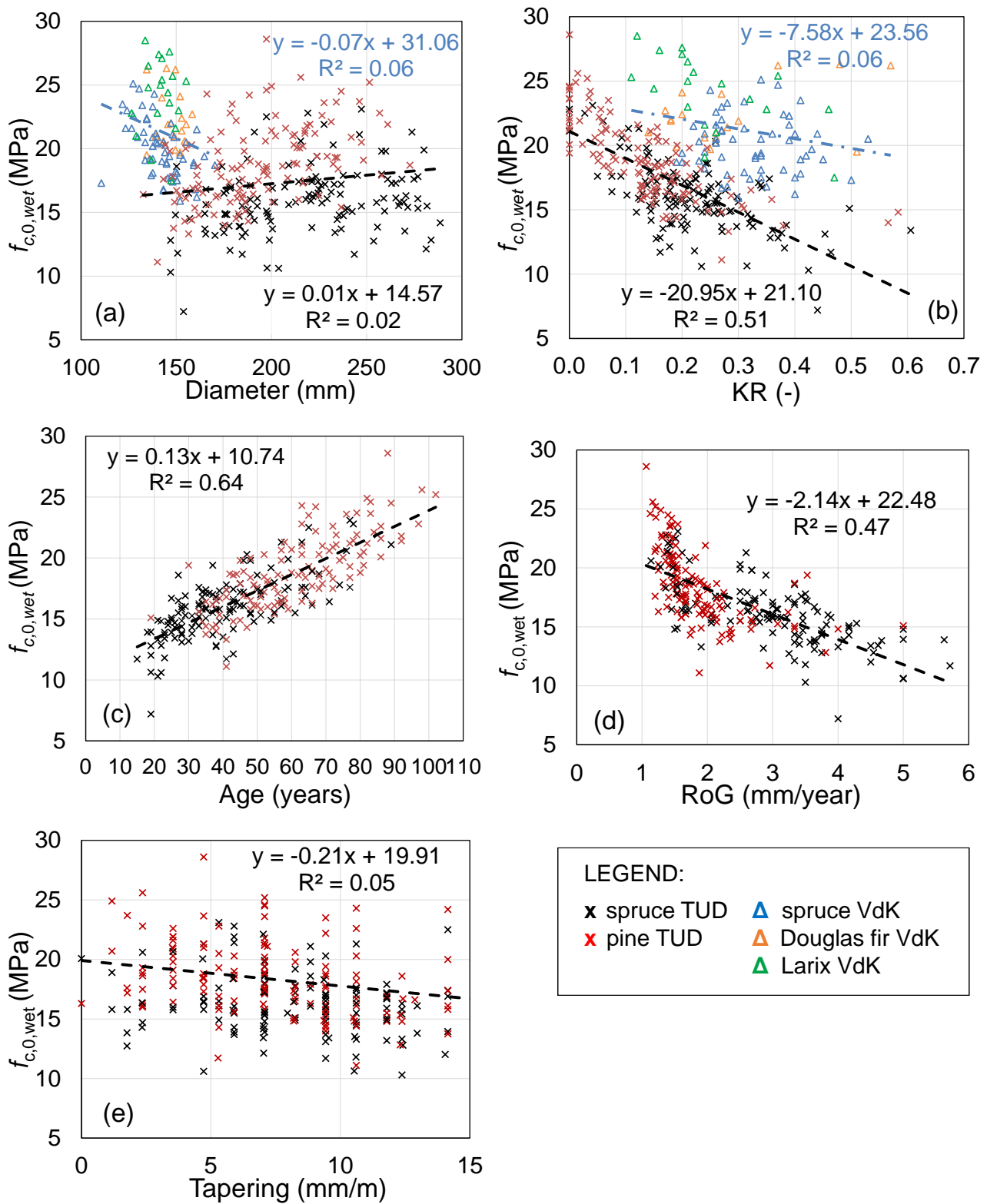


Figure 4: Relationship between  $f_{c,0,wet}$  and (a) diameter, (b) KR; (c) Age; (d) RoG; (e) tapering for spruce and pine (TUD) and literature data from [8].

Table 2. Correlation matrix for all spruce piles

	$f_{c,0,wet}$	$E_{c,0,wet}$	$\rho_{wet}$	$\rho_{12}$	Age	KR	RoG	MC	Tapering	D
$f_{c,0,wet}$	1									
$E_{c,0,wet}$	0.76	1								
$\rho_{wet}$	0.41	0.37	1							
$\rho_{12}$	0.53	0.54	0.62	1						
Age	0.72	0.63	0.34	0.35	1					
KR	-0.60	-0.48	-0.24	-0.24	-0.66	1				
RoG	-0.68	-0.54	-0.28	-0.29	-0.86	0.53	1			
MC	-0.14	-0.19	0.36	-0.49	-0.02	0.02	0.00	1		
Tapering	-0.22	-0.34	0.01	0.04	-0.34	0.37	0.23	-0.05	1	
D	0.27	0.34	0.11	0.10	0.44	-0.48	-0.12	0.01	-0.26	1

Table 3. Correlation matrix for all pine piles

	$f_{c,0,wet}$	$E_{c,0,wet}$	$\rho_{wet}$	$\rho_{12}$	Age	KR	RoG	MC	Tapering	D
$f_{c,0,wet}$	1									
$E_{c,0,wet}$	0.89	1								
$\rho_{wet}$	0.42	0.39	1							
$\rho_{12}$	0.64	0.70	0.70	1						
Age	0.76	0.74	0.24	0.49	1					
KR	-0.72	-0.66	-0.28	-0.46	-0.71	1				
RoG	-0.52	-0.47	-0.20	-0.32	-0.73	0.52	1			
MC	-0.24	-0.36	0.47	-0.28	-0.31	0.21	0.14	1		
Tapering	-0.31	-0.32	0.06	-0.17	-0.41	0.38	0.30	0.34	1	
D	0.46	0.46	0.06	0.29	0.64	-0.49	-0.09	-0.28	-0.32	1

## 5 Analysis

### 5.1 Characteristics values for spruce and pine

Characteristic values of  $f_{c,0,k,wet}$ ,  $E_{c,0,wet}$ , and  $\rho_{12,k}$  of all spruce and pine pile segments are reported in Table 4 in accordance with NEN-EN 14358 (2016). The characteristic values were calculated for visual grading boundaries (according to NEN 5491 2010 and draft EC5 2023), related to: KR < 0.5; Age between 20 and 100 years; RoG < 5 mm/year.

Table 4:  $f_{c,0,k,wet}$ ,  $E_{c,0,wet}$ , and  $\rho_{12,k}$  determined in accordance with the parametric calculation in NEN-EN 14358 (2016) along spruce and pine foundation piles.

Wood species	Segment	Sample size (No.)	$E_{c,0,wet}$ (MPa)	$f_{c,0,k,wet}$ (MPa)	$\rho_{12,k}$ (kg/m <sup>3</sup> )
Spruce ( <i>Picea abies</i> )	All	132	9800	11.3	390
	Head + Middle	81	10800	12.0	410
	Tip	51	8800	10.6	380
Pine ( <i>Pinus sylvestris</i> )	All	121	10000	13.4	410
	Head	35	11800	17.1	440
	Middle	37	10300	14.8	420
	Tip	49	8600	12.9	400

### 5.2 Possible strength classes based on visually-graded properties

KR, RoG and Age were selected as the most influencing properties for visual grading of the pile segments (See Chapter 5). Their cumulative distribution is shown in Figure 5 and Figure 6, for pine and spruce, respectively. All the parameters were normally distributed. Head, middle-part and tip present a distinction in terms of KR, Age, and RoG. Tips feature the highest KR and RoG values and the lowest Age, associated with the poorest mechanical properties (See Table 4).

In the light of this, the tip shall be considered as the critical part of a tapered pile since:

- The tip features the lowest mechanical properties of the pile;
- Depending on soil conditions, the tip corresponds to the critical cross section of the pile, primarily due to the high stresses associated with its smaller cross section.

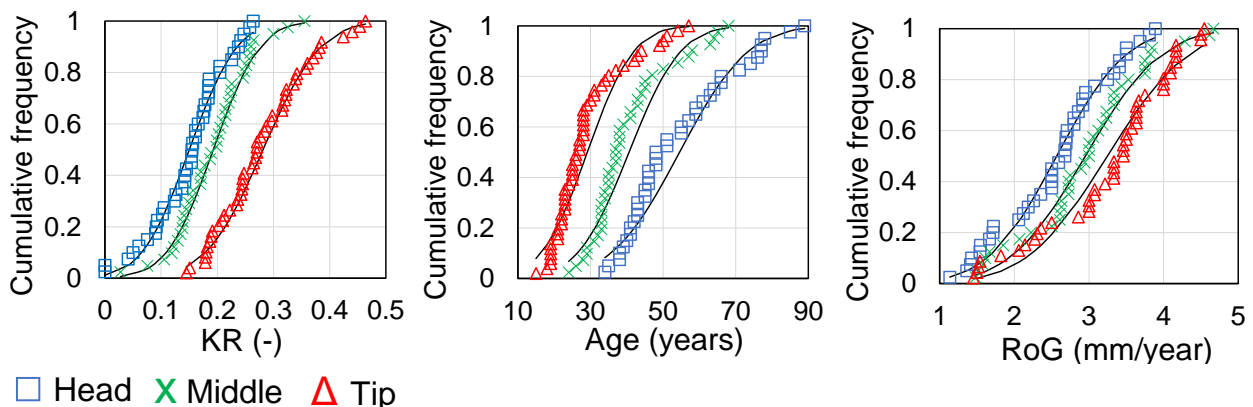


Figure 5: Cumulative distribution of KR, Age and RoG for pine head, middle-part and tip segments. The lines show the normal distribution fitted to the data.

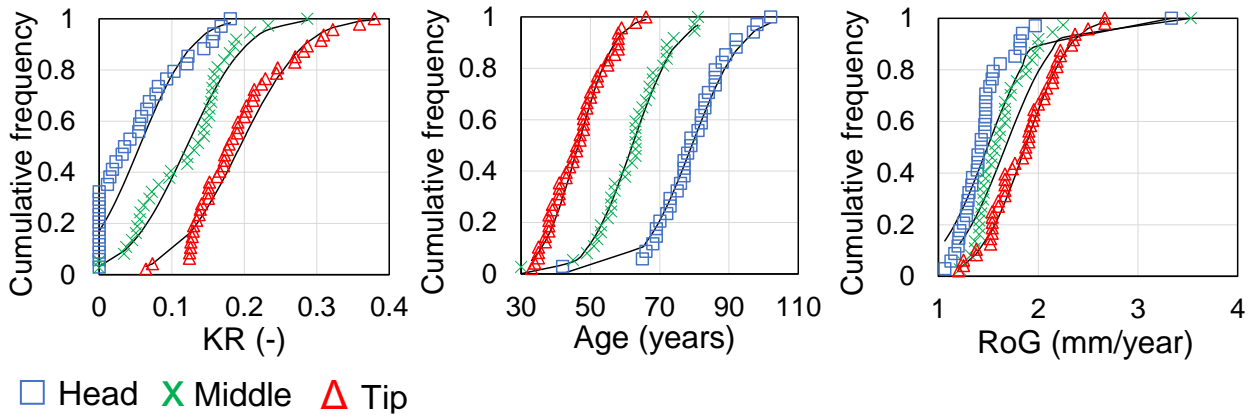


Figure 6: Cumulative distribution of KR, Age and RoG for spruce head, middle-part and tip segments. The lines show the normal distribution fitted to the data.

The possibility of combining spruce and pine for visual grading is studied with Equation 1.9, where  $IP_{SP}$  (SP stands for spruce and pine) is calculated based on common visually-graded independent variables for spruce and pine: KR and Age (Tab. 5). Only KR and Age were statistically significant ( $p$ -value < 0.05 in Tab. 3). Thus, RoG was not taken into account in the regression model. The multiple regression model of  $IP_{SP} (f_{c,0,wet})$  for spruce/pine had a F-value = 261.3 ( $n = 252$ ), a multiple coefficient of determination (adjusted  $R^2$ ) of 0.68 and a standard error of 1.8, indicating a high level of correlation of  $f_{c,0,wet}$  with Age and KR. All multipliers were significant and the residuals had relatively equal variances. The feasibility of combining spruce and pine is supported by Figure 7, where spruce and pine trendlines (calculated in Eq. 1.10) are superimposable and exhibit a similar trend. The results of  $f_{c,0,k,wet}$  for 4 possible grades A, B, C, for combined spruce and pine are presented in Table 6, together with the correspondent  $E_{c,0,wet}$ , and  $\rho_{12,k}$  values associated with that grade.

$$IP_{SP} (f_{c,0,wet}) = 13.92 + 0.097 \text{ Age} - 8.22 \text{ KR} \quad (1.9)$$

The possible grading classes are graphically shown in Figure 8. When grading a wooden pile, the characteristic strength values in Table 6 can be used for both spruce and pine. The visual grading has to be conducted at the tip section, correspondent to the weakest part of the pile. This is independent from the pile size. The grading can be applied also when a pile needs to be cut in smaller lengths to adapt it to different engineering project needs, or re-use it for other applications. In this case, the pile can be re-graded, always at the tip section.

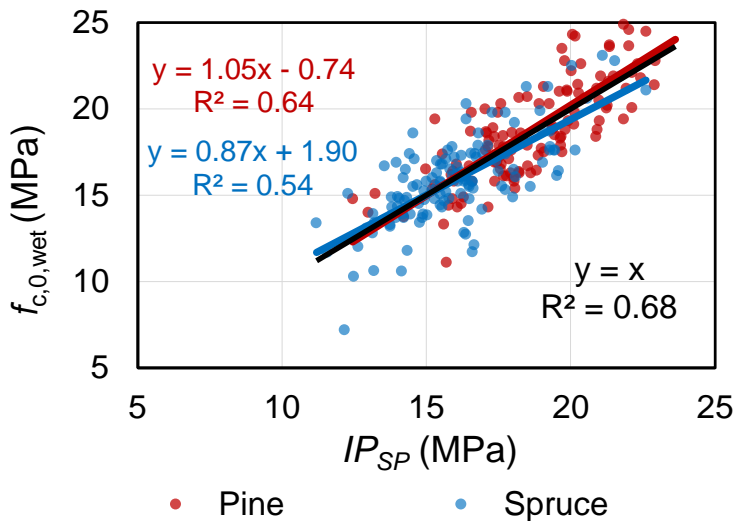


Figure 7: Multiple regression model  $IP_{SP}$  applied separately to spruce and pine.

Table 5: Multipliers and statistical parameters for 95% confidence interval in regression  $IP_{SP}$  for combined spruce and pine.

Variables	Coefficients	Standard Error	t-stat	p-value	Lower 95%	Upper 95%
Intercept	13.925	0.678	20.536	1.4E-55	12.589	15.26
Age	0.097	0.008	11.184	8.18E-24	0.08	0.114
KR	-8.22	1.548	-5.309	2.43E-07	-11.274	-5.172

Table 6: Grading classes A, B, C, for visual grading of pine and spruce pile segments according to draft EC5 2023 and the parametric calculation in NEN-EN 14358: 2016

Species	Possible grading classes	No. of segments (N ≥ 40)	IP limit (MPa)	$f_{c,0,wet}$ (MPa)			$E_{c,0,wet}$ (MPa)			$\rho_{12}$ (kg/m <sup>3</sup> )		
				mean	COV	$x_{05}$	mean	COV	mean	COV	$x_{05}$	
Spruce + Pine	Grade A	97	18.0	20.0	13%	15.1	10600	16%	500	12%	420	
	Grade B	106	15.0	16.4	11%	13.2	9000	17%	480	11%	400	
	Grade C	50	11.0	14.1	14%	10.5	8700	14%	460	10%	380	



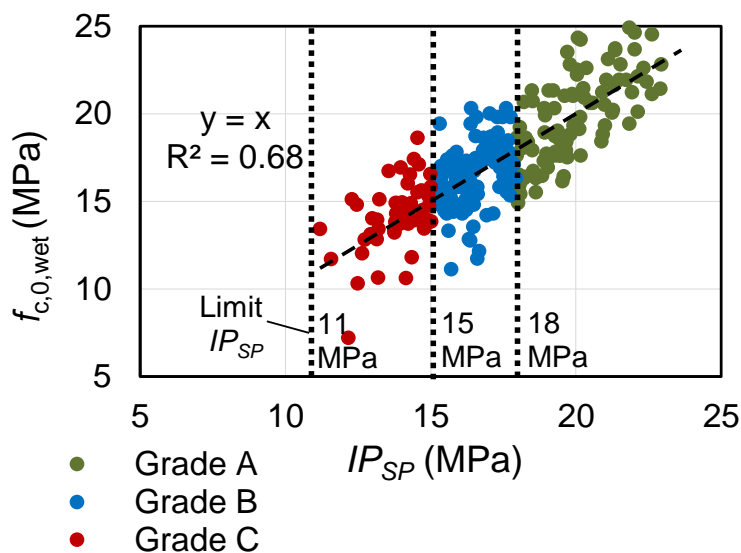


Figure 8: Grades A, B, C, based on  $IP_{SP}$  for combined spruce and pile segments.

### 5.3 Proposal for compressive strength design values according to draft EC5 2023

Based on  $f_{c,0,k,wet}$  correspondent to 3 different strength classes (See Table 6), the design values for engineering design of wooden piles can be calculated according to the indications provided in the draft EC5 2023. Design values are calculated for European spruce and pine in Table 7, by applying modification factors for long-term loading ( $k_{mod,sat} = 0.6$ ) and short-term loading ( $k_{mod,sat} = 0.9$ ), together with partial factors for resistances of timber piles  $\gamma_M = 1.3$  (Ultimate Limit State, ULS) to  $f_{c,0,k,wet}$ . These values do not consider the system strength factor ( $k_{sys} = 1.1$ ), applicable when the load is shared by a minimum of three piles. Table 7 includes also the calculation of design values according to the Dutch National Annex to EC5 2013 (EC5 NB 2013) [20], obtained by applying to the dry characteristic strength value ( $f_{c,0,rep} = 19.8$  MPa) the  $k_{mod}$  (0.7 for short- and 0.6 long-term loading corresponding to service class 3 for high moisture contents) and  $\gamma_M = 1.2$ .

The design values (Tab. 7) calculated according to the draft EC5 2023, based on spruce and pine piles characterized in this study, resulted to be up to 50% lower in long-term loading situations compared to the design values calculated with EC5 NB 2013. This highlights that the current approach in EC5 NB 2013 based on one single dry compressive strength value, might not be adequate for the calculation of design values of wooden foundation piles. More accurate design can be conducted using the provisions in the draft EC5 2023, by adopting directly  $f_{c,0,k,wet}$  and applying  $k_{mod,sat}$  only accounting for the effect of the duration of load in a timber pile, since the effect of moisture is already accounted in  $f_{c,0,k,wet}$  of spruce and pine piles tested in fully-saturated conditions. Furthermore, this research underlines the importance of considering the different strength distribution from the pile head to the tip when calculating the design strength values for tapered timber foundation piles.

Table 7: Design strength values for spruce and pine piles calculated according to the draft EC5 2023 and differences (Diff.) with those according to EC5 NB 2013.

Norm	Species	Grading class	$f_{c,0;rep}$	$f_{c,0,k,wet}$	$f_{c,0;d,short}$	$f_{c,0;d,long}$	Diff.	Diff.	$k_{mod}$	$k_{mod}$	$\gamma_M$
			(MPa)	(MPa)	(MPa)	(MPa)	$f_{c,0;d,short}$	$f_{c,0;d,long}$	$k_{mod,sat}$	$k_{mod,sat}$	ULS
Draft EC5 2023 [21]	EU spruce and pine	A	-	15.1	<b>10.5</b>	<b>7.0</b>	-8	-28	$k_{mod,sat} = 0.9$	$k_{mod,sat} = 0.6$	1.3
		B	-	13.2	<b>9.1</b>	<b>6.1</b>	-21	-38			
		C	-	10.5	<b>7.3</b>	<b>4.8</b>	-37	-51			
EC5 NB 2013 [20]	EU spruce	None	19.8	-	11.5	9.8	-	-	$k_{mod} = 0.7$	$k_{mod} = 0.6$	1.2

## 6 Conclusions

In this study, 132 spruce (*Picea abies*) and 121 pine (*Pinus sylvestris*) pile segments were characterized in saturated conditions, allowing to investigate the distribution of the material and mechanical properties along the piles' length. The mechanical properties resulted to decrease from head to tip. This was related to the variation of the most influencing parameters: knot-ratio (KR), annual rings (Age) and rate of growth (RoG). The tips exhibited the poorest mechanical properties, characterized by the larger number and size of knots and smaller diameters, resulting in higher KR values, lower Age and higher RoG compared to the pile's middle-part and head. Therefore, the mechanical properties of the spruce and pine piles revealed to be governed by the tips. The good correlation between compressive strength and visually-graded parameters opened up the opportunity for grading of multiple strength classes for combined visual grades (KR and Age), for spruce and pine together. The derived strength classes are applicable to the whole pile and/or its parts: head, middle-part and tip. However, the grading has to be conducted at the tip section, since it corresponds to the critical cross section of the pile, featuring the lowest compressive strength and subjected during service to higher stresses due to its smaller cross section. The strength classes proposed in this study are also applicable when a pile needs to be cut in shorter parts to be used for different design purposes; the shorter part can be re-graded to be assigned to a possible different strength class.

Based on the three possible strength classes determined in this research, design values for spruce and pine foundation piles were calculated in accordance with the provisions outlined in the draft of the new Eurocode 5 (2023). These design values resulted to be

up to 50% lower than those calculated according to the current Dutch National Annex to EC5 (2013) based on one single dry compressive strength value. This highlighted that more accurate and reliable design values of timber piles can be obtained according to the approach in the draft EC5 2023, by using saturated characteristic compressive strength values ( $f_{c,0,k,wet}$ ) and the modification factor ( $k_{mod,sat}$ ) applied in the new defined service class 4. Differently from the approach in the Dutch National annex to EC5 (2013),  $k_{mod,sat}$  only accounts for the effect of load duration in the piles, since the effect of moisture is already accounted in  $f_{c,0,k,wet}$  determined in fully-saturated conditions.

This research underlines the importance of considering the different strength distribution from the pile head to the tip when calculating the design strength values for tapered timber foundation piles. Further research will be developed for the prediction of the saturated compressive strength of timber foundation piles based on machine grading. The saturated compressive strength values and grading boundaries presented in this study contribute to the engineering design of timber piles and support the integration of reliable design values into future versions of Eurocode 5.

## 7 References

1. Van de Kuilen, J.W.G., Beketova-Hummel, O., Pagella, G., Ravenshorst, G.J.P., Wolfgang G. (2021). An integral approach for the assessment of timber pile foundations. In: WCTE 2021, pp. 2–8, Santiago, Chile.
2. Klaassen, R.K.W.M. et al. (2005). Preserving cultural heritage by preventing bacterial decay of wood in foundation poles and archaeological sites. Final report EVK4-CT-2001-00043. Wageningen 2005.
3. Natural Pavilion. ([www.thenaturalpavilion.eu/](http://www.thenaturalpavilion.eu/)). Last visited 20-06-2024.
4. Kim, Y.S., Singh, A.P. (2000). Micromorphological characteristics of wood biodegradation in wet environments: A review. IAWA journal 21 (2), 135-155.
5. Klaassen, R.K.W.M. (2008). Bacterial decay in wooden foundation piles—Patterns and causes: A study of historical pile foundations in the Netherlands, Int. Biodeterior. Biodegradation, Vol 61 (1), Pages 45-60, ISSN 0964-8305.
6. EN 1995-1-1 (2010)+AC (2006)+A1 (2008) Eurocode 5: design of timber structures—part 1-1: General—common rules and rules for buildings. CEN.
7. NEN 6760 (1997) TGB 1990: Timber Structures – basic requirements and determination methods. NEN.
8. Van de Kuilen, J.W.G. (1994). Bepaling van de karakteristieke druksterkte van houten heipalen. Toegepast-Natuurwetenschappelijk Onderzoek (TNO), order Nr. 94-con-RO271. Delft, The Netherlands (in Dutch).
9. Buiten, H., Rijdsijk, J.F. (1982). Compressive strength of larch, Douglas fir and spruce piles (in Dutch). Rapport HI 82.1140, Houtinstituut TNO, Postbus 151, 2600 AD Delft, order Nr.: 30.01.1.0002.

10. Aicher, S., Stapf, G. (2016). Compressive strength parallel to the fiber of spruce with high moisture content. *Eur. J. Wood Prod.* 74, 527–542.
11. Ramage, M.H., et al. (2017). The wood from the trees: The use of timber in construction, *Renewable and Sustainable Energy Reviews*, Vol. 68, Part 1, 333-359, ISSN 1364-0321.
12. Chauhan, S., Donnelly, R., Huang, Cl., Nakada, R., Yafang, Y., Walker, J.C.F. (2006). Wood quality: in context. In: *Primary Wood Processing*. Springer, Dordrecht.
13. Zobel, B.J., van Buijtenen, J.P. (1989). The Effect of Growth Rate on Wood Properties. In: *Wood Variation*. Springer Series in Wood Science.
14. Mohren, G.M.J., Vodde, F. (2006). Forests and Forestry in the Netherlands. Forests and forestry in European Union Countries. Arkuszewska, A., Warsaw: The State Forest Information Centre and the For. Research Ins. ISBN 9788389744425, 334 - 352.
15. Spathelf, P., Ammer, C. (2015). Forest management of scots pine (*Pinus sylvestris* L) in northern Germany-a brief review of the history and current trends. *Forstarchiv*. 86. 59-66.
16. Ross, R.J. (2021). Wood handbook wood as an engineering material. Forest Products Laboratory. General Technical Report FPL-GTR-282. Madison, WI: U.S. Department of Agriculture, Forest Service, Forest Products Laboratory. 543 p.
17. EN 408 (2010). Timber structures – Test methods – Pull through resistance of timber fasteners. CEN.
18. Pagella, G., Mirra, M., Ravenshorst, G.J.P., van de Kuilen, J.W.G. (2022). Influence of knots and density distribution on compressive strength of wooden foundation piles. In: *Current Perspectives and New Directions in Mechanics, Modelling and Design of Structural Systems*, 1st ed. CRC Press, London.
19. Pagella, G., Ravenshorst, G.J.P., Gard, W.F., Van de Kuilen, J.W.G. (2024). Characterization of the mechanical properties of saturated spruce (*Picea abies*) and pine (*Pinus sylvestris*) foundation piles. *Journal of Building Engineering*. (Forthcoming).
20. NEN-EN 1995-1-1/NB (2013). Dutch National annex to EC 5: Design of timber structures-Part 1-1: General-Common rules and rules for buildings. NEN.
21. prEN 1995-1-1 (2023). Draft of Eurocode 5: Design of timber structures - Common rules and rules for buildings - Part 1-1: General. NEN.
22. NEN 5491: Quality requirements for wood (KVH 2010) - Piles - European softwood. NEN. (In Dutch).
23. EN 14251 (2003). Structural round timber - Test methods, CEN.
24. NEN-EN 13183-1 (2002). Moisture content of a piece of sawn timber - Part 1: Determination by oven dry method. NEN.
25. NEN-EN 1309-3 (2018). Round and sawn timber - Methods of measurements - Part 3: Features and biological degradations. NEN.

26. EN 14358 (2016). Timber structures – Calculation and verification of characteristic values. CEN.
27. Dharmaraja, S., Dipayan, D. (2018). Introduction to Statistical Methods, Design of Experiments and Statistical Quality Control, Springer Nature Singapore Pte Ltd.

## DISCUSSION

**The paper was presented by G Pagella**

*There was a question whether one would consider a system factor in design. J W van de Kuilen said there is a system factor of 1.1 which could be considered.*

*O Sisman commented that as B and C grades are quite close, one should consider reducing the number of grades.*

*S Aicher commented that B and C grades differentiation was a bit superficial and different KR might be needed.*

*P Dietsch asked if moisture profile of the timber was considered to verify that the piles are saturated over the full cross-section before tetsing. G Pagella said piles were submerged for months and no consideration of moisture profile was taken. Small specimen moisture tests indicated small changes even after one hour.*

*S Aicher stated that the strength at tip of the pile should be considered rather than the strength along the length of the pile, and one should consider which part of the log diameter would not be important. G Pagella said if we only look at the tip KR will not be considered. Other data on the topic could support the findings but relying on data from existing buildings in other parts of Europe would be important but difficult.*



# Fatigue Behaviour of in Tension Axially-Loaded Self-Tapping Screws

Reinhard Brandner

Graz University of Technology, Institute of Timber Engineering and Wood Technology; Inffeldgasse 24/I 8010 Graz, Austria; [reinhard.brandner@tugraz.at](mailto:reinhard.brandner@tugraz.at)

Keywords: low-cycle fatigue; LCF; self-tapping screws; axial-loading; withdrawal; steel-tension

## 1 Introduction

Fatigue describes the decrease in material's resistance with increasing number of load cycles relative to the short-term resistance which is usually determined in monotonic ramp-load tests. The fatigue life or number of cycles until failure  $N$  is usually regulated in dependency of the applied stress level  $SL$  relative to the short-term strength for pulsating and / or alternating cyclic loading. The fatigue life can be separated in "low-cycle fatigue" (LCF; approx.  $N \leq 10^4$ ; plastic deformations expected), "high-cycle fatigue" (HCF; approx.  $10^4 < N \leq 2 \cdot 10^6$ ; elastic domain) and "ultra-high-cycle fatigue", associated with the endurance (fatigue) limit (UHCF; usually  $N > 2 \cdot 10^6$ ). Whereas LCF is of relevance for seismic actions, HCF is decisive for the design of, for example, bridges, lift shafts, crane tracks and wind towers. In case of HCF the relationship  $SL$  vs.  $\log_{10}(N)$  is usually modelled as linear and described by the well-known Wöhler-curve (Wöhler 1870). In case of timber, as radial anisotropic material, the dependency of its properties on the type (tension, compression, bending, shear) and direction of loading (parallel, perpendicular or under an angle to the grain) needs to be considered. There seems to be also an apparent analogy between fatigue and the creep strength, also known as static fatigue or duration-of-load phenomenon (DoL), which describes the relationship between the strength and time under sustained stress, i.e.  $SL$  vs.  $\log_{10}(t)$ ; see Figure 1 (left).

In Europe, the resistance of timber and timber connections against cyclic loading is currently regulated in EN 1995-2 (2004) and based on the comprehensive literature studies and works of Kreuzinger & Mohr (1994) and Mohr (2001). Drafts of the second generation of EC 5 shifted the current fatigue regulations to prEN 1995-1-1 (2023) essentially by adopting, correcting and specifying them. The fatigue design, here in notation of the revised version of EC 5, requires that the characteristic short-term strength  $f_k$  multiplied by the fatigue coefficient  $k_{fat}(R; N) \leq 1$  and divided by the



material safety factor  $\gamma_{M,fat}$  (for timber products and connections  $\gamma_{M,fat} = 1$ ) is higher than the design fatigue stress  $\sigma_{d,max}$ , with

$$f_{fat,d} = k_{fat,EC5}(R_T; N) \frac{f_k}{\gamma_{M,fat}} \geq \sigma_{d,max}, \quad (1)$$

with

$$k_{fat,EC5}(R_T; N) = 1 - \frac{1-R_T}{a_{fat}(b_{fat}-R_T)} \log_{10}(N), \text{ with } N = \beta n_{obs} T_{Lf} \quad (2)$$

and with  $R_T = \sigma_{d,min} / \sigma_{d,max}$  as stress ratio, with  $-1 \leq R_T \leq 1$  and  $|\sigma_{d,min}| < |\sigma_{d,max}|$ ,  $a_{fat}$  and  $b_{fat}$  as coefficients in dependency of the type of fatigue action,  $\beta$  as factor based on the damage consequence of the member, connection or component (1 ... design concept tolerant to damage; 3 ... to avoid substantial consequences of damage),  $n_{obs}$  as the number of constant amplitude stress cycles per year and  $T_{Lf}$  [a] as the design life acc. to EC 0.

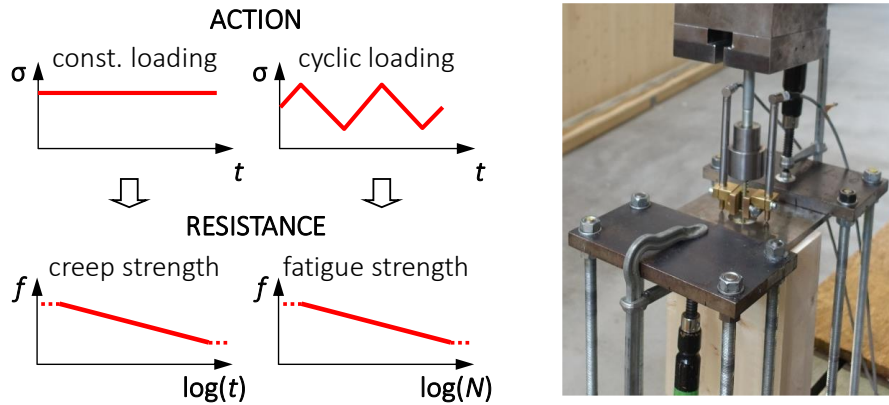


Figure 1. (left) Analogies between creep strength (static fatigue; DoL) and fatigue in timber; (right) push-pull test setup as applied in monotonic and cyclic tests with two opposite placed displacement transducers for local displacement measurement.

With regard to the focus of this work, self-tapping timber screws made of hardened steel could be associated to dowel-type fasteners for which prEN 1995-1-1 (2023) provides factors for nominal diameters  $d \leq 12$  mm with  $a_{fat} = 6.0$  and  $b_{fat} = 2.0$ . However, these coefficients are associated with dowels and fitted bolts which are inserted pre-drilled and usually loaded laterally whereas self-tapping timber screws are primarily loaded axially in tension. Nevertheless, for fasteners such as self-tapping screws, screw rods and glued-in rods loaded in tension comparable regulations are still missing. In this respect it needs to be mentioned, that in Europe self-tapping timber screw products are usually regulated via European Technical Assessments (ETAs). The EAD 130118-00-0603 (2016), as guideline to obtain such an ETA, however, restricts the use of such screws for static / quasi-static actions, i.e. their application in connections subjected to fatigue loading is not permitted.

So far, knowledge on the fatigue behaviour of self-tapping screws is rather limited, in particular with focus on in tension axially-loaded single screws with failure modes withdrawal, head-pull through and steel-tension, as well as groups of screws. Ringhofer (2017) and Ringhofer et al. (2019) investigated the HCF and UHCF behaviour of

single screws loaded in tension. Based on their findings they proposed to regulate such screws via the “detail category 100” acc. to EN 1993-1-9 (2009). Niebuhr & Sieder (2020) found comparable but more conservative results and outlined also the necessity to take also head tear-off fatigue failures into account. Stamatopoulos & Malo (2017) provide some test results on the HCF behaviour of in tension axially-loaded screw rods. By setting the fatigue behaviour of timber in shear analogue to the withdrawal behaviour of screw rods, the regulations in EN 1995-2 (2004) were found to be rather conservative. Compared to glued-in rods, screw rods seem also to be less affected by cyclic loading. This can be argued by the softer embedment of screw rods, c.f. Ringhofer et al. (2019). The same authors report also on some preliminary fatigue tests on self-tapping screws failing in withdrawal indicating a linear relationship between  $SL$  and  $\log_{10}(N)$  also in the LCF domain (approx.  $0 \leq \log_{10}(N) \leq 4$ ) and timber to be less affected by fatigue than the screw itself. For reports on some cyclic tests conducted on single and groups of in tension axially-loaded self-tapping screws aiming on their seismic resistance in case of withdrawal, head-pull through and steel-tension failure c.f. Bratulic et al. (2014), Gavric et al. (2015), Loss et al. (2018) and Hossain et al. (2018).

In conclusion, knowledge on the fatigue behaviour of in tension axially-loaded self-tapping timber screws is insufficient and limited in respect to the investigated failure modes, screw types and cyclic loading regimes, in particular in respect to impulse shape and frequency, parameters generally well-known to affect the fatigue resistance of timber (c.f. Marsoem et al. 1987; Okuyama et al. 1984; Majumdar & Maiya 1980; Okazaki et al. 1985; Gong & Smith 2003; Sugimoto & Yasutoshi 2006), and also in respect to possible analogies between fatigue and static fatigue (DoL) (c.f. Kohara & Okuyama 1992; Kreuzinger & Mohr 1994; Clorius et al. 2000; Mohr 2001; Clorius et al. 2009).

Motivated by the identified knowledge gaps related to the fatigue behaviour of in tension axially-loaded self-tapping timber screws, a comprehensive test campaign was established with focus on their LCF behaviour and on the failure mode withdrawal. The aim of this paper is to contribute to the existing knowledge on the fatigue behaviour of self-tapping timber screws. Furthermore, it is aimed to add knowledge on the successive cumulative damage of screws exposed to pulsating cycling loads failing in withdrawal as well as steel-tension by analysing the development of the slip modulus in loading and unloading phases, and the displacement at the upper load levels over the fatigue life, as well as to add some information on the influence of different impulse shapes on the fatigue life.

## 2 Materials and Methods

### 2.1 Test plan overview

For analysing the fatigue behaviour of in tension axially-loaded self-tapping timber screws with target failure mode withdrawal, the following parameter variations were

conducted: load-grain angle  $\alpha = \{0; 45; 90\}^\circ$ , expected fatigue life  $N_{\text{exp}} = \{10^1; 10^2; 10^3\}$  and impulse shape {triangle (as reference); trapezoidal}. This was done within nine cyclic test series with 15 replicates each and fixed  $R = 0.10$  in the LCF domain; see Table 1. In addition, three monotonic test series were necessary for determining the reference short-term withdrawal properties for the thread-grain angles  $\alpha = \{0; 45; 90\}^\circ$ , each with 20 replicates.

Table 1. Cyclic tests – final test plan: overview and series names;  $R = 0.10$ .

$\alpha$ ; impulse shape \ $N_{\text{exp}}$	$10^1$	$10^2$	$10^3$
$0^\circ$ ; triangle	F001A	F002A	–
$45^\circ$ ; triangle	F451A	F452A	F453A
$90^\circ$ ; triangle	F901A	F902A	F903A
$90^\circ$ ; trapezoidal	–	–	F903B

## 2.2 Tested materials

In all tests fully-threaded timber screws (Rapid®; ETA-12/0373 2020; Schmid Schrauben Hainfeld GmbH) from one batch were used. The screws featured a nominal diameter of  $d = 10$  mm and a total length of  $l = 200$  mm. They were inserted self-tapping, over an effective length of  $l_{\text{ef}} = 10 d = 100$  mm (excl. the tip length) and centricly in the middle layer of three-layer cross laminated timber (CLT) specimens made of Norway spruce (*Picea abies*) with layup 30 | 40 | 30 mm, built up of boards with a nominal strength class C24 / T14 acc. to EN 338 (2016) and conditioned at reference climate (20 °C & 65 % rel. humidity). Although conducted in CLT, the tests mirror withdrawal tests in structural timber (see e.g. Brandner et al. 2018). In preparing the specimens it was aimed on maximising the variety in tested boards within each series by minimising the variety between the series as far as possible. Furthermore, care was taken to ensure that each screw was anchored only in one board which was enabled by the 120 mm wide boards in the CLT middle layer.

## 2.3 Methods

### 2.3.1 Monotonic and cyclic “push-pull” withdrawal tests

All monotonic and cyclic tests were carried out at the universal testing frame “lignum\_uni\_275” (Z250; ZwickRoell) at the Lignum Test Centre (LTC; Institute of Timber Engineering and Wood Technology, Graz University of Technology) by means of a “push-pull” setup and specimen dimensions acc. to EN 1382 (1999). The measurement rate was 5 Hz in the monotonic (reference) tests and 50 Hz (at least for the first  $\approx 750$  load cycles) in the cyclic tests. In the monotonic tests time-to-failure was within  $90 \pm 30$  s which corresponds to a testing speed of approx. 2 mm/min, whereas it was 500 mm/min in the loading and unloading phases in the cyclic tests. In case of triangle impulses (type A) no holding time, neither at the lower nor at the upper load level, was applied, whereas it was 3 s at the lower and upper load levels in case of the trapezoidal impulses (type B). The local displacement was measured by means of two opposite placed displacement transducers; see Figure 1 (right). These displacement

transducers were left on the specimens over the whole testing period. The local displacement was calculated by averaging the measurements from both displacement transducers and by subtracting the extension of the free thread length which was calculated with a modulus of elasticity for steel of 210 GPa and for an effective cross section of the threaded part in the elastic stage acc. to Ringhofer (2017). The corrected load-displacement data served as basis for determining the slip modulus  $K_{ser}$  in the linear elastic part acc. to EN 408 (2012). During insertion of the screws care was taken on correct anchorage depth ( $l_{ef} = 100$  mm) and insertion angle  $\alpha$  by means of a screw-in aid; all specimens were prepared to allow screw insertion orthogonal to the specimen's surface. In some cases, screws penetrated knots or touched a knot or other local growth characteristic, such as bark inclusions or reaction wood, along the screw channel. Such tests were explicitly enabled but left to chance. To know more about the possible occurrence of local growth characteristics along the screw channel, after determining the local density acc. to ISO 13061-2/A1 (2017) and the moisture content acc. to EN 13183-1 (2004) on small specimens enclosing the tested zone each specimen was split centrally along the screw channel and analysed by recording all observations as well as the position and length of penetrated and touched local growth characteristics. The density was corrected to the reference moisture content  $u_{ref} = 12$  % acc. to EN 384 (2016). For more details on the monotonic tests, see Eckert & Brandner (2023), and on the cyclic tests, see Brandner & Eckert (2024).

As the LCF domain is dedicated to the ductile part of materials, i.e. that part in which plastic deformations occur, information on the transition region between the linear-elastic and ductile load-displacement curve was needed. Therefore, the modified "Glos model" (originally published in Glos 1978, modified by Brandner et al. 2018 and further optimised by Obermüller 2020), which consists of a linear and a non-linear part, was calibrated to each reference data set.

### **2.3.2 Monotonic steel tension tests on screws**

To know more about the tensile capacity and strength of the screws, from the same batch six screws were randomly selected for determining the geometric parameters and five screws for determining the steel tensile capacity. This information together with the effective cross section calculated acc. to the theory of plasticity (see Ringhofer 2017) was used to compute the tensile strength of the screws. Furthermore, by applying the approach of Obermüller (2020) again the transition region between the linear-elastic and ductile domain was determined.

### **2.3.3 Fatigue models considered in planning and evaluating of cyclic tests**

As already mentioned, versions of EC 5 (EN 1995-2 2004; prEN 1995-1-1 2023) do not provide any regulations for the fatigue resistance of axially-loaded fasteners and thus also none for in tension axially-loaded self-tapping timber screws. With focus on the failure mode withdrawal and depending on the load-grain angle  $\alpha$  it can be concluded that the timber surrounding the thread is mainly stressed in (rolling) shear and compression. By considering this, for a first estimation of the fatigue resistance

of axially, in tension loaded timber screws, the fatigue coefficients for shear could be applied (c.f. also Stamatopoulos & Malo 2017), with  $a_{fat} = 6.7$  and  $b_{fat} = 1.3$ , which gives a significantly lower fatigue resistance than currently regulated for laterally-loaded dowel-type fasteners.

Kreuzinger & Mohr (1994) used a slightly different formulation for the coefficient  $k_{fat}(R; N)$ , given as

$$k_{fat,KM}(R; N) = a + b(1 - R) \log_{10}(N), \text{ with } a = 1 \text{ and } b = -\frac{1}{a_{fat}(b_{fat}-R_T)} \quad (3)$$

Following the same analogy as before, based on the outcomes in Kreuzinger & Mohr (1994) for pulsating cyclic loading in shear the coefficients  $a = 1.00$  and  $b = -0.10$  are found. Later, Mohr (2001) introduced three fatigue classes in his design proposal and assigned pulsating as well as alternating cyclic loading in shear to class III, with

$$k_{fat,M}(R; N = 10^7) = 0.070 \cdot R^3 + 0.267 \cdot R^2 + 0.330 \cdot R + 0.333 \quad (4)$$

Based on boundary conditions for  $k_{fat,M}(R; N)$ , Mohr (2001) formulated three areas, with a linear relationship between  $k_{fat,M}(R)$  and  $\log_{10}(N)$  within  $0 \leq \log_{10}(N) \leq 4.5$ , the LCF domain. Given  $R \geq 0$ , for  $k_{fat,M}(R; N)$  the following simplification is made:

$$k_{fat,M}(R; N) = 1 - \frac{1 - k_{fat,M}(R; N = 10^7)}{\log_{10}(10^7)} \log_{10}(N) \quad (5)$$

For  $R = 0.10$  this formulation gives similar results as Eq. (3) whereas it becomes slightly conservative for higher values of  $R$ . Because of similar values for  $k_{fat}(R; N)$  given  $R = 0.10$  acc. to Eq. (3) and Eq. (5), for planning of the test campaign and evaluating the outcomes the simpler function of Kreuzinger & Mohr (1994; Eq. (3)) with the corresponding coefficients for shear  $\{a = 1.00; b = -0.10\}$  was applied.

In the conception phase of the cyclic tests acc. to the horizon method the expected fatigue life was set to  $N_{exp} = \{10^1; 10^2; 10^3\}$ . Based on  $N_{exp}$  and  $R$  the corresponding values for  $k_{fat,exp}(R; N)$  were calculated and used further to set the average upper and lower load levels, respectively, with  $F_{ax,UL} = k_{fat,exp}(R; N) F_{ax,mean,ref}$  and  $F_{ax,LL} = R F_{ax,UL}$ .

To enrich the information on cyclic tests with failure mode withdrawal and to allow for harmonisation of test outcomes in cases of deviating densities between the test series, the individual short-term withdrawal capacity was estimated acc. to the individual local density of each specimen following the proposal in Ringhofer et al. (2015) and Ringhofer (2018), with

$$F_{ax,\alpha,i,est} = F_{ax,\alpha,mean,ref} \left( \frac{\rho_{12,i}}{\rho_{12,\alpha,mean,ref}} \right)^{k_p} \quad (6)$$

with  $k_p = 1.10$  for  $\alpha = \{90; 45\}^\circ$  and  $k_p = 0.75$  for  $\alpha = 0^\circ$ . By means of this information individual fatigue coefficients  $k_{fat,W,est,i} = F_{ax,UL} / F_{ax,\alpha,i,est}$  could be calculated and individual fatigue lives  $N_{est,i,W}$  back-calculated from Eq. (3).

To gain knowledge on the development of the slip modulus in the loading and unloading phases of the cyclic tests, as well as of the displacement at the upper load

levels over the fatigue life, test series {F902A; F452A; F002A} were analysed in more detail.

To estimate the fatigue life of screws in tension in the planning phase of the cyclic tests, the proposal of Ringhofer et al. (2019) to apply “detail category 100” acc. to EN 1993-1-9 (2009) was followed, with

$$\Delta\sigma_R^m N_R = \Delta\sigma_C^m \cdot 2 \cdot 10^6 N_R, \text{ with } \Delta\sigma_C = 100, m = 3 \text{ and } N_R = N \leq 5 \cdot 10^6 \quad (7)$$

and  $\Delta\sigma_R$  as stress amplitude. Data on later partly observed steel-tension fatigue failures of screws was used to calculate the corresponding fatigue coefficient

$k_{\text{fat},T,\text{est},i} = F_{\text{ax},\text{UL}} / F_{\text{tens,max},i}$  and to calculate the fatigue life from Eq. (7).

## 3 Results and Discussion

### 3.1 Main outcomes of the reference steel-tension and withdrawal tests

The main statistics of the geometry and the tensile properties of the screws are summarised in Table 2, those of the monotonic withdrawal tests in Table 3. These are separated in statistics for “all specimens” and in those “without knots”.

Table 2. Main statistics of the geometric parameters & steel-tension properties determined on randomly chosen screws.

RAPID® 10 × 200	$d^{1)}$ [mm]	$d_1^{1)}$ [mm]	$p^{2)}$ [mm]	$l$ [mm]	$l_{\text{tip}}$ [mm]	$F_{\text{tens,max}}$ [kN]	$f_{\text{u,el}}$ [MPa]	$f_{\text{u,plas}}$ [MPa]
no. [-]	6	6	6	6	6	5	5	5
$X_{\text{mean}}$	9.97	6.55	4.64	198.65	14.71	46.12	1,175	1,335
CV[x] [%]	1.16	0.89	0.25	0.05	2.44	0.52	0.52	0.52

<sup>1)</sup> average values from three measurement per screw; <sup>2)</sup> average values over ten convolutions per screw

The outcomes in brief: the steel-tension properties are high but within a typical range for the tested screw type. By analysing the outcomes of the load-displacement model acc. to Obermüller (2020) calibrated to the screw test data, for the ratio between the load at the transition from linear-elastic to the non-linear part and the maximum load of ( $F_{\text{el}} / F_{\text{max}}$ ) on average 47 % (CV = 6.6 %) are found. As a consequence, the proportional limit is on average approx. at 21.7 kN which means, that during the cyclic tests the screws should be only loaded within the linear-elastic part.

The average moisture content of the monotonic reference test series is close to the reference value of 12 % whereas there is some unexpected variation in the average densities between the series. Whereas the values for  $\alpha = \{0; 45\}^\circ$  are typical for the nominal board strength class C24 / T14, in case of  $\alpha = 90^\circ$  the densities are clearly higher. The variabilities in the density as well as in the withdrawal properties, expressed as coefficients of variation, are higher than usual with the advantage of representing a wider bandwidth of the tested material. The differences in the statistics for “all” and those specimens “without knots” are overall small. By explicitly allowing knots also in the cyclic tests, for the reference values the statistics “all” apply. In the withdrawal tests the average values for the ratio  $F_{\text{el}} / F_{\text{max}}$  are approx. {75; 50; 55} %, respectively, for  $\alpha = \{0; 45; 90\}^\circ$ . The average values of the displacements at

maximum load  $w_{f,mean}$  clearly underline the less ductile behaviour of parallel to the grain inserted screws compared to those inserted inclined or perpendicular to the grain.

Table 3. Main statistics from monotonic withdrawal tests (reference tests).

	RF-00		RF-45		RF-90	
	all	excl. knots	all	excl. knots	all	excl. knots
no. [-]	20	16	20	19	20	17
$u_{mean}$ [%]	11.0	11.1	11.1	11.1	10.9	10.9
$\rho_{12,mean}$ [kg/m <sup>3</sup> ]	433	416	429	430	451	448
CV[ $\rho_{12}$ ] [%]	13.5	12.6	10.1	10.3	10.5	11.3
$F_{max,mean}$ [kN]	12.46	11.47	18.03	18.19	21.57	20.33
CV[ $F_{max}$ ] [%]	35.4	34.0	25.6	25.8	20.0	15.9
$f_{ax,mean}$ [MPa]	4.00	3.68	5.79	5.84	6.97	6.57
CV[ $f_{ax}$ ] [%]	35.1	33.5	25.1	25.2	19.9	20.8
$f_{ax,05}$ [MPa]	2.17	2.13	4.06	4.08	4.93	4.96
$K_{ser,mean}$ [kN/mm]	26.8	25.5	29.2	29.3	30.6	29.7
CV[ $K_{ser}$ ] [%]	22.7	21.4	24.4	24.8	17.3	17.8
$(F_{el} / F_{max})_{mean}$ [%]	74.7	74.4	47.3	46.7 (55.0 <sup>1)</sup> )	53.6	53.8
$(w_{lin} - w_{ini})_{mean}$ [mm]	0.34	0.33	0.30	0.30	0.38	0.38
$w_{f,mean}$ [mm]	0.80	0.77	1.15	1.15	1.55	1.54

<sup>1)</sup> excl. knots and extreme values

### 3.2 Main outcomes of the cyclic tests

#### 3.2.1 Excluded specimens

Based on the recordings made in parallel with the tests and subsequent data analyses, the following specimens had to be excluded from further analysis: F902A-14 because of an obvious mistake in the determined density and moisture content. In F451A-06, F001A-13, F452A-02, F452A-09, F452A-11, F452A-13, F902A-02 and F453A-11 the insertion of the screw was apparently not orthogonal to the specimen's surface which partly caused a horizontal movement of the screw in the hole of the supporting steel plate ( $d_h = 40$  mm) during the pulsating cyclic tests which in two cases even led to a contact of the screw with the steel plate. Specimens F001A-04 and F002A-06 featured extremely high fatigue lives, which, from the statistical point-of-view, were identified as extreme values. All those specimens were further excluded from data analyses as their influence on the final results is partly unclear as well as because of their obvious influence on some statistics, in particular on average values and coefficients of variation.

#### 3.2.2 Main statistics and observations

The main statistics of the fatigue tests are summarised in Table 4. As in most of the test series in addition to withdrawal also steel-tension failures occurred, the statistics are separated in withdrawal (W) and steel-tension (T). Groups of less than three valid specimens per test series and failure mode are not considered. As a consequence, for

series F453A only statistics for those specimens which failed in steel-tension are provided as only two of twelve finally tested specimens failed in withdrawal.

By looking at the statistics in Table 4 it is found that the average moisture content in the cyclic tests is overall 1 % higher than in the monotonic reference test series and well aligned with the reference moisture content  $u_{ref} = 12$  %. The average densities of the cyclic tests which failed in withdrawal vary between 408 and 466 kg/m<sup>3</sup>. The average densities for the steel-tension failures are clearly higher than those of the withdrawal failures of the same series and vary between 444 and 509 kg/m<sup>3</sup>. This observation aligns with the expectation that steel-tension failures are apparently more likely at higher densities. The observed fatigue lives within one series, i.e.  $N_{obs}$ , spans partly over five powers of ten and in other series only over one power of ten which expresses also in high coefficients of variation in the range of 100 to 200 % in case of withdrawal and 20 to 40 % in case of steel-tension failures. This means that the variation in fatigue lives is roughly ten-times higher than that of the corresponding strengths and capacities determined from monotonic tests. Clorius et al. (2000), for example, report comparable variations for the fatigue life in the range of 70 to 170 % from cyclic tests on timber loaded in compression parallel to the grain.

The average values of the individually and according to their density adjusted withdrawal capacities,  $F_{ax,est,mean}$ , are provided. Based on the individual capacities  $F_{ax,est,i}$  individual fatigue coefficients  $k_{fat,est}$  and individual fatigue lives  $N_{est}$  were calculated, latter for withdrawal failures by means of the approach of Kreuzinger & Mohr (1994; Eq. (3)) and for steel-tension failures by following the proposal of Ringhofer et al. (2019; Eq. (7)). With a look on the average and median values of the ratio ( $N_{obs} / N_{est}$ ) it turns out that the fatigue lives in absolute values (not on a logarithmic scale) in case of withdrawal are clearly underestimated whereas those in case of steel-tension go in the opposite direction, i.e. the median values  $(N_{obs} / N_{est})_{50}$  are between 0.40 and 23 for the withdrawal and between 0.43 and 0.57 for the steel-tension failures. The range in mean values is even larger which is because of the highly right-skewed fatigue lives. This characteristic consequence a lot of bias in mean values and coefficients of variation as both statistics are highly sensitive to extreme values. Median values provide significantly more stable statistics for estimating the location of the data and are also preferred in the literature. In principle, the fatigue lives of those specimens which failed in steel-tension prior to the target failure mode withdrawal are right-censored. It would be easy to consider this in the statistical analysis but this is not recommended. The reason is the clearly different behaviour of screws failing in steel-tension compared to those failing in withdrawal. Figure 2 shows typical load-displacement curves from fatigue tests. Whereas the behaviour within the first cycles is similar, in case of steel-tension the overall displacement seems to become constant whereas it steadily increases from cycle to cycle for screws which finally failed in withdrawal. Apart from this, the graphs in this figure also outline the non-linearity in the load-displacement curves close to the upper load level as a typical characteristic of cyclic tests in the LCF domain.



Table 4. Main statistics from cyclic tests separately for withdrawal (W) and steel-tension failures (T).

	F901A		F451A		F001A		F902A		F452A		F903A		F453A		F903B		F903B		
	W	T	W	T	W	T	W	T	W	T	W	T	W	T	W	T	W	T	
$\rho_{12,ref,mean}$ [kg/m <sup>3</sup> ]	451	429	433	451	451	429	433	451	451	451	451	451	451	451	451	451	451	451	451
$F_{ax,ref,mean}$ [kN]	21.57	18.03	12.46	21.57	21.57	18.03	12.46	21.57	21.57	18.03	12.46	21.57	21.57	18.03	12.46	21.57	21.57	21.57	21.57
$F_{tens,mean}$ [kN]																			
R	0.10	0.10	0.10	0.10	0.10	0.10	0.10	0.10	0.10	0.10	0.10	0.10	0.10	0.10	0.10	0.10	0.10	0.10	0.10
$F_{ax,ul}$ [kN]	19.75	16.47	11.47	17.79	17.79	14.84	10.33	15.84	15.84	14.84	10.33	15.84	15.84	14.84	10.33	15.84	15.84	15.84	15.84
$F_{ax,ll}$ [kN]	1.97	1.65	1.15	1.78	1.78	1.48	1.03	1.58	1.58	1.48	1.03	1.58	1.58	1.48	1.03	1.58	1.58	1.58	1.58
$N_{exp}$ [-]	10	10	10	100	100	100	100	100	100	100	100	1,000	1,000	1,000	1,000	1,000	1,000	1,000	1,000
$k_{fat,exp}$ [-]	0.92	0.91	0.92	0.82	0.82	0.82	0.83	0.73	0.73	0.82	0.83	0.73	0.73	0.73	0.82	0.73	0.73	0.73	0.73
$n$ ( $n_{knots}$ ) [-]	15 (1)	14 (3)	11 (1)	10 (0)	10 (0)	8 (1)	12 (0)	12 (0)	12 (0)	8 (1)	12 (0)	12 (0)	12 (0)	9 (1)	11 (2)	11 (2)	11 (2)	11 (2)	4 (1)
$\mu_{mean}$ [%]	12.1	12.1	12.0	11.7	11.7	12.1	12.0	11.7	12.1	12.1	12.0	11.7	11.7	11.9	11.8	11.7	11.7	11.7	11.8
$\rho_{12,mean}$ [kg/m <sup>3</sup> ]	448	431	411	466	466	408	443	443	443	408	443	417	443	444	443	443	443	443	491
CV[ $\rho_{12}$ ] [%]	10.2	7.5	14.3	4.8	4.8	6.2	11.2	6.4	6.4	6.2	11.2	6.4	6.4	3.2	7.7	9.1	9.1	9.1	4.1
$f_{mean,mean}$ [Hz]	0.70	0.77	0.82	0.72	0.72	0.76	0.94	0.76	0.76	0.76	0.94	0.76	0.76	0.82	0.86	0.14	0.14	0.14	0.14
$N_{obs,mean}$ [-]	195	1974	3.03	2,077	2,077	94.1	15,524	2,320	3,477	94.1	15,524	2,320	3,477	14,384	28,597	2,822	2,822	2,822	15,745
$N_{obs,50}$ [-]	58.0	35.0	0.48	1,235	1,235	68.5	14,813	168	1,212	68.5	14,813	168	1,212	13,064	28,006	732	732	732	14,180
CV[ $N_{obs}$ ] [%]	138	188	206	117	117	110	188	147	147	110	188	147	147	38.3	26.6	123	123	123	37.2
range[ $N_{obs}$ ] [-]	0.44/743	0.14/11,363	0.34/21	20/8,189	20/8,189	1.5/312	7,316/31,218	0.46/11,636	34/16,654	1.5/312	7,316/31,218	0.46/11,636	34/16,654	9,661/20,428	17,674/40,689	3/8,887	3/8,887	3/8,887	10,546/24,075
$F_{ax,est,mean}$ [kN]	21.43	18.11	11.96	22.35	22.35	17.05	19.88	12.64	19.77	17.05	19.88	12.64	19.77	21.20	18.98	21.16	21.16	21.16	23.71
$k_{fat,est,mean}$ ; $k_{fat,est}$ [-]	0.93	0.92	0.97	0.80	0.80	0.87	0.32	0.82	0.80	0.87	0.32	0.82	0.80	0.34	0.29	0.76	0.76	0.76	0.34
range[ $k_{fat,est}$ ] [-]	0.77/1.11	0.79/1.01	0.78/1.09	0.71/0.85	0.71/0.85	0.76/0.94	0.67/1.03	0.73/0.93	0.67/1.03	0.76/0.94	0.67/1.03	0.73/0.93	0.67/1.03	0.66/0.90	0.66/0.90	0.66/0.90	0.66/0.90	0.66/0.90	0.66/0.90
$N_{est,mean}$ ; $N_{est}$ [-]	50.1	38.0	34.6	328	328	73.4	34,560	481	301	73.4	34,560	481	301	28,421	49,029	1,671	1,671	1,671	28,421
$N_{est,50}$ [-]	6.4	13.8	2.30	178	178	24.9	135	201	201	24.9	135	201	201	767	767	767	767	767	767
$(N_{obs}/N_{est})_{mean}$ [-]	30.0	32.88	1.08	10.4	10.4	2.80	0.45	8.40	21.4	2.80	0.45	8.40	21.4	0.51	0.58	2.39	2.39	2.39	0.62
$(N_{obs}/N_{est})_{50}$ [-]	4.57	22.8	0.44	10.4	10.4	2.19	0.43	1.03	10.0	2.19	0.43	1.03	10.0	0.46	0.57	1.16	1.16	1.16	0.50
CV[ $N_{obs}/N_{est}$ ] [%]	307	124	122	88.0	88.0	126	35.5	197	164	126	35.5	197	164	38.3	26.6	133	133	133	33.4

The differences in the fatigue behaviour between specimens failing in withdrawal and steel-tension are also demonstrated in Figure 3, which shows the development of the displacement  $w_{UL,i}$  at the upper load levels along the relative fatigue life,  $N_i / N_{obs}$ , for test series F002A, F452A and F902A. In case of withdrawal failures, the development of the displacement reminds of creep curves. Such curves are usually separated in three phases: primary (initial) “creep”, here between 0 and 10 % of  $N_{obs}$ , secondary “creep” characterised by a linearly increasing damage, here between 10 and 80 %, and finally tertiary “creep”, characterised by a progressively increasing damage until “creep failure”. Interestingly, the gradient in the central part increases slightly from  $\alpha = 0^\circ$  to  $45^\circ$  and  $90^\circ$ . The curves are also compared with the displacement at maximum load from the short-term reference tests,  $w_f$ , visualised as average values  $\pm$  standard deviation (sd). Qualitatively it could be concluded that the “creep” reaches  $w_f$  roughly at 60 % of the fatigue life which could be associated with a turning point of the average “creep” curves.

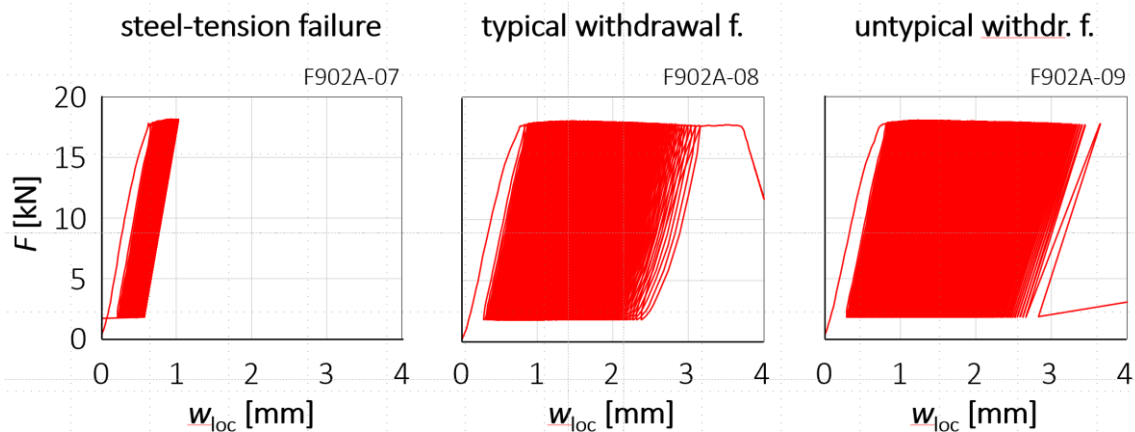


Figure 2. Typical load-displacement curves from cyclic tests of series F902A: (left) typical steel-tension failure; (middle) typical withdrawal failure; (right) untypical withdrawal failure.

Accumulated creep deformations together with stiffness reductions as measure for the progressive damage of cyclic loaded timber specimens was also analysed in Clorius et al. (2000). They found that the stiffness reduction is independent of the frequency of the applied load cycles whereas the fatigue life is not. Furthermore, they concluded that the accumulation in displacement is dominated by creep in case of low frequencies whereas it is dominated by successive damage in case of high frequencies. Dobraszcyk (1983) analysed acoustic emissions during cyclic tests and concluded that damage starts above 5 to 30 % whereas significant damage occurs above 90 % of the displacement at maximum load.

Those specimens which failed in steel-tension behave clearly different: after a short initial phase, the displacement  $w_{UL,i}$  of most of them remains nearly constant until failure and on a much lower level compared to the withdrawal failures; some others show a slight increase in  $w_{UL,i}$ . It appears that those specimens which ultimately failed in steel-tension were prevented from subsequently increasing displacements. Based on a detailed analyses of the opened screw channels and with a look at the densities it can be concluded that specimens which failed in steel-tension usually feature high

densities, very narrow annual ring widths and / or knots or bark inclusions along the screw channel. However, there are also other specimens featuring the same characteristics which failed in withdrawal, even cases with knots along the screw channel. At present there is no final and conclusive explanation for the made observations.

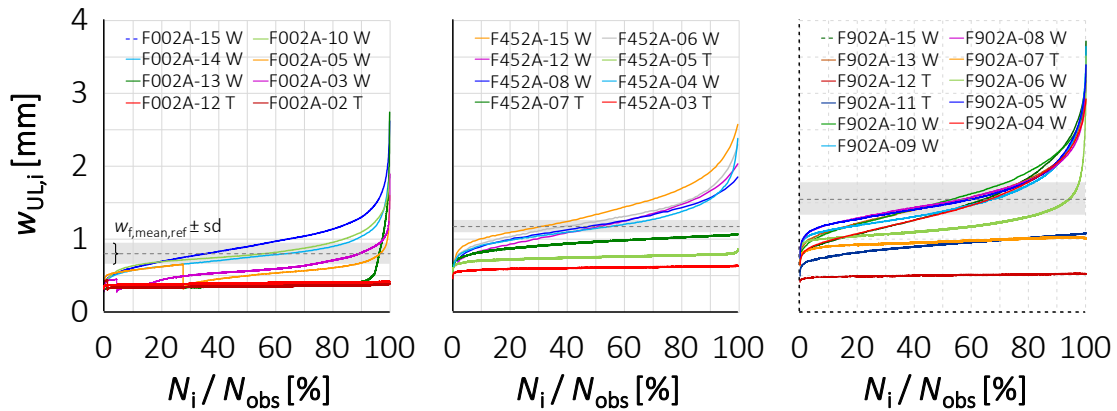


Figure 3. Development of the displacement  $w_{UL,i}$  at upper load level along the rel. fatigue life in comparison with the displacement at max. load  $w_f$  from monotonic tests; failure modes withdrawal (W) & steel-tension (T): (left)  $\alpha = 0^\circ$ ; (middle)  $\alpha = 45^\circ$ ; (right)  $\alpha = 90^\circ$ .

Looking at Figure 3 (left), specimens F002A-02, F002A-03 and F002A-05 exhibit a sudden step in their curves after which the displacement  $w_{UL,i}$  slowly recovers to the previous level before it continues the course before the step. The reason behind these steps is that the first cyclic tests stopped automatically after 500 cycles after which they were stored at reference climate and tested until fatigue failure some days later (three days in case of F002A-05; four days in case of F002A-03 and five days in case of F002A-02); thereby the screw remained in the specimen. The curves clearly show some recovery of the displacement expressed by the second “initial creep” phase after the drops. However, as the local displacement transducers had to be mounted again there might be also some bias in the data.

As next, the development of the slip modulus  $K_{ser,i}$  along the relative fatigue life  $N_i / N_{obs}$  is analysed; this again for the test series F002A, F452A and F902A. The outcomes are exemplarily demonstrated in Figure 4. The slip moduli were determined for each cycle in the loading and in the unloading phase. Overall, the slip moduli in the unloading phase are about 10 % lower than in the loading phase. In case of  $\alpha = 0^\circ$  the slip moduli steadily increase until a short drop in a very short final phase whereas it remains widely constant at  $\alpha = 45^\circ$  and steadily decrease in case of  $\alpha = 90^\circ$ . These differences can be explained by the circumstance, that in case of  $\alpha = 0^\circ$  the timber surrounding the thread is primarily stressed in longitudinal shear and compression parallel to the grain within a very local volume; the repeated loading leads to a successive compression and densification of the timber, which is reflected by increasing slip moduli. In case of  $\alpha = 90^\circ$  the timber surrounding the thread is primarily stressed in rolling and transverse shear as well as tension & compression perpendicular to the grain within a much larger volume. Repeated loading leads to a successive formation and opening of cracks which consequence in a softening of the timber, which is reflected by decreasing slip moduli. Decreasing stiffness properties with increasing

number of load cycles are frequently reported in the literature, c.f. Dobraszcyk (1983) and Clorius et al. (2000), and seen as clear indicator for the progressive damage of specimens exposed to cyclic load. Clorius et al. (2000) point out a higher decrease in stiffness in the loading than in the unloading phase. This indicates that the loading phase is of higher relevance for the fatigue damage process.

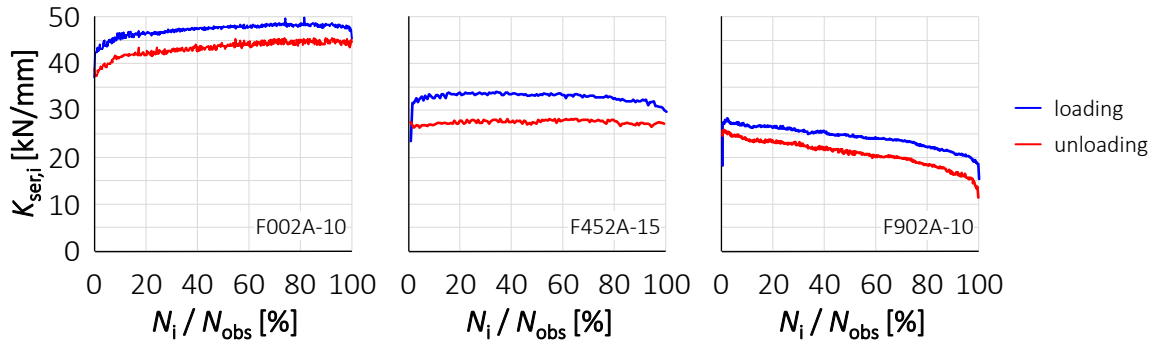


Figure 4. Representative examples for the development of the slip modulus  $K_{ser,i}$  along the relative fatigue life determined in the loading and unloading branch of load-displacement data: (left)  $\alpha = 0^\circ$ ; (middle)  $\alpha = 45^\circ$ ; (right)  $\alpha = 90^\circ$ .

Apart from these observations it needs to be addressed, that the testing speed is clearly different between the monotonic reference tests and the cyclic tests: whereas in the reference tests the speed was  $\{1.3; 1.7; 2.3\}$  mm/min, respectively, for  $\alpha = \{0; 45; 90\}^\circ$ , it was 500 mm/min in the fatigue tests. Mayr (2018), for example, analysed the influence of the testing speed on the withdrawal properties of self-tapping screws inserted parallel to the grain in beech (*Fagus sylvatica*). He found on average +15 % higher withdrawal strengths and lower slip moduli at a testing speed of 500 mm/min compared to those at reference test conditions. It is subject to further analyses on how this impacts the reference values for evaluation of cyclic tests. Anyway, the influence of the testing frequency on fatigue life was frequently investigated in the literature, c.f. Marsoem et al. (1987) with reference to Okuyama et al. (1984), Kohara & Okuyama (1992), Clorius et al. (2000), Gong & Smith (2003), Ando et al. (2005) and Sugimoto & Yasutoshi (2006), but without any adjustment of the reference values. The conclusions from these references are: the higher the frequency, the higher the loading rate and the longer the fatigue life, whereas the time-under-load (TUL) in most of the references decreases with increasing frequency. Furthermore, the influence of frequency seems to be more pronounced at higher load levels whereas it seems to diminish at lower load levels. This is explained by a change of the governing mechanisms: whereas the LCF domain seems to be dominated by the duration of load (DoL) phenomenon, the HCF domain is dominated by the number of load cycles.

### 3.2.3 Analysis of the fatigue coefficient $k_{fat}$

In the following, the fatigue coefficient  $k_{fat}(R = 0.10; N)$  of those specimens which failed in withdrawal is analysed in more detail. Figure 5 (left) presents the results from fatigue testing based on the applied horizon method. Apart from the individual data points (load level  $LL = k_{fat,exp}; N_{obs}$ ) also the average (mean) and median values

per series are given. Due to the sensitivity of the average values on extreme values in the obviously highly right-skewed fatigue lives, the variety in the average values is rather large and the trend in the median values much clearer. Simple linear regression models  $LL$  vs.  $\log_{10}(N_{obs})$  are presented and compared with the fatigue model of Kreuzinger & Mohr (1994) for “shear | pulsating loading”. It can be concluded that the regression models not meet the reference point ( $LL = 1$ ;  $N = 1$ ) as anchored in EC 5 and also frequently set in the literature. However, the trends for the withdrawal failures show a less pronounced fatigue behaviour than intended by Kreuzinger & Mohr's model for shear.

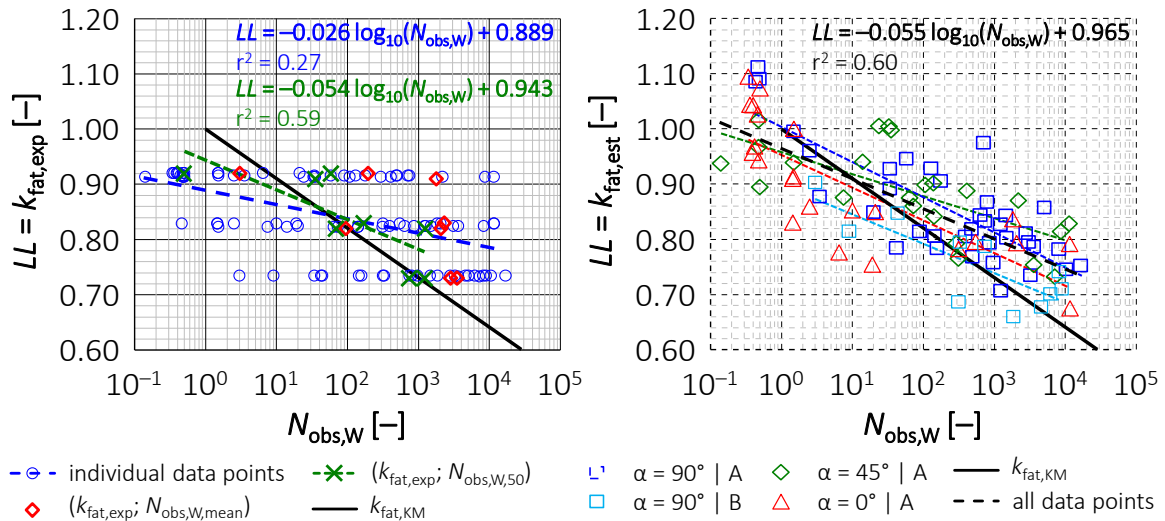


Figure 5. Cyclic tests with withdrawal failure mode: (left) expected load level  $LL = k_{fat,exp}$  vs. the observed fatigue life  $N_{obs,W}$  based on average reference capacities; (right) estimated load level  $LL = k_{fat,est}$  vs.  $N_{obs,W}$  based on individually estimated reference capacities.

Figure 5 (right) presents the individually estimated load levels  $LL = k_{fat,est}$  vs. the observed fatigue lives  $N_{obs}$  separately for each load-to-grain angle  $\alpha$  and the impulse shape {triangle (A); trapezoidal (B)}. The individual trend lines calibrated to the data sets are overall nearly parallel, which means that the fatigue behaviour seems not to be influenced by the load-grain angle  $\alpha$  and the impulse shape, although the data points of the trapezoidal tests ( $\alpha = 90^\circ | B$ ) are overall slightly shifted downwards and in case of  $\alpha = 0^\circ | A$  the course of the data is not as clear as for the others. Again, a less pronounced fatigue behaviour of in tension axially-loaded self-tapping timber screws than suggested by timber in shear acc. to Kreuzinger & Mohr (1994) is shown. In addition, the simple linear regression model calculated over all data points is given. This regression model also does not meet the reference point ( $LL = 1$ ;  $\log_{10}(N) = 1$ ) but it is rather close to the point ( $LL = 1$ ;  $N = 0.5$ ) which would confirm the assumption that the reference tests conducted as simple ramp-load tests represent only one half of a fatigue cycle in case of pulsating loading. It would even perfectly align with the point ( $LL = 1$ ;  $N = 0.25$ ) as recommended for example in Stamatopoulos & Malo (2017), however, this assumption rather agrees with an alternating than with a pulsating loading regime. Anyway, findings in Marsoem et al. (1987), Gong & Smith (2003), Sugimoto & Yasutoshi (2006) and others demonstrate that the loading rate

has a decisive influence on the fatigue behaviour and not the energy below the pulse form. Considering this it seems to be worth to stay with the common reference point, e.g. acc. to EC 5.

## 4 Summary and Conclusions

The focus of this paper was on the fatigue behaviour in the LCF domain of in tension axially-loaded self-tapping timber screws with failure mode withdrawal. The fatigue investigations were restricted to one type of screw, one diameter, one effective insertion length, one timber species, one timber strength class, one timber product, one testing speed and one stress ratio  $R$ . Varied parameters were the load-to-grain angle  $\alpha = \{0; 45; 90\}^\circ$ , the expected fatigue life  $N_{exp} = \{10^1; 10^2; 10^3; 10^4\}$  and corresponding fatigue coefficients in the applied horizon method and the impulse shape {triangle (as reference); trapezoidal}. In total, nine cyclic test series comprising overall 132 tests and three monotonic test series with in total 60 tests were conducted. Within the cyclic tests 98 specimens failed in withdrawal, the target failure mode, and 34 specimens in steel-tension of which 94 and 27, respectively, were considered in the data analyses. The main outcome is presented in Figure 6 which shows the individually calculated fatigue coefficients  $k_{fat,est}$  vs. the observed fatigue life  $N_{obs}$  for withdrawal and steel-tension failures together with calibrated simple linear regression models, fatigue models and test data from the literature and a new proposal for the regulation of the fatigue behaviour of in tension axially-loaded self-tapping timber screws failing in withdrawal. First of all, tests from the literature well align with the new test results and confirm that timber screws failing in withdrawal are less sensitive to fatigue failures than timber loaded in shear. However, it needs to be considered that although the literature data extends the range of investigated screw products, diameters and timber quality, all tests were done in Norway spruce and at approx. the same stress ratio  $R$ .

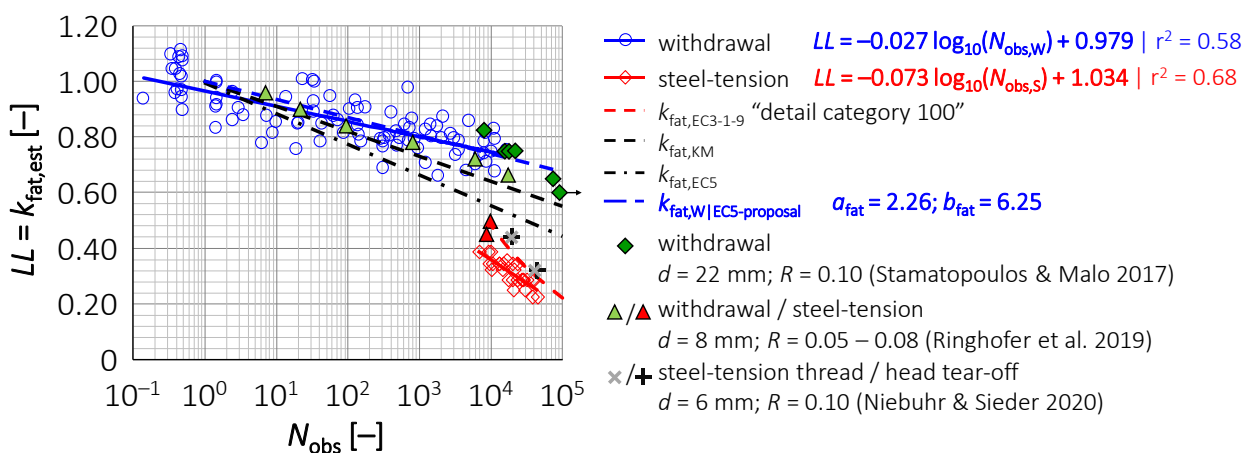


Figure 6. Individually est. load level  $LL = k_{fat,est}$  vs. obs. fatigue life  $N_{obs}$  together with regression models in comparison with fatigue models for shear acc. to EC 5 and Kreuzinger & Mohr (1994), the proposal of Ringhofer et al. (2019) for steel-tension, test data from the literature and a new proposal for screws failing in withdrawal.



By following the model for the fatigue coefficient  $k_{\text{fat}}(R; N)$  in EC 5 (see Eq. (2)) and based on the observed withdrawal failures the best choice for the model parameters  $\{a_{\text{fat}}; b_{\text{fat}}\}$  is  $\{2.26; 6.25\}$ . This would consequence in a model bias  $(k_{\text{fat,est}} / k_{\text{fat,model}})_{\text{mean}} = 0.98$  and a model uncertainty  $\text{CV}[k_{\text{fat,est}} / k_{\text{fat,model}}] = 7.90\%$ . For a bit more conservative regulation, the model of Kreuzinger & Mohr (1994; Eq. (3)) for shear appears meaningful. Transferred to the EC 5 approach the values corresponding to the model parameters  $\{a_{\text{fat}}; b_{\text{fat}}\}$  are  $\{1.84; 5.52\}$  which would result in a model bias  $(k_{\text{fat,est}} / k_{\text{fat,model}})_{\text{mean}} = 1.05$  and a model uncertainty  $\text{CV}[k_{\text{fat,est}} / k_{\text{fat,model}}] = 10.4\%$ .

The fatigue behaviour of observed steel-tension failures is below the predictions according to “detail category 100” of EC 3 as suggested by Ringhofer et al. (2019) as well as below the results of Niebuhr & Sieder (2020). The reasons behind this unexpected shorter fatigue lives and the clearly different behaviour of specimens failing in steel-tension compared to those failing in withdrawal, in particular the quasi-frozen displacement at the upper load levels, have not yet been fully clarified and are subjects of further analyses.

Other findings in brief: the individually estimated withdrawal capacities based on the individual densities, as basis for individually calculated fatigue coefficients, led to real added value in the data. Investigations in Eckert et al. (2023) demonstrate that the insertion energy would even by a more reliable and more powerful predictor for the withdrawal properties. Considering this, for future cyclic and DoL-tests it is highly recommended to enrich the information on each specimen by means of such or similar indicating properties. Furthermore, the analysis of the development of the slip moduli along the fatigue life reflected a dependency on the load-to-grain angle. An overall decreasing trend of the slip moduli as indicator for a progressively increasing fatigue damage, as frequently reported in the literature for other timber properties, could not be confirmed. However, the analysis of the development of the displacement at the upper load level along the fatigue life clearly indicated this progressive accumulation of fatigue damage also in some relationship to the displacement at maximum load from monotonic tests. This finding could be also of relevance for the monitoring of connections with groups of axially-loaded screws exposed to cyclic loads in the future.

There is still more room for further analyses of the test data, in particular in regard to possible analogies between static fatigue (DoL) and fatigue. In this respect it is planned to evaluate each test along the whole load vs. time curve by means of DoL-models and by considering the experiences gained from DoL-tests on in tension axially-loaded self-tapping timber screws over the last seven years.

## 5 Acknowledgement

The publication was written in frame of the research project FFG BRIDGE 1 “CLT\_joint” (no. 883672) and received public funding by the Austrian Research Promotion Agency (FFG). Their support and

the support by the commercial partners, Schmid Schrauben Hainfeld GmbH (Hainfeld, Austria) and TechnoWood AG (Alt St. Johann, Switzerland) are thankfully acknowledged.

## 6 References

- Ando K, Yamasaki M, Watanabe J, Sasaki Y (2005) Torsional fatigue properties of wood (in Japanese). *Mokuzai Gakkaishi*, 51(2):98–103.
- Brandner R, Ringhofer A, Grabner M (2018) Probabilistic models for the withdrawal behavior of single self-tapping screws in the narrow face of cross laminated timber (CLT). *Eur. J. Wood Prod.*, 76:13–30, DOI 10.1007/s00107-017-1226-3.
- Brandner R, Eckert A (2024) AP3 – BEHAVIOUR: Ermüdungsverhalten von Holz: Fokus Ausziehtragfähigkeit von Holzbauschrauben. Research report, Graz University of Technology (in German).
- Bratulic K, Flatscher G, Brandner R (2014) Monotonic and cyclic behaviour of joints with self-tapping screws in CLT structures. COST Action FP1004, Prague, Czech Republic.
- Clorius CO, Pedersen MU, Hoffmeyer P, Damkilde L (2009) An experimentally validated fatigue model for wood subjected to tension perpendicular to the grain. *Wood Sc. and Techn.*, 43:343–357.
- Clorius CO, Pederson MU, Hoffmeyer P, Damkilde L (2000) Compressive fatigue in wood. *Wood Sc. and Techn.*, 34:21–37.
- Dobraszczyk B (1983) An investigation into fracture & fatigue behaviour of wood. PhD Thesis, University of Bath.
- EAD 130118-00-0603 (2016) Screws for use in Timber Constructions. European Assessment Document (EAD), EOTA.
- Eckert A, Brandner R (2023) AP5 – MOUNT: Eindreh- und Ausziehprüfungen. Research report, Graz University of Technology, Austria (in German).
- Eckert A, Brandner R, Glasner D (2023) Experimental study on control parameters for automated application and in-situ performance assessment of joints with self-tapping timber screws. 13th World Conference on Timber Engineering (WCTE'23), Oslo, Norway.
- EN 338 (2016) Structural timber – Strength classes. CEN.
- EN 384 (2016) Structural timber – Determination of characteristic values of mechanical properties and density. CEN.
- EN 408 (2012) Timber structures – Structural timber and glued laminated timber – Determination of some physical and mechanical properties. CEN.
- EN 1382 (2016) Timber structures – Test methods – Withdrawal capacity of timber fasteners. CEN.
- EN 13183-1 (2004) Moisture content of a piece of sawn timber – Part 1: Determination by oven dry method (EN 13183-1 :2002 + AC:2003). CEN.
- EN 1993-1-9 (2005) + AC (2009) Eurocode 3: Design of steel structures – Part 1-9: Fatigue. CEN.
- EN 1995-2 (2004) Eurocode 5: Design of timber structures – Part 2: Bridges. CEN.
- ETA-12-0373 (2020) European Technical Assessment Schmid Schrauben Hainfeld GmbH. 23.12.2020.
- Gavric I, Fragiaco M, Ceccotti A (2015) Cyclic behaviour of typical screwed connections for cross-laminated (CLT) structures. *Eur. J. Wood Wood Prod.*, 73,179–191.
- Glos P (1978) Zur Bestimmung des Festigkeitsverhaltens von Brettschichtholz bei Druckbeanspruchung aus Werkstoff- und Einwirkungskenngrößen. Research report, TU Munich (in German).
- Gong M, Smith I (2003) Effect of waveform and loading sequence on low-cycle compressive fatigue life of spruce. *J. of Mat. in Civil Eng.*, 15:93–99.



- Hossain A, Popovski M, Tannert T (2018) Cross-laminated timber connections assembled with a combination of screws in withdrawal and screws in shear. *Eng. Struct.*, 168:1–11.
- ISO 13061-2/A1 (2017) Physical and mechanical properties of wood – Test methods for small clear wood specimens – Part 2: Determination of density for physical and mechanical tests – Amendment 1. ISO.
- Kohara M, Okuyama T (1992) Mechanical responses of wood to repeated loading V—Effect of duration of time and number of repetitions. *Mokuzai Gakkaishi*, 38(8):753–758.
- Kreuzinger H, Mohr (1994) Holz und Holzverbindungen unter nicht vorwiegend ruhenden Einwirkungen. Research report, TU Munich (in German).
- Loss C, Hossain A, Tannert T (2018) Simple cross-laminated timber shear connections with spatially arranged screws. *Eng. Struct.*, 173:340–356.
- Majumdar S, Maiya PS (1980) A Mechanistic Model for Time-Dependent Fatigue. *J. of Eng. Mat. and Techn.*, 102:159–167.
- Marsoem SN, Bordonné PA, Okuyama T (1987) Mechanical responses of wood to repeated loading II—effect of wave form on tensile fatigue. *Mokuzai Gakkaishi*, 33(5):354–360.
- Mayr P (2018) Einfluss konstanter Langzeitbeanspruchung (DoL) auf die Tragfähigkeit selbstbohrender Holzschrauben appliziert in Faserrichtung in Fichte, Buche und BauBuche. Master thesis, Graz University of Technology (in German).
- Mohr B (2001) Zur Interaktion der Einflüsse aus Dauerstands- und Ermüdungsbeanspruchung im Ingenieurholzbau. PhD thesis, TU Munich (in German).
- Niebuhr P, Sieder M (2020) High-cycle fatigue behaviour of a self-tapping timber screw under axial tensile loading. *J Fail. Anal. And Prev.*, 20:580–589.
- Obermüller M (2020) Gedrungene Brett-, BSH- und BSP-Querschnitte unter Druckbeanspruchung längs zur Faser sowie in Scheibenebene. Master thesis, Graz University of Technology (in German).
- Okazaki M, Hattori I, Ikeda T, Koizumi T (1985) Low Cycle Fatigue Crack Growth Behavior at Elevated Temperature Under the Combined Strain-Wave-Shape Cycling in Type 304 Stainless Steel. *J. of Eng. Mat. and Techn.*, 107:346–355.
- Okuyama T, Itoh A, Marsoem SN (1984) Mechanical responses of wood to repeated loading I—tensile and compressive fatigue fractures. *Mokuzai Gakkaishi*, 30(10):791–798.
- prEN 1995-1-1 (2023) Eurocode 5: Design of timber structures – Part 1-1: General rules and rules for buildings. V2023-04-19, CEN.
- Ringhofer A, Brandner R, Schickhofer G (2015) A Universal Approach for Withdrawal Properties of Self-Tapping Screws in Solid Timber and Laminated Timber Products. INTER/48-7-1, Sibenik, Croatia.
- Ringhofer A (2017) Axially Loaded Self-Tapping Screws in Solid Timber and Laminated Timber Products. PhD thesis, Graz University of Technology.
- Ringhofer A, Augustin M, Schickhofer G (2019) Basic steel properties of self-tapping timber screws exposed to cyclic axial loading. *Constr. Build. Mater.*, 211:207–216.
- Stamatopoulos H, Malo KA (2017) Fatigue strength of axially-loaded threaded rods embedded in glulam at 45° to the grain. 3rd International Conference on Timber Bridges, Skellefteå, Sweden.
- Sugimoto T, Yasutoshi S (2006) Effect of loading frequency on fatigue life and dissipated energy of structural plywood under panel shear load. *Wood Sc. and Techn.*, 40:501–515.
- Wöhler A (1870) Über die Festigkeitsversuche mit Eisen und Stahl. *Zeitschrift für Bauwesen*, 20:73–106 (in German).

## DISCUSSION

**The paper was presented by R Brandner**

*P Dietsch received confirmation that up to 10000 load cycles could be considered as low cycle fatigue. P Dietsch inquired on the potential influence of the hardening and forming processes of the screws on their fatigue behaviour. R Brandner said that the screws had the same hardening process. They discussed that the tensile failure mode was not expected at these percentages of failures and discussed potential effects. It was agreed that a solution would be needed for code and standard implementation.*

*P Vinco da Sesso asked if there are any studies planned to consider the influence of moisture exposure and climatic conditions. R Brandner agreed that this area is important but did not have an answer yet. It was agreed that without technical evidence one would need to be very conservative.*

*C Sandhaas commented about the process of fixing the screws using steel fixtures in fatigue tests as friction activated from the steel plate could influence the results. C Sandhaas also commented about the necessity to consider the fact that a connection always includes numerous screws.*

*A Frangi commented that as connections with multiple screws were not considered, can the results be trusted. R Brandner responded that one can trust the results. The tensile failure results were low but withdrawal failure information are okay.*

*U Kuhlmann commented that the boundary between low and high cycle fatigue of 10000 cycles is just a number. Toughness of the steel is an important factor and is covered in EN 1993-1-10. It is a question of choice of steel. Also hardness treatment from cold forming would decrease the toughness. It is also well known that manufacturers of screws produce screws with high hardness.*

*U Huebner discussed if this item could be covered in a product standard, differentiating between normal (quasi-static) and special applications (seismic, fatigue). P Dietsch mentioned that this would be challenging to control in practice.*



# On stiffness and strength of glued-in rods and threaded rods parallel to the grain

Charles Binck, Institute of Structural Engineering, ETH Zurich

Andrea Frangi, Institute of Structural Engineering, ETH Zurich

Keywords: Glued-in rods, screwed-in threaded rods, monotonic pull-out tests, withdrawal stiffness, withdrawal strength

## 1 Introduction

Connections in timber with glued-in rods and long threaded rods have gained attention in recent years. Both rod types show high stiffnesses and withdrawal strengths. For glued-in rods, extensive research has been carried out in the last decades to provide design procedures in the codes (Bainbridge et al., 2000, 2002; Bengtsson & Johansson, 2001; Bernasconi, 2001; Blaß & Laskewitz, 1999; Gustafsson et al., 2001; Mettem et al., 1999; Riberholt, 1988; Steiger et al., 2007, 2015; Stepinac et al., 2013; Tlustochowicz et al., 2011). However, most of the investigations have been devoted to the load bearing capacity of the glued-in rods, rather than to their stiffness. At ETH Zurich, the axial slip modulus of glued-in rods parallel to the grain was investigated (Ogrizovic et al., 2018), but only specimens with predefined parameters have been considered so far.

For long threaded rods with a wood screw threads, most of the conducted research was mainly focussed on rods with diameters of up to 12 mm. Investigations on the stiffness and withdrawal capacity of threaded rods above 12 mm have been received less attention. Apart from Hübner (2010; 2013), Jensen et al. (2010), Stamatopoulos & Malo (2015) and the research for product development (Krüger & Blaß, 2009), the few available investigations have mainly focused on rods set perpendicular or at a certain angle with respect to the grain.

Eurocode 5 (2010) provides no guidelines for the axial slip modulus of rods parallel to the grain – neither for glued-in rods, nor for threaded rods. Currently, the new draft of the Eurocode 5 (2023) also shows that no new information will be included in this area. Only the axial slip modulus for the perpendicular to the grain direction is intended to

be standardised for both rod types. For long threaded rods with wood screw threads, similar restrictions can be found in current approvals (ETA-Danmark A/S, 2019, 2022, 2023). None of the current products (HECO/SFS, EUROTEC, ROTHOBLOSS) are approved for rod configurations parallel to the grain. Furthermore, all approvals focus on softwood, where no differentiation with respect to the grain angle is made for the provided axial slip modulus. In light of these limitations, an experimental campaign of pull-out tests for rods set parallel to the grain has been carried out.

## 2 Experimental investigations

### 2.1 Overview

Monotonic pull-out tests are conducted on glued-in rods with metric threads and screwed-in threaded rods with wood screw thread. A total of 195 tests are carried out, where 120 tests are conducted on GL28h glulam made of Norway spruce, and 75 tests on European ash at the SSH48 strength class. The main goal of the campaign is to investigate the stiffness of the connections subjected to monotonic loading. Furthermore, attention is given to evaluating the ultimate failure loads, the withdrawal shear strength, the ductility capacity, and the failure modes of both rod types.

### 2.2 Experimental set-up

The experiments are performed in a universal testing machine in a pull-pull configuration. The test set up is presented in Figure 1.

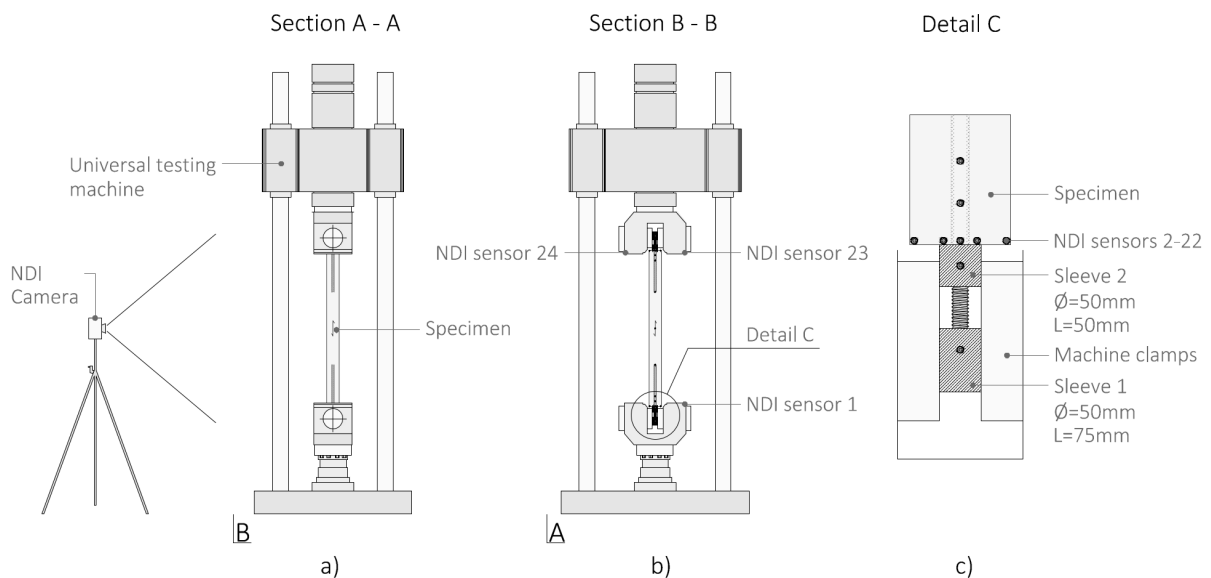


Figure 1. Test set up of the pull-out experiments. a) Front view. b) Side view. c) Clamping detail.

The specimens are clamped with 50 mm diameter steel sleeves. Two sleeves with the corresponding thread are mounted on each rod, with the machine's pulling force applied directly to the sleeves. For the displacement measurement, an optical 3D measurement system, the "Optotrak Certus" from Northern Digital Inc. (NDI) is used. In total

24 light emitting diodes are connected. Three diodes are fixed on the testing machine and 21 diodes are distributed along the length of each specimen. Figure 2 shows the diode positions. The exact 3D coordinates of the diodes are recorded by a camera unit with three lenses. The determination of the absolute and relative displacements of all placed diodes is recorded by the optical 3D measurement system at a measurement frequency of 10 Hz and with a resolution of 0.01 mm. The applied load is measured by the machine's integrated load cell.

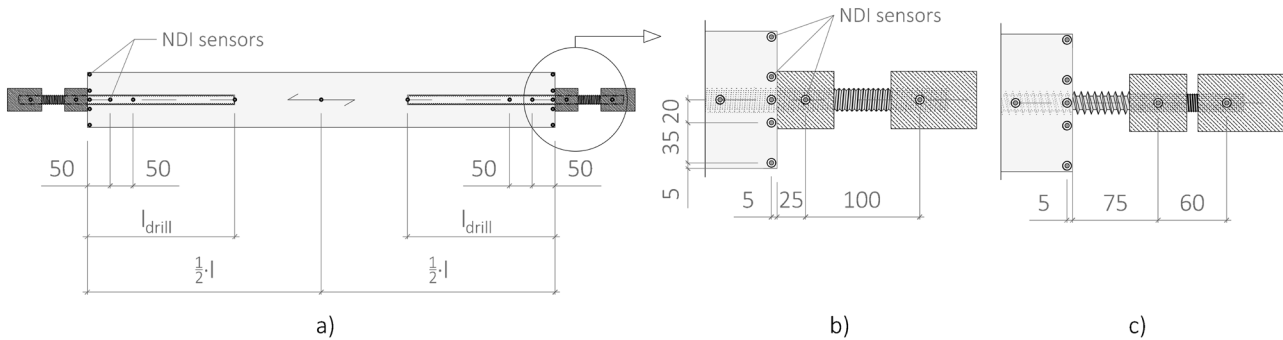


Figure 2. Sensor layout for the optical 3D measurement system. a) Sensor layout on the specimens. b) Clamping detail of the Glued-in rods. c) Clamping detail of the screwed-in rods. Dimensions in [mm].

## 2.3 Materials

The timber members are made of GL28h, machine graded glued-laminated Norway spruce, according to EN 14080 (2013), and square-laminated European ash of grade SSH48 according to Fagus Suisse specifications (Fagus Suisse SA, 2023). The GL28h specimens are fabricated with 40 mm thick lamellas, resulting in three lamellas per specimen. The SSH48 specimens are glued with melamine resin and produced with squared lamellas of 40 mm. One SSH48 specimen is composed of nine lamellas. Further product information related to these SSH48 sections are available (Fagus Suisse SA, 2023; Lignatec, 2021).

The specimens with glued-in rods are produced with SFS rods of strength classes 4.6/4.8 (DIN 975-4.6/4.8) and 8.8 (DIN 975-8.8). For both strength classes, rod diameters of 16 mm, 20 mm and 24 mm are investigated. The rods are glued-in with the two-component epoxy Hilti HIT-RE 500 V4, (OIB, 2023). The specimens with the wood screw threaded rods are produced with HECO/SFS WB-T rods (ETA-Danmark A/S, 2019) with diameters of 16 mm and 20 mm. The WB-T 20 rods are produced and delivered with a metric thread diameter of  $d_2 = 16$  mm (M16) at the rod ends. The WB-T 16 rods are post-processed to guaranty a consistent mounting thread, as no standard product exists. For this purpose, an M12 thread is rolled on the WB-T 16 rods in the same cold forming procedure as the WB-T 20 rods.

An overview of the rod's geometry is given in Table 1, where  $d$  is the rod diameter,  $d_1$  is the inner core diameter,  $d_{drill}$  is the drill hole diameter and  $d_2$  is the metric thread diameter at the end of the WB-T rods, Figure 3. In general, all rods are tested with embedment lengths  $l_w$  of 200 mm, 300 mm, 400 mm, 500 mm, and 600 mm.

Table 1. Geometry of the rods. Dimensions in [mm].

Description	Type	Thread	d [mm]	d <sub>1</sub> [mm]	d <sub>drill</sub> [mm]	d <sub>2</sub> [mm] <sup>(*)</sup>	Sketch
SFS 4.6/4.8 & 8.8	M16	Metric	16.0	13.508	18	d <sub>2</sub> =d	
	M20	Metric	20.0	16.891	22	d <sub>2</sub> =d	
	M24	Metric	24.0	20.271	26	d <sub>2</sub> =d	
HECO/SFS WB-T	W16	Wood screw	16.0	12.0	13	12.0	
	W20	Wood screw	20.0	15.0	16	16.0	

## 2.4 Specimens

Table 2 gives an overview of the test campaign with the glued-in rods (GIR) and long threaded rods (WB-T). Beside the timber grade and the rod type, the varying parameters are the steel class, the rod diameters  $d$ , and the embedment length  $l_w$ . For both timber grades, no tests on 24 mm diameter WB-T could be performed, as no products exist at such large diameter.

Table 2. Overview of the specimens with 3 specimens per test series.

Timber grade	GL28h												SSH48																		
	Rod type		GIR 4.6					GIR 8.8					WB-T		GIR 4.6					GIR 8.8					WB-T						
$d$	$l_w$ [mm]	200	300	400	500	600	200	300	400	500	600	200	300	400	500	600	200	300	400	500	600	200	300	400	500	600	200	300	400	500	600
16 mm		3	3	3	3	3	3	3	3	3	3	3	3	3	3	3	-	-	-	-	-	3	3	3	3	3	3	3	3	3	3
20 mm		3	3	3	3	3	3	3	3	3	3	3	3	3	3	3	-	-	-	-	-	3	3	3	3	3	3	3	3	3	3
24 mm		3	3	3	3	3	3	3	3	3	3	-	-	-	-	-	-	-	-	-	-	3	3	3	3	3	-	-	-	-	-

Figure 3 summarises the specimen dimensions. The glued-in rods are glued with an unbonded length of  $l_u = 20$  mm. The adhesive joint thickness  $t$  is 1 mm in accordance with the approval (OIB, 2023). The free outer length is 150 mm. The screwed-in rods with wood screw threads have the same outer rod length of 150 mm, where  $l_b = 50$  mm is the free length of a rod with a wood screw thread. Prior to the rod insertion, the specimens are pre-drilled with a diameter  $d_{drill}$  according to Table 1. The adhesive injection is carried out with a battery-powered adhesive dispenser Hilti HDE 500-22.

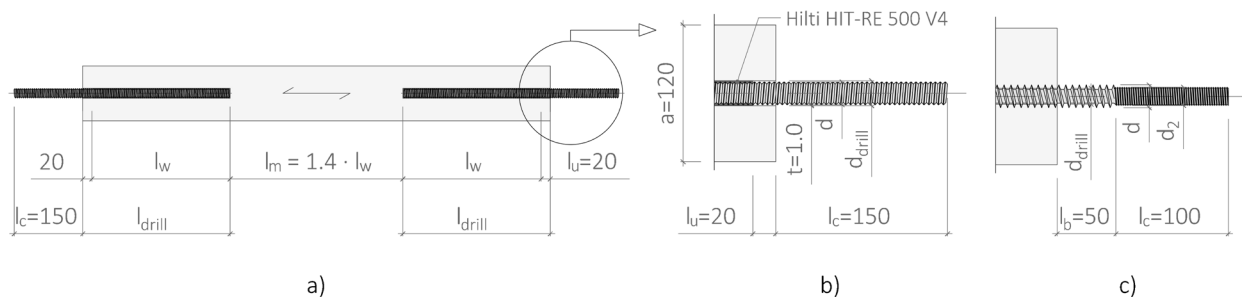


Figure 3. Schematic representation of the test specimens. a) Dimensions of the specimens. b) Detail of the glued-in rods. c) Detail of the threaded rods with wood screw threads. Distances in [mm].

The specimen dimensions and the test method follow EN 17334 (2021). Only the cross-sectional dimensions of the timber specimens deviate from EN 17334. For all rod diameters, the timber cross-sections show constant widths of  $a = 120$  mm (Figure 3), resulting in cross-sectional edge lengths of  $a = 7.5d$  for  $d = 16$  mm,  $a = 6.0d$  for  $d = 20$  mm and  $a = 5.0d$  for  $d = 24$  mm. The specimens are produced in double symmetry.

## 2.5 Method

All configurations are tested under monotonic loading. The tensile tests are performed with displacement control according to EN 26891 (1991). The specimens are firstly loaded up to 40 % of the expected pull-out capacity, unloaded to approximately 10 % of the estimated ultimate load, and reloaded until failure. A constant displacement rate of 0.01 mm/s is chosen to achieve the failure of the connection within 300 +/- 120 s, according to EN 26891 (1991). The expected pull-out capacity is conservatively estimated to the characteristic withdrawal resistance according to the german national annex of the Eurocode 5 (DIN, 2013). The measured data are the applied loads, the deformations, the testing time and the failure modes. In order to categorise the test specimens, moisture measurements are carried out and the bulk densities are determined.

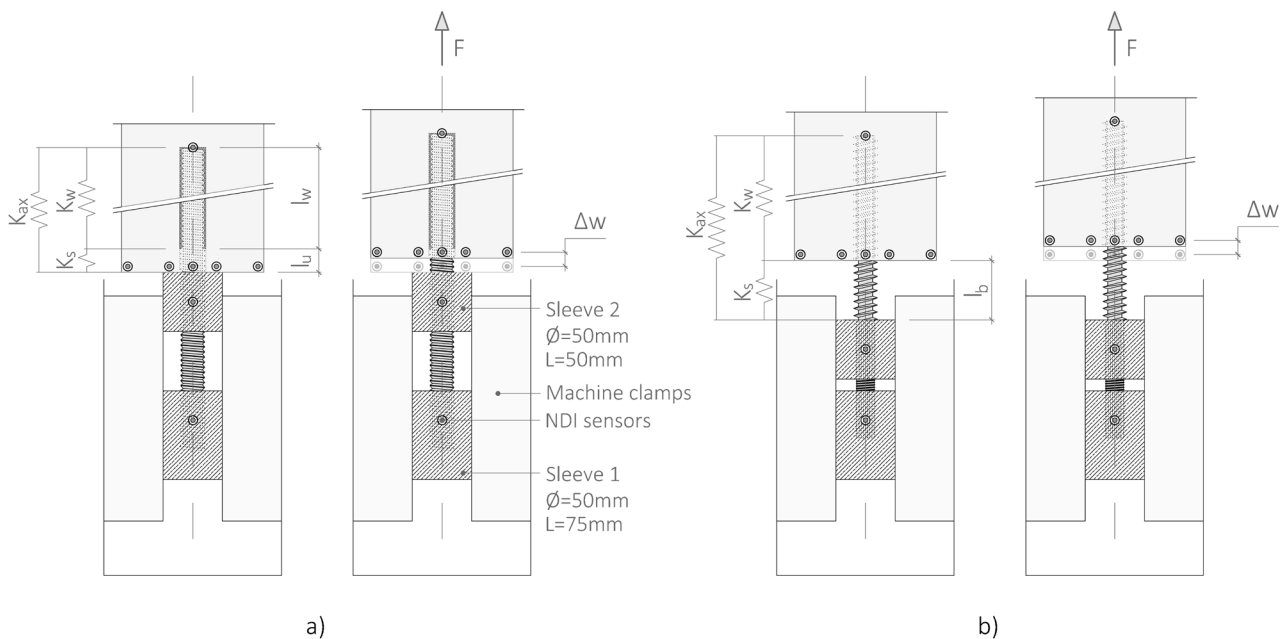


Figure 4: Deflection measurement and stiffness determination. a) Specimens with the glued-in-rods. b) Specimens with the screwed-in rods.

The measured stiffness  $K_{ax}$  is determined as:

$$K_{ax} = \frac{\Delta F}{\Delta w}, \quad (1)$$

where  $\Delta F$  and  $\Delta w$  are the relative forces and displacements, measured between the 10% estimated ultimate load and the 60% measured failure Load. As  $K_{ax}$  corresponds to the axial slip modulus, which includes the unbonded length  $l_u$  of the glued-in rods



and the free length  $l_b$  of the screwed-in rods, the withdrawal stiffness  $K_w$  is back calculated to:

$$K_w = \left( \frac{1}{K_{ax}} - \frac{1}{K_s} \right)^{-1}, \quad (2)$$

where  $K_s$  is the determined steel stiffness of the unbonded length  $l_u$  or  $l_b$  respectively (Figure 4) and determined as:

$$K_s = \frac{EA}{L} \quad (3)$$

In equation (3),  $L$  corresponds to  $l_u = 20$  mm (glued-in rods) or  $l_b = 50$  mm (screwed-in rods) respectively.  $EA$  is determined by preliminary tensile tests on the single rods with  $n = 5$  tests per rod configuration (Table 3).

Regarding the withdrawal strength, for both the glued-in rods and screwed-in rods with wood screw threads, the withdrawal strength  $f_{w,k}$  is determined by:

$$f_{w,k} = \frac{F_{max}}{\pi \cdot d \cdot l_w}, \quad (4)$$

where  $F_{max}$  denotes the failure load,  $d$  is the rod diameter and  $l_w$  is the embedment length.

### 3 Results

#### 3.1 Materials

Before and after testing, moisture measurements on the specimens are performed with a hygrometer at depth of either 10 mm (SSH48) or 20 mm (GL28h). Figure 5 (left) shows the moisture content in relation to the mean density. The plotted moisture content data are the mean values of the four measurements per specimen.

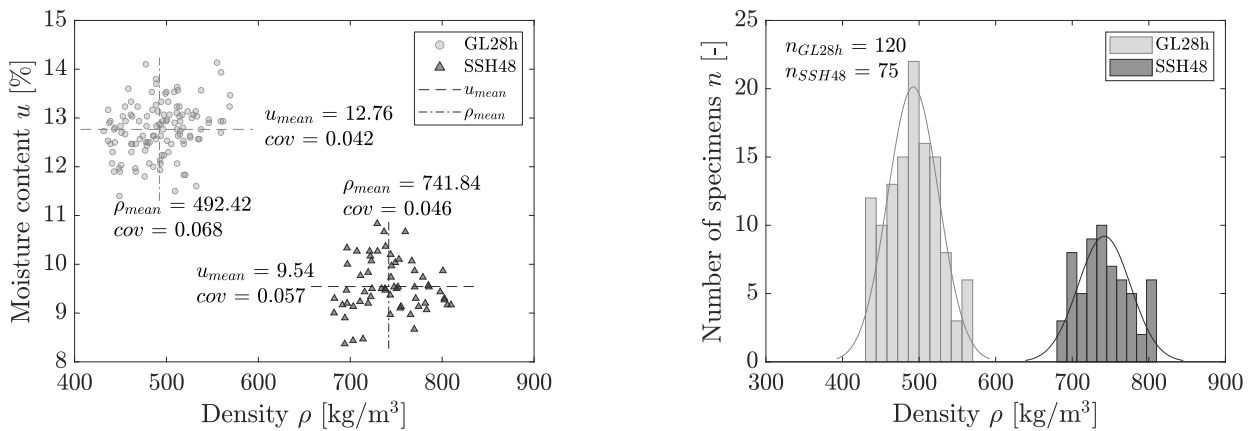


Figure 5. Moisture content and densities of the timber specimens, showing a scatter plot with mean values and coefficients of variation (left) and a histogram of the timber densities (right).

The densities of the specimens are determined from the mass and the volume. The translation to the reference moisture content follows EN 384 (2022). For the GL28h specimens, the densities range from 431 kg/m<sup>3</sup> to 569 kg/m<sup>3</sup>, resulting in a mean density of  $\rho_{mean} = 492$  kg/m<sup>3</sup>. According to EN 14080 (2013), the mean and characteristic densities of GL28h are  $\rho_{g,mean} = 460$  kg/m<sup>3</sup> and  $\rho_k = 425$  kg/m<sup>3</sup>. The mean density of the SSH48 specimens is determined as  $\rho_{mean} = 742$  kg/m<sup>3</sup> ranging from 682 kg/m<sup>3</sup> to 810 kg/m<sup>3</sup>. The standardised characteristic density is  $\rho_k = 680$  kg/m<sup>3</sup>.

Yielding and steel fracture of the rods occurred at load levels which were significantly higher than the standardised nominal yield and ultimate strength properties. Table 3 lists the experimental results of the characteristic yield strength  $f_{0.2,k}$ , characteristic tensile strength  $f_{t,k}$  and mean elastic modulus  $E_{mean}$ , by determining the results with the nominal cross section  $A_{nom}$  for the glued-in rods and the core cross section  $A_{core}$  for the screwed-in rods.

Table 3. Experimental results for the steel rod properties.

$d$ [mm]	DIN 975 4.6/4.8			DIN 975 8.8			WB-T	
	16	20	24	16	20	24	16	20
$f_{0.2,k}$ [N/mm <sup>2</sup> ]	420.5	428.9	366.6	836.4	798.5	778.8	862.7	843.3
$f_{t,k}$ [N/mm <sup>2</sup> ]	461.4	469.4	419.6	912.2	895.3	891.7	963.2	974.0
$E_{mean}$ [kN/mm <sup>2</sup> ]	200.5	194.9	193.9	197.8	192.8	189.8	187.3	193.5

### 3.2 Withdrawal stiffness

The experimental results of the withdrawal stiffnesses are given in Figure 6 and Figure 7 for the GL28h and SSH48 specimens, respectively. The boxplots show the pull-out stiffnesses  $K_w$  in relation to the rod types, rod diameters  $d$ , embedment lengths  $l_w$  and timber grades. “M – 4.8” and “M – 8.8” denote the results for the glued-in rods of strength classes 4.6/4.8 and 8.8, respectively. The screwed-in threaded rods are denoted by “W – 8.8”. Derived mean values  $\mu$  (dashed lines) are plotted and summarised with the coefficients of variation (COV in brackets). The swarmcharts of Figure 6 and Figure 7 (right) illustrate the frequencies of the results by reference to the swarm width. While the smallest markers visualise the shortest embedment lengths of  $l_w = 200$  mm, the biggest markers illustrate the embedment lengths of  $l_w = 600$  mm.

For the GL28h specimens, the glued-in rods achieve approximately the double withdrawal stiffness than the screwed-in rods. No significant difference is noticed between the glued-in rods M – 4.8 and M – 8.8. Compared to the softwood specimens, the stiffness increase of the SSH48 hardwood specimens is with 15 % - 50 % particularly noticeable for the 20 mm and 24 mm rod diameters.

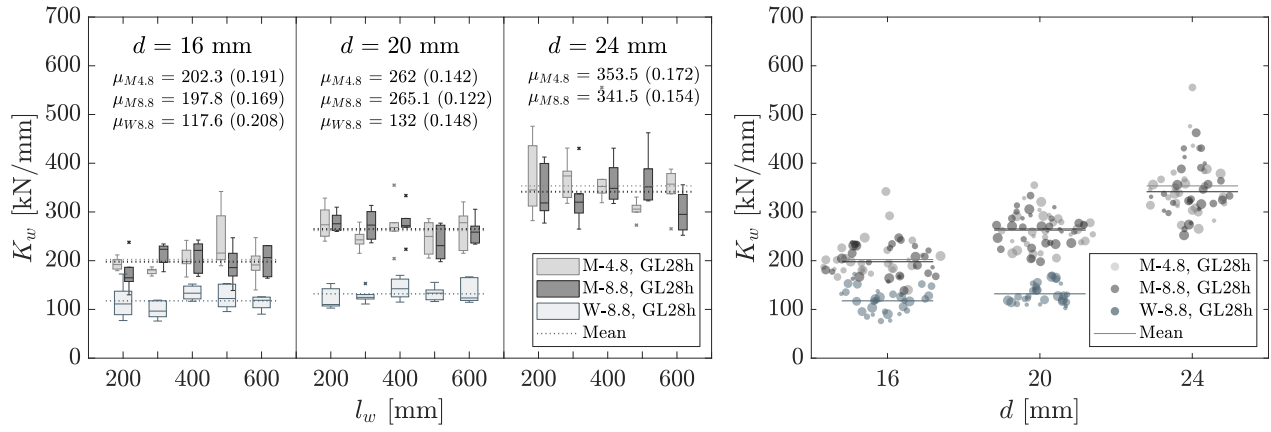


Figure 6. Experimental results of the withdrawal stiffnesses in GL28h. Boxplot for the different specimen configurations (left). Scatter plot (Swarmchart) with the illustration of the frequency (right).

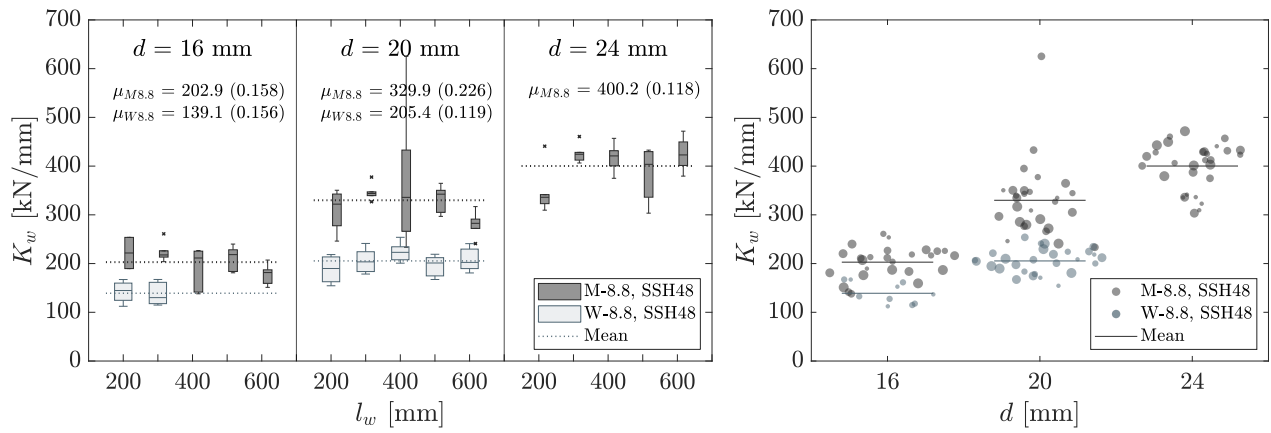


Figure 7. Experimental results of the withdrawal stiffnesses in SSH48. Boxplot for the different specimen configurations (left). Scatter plot (Swarmchart) with the illustration of the frequency (right).

The increase of embedment length shows no noteworthy correlation on the withdrawal stiffness of the glued-in rods. For the threaded rods with wood screw threads, the stiffness increase becomes smaller with increasing embedment lengths. Stiffness peaks are reached for  $l_w = 400$  mm. Similar empirical observations were already established (Jensen et al., 2010; Stamatopoulos & Malo, 2015). As shown in Figure 7, only tests with embedment lengths of  $l_w = 200$  mm and  $l_w = 300$  mm are performed on WB-T 16 rods in the hardwood specimens. Test with longer rods were discontinued early on, as all tests failed in the tensile capacity of the rods with yielding in the metric thread part.

### 3.3 Withdrawal resistance

An overview on the withdrawal resistances is given on the left in Figure 8 and Figure 9, respectively. Figure 8 and Figure 9 (right) provide the correlation between the withdrawal stiffness  $K_w$  and the withdrawal resistance  $F_{max}$  for the different rod types.

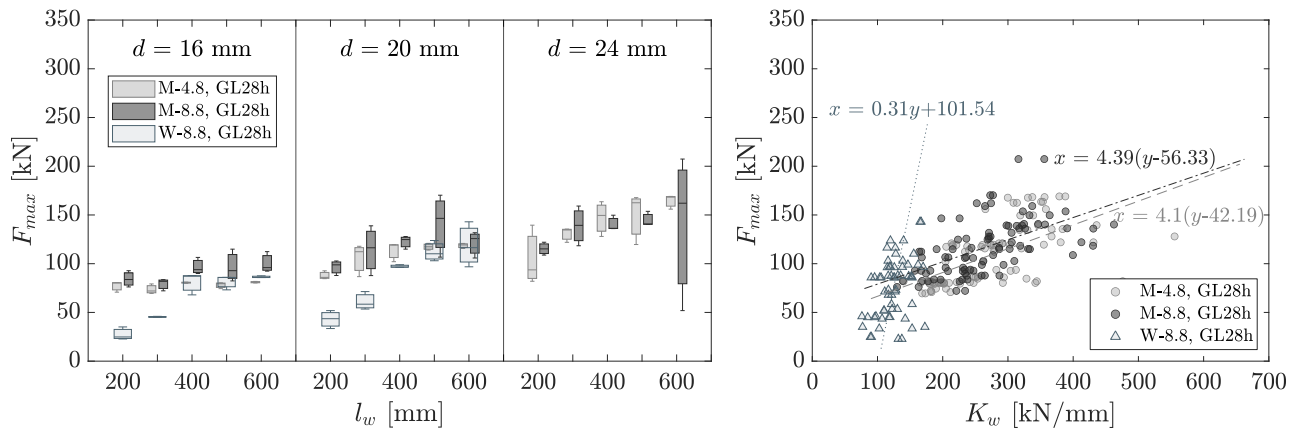


Figure 8. Measured withdrawal resistances in GL28h; as function of the rod type,  $l_w$  and  $d$  (left); as function of the pull-out stiffness (right).

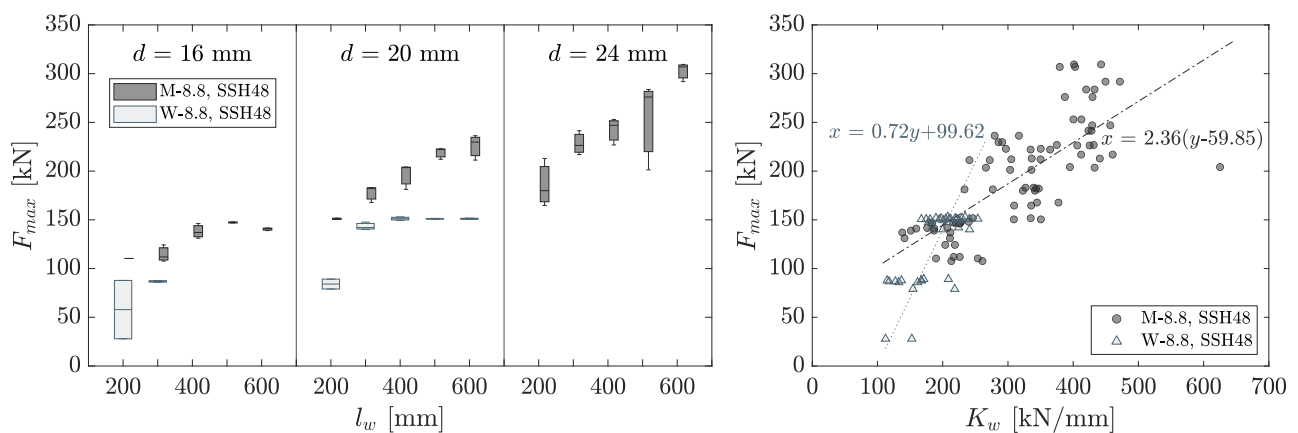


Figure 9. . Measured withdrawal resistances in GL28h; as function of the rod type,  $l_w$  and  $d$  (left); as function of the pull-out stiffness (right).

While the ratio of the mean softwood density to the mean hardwood density is  $\rho_{mean, GL28h} / \rho_{mean, SSH48} = 0.66$ , the ratio of the mean failure loads  $F_{max, GL28h} / F_{max, SSH48}$  ranges from 0.53 to 0.64 for the glued-in rods, and from 0.43 to 0.79 for the rods with wood screw threads, depending on the single rod series. As the presented experimental campaign is limited to two timber grades, a more thorough correlation cannot be investigated.

Regarding the embedment lengths, the graphs reveal the influence of  $l_w$  on  $F_{max}$ . With increasing  $l_w$ , the influence is higher with the screwed-in than with the glued-in rods. With  $l_w = 600$  mm in GL28h, the WB-T 16 and WB-T 20 achieve withdrawal capacities in the same range as the respective glued-in rods with strength class 4.6/4.8 (M – 4.8).

### 3.4 Failure Modes

The failure modes of the specimens are visually and audibly identified during the tests. Figure 10 and Figure 11 show the examined failure modes for the different rod types, rod diameters, embedment lengths and failure loads. The frequencies of the failure modes are given in the bar plots.

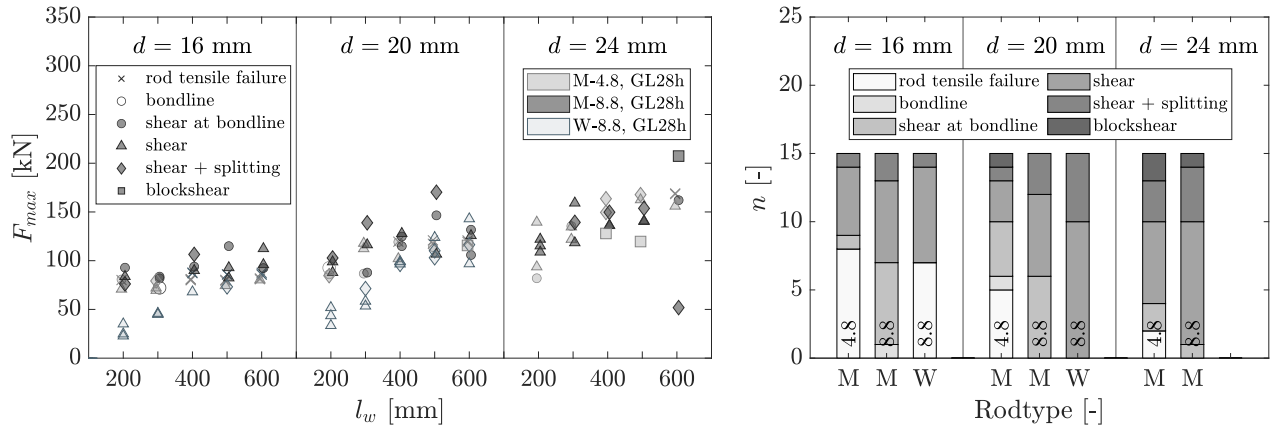


Figure 10. Failure modes in the GL28h specimens. Scatter plot with the corresponding failure load (left). Frequency of the failure modes (right).

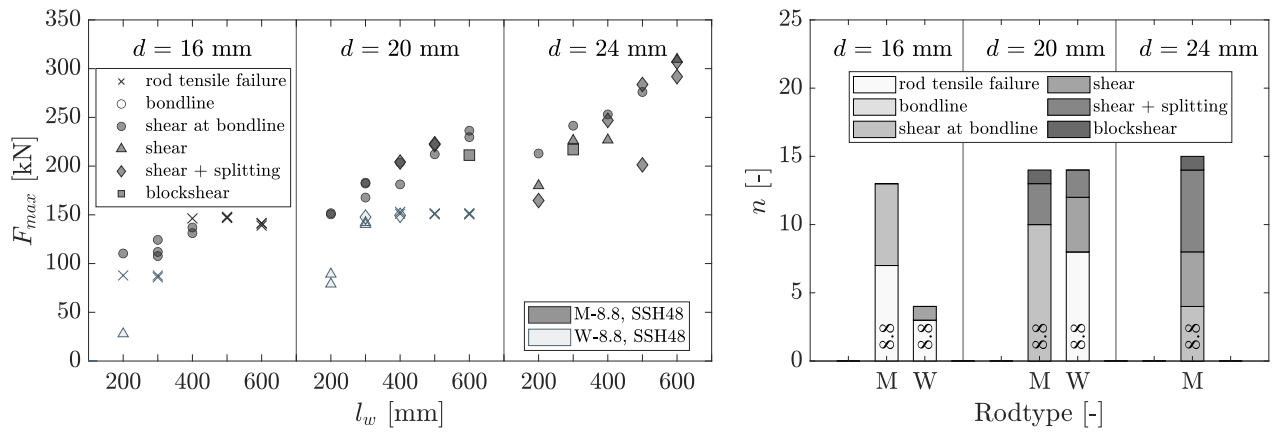


Figure 11. Failure modes in the GL28h specimens. Scatter plot with the corresponding failure load (left). Frequency of the failure modes (right).

In total, the failure modes of the glued-in rods are identified to 1% in the bondline, to 22% in shear immediate adjacent to the bondline, 34 % in pure shear, 17% in shear with splitting, to 4 % in blockshear failure, and to 22% in steel yielding. Bondline failure was only observed twice in the GL28h specimens, in combination with a timber shear failure. The reason for the deficient bondline can be traced back to trial specimens, where the rods were pulled out once after glueing for the verification of the adhesive application. After the verification, these rods were pushed back in the drilled hole.

Regarding the splitting failure, various reasons can be possible triggers. Beside the excessively large forces, the use of high-strength steel leads to brittle failure of the timber, as high tensile stresses perpendicular to the grain occur. A further contributing reason can be related to the constant timber cross-sections, resulting in decreasing edge distances for increasing rod diameters. A further reason can result from the increase of the bondline stresses at the end of the grain due to the short unbonded lengths of  $l_u = 20$  mm. However, as splitting occurred mostly at the bigger rod diameters, the first three reasons are likely more significant.

In the cases showing steel yielding, the plateau can be seen on the withdrawal strength results. For the rods with wood screw threads, the rod yielding is given by the failure capacity of the metric thread, where the net cross-section is reduced. The WB-T16 rods are here limited to the M12 net area, the WB-T20 to the M16 net area respectively.

### 3.5 Withdrawal strength

Withdrawal strengths  $f_{w,k}$  are determined according to Equation (4). For the glued-in rods,  $f_{w,k}$  corresponds with the density-influenced bond shear strength  $f_{vr,\rho}$  according to EN 17334 (2021) and not to the density corrected bond strength  $f_{vr,\rho ref}$ . For the different rod types, Figure 12 and Figure 13 show on the left the correlation with the rod diameter  $d$  and the embedment length  $l_w$ , while the relation for the rod slenderness  $\lambda$  is given on the right side of the figures. All measured results are plotted, including the tests failing by steel yielding.

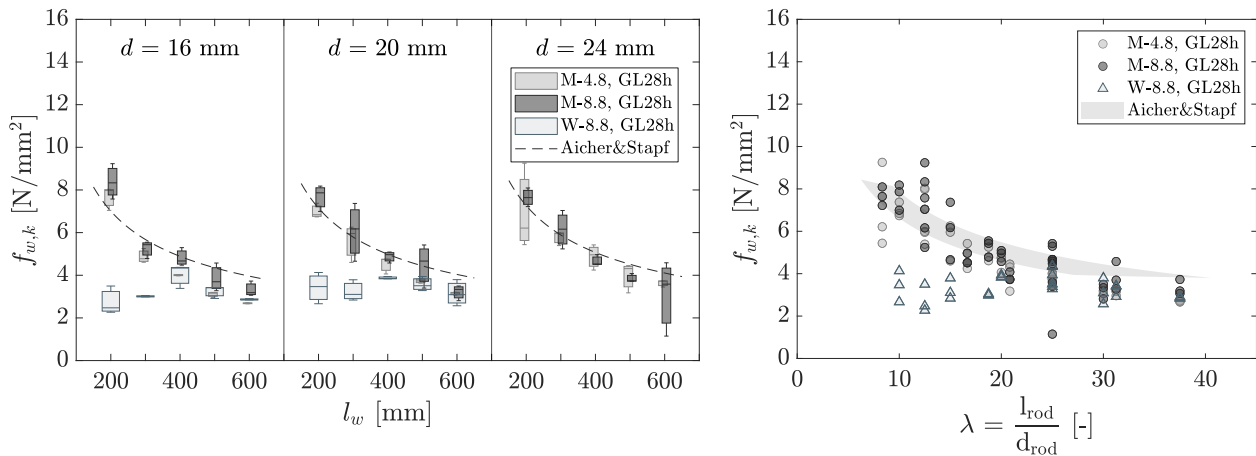


Figure 12: Determined withdrawal strengths in GL28h for both rod types; as function of the rod dimensions  $l_w$  and  $d$  (left), as function of the rod slenderness  $\lambda$  (right).

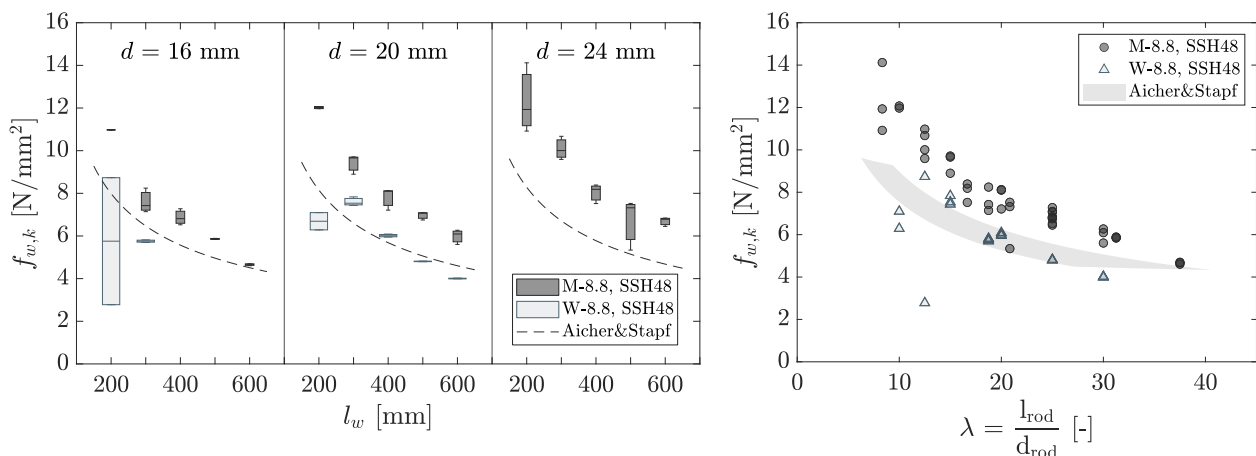


Figure 13. Determined withdrawal strengths in SSH48 for both rod types; as function of the rod dimensions  $l_w$  and  $d$  (left), as function of the rod slenderness  $\lambda$  (right).

For a result comparison of the glued-in rods, the fitting equations by Aicher and Stapf (2017) are highlighted, where the mean density of the respective test series is used for  $\rho$  ( $\rho_{mean, GL28h} = 492$  kg/m<sup>3</sup>,  $\rho_{mean, SSH48} = 742$  kg/m<sup>3</sup>). Figure 12 shows that the measured

bond shear strengths of the glued-in rods fits well with the predictions of Aicher and Stapf (2017) for embedment lengths of  $l_w < 500$  mm in GL28h. For  $l_w \geq 500$  mm the conducted tests tend to show lower withdrawal strengths. The results in SSH48 however exceed the predictions. The assessment of the results with respect to DIN EN 1995-1-1/NA (2013) and prEN 1995-1-1 (2023) for both rod types is given in section 4.

## 4 Discussion and Recommendation

### 4.1 Withdrawal stiffness

In Figure 14 and Figure 15, a comparison of the resulting stiffnesses and the proposed  $K_{SLS,ax}$  for rod installations perpendicular to the grain of prEN 1995-1-1 (2023) is shown. For threaded rods with wood screw threads, the experimental results fit adequately with the predictions for rods set perpendicular to the grain. The measured withdrawal stiffnesses for the parallel to the grain rods are around 1.5 – 2.5 times higher than the predictions in the new draft of Eurocode 5 (2023). For glued-in rods however, no direct correlation with the predicted stiffnesses can be observed.

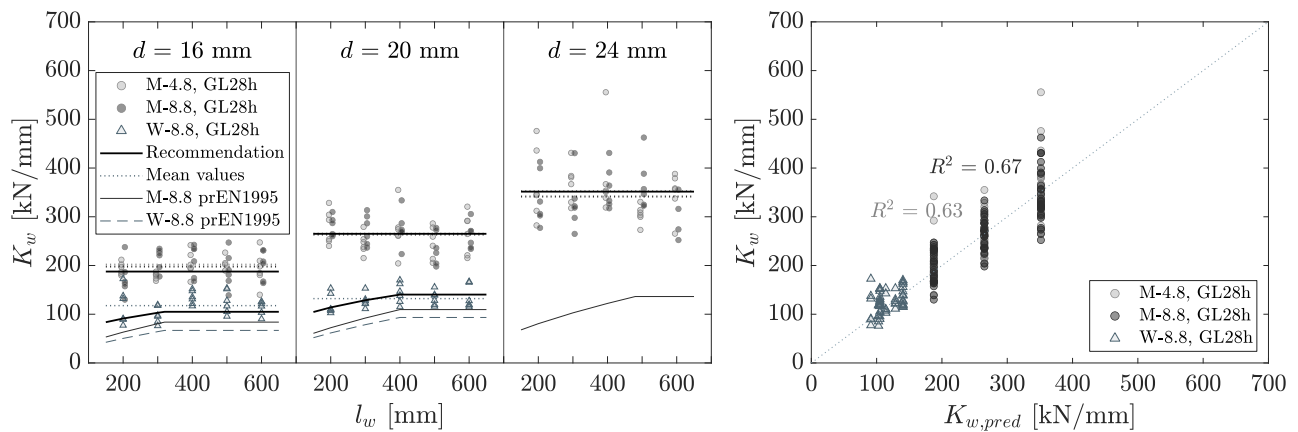


Figure 14. Withdrawal stiffnesses for GL28h with mean values, slip moduli predictions  $K_{SLS,ax}$  according to prEN 1995-1-1:2023 and recommendations (left). Results against predictions (right).

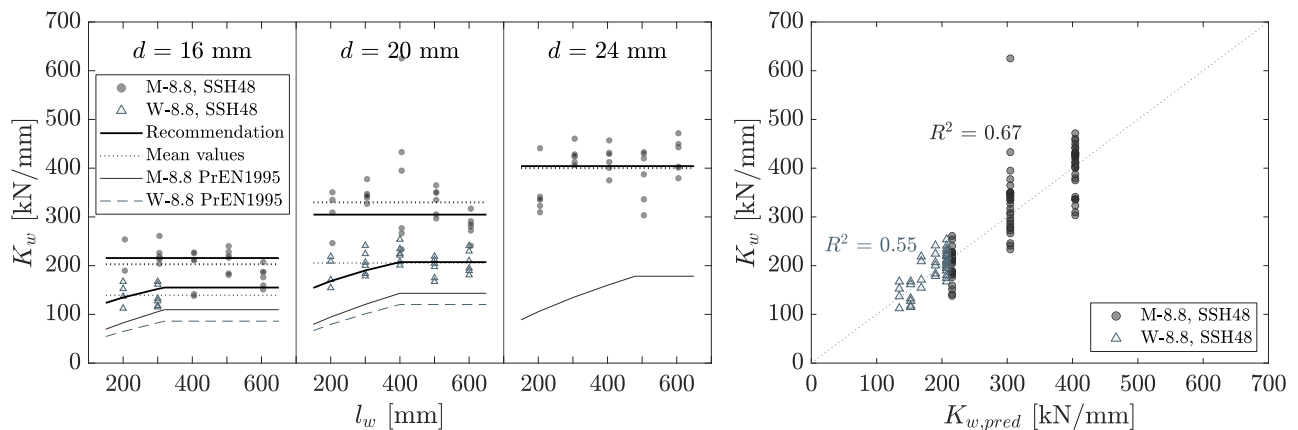


Figure 15. Withdrawal stiffnesses for SSH48 with mean values, slip moduli predictions  $K_{SLS,ax}$  according to prEN 1995-1-1:2023 and recommendations (left). Results against predictions (right).

Due to the lack of withdrawal stiffness predictions for rod installations parallel to the grain ( $\varepsilon = 0^\circ$ ), the following correlation

$$K_w = 310 \cdot d^{1.55} \cdot \rho_{mean}^{0.34} \quad [\text{N/mm}] \quad (5)$$

was found for the glued-in rods, where the mean timber densities of the test results  $\rho_{mean, GL28h} = 492 \text{ kg/m}^3$  and  $\rho_{mean, SSH48} = 742 \text{ kg/m}^3$  are used. In comparison to the equation given in prEN 1995-1-1 (2023) with  $K_{SLS,ax} = 2 \cdot d^{0.6} \cdot l_w^{0.6} \cdot \rho_{mean}^{0.9}$  for rod installations perpendicular to the grain, the rod diameter  $d$  has a higher significance for  $\varepsilon = 0^\circ$ , while the timber density has a smaller influence. For rods in GL28h with  $d = 16 \text{ mm}$ , the stiffness prediction of prEN 1995-1-1 (2023) for the perpendicular to the grain rods results in  $K_w = 84 \text{ kN/mm}$ , while the measured mean values of the experimental tests are  $202.3 \text{ kN/mm}$  and  $197.8 \text{ kN/mm}$  for the rod strengths classes 4.6/4.8 and 8.8, respectively. For the same rods, Ogrizovic et al. (2018) measured a mean stiffness of  $170 \text{ kN/mm}$  in GL24h, which is consistent with the E-modulus difference of the timber.

For the threaded rods with wood screw threads, an adapted equation of the proposal in prEN 1995-1-1(2023) can be recommended for rod installations parallel to the grain:

$$K_w = 1000 \cdot \left(\frac{\rho_{mean}}{420}\right)^{0.95} \cdot d \cdot l_w^{0.3} \quad [\text{N/mm}] \quad \text{for } l_w \leq 20 \cdot d \quad (6)$$

Compared to prEN 1995-1-1 (2023) with  $K_{SLS,ax} = 160 \cdot (\rho_{mean}/420)^{0.85} \cdot d^{0.9} \cdot l_w^{0.6}$  for rod installations perpendicular to the grain, the timber density shows a slightly higher influence, while for the rod diameter  $d$  and the withdrawal length  $l_w$  smaller influence are found for installations parallel to the grain. For both rod types, the plotted withdrawal stiffness recommendations correspond to the given equations (5) and (6).

## 4.2 Withdrawal strength

The test results allow a comparison between the withdrawal strengths and existing calculation models. Figure 16 and Figure 17 show the fitted strength model for the calculation of the withdrawal strengths.

With regard to the embedment length  $l_w$ , the rod diameter  $d$ , and the mean density  $\rho_{mean, GL28h} = 492 \text{ kg/m}^3$  and  $\rho_{mean, SSH48} = 742 \text{ kg/m}^3$ , the regression function for the glued-in rods is determined as

$$f_{w,k} = \left(\frac{l_w}{600} \cdot d^{0.1}\right)^{\frac{2.3}{k \cdot d}} \cdot (0.6 \cdot d \cdot \rho_{mean})^{\frac{\pi \cdot d}{1000}} \cdot \rho_{mean}^k \quad [\text{N/mm}^2], \quad (7)$$

where

$$k = \frac{\rho_{mean}}{3500}. \quad (8)$$

The respective coefficients of determination are between  $R^2 = 0.81$  and  $R^2 = 0.84$  for the GL28h specimens and  $R^2 = 0.89$  for the SSH48 specimens.



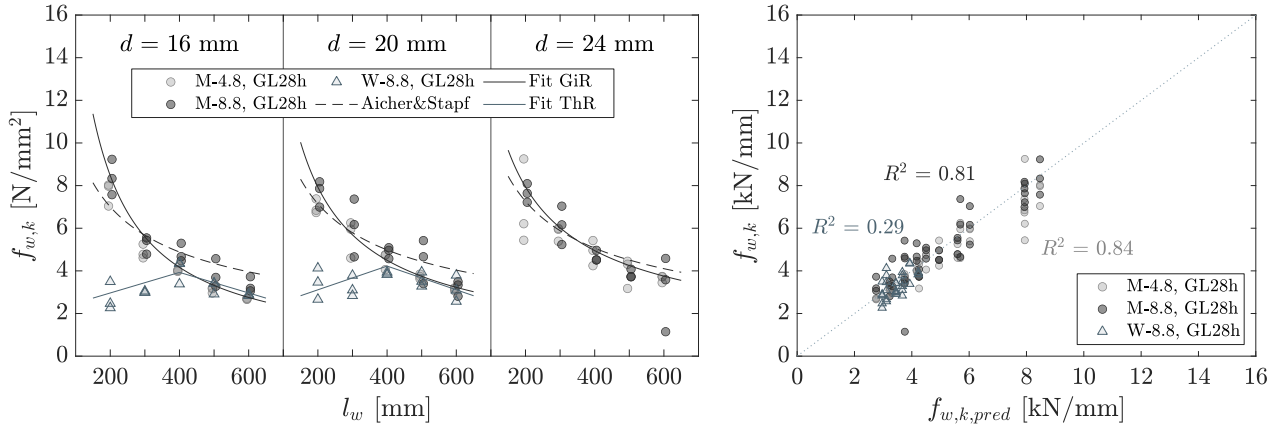


Figure 16. Withdrawal strengths for GL28h. Comparison of existing calculation proposals with the predictions for the experimental results (left). Results against predictions (right).

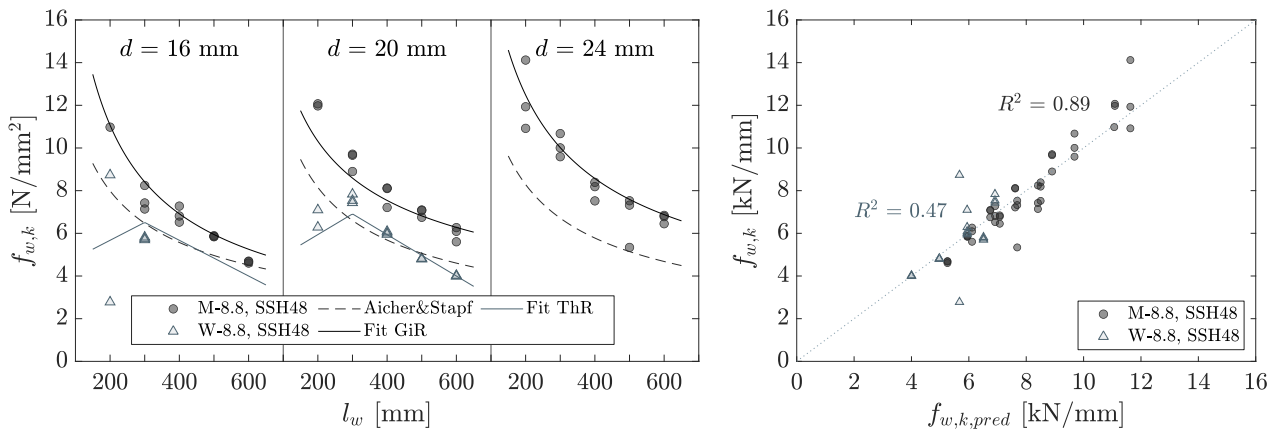


Figure 17. Withdrawal strengths for SSH48. Comparison of existing calculation proposals with the predictions for the experimental results (left). Results against predictions (right).

If a similar equation should be found for the threaded rods with wood screw threads, the withdrawal strength can be expressed by

$$f_{w,k} = \begin{cases} a + \frac{l_w \cdot d^{0.1}}{1000} \cdot (0.6 \cdot d \cdot \rho_{mean})^{\frac{\pi \cdot d}{1000}} \cdot \rho_{mean}^k & \text{for } l_w \leq l_{ref} \text{ mm} \\ a + f_{w,k,l_w=300} - \frac{l_w \cdot d^{0.1}}{1000} \cdot (0.6 \cdot d \cdot \rho_{mean})^{\frac{\pi \cdot d}{1000}} \cdot \rho_{mean}^k & \text{for } l_w > l_{ref} \text{ mm,} \end{cases} \quad (9)$$

where \$k\$ is given by equation (8), \$a = (2; 4)\$ for (GL28h; SSH48) and \$l\_{ref} = (400; 300)\$ for (GL28h; SSH48).

For equation (9), the coefficients of determination are \$R^2 = 0.29\$ for the GL28h specimens and \$R^2 = 0.47\$ for the SSH48 specimens. Due to the small number of specimens (\$n = 30\$ for GL28h and \$n = 19\$ for SSH48) and the small differences in the withdrawal strengths, more investigations are needed to predict \$f\_{w,k}\$ for the rods with wood screw threads.

### 4.3 Recommendations

The following recommendations for single rods set parallel to the grain can be given:

- For stiffness specifications, the given equations in prEN 1995-1-1 (2023) for perpendicular to the grain rods can be slightly adjusted to predict the withdrawal stiffness for rods set parallel to the grain. The respective withdrawal stiffness  $K_w$  is proposed by equations (5) and (6).
- If a more precise withdrawal strength is being sought for glued-in rods, equation (7) gives a recommendation for the conducted tests.

With regard to the production, the subsequent recommendations can be made based on experience:

- The adhesive injection with millilitre dosing accuracy by the electronic dispenser is easy to handle and works well for the adhesive application of glued-in rods. However, the accuracy is not guaranteed, when the drill length would be imprecise. Furthermore, the battery-powered millilitre dosing seems to be vulnerable with respect to temperature change. Improvements in dosing accuracy are recommended.
- Straightness of the rods and the boreholes should be guaranteed by CNC-driven drilling. Manual drilling is not precise enough.
- Before gluing, a degreasing of the rods is recommended.
- For threaded rods screwed-in manually, pre-drilling diameters in hardwood of  $d+2$  mm are recommended. Following the recommendation of  $d+1$  mm given in the approval (ETA-Danmark A/S, 2019) for softwood elements, can't ensure the screwing-in of the rods with the four-speed hand drill machine BOZ 32-4 M from Fein company.

## 5 Summary and conclusion

In this paper, the withdrawal properties of glued-in rods and long threaded rods with wood screw threads are experimentally analysed and discussed for single rods set parallel to the grain. The main objective of the test campaign is the investigation of the withdrawal stiffness of both rod types. Based on the results, recommendations for the withdrawal stiffnesses are given. Furthermore, failure loads, failure modes and the withdrawal strengths are presented.

The findings and recommendations are based on the conducted experimental tests. A detailed comparison of both rod types with respect to pull-out strengths, stiffnesses and failure modes is thus provided. Further experimental investigations are required to obtain results in the untested intermediate ranges of the tested parameters. The results are based on the given conditions. As only three experiments per test series have been carried out, further investigations are suggested. The following conclusions can be drawn:

- The results confirm that the different use of steel grades has no influence on the withdrawal properties.
- For the withdrawal stiffness of the glued-in rods, no significant influence of the embedment length  $l_w$  can be observed for the tested lengths. For the threaded rods with wood screw threads, the stiffness increase becomes smaller with increasing embedment lengths. Furthermore, the withdrawal stiffnesses stay constant and do not further increase when  $l_w > 400$  mm, i.e. for rod slenderness  $\lambda > 15$ -25.
- The proposed withdrawal stiffnesses in prEN1995 (2023), for rods installed perpendicular to the grain, are below the experimental results of the rods set parallel to grain presented in this paper. While the glued-in rods of the present test campaign exceed the axial slip modulus in prEN1995 (2023) by a factor 2, the threaded rods with wood screw threads pass the predictions for the perpendicular to the grain rods by a factor 1.5-1.75.
- The predictions of the withdrawal strengths in prEN 1995 (2023) are on the safe side. However, with a factor 1.5 to 2.0, the observed results exceed the predictions significantly.

## 6 References

- Aicher, S., & Stapf, G. (2017, June). Eingelebte Stahlstäbe - state-of-the-art -Einflussparameter, Versuchsergebnisse, Zulassungen, Klebstoffnormung, Bemessungs- und Ausführungsregeln. *23. Internationales Holzbau-Forum IHF*.
- Bainbridge, R. J., Harvey, K., Mettem, C. J., & Ansell, M. P. (2000). Fatigue performance of bonded-in rods in glulam, using three adhesive types. *CIB-W18 Meeting Thirty-Three*.
- Bainbridge, R. J., Mettem, C., Harvey, K., & Ansell, M. (2002). Bonded-in rod connections for timber structures—development of design methods and test observations. *International Journal of Adhesion and Adhesives*, 22(1), 47–59. [https://doi.org/https://doi.org/10.1016/S0143-7496\(01\)00036-7](https://doi.org/https://doi.org/10.1016/S0143-7496(01)00036-7)
- Bengtsson, C., & Johansson, C. J. (2001). GIROD - Glued-in rods for timber structures. *CIB-W18 Meeting Thirty-Four*.
- Bernasconi, A. (2001). Behaviour of axially loaded glued-in rods - Requirements and resistance, especially for spruce timber perpendicular to the grain direction. *CIB-W18 Meeting Thirty-Four*.
- Blaß, H. J., & Laskewitz, B. (1999). Effect of spacing and edge distance on the axial strength of glued in rods. *CIB-W18 Meeting Thirty-Two*.
- CEN. (1991). *EN 26891 Joints made with mechanical fasteners - General principles for the determination of strength and deformation characteristics*.

- CEN. (2010). *EN 1995-1-1 Eurocode 5: Design of timber structures - Part 1-1: General - Common rules and rules for buildings.*
- CEN. (2013). *EN 14080 Timber structures - Glued laminated timber and glued solid timber - Requirements.*
- CEN. (2021). *EN 17334 Glued-in rods in glued structural timber products - Testing, requirements and bond shear strength classification.*
- CEN. (2022). *EN 384 Structural timber - Determination of characteristic values of mechanical properties and density.*
- CEN/TC 250/SC5. (2023). *prEN 1995-1-1 Eurocode 5: Design of timber structures - Part 1-1: General - Common rules and rules for buildings.*
- DIN. (2013). *EN 1995-1-1/NA National Annex Eurocode 5: Design of timber structures - Part 1-1: General - Common rules and rules for buildings.*
- ETA-Danmark A/S. (2019). *ETA-19/0129 - SFS WB-T Gewindestange. Gewindestangen in tragenden Holzkonstruktionen.*
- ETA-Danmark A/S. (2022). *ETA-11/0030 - Rotho Blaas Self-tapping screws and threaded rods. Screws and threaded rods for use in timber constructions.*
- ETA-Danmark A/S. (2023). *ETA-11/0024 - E.u.r.o. TEC screws type "BRUTUS" threaded rods. Screws for use in timber constructions.*
- Fagus Suisse SA. (2023). *Fagus Stabschichtholz - Bemessungswerte für Esche.*  
<https://fagussuisse.ch/wp-content/uploads/2023/08/230823-bemessungswerte-esche.pdf>
- Gustafsson, P., Serrano, E., Aicher, S., & Johansson, C. J. (2001). A strength design equation for glued-in rods. *Proc. Int. RELEM'S.*, 22, 324–327.
- Hübner, U. (2013). *Mechanische Kenngrößen von Buchen-, Eschen- und Robinienholz für lastabtragende Bauteile.*
- Hübner, U., Rasser, M., & Schickhofer, G. (2010). Withdrawal capacity of screws in European ash (*Fraxinus excelsior* L.). *11th World Conference on Timber Engineering 2010, WCTE 2010.*
- Jensen, J., Quenneville, P., & Nakatani, M. (2010). Withdrawal of lag screws in end-grain. *World Conference on Timber Engineering, 3*, 1921–1925.
- Krüger, O., & Blaß, H. J. (2009). *Prüfbericht Nr. 086129 - Tragfähigkeitsversuche mit SFS Gewindestangen WB mit 16 mm und 20 mm Durchmesser.*
- Lignatec. (2021). *Verklebte Laubholzprodukte für den statischen Einsatz.*
- Mettem, C. J., Bainbridge, R. J., Harvey, K., & Ansell, M. P. (1999). Evaluation of material combinations for bonded in rods to achieve improved timber connections. *CIB-W18 Meeting Thirty-Two.*

- Ogrizovic, J., Jockwer, R., & Frangi, A. (2018). Seismic response of connections with glued-in steel rods. *INTER Meeting Fifty-One*.
- OIB. (2023). *ETA-20/0834 - Hilti HIT-RE 500 V4. Glued in rods for timber connections*.
- Riberholt, H. (1988). Glued bolts in glulam - Proposal for CIB Code. *CIB-W18A/21-7-2 Meeting Twenty-One*.
- Stamatopoulos, H., & Malo, K. (2015, March). Characteristic withdrawal capacity and stiffness of threaded rods. *INTER Meeting Forty-Eight*.
- Steiger, R., Gehri, E., & Widmann, R. (2007). Pull-out strength of axially loaded steel rods bonded in glulam parallel to the grain. *Materials and Structures*, 40(1), 69–78. <https://doi.org/10.1617/s11527-006-9111-2>
- Steiger, R., Serrano, E., Stepinac, M., Rajčić, V., O’Neill, C., McPolin, D., & Widmann, R. (2015). Strengthening of timber structures with glued-in rods. *Construction and Building Materials*, 97, 90–105. <https://doi.org/10.1016/j.conbuildmat.2015.03.097>
- Stepinac, M., Hunger, F., Tomasi, R., Serrano, E., Rajcic, V., & van de Kuilen, J.-W. (2013, March). *Comparison of design rules for glued-in rods and design rule proposal for implementation in European standards*.
- Tlustochowicz, G., Serrano, E., & Steiger, R. (2011). State-of-the-art review on timber connections with glued-in steel rods. *Materials and Structures*, 44(5), 997–1020. <https://doi.org/10.1617/s11527-010-9682-9>

## DISCUSSION

**The paper was presented by C Binck**

*E Serrano asked how was the stiffness of the joint measured. C Binck responded that deformation between end of timber and the sleeve of the GIR was measured.*

*D Moroder questioned how the bond quality in manufacturing be controlled in the chosen sequence of installation.*

*H Stamatopoulos and C Binck discussed parallel to grain application versus small angle application which can potentially reduce the influence of shrinkage cracks.*

*H Stamatopoulos received clarification of whether a camera system was used from one or both sides of the specimen.*

*P Vinco da Sesso commented on possible tolerance issues during manufacturing of the GIR and not to consider the full length as embedment length due to the increased splitting potential.*

*S Aicher commented that too much recommendations are given based on testing of only one product from a single manufacturer. Typical construction practice would use a larger hole to ease production which would influence performance of the connection. He emphasized that one should not provide a proposal based on a single producer. A Frangi responded that one did not observe bond line failure and stiffness of the connection could be achieved easily. Therefore the results should be applicable to other producers. S Aicher said results from testing with one mm oversized holes cannot be generalized to other situations.*

*R Jockwer questioned measurement of stiffness for different unbonded lengths.*

*C Binck responded if the 5 cm unbonded length was neglected, stiffness would be 5% higher. Stiffness values for different unbonded length could be corrected but was not done in the original version of the paper.*

*C Sandhaas received confirmation that the measurement differences across the specimen width were so small that taking an average was acceptable.*

*S Winter discussed failure mode versus capacity in slide 75 and received explanation that in some cases yield point of the rod was close to shear failure load.*



# Embedment strength of glued-in rods and dowels oriented parallel to grain

Simon Aicher; Kai Simon

Materials Testing Institute, University of Stuttgart

Keywords: embedment strength, glued-in rods, dowel-type-fasteners, connections

## 1 Motivation

Glued-in rod connections represent an efficient method for transfer of high loads in timber to timber and timber to steel / concrete connections, proven widely in practice and research ( (Schmid & Fischer, 2010), (Hezel, Aicher, & Helbig, 2015), (Aicher & Simon, 2021)). While loading parallel to rod axis represents a rather robust solution, lateral forces are rather crucial in case of rods glued-in parallel to grain with regard to splitting due to tensile forces acting perpendicular to grain, especially in unreinforced joints.

Joints with glued-in rods are now tackled in the second generation of Eurocode 5 (prEN 1995-1-1 (2023)). The respective design of lateral forces given in the new EC5 is closely aligned with DIN EN 1995-1-1/NA (2013) and resembles the design of connections with dowel type fasteners. The design depends apart from geometrical boundaries on embedment strength of the wood in any case and additionally on yield moment of the rod in case of a failure mode including rod yielding, see Figure 1. Embedment strength influences the lateral capacity in all cases and prevailingly in linear manner hence being a highly decisive capacity parameter.

The equations for embedment strength for the situation of a rod glued-in parallel to grain or slightly inclined given in prEN 1995-1-1 deliver apparently very low strength results. When comparing with EC5 design solutions for screws and rods with wood screw thread inserted parallel to grain where much higher embedment strengths are proposed. This assessment is further supported by a small number of previous test results and evaluations which delivered throughout much or extremely higher values (e.g. (Riberholt, 1977, 1986), (Möhler & Hemmer, 1981), (Ehlbeck & Gerold, 1989)). The issue of embedment strength of fasteners inserted parallel to grain is of utmost importance for the effectiveness of joints with rods glued-in parallel or inclined to grain as the joint design specifications stipulate an interaction verification of axial and lateral forces with the same exponent on the respective utilization.

To spread light on ratio empiric-based embedment values an experimental campaign was initiated for clarification. Hereby the eventual increase of the embedment strength of resin-injected bolts vs. tight fitting dowels in holes predrilled with nominal dowel diameter as revealed previously by Rodd (Rodd, Hilson, & Spriggs, 1989) is addressed, too.



## 2 Lateral resistance of bonded-in rods

The design clauses in (prEN 1995-1-1:2023-10, 2023) specify that the characteristic resistance  $F_{D,k}$ , termed awkwardly dowel-effect contribution, vs. the lateral load  $F_{lat}$  acting at a distance  $l_{can} > 0$  from the bond line should be calculated as

$$F_{D,k} = \min \begin{cases} d \cdot f_{h,k} \cdot \left( \sqrt{(l_h + 2 \cdot l_{can})^2 + l_h^2} - l_h - 2l_{can} \right) & (1a) \\ d \cdot f_{h,k} \cdot \left( \sqrt{l_{can}^2 + \frac{2M_{y,k}}{d \cdot f_{h,k}}} - l_{can} \right) & (1b) \end{cases}$$

where

- $d$  nominal diameter of the bonded-in rod
- $f_{h,k}$  characteristic embedment strength of the wood as defined below
- $l_h$  embedment length of the rod
- $M_{y,k}$  characteristic yield moment of the rod

Equations (1a) and (1b) based on Johansen yield theory (Johansen, 1949) are related to the failure modes depicted in Figs. 1 a) and b), respectively.

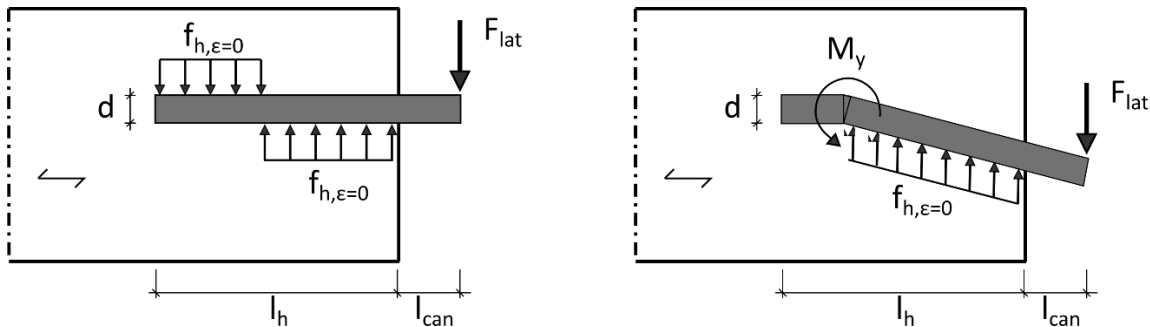


Figure 1: Failure modes a) and b) and according design equations (prEN 1995-1-1:2023-10, 2023)

The Eqs. (1a, b) which consider an off-set / air gap  $l_{can}$  between load and begin of the bond line, firstly derived by Johansen (1949) and Riberholt (1977) rely on the fact that the load  $F_{lat}$  is introduced quasi point like over a very short application length. In the limit case of  $l_{can} = 0$ , Eqs. (1a) and (1b) then reduce to

$$F_{D,k} = 0,41 \cdot f_{h,k} \cdot l_h \cdot d \quad \text{and} \quad (2a)$$

$$F_{D,k} = \sqrt{2} \cdot \sqrt{M_{y,k} \cdot f_{h,k} \cdot d} \quad . \quad (2b)$$

Expressions (2a, b) conform fully (Eq. (2a)) and predominantly (Eq. (2b)) to the Johansen equations for the characteristic load carrying resistance of a single fastener per shear plane between a timber member and a thin steel plate as specified in EN 1995-1-1 (2010). Equation (2b) is more conservative as compared to the solution for a thin

steel plate with  $l_{can} = 0$  in (Eurocode 5, 2010) as the pre-factor 1,15 is missing and no rope effect accounting for an activation of the pull-out resistance is addressed.

In case the lateral force is not applied point-like but via a thick, stiff and high strength embedment material as present in case of a tight fitting, thick steel-plate or a concrete abutment in which the rods are cast the additional capacity gain by either moment free embedment or by development of a second yield moment can be considered by the respective Johansen equations, e.g. Blaß (2000).

The numerical evaluation of the above given equations for  $F_{D,k}$  relies apart from the geometry data being bolt diameter  $d$  or better drill hole diameter  $d_h$  in case of glued-in rods, bond length  $l_h$  and eccentricity  $l_{can}$  on two material parameters being characteristic yield moment  $M_{y,k}$  and characteristic embedment strength  $f_{h,k}$ . The calculation of  $M_{y,k}$  by  $M_{y,k} = 0,3 \cdot f_{u,k} \cdot d^{2,6}$  (Eurocode 5, 2010) based on the characteristic tensile strength  $f_{u,k}$  is substantiated and not considered here any further. Regarding embedment strength the issue of realistic values is, however, much less clear. In this context for clarity the hereinafter used angle definitions relevant for embedment strengths are precised in Fig. 2 illustrating the different angles between load and fastener axis ( $\alpha$ ) and fastener axis and grain direction ( $\epsilon$ ). Dowels and bolts are design-wise and practically throughout inserted perpendicular to grain ( $\epsilon = 0^\circ$ ) and hence exclusively angle  $\alpha$  between load and grain can vary ( $0^\circ \leq \alpha \leq 90^\circ$ ). This is different for self-tapping screws with or without predrilling which can be / are inserted at deliberate angles  $\epsilon$  to grain. When considering the case of rods glued-in perpendicular to grain, i.e.  $\epsilon = 90^\circ$  (see Fig. 2), draft Eurocode 5 specifies that an embedment strength should be applied as for a dowel type fastener inserted perpendicular to grain. Hereby as shown below angle  $\alpha$  between load and grain direction and the respectively used wood materials shall be considered.

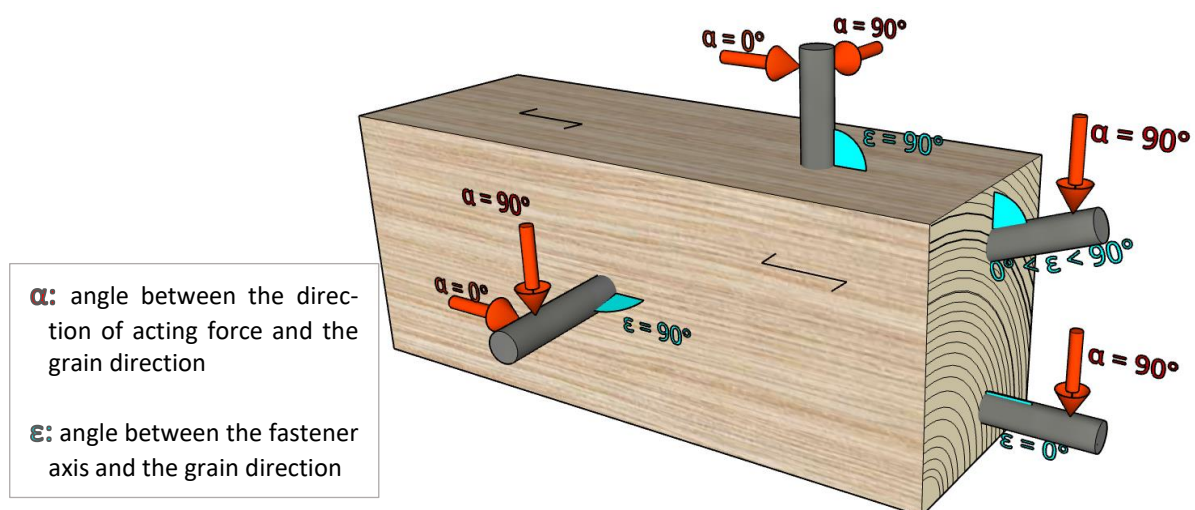


Figure 2: Denotation of angles  $\alpha$  and  $\epsilon$  acc. to prEN1995-1-1 (2023)

However, in case of rods bonded-in parallel to grain into the end-grain face ( $\varepsilon = 0^\circ$ ) or at an angle to grain ( $0^\circ < \varepsilon < 90^\circ$ ) either at the end grain face or at one of the side faces all present code specifications are much less based on science and validated material parameters. EC5 draft (2023) specifies for the case of laterally loaded rods bonded-in parallel to grain ( $\varepsilon = 0^\circ$ ) that the embedment strength should be taken as 10% of the embedment strength of a laterally loaded rod inserted perpendicular to grain ( $\varepsilon = 90^\circ$ ). However, with regard to lateral loading no angle  $\alpha$  is specified. This has to be seen in view of the possible angle range of  $0^\circ \leq \alpha \leq 90^\circ$  which relates to significantly differing embedment strength values. For rods bonded in at angles  $0^\circ < \varepsilon < 90^\circ$  the EC5 draft then stipulates a linear interpolation between the solutions for  $\varepsilon = 0^\circ$  and  $\varepsilon = 90^\circ$  whereby the unclarity with regard to angle  $\alpha$  remains. The uncertainty on the correct / appropriate choice of angle  $\alpha$  for embedment strength at  $\varepsilon = 90^\circ$  has been addressed previously in (Blaß, Ehlbeck, Kreuzinger, & Steck, 2004) then stipulating the higher embedment strength at  $\alpha = 0^\circ$ , i.e. the value for loading parallel to fiber. Concluding it can be stated that no convincing scientific explanation can be found in literature for setting  $f_{h,\alpha=90,\varepsilon=0}$  to 10% of either  $f_{h,\alpha=0,\varepsilon=90}$  or  $f_{h,\alpha=90,\varepsilon=90}$  of a dowel type fastener. In addition to the above it has to be mentioned that DIN EN 1995-1-1/NA (2013) specifies different from prEN1995-1-1 (2023) for glued-in rods a 25% increase vs. the basic strength for bolts in predrilled holes  $f_{h,\alpha=0,\varepsilon=90}$  based on the work by Rodd et al. (1989).

### 3 Embedment strengths of fasteners given in EC5

#### 3.1 Dowels and bolts inserted perpendicular to grain

Embedment strength of dowel type fasteners inserted in predrilled holes of softwoods perpendicular to grain ( $\varepsilon = 90^\circ$ ) and loaded at an angle  $\alpha$  ( $0^\circ \leq \alpha \leq 90^\circ$ ) to grain (see Figure 2) has been extensively investigated especially by Whale and Smith (1986) and Ehlbeck and Werner (1992) in loading parallel and perpendicular to grain, respectively. The wood species used was mainly European spruce. The results of the mentioned research work are implemented in the present Eurocode 5 part 1-1 (2010) and principally alike in prEN 1995-1-1 (2023) as ( $\rho_k$  = characteristic wood density)

$$f_{h,\alpha,k} = \frac{f_{h,0,k}}{k_{mat}(\alpha)} \quad (3)$$

where

$$f_{h,0,k} = 0,082 \cdot (1 - 0,01 \cdot d) \cdot \rho_k \quad (4)$$

$$k_{mat}(\alpha) = k_{90} \cdot \sin^2 \alpha + \cos^2 \alpha . \quad (5a)$$

$$\text{with } k_{90} = \frac{f_{h,0,k}}{f_{h,90,k}} = 0,015 \cdot d + \begin{cases} 1,35 & \text{softwood SL, PL and GL} \\ 1,30 & \text{softwood LVL} \\ 0,90 & \text{hardwood ST, GL, LVL and GLVL} \end{cases} \quad (5b)$$

Note that factor 1,3 for softwood LVL in Eq. (5b) has been changed in the draft of EC5 (2023) to 1,15. In the Hankinson-type equation format of Eq. (3) and (5 a,b)  $k_{90}$  actually representing the ratio  $f_{h,0,k} / f_{h,90,k}$  depends slightly on the dowel diameter and varies in case of softwood SL, PL and GL for typical diameters of 16 to 24 mm marginally from 1,6 to 1,7. No specifications are provided for angles  $\varepsilon \neq 90$ .

### 3.2 Screws and rods with wood screw thread inserted at various angles to grain

Although the lateral force design provisions for joints with glued-in rods address code-wise (prEN 1995-1-1:2023-10, 2023) with regard to embedment strength exclusively dowel type fasteners it is tempting to look on  $f_h$  values existing for screws and rods with wood-screw thread. Extensive experimental investigations with self-tapping screws of diameters  $d = 6$  mm, 8 mm and 12 mm are reported in (Blaß, Bejtka, & Uibel, 2006). The screws were inserted at different angles  $\varepsilon$  between screw axis and wood fiber direction ( $0^\circ \leq \varepsilon \leq 90^\circ$ ) and further different angles  $\alpha$  between load and fiber direction ( $0^\circ \leq \alpha \leq 90^\circ$ ) were considered. Based on regression analysis of the entity of results the characteristic embedment strength of the self-tapping screws was derived as ( $\rho_k$  in  $\text{kg/m}^3$ )

$$f_{h,k} = f_{h,\varepsilon,k} = \frac{0,019 \cdot \rho_k^{1,24} \cdot d^{-0,3}}{2,5 \cdot \cos^2 \varepsilon + \sin^2 \varepsilon} \quad \text{in N/mm}^2. \quad (6)$$

As can be seen from Eq. (6), now proposed for prEN 1995-1-1 (2023), embedment strength is specified independent of variable  $\alpha$  similarly as for nails and staples indicating no influence of the angle between load and grain direction. The disregard of an  $\alpha$ -influence in Eq. (6), however, is bound to an embedment displacement of about 4-5 mm, whereas some differences occur at smaller embedment indentations where embedment strength at  $\alpha = 90^\circ$  is noticeably smaller as compared to  $\alpha = 0^\circ$  (Blaß, Bejtka, & Uibel, 2006).

## 4 Experimental program, test set-up and evaluation

In order to provide a consistent experimental verification on the highly divergent literature and design standard specifications for embedment strength of glued-in rods an extensive test campaign was realized. The prime focus was on steel dowels and rods inserted parallel to grain in the end grain face ( $\varepsilon = 0^\circ$ ) of solid wood then loaded perpendicular to dowel axis and grain direction ( $\alpha = 90^\circ$ ). Hereby two configurations were regarded being i) smooth shanked steel dowels inserted without additional adhesive in tight fitting drill holes (diameter  $d_h$ ) of same diameter as the dowels ( $d_d$ ) and ii) threaded steel rods bonded centrically into the drill holes. To enable an immediate comparison of the results obtained for the bolts without and with resin injection the

diameter of the drill hole was equally  $d_h = 20$  mm in all cases. The diameter of the smooth dowels was 20 mm as well whereas the nominal diameter of the glued-in steel rods was  $d_d = 16$  mm resulting in a nominal bond line thickness of  $t_b = 2$  mm.

For an assessment of the test results vs. the code provisions (prEN 1995-1-1:2023-10, 2023) where embedment strength of rods bonded-in parallel to grain are based on values for dowels inserted perpendicular to grain, i.e.  $\varepsilon = 90^\circ$ , such a rod placement was investigated as well. Hereby two different configurations were regarded being in principle equally relevant, i.e. loading of the dowel parallel ( $\alpha = 0^\circ$ ) and perpendicular ( $\alpha = 90^\circ$ ) to grain, respectively.

To ensure a best possible matching of all four investigated test configurations the wood slabs or segments of each single test were cut adjacent from one timber scantling piece. The reported experimental campaign was conducted with solid wood (SL) from European spruce softwood. The specimens shown in Fig. 3 were cut from a total of 30 scantlings with cross-sectional dimensions of 120 mm x 140 mm and a length of about 500 mm. The mean and characteristic wood density as determined from all scantlings was  $\rho_{12} = 446 \pm 58$  kg/m<sup>3</sup> and  $\rho_{12,k} = 348$  kg/m<sup>3</sup>, respectively. The wood slab shown in front of Figure 3 served for testing of the rod bonded in parallel to grain and the second slab with a thickness of 50 mm, too, was used for embedment investigations of the corresponding tight fitting not bonded dowel. The third scantling piece with a length of 350 mm served for embedment testing of not resin-injected dowels inserted perpendicular to grain. In this scantling two holes had to be placed to enable both loading directions  $\alpha = 0^\circ$  and  $90^\circ$ . The dimensions of the wooden specimens were chosen in close alignment with EN 383 (2007) especially regarding the edge distances.

The bond manufacture of the specimens with glued-in rods is revealed in Figs. 4 a) and b). The protruding ends (25 mm) of the rods ( $d = 16$  mm) with metrical thread as well as the wood end-grain faces around the drill hole were sealed with a tape and the 2C-epoxy adhesive (WEVO EP32S with hardener B22 TS, DIBt Z-9.1-705 (2021)) was pressed in the gap between rod and drill hole with a syringe.

Figure 5 a) shows the scheme of the test set-up conforming to EN 383 (2007); the realized test arrangement is depicted in Figure 5 b). The embedment displacement was measured with two LVDT's mounted diagonally opposite at both wide specimens faces as depicted in Fig. 5 b). The embedment tests were conducted in a screw-driven electro-mechanical test machine (capacity 100 kN) in displacement control with constant movement of the loading cross-head at a rate of about 1 mm/min. The load was applied in all cases until an embedment displacement of at least 5 mm had been reached. Similar to the provisions of EN 383 the load was applied with a first loading up to about 30%-40% of the estimated load  $F_{est}$  followed by unloading to 10% of  $F_{est}$  after a waiting period of 30 sec then followed by ramp loading up to  $\delta_{max} = 5$  mm. The load and

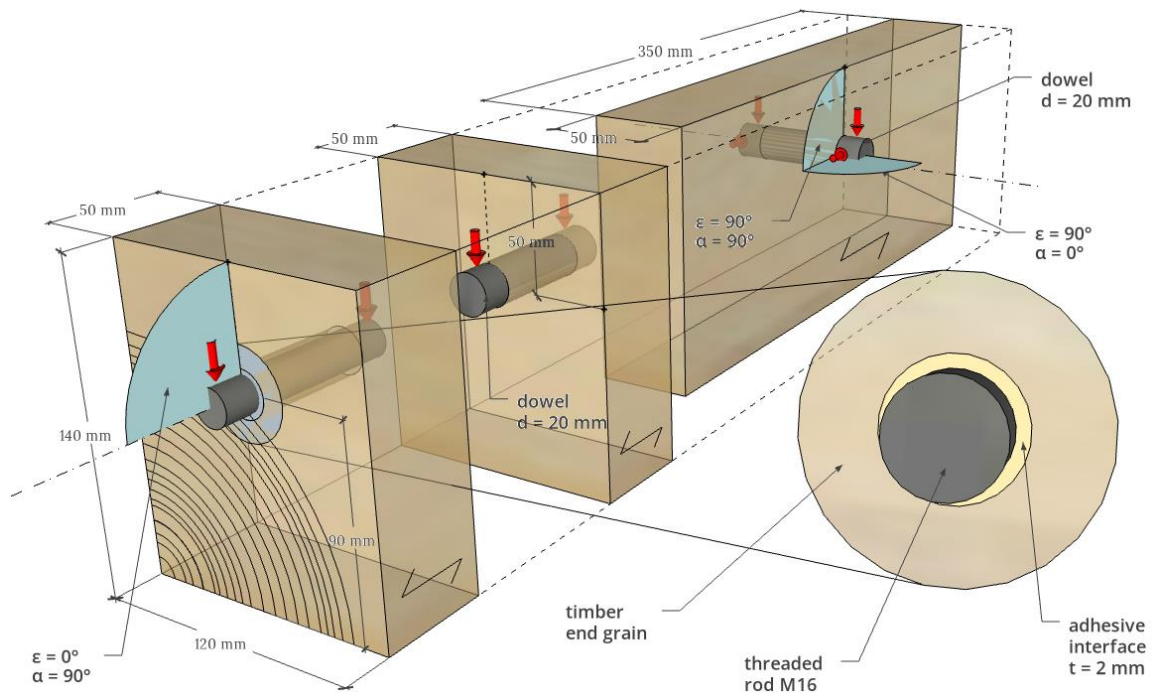


Figure 3: Cutting scheme of the matching samples for the four embedment test configurations

displacement were continuously recorded in a computer-controlled data acquisition system. Embedment strength was determined as usual by

$$f_h = \frac{F_u}{d_{hole} \cdot l_h} \quad \text{in N/mm}^2 \quad (7)$$

where

- $F_u$  maximum load within embedment range of  $\delta_u = 0 - 5$  mm
- $d_{hole}$  drill hole diameter
- $l_h$  embedment length of the fastener inside the wood specimen

The tests were conducted in a heated (19 – 22°C) yet not climatized test room. Immediately after test end a slice with thickness of 30 mm was cut from each specimen for determination of moisture content by oven-drying acc. to EN 13183-1 (2002). The density was determined by weight and dimension measurements of the moisture slice.

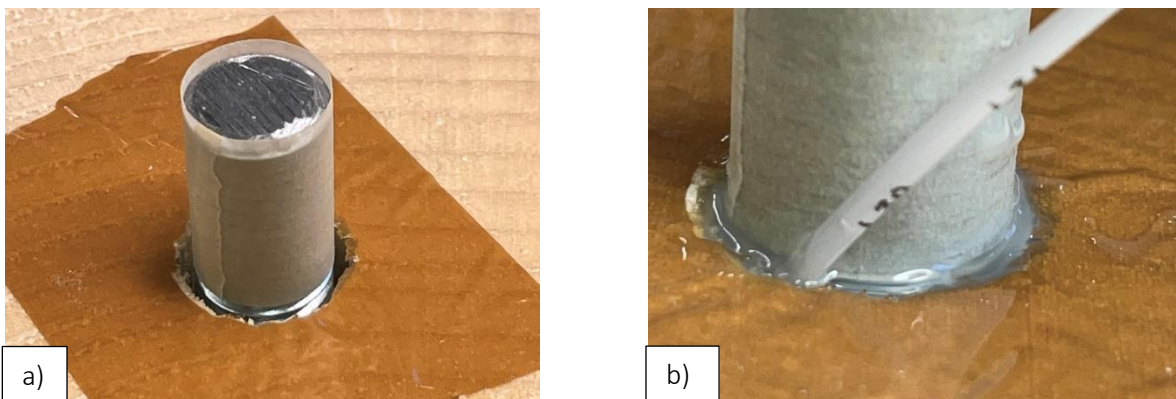


Figure 4: Manufacture of glued-in rod embedment joints a) prepared M16 rod in drill hole, b) adhesive filling process with syringe

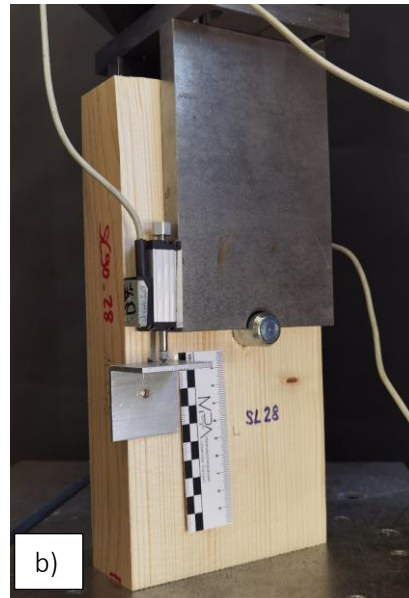
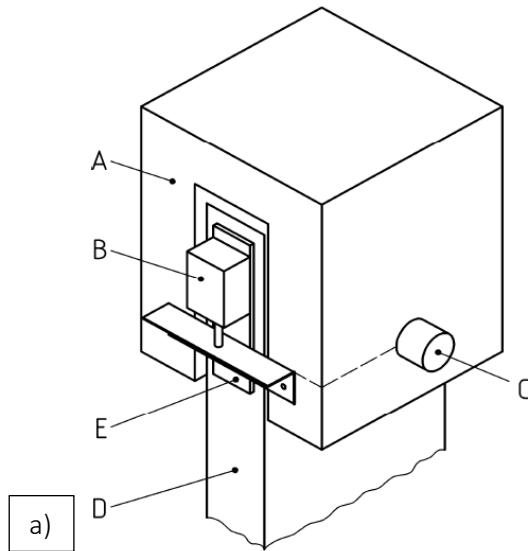


Figure 5: a) Testing scheme acc. to EN 383 (2007) and b) realized test set-up

## 5 Test results of dowels inserted perpendicular to grain

Figure 6 a) depicts typical load indentation / embedment curves which resemble shape-wise rather well in case of loading parallel ( $\alpha = 0^\circ$ ) and perpendicular ( $\alpha = 90^\circ$ ) to grain. A difference can be observed after the nonlinear yielding phase where stiffness of the  $\alpha = 90^\circ$  - specimens is linearly increasing while in case of  $\alpha = 0^\circ$  the slope is horizontal or slightly negative.

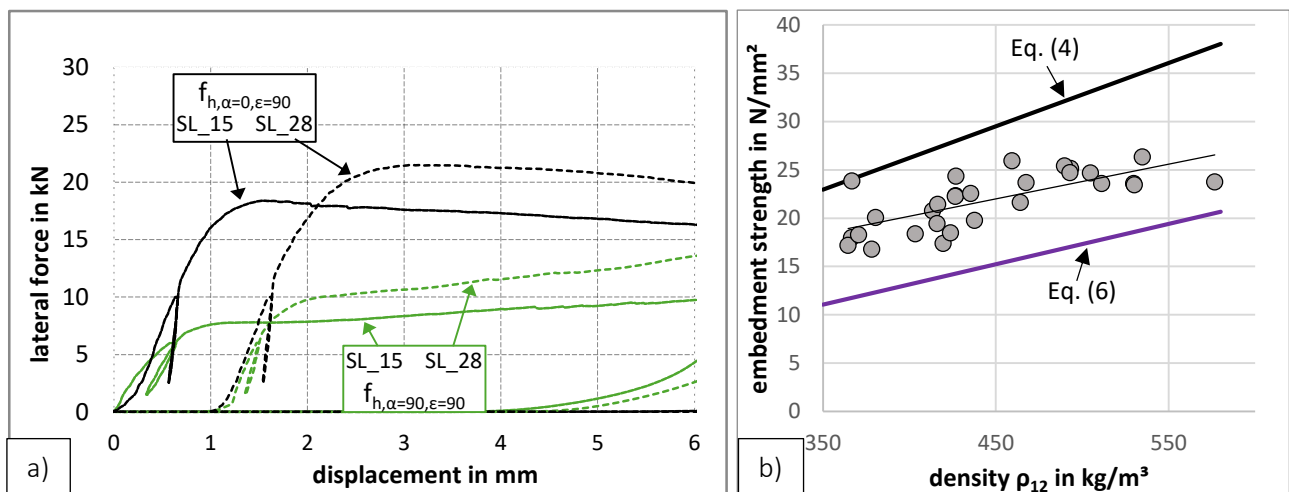


Figure 6: a) Typical load-displacement curves of embedment tests with dowels oriented perpendicular ( $\epsilon=90^\circ$ ) and loaded parallel ( $\alpha=0^\circ$ ) (black) or perpendicular ( $\alpha=90^\circ$ ) (green) to fiber for specimen pairs No. SL15 and SL28  
 b) Embedment strength results  $f_{h,0,90}$  of specimens made from spruce solid wood lumber

Figure 6 b) shows the relationship of embedment strength  $f_{h,0,90}$  with density  $\rho = \rho_{12}$  in loading parallel to grain. A linear regression on the test results delivers ( $\rho_{12}$  in  $\text{kg/m}^3$ )  
 $f_{h,0,90} = 5,8846 + 0,0358 \rho$  (in  $\text{N/mm}^2$ ), (8)

with a coefficient of correlation of  $R^2 = 0,52$ . Besides the test results and their linear approximation, the embedment strengths acc. to Eqs. (4) and (6) is shown whereby the characteristic values  $f_{h,k}$  and  $\rho_k$  are replaced by individual values  $f_h$  and  $\rho$  as done vice versa in the derivation of the respective equations. The test results reveal a similar relationship with density as predicted by the EC5 specifications. Most important, however, is the striking off-set of the experimental results from the code equation (4) in terms of strength level. The EC5 Eq. (4) for dowels delivers a much higher embedment strength. Contrary Eq. (6) for (self-) tapping screws, which is however, limited to a maximum diameter of 12 mm, underestimates the test results significantly. To enable a concise quantitative comparison firstly the individual embedment strength results  $f_{h,i}$  are normalized vs. their respective individual densities  $\rho_i$ , resulting in

$$(f_h/\rho)_{\text{mean}} = 49,2 \pm 0,6 \cdot 10^{-3} \quad \text{in } \text{N m}^3 / (\text{mm}^2 \cdot \text{kg}) . \quad (9)$$

At the mean density level of  $450 \text{ kg/m}^3$  the test results undercut the embedment strength level predicted by dowel equation (4) by 25%. Contrary, the strength prediction by Eq. (6) is exceeded significantly by 47%. The presented differences are very similar in the typical density range of about  $350$  to  $500 \text{ kg/m}^3$ . The extreme quantitative differences between Eqs. (4) and (6) and further the pronounced undercut of the embedment prediction of Eq. (4) by the test results gives rise to questions not followed up here and stipulate further investigations.

As mentioned above the choice of  $f_{h,\alpha=0,\varepsilon=90}$  as a basis for embedment strength at  $\varepsilon = 0^\circ$  is not self-evident and  $f_{h,\alpha=90,\varepsilon=90}$  seems to be justified as well. In order to present the conducted  $f_{h,90,90}$  tests in condensed manner altogether with the matched  $f_{h,0,90}$  results exclusively the ratio of both strengths, i.e.  $f_{h,90} / f_{h,0} = 1/k_{90} = k_{\text{mat},90}^{-1}$  is discussed.

The approximation of the  $1/k_{90}$  test results by a linear regression forwards as anticipated almost no correlation with density. Density normalization of  $1/k_{90}$  then delivers

$$(\rho \cdot k_{90})^{-1}_{\text{mean}} = (1,38 \pm 0,16) \cdot 10^{-3} \quad \text{in } \text{m}^3/\text{kg} \quad (10)$$

and for the average density of  $450 \text{ kg/m}^3$

$$(k_{90,\text{mean}})^{-1} = f_{h,90} / f_{h,0} = 0,61 \pm 0,08 .$$

Compared hereto code Eq. (5) results for a dowel diameter of 20 mm and softwood SL in a coinciding value of

$$(k_{90})^{-1} = (k_{\text{mat},90})^{-1} = 0,606 \approx 0,61.$$



In conclusion it can be stated that the performed tests with dowels inserted perpendicular to grain ( $\varepsilon = 90^\circ$ ) delivered pronouncedly (25%) lower embedment strengths at  $\alpha = 0^\circ$  and  $90^\circ$  as stipulated by EC5. Deriving embedment values for  $\varepsilon = 0^\circ$  from the test results by the mentioned 10% procedure would then result in much lower values than code predicted.

## 6 Test results of fasteners inserted parallel to grain

### 6.1 Not bonded dowels

Figures 7 a) and b) depict typical load-indentation curves (dotted lines) of solid wood specimens No. SL\_15 and SL\_17 with dowels of 20 mm in diameter inserted tight fitting parallel to grain in drill holes of same diameter. Apart from the load-indentation curves for the joints with tight fitting dowels ( $d_{\text{hole}} = d_{\text{dowel}} = 20 \text{ mm}$ ) inserted without presence of adhesive also the F- $\delta$  curves for the matched twin specimens with rods of  $d_{\text{rod}} = 16 \text{ mm}$  glued with a gap-filling adhesive into the drill holes ( $d_{\text{hole}} = 20 \text{ mm}$ ) are given. The latter curves and their respective differences with dowel-type fastener joints are discussed below.

The load displacement / embedment curves are characterized by three rather clearly separable stiffness ranges. The initial load displacement evolution in range I is rather linear. The constant initial stiffness  $K_{\text{init}}$  is limited to about 30 to 50% of maximum load and a displacement of less than 0,5 mm. The subsequent load-displacement range II is characterized by a progressively nonlinear stiffness decrease occurring up to a displacement of about 1 mm. Range II ends up in a quasi-constant slightly increasing stiffness. The hardening range III stretches beyond a displacement of 5 mm when tests were ended throughout.

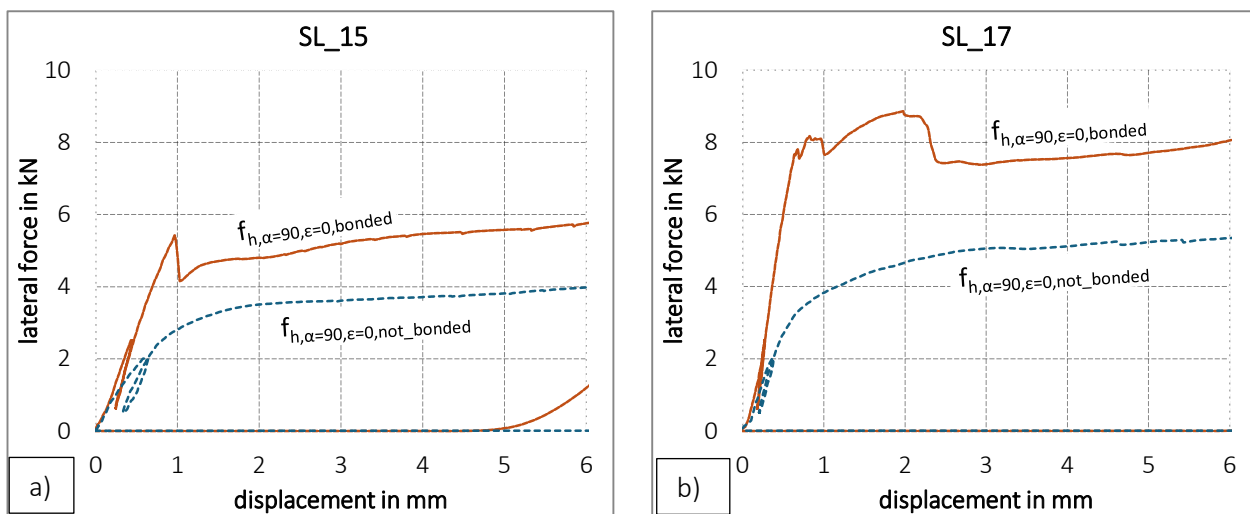


Figure 7: Typical load displacement / indentation curves in lateral load tests on steel dowels and glued-in rods inserted parallel to grain ( $d_{\text{hole}} = 20 \text{ mm}$ ,  $d_{\text{dowel}} = 20 \text{ mm}$ ,  $d_{\text{rod}} = 16 \text{ mm}$ ) into a) structural lumber specimen pair SL\_15, b) structural lumber specimen pair SL\_17

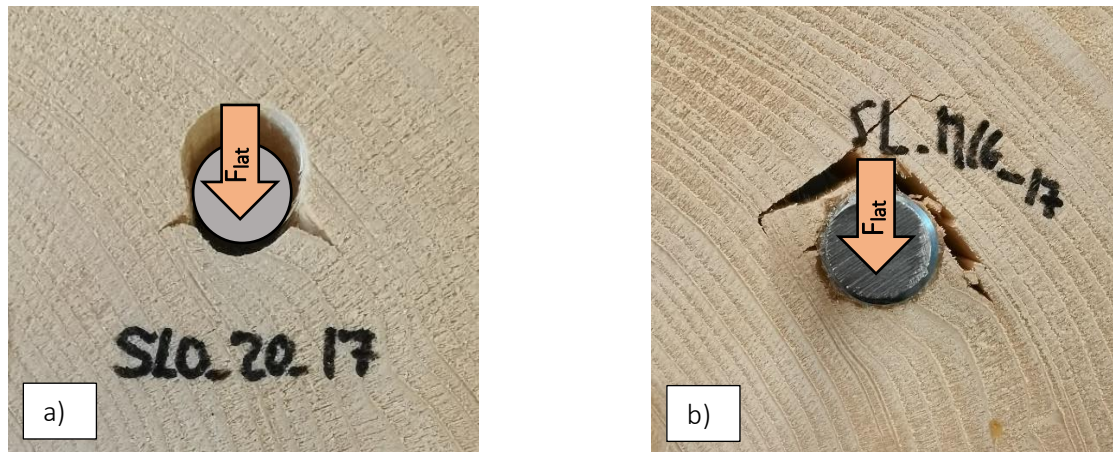


Figure 8: Typical fracture appearances in lateral load tests on dowels and glued-in rods inserted parallel to grain in solid spruce lumber  
a) non-bonded dowel joint No. SL\_17 and b) glued-in rod joint No. SL\_17

The typical embedment and fracture appearance of a not bonded dowel inserted parallel to grain and loaded laterally is shown in Fig. 8 a). At both sides of the compressed, dowel embedment / contact area a crack spreads roughly normal to the hole periphery. The cracks result from the high peaks of the tensile stresses perpendicular to grain equilibrating the compressive stresses in the wood-dowel contact area. Interestingly these cracks do not show up as discontinuities in the load displacement / embedment as curves shown in Figs. 7 a) and b).

Figure 9 a) depicts the relationship of embedment strength  $f_{h,\alpha=90,\epsilon=0,\text{not bonded}} = f_{h,\text{nb}}$  with density for all test specimens. The approximation of the data by linear regression yields ( $\rho_{12}$  in  $\text{kg/m}^3$ )

$$f_{h,\text{nb}} = 0,0155 \rho - 0,8084 \quad \text{in N/mm}^2, \quad R^2 = 0,44 . \quad (11)$$

The data and the respective linear approximation reveals a weakly correlated, positive trends towards higher embedment strengths with increasing densities. The mean value of the density normalized embedment strengths ( $\pm$  std.) evolves as

$$(f_{h,\text{nb}} / \rho)_{\text{mean}} = (13,4 \pm 1,8) \cdot 10^{-3} \text{ N m}^3 / (\text{mm}^2 \text{ kg}) \quad (12)$$

and for mean density of  $450 \text{ kg/m}^3$  embedment strength  $f_{h,\text{mean,nb}} = 6,0 \text{ N/mm}^2$  is obtained.

Besides the test results Fig. 9 a) also presents the relationship  $0,1 \cdot f_h(\rho)$  with  $f_h$  acc. to Eq. (3) as proposed by design code (prEN 1995-1-1:2023-10, 2023) here applied to the nominal strength-density level. Hereby the higher base-value  $f_{h,0}$  as stipulated by Blaß (2000) was assumed.

The graph reveals an expressed offset of the test results from the significantly smaller code proposed strengths. A comparison of the density normalized results forwards on the mean level a 2,1 times higher embedment strength obtained in the conducted

tests. In case the code predictions would not be based on  $f_{h,0,90}$  but on  $f_{h,90,90} = 0,61 \cdot f_{h,0,90}$  the difference would even amount to a factor of 3,4.

### 6.2 Bonded-in rods

The bonded-in rods of diameter  $d_{rod} = 16$  mm in a fully epoxy resin filled drill hole of  $d_{drill} = 20$  mm revealed significantly different load displacement and fracture features as compared to dowels with diameter  $d_d = 20$  mm inserted smooth fitting without bonding. Figures 7 a) and b) show exemplarily typical load-embedment displacement curves of the epoxied rods in comparison with their wood-wise matched not bonded specimens characterized by almost identic wood and hence fastener embedment conditions. Apart from the generally higher load level of the bonded-in rods, discussed below, the stiffness evolution and hence the fracture appearances and the underlying fracture mechanism differ profoundly from the not bonded rods.

The bonded-in rods revealed mechanically plausible a significantly higher embedment stiffness as compared to the not bonded joints. Further, the linear stiffness range reaches up to maximum load or more often to a pre-peak load  $F_{u,1}$  at about 90-100% of maximum load  $F_u$ , then followed by a sudden load drop. In some cases the first load drop occurs at  $F_u$ , i.e.  $F_{u,1} = F_u$ . Load  $F_{u,1}$  and hence the end of the linear range is associated with displacement values of 0,8 to 1,1 mm. In the follow-up of the differently expressed load drop ( $\Delta F \approx 0,02 - 0,2 \cdot F_{u,1}$ ) the force displacement evolution is characterized either by a rather steady hardening as shown in Fig. 7 a), quasi plasticity, or by a rather fast non-linear load recovery to peak load, followed by subsequent load decrease and then by hardening. The sketched stiffness evolution resembles closely the load displacement behavior found previously by Rodd et al. (1989) in investigations on resin injected dowels inserted perpendicular to grain.

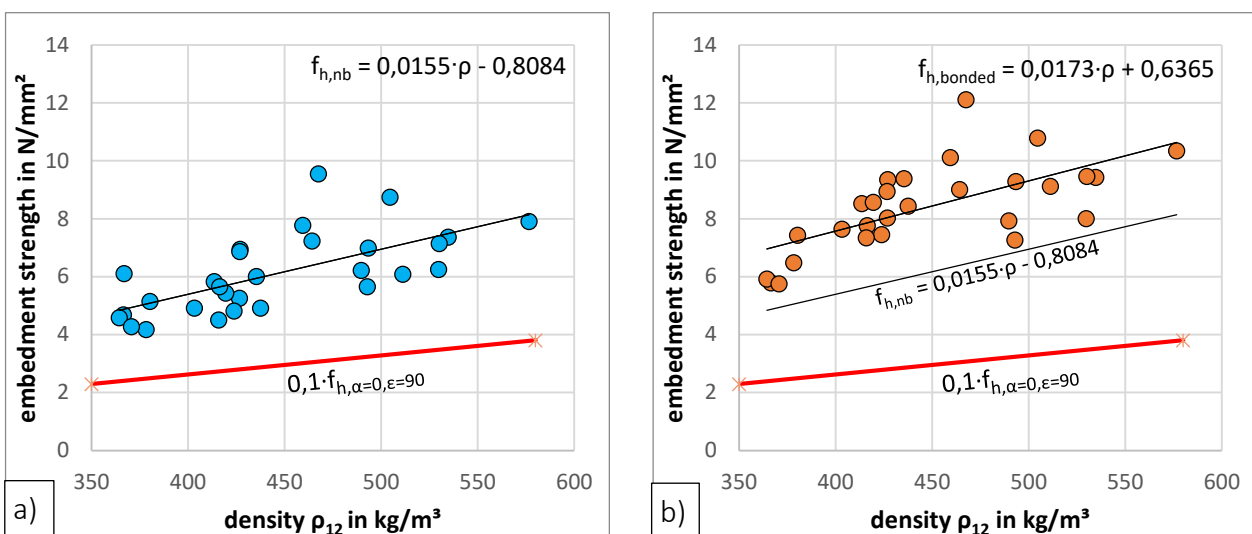


Figure 9: Embedment strength  $f_{h,90,0}$  of fasteners inserted parallel to grain in solid wood made from spruce a) non-glued dowels and b) glued-in rods

The reported sudden stiffness drop of the load embedment curves, which was not experienced in the not bonded specimens, is related to a significantly different load transfer and fracture mechanism of a bonded rod as compared to a not bonded rod. Fig. 8 b) depicts a typical embedment fracture appearance of a bonded rod inserted parallel to grain and loaded laterally. Now, different from the not bonded dowel the fracture takes place at the tension (here upper) side of the glued-in rod. In the shown picture the fracture occurred mainly as a tension failure perpendicular to grain in the wood. In other cases, bond line and mixed wood-bond-line failures were encountered. The failure mode explains the higher embedment stiffness of the bonded rod as the load is distributed by tension, shear and compression to the whole rod periphery. Further, after crack formation the embedment area of the dowel at the compression side of the drill hole is significantly larger as compared to the not bonded dowel due to the still existing glued interface, which explains that the much higher fracture load level (see below) vs. the not bonded dowel is preserved in the post crack range, too. The forwarded explanation on the mechanical reason of the crack formation could unfortunately not be proven visually during testing due to the realized test set-up hiding the crucial bond line edge / area. However, the fracture appearance shown in Fig. 8 b) supports this assumption strongly.

Maximum load and consequently embedment strength were evaluated by two approaches. In a first evaluation the ultimate load was taken as the maximum load value within the whole (5 mm) displacement range. This was done irrespective whether the load level after the load drop remained below the peak value or not. In a second evaluation the peak load was taken at  $\delta = 5,0$  mm. The differences between both evaluation methods are however marginal. At the mean value level, the evaluation based on the peak load of the whole displacement range  $F_{u,0-5mm}$  delivers a 5% higher value as compared to the use of  $F_{u,5mm}$ . The hereinafter presented embedment strengths rely on  $F_{u,0-5mm}$ .

Figure 9 b) shows the obtained embedment strength - density relationship of all specimens altogether with their linear regression approximation ( $\rho = \rho_{12}$  in  $\text{kg}/\text{m}^3$ )

$$f_{h,\text{bonded}} = 0,0173 \rho + 0,6365 \quad \text{in } \text{N}/\text{mm}^2, \quad R^2 = 0,43. \quad (13)$$

Further, the approximation lines obtained for the not bonded dowels acc. to Eq. (11) and the code-based prediction  $0,1 f_h(\rho)$  with  $f_h$  acc. to Eq. (3) are given. The mean value of the density normalized embedment strength evolves as

$$(f_{h,\text{bonded}} / \rho)_{\text{mean}} = (18,8 \pm 2,5) \cdot 10^{-3} \text{ N m}^3 / (\text{mm}^2 \text{ kg}). \quad (14)$$

Figure 9 b) and Eqs. (11) and (13) reveal i) an almost equal relationship of embedment strengths of the bonded and not bonded specimen configurations vs. density and ii) a

significantly higher embedment strength level of the bonded rods. A comparison on the basis of the density normalized mean values acc. to Eq. (12) and (14) delivers a strength gain of the bonded rods by a factor of 1,4. Comparing  $(f_{h,bonded} / \rho)_{mean}$  to the EC5 specified density normalized value  $(0,1 \cdot 0,082 \cdot (1 - 0,01 \cdot d) \cdot \rho_k) / \rho$  delivers a factor of 2,9.

## 7 Conclusions

The performed investigations have revealed that the embedment strength specified in draft EC5-1-1 (2023) for glued-in steel rods inserted parallel to grain and loaded laterally, lacking convincing scientific justifications, is by far, roughly by a factor of 3, too low. Hereby it has to be beard in mind that the presented results are even highly conservative in view of scarce former literature data. In order to enable mechanical-wise competitive connections for glued-in rod joints it is deemed necessary to alter the presently proposed respective EC5-1-1 specifications for embedment strength of steel rods glued-in parallel or inclined to grain direction. The fact that the results of the complementary lateral force tests with dowels inserted perpendicular to grain delivered much lower values than code proposed, rises further questions.

## 8 References

- Aicher, S., & Simon, K. (2021). Rigid Glulam Joints with Glued-in Rods subjected to Axial and Lateral Force Action, paper 54-7-3. In *Proceedings International Network on Timber Engineering Research (INTER), Meeting 54* (S. 113-128). Online.
- Blaß, H. J. (2000). Eingeleimte Gewindestangen - Bemessung nach E DIN 1052 und neuere Forschungsergebnisse. In *Tagungsband. Ingenieurholzbau, Karlsruher Tage, Forschung für die Praxis* (S. 19-28). Karlsruhe: Bruderverlag.
- Blaß, H. J., Ehlbeck, J., Kreuzinger, H., & Steck, G. (2004). *Explanations to DIN 1052:2004-08 - Design, Calculation and Dimensioning of Timber Structures (in German)*. München: DGfH Deutsche Gesellschaft für Holzforschung.
- Blaß, H., Bejtka, I., & Uibel, T. (2006). Tragfähigkeit von Verbindungen mit selbstbohrenden Holzschrauben mit Vollgewinde. In L. f. Universität Karlsruhe, *Karlsruher Berichte zum Ingenieurholzbau* (S. Band 4). Karlsruhe, Germany.
- Ehlbeck, J., & Gerold, M. (1989). End grain connections with laterally loaded steel bolts. *International Council for Building Research Studies and Documentation (CIB) W18A*, (S. paper 22-7-1). Berlin, Germany.
- Ehlbeck, J., & Werner, H. (1992). Softwood and hardwood embedding strength for dowel-type fasteners - Background of the formulae in Eurocode 5, draft April 1992. In: *Proceedings. CIB-W18A Meeting No. 25*. Åhus, Sweden.

- EN 13183-1:2002-07. (2002). Moisture content of a piece of sawn timber - Part 1: Determination by oven dry method. Brussels, Belgium: European Committee for Standardization.
- EN 383. (2007). *Timber Structures - Test methods - Determination of embedment strength and foundation values for dowel type fasteners*. Belgium, Brussels: CEN.
- Eurocode 5 / NA. (2013). *DIN EN 1995-1-1/NA:2013-08: National Annex - Nationally determined parameters - Design of timber structures - Part 1-1: General - Common rules and rules for buildings*. Berlin, Germany: DIN.
- Eurocode 5. (2010). *EN 1995-1-1:2010-12: Design of timber structures - Part 1-1: General - Common rules and rules for buildings*. Brussels, Belgium: CEN.
- Hezel, J., Aicher, S., & Helbig, T. (2015). Integral, bonded Timber-Concrete-Abutment-Connection (in German). *Proceedings 3rd Stuttgarter Holzbau-Symposium*, (S. 97-107). Stuttgart (Germany).
- Johansen, K. (1949). Theory of timber connections. In *International Association for Bridge and Structural Engineering, Vol. 9* (S. 249-262).
- Möhler, K., & Hemmer, K. (1981). *Versuche mit eingeleimten Gewindestangen*. Lehrstuhl für Ingenieurholzbau und Baukonstruktionen, Universität Karlsruhe.
- prEN 1995-1-1:2023-10. (2023). *E DIN EN 1995-1-1: Design of timber structures - Part 1-1: General and rules for buildings (NA 005-04-01 AA N 4927)*. Brussels, Belgium: CEN.
- Riberholt, H. (1977). *Bolte indlimet i limtrae Rapport Nr. R 83 (Raport Nr. R 99 1978: Eingleimte Gewindestangen (in German))*. Technical University of Denmark.
- Riberholt, H. (1986). *Glued bolts in glulam. Serie R, No 210*. Department of Structural Engineering, Technical University of Denmark.
- Rodd, P. D., Hilson, B. O., & Spriggs, R. A. (1989). Resin injected mechanically fastened timber joints. *Proceedings of The Second Pacific Timber Engineering Conference*, (S. 131-136). Auckland, New Zealand.
- Schmid, V., & Fischer, M. (2010). Metropol Parasol Sevilla – ein neues Wahrzeichen für den Ingenieurholzbau. *16. Internationales Holzbauforum*. Garmisch-Partenkirchen: FORUM HOLZBAU.
- Whale, L., & Smith, I. (1986). *Mechanical Timber Joints*. Timber Research and Development Association.
- Z-9.1-705. (2021). *2K-EP-Adhesive WEVO special resin EP 32 S with WEVO hardener, valid until 26/11/2022, WEVO-CHEMIE GmbH, Ostfildern-Kemnat, Germany*. Berlin, Germany: DIBt.

DISCUSSION

**The paper was presented by S Aicher**

*A Salenikovich asked about the limits to use in terms of deformation to establish the resistance. S Aicher responded that maximum value at 5 mm seemed to make sense in most cases. In situations where reinforcements were involved, loads associated with much smaller deformations would be reasonable. One should keep in mind that the design equation from EC5 is very conservative. A Salenikovich suggested that potential splitting failures might be the reason of setting the conservative EC5 approach.*

*R Jockwer and H Blass commented and discussed the origin of EC5 provisions that could be based on embedment tests from the UK.*

*U Hübner commented that the current project team for EC5 studied embedment strength including density correction, 75%CI on characteristic strength and embedment tests for hardwood. They could not reach past values with today's analysis. He mentioned that their own and Gehris' back calculations also showed inconsistencies with EC5 provisions.*







# A Proposal for the Stiffness of Steel-Timber Dowel-Type Connections

Lea Buchholz, M.Sc., Scientific Researcher

Prof. Dr.-Ing. Ulrike Kuhlmann, University Professor

Institute of Structural Design, University of Stuttgart, Germany

Dr.-Ing. Julius Gauß, Structural Engineer

müllerblaustein Ingenieure, Germany

Keywords: Connection stiffness, steel-timber dowel-type connections, experimental results, beech LVL

## 1 Introduction

In times of climate change, timber structures are coming under increasing political and social focus as a sustainable and resource-efficient construction method. At the same time, the forest structure in Germany is changing due to extended drought, with the high proportion of spruce being replaced mainly by beech. As a result, beech will be increasingly used in construction practice. This requires a reliable and economical design, also for hardwoods. In particular, the prediction of the load-deformation behaviour of high-performance joints is crucial for the design of complex timber structures. Especially for highly indeterminate structures, the use of computer-based design methods is state of the art and is indispensable today. At first sight, these numerical design methods provide very precise results for the internal forces and the deformations of the structure, but require just as precise input parameters.

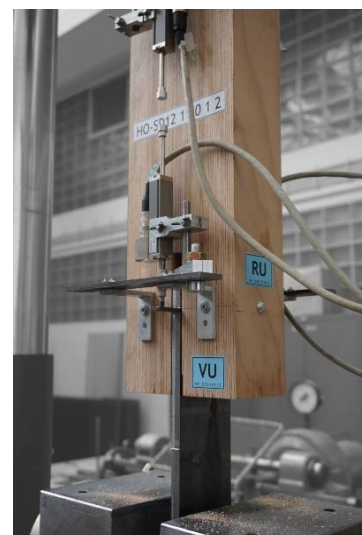


Figure 1.1. Tensile test on steel-timber dowel-type connection in beech LVL

As part of the changes of prEN 1995-1-1 (2023) compared to EN 1995-1-1 (2004), the equation for determining the slip modulus  $K_{ser}$  of steel-timber dowel-type fasteners (see equation (1)) has been adapted.

$$K_{ser,prEN1995-1-1} = 2 \cdot \rho_{mean}^{1.5} \cdot d/23 \cdot (1 - \alpha/180) \text{ [N/mm]} \quad (1)$$

The load-to-grain angle  $\alpha$  is now taken into account as an additional parameter. Comparable to the Swiss standard SIA 265 (2012) (see equation (2) and (3)), the slip modulus is reduced by 50 % for a load-to-grain angle of 90°. Linear interpolation should be used for intermediate angles.

$$K_{ser,0,SIA} = 6 \cdot \rho_k^{0.5} \cdot d^{1.7} \text{ [N/mm]} \quad (2)$$

$$K_{ser,90,SIA} = 3 \cdot \rho_k^{0.5} \cdot d^{1.7} \text{ [N/mm]} \quad (3)$$

## 2 Research on softwood connections

Within two former INTER publications (KUHLMANN & GAUß (2019b), KUHLMANN & GAUß (2021b)), the possibilities and advantages of the application of the component method in timber construction were pointed out, but also the need of an accurate prediction of the joint load-displacement behaviour. It was shown that the stiffness calculation according to EN 1995-1-1 (2004) is not satisfactory.

The results of two extensive research projects (KUHLMANN & GAUß (2019a), KUHLMANN & GAUß (2021a)) with 326 tested softwood connections are summarized in GAUß (2024). The most important findings of the experimental, numerical and analytical investigations of the influencing factors on the connection stiffness are summarized below.

The evaluation of the influence of the embedment properties on the connection stiffness has shown that by using average embedment properties, the connection behaviour can be predicted relatively accurately despite the large material scatter. An estimation of the scatter range of the connection stiffness can be made by using minimum and maximum embedment properties.

The influence of the fastener diameter on the connection stiffness is underestimated by the formula in EN 1995-1-1 (2004) and also by the new formula in prEN 1995-1-1 (2023), see Eq. (1). An adaptation of the formula of the connection stiffness  $K_{ser}$  is therefore recommended. The introduction of an exponent for the diameter  $d$  leads to a significantly better prediction of the connection stiffness. This is already integrated in a similar way in the Swiss standard SIA 265 (2012), see for example Eq. (2) & (3).

Furthermore, it is recommended to reduce the initial stiffness by 50 % for a load-to-grain angle  $\alpha = 90^\circ$  compared to a load in grain direction ( $\alpha = 0^\circ$ ). With increasing load-to-grain angle, there was a disproportionate decrease in connection stiffness, which can be described, for example, with a modified Hankinson equation. However, a linear reduction between  $0^\circ$  and  $90^\circ$  could simplify the determination of the connection stiffness and to take account of the large scatter that occurs.

The hole tolerance of the connection has proven to be an important influencing factor for the connection stiffness. However, due to the complexity of taking the hole tolerance into account directly, it is recommended to reduce the stiffness of fastener groups.

The influence of the timber density seems to be overestimated by prEN 1995-1-1 (2023). However, since the database of hardwood tests was very small the influence of the density on the connection stiffness was difficult to assess.

On the basis of the collected test data of mainly softwood connections from own and third-party investigations, the following formula for the initial stiffness  $K_{ser}$  was derived. This was evaluated for different input values and in comparison to existing normative prediction models. Besides the mean density  $\rho_{mean}$ , the fastener diameter  $d$ , the load-to-grain angle  $\alpha$  and the number of fasteners  $n$  are considered.

$$K_{ser,Gau\beta} = \frac{11 \cdot \rho_{mean}^{0.25} \cdot d^{1.9}}{\sin^{1.9} \alpha + 0.5 \cdot \cos^{1.9} \alpha} \cdot n^{0.8} \text{ [N/mm]} \quad (4)$$

The influence of the individual parameters on the connection stiffness is summarized within a comparison of the different prediction models in Chapter 4.3.

## 3 Research on hardwood connections

### 3.1 General

The database on the connection stiffness with hardwoods was far too small to derive reliable predictions. As part of the research project of the „Timber Building Initiative“ of the state of Baden-Württemberg (see KUHLMANN & BUCHHOLZ (2023)), tensile tests were therefore carried out on over 300 steel-timber dowel-type connections in beech laminated veneer lumber (beech LVL). The main results are listed below. More detailed information can be found in the project reports.

### 3.2 Test programme and setup

The experimental programme of the tensile tests on steel-timber dowel-type connections in beech LVL is given in Table 3.1. In addition to the number of fasteners, the type and diameter  $\emptyset$  of the fasteners, the load-to-grain angle  $\alpha$ , the type of reinforcement of the timber element and the side member thickness  $t_{1-3}$  (slenderness of the connection) were varied. The different side member thicknesses  $t_{1-3}$  were intended to induce all three possible European Yield Model (EYM) failure modes according to EN 1995-1-1 (2004) in the tests. For the standard side member thickness  $t_1$  two plastic hinges per shear plane could be observed. The additional side member thicknesses led to one plastic hinge per shear plane ( $t_2$ ) or to embedment failure in timber ( $t_3$ ). The reinforcement of the timber was partly achieved by fully threaded screws and partly by internal reinforcement using veneer cross-layers (GL 60Q).

Table 3.1. Experimental programme of tensile tests on steel-timber dowel-type connections in beech LVL

Fastener	$\varnothing$ [mm]	$n_{\perp} \times n_{\parallel}$	$\alpha$ [°]	Reinforcement	Timber grade	t
Single dowel	8, 12	1 x 1	0	Fully threaded screws Veneer cross-layers	GL 75	t <sub>1</sub>
	16, 20		90		GL 60Q	t <sub>2</sub>
						t <sub>3</sub>
Single bolt	8, 12 16, 20	1 x 1	0	-	GL 75	t <sub>1</sub>
Group of bolts and dowels	8, 12	1 x 3	0	Fully threaded screws Veneer cross-layers	GL 75	t <sub>1</sub>
	16, 20	1 x 5			GL 60Q	
		2 x 3				
Self-drilling dowels	7	1 x 3	0	-	GL 75	t <sub>1</sub>

An example of a tensile test specimen loaded parallel to the grain, with 1 x 5 fasteners per connection and reinforcement with fully threaded screws is shown in Figure 3.1. The symmetrical design allowed two connections to be tested simultaneously, providing two sets of data for each specimen to evaluate connection stiffness. The displacement transducers were positioned according to EN 383 (2007) and measured the relative deformation between the slotted-in steel plate and the timber at the level of the centre line of the connection (see Figure 1.1 and Figure 3.2). The load was applied according to EN 26891 (1991). Further information on the geometry and test setup of the tensile tests can be found in KUHLMANN & BUCHHOLZ (2023).

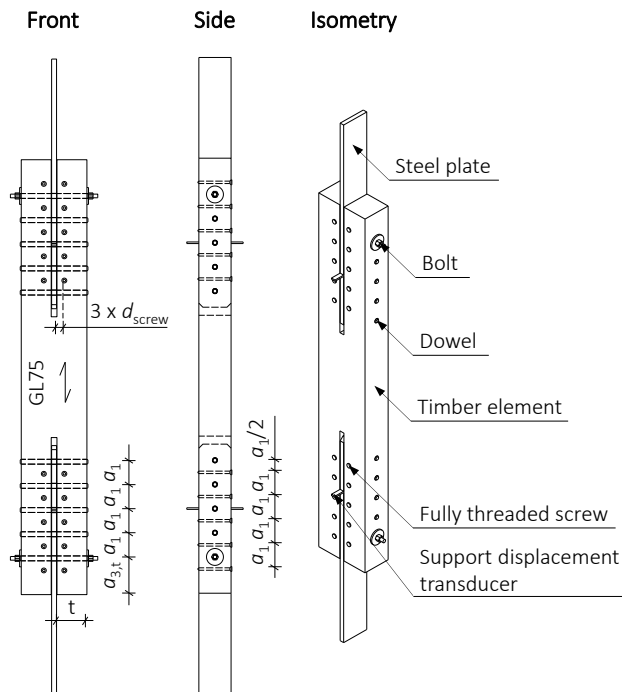


Figure 3.1. Example of a tensile test parallel to the grain specimen with 1 x 5 fasteners per connection and screw reinforcement



Figure 3.2. Splitting of the timber after ductile deformation of the dowel and deformation of a bolt and the washer ( $\alpha = 0^\circ$ )

### 3.3 Test results

#### 3.3.1 Failure modes

Depending on the side member thickness, two ( $t_1$ ) or one ( $t_2$ ) plastic hinge(s) per shear plane or embedment failure in timber ( $t_3$ ) could be observed. In addition, there were other types of subsequent failure for the connections with a large side member thickness. For example, splitting of the side members at large deformations was frequently observed, particularly in unreinforced connections (see Figure 3.2). In some cases, this was accompanied by partial block shear behaviour. The connections loaded perpendicular to the grain showed lateral splitting of the timber. This resulted in a relatively brittle failure after about 11 mm of deformation at the dowel. The splitting of the timber could be prevented by reinforcing the timber with screws or veneer cross-layers. Then, often no cracks were externally visible, especially on specimens with cross-layers. For bolted connections, the washer of the bolt was deformed and slightly pressed into the timber (see Figure 3.2). Compared to the failure of bolted connections in spruce glulam due to head pull-through (see KUHLMANN & GAUB (2019a)), the deformations at the washers in beech LVL were significantly smaller. As a special case, and only for connections reinforced with screws or veneer cross-layers with 1 x 5 fasteners, the outer bolt sheared off close to the slotted-in steel plate (see Figure 3.3). This failure was observed for fastener diameters of 8 mm, 12 mm and 16 mm. For example, for the 12 mm diameter, shearing occurred at a displacement of approximately 15 mm. FRANKE & FRANKE (2020) have also already described the shearing off of dowels with groups of fasteners in beech glulam.



Figure 3.3. Sheared bolt after testing (specimen HO-SD16 15 0 Q 1 Top)

A significant indentation in the area of the steel plate was characteristic for the deformation figure of a fastener after testing, also shown in Figure 3.3. Further photos describing the failure modes can be found in KUHLMANN & BUCHHOLZ (2023).

#### 3.3.2 Connection stiffness

Table 3.2 to Table 3.6 summarise the main test results of the initial stiffness  $K_{ser}$  and the reloading stiffness  $K_e$  for the different fastener diameters and compare them with the stiffnesses calculated according to prEN 1995-1-1 (2023) (see Eq. (1)). The corresponding standard deviation (SD) and the coefficient of variation (COV) are also given. See KUHLMANN & BUCHHOLZ (2023) for detailed information on the calculation of the stiffnesses. The main characteristics of each test series are briefly explained below to better understand the tables. The test series are named as follows:

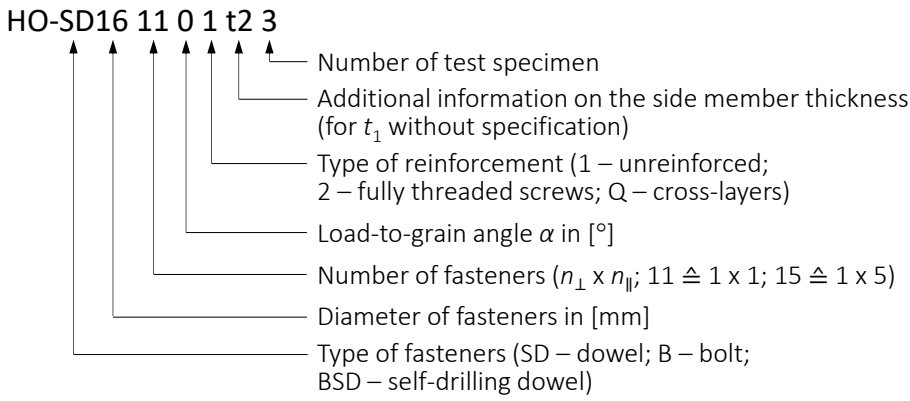


Figure 3.4. Nomenclature of test specimens

The focus of the evaluation was to analyse the influence of each parameter on the connection stiffness. Parameters that have a major influence on stiffness include fastener diameter, load-to-grain angle and number of fasteners. The comparison between the experimentally determined initial stiffnesses  $K_{ser,test}$  and the stiffnesses  $K_{ser,prEN1995}$  calculated according to prEN 1995-1-1 (2023) shows that the current draft tends to overestimate the stiffness for small diameters, while it tends to underestimate the stiffness for larger diameters. In prEN 1995-1-1 (2023), the diameter is included linearly in the stiffness calculation, so that the influence is underestimated in the standard. Furthermore, the results for almost all test series show that the stiffness is approximately 50 % lower for loading perpendicular to the grain than for loading parallel to the grain. This effect applies equally to both the unreinforced and cross-laminated series. The test results thus show that the 50 % reduction in stiffness for loading perpendicular to the grain in the current draft prEN 1995-1-1 (2023) is also appropriate for connections in beech LVL.

Table 3.2. Initial stiffness  $K_{ser}$  and reloading stiffness  $K_e$  from tensile tests on steel-timber dowel-type connections in beech LVL  $\varnothing = 8$  mm; SD = standard deviation, COV = coefficient of variation

$\varnothing$ 8 mm Series	Mean [kN/mm] ( $K_{test} / K_{prEN1995}$ )		SD [kN/mm]		COV [%]	
	$K_{ser}$	$K_e$	$K_{ser}$	$K_e$	$K_{ser}$	$K_e$
HO-SD8 11 0 1	26.9 (85%)	51.6 (164%)	6.3	9.3	23.4	18.0
HO-B8 11 0 1	30.8 (98%)	57.9 (184%)	7.4	3.8	24.2	6.6
HO-SD8 11 0 1 t2	22.8 (72%)	37.4 (119%)	4.4	4.8	19.5	12.8
HO-SD8 11 0 1 t3	19.5 (62%)	34.7 (110%)	4.6	5.6	23.5	16.2
HO-SD8 11 0 2	22.0 (70%)	49.4 (157%)	6.0	5.7	27.2	11.5
HO-SD8 11 0 Q	17.0 (54%)	51.7 (164%)	3.3	4.8	19.1	9.3
HO-SD8 11 90 1	12.9 (82%)	23.6 (150%)	2.5	1.8	19.3	7.4
HO-SD8 11 90 Q	12.5 (80%)	29.5 (188%)	2.1	2.0	16.6	6.9
HO-SD8 13 0 1	61.9 (66%)	145.5 (154%)	3.3	9.0	5.3	6.2
HO-SD8 15 0 1	87.6 (56%)	249.8 (159%)	14.3	21.0	16.3	8.4
HO-SD8 15 0 2	99.0 (63%)	246.0 (156%)	8.4	16.7	8.5	6.8
HO-SD8 15 0 Q	91.1 (58%)	242.2 (154%)	18.9	18.6	20.8	7.7

Table 3.3. Initial stiffness  $K_{ser}$  and reloading stiffness  $K_e$  from tensile tests on steel-timber dowel-type connections in beech LVL  $\varnothing = 12$  mm; SD = standard deviation, COV = coefficient of variation

$\varnothing$ 12 mm Series	Mean [kN/mm] ( $K_{test} / K_{prEN1995}$ )		SD [kN/mm]		COV [%]	
	$K_{ser}$	$K_e$	$K_{ser}$	$K_e$	$K_{ser}$	$K_e$
HO-SD12 11 0 1	48.2 (102%)	80.8 (171%)	3.7	5.0	7.7	6.1
HO-B12 11 0 1	49.9 (106%)	86.4 (183%)	4.0	7.5	8.0	8.7
HO-SD12 11 0 1 t2	52.3 (111%)	76.7 (162%)	9.5	11.0	18.2	14.4
HO-SD12 11 0 1 t3	45.5 (96%)	78.8 (167%)	7.6	8.7	16.6	11.1
HO-SD12 11 0 2	40.6 (86%)	95.3 (202%)	3.4	9.3	8.5	9.8
HO-SD12 11 0 Q	49.0 (104%)	99.4 (210%)	8.5	2.0	17.4	2.0
HO-SD12 11 90 1	24.9 (105%)	37.8 (160%)	1.8	2.4	7.1	6.4
HO-SD12 11 90 Q	26.5 (112%)	46.2 (196%)	2.8	3.1	10.5	6.7
HO-SD12 13 0 1	139.7 (99%)	241.6 (171%)	15.1	35.7	10.8	14.8
HO-SD12 15 0 1	210.9 (89%)	380.5 (161%)	23.1	37.0	10.9	9.7
HO-SD12 15 0 2	222.1 (94%)	462.1 (196%)	17.6	23.5	7.9	5.1
HO-SD12 15 0 Q	230.6 (98%)	388.0 (164%)	29.4	33.3	12.8	8.6

Table 3.4. Initial stiffness  $K_{ser}$  and reloading stiffness  $K_e$  from tensile tests on steel-timber dowel-type connections in beech LVL  $\varnothing = 16$  mm; SD = standard deviation, COV = coefficient of variation

$\varnothing$ 16 mm Series	Mean [kN/mm] ( $K_{test} / K_{prEN1995}$ )		SD [kN/mm]		COV [%]	
	$K_{ser}$	$K_e$	$K_{ser}$	$K_e$	$K_{ser}$	$K_e$
HO-SD16 11 0 1	76.0 (121%)	131.2 (208%)	3.4	3.4	4.5	2.6
HO-B16 11 0 1	74.7 (119%)	129.9 (206%)	4.7	4.0	6.3	3.1
HO-SD16 11 0 1 t2	84.9 (135%)	127.2 (202%)	7.7	8.9	9.1	7.0
HO-SD16 11 0 1 t3	71.3 (113%)	101.4 (161%)	4.9	6.0	6.9	5.9
HO-SD16 11 0 2	68.8 (109%)	129.0 (205%)	10.4	9.1	15.2	7.0
HO-SD16 11 0 Q	70.7 (112%)	139.3 (221%)	2.5	3.6	3.5	2.6
HO-SD16 11 90 1	32.8 (104%)	64.6 (205%)	8.6	10.2	26.1	15.9
HO-SD16 11 90 Q	37.0 (118%)	72.8 (231%)	6.3	3.5	17.1	4.8
HO-SD16 13 0 1	180.5 (96%)	320.9 (170%)	12.6	28.0	7.0	8.7
HO-SD16 15 0 1	297.5 (94%)	583.8 (185%)	18.5	25.2	6.2	4.3
HO-SD16 15 0 2	267.2 (85%)	566.5 (180%)	47.9	42.7	17.9	7.5
HO-SD16 15 0 Q	246.2 (78%)	545.4 (173%)	33.3	79.6	13.5	14.6
HO-SD16 23 0 1	374.1 (99%)	640.2 (169%)	44.3	48.4	11.8	7.6

In addition to connections with a single fastener, connections consisting of a row of three or five fasteners parallel to grain (1 x 3 or 1 x 5) were analysed. As expected, an increase in the number of fasteners resulted in a significant increase in the overall stiffness of the connection. At the same time, the tests showed a reduction in stiffness per fastener as the number of fasteners increased. However, according to prEN 1995-1-1 (2023) (see Eq. (1)), the number of fasteners is included linearly in the stiffness calculation. For other parameters analysed, such as reinforcement, fastener type and side



member thickness (slenderness), there were no clear tendencies to their influence on the connection stiffness.

Table 3.5. Initial stiffness  $K_{ser}$  and reloading stiffness  $K_e$  from tensile tests on steel-timber dowel-type connections in beech LVL  $\varnothing = 20$  mm; SD = standard deviation, COV = coefficient of variation

$\varnothing$ 20 mm Series	Mean [kN/mm] ( $K_{test} / K_{prEN1995}$ )		SD [kN/mm]		COV [%]	
	$K_{ser}$	$K_e$	$K_{ser}$	$K_e$	$K_{ser}$	$K_e$
HO-SD20 11 0 1	74.8 (95%)	142.4 (181%)	7.1	9.2	9.4	6.5
HO-B20 11 0 1	83.4 (106%)	165.7 (211%)	12.2	14.6	14.7	8.8
HO-SD20 11 0 1 t2	104.1 (132%)	166.3 (211%)	6.3	7.0	6.0	4.2
HO-SD20 11 0 1 t3	89.6 (114%)	135.5 (172%)	9.0	7.8	10.0	5.8
HO-SD20 11 0 2	81.3 (103%)	165.2 (210%)	7.6	9.8	9.3	5.9
HO-SD20 11 0 Q	121.1 (154%)	187.7 (238%)	5.1	5.4	4.2	2.9
HO-SD20 11 90 1	46.9 (119%)	86.8 (221%)	3.0	9.2	6.3	10.6
HO-SD20 11 90 Q	62.4 (159%)	100.9 (256%)	7.7	4.3	12.4	4.2
HO-SD20 13 0 1	229.7 (97%)	391.0 (166%)	37.4	39.4	16.3	10.1
HO-SD20 15 0 1	416.5 (106%)	717.7 (182%)	72.7	66.2	17.5	9.2
HO-SD20 15 0 2	425.2 (108%)	742.6 (189%)	48.1	75.9	11.3	10.2
HO-SD20 15 0 Q	469.7 (119%)	827.9 (210%)	34.7	23.5	7.4	2.8

Table 3.6. Initial stiffness  $K_{ser}$  and reloading stiffness  $K_e$  from tensile tests on steel-timber connections with self-drilling dowels in beech LVL  $\varnothing = 7$  mm; SD = standard deviation, COV = coefficient of variation

$\varnothing$ 7 mm Series	Mean [kN/mm] ( $K_{test} / K_{prEN1995}$ )		SD [kN/mm]		COV [%]	
	$K_{ser}$	$K_e$	$K_{ser}$	$K_e$	$K_{ser}$	$K_e$
HO-BSD7 13 0 1	47.1 (57%)	164.1 (199%)	6.1	45.8	12.9	27.9
HO-BSD7 13 0 1 a1	43.6 (53%)	143.7 (174%)	1.8	17.5	4.1	12.2
HO-BSD7 13 0 1 ZK	47.0 (57%)	114.2 (138%)	5.1	8.2	10.9	7.2

## 4 Proposal for the determination of the initial connection stiffness

### 4.1 General

The stiffness calculation according to prEN 1995-1-1 (2023) is still unsatisfactory, as shown by experimental investigations on steel-timber dowel-type connections with softwood and hardwood (KUHLMANN & GAUß (2019a), KUHLMANN & GAUß (2021a), KUHLMANN & BUCHHOLZ (2023)). With the aim of developing a more suitable equation for predicting connection stiffness, a comprehensive database on the stiffness of steel-timber dowel-type connections has been compiled. The results obtained from this database are presented and discussed in this paper, and a proposal for the stiffness calculation of steel-timber dowel-type connections is given.

One of the main challenges in deriving an equation for the initial stiffness  $K_{ser}$  of steel-timber dowel-type connections is the large scatter of the test data. It is therefore practically impossible to derive a perfect equation as there is no “correct stiffness value”. Thus, the aim was to map the range of scattering as well as possible by means of an empirical equation. The equation proposed by GAUß (2024) has been taken as a basis and adapted to an extended database, which now includes a larger range of stiffness values of connections in hardwood.

#### 4.2 Proposed equation for the initial stiffness $K_{ser}$

The influencing factors included in the proposed equation are the fastener diameter  $d$ , the load-to-grain angle  $\alpha$  and the number of fasteners  $n$ . These parameters were also found to be the most important influencing parameters in the evaluation of the tests (see section 3.3.2). In addition, the influence of the mean density  $\rho_{mean}$  is considered in the equation. The mean initial stiffness  $K_{ser}$  of a steel-timber dowel-type connection per fastener and per shear plane can then be determined using the following equation:

$$K_{ser,proposal} = 1.4 \cdot \rho_{mean}^{0.7} \cdot d^{1.9} \cdot (1 - \alpha/180) \cdot n^{0.8} \text{ [N/mm]} \quad (5)$$

A single equation both for softwood and hardwood is proposed as the stiffness values of hardwoods are within the range of the values of softwoods. This also contributes to a more user-friendly rule.

#### 4.3 Evaluation of the proposed equation

The equation presented for determining the initial stiffness  $K_{ser}$  is discussed below. Figure 4.1 shows the influence of different parameters on the initial stiffness  $K_{ser}$  for the prediction models investigated. The proposal (blue curve) is compared with the prediction models according to prEN 1995-1-1 (2023) (red curve), SIA 265 (2012) (green curve) and GAUß (2024) (purple curve). The initial values of the curves are used as reference values and the proportional change in stiffness is plotted over the investigated parameters.

Compared to the other models, the prediction according to prEN 1995-1-1 (2023) shows a clearly disproportionate increase in stiffness with increasing density (see Figure 4.1 (a)). The difference between the prediction according to GAUß (2024) and the current proposal can be explained by the additional consideration of the tests by KUHLMANN & BUCHHOLZ (2023) in the database. In prEN 1995-1-1 (2023), the diameter of the fastener only has a linear effect on the stiffness (see Figure 4.1 (b)). For the other models, a disproportionate influence is shown, whereby the proposal is still above SIA 265 (2012). The influence of the load-to-grain angle is taken into account in almost the same way in all models (see Figure 4.1 (c)). The prediction according to GAUß (2024) uses a variant of the Hankinson equation, the other models use a linear interpolation between 0° and 90°. Currently, SIA 265 (2012) and prEN 1995-1-1 (2023) do not consider an effective number of fasteners when determining the stiffness of fastener groups. Therefore, in Figure 4.1 (d), the rules for the effective number of fasteners for

the load-bearing capacity according to prEN 1995-1-1 (2023) and to SIA 265 (2012) are compared with the rules according to the proposal and to GAUß (2024) for the stiffness. The decrease in stiffness is initially somewhat smaller for the proposed equation than this is the case for the load-bearing capacity rules.

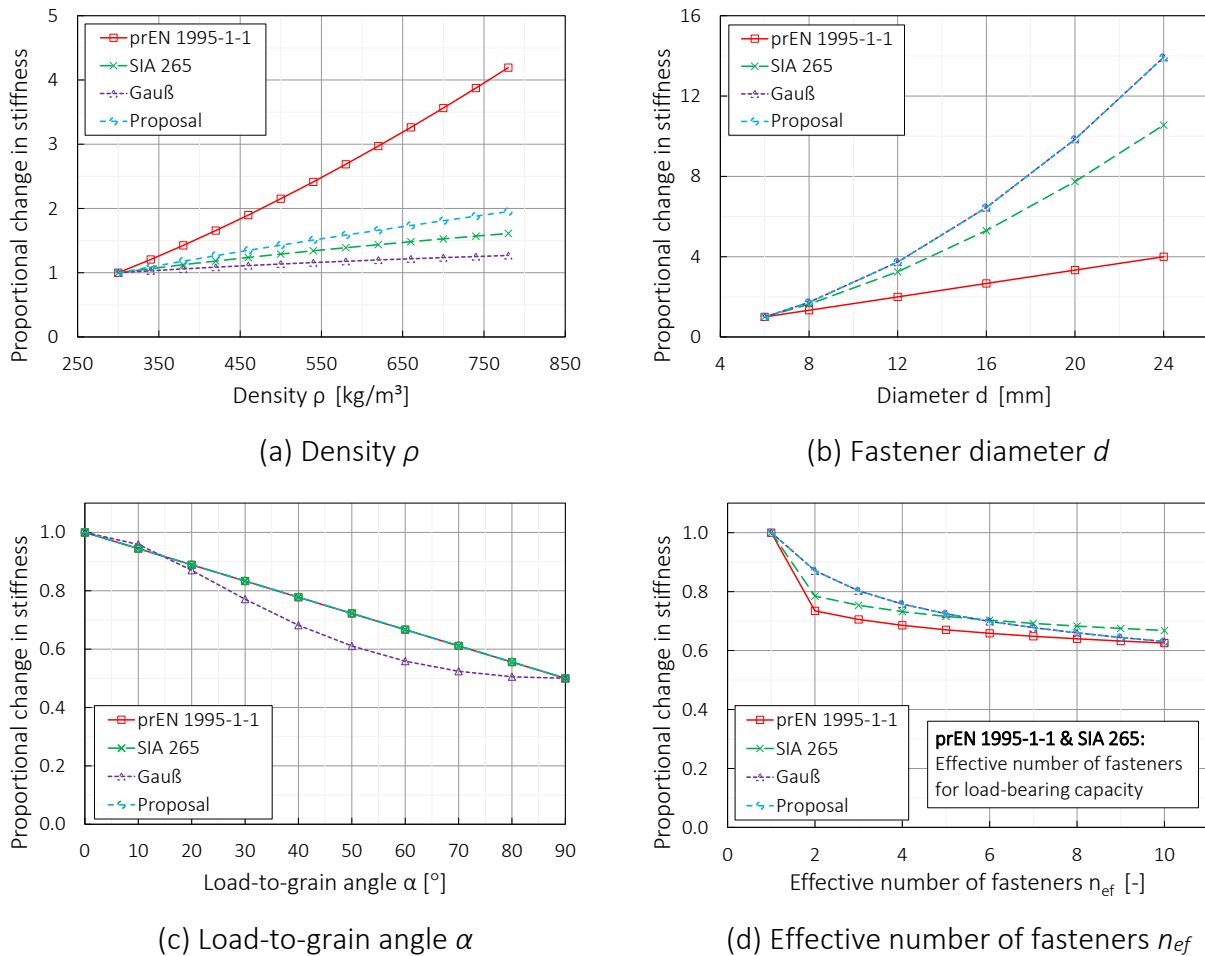


Figure 4.1. Relative influence of individual parameters on the predicted initial stiffness  $K_{ser}$  according to prEN 1995-1-1 (Eq. (1)), SIA 265 (Eq. (2 & 3)), Gauß (Eq. (4)) and proposal (Eq. (5)); initial values of the curves as reference values

In order to evaluate the individual models based on test data, a comprehensive database has been compiled containing stiffness values from tests on steel-timber dowel-type connections in softwoods (spruce glulam) as well as tests on hardwoods (beech glulam, beech LVL, azobé glulam).

The following research has been taken into account (*shortcut*):

- Julius Gauß softwood (JG-S), beech LVL (JG-LVL), GAUß (2024)
- Frank Brühl softwood (FB), BRÜHL (2020)
- Markus Dorn softwood (MD), DORN (2012)
- Ireneusz Bejtka softwood (IB), BEJTKA (2005)
- Carmen Sandhaas softwood (CS-S), azobé (CS-A), beech (CS-B), SANDHAAS (2012)
- Holzbau-Offensive research project beech LVL (HO), KUHLMANN & BUCHHOLZ (2023)

Figure 4.2 shows the comparison of the initial stiffness  $K_{ser}$  proposed in Equation (5) with the experimentally determined stiffnesses. The black solid line is obtained by ideally matching the prediction based on calculations and experimental stiffness values. The lower black dashed line indicates that the predicted values are 50 % below the experimental values, while the upper dashed line indicates that the predicted values are 50 % above the experimental values. The green data points represent stiffness values of connections with softwood and the red points represent stiffness values of connections with hardwood.

It can clearly be seen, that the majority of the tests fall within a range of  $\pm 50\%$  of the ideal value. The proposed equation therefore seems to be equally suitable for predicting the initial stiffness of softwood and hardwood. The easily recognizable vertical bars usually represent the results of a single test series and thus clearly show the scattering of results that occurs although the same geometry and material were used. The circled test series by KUHLMANN & BUCHHOLZ (2023) shows individual measured values for tests with five fasteners and different types of reinforcement, where the reinforcement had no significant influence on the initial stiffness. This means, that the deviation of the individual measured values is not necessarily due to the poor prediction accuracy of the equation, but rather arises from the large coefficients of variation present.

Even with nominally identical boundary conditions, there are sometimes huge differences in the measured stiffnesses between the different research projects. This can be explained on one hand by the material scatter, but on the other hand also by the large influence of manufacturing accuracy (e.g. drill hole roughness) and different measurement methods. GAUß (2024) found systematic deviations of about 50 % between the reference series of his own two research projects, which can probably be explained by geometric imperfections of the test specimens.

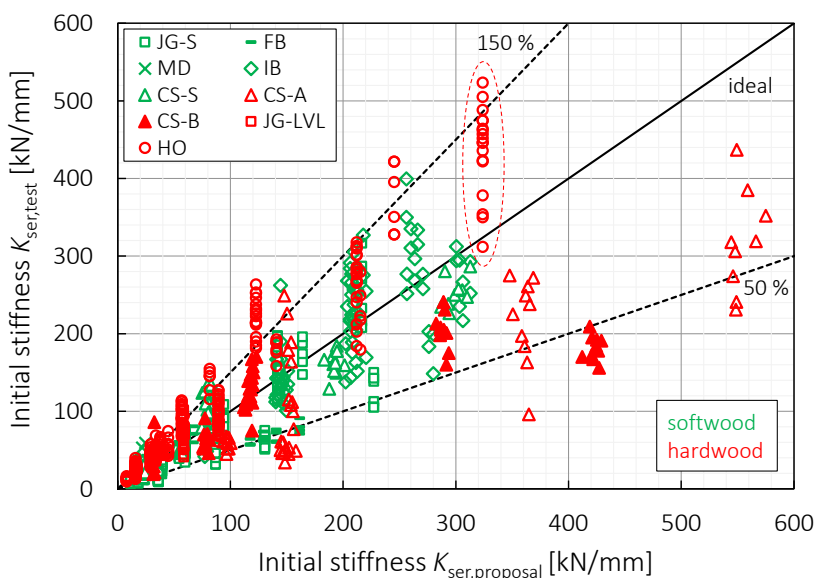


Figure 4.2. Comparison of the stiffness  $K_{ser}$  of the proposed equation with experimentally determined stiffnesses

In Figure 4.3, the predicted stiffnesses according to prEN 1995-1-1 (2023) (red), SIA 265 (2012) (green) and the proposed equation (blue) are compared with the experimentally determined stiffnesses.

For the prediction according to prEN 1995-1-1 (2023) there are significantly more measuring points below and above the 50 % line than for the prediction models according to SIA 265 (2012) and the proposed equation. This can also be clearly seen in the coefficient of determination  $R^2$  for the individual models (see Figure 4.2). The horizontal shift of the measuring points, indicated by the circle, clearly shows the influence of density on the stiffness prediction. While the rule given in prEN 1995-1-1 (2023) considers density by an exponent of 1.5, the rule given in SIA 265 (2012) considers it by an exponent of 0.5 and the proposed equation by 0.7.

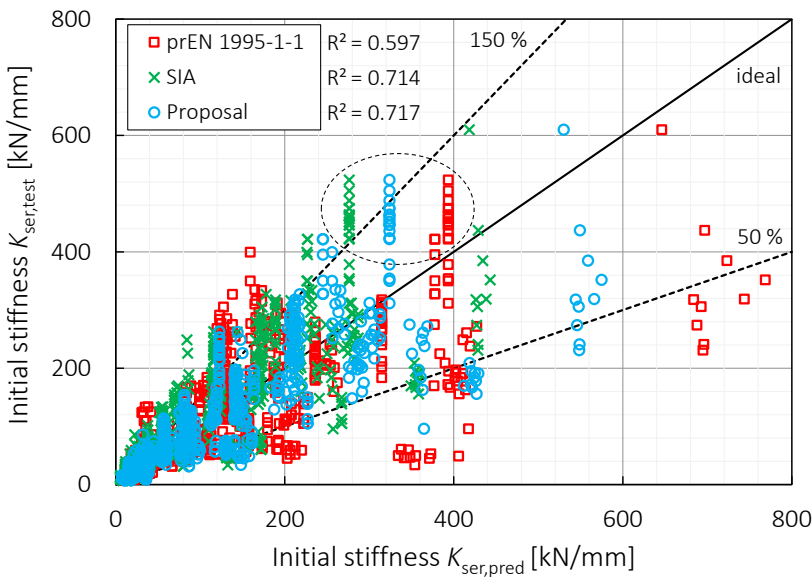


Figure 4.3. Comparison of the stiffness  $K_{ser}$  according to prEN 1995-1-1 (2023), SIA 265 (2012) and the proposed equation with the experimentally determined stiffnesses

Figure 4.4 shows an extract from Figure 4.3 for stiffnesses up to 400 kN/mm. This section contains the test results for single dowel connection, so many data points can now easier be seen in this plot. It becomes even clearer that there are many measuring points below and above the 50 % line for the prediction according to prEN 1995-1-1 (2023). For the SIA 265 (2012) prediction, there are some measuring points especially above the 50 % line. For the prediction with the proposed equation, almost all measuring points are within these limits of +/- 50 %.

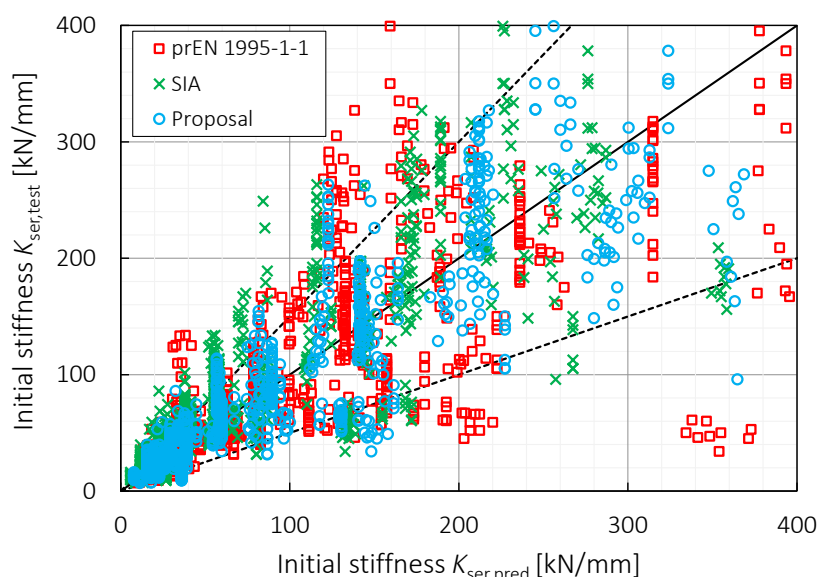


Figure 4.4. Comparison of the stiffness  $K_{ser}$  according to prEN 1995-1-1 (2023), SIA 265 (2012) and the proposed equation with the experimentally determined stiffnesses (extract from Figure 4.3)

## 5 Summary and Outlook

Based on the results of a large number of tests on steel-timber dowel-type connections in both softwood and hardwood, an empirical equation for determining the initial stiffness has been derived. In addition to the density, the fastener diameter and the load-to-grain angle, the number of fasteners is also taken into account. The evaluation of the deviation of the predicted stiffness from the measured stiffness shows that, despite of the large scatter that occurs, a prediction within a scatter band of +/- 50 % can be achieved for all types of timber. For practical application, this means that the average value of the expected initial connection stiffness as well as the expected upper and lower limit of stiffness can be determined using the proposed formula. To determine the minimum or maximum expected stiffness, the mean value must be multiplied by a factor of 0.5 or 1.5.

To realistically account for the stiffness and load-deformation behaviour of complex joints and thus be able to benefit from reserves, flexible and easy-to-use design concepts are needed. Within a new research project at the University of Stuttgart, a design method for timber joints inspired by the component method is under development, which enables the designer to combine in a very flexible way different components in order to optimize joints for a performance-based design.

## 6 Acknowledgements

This project is supported by the Ministry of Food, Rural Affairs and Consumer Protection of the State of Baden-Württemberg as part of the “Timber Building Initiative”. We would also like to thank Pollmeier Massivholz GmbH & Co. for providing the beech LVL and Adolf Würth GmbH & Co. KG for donating the screws and self-drilling dowels.

## 7 References

- Bejtka, I. (2005): Verstärkung von Bauteilen aus Holz mit Vollgewindeschrauben (in German). Dissertation, Karlsruhe Institute of Technology, Germany.
- Brühl, F. (2020): Ductility in timber structures – possibilities and requirements with regard to dowel type fasteners. Dissertation, Publication of Institute of Structural Design no. 2020-1, University of Stuttgart, Germany.
- Dorn, M. (2012): Investigations on the Serviceability Limit State of Dowel-Type Timber Connections. Dissertation, TU Vienna, Austria.
- EN 383 (2007): Timber Structures – Test methods – Determination of embedment strength and foundation values for dowel type fasteners. CEN, Brussels.
- EN 1995-1-1 (2004): Eurocode 5: Design of timber structures – Part 1-1: General – Common rules and rules for buildings. European Committee for Standardization (CEN), Brussels, with corrections and amendments + AC:2006 and A1:2008.
- EN 26891 (1991): Timber Structures – Joints made with mechanical fasteners – General principles for the determination of strength and deformation characteristics. CEN, Brussels.
- Franke, S. & Franke, B. (2020): Bemessung von Stabdübelverbindungen in Buchen-Brett-schichtholz (in German). Bautechnik 97, special issue „Holzbau“, pp. 35-43.
- Gauß, J. (2024): Zum Trag- und Verformungsverhalten von Stahl-Holz-Stabdübelverbindungen (in German). Dissertation, Publication of Institute of Structural Design no. 2024-1, University of Stuttgart, Germany.
- Kuhlmann, U. & Buchholz, L. (2023): Innovative Holzknoten durch Modellierung der Steifigkeit für leistungsfähige Holztragwerke aus Laub- und Nadelholz (in German). Research report, research project within the „Timber Building Initiative“ of the Ministry of Food, Rural Affairs and Consumer Protection of Baden-Württemberg, Institute of Structural Design, University of Stuttgart.
- Kuhlmann, U. & Gauß, J. (2019a): Optimierung von Anschlüssen im Holzbau zur Verbreitung der ressourcenschonenden Bauweise (in German). Research report, Zukunft Bau (SWD-10.08.18.7-17.12), Institute of Structural Design, University of Stuttgart.
- Kuhlmann, U. & Gauß, J. (2019b): Component Method in Timber Construction – Experimental and Numerical Research. INTER, 52-7-11, Tacoma, University of Stuttgart.
- Kuhlmann, U. & Gauß, J. (2021a): Wirtschaftliche Dimensionierung von Holztragwerken durch leistungsfähige Stahl-Holz-Stabdübelverbindungen (in German). Research report, IGF research project No. 20625 N (AiF/iVTH), Institute of Structural Design, University of Stuttgart.
- Kuhlmann, U. & Gauß, J. (2021b): Stiffness of Steel-Timber Dowel Connections – Experimental and Numerical Research. INTER, 54-7-9, Online-Meeting, University of Stuttgart.
- prEN 1995-1-1 (2023): Eurocode 5: Design of timber structures – Part 1-1: General – Common rules and rules for buildings. European Committee for Standardization (CEN), Brussels
- Sandhaas, C. (2012): Mechanical behavior of timber joints with slotted-in steel plates. Dissertation, TU Delft, Netherlands.
- SIA 265 (2012): Timber Structures. Zürich, Swiss Society of Engineers and Architects.

## DISCUSSION

**The paper was presented by L Buchholz**

*A Salenikovich commented that how stiffness was determined needed to be considered carefully when combining data from different projects. L Buchholz described how the testing was established which was similar to other cases.*

*H Blass questioned whether the approach of estimating the maximum load for stiffness estimation was used in all cases especially for the reinforced connections as there seemed to large differences from C Sandhaas' results on beech. L Buchholz responded that this could be due to difference in manufacturers. L Buchholz also confirmed that the evaluation of the effect of number of fasteners was also done with databases from others.*

*A Frangi commented he could share more ETH data (Gehri, Wydler) on the topic.*

*P Dietsch discussed with U Hübner if there would be room to consider this issue in the code. They agreed that more discussion would be needed as all kinds of connections would need to be considered and influence of number of dowels also play a role.*

*A Frangi commented that the paper should show equations for the +- 50% band.*





# Design proposal for the final slip modulus of dowel-type timber connections based on the Beam-on-Foundation approach

Romain Lemaître, CERIB Fire Testing Centre, Épernon, France

Michael Schweigler, Dept. of Building Technology, Linnæus University, Växjö, Sweden

Eva Binder, Dept. of Building Technology, Linnæus University, Växjö, Sweden

Eric Sauvignet, BE2S engineering office, Saint-Symphorien-des-Bois, France

Jean-François Bocquet, work4cad, Saône, France

Keywords: final slip modulus, dowel-type timber connections, timber-to-timber, steel-to-timber, concrete—to-timber, beam-on-foundation

## 1 Introduction and motivation

In EN 1995-1-1 (2004), the final slip modulus of a dowel-type connection is given by the following relationship

$$K_{SLS,fin} = K_{SLS} / (1 + k'_{def}), \quad (1)$$

with

$$k'_{def} = \eta \cdot k_{def}, \quad (2)$$

with  $\eta = 2$  for timber-to-timber, and  $\eta = 1$  for steel-to-timber connections or

$$k'_{def} = \eta \cdot (k_{def,1} \cdot k_{def,2})^{1/2}, \quad (3)$$

with  $\eta = 2$  for hybrid timber-to-timber connections,

where  $\eta$  is a prefactor to consider the connection type, and  $k_{def}$  is the creep deformation factor of the wood-based members comprising the connection, as given in Table 3.2 of EN 1995-1-1 (2004). In 5.1.6(3) of prEN 1995-1-1 (2023), the same values for  $\eta$  respectively  $k'_{def}$  are proposed.

In CEN/TS 19103 (2021), the final slip modulus is given by the same relationship than equation (1) and with

$$k'_{\text{def}} = \psi_{\text{conn}} \cdot \eta \cdot k_{\text{def}}, \quad (4)$$

where  $\psi_{\text{conn}}$  is a time-dependent factor relating to the effect of the mixed action on the creep deformation factor  $k'_{\text{def}}$ . The value of  $\psi_{\text{conn}}$  is equal to 1 or 0.65 for long-term period or a period between 3 and 7 years, respectively. As given in 4.3.2(6) of CEN/TS 19103 (2021), the prefactor  $\eta$  is equal to 2.

To the best of our knowledge, there is no background to use  $\eta = 2$  in the design of dowel-type timber-to-timber or concrete-to-timber connections, while  $\eta = 1$  is used for steel-to-timber connections. The creep deformation factor of wood,  $k_{\text{def}}$ , is derived from bending tests, and according to EN 1995-1-1 (2004) is identical for all stiffness properties. Recent works showed that  $k_{\text{def}}$  can be lower when timber is mainly subjected to compression load (Dubois et al., 2023) or higher when timber is subjected to rolling shear (Allemand et al., 2021). Very few studies can be found in the literature about long-term connection behaviour (e.g. van de Kuilen, 1992 and Brandon, 2015), and even less on the embedment behaviour (e.g. Brandon, 2015). However, it can be thought that larger creep deformations appear in connections due to higher local stress-levels in the vicinity of the dowels, which might even lead to non-linear creep. In addition, for connections a stronger influence of mechano-sorption on the long-term deformations can be expected due to more “open end-grain surfaces”. In van de Kuilen (1992), it is mentioned that for nailed connections without predrilling in service class 2, the  $k'_{\text{def}}$  factor should be higher than  $k_{\text{def}}$  proposed in the design standard at this time. Enhancing the understanding of  $k'_{\text{def}}$  is crucial for improved deflection estimates in timber structures, particularly for those with numerous connections like tall timber buildings or long-span truss beams.

The purpose of this paper is to investigate the reliability of  $k'_{\text{def}}$  for different connection types, i.e., timber-to-timber, steel-to-timber, and concrete-to-timber, with the aim to propose connection specific prefactors  $\eta$  for definition of  $k'_{\text{def}}$  based on  $k_{\text{def}}$ . This is achieved by a parameter study, where the Beam-on-Foundation (BoF) approach is utilized to study the influence of modification of the local material property, i.e. the instantaneous and final elastic foundation modulus, on the global connection property, i.e., the instantaneous and final connection slip modulus.

## 2 Method for determining prefactors $\eta$

With the aim of investigating the most common types of connections, three types were studied: (i) timber-to-timber and (ii) steel-to-timber connections (slotted-in steel plate), both with double shear planes, as well as (iii) concrete-to-timber connections with single shear plane.

The creep deformation factor of the connection,  $k'_{def}$ , is determined by comparing the instantaneous,  $K_{SLS}$ , and the final connection slip modulus,  $K_{SLS,fin}$ , where these values are calculated from connection slip curves based on the Beam-on-Foundation (BoF) approach. Thus, for determination of  $k'_{def}$ , two BoF simulations are required. One for calculation of the instantaneous slip modulus,  $K_{SLS}$ , and a second for prediction of the final connection slip modulus,  $K_{SLS,fin}$ . The general approach to determine  $k'_{def}$ , giving access to the prefactor  $\eta$  (equations (2)-(4)), is illustrated in Figure 2.1 and described in more details in Section 2.1.

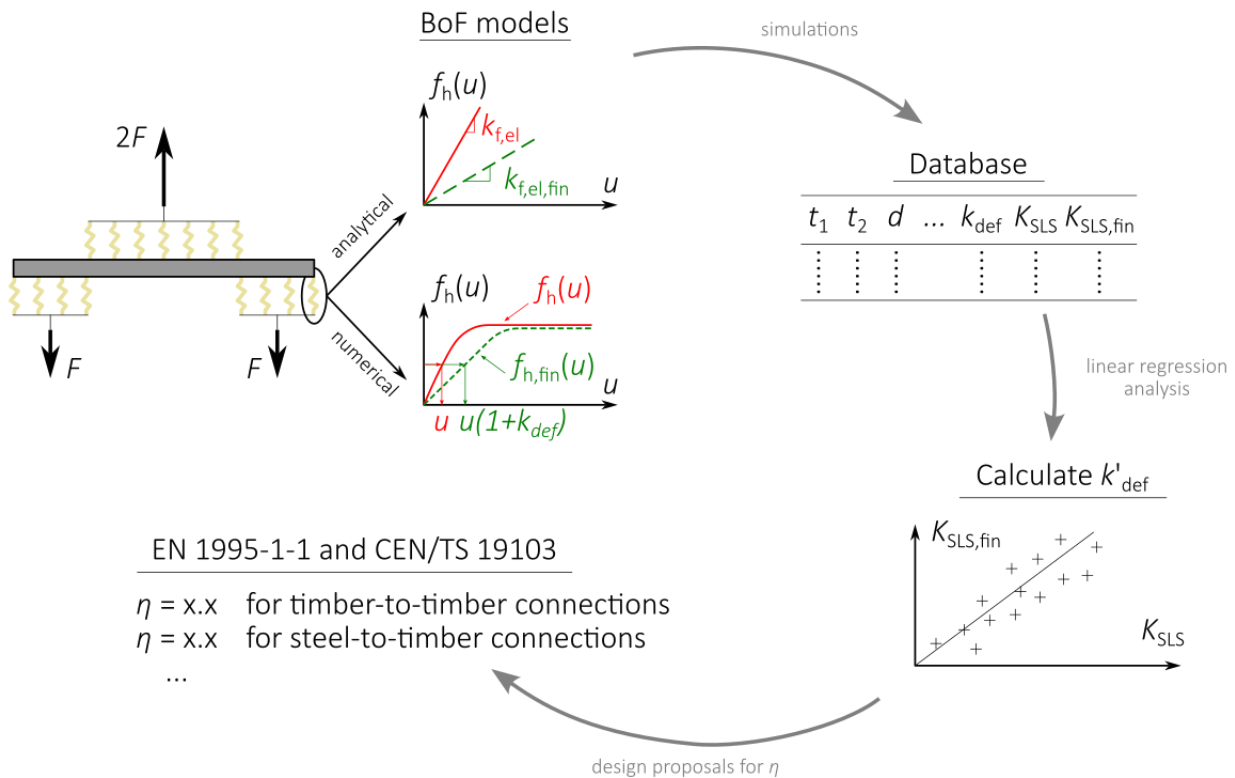


Figure 2.1. Methodology to investigate the reliability of  $k'_{def}$  and  $\eta$  based on equations (1)-(4).

## 2.1 Definition of $k'_{def}$ and $\eta$

The connection creep factor,  $k'_{def}$ , was calculated by applying a linear regression analysis between  $K_{SLS,fin}$  and  $K_{SLS}$ , utilizing the simulation results for the connections defined in Section 2.2. Considering equation (1), the slope of the regression line was assumed to be equal to  $1 / (1 + k'_{def})$ , resulting in

$$k'_{def} = K_{SLS} / K_{SLS,fin} - 1. \tag{5}$$

For simulation with the analytical BoF approach, the instantaneous  $K_{SLS}$  and the final  $K_{SLS,fin}$  slip moduli were given directly since this approach is elastic (see Section 2.2.1). However, for simulation with the numerical model (see Section 2.2.2),  $K_{SLS}$  and  $K_{SLS,fin}$  needed to be extracted from the corresponding non-linear load-slip curves. In this case, the slip modulus was defined as the slope of the load-slip curve between 10 and 40 % of the load at 5 mm slip.

The prefactor,  $\eta$ , describes the relationship between the material creep factors,  $k_{def}$  and  $\varphi_c$ , and the connection creep factor,  $k'_{def}$ . Following equations (2) to (4),  $\eta$  is defined for timber-to-timber and steel-to-timber connections as:

$$\eta = k'_{def} / k_{def}, \quad (6)$$

and for concrete-to-timber connections as:

$$\eta = k'_{def} / (\varphi_c \cdot k_{def})^{0.5}. \quad (7)$$

## 2.2 Beam-on-foundation approaches

Two different types of Beam-on-Foundation approaches were utilized in this study. For single-dowel connections the analytical approach proposed by Kuenzi (1955), and for multiple-dowel connections the numerical approach proposed by Lemaître et al. (2021) was utilized.

### 2.2.1 Analytical approach: Kuenzi (1955)

The analytical beam-on-elastic foundation approach developed by Kuenzi (1955) is used to investigate the reliability of  $k'_{def}$  for single dowel connections ( $n_0 = 1$ ). In Kuenzi (1955), the author presented relationships between load and slip, based on the theory of the beam-on-elastic foundation, for single and double shear nailed timber-to-timber connections. These relationships enable to find analytical equations to estimate the slip moduli which depend on both geometrical and mechanical parameters such as: thickness of the connection members,  $t_1$  and  $t_2$ , dowel diameter,  $d$ , elastic moduli of foundation of the connection members  $k_{f,el}^{1 \text{ or } 2}$ , which are in the case of this paper,  $k_{f,el}^{wood}$ ,  $k_{f,el}^{steel}$  and  $k_{f,el}^{concrete}$ , and the bending stiffness of the dowel,  $E_s I_s$ . For more details the reader is referred to Kuenzi (1955).

Kuenzi's analytical equations were used to calculate the instantaneous,  $K_{SLS}$ , and the final connection slip modulus,  $K_{SLS,fin}$ .  $K_{SLS}$  was calculated from the instantaneous elastic foundation modulus  $k_{f,el}$  (given in Subsection 2.2.3) while as model input for calculation of  $K_{SLS,fin}$ , the final elastic foundation modulus,  $k_{f,el,fin}$ , was used and defined as

$$k_{f,el,fin}^{wood} = k_{f,el}^{wood} / (1 + k_{def}), \quad (8)$$

$$k_{f,el,fin}^{concrete} = k_{f,el}^{concrete} / (1 + \varphi_c), \quad (9)$$

with  $k_{def}$  is creep deformation factor given in EN 1995-1-1 (2004) and  $\varphi_c$  is creep coefficient given in EN 1992-1-1 (2004). No creep was considered for steel, i.e.,

$$k_{f,el,fin}^{steel} = k_{f,el}^{steel}. \quad (10)$$

The dowel bending stiffness  $E_s I_s$  was assumed to be the same value for the calculation of  $K_{SLS}$  and  $K_{SLS,fin}$ . The Young's modulus of the steel dowel  $E_s$  was set equal to 210 000 MPa and the second moment of area for circular cross section was equal to

$$I_s = \pi \cdot d^4 / 64, \quad (11)$$

with  $d$  as the dowel diameter.

### 2.2.2 Numerical approach: Lemaître et al (2021)

The numerical beam-on-foundation approach was used for investigation of multiple-dowel connections, as the analytical approach, presented in Section 2.1.1, cannot include the non-linear effect of multiple dowels on the slip modulus (Sandhaas & van de Kuilen, 2017; Jockwer & Jorissen, 2018). This study was limited to timber-to-timber connections with a single row of dowels ( $n_0 = \{1; 2; 6; 10\}$ ).

In this approach, the numerical model integrates the different material behaviours of the dowel-type connection, i.e., the elastic behaviour of the wood and steel members (shell elements), the elasto-plastic behaviour of the steel dowel, and the non-linear behaviour of the dowel-wood interaction, i.e., the embedment behaviour expressed by non-linear spring elements. For calculation of the instantaneous slip modulus,  $K_{SLS}$ , the phenomenological equation proposed in Richard & Abbott (1975) was utilized to describe the spring behaviour representing the instantaneous embedment stress parallel to the grain  $f_h$  as a function of the dowel displacement  $u$ :

$$f_h(u) = (k_{f,el} - k_{f,pl}) \cdot u / (1 + ((k_{f,el} - k_{f,pl}) \div f_{h,inter})^a)^{1/a} + k_{f,pl} \cdot u. \quad (12)$$

For more information on this model, the reader is referred to Lemaître et al., (2021).

For calculation of  $K_{SLS,fin}$ , Richard and Abbott's equation (12) was utilized by applying following long-term embedment parameters for calculation of the final embedment slip behaviour:

$$k_{f,pl,fin}^{wood} = k_{f,pl}^{wood} / (1 + k_{def}), \quad (13)$$

$$f_{h,inter,fin}^{wood} = f_{h,inter}^{wood}. \quad (14)$$

The shape coefficient  $a$  given in equation (12) was set equal to 3 for calculation of the instantaneous and final load-slip response of the connection. In addition of the above long-term embedment parameters, equation (8) was also utilized.

Edge and end distances followed the provision from EN 1995-1 (2004), except for  $a_1$ , which was varied in the range of  $\{5d; 7d; 9d\}$ . The elastic material properties for the timber members, i.e., the two moduli of elasticity  $E_1$  and  $E_2$ , in the directions parallel and perpendicular to the grain were set equal to 11 500 MPa and 300 MPa, respectively. A Poisson's ratio  $\nu_{12}$  in the plane of the plate was set equal to 0.41 and a shear modulus  $G_{12}$  was set equal to 650 MPa. These four parameters are standard values for GL24h. Regarding the steel dowel bending stiffness, the same assumption and values as described in Section 2.1.1 were applied.

### 2.2.3 Input parameters for the Beam-on-Foundation approaches

The following equations were used to define the instantaneous embedment parameters required for the BoF simulations, i.e., the elastic foundation modulus (for analytical and numerical BoF)

$$k_{f,el}^{wood} = 0.1374 \cdot \rho - 12.29, \quad (15)$$

the plastic foundation modulus (for the numerical BoF)

$$k_{f,pl}^{wood} = 0.0047 \cdot \rho - 2.00, \quad (16)$$

the embedment stress at the intersection of  $k_{f,pl}$  with the stress axis (for the numerical BoF)

$$f_{h,inter}^{wood} = 0.1018 \cdot \rho - 10.32, \quad (17)$$

with  $\rho$  as timber member density (in  $\text{kg/m}^3$ ).

Equations (16) to (18) were defined from a regression analysis of a database comprising the embedment parameters of 1 565 tests (Schweigler et al. (2019)).

For this study, the factors  $k_{f,el}^{steel}$  and  $k_{f,el}^{concrete}$ , were assumed as the ratio between steel, respectively concrete, and wood Young's moduli.

$$k_{f,el}^{steel} = 20 \cdot k_{f,el}^{wood}, \quad (18)$$

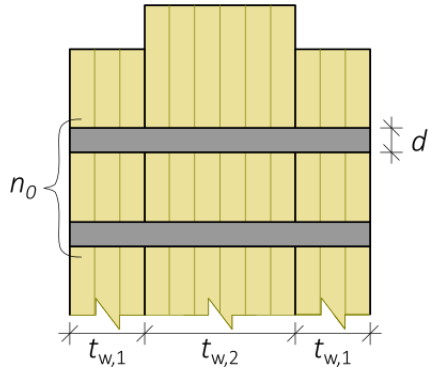
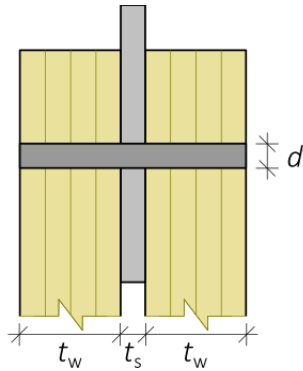
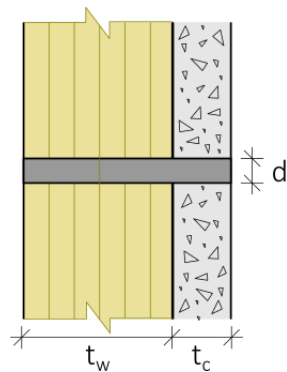
$$k_{f,el}^{concrete} = 3 \cdot k_{f,el}^{wood}. \quad (19)$$

Values of  $\rho$ ,  $k_{def}$ , and  $\varphi_c$  used in the parameter study are given in Section 2.3.

### 2.3 Parameter study variables

Input parameters, by means of geometrical and material parameters, were selected to reflect common connections used in building practice (see Table 1).

Table 1. List of studied variables for each connection type.

Connection types	Parameter study variables
	$n_0 \in \{1; 2; 6; 10\}$ $\rho_1 = \rho_2 \in \{420 \text{ kg/m}^3\}$ $d \in \{8; 12; 16; 20; 24 \text{ mm}\}$ $t_{w,1} / d \in \{1 \text{ to } 10, \text{ in steps of } 0.5\}$ $t_{w,2} = 2 \cdot t_{w,1}$ $k_{\text{def},1} = k_{\text{def},2} \in \{0.3; 0.6; 0.8; 1.2; 2.4; 4.8\}$
	$n_0 \in \{1\}$ $\rho \in \{420 \text{ kg/m}^3\}$ $d \in \{8; 12; 16; 20; 24 \text{ mm}\}$ $t_w / d \in \{1 \text{ to } 10, \text{ in steps of } 0.5\}$ $t_s = d$ $k_{\text{def}} \in \{0.3; 0.6; 0.8; 1.2; 2.4; 4.8\}$
	$n_0 \in \{1\}$ $\rho \in \{420 \text{ kg/m}^3\}$ $d \in \{12; 16; 20 \text{ mm}\}$ $t_c \in \{60; 80; 100; 120 \text{ mm}\}$ $t_w \in \{100 \text{ to } 475, \text{ in steps of } 25 \text{ mm}\}$ $\varphi_c \in \{2.2; 3.8\}$ $k_{\text{def}} \in \{0.3; 0.6; 0.8; 1.2; 2.4; 4.8\}$

### 3 Results and discussion

#### 3.1 Simulation results – $K_{\text{SLS,fin}}$ vs $K_{\text{SLS}}$

As explained in Section 2, determining  $k'_{\text{def}}$  is a preliminary step before determining prefactors  $\eta$ . Therefore, two BoF simulations are required: one for calculation of the instantaneous slip modulus,  $K_{\text{SLS}}$ , and a second for prediction of the final connection slip modulus,  $K_{\text{SLS,fin}}$ . Figures 3.1 to 3.3, show the comparisons between  $K_{\text{SLS,fin}}$  and  $K_{\text{SLS}}$  for different connection types and different creep deformation factors  $k_{\text{def}}$ . For each case, a regression line is plotted as well as two lines defined by slopes of  $1 / (1 + k_{\text{def}})$



and  $1 / (1 + 2 \cdot k_{\text{def}})$  which represent the provisions given in EN 1995-1-1 (2004) and CEN/TS 19103 (2021). For all graphs, the slope of the regression lines is used to calculate the connection creep deformation factor  $k'_{\text{def}}$  using Equation (5).

In Figure 3.1, a comparison between  $K_{\text{SLS,fin}}$  and  $K_{\text{SLS}}$ , is shown for timber-to-timber connections with different creep deformation factor  $k_{\text{def}}$  values. Results for single dowel connections, i.e.,  $n_0 = 1$  (with the analytical BoF) and multiple-dowel connections, i.e.,  $n_0 = \{1; 2; 6; 10\}$  (with the numerical BoF), are also included. In total, around 1 500 simulations were performed. Figure 3.1 shows that all regression lines are consistently above the line representing by the slope of  $1 / (1 + k_{\text{def}})$ , which is in contradiction with the provisions given in EN 1995-1-1 (2004) for timber-to-timber connections, see Equation (3). For single dowel connections,  $k'_{\text{def}}$  is equal to 0.22 ( $R^2 = 0.9998$ ), 0.44 ( $R^2 = 0.9992$ ), 0.57 ( $R^2 = 0.9987$ ), 0.84 ( $R^2 = 0.9977$ ), 1.58 ( $R^2 = 0.9943$ ) and 2.91 ( $R^2 = 0.9881$ ), for a creep deformation factor  $k_{\text{def}}$  equal to 0.3, 0.6, 0.8, 1.2, 2.4, and 4.8, respectively. For multiple-dowel connections,  $k'_{\text{def}}$  is equal to 0.47 ( $R^2 = 0.9996$ ) and 0.63 ( $R^2 = 0.9993$ ), for a  $k_{\text{def}}$  equal to 0.6 and 0.8, respectively. A comparison of  $k'_{\text{def}}$  values between single dowel and multiple-dowel connections, shows that there is no significant influence of the number of fasteners  $n_0$ .

In Figure 3.2 a comparison between  $K_{\text{SLS,fin}}$  and  $K_{\text{SLS}}$ , is shown for steel-to-timber connections with different  $k_{\text{def}}$  values. In total, 665 simulations were performed. Figure 3.2 shows that all regression lines are consistently above the line representing by the slope of  $1 / (1 + k_{\text{def}})$ , which contradicts the provisions given in EN 1995-1-1 (2004) for steel-to-timber connections, see Equation (3).  $k'_{\text{def}}$  is equal to 0.18 ( $R^2 = 0.9998$ ), 0.35 ( $R^2 = 0.9992$ ), 0.46 ( $R^2 = 0.9988$ ), 0.68 ( $R^2 = 0.9978$ ), 1.28 ( $R^2 = 0.9947$ ) and 2.37 ( $R^2 = 0.9890$ ), for a creep deformation factor  $k_{\text{def}}$  equal to 0.3, 0.6, 0.8, 1.2, 2.4, and 4.8, respectively. Slightly lower  $k'_{\text{def}}$  values were found for steel-to-timber compared to timber-to-timber connections.

In Figure 3.3 a comparison between  $K_{\text{SLS,fin}}$  and  $K_{\text{SLS}}$ , is shown for concrete-to-timber connections with different  $k_{\text{def}}$  and  $\varphi_c$  values, i.e., creep factor deformations for timber and concrete, respectively. In total, 2688 simulations were performed. Figure 3.3 shows that the regression lines are above or below the line representing by the slope of  $1 / (1 + 2 \cdot k_{\text{def}})$ , which contradicts the provisions given in CEN/TS 19103 (2021) for concrete-to-timber connections, see Equation (4). The latter observation depends on the definition of  $k'_{\text{def}}$  used for connection members with different time-dependent behaviour. This point is discussed in Subsection 3.2.3. For a creep deformation factor  $\varphi_c$  equals to 2.2,  $k'_{\text{def}}$  is equal to 0.73 ( $R^2 = 0.9990$ ), 0.88 ( $R^2 = 0.9989$ ), 0.98 ( $R^2 = 0.9988$ ), 1.16 ( $R^2 = 0.9986$ ), 1.63 ( $R^2 = 0.9980$ ) and 2.42 ( $R^2 = 0.9871$ ), for a creep deformation factor  $k_{\text{def}}$  equal to 0.3, 0.6, 0.8, 1.2, 2.4, and 4.8, respectively. For  $\varphi_c$  equals to 3.8,  $k'_{\text{def}}$  is equal to 1.06 ( $R^2 = 0.9987$ ), 1.23 ( $R^2 = 0.9986$ ), 1.34 ( $R^2 = 0.9985$ ), 1.53 ( $R^2 = 0.9982$ ), 2.05 ( $R^2 = 0.9974$ ) and 2.92 ( $R^2 = 0.9961$ ), for a creep deformation factor  $k_{\text{def}}$  equal to 0.3, 0.6, 0.8, 1.2, 2.4, and 4.8, respectively.

Timber-to-timber connections

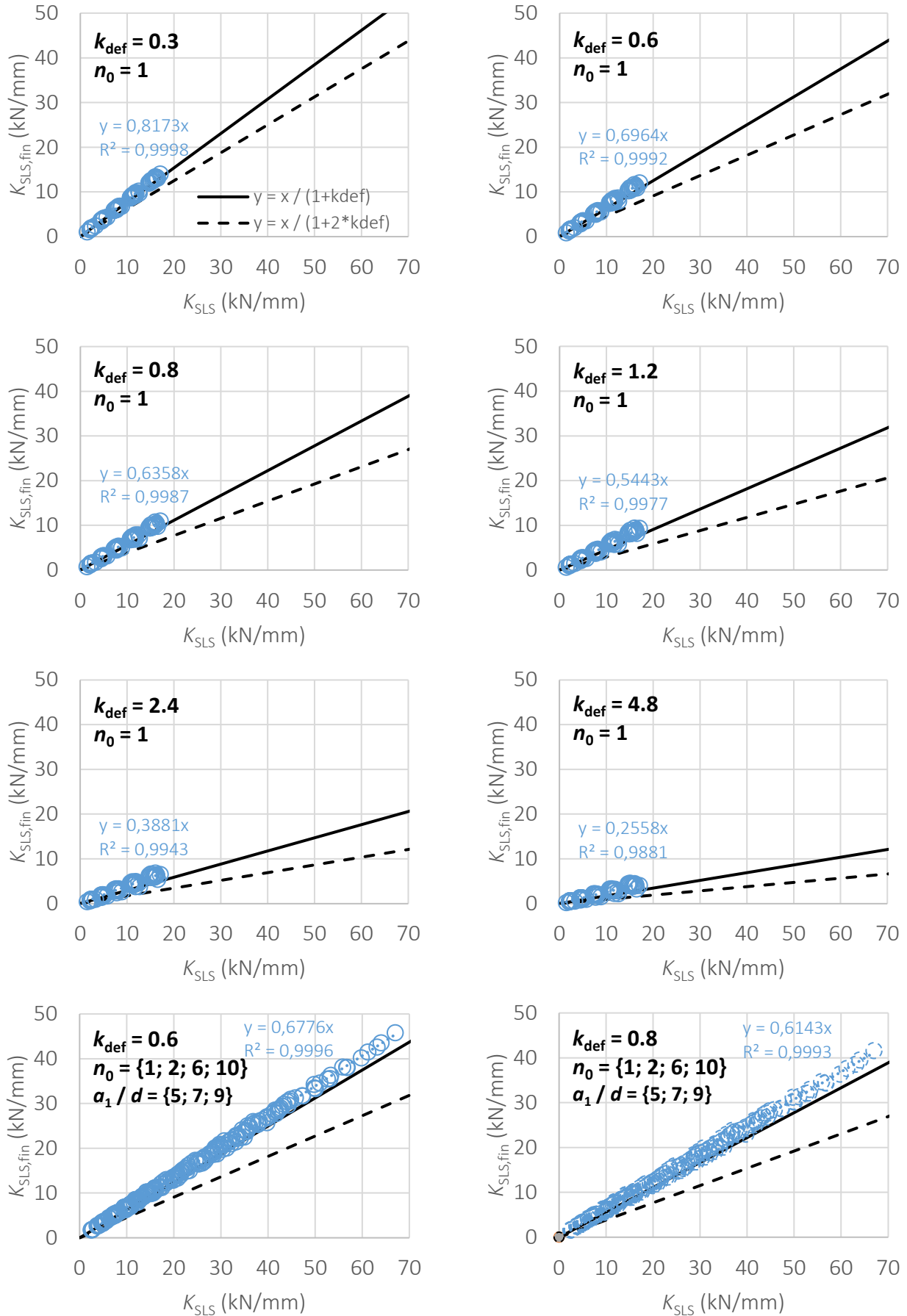


Figure 3.1. Comparison between instantaneous  $K_{SLS}$  and final slip  $K_{SLS,fin}$  moduli of timber-to-timber connections for different creep deformation factors  $k_{def}$ .

Steel-to-timber connections

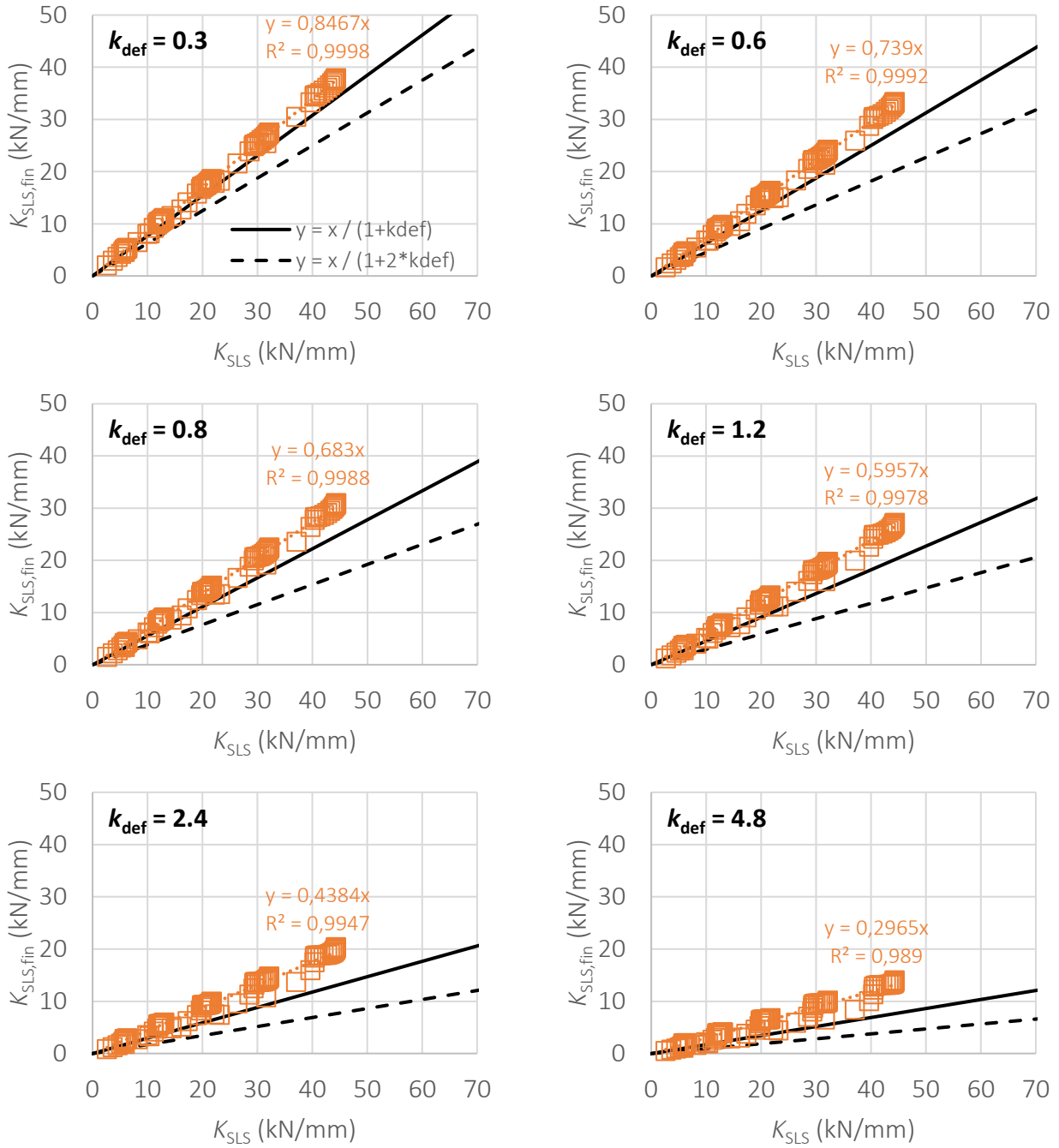


Figure 3.2. Comparison between instantaneous  $K_{SLS}$  and final slip  $K_{SLS,fin}$  moduli of steel-to-timber connections for different creep deformation factors  $k_{def}$ .

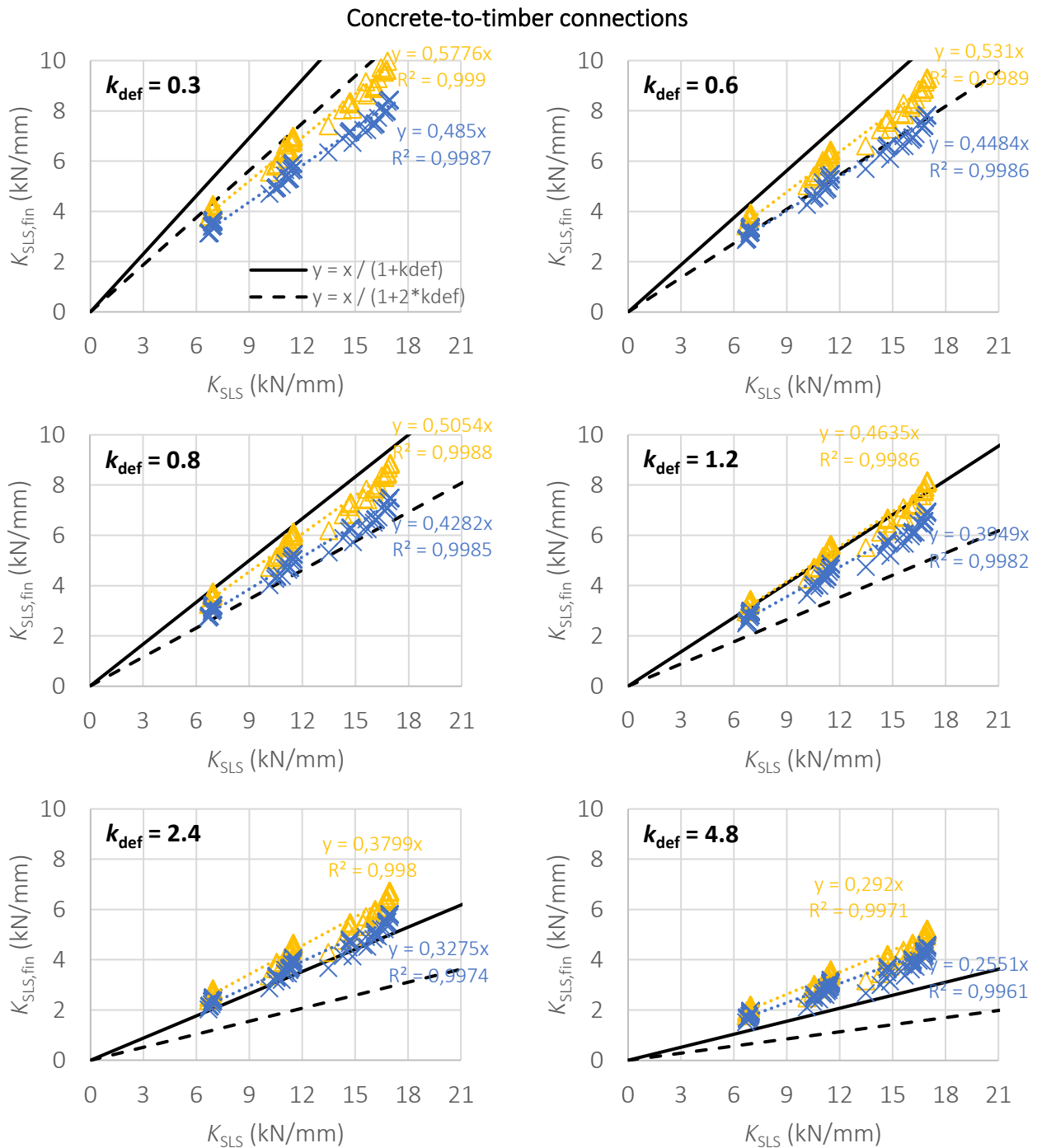


Figure 3.3. Comparison between instantaneous  $K_{SLS}$  and final slip  $K_{SLS,fin}$  moduli of concrete-to-timber connections for different creep deformation factors  $k_{def}$  and  $\varphi_c$ .  $\varphi_c = 2.2$  (△) and  $\varphi_c = 3.8$  (×).

### 3.2 Estimation of prefactor $\eta$

#### 3.2.1 Influence of the dowel slenderness $t / d$

Figure 3.4 shows the influence of the dowel slenderness  $t / d$ , i.e., connection failure mode (in accordance with Johansen's theory) on the prefactor  $\eta$ . The presented results are limited to a dowel diameter of 12 mm and  $k_{def}$  equal to 0.6. It is observed that  $\eta$  is almost independent of the dowel slenderness for different connection types. It is observed that for a small dowel slenderness the prefactor converges to 1.

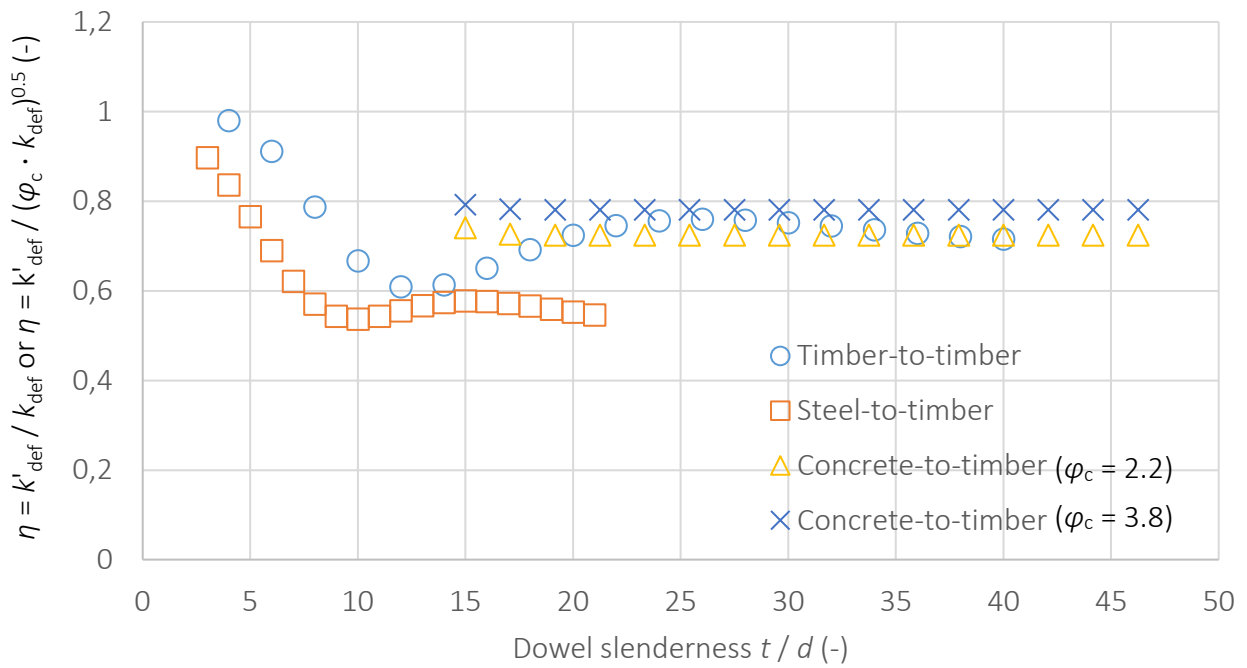


Figure 3.4. Prefactor  $\eta$  versus dowel slenderness  $t/d$  for different connection types. Results are based on a dowel diameter  $d = 12$  mm, concrete thickness  $t_c = 80$  mm and a creep deformation factor  $k_{def} = 0.6$ .

### 3.2.2 Influence of the creep deformation factors $k_{def}$ and $\varphi_c$

Using Equations (6) and (7), and connection creep deformation  $k'_{def}$  values presented in Subsection 3.1,  $\eta$  values are calculated for different connection types and creep deformation factors. The results are presented in Table 2 and illustrated in Figure 3.5. Slightly lower  $\eta$  values are found for steel-to-timber compared to timber-to-timber connections, which however does not justify to used  $\eta = 2$  for timber-to-timber, while  $\eta = 1$  is used for steel-to-timber connections. Finally, the Figure 3.5 shows that the prefactor  $\eta$  is almost independent of the  $k_{def}$  value for steel-to-timber and timber-to-timber connections but not for concrete-to-timber connections, as also the creep behaviour of the concrete is influencing the connection deformation.

Table 2. Values of prefactor  $\eta$  for different connection types and creep deformation factors.

Connection types	$n_0$	$\varphi_c$	$k_{def}$					
			0.3	0.6	0.8	1.2	2.4	4.8
Timber-to-timber	{1}	-	0.75	0.73	0.72	0.70	0.66	0.61
Timber-to-timber	{1; 2; 6; 10}	-	-	0.79	0.78	-	-	-
Steel-to-timber	{1}	-	0.60	0.59	0.58	0.57	0.53	0.49
Concrete-to-timber	{1}	2.2	0.90	0.77	0.74	0.71	0.71	0.75
Concrete-to-timber	{1}	3.8	0.99	0.81	0.77	0.72	0.68	0.68

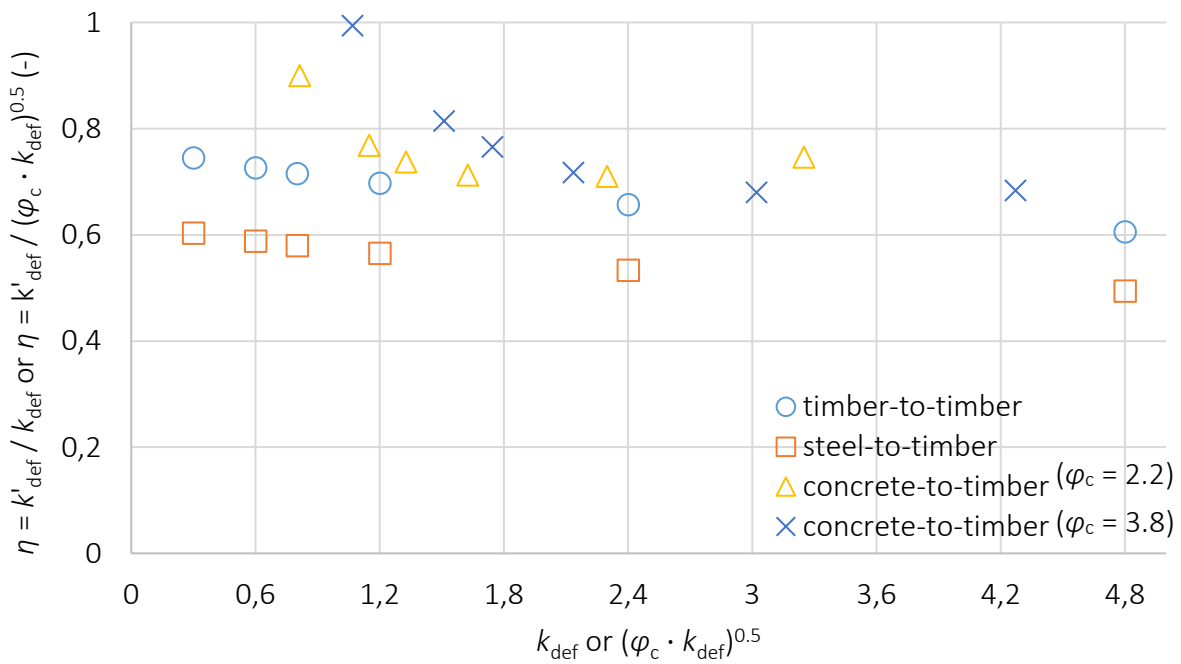


Figure 3.5. Comparison of the prefactor  $\eta$  for different connection types and creep deformation factors. Values of  $\eta$  for timber-to-timber and steel-to-timber connections were calculated from Equation (6), while Equation (7) was used for concrete-to-timber connections.

### 3.2.3 Connections including members with different time-dependent behaviour

Figure 3.6 shows  $\eta$  values calculated using Equations (6) and (7), for concrete-to-timber connections. The use of Equation (7) shows that the values of  $\eta$  are smaller and less dependent on the creep deformation factors  $k_{def}$  and  $\varphi_c$  than with the use of Equation (6). The latter shows that  $\varphi_c$  should be introduced into Equation (4) to consider the different time-dependent behaviour of connection members.

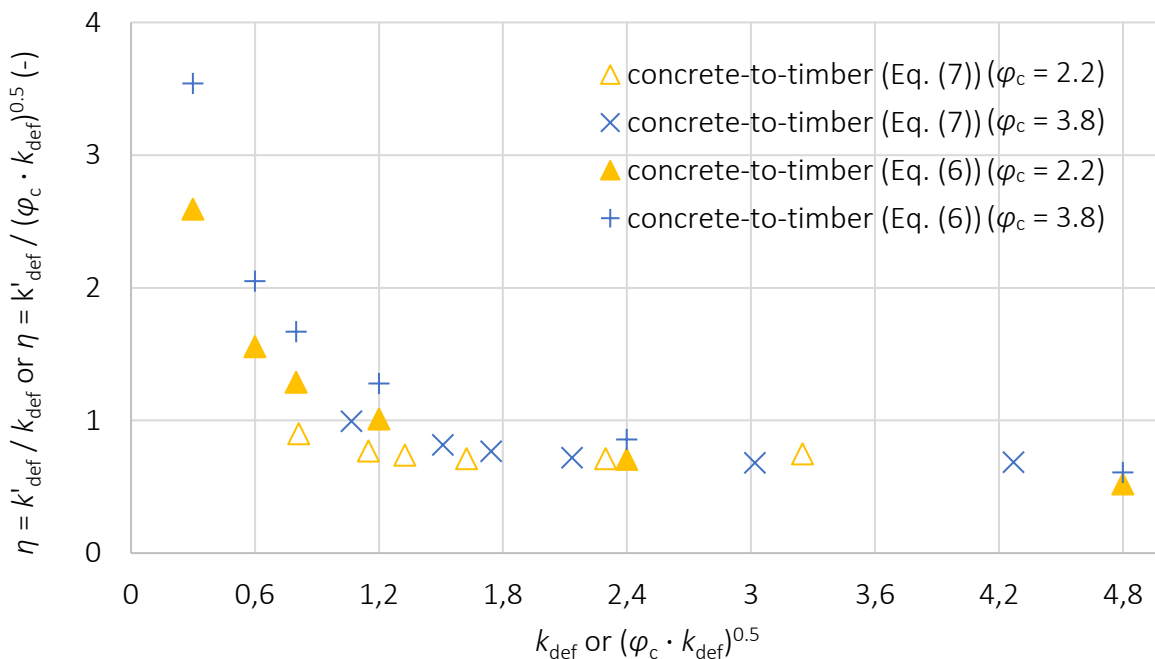


Figure 3.6. Comparison of the prefactor  $\eta$  definition for concrete-to-timber connection types and creep deformation factors.

## 4 Conclusions and proposal

The purpose of this paper was to investigate the reliability of the connection creep deformation factor,  $k'_{\text{def}}$ , for different connection types, i.e., timber-to-timber, steel-to-timber, and for connections including members with different time-dependent behaviour, e.g. concrete-to-timber connections. The aim was to propose connection specific prefactors  $\eta$  to calculate  $k'_{\text{def}}$ , and thus the final slip modulus,  $K_{\text{SLS,fin}}$ , based on the basic material creep deformation factors,  $k_{\text{def}}$  and  $\varphi_c$ , i.e., creep deformation factors for timber and concrete, respectively. This was achieved by a parameter study, where the Beam-on-Foundation (BoF) approach was utilized to study the influence of different basic material creep deformation factors on the final  $K_{\text{SLS,fin}}$  connection slip modulus. Due to the lack of established correlation of basic material creep parameters,  $k_{\text{def}}$  and  $\varphi_c$ , and input values for the BoF, a large variation in  $k_{\text{def}}$  and  $\varphi_c$  was included in the parameter study.

From the comparison between instantaneous  $K_{\text{SLS}}$  and final slip  $K_{\text{SLS,fin}}$  moduli carried out in this study, the following conclusions can be drawn:

- $\eta = 2$  for timber-to-timber connections as recommended in EN 1995-1-1 (2004) is not justified;
- $\eta = 1$  for steel-to-timber connections as recommended in EN 1995-1-1 (2004) is an upper limit;
- $\eta$  for steel-to-timber connections is smaller than for timber-to-timber connections;
- $\eta = 2$  for concrete-to-timber connections as recommended in CEN/TS 19103 is not justified;
- similar  $\eta$ -values were found for single and multiple-dowel connections;
- $\eta$  is almost independent from the connection failure mode, i.e. the dowel slenderness;
- $\eta$  is almost independent from  $k_{\text{def}}$  for timber- and steel-to-timber connections;
- $\eta$  is dependent on  $k_{\text{def}}$  and  $\varphi_c$  for concrete-to-timber connections and lower than 1.0;

Based on the findings from this study, the following expressions to calculate the connection creep factor  $k'_{\text{def}}$ , are proposed:

- $k'_{\text{def}} = \eta \cdot k_{\text{def}}$  for timber-to-timber and steel-to-timber connections;
- $k'_{\text{def}} = \eta \cdot (\varphi_c \cdot k_{\text{def}})^{0.5}$  for concrete-to-timber connections.

with  $k_{\text{def}}$  given in EN 1995-1-1 (2004) and  $\varphi_c$  given in EN 1992-1-1 (2004), where the prefactor  $\eta$  to calculate  $k'_{\text{def}}$ , and thus the final slip modulus  $K_{\text{SLS,fin}}$  of dowel-type connections, is assumed to be:

- $\eta = 0.8$  for timber-to-timber connections;
- $\eta = 0.6$  for steel-to-timber connections;
- $\eta = 1.0$  for concrete-to-timber connections.

However, we like to emphasize the need for future research to confirm the suitability of the basic material creep deformation factor,  $k_{\text{def}}$ , to be applied for the design of dowel-type connections.

## 5 Acknowledgements

The authors gratefully acknowledge the financial support by the Swedish research council FORMAS through the project “Long-term mechanical behavior of dowel connections in timber structures as the basis for an extended service life and reuse” (2022-01367).

## 6 References

- Allemand, C., et al. (2021). Characterization of Rolling and Longitudinal Shear Creep for Cross Laminated Timber Panels In: Proceedings of INTER/54-12-6.
- Brandon, D. (2015). Fire and structural performance of non-metallic timber connections, Doctoral dissertation, University of Bath.
- CEN/TS 19103 (2021). Eurocode 5: Design of Timber Structures — Structural design of timber-concrete composite structures – Common rules and rules for buildings. European Committee for Standardization (CEN), Brussels, Belgium.
- Dubois, F. et al. (2023). Long-term creep behavior of timber columns: Experimental and numerical protocols. *Engineering Structures*, 275, 115283.
- EN 1992-1-1 (2004). Eurocode 2: Design of concrete structures – Part 1-1: General rules and rules for buildings, and its amendments and corrigenda. European Committee for Standardization (CEN), Brussels, Belgium.
- EN 1995-1-1 (2004). Eurocode 5: Design of timber structures – Part 1-1: General – Common rules and rules for buildings, and its amendments and corrigenda. European Committee for Standardization (CEN), Brussels, Belgium.
- Jockwer, R. & Jorissen, A. (2018). Load-deformation behaviour and stiffness of lateral connections with multiple dowel type fasteners. In: Proceedings of INTER/51-07-07.
- Kuenzi, E. W. (1955): Theoretical design of a nailed or bolted joint under lateral load. Research Paper D1951 Madison, US: Department of Agriculture, Forest Service, Forest Products Laboratory Report.
- Lemaître, R. et al. (2021). Beam-on-Foundation Modelling as an Alternative Design Method for Timber Joints with Dowel-Type Fasteners Part 4: Joints Subjected to In-Plane Loading. In: Proceedings of INTER/54-7-7.
- prEN 1995-1-1 (2023). Eurocode 5: Design of timber structures – Part 1-1: General rules and rules for buildings. European Committee for Standardization (CEN), Brussels, Belgium.
- Richard, R. M. & Abbott, B. J. (1975). Versatile elastic-plastic stress-strain formula. *Journal of the Engineering Mechanics Division* 101.4, pp. 511–515.
- Sandhaas, C. & van de Kuilen, J.-W. G. (2017). Strength and stiffness of timber joints with very high strength steel dowels. *Engineering Structures*, 131:394–404.
- Schweigler, M. et al. (2019): Embedment test analysis and data in the context of phenomenological modeling for dowelled timber joint design. In: Proceedings of INTER/52-7-8, Tacoma, USA.
- Van de Kuilen, J. W. G. (1992). Determination of  $k_{def}$  for nailed joints. In: Proceedings of CIB-W18/25-7-9.



DISCUSSION

**The paper was presented by R Lemaître**

*A Frangi asked if experimental data was available to check the approach. R Lemaître responded not yet but they will have information from long term tests.*

*M Fragiaco stated that test data from other organizations exist to benchmark the results. He commented about the use of viscoelastic spring versus localized effects. R Lemaître said that elastic springs were used. M Fragiaco questioned why EC5 are higher. Some of these springs should be outside the elastic range. M Fragiaco stated that test data for model verification would be needed.*

*H Stamatopoulos commented that experimental data should be used to back calculate the spring parameters and changing local properties of the springs could ameliorate the results. Currently  $K_{SLS,fin}$  seems a fictitious number.*

*D Moroder and R Lemaître discussed difficulties in finding  $k'_{def}$  values in EC5.*

*J Töpler and JW van de Kuilen discussed  $k_{def}$  factors established from past papers.*

*J Töpler asked if primary and secondary creep was considered and mentioned that the reduction of stiffness could be an approach. P Dietsch suggested further clarification in the paper on this issue would be needed.*





# Parametrization of the non-linear behaviour of timber joints with self-tapping screws

Dorotea Caprio, Chalmers University of Technology, Sweden

Robert Jockwer, TUD Dresden University of Technology, Germany

Andreas Ringhofer, Graz University of Technology, Austria

Keywords: non-linear behaviour, slip-modulus, self-tapping screws

## 1 Introduction

The recent developments in the timber construction industry highlight the aim to design more cost-effective, adaptable, and reliable connections with high-performance fasteners. Examples of such modern connections are timber-to-timber or steel-to-timber joints with (inclined) self-tapping screws (STS) that exhibit highly non-linear mechanical behaviour. The design rules in prEN 1995-1-1:2023 *prEN 1995-1-1:2023 Eurocode 5 - Design of timber structures — Part 1-1: General rules and rules for buildings*. (2023) are partly insufficient to consider this complex mechanical behaviour: the analysis of joints is mainly linear elastic, and ductility is not considered explicitly. Considering the non-linear behaviour of joints is crucial for the design of statically indeterminate timber structures or in push-over and seismic analysis (Caprio et al. (2022) and De Santis et al. (2023)). Past studies investigated the resistance and stiffness of self-tapping screws loaded axially or laterally (Brandner et al. (2018)) while others focused on the mechanical behaviour of joints with STS being subjected to combined lateral and axial loads (Bejtka & Blaß (2002), Tomasi et al. (2010), Krenn (2017), Jockwer et al. (2014), and De Santis et al. (2023)). Questions about the detailed load-deformation behaviour and the influence of other parameters (such as additional load-to-screw axis angles, friction, torque, and screw length) on the load-deformation behaviour and the related variability were still unanswered. As a first step, Krenn (2017) and Jockwer et al. (2014) performed up to 8-20 repetitions of tests for each parameter investigated, providing insight into the variability of the load-deformation behaviour of steel-to-timber and timber-to-timber, respectively, with STS, but more tests are needed to characterize the variability

of these joints. Knowledge of the variability of the load-deformation behaviour is essential to perform reliability analyses of the structure and to provide design guidance for more reliable complex timber structures.

In this study, the regression model of Richard-Abbott is fitted to load-displacement curves of joints with STS to provide a more accurate description of the non-linear load-deformation and their variability. The probabilistic distribution type of each regression model parameter is determined (and partly assigned). From this, load-displacement curves are generated by sampling from a multivariate distribution that considers the correlation among the parameters. The data used in this study are taken from existing experimental data from Empa/ETHZ on timber-to-timber joints (*Jockwer et al. (2014)*) and from TU Graz on steel-to-timber joints (*Krenn (2017)*). Complementary experiments have been performed at Chalmers on steel-to-timber joints to better characterize the variability of the load-displacement curves. This is done using an asymmetric test set-up where only one single screw is loaded at a time. This enables to isolate the effects of the load on each single screw, preventing any homogenisation effects from multiple fasteners. From the parameterized load-displacement behaviour, on the one hand, the conventional parameters slip-modulus at serviceability limit state (SLS) and ultimate limit state (ULS), resistance, and ductility can be derived and compared with the standardized values, and on the other hand, improved design rules/guidance can be developed taking into account the full, real load-displacement curve.

## 2 Experiments and material

### 2.1 Overview of the tests

The database includes load-displacement curves taken from experimental campaigns conducted at Empa, TU Graz, and Chalmers. In this study, the analysis is limited to joints with one STS in a row. Nevertheless, the tests at Empa were performed on symmetric push-out tests on a total of 4 screws, and the tests at Graz on symmetric pull-out tests on a total of 2 STS. An overview of the tests is given in the table below:

Table 1. Overview of the main test series

	Timber	$d$ [mm]	$l$ [mm]	Test set-up	Institution	Parameters	Ref.
T-T	Glulam	13	400	Push-out	Empa	$\alpha$ , density	<i>Jockwer et al. (2014)</i>
S-T	GL28h	8	200	Pull-out	TU Graz	$\alpha$ , friction	<i>Krenn (2017)</i>
S-T	GL30c	8	200	Pull-out	Chalmers	$\alpha$ , friction	-

\*  $d$  is the diameter of the screw,  $l$  is the length of the screw,  $\alpha$  is the load-to-screw axis angle, T-T is timber-to-timber, S-T is steel-to-timber.

### 2.2 Tests from the literature

*Jockwer et al. (2014)* conducted monotonic push-out tests on timber-to-timber joints with STS inclined at different load-to-screw axis angles and densities. The tests were divided into two groups: 15 specimens were characterized by low density ( $\rho_m = 360 \frac{kg}{m^3}$ ),

and 14 specimens were characterized by high density ( $\rho_m = 460 \frac{kg}{m^3}$ ). The load-to-screw axis angles were varied between three values (90°, 60° and 45°). The governing failure mode was withdrawal failure for the tests with STS inclined at 45° and 60°, while it was the formation of two plastic hinges when the STS were inclined at 90°. *Krenn* (2017) performed a large experimental campaign on pull-pull tests on steel-to-timber joints with an inclined STS at TU Graz. The parameters that have been varied are the load-to-screw axis angle (30° and 45°), the number of rows (for the joints with STS inclined at 45°), and the number of STS (up to 20), the type of fastener, fully threaded and partially (FT) threaded (PT) and the friction (with and without Teflon sheet).

## 2.3 Experimental campaign at Chalmers

### 2.3.1 Test setup and configurations

The existing large experimental data set provides the basis for additional studies and evaluation. To extend the database of experiments on steel-to-timber joints by further inclined and not inclined STS, additional experiments have been conducted at the Laboratory of Structural Engineering at Chalmers University of Technology. A special test set-up for an asymmetric configuration was designed to apply a tension force to the steel plate screwed on one side of the timber specimen (see Figure 1). The timber piece is tied down to the clamping plate of the machine. The load was applied using a servo-hydraulic testing machine and the test was run displacement-controlled with a speed of 1 mm/min up to failure (rupture of the screw) or a maximum relative displacement between the steel plate and timber of 18 mm, close to the maximum displacement ranges of the LVDTs. The experimental campaign was divided into preliminary and main test series. In the preliminary test series, the influence of the length of the screw, the torque, and the friction has been investigated. In addition, the asymmetric test configuration has been compared with a symmetric test set-up in which the displacement was applied simultaneously to two steel plates, one of each fastened on the right and left side of the timber piece. For the comparison, the DIC system was used to measure the displacement filed on the surfaces of both the timber and the steel plate. The analysis indicated that the asymmetry of the test setup does not influence the load-displacement curve, which remains comparable to that of the symmetric case for both joint configurations with load-to-screw axis angles of 45° and 90°. Some details of this comparison and results from the preliminary tests serie are reported in *Dahlberg & Vallström* (2024). In the main test series, a larger number of repetitions of tests have been performed on selected configurations, quantifying the variability of the load-deformation behaviour for different load-to-screw axis angles. In the main test series, the relative displacement between the steel plate and the timber piece was measured at the location of the screw head (10 cm from the loaded end-grain) with LVDTs. Two additional LVDTs were placed on the steel plate to measure the horizontal movement of the steel plate. The setup with the placement of the LVDTs, the geometry of the steel plate with the milled

hole, and the fully threaded self-tapping screw are illustrated in Figure 1. In this present study, the analysis is done on tests belonging to the main test series and on joints with only one STS.

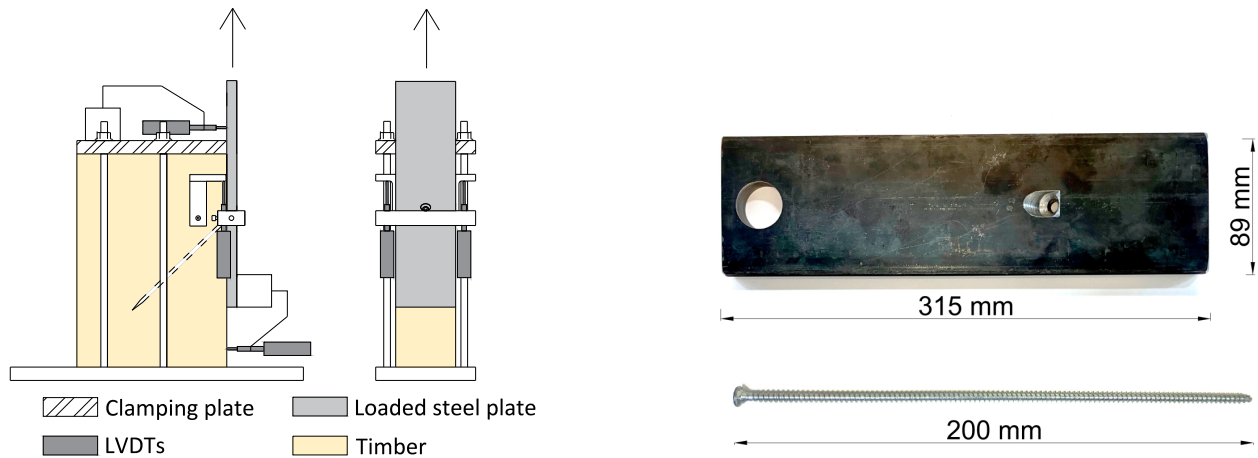


Figure 1. Asymmetric test set-up and details of the steel plate and the screws.

Table 2. Overview of the failure modes for tests on S-T joints with one STS conducted at Chalmers.  $\alpha$  is the load-to-screw axis angle,  $n$  is the total number of tests,  $n_{WITH}$  is number of withdrawal failures,  $n_{HTO}$  is the number of head tear-off failures

$\alpha$ [°]	$n$	$n_{WITH}$	$n_{HTO}$
30	10	4	6
45	20	1	19
60	10	0	10
90	20	0	20

### 2.3.2 Test results

Two types of failure governed the joint behaviour: withdrawal (WITH) and screw head tear-off (HTO). Head tear-off was always the governing failure for load-to-screw axis angles of 60° and 90°. The withdrawal failure governed 40% of the total tests for the load-to-screw axis angle of 30° and about 10% of the tests for a load-to-grain angle of 45°. When the failure is governed by head tear-off and the STS is arranged at angles < 90° to the applied load, the load-displacement curve stops abruptly before any large plastic deformation can take place, while when the withdrawal failure occurs, the curve presents a long softening behaviour.

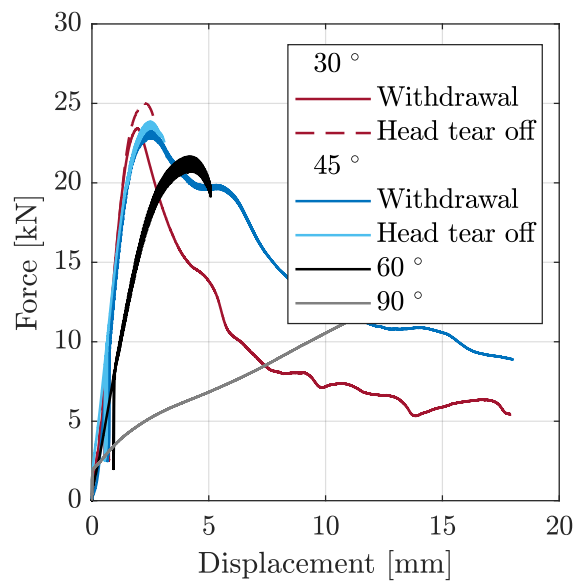


Figure 2. Typical load-displacement curves for different load-to-screw axis angles.

For joints with STS arranged perpendicularly to the grain, the head-tear-off failure occurs at a larger value of displacement (Figure 2). In this case, the failure is due to the bending of the STS due to the formation of two plastic hinges and the tension due to the rope effect.

### 3 Analytical Methods

#### 3.1 Models

Analytical expressions (such as exponential, analytical, logarithm and polynomial function etc) can be used to more accurately describe the load-displacement curve of joints. Analytical models provide a more precise way to describe the load-displacement behaviour of joints (*Foschi, 1974; Richard & Abbott, 1975; Glos, 1978; Brandner et al., 2018; Flatscher, 2017*). In *Caprio & Jockwer (2023)* it has been shown that the Richard-Abbott model is well suitable to represent the analyzed load-displacement shapes of joints. Additionally, the model has the ability to represent the intrinsic variability of the data.

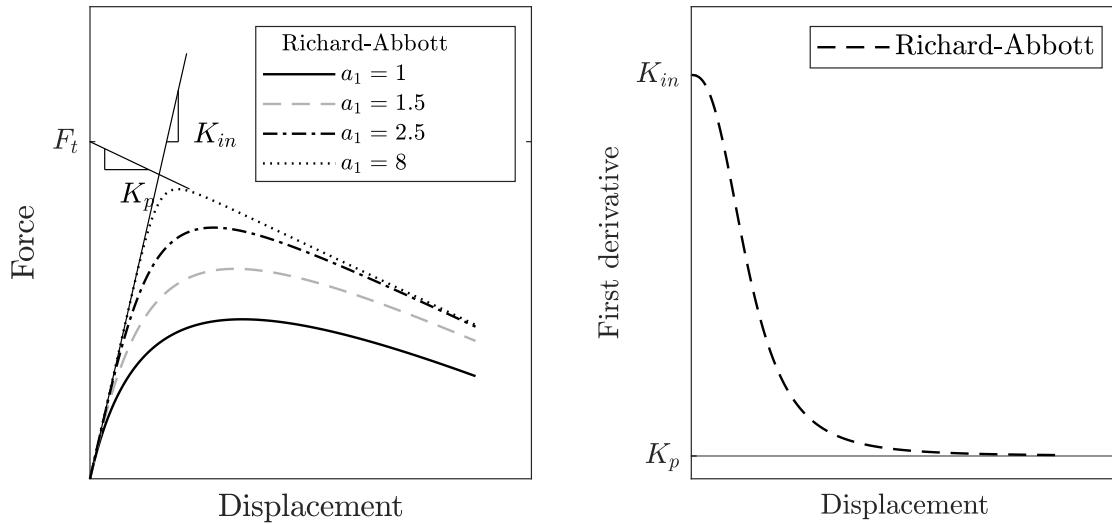
The Richard-Abbott model is a function of four parameters (Equation 1:  $K_{in}$  represents the initial inclination of the curve,  $K_p$  is the inclination in the plastic region, i.e. after the peak (or yield point) of the curve, and the shape parameter  $a_1$  regulates the shape of the transition between the elastic and the plastic region. The effect of  $a_1$  on the shape of the model is illustrated in Figure 3a. The derivative of the Richard-Abbott model is characterized by a non-linear behaviour almost from the beginning of the curve, as illustrated in Figure 3b.

$$F(v) = \frac{(K_{in} - K_p) \cdot v}{\left(1 + \left(\frac{(K_{in} - K_p)}{F_t} v\right)^{a_1}\right)^{\frac{1}{a_1}}} + K_p \cdot v \quad (1)$$

#### 3.2 Fitting of the curves

Weighted non-linear regression analysis has been used to fit the Equation 1. The range of the load-displacement curve for the regression has been chosen up to a 30% load drop from the maximum load for the curve corresponding to joints with STS arranged at an angle and characterized by a withdrawal failure. In contrast, the entire load-displacement curve up to maximum load has been used for the tests with STS perpendicular to the grain and up to the load drop for tests with inclined STS but characterized by head-tear-off failure. By choosing these ranges for regression, a direct comparison with the dataset from *Krenn (2017)* is possible, where the same range of the load-displacement curves is given. However, the fit of the curve appears to be good enough even after the end point of the displacement regression range (Figure 4a). For curves





(a) The effect of the parameter  $a_1$  (b) The Richard-Abbott model first derivative

Figure 3. Illustration of the Richard-Abbott model and its first derivative. Similar figures are shown in Caprio & Jockwer (2023).

characterized by shorter softening branches, the parameter  $K_p$ , defined as the asymptote of the derivative of the Richard-Abbott equation for very large displacement values, can hardly be defined. Therefore, in this case, it does not possess a physical meaning. Still, the parameter is determined from the non-linear regression (dashed line in Figure 4a). The displacement at failure has also been defined, at which the regression curve must be stopped.

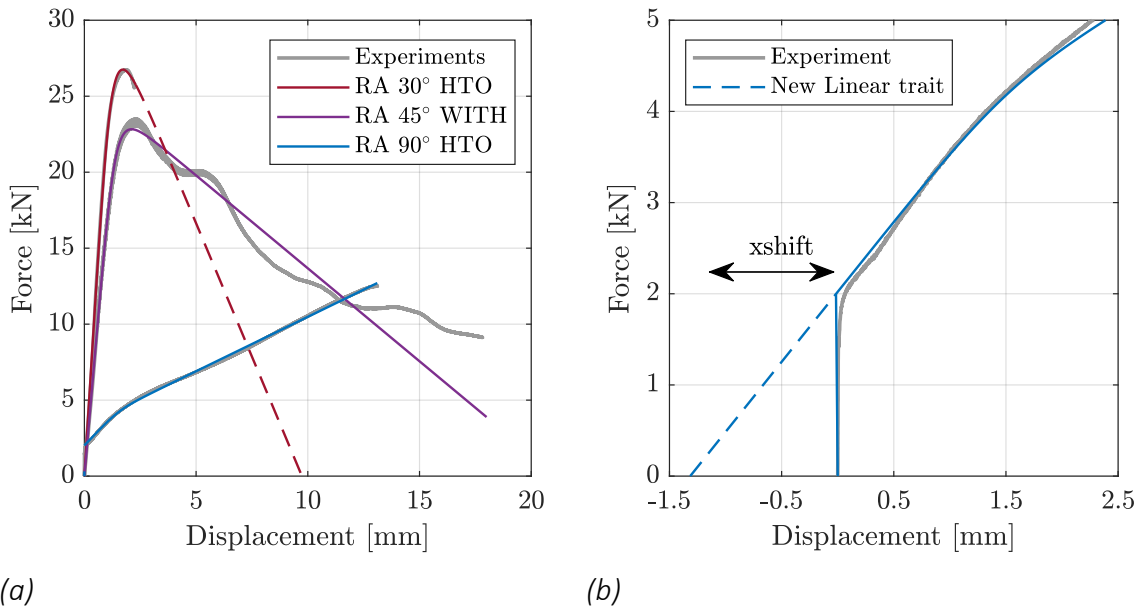


Figure 4. (a): typical load-displacement curves for different load-to-grain angels, (b): approximation of the initial rigid region by a linear trait.

In some of the tests, an initial rigid region occurred at the beginning of the load-displacement curve due to friction between the steel plate and timber induced by pre-tensioning force in the STS. This initial rigid region was particularly evident for joints with STS inclined at

90° from the experimental campaign at Chalmers and for joints with screws inclined at 30° and 45° from the test campaign conducted at Graz. In these cases, the fitting of the Richard-Abbott model appears challenging due to the vertical load-displacement curve. Hence, the initial rigid region was replaced with a trait whose inclination equals the tangential stiffness at the end of the rigid region (Figure 4b), then the curve has shifted back again to match the experimental curve.

## 4 Results and Discussion - Parameters and their variability

### 4.1 Chalmers

For the tests performed at Chalmers, the boxplots of the regression parameters are plotted against the value of the load-to-screw axis angle in Figure 5. The analysis is limited to the head-tear-off failure tests since they were more prevalent, while the values relative to withdrawal failure are represented with a cross.

The median value of  $K_{in}$  and the variance decrease with increasing load-to-screw axis angle (Figure 5a). The load transfer mechanism in the case of inclined screws involves not only the embedment but also the withdrawal of the fastener and the friction in the shear plane. As a result, the stiffness for lower values of load-to-screw axis angles (30°) is associated with larger variability compared to combined behaviour at larger angles (60°). The variance decreases in correspondence to a load-to-screw axis angle of 90°; however, the variance is not always indicative of the scatter of the data. In this case, for example, the corresponding CoV of  $K_{in}$  for a load-to-screw axis angle of 90° increases again respect to the case of 60°, being approximately 0.28 (Table 3). The parameter  $K_p$  is positive for load-to-screw axis angle of 90° while it is negative for tests with smaller angles characterized by a softening behaviour (Figure 5a). The median and the variance of  $K_p$  decreases for a change in the STS inclination from 60° to 90°. No clear trend for changes in the median or the CoVs is seen between 30° and 60°. In general, the larger values of CoVs for  $K_p$  for joints with inclined STS might be due to the more brittle behaviour of the head-tear-off failures for these cases. A clearer trend can be seen for the parameter  $F_t$  (Figure 5b). The variance of the parameters  $F_t$  increases when the load-to-screw axis angle increases from 30° to 60°, while it drops for a load-to-screw axis angle of 90°. The median value of  $F_t$  stays approximately constant between the load-to-screw axis angle of 30° and 45°, while it slightly increases from 45° and 60° to drop again in correspondence of a load-to-screw axis value of 90°. The CoVs of  $F_t$  have an increasing trend with increasing load-to-screw axis angle (Table 3). The median and the variance of the shape parameter  $a_1$  decrease between a load-to-screw axis angle of 30° and 60° (due to the less sharp kink of the curve), while it increases between the value of 60° and 90° (Figure 5c). The CoVs of  $a_1$  stay constant between 30° and 60° and it increases from 60° to 90°. The median and the variance of the ultimate displacement  $v_u$

increase with increasing load-to-screw axis angle for the head tear-off failure (Figure 5d). However, the CoVs show a relevant difference only between the load-to-screw angle of 30° and 45° (from 0.07 to 0.14) (Table 3).

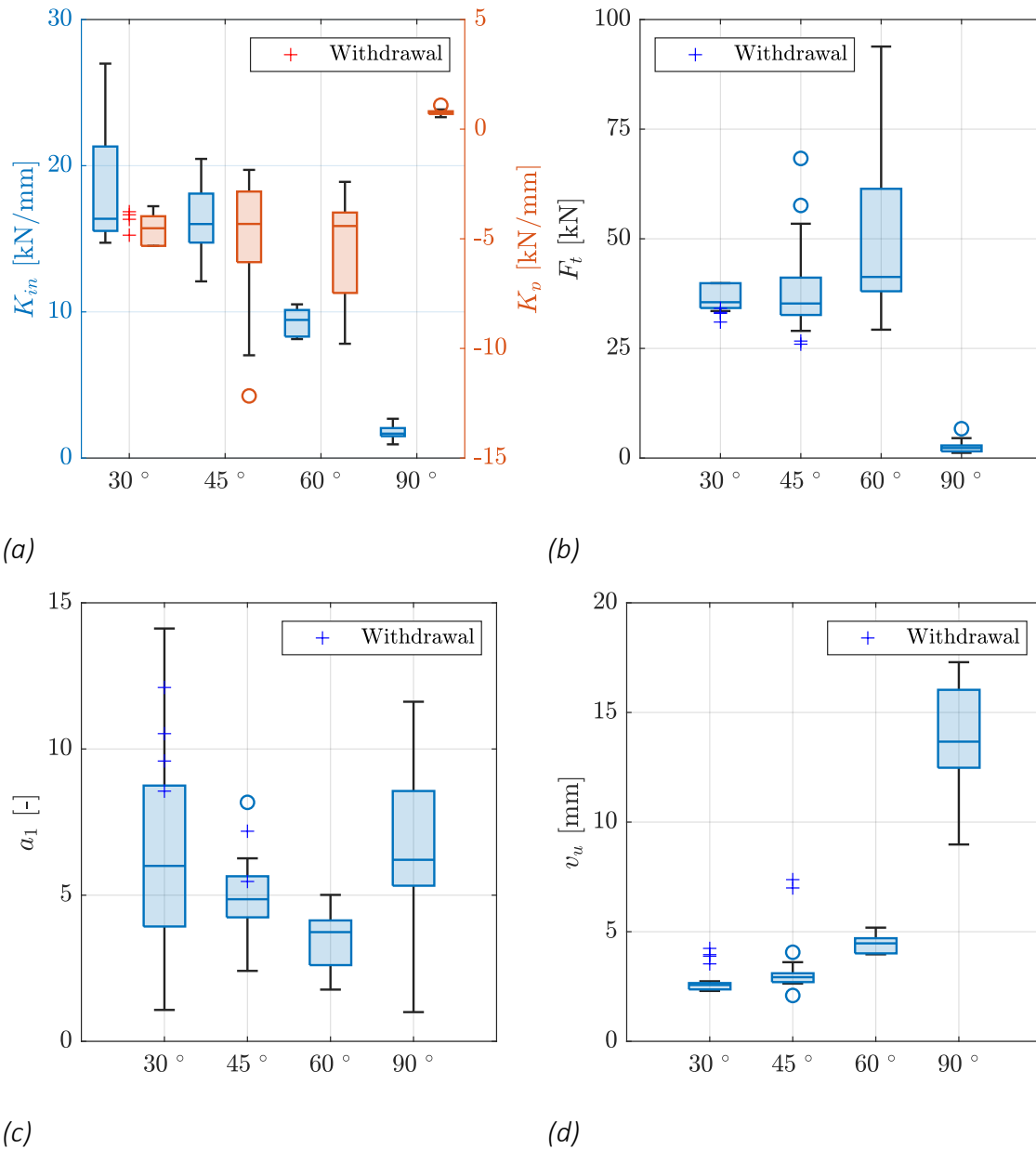


Figure 5. Boxplots of the Richard-Abbott parameters in function of the load-to-screw axis angle. (a):  $K_{in}$  and  $K_p$ , (b):  $F_t$ , (c):  $a_1$ , (d):  $v_u$ .

## 4.2 Tests from literature

### 4.2.1 TU Graz

In general, the same trends of the parameters over the load-to-screw axis angle from the Chalmers tests can be confirmed in the tests performed at TU Graz. However, the median values of the coefficient for  $K_{in}$  and  $F_t$  are almost double in values compared to Chalmers tests. This could be due to different test setups and friction coefficient values. In fact, *Krenn* (2017) used a symmetric test set-up with two simultaneously tested

screws, highly processed surfaces of the steel plates, and rough-sawn timber specimens. The geometry of the timber specimen and the steel plate were also different. Therefore, herein are discussed only the differences between the dataset in TU Graz with and without the Teflon sheet and between the joints with FT and PT screws.

The median, variance, and the CoVs of the parameter  $K_{in}$  decrease for the tests conducted with the Teflon sheet compared to those performed without the Teflon sheet. This result for the median value is expected as the contribution of friction to the initial slip-modulus decreases when using the Teflon sheet with a low friction coefficient. The median for the parameters  $K_p$  and  $F_t$  stay constant between the case of joints with and without Teflon, while the variance and CoVs slightly increase in the case of joints with the Teflon sheet. Reduced friction also shows no remarkable effect on the shape parameter  $a_1$  and the displacement at failure  $v_u$ . The tests performed with PT show lower median values compared to those with FT screws, but lower CoVs only for the parameter  $K_{in}$ . The median values of  $a_1$  and  $v_u$  increase for joints with PT.

#### 4.2.2 EMPA

Regarding the tests performed at Empa, the median and the variance of the parameter  $K_{in}$ , decrease with increasing load-to-screw axis angle (Figure 6a). This trend has to be confirmed for a load-to-screw axis angle of  $90^\circ$  since only three tests were performed for both high and low density. The median and the variance of parameters  $F_t$  and  $K_p$  in absolute value decrease with increasing load-to-screw axis angle (Figure 6b and Figure 6c). The CoV of  $a_1$  decreases with increasing load-to-screw axis angle, while the median value decreases. The larger variance and CoVs of the parameters for timber-to-timber joints for increasing the inclination of the STS can be explained by the failure mode involved. In fact, in the case of the STS inclined at  $90^\circ$ , the failure is characterized by the bending and forming of plastic hinges in the STS, whose material properties have low variability. Failure in joints with inclined STS involves the withdrawal of the screws and a shear transfer load mechanism characterized by larger variability.

The impact of the density can also be identified: the larger the density value, the larger the median values of the parameters. The difference between higher and lower density in terms on median and variance increases with decreasing angle for  $K_{in}$ ,  $K_p$  and  $F_t$ . Similar considerations are reported in *Caprio & Jockwer (2023)*.

## 5 Probabilistic modelling of load-displacement curves

### 5.1 Determination of the distribution characteristics

The probability distribution of each regression parameter must be identified to accurately model the mechanical behaviour of joints and their variability. Fitting a distribution can also provide insights into the data behavior, variability, and underlying physical phenomena. The distribution is selected based on the variability of the data and the

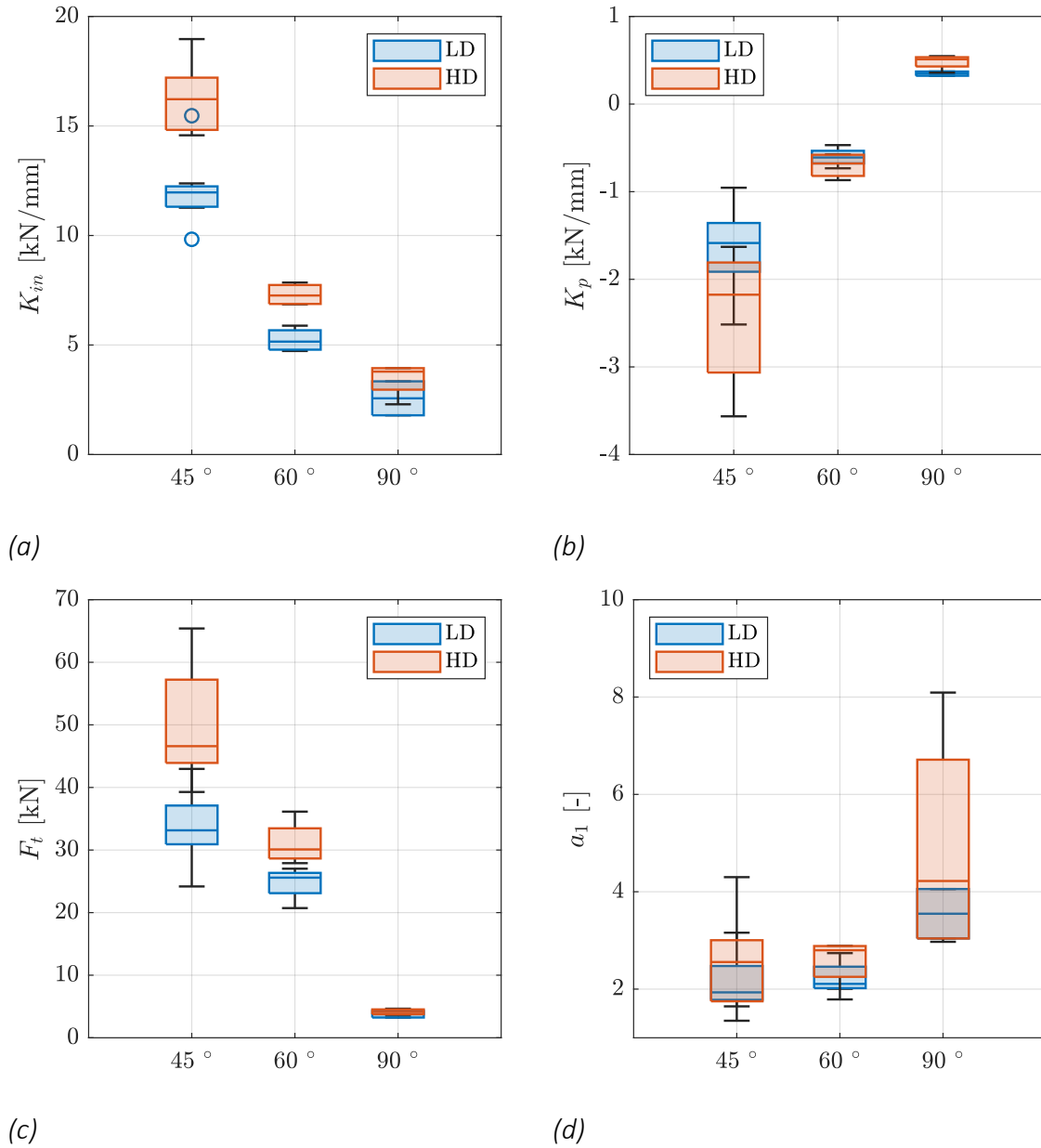


Figure 6. Boxplots of the Richard-Abbott parameters in function of load-to-screw axis angle for the tests by Jockwer et al. (2014) for the high (HD) and low (LD) density groups of specimens. (a):  $K_{in}$ , (b):  $K_p$ , (c):  $F_t$ , (d):  $a_1$ .

physical meaning of distribution parameters. A lognormal distribution looks suitable to represent the variability associated with  $K_{in}$ ,  $F_t$ ,  $a_1$ , and  $v_u$ . The values of these parameters are expected always to be positive; thus, a lognormal distribution is selected for these parameters. A normal distribution is chosen for the parameter  $K_p$  and  $x_{shift}$  since it follows the data and can also assume both negative and positive values. It adapts to the case of joints with inclined STS and softening behaviour (negative mean value) and to the case of joints with STS perpendicular to the grain with a hardening behaviour (positive mean value). The log-normalized and the normalized data for the parameter  $K_{in}$  and  $K_p$  for all the values of load-to-screw axis angles are plotted in Figures 7a and 7b respectively. An offset was applied to each dataset to visualize multiple Q-Q plots within a single figure without overlapping.

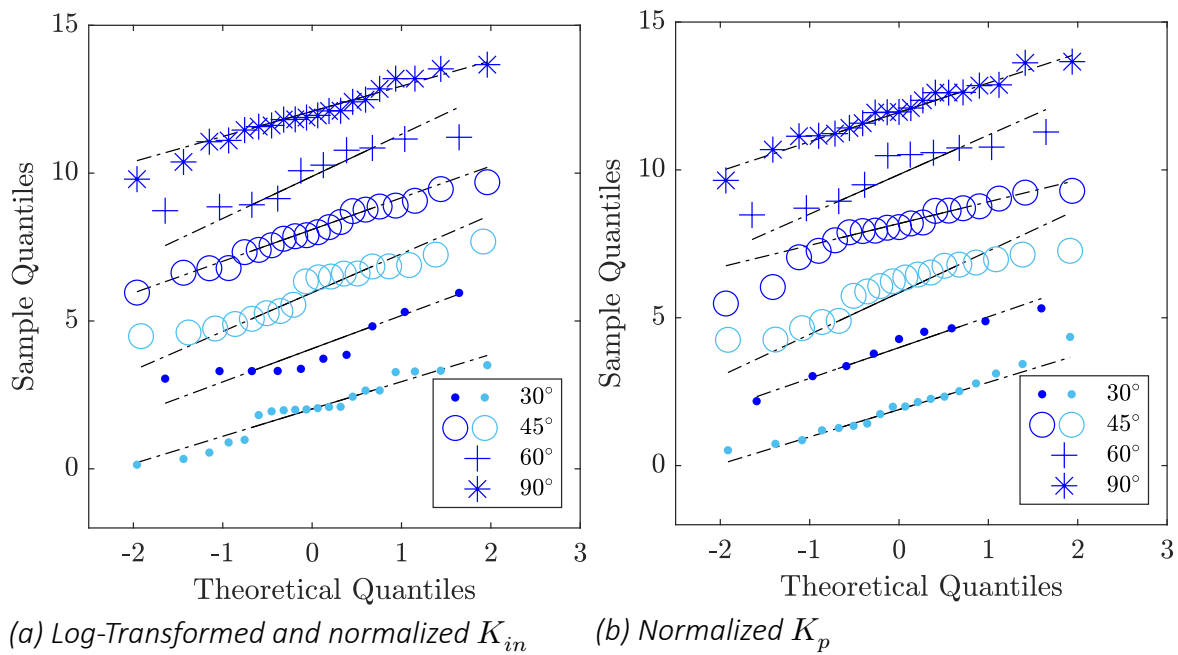


Figure 7. QQ-Plots for the normalised parameters  $K_{in}$  and  $K_p$  vs. Normal Distribution. Blue markers are data from Chalmers tests, while light blue are data from TU Graz tests.

In the case of STS arranged perpendicular to the grain, an additional regression parameter must be defined: the horizontal shift determined by the intersection with the horizontal axis by the tangent at the end of the rigid region ( $x_{shift}$ ). The normal distribution can be assumed for this parameter. In fact, it can assume both negative and positive values. A rigid region is generated when  $x_{shift}$  is negative, while a curve with an initial slip is represented when it is positive. An initial slip, even if this did not occur in the analyzed test, might be always possible. The distribution characteristics for each value of load-to-screw axis angle are summarized in Table 3. The considerations on the type of distribution can be applied to both the cases of timber-to-timber joints and steel-to-timber joints.

## 5.2 Generation of the load-displacement curves

Given the variability of the parameters, it is necessary to consider the correlations among them to generate the corresponding load-displacement curves. This can be done using the Pearson coefficient, and the (shortened) correlation matrices are given for selected cases in Table 4. From the determined regression parameters and the correlation among them, load-displacement curves using the Richard-Abbott model can be generated as shown in Figure 8. It should be considered that due to the correlation among the parameters, the load-displacement curve that corresponds to the  $i$ -fractile of the family of the curve associated with the curve variability does not correspond to the curve generated using the  $i$ -fractile values of each parameter.

Table 3. Overview of the parameters and their CoV for different load-to-screw angles

S-T joints (Chalmers)						
$\alpha$ [°]	Failure	$K_{in}$ [kN/mm]	$F_t$ [kN]	$K_p$ [kN/mm]	$a_1$ [-]	$v_u$ [mm]
30	HTO	18.35 (0.21)	35.75 (0.07)	-4.37 (0.16)	6.28 (0.38)	2.53 (0.07)
	WITH		32.85 (0.04)	-4.15 (0.12)	10.22 (0.15)	3.90 (0.08)
45	HTO	16.28 (0.14)	38.84 (0.24)	-4.92 (0.51)	4.92 (0.31)	2.97 (0.14)
	WITH		26.32 <sup>(1)</sup>	-1.31 <sup>(1)</sup>	6.39 <sup>(1)</sup>	7.19 <sup>(1)</sup>
60	HTO	9.33 (0.10)	50.38 (0.38)	-5.40 (0.46)	3.46 (0.34)	4.47 (0.10)
90	HTO	1.77 (0.28)	2.46 (0.48)	0.75 (0.21)	6.82 (0.59)	13.85 (0.16)
S-T joints (Graz TU)						
$\alpha$ [°]	Failure	$K_{in}$ [kN/mm]	$F_t$ [kN]	$K_p$ [kN/mm]	$a_1$ [-]	$v_u$ [mm]
30	HTO	65.87 (0.54)	30.14 (0.09)	-2.65 (0.30)	1 <sup>(2)</sup>	2.78 (0.15)
	WITH		35.87 (0.07)	-1.30 (0.10)	1.17 <sup>(2)</sup>	4.95 (0)
30-Tef	HTO	43.14 (0.44)	30.03 (0.13)	-2.94 (0.13)	1.01 <sup>(2)</sup>	2.57 (0.28)
	WITH		26.63 (0.21)	-2.44 (0.15)	1.00 <sup>(2)</sup>	4.72 (0.15)
30-PT	WITH	24.82 (0.29)	16.44 (0.16)	1.66 (0.27)	3.22 (0.47)	3.91 (0.16)
45	HTO	26.70 (0.48)	57.88 (0.37)	-12.71 (0.73)	2.35 (0.51)	3.71 (0.71)
	WITH		34.00 (0.10)	-4.78 (0.20)	3.31 (0.84)	2.76 (0.08)
T-T joints (Empa)						
$\alpha$ [°]	Failure	$K_{in}$ [kN/mm]	$F_t$ [kN]	$K_p$ [kN/mm]	$a_1$ [-]	$v_u$ [mm]
High density						
45	WITH	16.23 (0.10)	49.88 (0.19)	-2.38 (0.31)	2.55 (0.38)	-
60	WITH	7.30 (0.07)	31.06 (0.11)	-0.70 (0.20)	2.57 (0.21)	-
90	EYM	3.83 <sup>(1)</sup>	4.3 <sup>(1)</sup>	0.52 <sup>(1)</sup>	5.51 <sup>(1)</sup>	-
Low density						
45	WITH	12.05 (0.13)	33.76 (0.17)	-1.65 (0.29)	2.11 (0.29)	-
60	WITH	5.24 (0.10)	24.77 (0.12)	-0.61 (0.18)	2.25 (0.15)	-
90	EYM	2.51 <sup>(1)</sup>	3.74 <sup>(1)</sup>	0.35 <sup>(1)</sup>	3.37 <sup>(1)</sup>	-

<sup>1</sup> The number of tests in this case is only 2-3. Thus, only the mean value is provided.

<sup>2</sup> The CoV in this has is very small, thus the parameter can be considered constant.

\* The  $x_{shift}$  has a significant value only for steel-to-timber joints with STS arranged at 90°: -1.66 (0.37). It can be approximated to zero for all the other cases.

\* EYM: European Yield Model: two plastic hinges formed in the STS.

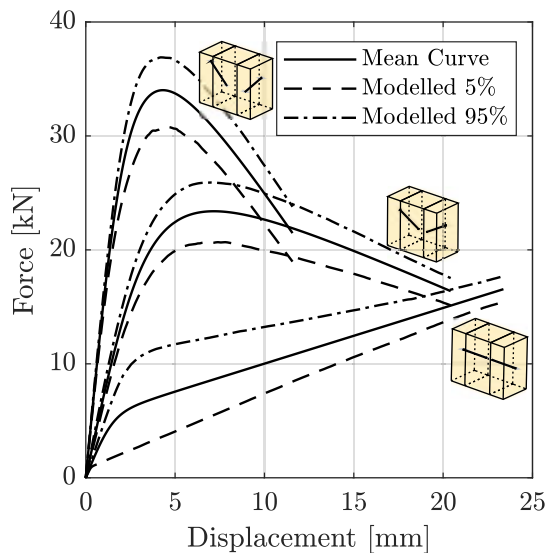
## 6 Recommendations for and relation to EC5

### 6.1 Current challenges with the standard

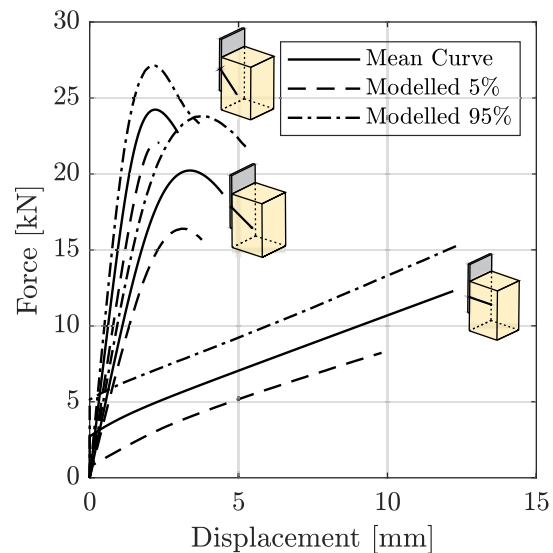
The current version and even the next generation of EC5 (EN 1995-1-1, *prEN 1995-1-1:2023 Eurocode 5 - Design of timber structures — Part 1-1: General rules and rules for buildings*. 2023) still contain some issues regarding the description of the mechanical behavior of joints. The description of the behavior of joints is mainly linear, and only (mean) slip-modulus values are given ( $K_{SLS}$ ). The stiffness of different types of connections is just distinguished rudimentary: for laterally loaded dowel type fasteners,  $K_{SLS}$  is very similar despite considerable differences in the fastener characteristics; for inclined fasteners, a simplified model is presented in the new generation of EC5. At ULS, the non-linearity is only considered through the definition of one single mean slip modulus  $K_{ULS}$ , taken as  $\frac{2}{3}$  of the mean value of slip modulus at SLS  $K_{SLS}$ , regardless of the type and failure mode of the joint.

Table 4. Correlation matrix of Chalmers tests (steel-to-timber joints) for some of the load-to-screw axis angle.

	30 [°]				45 [°]				60 [°]			
	$F_t$	$K_p$	$a_1$	$v_u$	$F_t$	$K_p$	$a_1$	$v_u$	$F_t$	$K_p$	$a_1$	$v_u$
$K_{in}$	0.72	-0.72	-0.85	-0.77	0.42	-0.49	-0.44	-0.71	-0.06	0.03	-0.05	-0.73
$F_t$	1	-1.00	-0.60	-0.47	1	-0.99	-0.81	-0.15	1	-0.95	-0.93	0.64
$K_p$		1	0.60	0.47		1	0.8	0.2		1	0.96	-0.52
$a_1$			1	0.46			1	-0.07			1	-0.44
$v_u$				1				1				1



(a) Timber-to-timber joints



(b) Steel-to-timber joints

Figure 8. Generated load-displacement curves and their fractiles for T-T joints (high density) and S-T joints for load-to-screw axis angle of 90°, 60°, and 45°.

This is then divided by the partial safety factor  $\gamma_m$ . The Swiss standard SIA 265 (SIA 265 - Timber structures (2012)) defines  $K_{ULS}$  as the second stiffness between 0 load level and the maximum carrying capacity. These definitions do not consider the variability that characterizes the load-displacement curves of timber joints. The latter complicates the interpretation and the meaning of  $K_{ULS}$  (Figure 9). Although EC5 (EN 1995) does incorporate statements to enhance the ductility of certain types of joints, this aspect is not explicitly detailed or specified for the application. More indications are given in EC8 (EN 1998-1:2004 Eurocode 8: Design of structures for earthquake resistance - Part 1: General rules, seismic actions and rules for buildings (2004)) for the design of structures under seismic

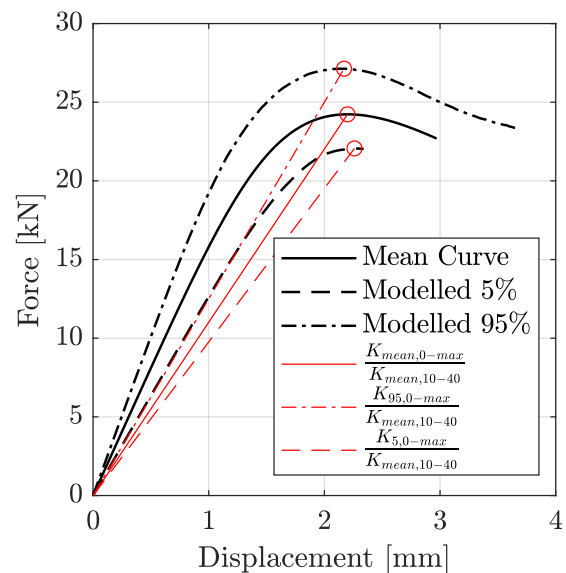


Figure 9. The variability of the load-displacement curve complicates the interpretation of  $K_{ULS}$ .



actions. To complicate this, different relative and absolute ductility definitions exist in the literature (*Jorissen & Fragiaco* (2011)), and as the slip-modulus, ductility is characterized by variability. These issues could be solved by incorporating parametrized load-displacement curves and corresponding parameters as shown in Figure 8 in the standards. Some benefits of such a definition of the load-displacement behaviour are discussed in the following.

The new generation of EC5 provides a formula for the stiffness at the serviceability limit state for joints with inclined screws. The formula is a combination of the axial and lateral stiffnesses:

$$K_{ser} = K_{SLS,ax} \cdot \sin \alpha \cdot (\sin \alpha + \mu \cdot \cos \alpha) + K_{SLS,v} \cdot \cos \alpha \cdot (\cos \alpha - \mu \cdot \sin \alpha) \quad (2)$$

### 6.2 Comparison and evaluation of $K_{SLS}$

For the comparison of slip-modulus at SLS, 1000 synthetic curves have been generated based on the parameters described in the previous chapter. The regression values of the parameters  $K_{in}$  are compared with the prediction of  $K_{SLS}$  for joints with inclined STS in the new generation of EC5 in Figure 10. It can be seen that the trend follows more or less accurately the parameters for both the timber-to-steel and timber-to-timber joints. For timber-to-timber joints, the EC5 is less accurate for inclined STS, particularly for a load-to-screw axis angle of 45°.

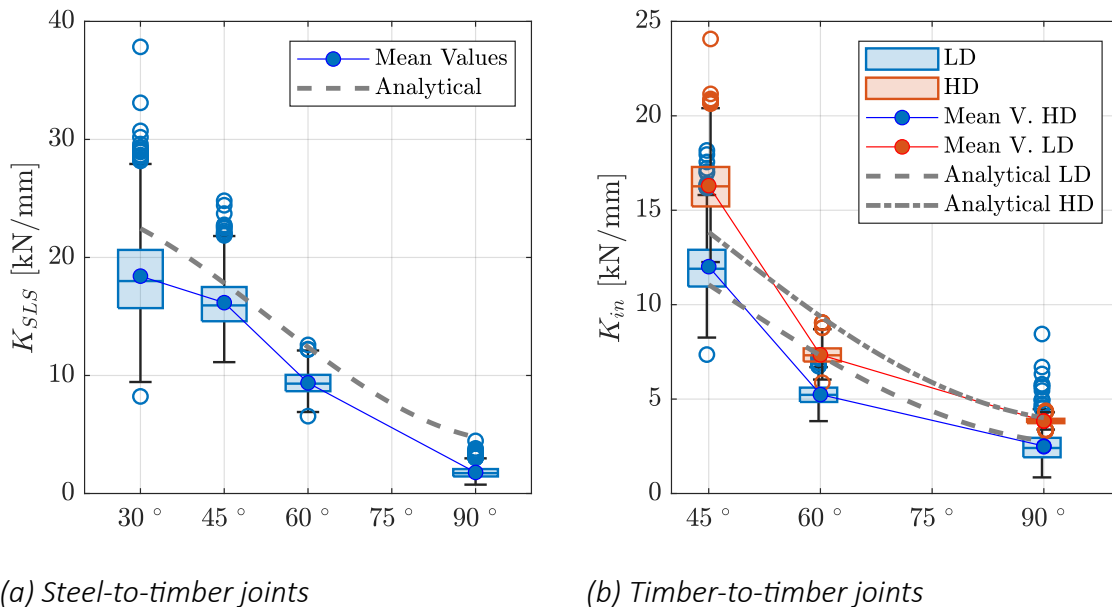


Figure 10. Comparison between  $K_{in}$  values from 1000 generated synthetic curves and  $K_{SLS}$  values according to the new generation of EC5.

### 6.3 Comparison and evaluation of $K_{ULS}$

In EC5, the relation of  $K_{ULS}$  and  $K_{SLS}$  is based on studies by *Ehlbeck et al. (1988)* where the slip modulus at 0.5mm and 1.0mm joint deformation are compared based on load-deformation curves on nailed joints derived by *Mack (1966)*. For comparison with this definition, 1000 synthetic curves have been generated, and the ratio between the two secant stiffness ( $\frac{K_{0-1mm}}{K_{0-0.5mm}}$ ) as specified by *Ehlbeck et al. (1988)* and the related variability have been calculated and are shown in Figure 11. The initial rigid region that characterizes the joints with STS at 90° has been excluded from the analysis.

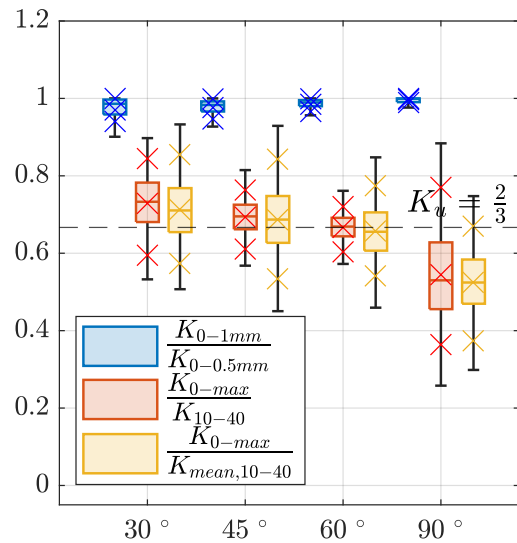


Figure 11. Boxplots in dependency of the load-to-screw axis angle for different ratios.

In addition to the values of the boxplot, the 5%— and 95%—fractiles are given and marked with a cross. The variability of the ratio  $\frac{K_{0-1mm}}{K_{0-0.5mm}}$  decreases with increasing load-to-screw axis angles. The mean is always close to 1. This shows that the classic definition of  $K_{ULS}$  is not suited for these types of joints since the second stiffness at these two specific deformation levels is closer to each other, leading to a ratio value close to 1 for all the load-to-screw axis angles. For this reason, a comparison is made with the ratio  $\frac{K_{0-max}}{K_{10-40}}$ .  $K_{10-40}$  is the stiffness in the elastic range, for this reason in the case of the joints with STS at 90°, the stiffness is a secant through 10% and 40% of the yielding point. The mean and the 5%— fractile of the distribution of the ratio are closer to the prescribed ratio of  $\frac{2}{3}$  between the load-to-screw axis angle of 30° and 60°. However, the variability is larger than the ratio  $\frac{K_{0-1mm}}{K_{0-0.5mm}}$ . For joints with a load-to-screw axis ratio of 90°, the ratio  $\frac{K_{0-max}}{K_{10-40}}$  presents a large scatter with values that ranges between 0.3 and 0.9. Comparing the secant stiffness  $K_{0-max}$  with the mean value of  $K_{mean,10-40}$ , considerable variability of the ratio for all the load-to-screw axis angles is observed with values close to 1. The variability is similar to the ratio  $\frac{K_{0-max}}{K_{10-40}}$ . This is because the secant stiffness  $K_{mean,10-40}$  stiffness is characterized by a certain variability. Thus, it can assume values close to the mean value of the initial stiffness.

## 7 Conclusions and future work

The load-deformation behaviour of joints with STS is highly non-linear and dependent on various parameters such as the load-to-screw axis angle. This non-linearity has not been adequately considered in EC5 so far. The Richard-Abbott model is suitable to represent the non-linear load-deformation behaviour of different joint configurations and

even the variability of test data. The distribution characteristics of the model parameter of the Richard-Abbott model and the corresponding correlations were determined from tests on Timber-to-Timber and Steel-to-Timber joints carried out at Chalmers, TU Graz, and Empa. These parameters can be used to generate synthetic load-deformation curves for further analysis.

Based on the current analysis, the following conclusion can be drawn:

- The study of the regression parameters in function of the load-to-screw axis angle for the experiments conducted at Chalmers and at TU Graz led to different results in terms of mean values and CoVs, but similar results in terms of trends, i.e. how the variance, CoVs and the mean value change in correspondence to different load-to-screw axis angle. The regression parameters is particularly important in order to obtain the load-displacement curve at the fractile of interest.
- The validity of the current definition of  $K_{ULS}$  in EC5 as a simple ratio of  $K_{SLS}$  can be questioned for modern joints and it is not suitable for joints with inclined STS. The incorporation of parametrized load-deformation curves in EC5 may be preferable. This will allow structural analysis of complex structures at different load levels.
- Defining  $K_{ULS}$  as the secant stiffness between the 0 load level and the load level corresponding to the maximum leads to mean values of the ratio closer to  $\frac{2}{3}$ , except in the case of joints with perpendicularly arranged STS, when it is lower.

Further reliability analyses are necessary to derive adequate slip-modulus values for the ULS. More experimental data are needed to confirm and clarify the observed trends and to determine more reliable values, in particular for a load-to-screw axis angle of  $90^\circ$  in the case of timber-to-timber joints and to explore additional parameters of influence, such as other joint configurations, number of fasteners, screw length, and friction coefficient. Moreover, although the present analysis focused on the definition of  $K_{ULS}$ , from the generated synthetic curves the ductility values can be derived in function of the load-to-screw axis angles. A possible incorporation of the ductility definition in EC5 could then be discussed.

## 8 Acknowledgments

This work was carried out within the project “RelyConnect – Reliable and high-performance timber structures with modern connections” (project number 2023-01603), funded by FORMAS, the Swedish research council for sustainable development, and was partly funded by Svensk Trä, the Swedish association of the timber industries, and TMF, the Swedish Federation of Wood and Furniture Industry. This financial support is gratefully acknowledged. Parts of the work presented in this paper were performed during a Short Term Scientific Mission at TU Graz and were financially supported by COST Action CA 20139 ([www.cahelen.eu](http://www.cahelen.eu)).

## 9 References

- Bejtka, I. & H. Blaß (2002). "Joints with inclined screws." In: Paper No. CIB-W18/35-7-4. Kyoto, Japan: Proc. of the Meeting 35 of Working Commission W18 – Timber Structures.
- Brandner, R.; A. Ringhofer & M. Grabner (2018). "Probabilistic models for the withdrawal behavior of single self-tapping screws in the narrow face of cross laminated timber (CLT)." en. In: *European Journal of Wood and Wood Products* 76.1, pp. 13–30. ISSN: 1436-736X. DOI: 10.1007/s00107-017-1226-3.
- Caprio, D.; R. Jockwer & M. al-Emrani (2022). *Reliability of statically indeterminate timber structures: Modelling approaches and sensitivity study*, pp. 1649–1655. DOI: 10.1201/9781003348443-270.
- Caprio, D. & R. Jockwer (2023). "Regression Models for the Description of the Behaviour of Modern Timber Joints." In: *Buildings* 13.11. ISSN: 2075-5309. DOI: 10.3390/buildings13112693.
- Dahlberg, O. & N. Vallström (2024). "Experimental investigation of steel-to-timber joints with inclined self-tapping screws: A parametric study evaluating load-displacement behavior and testing configurations in quasi-static testing." swe. In: URL: <http://hdl.handle.net/20.500.12380/308156>.
- De Santis, Y.; A. Aloisio; I. Gavrić; I. Sustersic & M. Fragiaco (2023). "Timber-to-steel inclined screws connections with interlayers: Experimental investigation, analytical and finite element modelling." In: *Engineering Structures* 292, p. 116504. DOI: 10.1016/j.engstruct.2023.116504.
- Ehlbeck; J & H. Werner (1988). "Untersuchungen über die Tragfähigkeit von Stabdübelverbindungen." In: *Holz als Roh-und Werkstoff* 46, pp. 281–288. DOI: <https://doi.org/10.1007/BF02615055>.
- EN 1998-1:2004 Eurocode 8: *Design of structures for earthquake resistance - Part 1: General rules, seismic actions and rules for buildings* (2004). Bruxelles, Belgium: European Committee for Standardization CEN.
- Flatscher, G. (2017). *Evaluation and approximation of timber connection properties for displacement-based analysis of CLT wall systems*. English. Ed. by G. Schickhofer & R. Brandner. Vol. TET 6. Monographic Series TU Graz: Timber Engineering & Technology. Graz, Austria: Verlag der Technischen Universität Graz. ISBN: 978-3-85125-557-7.
- Foschi, R. O. (1974). "Load-slip characteristics of nails." In: *Wood science* 7, pp. 69–76.
- Glos, P. (1978). "Zur Bestimmung des Festigkeitsverhaltens von Brettschichtholz bei Druckbeanspruchung aus Werkstoff-und Einwirkungskenngrößen." PhD Thesis, Berichte zur Zuverlässigkeitstheorie der Bauwerke, No. 35/78. Munich, Germany: Technische Universität München.
- Jockwer, R.; R. Steiger & A. Frangi (2014). "Design model for inclined screws under varying load to grain angles." In: Paper No. INTER/47-7-5. Bath, UK: Proc. of the INTER Meeting 47.
- Jorissen, A. & M. Fragiaco (2011). "General notes on ductility in timber structures." In: *Engineering Structures* 33.11, pp. 2987–2997. DOI: 10.1016/j.engstruct.2011.07.024.
- Krenn, H. (2017). "The sheet steel-wood strap connection with slanted screws." PhD Thesis, Monographic Series TU Graz - Timber Engineering & Technology, Volume 7. Graz, Austria: TU Graz.
- Mack, J. J. (1966). *The strength and stiffness of nailed joints under short-duration loading*. Division of Forest Products technological paper. Melbourne, Australia: Commonwealth Scientific and Industrial Research Organization, Australia.
- prEN 1995-1-1:2023 Eurocode 5 - *Design of timber structures — Part 1-1: General rules and rules for buildings*. (2023). Bruxelles, Belgium: European Committee for Standardization CEN.
- Richard, R. M. & B. J. Abbott (1975). "Versatile Elastic-Plastic Stress-Strain Formula." EN. In: *Journal of the Engineering Mechanics Division* 101.4, pp. 511–515. DOI: 10.1061/JMCEA3.0002047.
- SIA 265 - *Timber structures* (2012). Swiss Society of Engineers and Architects.

Tomasi, R.; A. Crosatti & M. Piazza (2010). "Theoretical and experimental analysis of timber-to-timber joints connected with inclined screws." In: *Construction and Building Materials* 24, pp. 1560–1571. DOI: 10.1016/j.conbuildmat.2010.03.007.

## DISCUSSION

**The paper was presented by D Caprio**

*A Frangi questioned how the experimental data from different sources was put together. D Caprio stated in some cases there was high variability. A Frangi stated that rationale to justify ignoring some cases would be needed.*

*M Fragiacommo commented that what is needed by designers are reliable formulae. Equations to get the non-linearity are not needed. He asked if there is a plan to do research to receive analytical predictions of the behaviour. He further commented that an analytical way to predict the stiffness was also missing.*

*A Salenikovich mentioned that he could contribute data to the database.*

*D Moroder received clarifications about comparison with test data, higher coefficient of variation with high stiffness and envelope of the curves were provided.*

*C Tapia Camu commented that some of the parameters in the model do not have physical meaning and questioned how these were treated in the correlation matrix.*

*P Dietsch suggested that further clarifications as well as editorial work on the paper would be needed.*



# The effective timber thickness for brittle failure assessment of dowel-type connections

Caroline D. Aquino, ISISE, University of Minho, Guimarães, Portugal

Michael Schweigler, Dept. of Building Technology, Linnaeus University, Växjö, Sweden

Leonardo Rodrigues, XAIS Asset Management Ltd., Doncaster, UK

Romain Lemaître, CERIB Fire Testing Centre, Epernon, France

Jean-François Bocquet, Work4Cad Group, Saône, France

Jorge M. Branco, ISISE, University of Minho, Guimarães, Portugal

Thomas K. Bader, Dept. of Building Technology, Linnaeus University, Växjö, Sweden

Keywords: steel-to-timber connections , beam-on-foundation model , effective thickness

## 1 Introduction

Connections with laterally loaded steel fasteners are widely used in timber engineering for various structural applications. Loads are transferred through timber embedment stresses and steel dowel-type fasteners' shear and bending. The timber in dowelled connections may fail prematurely before achieving a desirable ductile response because of high-stress concentrations due to localised shear and parallel and perpendicular to the grain tensile stresses (*Blaß & Schädle, 2011; Yurrita & Cabrero, 2020b*). Experimental studies have indicated that timber connections, designed following Eurocode 5 (EN 1995-1-1, 2004) provisions, may exhibit brittle failures, even when spacing requirements are satisfied (*Jorissen, 1998; Hanhijärvi & Kevarinmäki, 2008*).

The scientific community has endeavoured to develop more accurate and reliable design models to overcome this limitations. Models suitable for engineering design aim to predict the load-carrying capacity of timber connections with potential brittle failure in a straightforward way (*Quenneville, 2018; Yurrita & Cabrero, 2020b*). In the draft of the second generation of Eurocode 5 (prEN 1995-1-1, 2023), the brittle failure is determined through the strength of potential failure planes, such as shear lateral planes (row shear and block shear) and the head tension plane (block shear and net tension). For connections with rigid fasteners, embedment stresses are almost uniform across the



thickness of the timber member, allowing the entire member thickness of the activated plane to resist the applied load. However, the embedment stresses can vary significantly over the member thickness in connections with slender fasteners, leading to fastener bending. Consequently, for the proposed design model, it is essential to assess the effective thickness of timber that contributes to the connection load-carrying capacity.

The main objective of this contribution is to establish a mechanical understanding of the effective thickness of timber used in the design for brittle failure of dowel-type connections. This is achieved by drawing insights from a numerical non-linear beam-on-foundation (BoF) model (Lemaître et al., 2018), allowing to obtain the effective thickness as a function of the dowel displacement, and comparison of results with both the formulation in EN 1995-1-1 (based on the European Yield Model — EYM (Johansen, 1949)) and the one proposed in prEN 1995-1-1 (based on an analytical elastic BoF model (Yurrita & Cabrero, 2020a)).

## 2 Theoretical definition of the effective thickness

Various models are available in the literature for estimating the effective thickness ( $t_{ef}$ ) of timber derived from the bending deformation of the fastener. The existing models primarily differ in the theoretical definition. In EN 1995-1-1 (2004), the effective thickness is defined as the distance between plastic hinges obtained from the EYM, denoted as length  $y$  (see Figure 1). On the other hand, Yurrita & Cabrero (2020a) define effective thickness as the timber member region where the embedment stress is positive, denoted by  $y_1$ , as illustrated in Figure 1. This definition is derived from an analytical elastic BoF model and forms the basis for determining  $t_{ef}$  in prEN 1995-1-1 (2023).

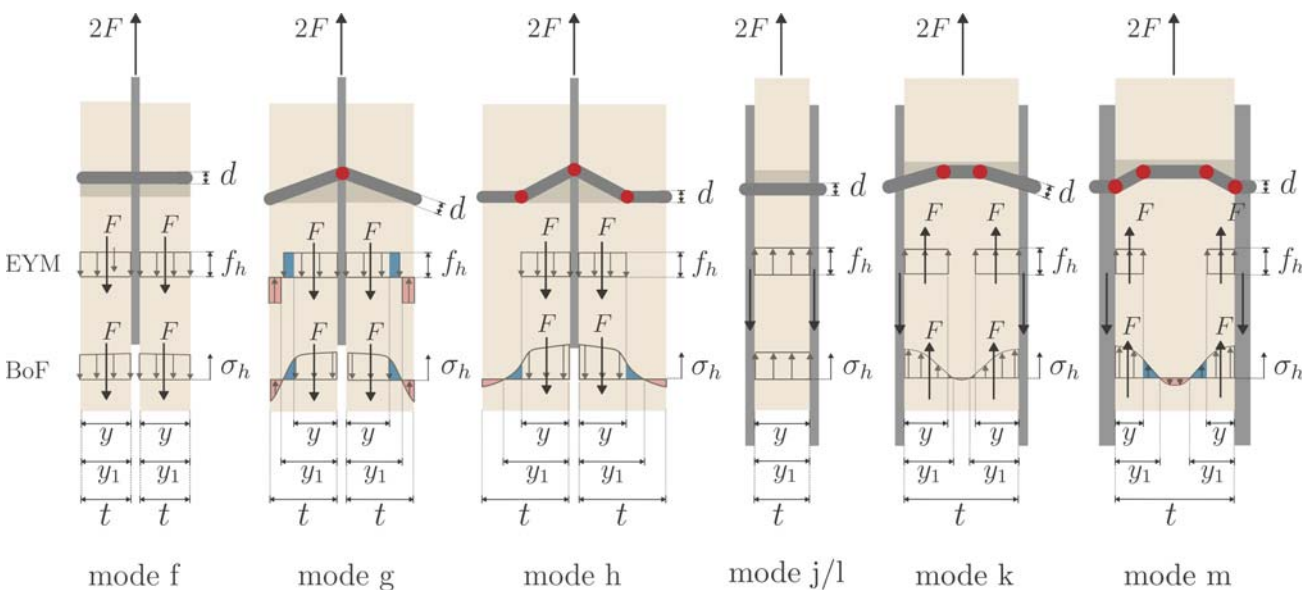


Figure 1. Effective thickness and stress distribution for steel-to-timber connections for the failure modes defined in EN 1995-1-1 (2004). The stress distribution is illustrated according to the EYM (adapted from Jorissen (1998)) at the top and the BoF at the bottom.

In the work of Jorissen (1998) (based on the EYM), the embedment stress was assumed to be uniform over the length  $y$ , and a failure plane would develop at length  $y_a$ . This length

$y_o$  was considered slightly greater than  $y$  through an empirical expression. This adjusted length was implemented in the analytical brittle failure models proposed by *Jorissen* (1998) as the effective thickness. From a theoretical point of view, the length  $y$ , obtained by *Jorissen* (1998) based on the EYM, can be understood as the length that effectively contributes to the connection's load-carrying capacity ( $F$ ) per shear plane, which can be expressed as  $y = F/(d f_h)$ , where  $f_h$  is the timber embedment strength defined according to EN 1995-1-1 (2004) and  $d$  is the fastener diameter. However, the size of  $y$  depends on the embedment stress distribution, which depends on the achieved failure mode.

The distinction between these definitions is critical and directly impacts the evaluation of brittle failure in dowel-type timber connections. The use of  $t_{ef}$  for verifying brittle failure modes in EN 1995-1-1 (2004) and prEN 1995-1-1 (2023) assumes a uniform stress distribution over the effective thickness. It defines the failure plane's position for the resistant plane's design strength. Based on the illustration of the stress distribution, as given in Figure 1, is clear that  $y_1 \geq y$ . This implies that considering a uniform stress distribution of  $F$  on the area obtained with  $t_{ef} = y_1$  would potentially overestimate the strength of the resistant plane if not compensated in the design procedure.

### 3 Determination of the effective timber thickness

#### 3.1 Design standards

##### 3.1.1 EN 1995-1-1 (2004)

The effective timber thickness, as defined in the Annex A of EN 1995-1-1 (2004), is based on the length  $y$  following the same principle proposed by *Jorissen* (1998), obtained as  $y = F/(d f_h)$ , where  $F$  is the load-carrying capacity per shear plane and  $f_h$  is the embedment strength. Hence, the effective thickness is defined according to the obtained failure mode (see Figure 2) as

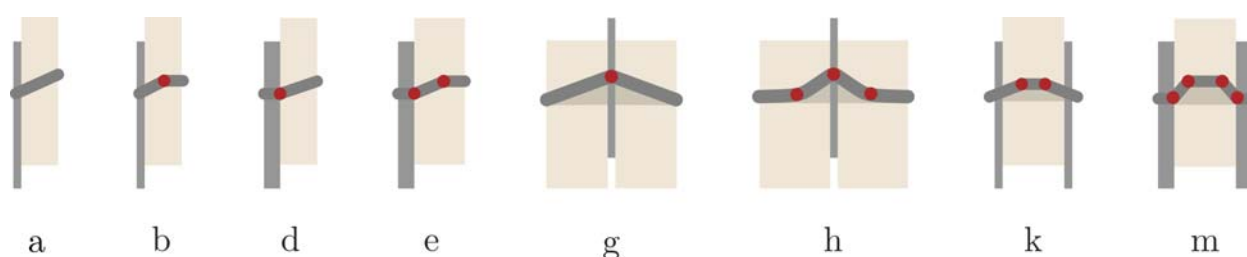


Figure 2. Failure modes for steel-to-timber connections with fastener deformation (adapted from EN 1995-1-1 (2004)).

$$t_{ef} = y = \begin{cases} (2^{0.5} - 1) t & \text{(a),} \\ 1.4 \sqrt{\frac{M_y}{f_h d}} & \text{(b)(k),} \\ t \left[ \sqrt{2 + \frac{4M_y}{f_h d t^2}} - 1 \right] & \text{(d)(g),} \\ 2 \sqrt{\frac{M_y}{f_h d}} & \text{(e)(h)(m),} \end{cases} \quad (1)$$

where the respective failure modes are given in brackets, and  $M_y$  is the fastener yield moment defined as  $M_y = 0.3 f_u d^{2.6}$ , with  $f_u$  being the steel ultimate tensile strength.

For failure modes related to connections with outer steel plates, brittle failure is evaluated only for the tensile head plane, considering the entire thickness of the timber member. Nonetheless, as depicted in Figure 2, failure modes (k) and (m) correspond to the modes (b) and (e), respectively, when symmetry is taken into account. Since connections with outer steel plates may also experience brittle failure modes where the stress distribution is non-uniform and only a portion of the thickness is activated (this was observed in *Quenneville & Mohammad (2000)* and in *ADIVbois (2022)* for reinforced connections), it is crucial to consider the effective thickness in such cases. This is also true for inner timber members in multiple shear connections, where a similar behaviour can be expected. The equations proposed for the single shear plane connections are recommended to address this.

### 3.1.2 prEN 1995-1-1 (2023)

*Yurrita & Cabrero (2020a)* argue that brittle failure in dowel-type timber connections usually appears before the yielding of the fastener. Therefore, an effective thickness based on the elastic behaviour should be adopted instead of the one based on the EYM as in EN 1995-1-1 (2004). From a parametric analysis using an analytical elastic BoF (discussed in Section 3.2), *Yurrita & Cabrero (2020a)* concluded that the fastener slenderness ratio ( $t/d$ ) is the only parameter having a significant influence on the effective timber thickness. Simplified formulae were then proposed through linear regression analysis and are presented in their study. These formulae were further adapted and included in prEN 1995-1-1 (2023) for the failure planes of inner timber members as

$$t_{ef} = y_1 = \begin{cases} 0.5t & \text{if } \frac{0.5t}{d} \leq 11 \alpha_{cl} \quad , \\ \max \left\{ \left( 2 - \frac{0.5t}{11d} \right) \alpha_{cl} 0.5t, 0.65 \alpha_{cl} 0.5t \right\} & \text{if } \frac{0.5t}{d} > 11 \alpha_{cl} \quad , \end{cases} \quad (2)$$

and for the failure planes of outer timber members as

$$t_{ef} = y_1 = \begin{cases} \alpha_{cl} t & \text{if } \frac{t}{d} \leq 3 \quad , \\ \max \left\{ \left( 1.17 - \frac{t}{18d} \right) \alpha_{cl} t, 0.35 \alpha_{cl} t \right\} & \text{if } \frac{t}{d} > 3 \quad . \end{cases} \quad (3)$$

Where  $\alpha_{cl}$  is a factor related to the clamping condition of the fastener.  $\alpha_{cl} = 1.0$  for failure modes with two plastic hinges per shear plane, while  $\alpha_{cl} = 0.65$  for other failure modes.

### 3.2 Analytical elastic beam-on-foundation

The differential equation for the deflection curve of a beam-on-elastic-foundation is given by

$$E_s I_s d^4 u / dx^4 + k_t u = 0 \quad , \quad (4)$$

where  $E_s$  and  $I_s$  are the modulus of elasticity and moment of inertia of the beam, respectively, and  $k_t$  is the foundation modulus. When applied to dowel-type timber connections, the steel fastener is represented by the beam and the timber embedment behaviour by the foundation support, where  $k_t = k_{el} d$ . Here  $k_{el}$  is the elastic embedment stiffness, and  $d$  is the fastener diameter.

The homogeneous solution to this differential equation is given by

$$u(x) = A \cos(\beta x) \cosh(\beta x) + B \cos(\beta x) \sinh(\beta x) + C \sin(\beta x) \cosh(\beta x) + D \sin(\beta x) \sinh(\beta x), \quad (5)$$

with  $\beta = \left( \frac{k}{4EI} \right)^{1/4}$ . Here,  $u(x)$  is the deflection curve of the fastener, and the parameters  $A, B, C,$  and  $D$  are integration constants determined by solving the differential equation subject to specific boundary conditions (the reader is referred to *Kuenzi (1955)* for the complete derivation).

In the work of *Yurrita & Cabrero (2020a)*, in which the analytical BoF approach was adopted for the determination of the timber effective thickness, two main configurations were considered: inner timber members, where loads were symmetrically applied at both ends of the fasteners and outer timber members, where the load was applied on one side of the element, coinciding with the position of the steel plate(s). The type of support (pinned or clamped) was prescribed based on whether thin plates or connections with thick plates were used.

The analytical elastic BoF model was implemented in this study to compare with the numerical non-linear BoF and the formulations proposed in EN 1995-1-1 (2004) and prEN 1995-1-1 (2023). The embedment stress along the fastener axis was obtained by  $\sigma_h(x) = -k_{eI} u(x)$ , which was used to estimate the length  $y_1$  and  $y$ , following the observations from *Jorissen* (1998).

Given that the stress obtained from the BoF model is non-uniform,  $F$  is calculated by integrating the embedment stress function ( $\sigma_h$ ) over the member thickness ( $t$ ). The integration can be divided into three intervals  $[0; y]$ ,  $[y; y_1]$  and  $[y_1; t]$ , defined from the shear plane position (see Figure 1), which yields

$$F = d \left( \int_0^y \sigma_h(x) dx + \int_y^{y_1} \sigma_h(x) dx + \int_{y_1}^t \sigma_h(x) dx \right) . \quad (6)$$

The first integral is the one that corresponds to the member load-carrying capacity. The sum of the last two intervals, highlighted in Figure 1, is zero. The length  $y_1$  is found by solving the root of the stress function  $\sigma_h(x) = 0$ . Subsequently, an iterative approach is employed to estimate the value of  $y$ , such that equation

$$\int_y^{y_1} \sigma_h(x) dx = - \int_{y_1}^t \sigma_h(x) dx \quad (7)$$

is fulfilled. This equation corresponds to the balance between positive and negative embedment stress distribution along the fastener axis. It is important to note that for connections with outer steel plates, half of  $t$  should be considered in Equations (6) and (7).

### 3.3 Numerical non-linear beam-on-foundation

#### 3.3.1 Modelling strategies

Following the BoF strategy, the steel fastener is represented using 2D beam elements with isotropic strain hardening material properties, and the timber embedment is modelled with zero-length non-linear spring elements attached to each node of the beam elements, creating a spring foundation support. The load-displacement law assigned to each spring is calculated by multiplying the embedment stress ( $\sigma_h$ ) with the contact area of the fastener, given by the product of its diameter ( $d$ ) and the spacing between springs ( $s$ ). The regression equation proposed by *Richard & Abbott* (1975) is applied to model the embedment stress parallel to the grain ( $\sigma_h$ ) as a function of fastener displacement ( $u_h$ ) as obtained from an embedment test, reading as

$$\sigma_h(u_h) = \frac{(k_{el} - k_{pl}) \cdot u_h}{\left[1 + \left(\frac{(k_{el} - k_{pl}) \cdot u_h}{f_{h,inter}}\right)^a\right]^{\frac{1}{a}}} + k_{pl} \cdot u_h \quad , \quad (8)$$

in which  $k_{el}$  and  $k_{pl}$  are the elastic and plastic stiffness terms, respectively;  $f_{h,inter}$  denotes the intersection of  $k_{pl}$  with the vertical axis; and the parameter  $a$  governs the transition between the elastic and plastic segments of the curve. The load-displacement behaviour of such springs is provided following uni-axial embedment data from experimental tests (see e.g. *Schweigler et al. (2019)*). It is worth noting that the non-linear springs exclusively provide loads parallel to the displacement direction, i.e., no axial withdrawal resistance or friction along the fastener-timber interface, neither in between the steel plate and timber member, were considered in the implementation.

The forces acting on each spring element can be used to estimate the embedment stress along the fastener axis. The approach discussed in Section 3.2 is then adopted for deriving the lengths  $y$  and  $y_1$ . These lengths are calculated for all displacement increments in the numerical BoF model, allowing the effective thickness to be obtained as a function of the fastener displacement at the steel plate,  $u_s$ .

### 3.3.2 Model validation

The model validation is based on tests from *Wydler (2023)* and *Palma & Wydler (2024)* of single-dowel timber connections with slotted-in steel plates loaded in parallel to the grain direction. The timber used was spruce (*Picea abies*), Laminated Veneer Lumber (LVL) (Kerto-S, Metsä Wood, Finland) and the steel dowels of grade S235. The material properties of both the timber and the steel dowels were thoroughly characterised in the study of *Wydler (2023)* and *Palma & Wydler (2024)*.

The embedment parameters for the Richard-Abbot slip-curve (Eq. (8)) were derived from embedment test results by *Wydler (2023)*, resulting in  $k_{el} = 31.7 \text{ N/mm}^3$ ,  $k_{pl} = 0.63 \text{ N/mm}^3$ ,  $f_{h,inter} = 33.3 \text{ N/mm}^2$ , and  $a = 3.9$ . Similarly, the steel dowel material properties, obtained from uni-axial tensile tests, were also presented through the Richard-Abbott model adapted to stress-strain parameters, resulting in  $\sigma_{s,inter} = 581.6 \text{ N/mm}^2$  for the intersection of the stress axis with the plastic tangent,  $E_s = 198875 \text{ N/mm}^2$  for the elastic modulus,  $E_{pl} = 381.9 \text{ N/mm}^2$  for the plastic modulus, and  $a = 13.5$ . The resulting curve was corrected to true stress and logarithmic strain for use in the non-linear BoF model implemented in ABAQUS (version 2023), considering the steel tensile strength as  $f_y = 582.7 \text{ N/mm}^2$  and the ultimate tensile strength as  $f_u = 600.5 \text{ N/mm}^2$ . The interaction between the steel plate and dowel is modelled with isotropic elastic behaviour governed by the steel dowel due to the high-strength steel of the plates. Thus, the elastic embedment stiffness for the springs in the contact region is adopted as  $E_s$  times  $s$ .



The load-displacement curve obtained from the numerical model is compared to the experimental ones from *Wydler (2023)* and *Palma & Wydler (2024)* in Figure 3. The model effectively predicts the connection slip curve, showcasing the BoF model's capability to capture the non-linear behaviour of single-dowel connections. A similar good agreement was also found for other connections and documented in earlier BoF-model validations, see e.g. *Lemaître et al. (2018)* and *Basterrechea-Arévalo et al. (2023)*.

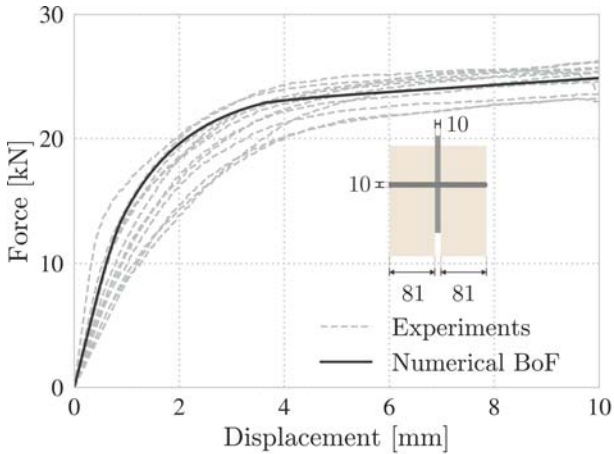


Figure 3. Comparison of the load-displacement curve obtained from the numerical BoF model with the experimental results from *Wydler (2023)* and *Palma & Wydler (2024)* for a single-dowel connection (dimensions are given in mm).

## 4 Comparison between models

A comparison between the fastener deformed shape according to different models and between formulations for the effective timber thickness for two exemplary connections with slotted-in steel plates are illustrated in Figure 4. The timber member thicknesses of  $t = 60$  mm and  $t = 140$  mm were chosen to consistently compare the models for failure modes  $g$  and  $f$  (see Figure 1), respectively. A similar comparison was conducted for connections with outer steel plates. In this case, the timber member thicknesses were kept constant at  $t = 140$  mm and the steel plate thicknesses were considered to be  $t_s = 4$  mm and  $t_s = 10$  mm, as shown in Figure 5. These thicknesses were selected to facilitate a comparison with the assumptions of clamping or pinned boundary conditions assumed in the analytical BoF model adopted by *Yurrita & Cabrero (2020a)*, for thin and thick steel plates (respectively modes  $k$  and  $m$  in Figure 1). On the other hand, the comparison shown in Figure 4 only considers the clamped boundary condition for the analytical BoF, as it represents the most appropriate configuration for connections with slotted-in steel plates.

The material properties utilised for the timber member and the fastener were kept constant for all the examples and are derived from the experimental campaign documented in *Wydler (2023)* and *Palma & Wydler (2024)* for Spruce LVL, as discussed in Section 3.3.2. For comparisons of the fasteners' deformed shape between numerical and analytical BoF models, a load level of about 25% of the maximum connection

load-carrying capacity ( $F_{max}$ ) derived from the numerical BoF model was used. This load level was chosen to ensure that the comparison was performed within the elastic range of the load-displacement curve, as the analytical BoF model is only valid within this range. For the determination of the effective thickness according to EN 1995-1-1 (2004), the parameters  $M_y = 0.3 f_u d^{2.6}$  and  $f_h = \sigma_h(u_h = 5 \text{ mm})$  were adopted. Where the ultimate tensile strength  $f_u = 600.5 \text{ N/mm}^2$  and the embedment parameters that describe the Richard-Abbott Equation (see Eq. (8)) were consistently the same as those used for the numerical and analytical models (see also Section 3.3.2).

#### 4.1 Connections with slotted-in steel plates

The comparisons of the fastener deformed shape illustrated in Figures 4a and 4c show an overall good agreement between models, with the analytical elastic BoF yielding a slightly stiffer response. This difference can be attributed to the difference in boundary conditions between the models; specifically, the numerical BoF incorporated linear springs at the contact interface between the steel plate and fastener, facilitating elastic deformations and small rotations, which were not allowed in the analytical BoF model. Additionally, while the numerical BoF model is implemented with Timoshenko beam elements, the analytical BoF follows the Bernoulli beam formulation, which neglects shear effects. This difference in shear treatment could also contribute to the observed difference between the models.

The plots given in Figures 4b and 4d illustrate the variation in the effective thickness according to the different definitions, encompassing the expressions in EN 1995-1-1 (2004) and prEN 1995-1-1 (2023). It is worth noting that for a displacement approximately equal to 1.5 mm (close to the connection yield point), the effective thickness variation with the fastener displacement derived from the numerical BoF tends to stabilise. The comparisons between elastic analytical and non-linear numerical BoF models show that the analytical BoF yields higher values of  $y$  and  $y_1$ , which can be attributed to the stiffer response of the analytical BoF model, observed in Figures 4a and 4c.

#### 4.2 Connections with outer steel plates

Concerning the connections with outer steel plates, the deformed shapes obtained with the analytical BoF model could be the lower and upper bounds of the fastener's deformed behaviour. For the connection with thin plates ( $t_s \leq 0.5d$ ), shown in Figure 5a, the pinned boundary condition approaches better the numerical solution, whereas, for the thick steel plates ( $t_s \geq d$ ), shown in Figure 5c, the clamped one resulted in a better approximation, as expected. It is noteworthy that the effective thickness obtained from the BoF model for thick steel plates could be used to define effective thickness for inner timber members in multiple shear connections.

From Figures 5b and 5d, one can note that the behaviour of  $y$  and  $y_1$  as a function of the fastener displacement (obtained from the numerical BoF) deviates significantly



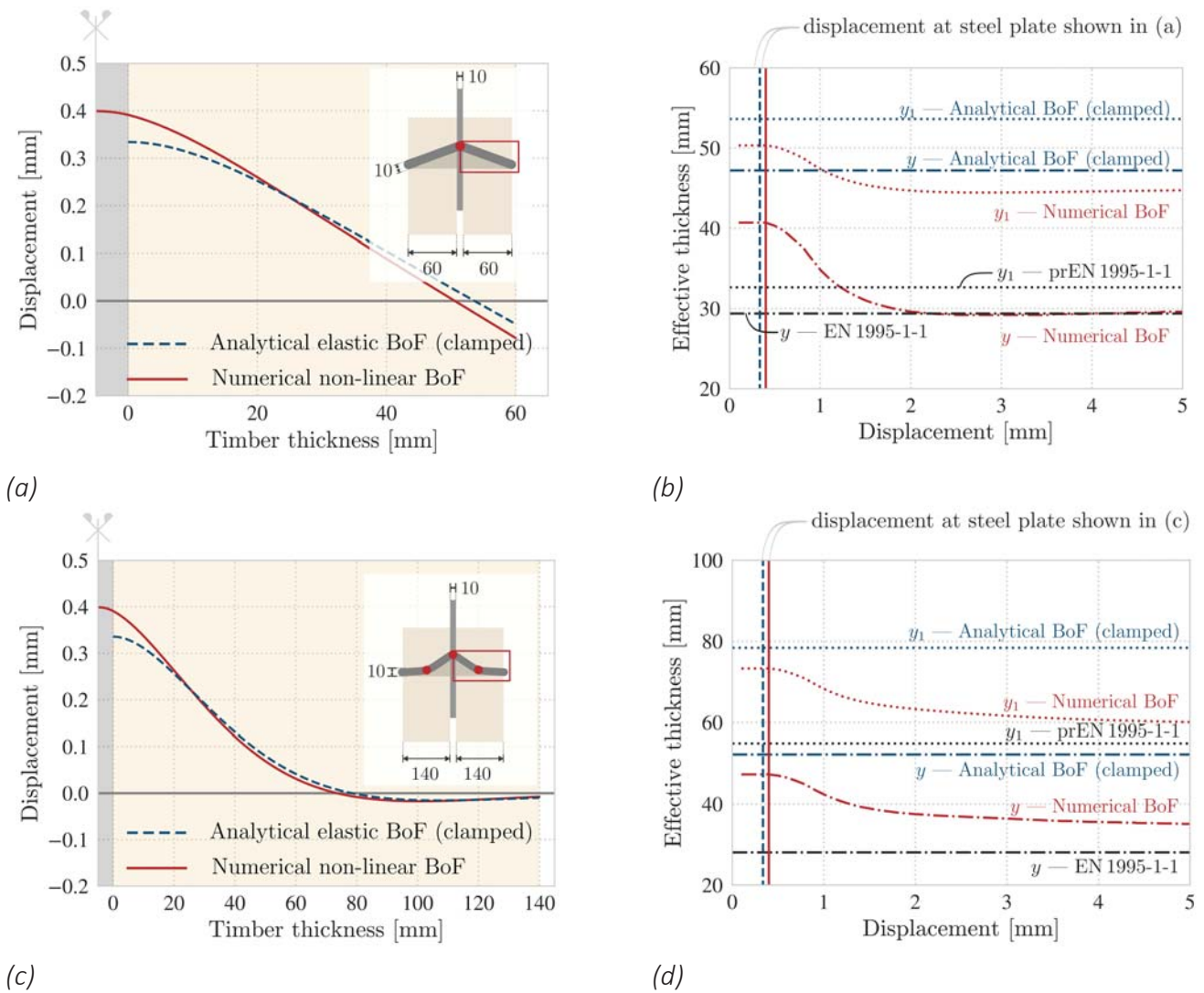


Figure 4. Comparison of different models for connections with slotted-in steel plate for (a)(c) the deformation of the steel fastener for a load level approximately 25% of the connection maximum load-carrying capacity (dimensions are given in mm); and (b)(d) the variation in the effective thickness.

between the two connections (thin and thick steel plate). This phenomenon is due to the embedment stress distribution, which is highly influenced by the thickness and stiffness of the steel plate. In addition, both EN 1995-1-1 (2004) and prEN 1995-1-1 (2023) result in  $t_{ef} = y = y_1 = 0.5t$ , considerably different than the values obtained according to the numerical BoF model.

### 4.3 Parametric and sensitivity analyses

The variation of  $t_{ef}$  with increasing timber thickness for steel-to-timber connections is presented in Figure 6. The diameter of the fastener ( $d = 10$  mm) and the thickness of the steel plate ( $t_s = 10$  mm for the slotted-in plate and  $t_s = 4$  mm for the outer plates) were kept constant in the analysis. Only the length  $y$  is considered here for the different models, except for  $y_1$  from prEN 1995-1-1 (2023). For the numerical BoF, a range of values is presented in Figure 6, encompassing the variation of the length  $y$  within the elastic ( $y$  at  $0.25F_{max}$ ) and plastic range ( $y$  at  $F_{max}$ ), as shown in Figures 4 and 5. Additionally, since

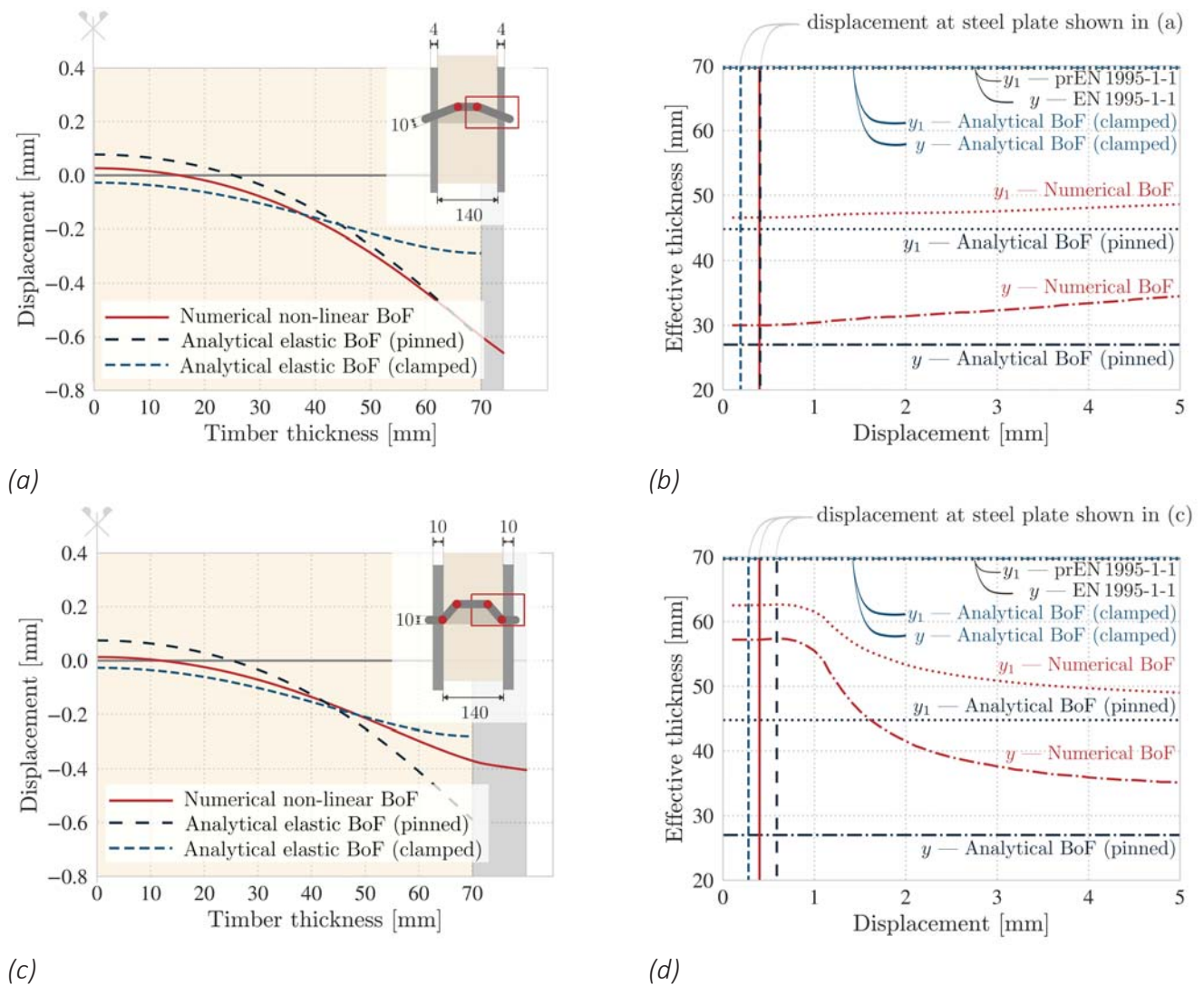


Figure 5. Comparison of different models for connections with outer steel plates for (a)(c) the deformation of the steel fastener for a load level approximately 25% of the connection maximum load-carrying capacity (dimensions are given in mm); and (b)(d) the variation in the effective thickness.

no effective thickness is considered for connections with outer steel plates (EN 1995-1-1, 2004), the equations proposed for single shear connections, as discussed in Section 3.1.1, were adopted herein for comparison, denoted by  $y$ —EN 1995-1-1\* in Figure 6b .

The results presented in Figure 6 show that the EN 1995-1-1 expressions for  $t_{ef}$  (modified to account for outer steel plates), align well with the numerical BoF model within the lower bound obtained for the length  $y$ . This alignment suggests that the EN 1995-1-1 (2004) approach could serve as a lower bound for the effective thickness. This conclusion also holds for connections with thick outer steel plates.

In addition, the curves obtained from prEN 1995-1-1 (2023) do not correspond to those obtained from the BoF models. Notably, the curves obtained for  $y_1$  from the numerical and analytical BoF models follow the same pattern as those for  $y$  but are consistently higher. *Teichmann* (2023) conducted a parametric investigation of the proposed formulation by prEN 1995-1-1 (2023) for  $t_{ef}$  and found several inconsistencies in the shape of the proposed curve. These inconsistencies can be observed in Figure 6,

namely: a jump in  $t_{ef}$  values between modes  $g$  and  $h$ , a parabolic behaviour and an unlimited increase in the curves under modes  $h$  and  $k$ . *Teichmann* (2023) concluded that these inconsistencies are mainly a reflex of the chosen regression equations and the implementation of the clamping factor  $\alpha_{CL}$ .

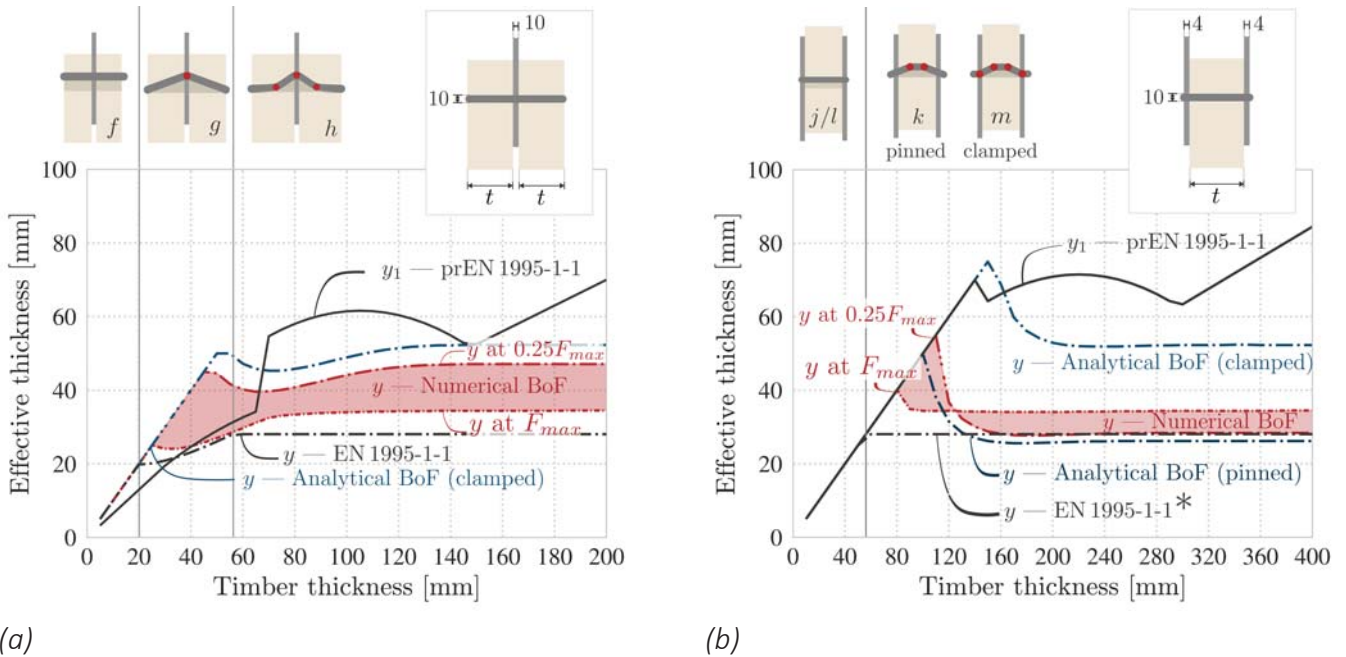


Figure 6. Variation in the effective thickness with varying timber member thickness for connections with (a) slotted-in steel plates and (b) outer thin steel plates.

A sensitivity analysis was conducted to evaluate the relative importance of each material parameter on  $t_{ef}$ , by including the following variables: the timber embedment parameters  $k_{el} = 31.7 \pm 15.3 \text{ N/mm}^3$ ,  $k_{pl} = 0.63 \pm 0.35 \text{ N/mm}^3$ , and  $f_{h,inter} = 33.3 \pm 2.8 \text{ N/mm}^2$ ; and the steel fastener parameters  $E_s = 198875 \pm 22488 \text{ N/mm}^2$  and  $f_y = 582.7 \pm 47.8 \text{ N/mm}^2$ . Here, the values are presented as the mean  $\pm$  standard deviation, obtained from *Wydlar* (2023) and *Palma & Wydlar* (2024). The Log-Normal distribution was adopted for all the variables ( $p$  – value  $\geq 0.05$  according to the Kolmogorov-Smirnov (K-S) statistical test), except for  $k_{pl}$  which was verified to follow a Normal distribution according to the K-S test. Two simulations were performed for each studied variable by considering the lower (5% percentile-  $P_{05}$ ) and upper bounds (95% percentile-  $P_{95}$ ) with the numerical non-linear BoF. The effective thickness, determined according to length  $y$  was obtained for each simulation in the elastic (at  $0.25F_{max}$ ) and in the plastic (at  $F_{max}$ ) ranges. Results are presented through bar diagrams in Figure 7 for the four studied connections. The variables are positioned in the ordinates, and the bar length represents the relative difference obtained in  $y$  by changing the variable to a lower and upper bound with respect to the mean value.

The elastic embedment stiffness  $k_{el}$  was the parameter with the most significant influence on the value of  $y$  at the elastic range, followed by the steel fastener modulus of elasticity  $E_s$ . The values of  $y$  in the plastic range are almost not influenced by the variation in material parameters. To further investigate the influence of  $k_{el}$ , the parametric analysis



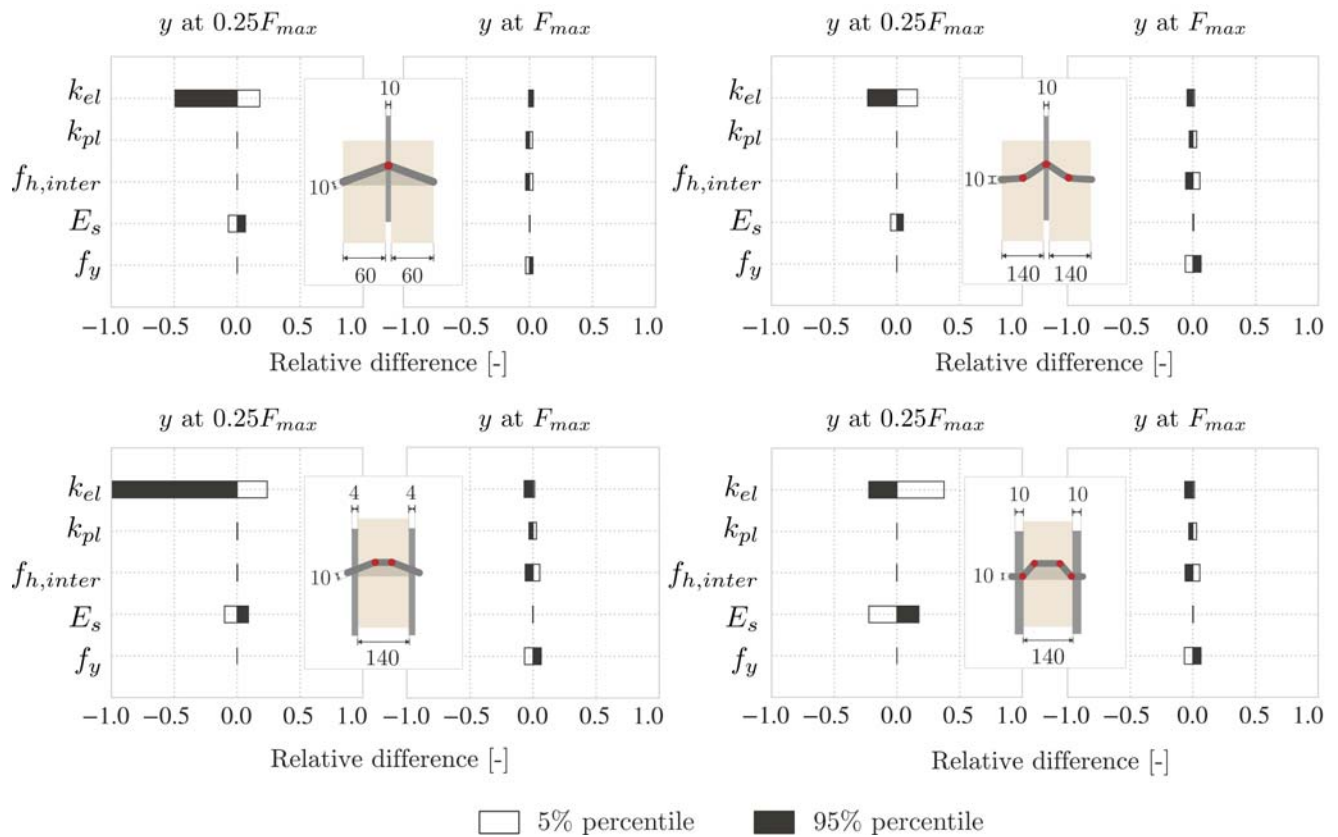


Figure 7. Sensitivity analysis of the material parameters for the effective thickness  $y$  according to the numerical non-linear BoF model.

regarding variation in  $t_{ef}$  as a function of the timber member thickness is repeated considering both the 5% and 95% percentiles of  $k_{el}$  (cf. Figure 6). All the other material parameters are kept to their mean values. The results are shown in Figure 8a, where the length  $y$  obtained in the elastic range (at  $0.25F_{max}$ ) from the numerical BoF is compared with the approaches from design standards. It can be observed that the lower bound of  $y$ , given by the 95% percentile of  $k_{el}$  is greater than the values obtained with EN 1995-1-1 (2004). This suggests that the standard approach could serve as a lower bound for the effective thickness of timber. For  $y$  obtained in the plastic range (at  $F_{max}$ ), the curves from the numerical model overlap and shift closer to the results from EN 1995-1-1 (2004).

These conclusions are further validated through the results presented Figure 8b, where a parametric analysis was performed to infer the influence of the timber density ( $\rho$ ) on the effective thickness. The timber embedment properties were derived using the regression equations proposed by Schweigler et al. (2019), which are functions of  $\rho$ . The fastener parameters remained consistent with the previous analysis (grade S235), but diameters of  $d = 12$  mm, 16 mm and 20 mm were considered, consistently with the embedment tests database. The results, shown for the length  $y$  obtained in the elastic range for  $d = 12$  mm, confirm that the EN 1995-1-1 (2004) equations could be viewed as a lower bound for  $t_{ef}$ . Similarly, the numerical BoF curves shift closer to the results from EN 1995-1-1 (2004) in the plastic range. Similar conclusions were found for fasteners with  $d = 16$  mm and  $d = 20$  mm.

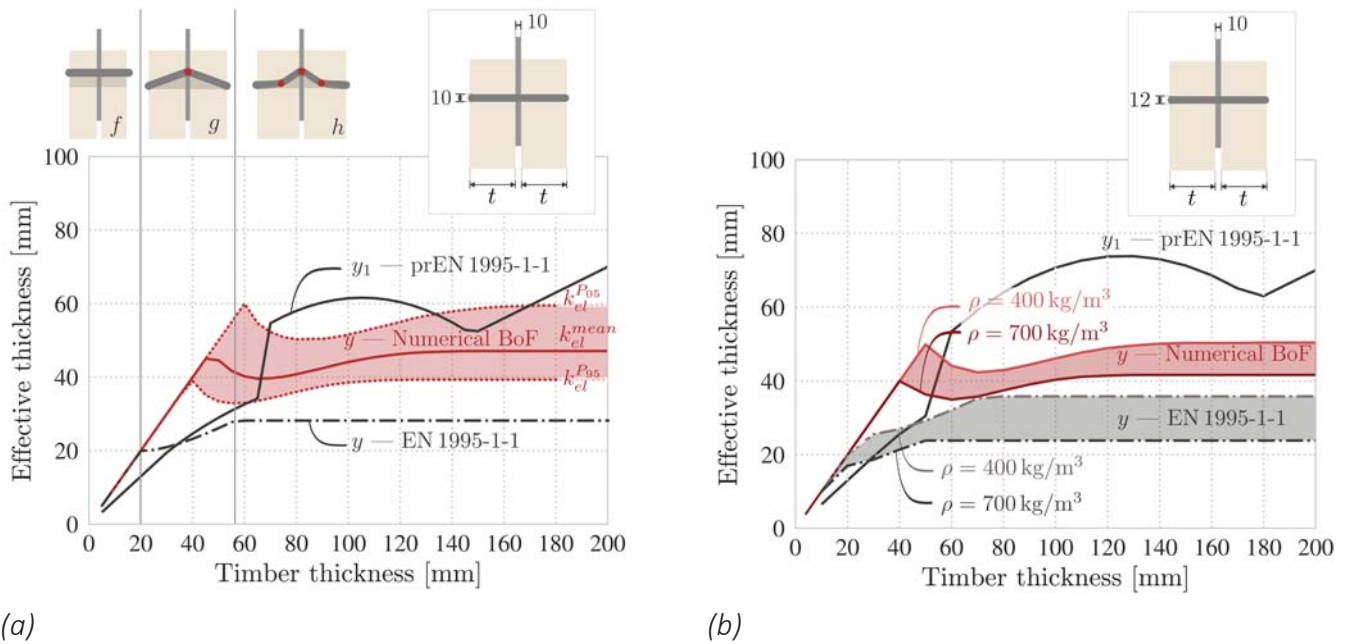


Figure 8. Variation in the effective thickness with varying timber member thickness for connections with slotted-in steel plates considering: (a) the 5% percentile and 95% percentile of the elastic embedment stiffness  $k_{el}$ , and (b) the embedment properties based on the regression equations proposed by Schweigler et al. (2019) for different timber densities  $\rho$ .

## 5 Conclusions

This paper discussed different theoretical definitions and modelling approaches for the effective timber thickness ( $t_{ef}$ ) in steel-to-timber dowel-type connections used in the design for brittle failure. Two modelling strategies were implemented: an analytical elastic beam-on-foundation (BoF) model and a numerical non-linear BoF model. The effective timber thickness was obtained using the stress distribution along the fastener axis. The theoretical definitions differ on whether  $t_{ef}$  is defined based on the region where the stress is positive, given by  $y_1$ , or in a smaller region, given by  $y$ , which consists in the region that effectively contributes to the connection's load carrying capacity.

By conducting parametric and sensitivity analyses, varying the connection arrangement and material properties, it was possible to evaluate the results from different models and to compare them with design standard formulae. The effective thickness obtained using the analytical elastic BoF exhibited a displacement shape and stress distribution similar to the numerical non-linear BoF in the elastic range. The observed differences can mainly be attributed to the boundary conditions of the fastener, which assume either a pinned or clamped support. In reality, the fastener behaviour is likely to fall somewhere in between, closer to the numerical non-linear BoF model.

Based on the comparisons, it was observed that the formulae from EN 1995-1-1 (2004), based on the European Yield Model (EYM), can be adopted as a lower bound for  $t_{ef}$ . For connections with outer steel plates and/or multiple shear planes, using the  $t_{ef}$  values given for single-shear plane connections is recommended. The model from prEN 1995-1-1 (2023) consistently provides higher  $t_{ef}$  values compared to EN 1995-1-1 (2004); thus,

it would result in higher capacity for brittle failure if not adjusted in the design model. This discrepancy is mainly due to the definition of  $t_{ef}$  based on the length  $y_1$  defined in the elastic range. Therefore, the model from prEN 1995-1-1 (2023) can be considered as an upper bound for the effective timber thickness, provided that the inconsistencies found in the regression curves adopted are corrected.

Nonetheless, the primary objective of this contribution was to establish a mechanical understanding and draw insights from different design and modelling approaches. Further recommendations for  $t_{ef}$  can only be made by evaluating the various definitions within the design models for brittle failure and validating them with comprehensive experimental results. In this context, the most significant advantage of the numerical non-linear BoF model is its ability to obtain the effective timber thickness as a function of the connection displacement. By implementing this feature in the brittle design model, the brittle capacity could also be determined as a function of the connection displacement. This approach could provide valuable insights into the displacement level at which brittle failure would occur for different connection arrangements. It could also offer more confidence in determining whether  $t_{ef}$  should be considered in the elastic range (as suggested by prEN 1995-1-1 (2023)) or the plastic range (as suggested by EN 1995-1-1 (2004)).

## 6 Acknowledgements

The authors gratefully acknowledge FCT – Foundation for Science and Technology (grant 2021.07308.BD) and COST Action CA20139 for the STSM Scholarship at Linnaeus University granted to the first author. Jonas Wydler and Pedro Palma (ETH Zurich and EMPA) are thanked for their support with experimental data during this study. Michael Schweigler and Thomas K. Bader gratefully acknowledge the Knowledge Foundation’s support for the project ‘Competitive timber structures- Resource efficiency and climate benefits along the wood value chain through engineering design’ (grant 20230005).

## 7 References

- ADIVbois (2022). *Experimental Characterization of Connection Stiffness in Timber Structures, Part 2*. Technical Report. Characterisation de la raideur d’assemblages de structures en bois, Partie 2 (in French).
- Basterrechea-Arévalo, M.; M. Schweigler; R. Lemaître & T. Bader (2023). “Numerical modelling of moment-transmitting timber connections.” In: *Engineering Structures* 297, p. 116923.
- Blaß, H. & P. Schädle (2011). “Ductility aspects of reinforced and non-reinforced timber joints.” In: *Engineering Structures* 33.11, pp. 3018–3026.

- Cabrero, J.; N. Rodríguez; T. Tannert; A. Salenikovich & Y. Chui (2024). “Brittle Failure Modes of Connections with Dowel-Type Fasteners Loaded Parallel to the Grain: A Comparison between Eurocode 5 and CSA O86 (Paper 57-7-9).” In: *Proceedings of the 57th INTER Meeting, Padova, Italy*. KIT Holzbau und Baukonstruktionen.
- EN 1995-1-1 (2004). *Design of timber structures – Part 1-1: General – Common rules and rules for buildings*. EN 1995-1-1:2004/AC:2006/A1:2008/A2:2014. Brussels, Belgium: European Committee for Sandardization.
- Hanhijärvi, A. & A. Kevarinmäki (2008). “Timber failure mechanisms in high-capacity dowelled connections of timber to steel.” In: *Espoo, VTT publication 677*, p. 53.
- Johansen, K. (1949). “Theory of timber connections.” In: *International Assoc. of Bridge and Structural Engineering Publication 9*, pp. 249–262.
- Jorissen, A. (1998). “Double shear timber connections with dowel type fasteners.” PhD thesis. Delft University of Technology.
- Kuenzi, E. (1955). *Theoretical design of a nailed or bolted joint under lateral load*. Forest Products Laboratory, Forest Service U.S. Department of Agriculture.
- Lemaître, R.; J. Bocquet; M. Schweigler & T. Bader (2018). “Beam-on-Foundation Modelling as an Alternative Design Method for Timber Joints with Dowel-Type Fasteners – Part 1: Strength and stiffness per shear plane of single-fastener joints (Paper 51-7-13).” In: *INTER meeting 51, Tallin, Estonia*. KIT Holzbau und Baukonstruktionen.
- Palma, P. & J. Wydler (2024). *Dataset with results of multi-scale experiments on timber connections*. DOI: 10.5281/zenodo.10602292.
- prEN 1995-1-1 (2023). *Design of timber structures – Part 1-1: General and rules for buildings*. prEN 1995-1-1 v2023-04-19 (Formal CEN Enquiry). Brussels, Belgium: European Committee for Sandardization.
- prEN 1995-1-1 (2024). *Design of timber structures – Part 1-1: General and rules for buildings*. CEN/TC250/SC5/WG5 (ed.)(2024)(unpublished) N619 prEN 1995-1-1 v0 to v1A. Connections. Status: July, 2024. Brussels, Belgium: European Committee for Sandardization.
- Quenneville, P. (2018). “Brittle Failures of Connections Loaded Parallel-to-Grain.” In: *Proc., Conference of COST Action FP1402, International Conference on Connections in Timber Engineering—From Research to Standards, Graz, Austria*, pp. 154–165.
- Quenneville, P. & M. Mohammad (2000). “On the failure modes and strength of steel-wood-steel bolted timber connections loaded parallel-to-grain.” In: *Canadian journal of civil engineering* 27.4, pp. 761–773.
- Richard, R. & B. Abbott (1975). “Versatile elastic-plastic stress-strain formula.” In: *Journal of the Engineering Mechanics Division* 101.4, pp. 511–515.
- Schweigler, M.; T. Bader; J. Bocquet; R. Lemaître & C. Sandhaas (2019). “Embedment test analysis and data in the context of phenomenological modeling for dowelled timber joint design (Paper 52-7-8).” In: *Proceedings of the 52nd INTER Meeting, Tacoma, USA*. KIT Holzbau und Baukonstruktionen.

- Teichmann, S. (2023). “Spröde Versagensarten in Holzverbindungen mit auf Abscheren beanspruchten Verbindungsmitteln- Vergleich von Bemessungsvorschlägen.” Master’s thesis. Karlsruhe, Germany: Karlsruhe Institute of Technology.
- Wylder, J. (2023). “Stress-Based Failure Model for Dowelled Steel-to-Timber Connections under Eccentric Loading.” PhD thesis. ETH Zurich.
- Yurrita, M. & J. Cabrero (2020a). “Effective thickness of timber elements for the evaluation of brittle failure in timber-to-steel connections with large diameter fasteners loaded parallel-to-grain at the elastic range: A new method based on a beam on elastic foundation.” In: *Engineering Structures* 209, p. 109959.
- Yurrita, M. & J. Cabrero (2020b). “New design model for brittle failure in the parallel-to-grain direction of timber connections with large diameter fasteners.” In: *Engineering Structures* 217, p. 110557.

## A Annex

### A.1 Updated parametric analyses based on prEN 1995-1-1 (2024)

The equations proposed for the effective timber thickness have been updated in the draft of Eurocode 5 (prEN 1995-1-1, 2024). A discussion of the new proposal can be found in *Cabrero et al. (2024)*. The updated equations for fully penetrated fasteners in inner timber members are

$$t_{ef} = y_1 = \min \left( t_h, \alpha_{cl} \frac{14t_h}{3 + t_h/d} \right) , \quad (\text{A.1})$$

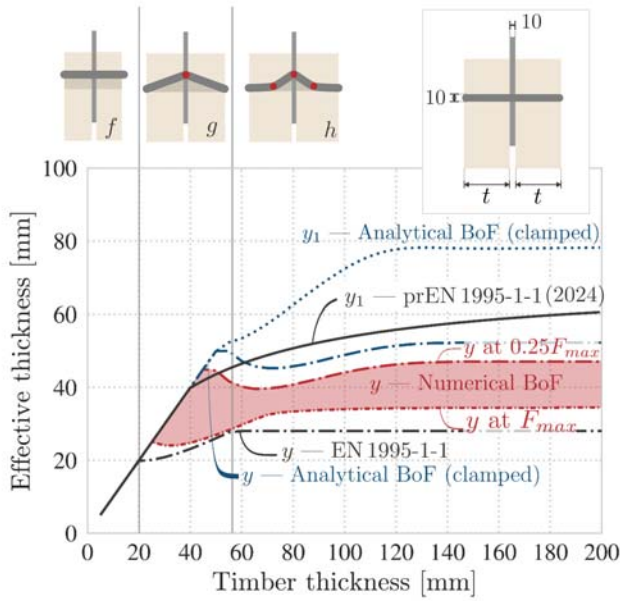
and for outer or partially penetrated timber members the failure planes of outer timber members as

$$t_{ef} = y_1 = \min \left( \alpha_{cl} t_h, \alpha_{cl} \frac{7t_h}{3 + t_h/d} \right) , \quad (\text{A.2})$$

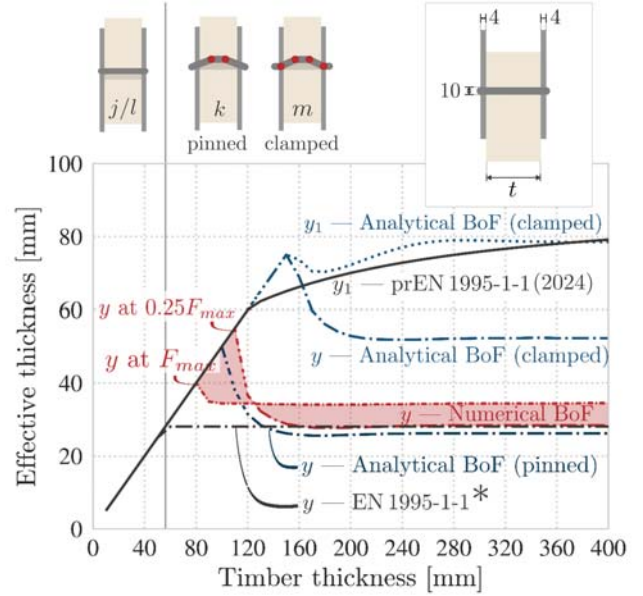
where  $t_h$  is the penetration length of the fasteners in the timber member. The clamping factor,  $\alpha_{cl}$ , is 0.65 for timber-to-timber connections and for steel-to-timber connections with  $t/d \leq 0.5$ , and 1.0 for steel-to-timber connections with  $t/d \geq 1.0$ . For intermediate cases,  $\alpha_{cl}$  is determined by linear interpolation.

In this annex, the original parametric analyses and comparisons between models presented in Figure 6 from Section 4.3 are updated to consider the new proposals. In addition, the effective thickness ratio ( $t_{ef}/t$ ) is also plotted in comparison to the slenderness ratio ( $t/d$ ) to facilitate the comparison with previous studies (e.g. *Yurrita & Cabrero (2020a)* and *Cabrero et al. (2024)*). Since no effective thickness is considered for connections with outer steel plates (EN 1995-1-1, 2004), the equations proposed for single shear connections, as discussed in Section 3.1.1, were adopted for comparison, denoted by  $y$ —EN 1995-1-1\* in Figures A.1b and A.2b.



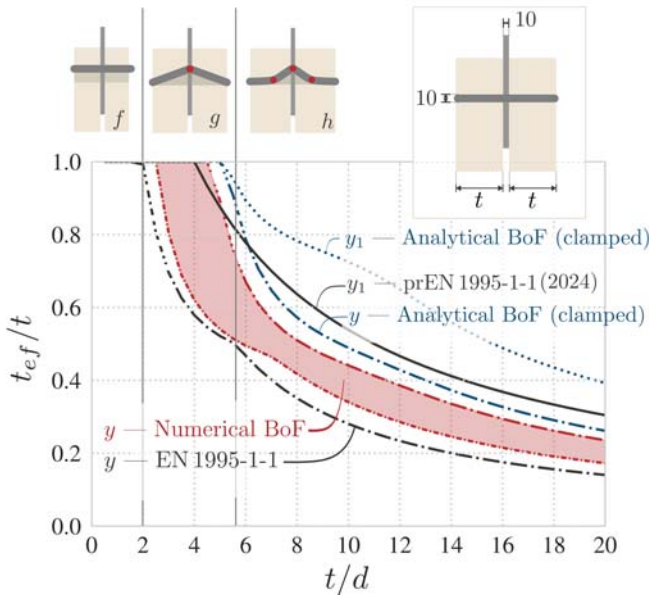


(a)

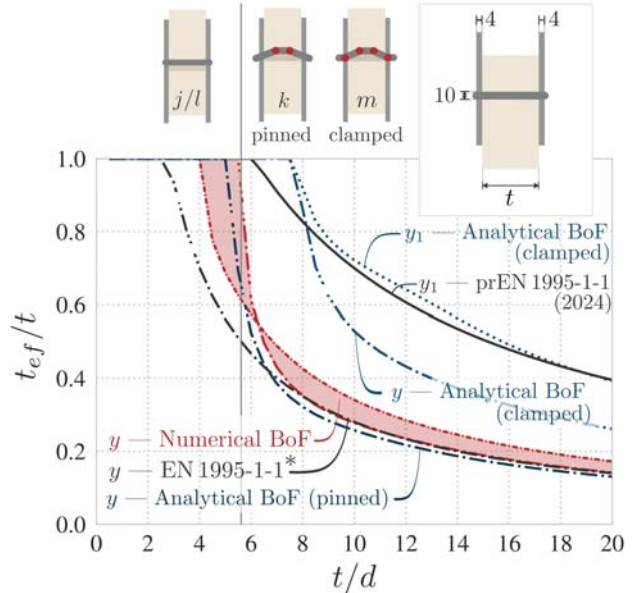


(b)

Figure A.1. Variation in the effective thickness with varying timber member thickness for connections with (a) slotted-in steel plates and (b) outer thin steel plates.



(a)



(b)

Figure A.2. Relation between the effective thickness of the timber member and the slenderness ratio  $t/d$  for connections with (a) slotted-in steel plates and (b) outer thin steel plates.

## DISCUSSION

**The paper was presented by C D Aquino**

*P Dietsch commented that the current EC5 model seemed to be not far from results of the paper.*

*T Tannert received confirmation which version of the proposed standard was compared. C D Aquino stated that the enquiry version was used but the changed proposal still represents an upper bound.*

*A Frangi commented that the upper limit cannot be accepted as design approach.*

*P Palma commented that based on experiments performed, the coefficient of variation should be higher.*

*T Ehrhart pointed out a couple of typo and illustration issues.*



# Brittle Failure Modes of Connections with Dowel-Type Fasteners Loaded Parallel to the Grain: A Comparison between Eurocode 5 and CSA O86

José Manuel Cabrero, Onesta Wood Chair, University of Navarra, Pamplona, Spain, [jcabrero@unav.es](mailto:jcabrero@unav.es)

Nicol López Rodríguez, Onesta Wood Chair, University of Navarra, Pamplona, Spain, [nlopezrodri@unav.es](mailto:nlopezrodri@unav.es)

Thomas Tannert, UNBC, Prince George, Canada; [thomas.tannert@unbc.ca](mailto:thomas.tannert@unbc.ca)

Alexander Salenikovitch, Université Laval, Canada, [alexander.salenikovitch@sbf.ulaval.ca](mailto:alexander.salenikovitch@sbf.ulaval.ca)

Ying Hei Chui, University of Alberta, Edmonton, Canada, [yhc@ualberta.ca](mailto:yhc@ualberta.ca)

Keywords: Bolts and dowels, effective depth, failure planes, self-tapping screws

## 1 Introduction

### 1.1 Background

Timber exhibits brittle failure when loaded in tension or shear. Considering these failure modes is particularly important for connections with dowel-type fasteners, such as bolts, dowels, or self-tapping screws (STS). Timber connections can exhibit either ductile behaviour, characterized by wood crushing and fastener yielding, or brittle behaviour, where the wood fails in shear and/or tension with minimal plastic deformation. The ductile failure modes of connections with dowel-type fasteners are described by the European Yield Model (EYM), introduced by Johansen [1]. This model has been incorporated into design standards like Eurocode 5 [2] and CSA O86 [3] for decades.

When a group of fasteners are loaded parallel to the grain, various brittle failure modes can occur depending on the connection geometry, including the member size, fastener diameter, penetration depth, and spacing. These modes include splitting, row shear, block shear (group tear-out), plug shear, step shear, and net tension, see Figure 1.

Traditionally, brittle failure modes of connections with large-diameter dowel-type fasteners loaded parallel to the grain have been addressed using group effect factors [4]. Splitting parallel to the grain is implicitly accounted for using minimum spacing requirements and an effective number of fasteners in Eurocode 5 [2]. In 2009, CSA O86, based on the work by Mohammad and Quenneville [5,6], incorporated provisions to explicitly

account for the brittle failures of bolted connections loaded parallel to the grain where the bolts fully penetrate the wood member. These failure modes include row shear, group tear-out, and net tension. However, for connections with partial fastener penetration, plug shear and step shear failure modes must also be considered.

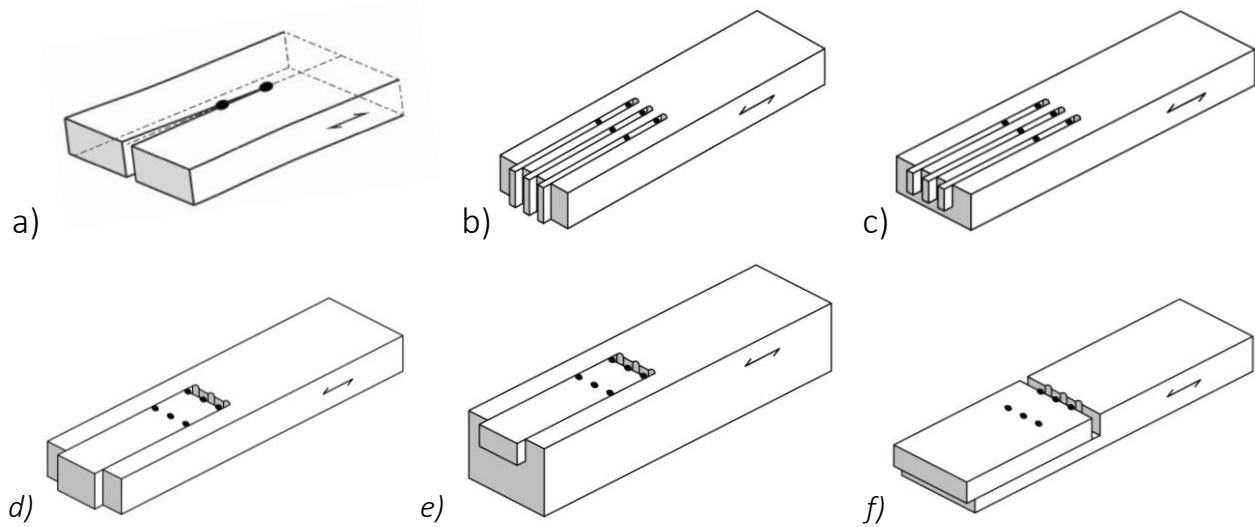


Figure 1. Brittle failure modes in connections with dowel type fasteners as depicted in Eurocode 3 draft [8] and CSA O86 [7]: splitting (a), row shear with full (b) and partial penetration (c), block shear or tear-out (d), plug shear (e) and step shear (f). Net tensile failure is not shown.

## 1.2 Objectives

The 2024 edition of CSA O86 provides design rules for brittle failure modes of connections with dowel-type fasteners [7]. Similarly, the latest draft of Eurocode 5, prEN1995 [8], currently under development, integrates revised design rules for brittle failure modes of connections with dowel-type fasteners. Both standards draw heavily from the model developed by Yurrita and Cabrero, which was presented in previous INTER meetings [9-11]. However, recent research from the Karlsruhe Institute of Technology [12,13], based on a parametric analysis of the model in the Formal Enquiry Eurocode 5 draft [14], highlighted several issues such as kinks when plotting the resistance versus the timber member thickness, ambiguity about the plastic effective depth and the absence of an upper limit for the effective depth. Subsequently, modifications to the formulation were proposed and incorporated in the most recent draft of prEN1995 [8], as discussed in section 2.1.

The objectives of this work are to: (i) present the current design provisions in the latest Eurocode 5 draft [8] and CSA O86:24 [7] for brittle failure modes of connections with dowel-type fasteners loaded parallel to the grain; and (ii) discuss the differences to enable international harmonization.

## 2 Design provisions for brittle failure modes

### 2.1 Eurocode 5 draft

The latest draft of prEN1995 [8] covers brittle failure modes of connections with dowel-type fasteners loaded parallel to grain in section 11.5. It states that brittle failure caused by splitting, row shear, block shear, plug shear, and net tensile failure shall be considered if multiple fasteners are used in steel-to-timber and timber-to-timber connections. Splitting is deemed prevented by using minimum spacing requirements and considering the number of effective fasteners,  $n_{ef}$ .

Eurocode 5 draft further allows for the simplification to completely neglect brittle failure modes of connections provided that yield mode (f) (with two plastic hinges in the fastener) governs the ductile design and the minimum spacings are met, with spacings  $a_1$ ,  $a_2$  and loaded end distance  $a_{3,t}$  being increased by the factor  $k_{br}$ . This simplification is still under discussion, and maybe modified or replaced in the final version.

Otherwise, for a timber member with a single row of fasteners, the brittle failure resistance should be determined by the minimum resistance of a) splitting (through  $n_{ef}$ ); b) row shear failure; and c) net tensile failure. For connections with more than one row of fasteners, the design brittle failure resistance should be determined by further considering: d) block shear failure (for fully penetrated members); and e) plug shear failure (for partially penetrated members).

The row shear resistance of a timber member<sup>1</sup>  $F_{rs,EC5}$  is taken as:

$$F_{rs,EC5} = 2n_{90}F_{v,la,EC5} \quad (1)$$

where  $n_{90}$  is the number of fasteners in a row perpendicular to grain; and  $F_{v,la,EC5}$  is the design shear resistance per side shear plane in the timber member.

The block shear resistance  $F_{bs,EC5}$  for fully penetrated timber members is taken as:

$$F_{bs,EC5} = \max \left\{ \begin{array}{l} 2F_{v,la,EC5} \\ F_{t,EC5} \end{array} \right. \quad (2)$$

where  $F_{t,EC5}$  is the tensile resistance parallel to grain of the head tensile plane.

For reinforced connections, the block shear resistance can be taken as:

$$F_{bs,EC5} = 2F_{v,la,EC5} + F_{t,EC5} \quad (3)$$

---

<sup>1</sup> For comparison purposes, the notation indicates Eurocode 5 symbols with subscript "EC5" and CSA O86 symbols with subscript "CSA". This notation differs from that used in the actual standards.

The plug shear resistance  $F_{ps,EC5}$  for partially penetrated timber members is taken as:

$$F_{ps,EC5} = \max \begin{cases} 2F_{v,la,EC5} \\ F_{t,EC5} + F_{v,b,EC5} \end{cases} \quad (4)$$

where  $F_{v,la,EC5}$  is the shear resistance per side shear plane;  $F_{t,EC5}$  is the tensile resistance of the head plane; and  $F_{v,b,EC5}$  is the shear resistance of the bottom shear plane.

The shear resistance per side shear plane,  $F_{v,la,EC5}$  is taken as follows:

$$F_{v,la,EC5} = k_v t_{ef} L_{con} f_v \quad (5)$$

with  $L_{con} = a_1(n_0 - 1) + a_{3,t}$ ; where  $k_v$  is the adjustment factor for shear strength (varies for different products, e.g.  $k_v = 0.75$  for glulam);  $t_{ef}$  is the effective depth (effective thickness)<sup>2</sup> of the plane;  $L_{con}$  is the length parallel to grain of the connection;  $f_v$  is the shear strength;  $a_1$  is the spacing of fasteners parallel to grain;  $n_0$  is the number of fasteners in a row parallel to grain; and  $a_{3,t}$  is the loaded end distance parallel to grain.

The shear resistance of the bottom shear plane,  $F_{v,b,EC5}$  is taken as follows:

$$F_{v,b,EC5} = k_v L_{con} b_{con} f_v \quad (6)$$

with  $b_{con} = a_2(n_{90}-1)$ , where  $k_v$ ,  $L_{con}$ , and  $f_v$  are as defined above;  $b_{con}$  is the width of the connection;  $n_{90}$  is the number of fasteners in a row perpendicular to grain; and  $a_2$  is the spacing of fasteners perpendicular to grain.

The tensile resistance parallel to grain of the head tensile plane,  $F_{t,EC5}$ , is taken as:

$$F_{t,EC5} = k_t b_{net} t_{ef} f_{t,0} \quad (7)$$

with  $b_{net} = (a_2 - d_{hole,max})(n_{90} - 1)$ , where  $k_t$  is the increase factor for tension (varies for different products, e.g.  $k_t = 1.25$  for glulam);  $b_{net}$  is the net width of area that fails in block shear;  $t_{ef}$ ,  $a_2$  and  $n_{90}$  are as defined above;  $f_{t,0}$  is the design tensile strength, is the spacing of fasteners perpendicular to grain;  $d_{hole,max}$  is the larger of the diameter of the predrilled hole and fastener diameter.

The Eurocode 5 draft proposes two equations to determine the effective depth, which is the penetration depth of the fastener considered to obtain the area of the failure planes in the model (see Figure 2), based on the relative position of the fasteners

---

<sup>2</sup> The term is coined as “thickness” in the Eurocode 5 draft [8] and in the works by Yurrita and Cabrero [9-11], and as “depth” in the CSA O86 [7]. The authors agree “depth” conveys more clearly the idea of the penetration of the fastener. Therefore, “depth” is the term used in this paper.

within the connection of the analysed timber member, and the fastener slenderness. For fully penetrating fasteners in inner members, it is taken as:

$$t_{ef} = \min \left\{ \begin{array}{l} t_h \\ \alpha_{cl} \frac{14 t_h}{3 + \frac{t_h}{d}} \end{array} \right. \quad (8)$$

where  $t_h$  is the penetration length of the fasteners in the timber member, which corresponds to the thickness of the inner timber member;  $\alpha_{cl}$  is a clamping factor (see discussion below),  $d$  is the fastener diameter. For multiple inner timber members, the effective depth  $t_{ef}$  is reduced to  $0.85t_{ef}$ .

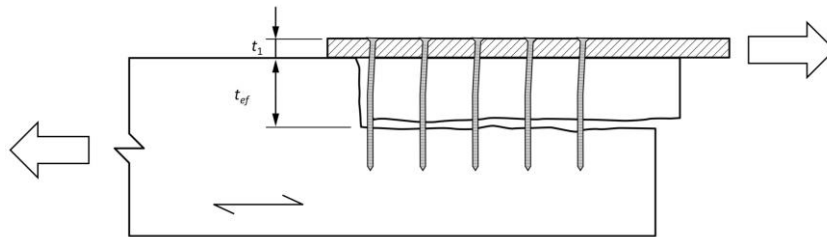


Figure 2. Definition of effective depth of the failure planes, as depicted in CSA O86 [7].

In the case of outer or partially penetrated timber members,  $t_{ef}$ , is taken as:

$$t_{ef} = \min \left\{ \begin{array}{l} \alpha_{cl} t_h \\ \alpha_{cl} \frac{7 t_h}{3 + \frac{t_h}{d}} \end{array} \right. \quad (9)$$

The clamping factor  $\alpha_{cl}$  is introduced to account for the different boundary conditions of the fastener in thin and thick side plates. The clamping condition is defined based on the ratio of the steel plate thickness,  $t_s$ , and the fastener diameter,  $d$ , in a similar manner as in the original thin-thick plate equation. It becomes  $\alpha_{cl} = 0.65$  for timber-to-timber connections and for  $t_s/d \leq 0.5$  (thin plate condition) in steel-to-timber connections, and  $\alpha_{cl} = 1.0$  for  $t_s/d \geq 1.0$  (thick plate condition). An additional equation provides a linear interpolation between these two limits, as follows:

$$\alpha_{cl} = 0.7 t_s/d + 0.3 \quad (10)$$

The proposed clauses differ in several aspects from the model proposed by Yurrita and Cabrero [9-11], due to discussion within the Working Group 5, and changes arising from the work at Karlsruhe Institute of Technology [12,13]. If a brittle failure mode governs, it should occur before yielding, therefore the concept of plastic effective depth does not seem logical. Consequently, it has been dismissed in the revised Eurocode 5 draft.

Most divergences relate to the calculation of the effective depth. The linear simplification for the effective depth proposed by Yurrita and Cabrero [9] has been modified to



rational expressions (8) and (9), which fit closer to the original results from the beam on elastic foundation analytical model used in the original work [9], see Figure 3, where the effective depth ratio is the ratio of the effective depth and the penetration length of the fastener. The proposed linear simplification showed flaws in case of fasteners with high slenderness.

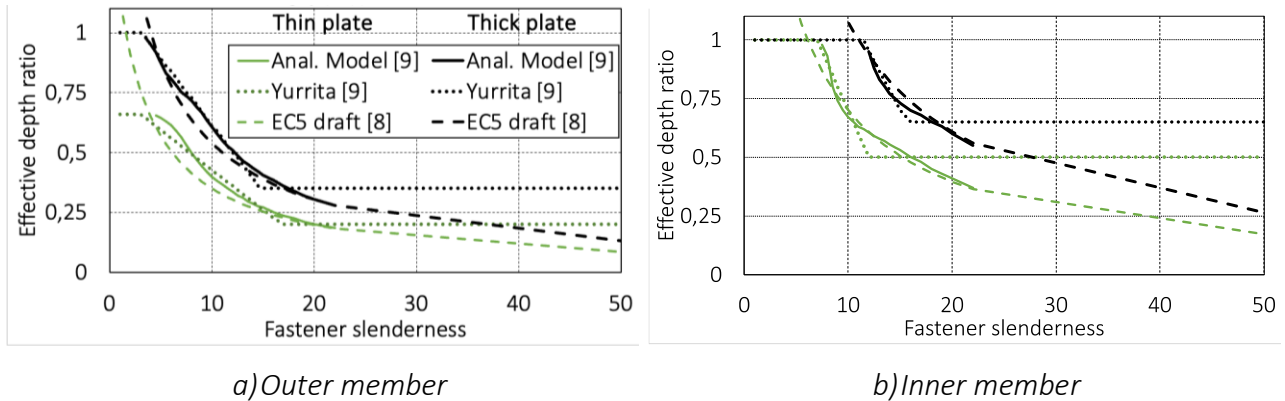


Figure 3. Comparison of the different formulations for the effective depth: analytical model [9], trilinear simplification proposed by Yurrita [9], new rational fitting in Eurocode 5 draft [8]. Thin plate condition corresponds to clamping factor  $\alpha_{cl} = 0.65$ ; thick plate condition,  $\alpha_{cl} = 1.00$ .

A different way of presenting the shear,  $k_v$ , and tensile,  $k_t$ , factors is adopted in the Eurocode 5 draft in comparison to the original proposal. Instead of giving a general formula, only values for those products contained in the validation database [10,11] are given.

Although the original model for block shear failure [10] combined the resistance of all failure planes, a more conservative approach was proposed by the EC5 Working Group 5. Due to the limited information on the long-term performance of connections, and the possible influence of cracks in timber members on connection resistance, it was decided to consider only the resistance of the side shear or head tensile planes, whichever is greater, for unreinforced connections. For reinforced connections, combining the resistance of these two planes is permitted.

The head tensile plane depth has been modified to the same effective depth as considered for the shear planes, while in the original model it was taken as the full member thickness. This makes the draft model more user-friendly, and less prone to mistakes, since the same effective depth is considered for both head tension and side shear plane resistance calculations.

In the case of plug shear, the total connection width is considered to obtain the area of the bottom plane. The original model from Yurrita and Cabrero [11] proposed to use the net width instead, which led to an unrealistic reduction. The effective depth has also been modified for plug shear, assuming the outer member condition (it was the inner member condition in the original proposal).

## 2.2 CSA O86:24

Clause 12.4 of CSA O86 [7], which covers the design of connections with bolts and dowels, remained unchanged in the 2024 edition of the standard. A new Clause 12.12 was added to cover connections with STS, where Clause 12.12.10.7 covers the resistance to brittle failures of wood members loaded parallel to grain.

For STS connections loaded parallel to the grain, the following brittle failure modes are included: a) net tension resistance; row shear resistance,  $F_{rs,CSA}$ ; b) group tear-out (block shear) resistance,  $F_{bs,CSA}$ ; c) plug shear resistance,  $F_{ps,CSA}$ ; and d) step shear resistance,  $F_{ss,CSA}$ . Each of these is calculated as the sum of the resistances of wood members resisting the load. Net tension resistance will not be further discussed herein; it is just reminded that both gross and net sections are being checked. For comparison purposes, the resistance factor  $\phi_W$  and the load-duration factor  $K_D$  included in the standard equations are dismissed here, and the symbols are harmonized with those used in the Eurocode 5 draft [8].

Row shear resistance of a wood member,  $F_{rs,CSA}$ , is determined as the product of the minimum side shear plane resistance of a fastener row and the number of fastener rows  $n_{90}$ :

$$F_{rs,CSA} = n_{90} F_{rs,j,CSA} \quad (11)$$

where  $F_{rs,j,CSA}$  is the row shear resistance per row of fasteners (including two shear planes) in the timber member.

The block shear (group tear-out in CSA O86) resistance of a wood member,  $F_{bs,CSA}$ , is determined as the sum of the row shear resistance of the first,  $F_{rs,1,CSA}$ , and the last row,  $F_{rs,nR,CSA}$ , divided by two and head tensile plane resistance of the critical net area between the first and the last rows,  $F_{t,CSA}$ , (the critical net area is the net width of the connection multiplied by the member thickness):

$$F_{bs,CSA} = [F_{t,CSA} + (F_{rs,1,CSA} + F_{rs,nR,CSA})/2] \quad (12)$$

In single-shear, three-member connections with STS installed from both sides, the central (point-side) member is considered as fully penetrated and  $F_{bs,CSA}$  shall be checked.

Plug shear resistance of a partially penetrated wood member (sawn timber and glulam),  $F_{ps,CSA}$ , is determined as the greater of the sum of head tensile plane resistance,  $F_{t,CSA}$ , and bottom shear plane resistance,  $F_{v,b,CSA}$ , and the sum of the row shear resistance of the first,  $F_{rs,1,CSA}$ , and the last row,  $F_{rs,nR,CSA}$ , divided by two:

$$F_{ps,CSA} = \max \left\{ \begin{array}{l} F_{t,CSA} + F_{v,b,CSA} \\ \frac{(F_{rs,1,CSA} + F_{rs,nR,CSA})}{2} \end{array} \right. \quad (13)$$

## INTER / 57 - 7 - 8

Step shear resistance,  $F_{ss,CSA}$ , is determined as the sum of head tensile plane,  $F_{t,CSA}$ , and bottom shear plane resistance,  $F_{v,b,CSA}$ :

$$F_{ss,CSA} = (F_{t,CSA} + F_{v,b,CSA}) \quad (14)$$

The head tensile plane resistance is determined as:

$$F_{t,CSA} = f_{t,0} b_{net} t_{ef} \quad (15)$$

where  $f_{t,0}$  is the specified strength in tension parallel to grain,  $b_{net}$  is the critical width of head tensile plane and  $t_{ef}$  effective depth of head tensile plane.

The row shear resistance is determined considering side shear planes on both sides of the fastener row as:

$$F_{rs,CSA} = K f_v L_s t_{ef} \quad (16)$$

where  $f_v$  is the specified longitudinal shear strength,  $L_s$  is the critical length of side shear plane and  $t_{ef}$  is the effective depth of head tensile plane, with  $L_s = n_{90} a_{cr}$  where  $a_{cr}$  is the minimum of end distance and the spacing of fasteners in a row parallel-to-grain.

The factor  $K$  is 1.2 (2 x 0.6) for bolts and dowels, and 1.5 (2 x 0.75) for STS. The effective depth  $t_{ef}$  is obtained as  $t_{ef} = K_{ls} t_i$  for bolts and dowels, being  $K_{ls} = 0.65$  for side members, and  $K_{ls} = 1.0$  for inner members and for the head tensile plane. For partially penetrated wood members, the effective depth of the head tensile and side shear planes,  $t_{ef}$ , is determined as:

$$t_{ef} = \alpha_{cl} \left( \frac{7t_h}{3 + \frac{t_h}{d}} \right) \leq t_h \quad (17)$$

which is the same as in the Eurocode 5 draft (see equation (9) in Section 2.1).

The bottom shear plane resistance is determined as:

$$F_{v,b,CSA} = f_v A_{p, sb} = f_v L_s b_{con} \quad (18)$$

where  $A_{p, sb}$  is the critical area of bottom shear plane, considering the length  $L_s$  based again on  $a_{cr}$ , and the connection width  $b_{con}$ .

## 3 Discussion

### 3.1 Comparison between Eurocode 5 draft and CSA O86:24

The comparisons discussed in this section pertain to the predictions of the mean resistance values. The additional differences between load and resistance factors used in European and Canadian codes are beyond the scope of this paper. The main differences between the two standards are:

1) CSA O86 distinguishes between the type of fastener, mainly bolts/dowels vs. STS, while the Eurocode 5 draft only differentiates based on the penetration type.

2) Regarding the geometry of the failure planes, the standards differ in the calculation of the parallel-to-grain length of the side and bottom shear planes. While the Eurocode 5 draft uses the actual connection length, CSA O86 uses the distance based on the minimum of the parallel to grain spacing and the edge distance.

3) The effective depth of failure planes for plug shear is calculated using the same approach in the case of STS. However, for bolts and dowels, CSA O86 provides a fixed thickness ratio based on the member boundary condition (inner or outer), whereas in the Eurocode 5, the ratio depends on the fastener slenderness. In both standards the same limits apply to the effective depth ratio: 0.65 and 1.0.

4) Both standards use pre-factors for tensile and shear strength, and in the case of screws, the same values are used for glulam; however, for other products, Eurocode 5 provides different values. And for bolts and dowels, CSA O86 considers a lower factor of 0.6 for shear strength, and no factor is applied for the tensile strength.

5) The approaches differ in the calculation of the block shear (group tear-out) resistance. CSA O86 adds the resistance of head tension and side shear planes, while Eurocode 5 draft combines the resistance of all the planes only for reinforced connections. For unreinforced connections, Eurocode 5 draft considers the maximum of the head tension and side shear plane resistance in block shear. For plug shear, both CSA O86 and Eurocode 5 draft consider the maximum resistance between side shear planes and the head and bottom planes.

6) CSA O86 includes some additional considerations, which are not found in Eurocode 5 draft: step shear and row shear failure modes for STS, and an additional block shear check of internal member partially penetrated from both sides.

### 3.2 CSA O86:24 experimental validation for STS

To evaluate the predictive capability of the CSA O86 design approach for STS connections with partially penetrated wood members, two series of connection tests were conducted by FPInnovations, including both glulam and CLT [15,16] (CLT results are not included in the comparisons presented in the following sections).

In the first series, 8 mm and 12 mm diameter STS were tested. The number of fasteners in connection ranged from 6 to 16. Though brittle failure modes were 'forced' via a reduced spacing perpendicular to grain and end distance, 14 of the 18 groups had first failure due to yielding of the fasteners. It was also noted that the proposed design approach, based on the work of Yurrita and Cabrero [9-11], significantly underestimated the failure load.

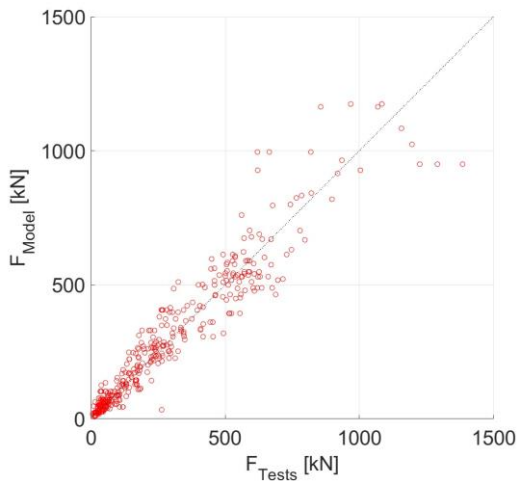
The second series of connection tests was conducted with 3 groups of glulam and 9 groups of CLT specimens using the same test setup. Only 12 mm diameter STS were tested in a staggered fastener pattern, with the number of fasteners ranging from 12 to 23, and the fastener spacing was again reduced from the minimum requirements [7]. A key observation from the second test series was the accurate prediction of failure modes and adequate predictions of load-carrying capacities. These tests led to some major deviations in the CSA O86 STS design provisions from the proposed model by Yurrita and Cabrero [9-11]: the calculation of the effective depth could be simplified, and the plastic effective depth was removed from the provisions.

### 3.3 Validation with an expanded experimental database

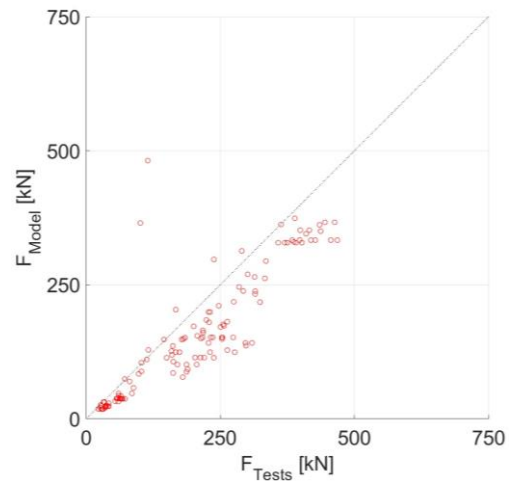
Additional tests from literature [19-40] were incorporated to expand the database originally used by Yurrita and Cabrero [9-11]. This expanded database was used for a re-validation of Yurrita's original model and to verify the approaches in each standard. The expanded database incorporated 194 additional tests in the case of full penetration, and 39 additional tests for partial penetration. The expanded database contains tests with both brittle (86%) and ductile (14%) failures of connections in double shear configurations (31% steel-wood-steel, 21% wood-wood-wood, 14% wood-steel-wood), 21% multiple shear plane configurations, and 13% single shear (12% wood-steel, 1% wood-wood). Most (56%) of the tests were glulam, the rest being solid lumber (27%) and LVL (17%). Regarding the type of fasteners, bolts (22%) and dowels (50%) are the most represented, with a reduced representation of nails (11%), screws (10%) and rivets (7%).

The validation was done, as in previous works [9-11], at the mean level. Consequently, the same values and procedures as described by Cabrero et al. [17] were used in those cases where the actual material properties were not provided in the references. The performance comparison of the models is based on the metrics described in [18]. The influence of the different applicable factors and design provisions and their effect on the failure mode at the characteristic and design level deserve a separate discussion.

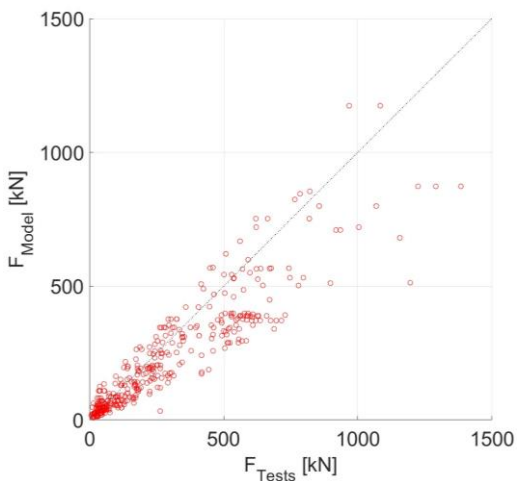
For ease of explanation, the results for full penetration and partial penetration of fasteners are separated. Resulting metrics for the original model and both standards are given in Table 1, while the resulting comparison plots are shown in Figure 4.



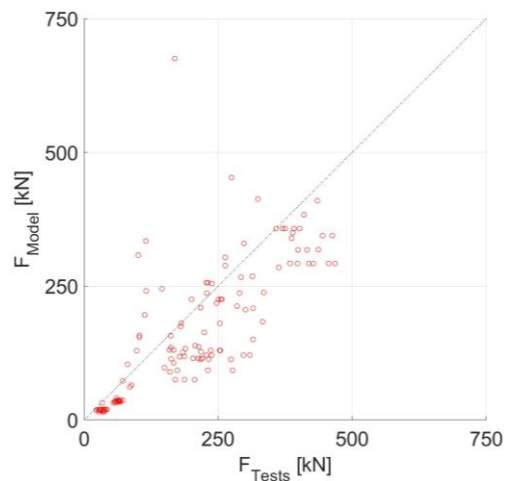
a) Full penetration, Yurrita and Cabrero[10]



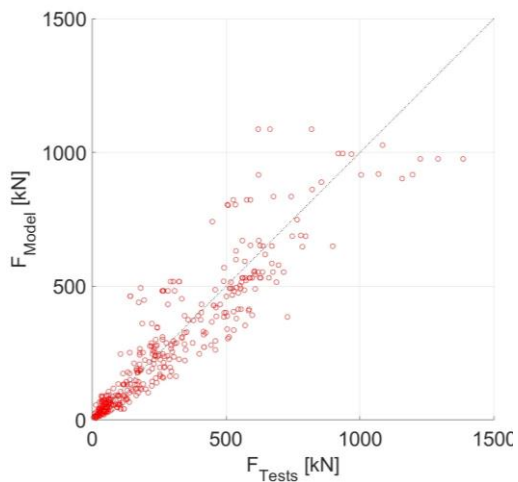
b) Partial penetration, Yurrita and Cabrero [11]



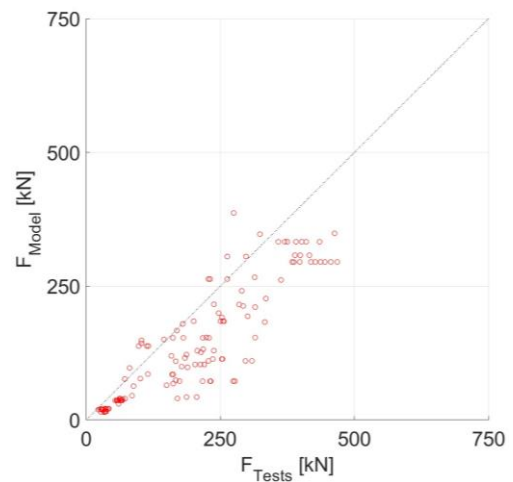
c) Full penetration, EC5 draft [8]



d) Partial penetration, EC5 draft [8]



e) Full penetration, CSA O86 [7]



f) Partial penetration, CSA O86 [7]

Figure 4. Comparison of experimental results and predicted results by each of the models. Left column: full penetration; right column: partial penetration; rows (starting above): a), b), original model by Yurrita and Cabrero [10,11]; c), d), Eurocode 5 [8]; e), f), CSA [7]. Only tests considered as brittle failure in the database are included.

Table 1. Metrics obtained for the different models for the results shown in Figure 4.

Fastener penetration	Model	R <sup>2</sup>	Mean Relative Error	Standard Deviation Error	Slope through origin	Correlation coefficient	Conc. Corr. Coef.
Full penetration	Yurrita [10]	0.91	0.18	0.22	0.98	0.96	0.95
	EC5 [8]	0.78	0.28	0.33	0.77	0.94	0.87
	CSA [7]	0.84	0.22	0.28	0.94	0.95	0.92
Partial penetration	Yurrita [11]	0.50	0.30	0.35	0.79	0.90	0.75
	EC5 [8]	0.50	0.33	0.33	0.80	0.85	0.75
	CSA [7]	0.58	0.33	0.26	0.71	0.90	0.78

### 3.4 Full penetration tests

Overall, the model proposed by Yurrita and Cabrero [10] provides the best predictions. It consistently achieves the best performance across all used metrics. Among the standards, CSA O86 [7] generally shows better performance than the Eurocode 5 draft [8], as evidenced by the Concordance Correlation Coefficient (CCC) factor. The Eurocode 5 draft [8] is more conservative, as indicated by the lowest slope through the origin. This conservatism is consistent with the Eurocode's 5 approach of adopting the maximum resistance of individual failure planes, instead of combining them. Both standards exhibit similar performance in the remaining metrics.

### 3.5 Partial penetration tests

In the case of the partial penetration, the model from the CSA O86 [7] exhibits the best general performance (highest CCC), closely followed by the original model [11] and the Eurocode 5 draft [8]. The original model produces the lowest error, while the Eurocode 5 draft results in the highest slope, although still conservative.

Both standards consider only the elastic effective depth, and conversely to the original model, the outer member condition for it (which results roughly in half the depth in comparison to the one originally proposed). Additional differences appear in the consideration of the bottom shear plane area, which is taken as the actual area in Eurocode 5 draft, whereas its length is reduced (based on the critical dimension) in CSA O86. The original model [11] reduced this bottom area by considering the net width.

## 4 Conclusions

The latest Eurocode 5 draft and CSA O86:24 provide detailed provisions for brittle failure modes of connections with dowel-type fasteners loaded parallel to the grain. Some of the implemented and proposed provisions are the results of an extensive exchange between working groups from Europe and Canada aimed at ensuring consistency

within the standards. The resolution of various issues necessitated further clarification and analysis, and among others, two main technical issues have been addressed:

1. The effective depth, as proposed by Yurrita, was modified for consistency within Eurocode 5. The originally proposed linear simplification, which resulted in kinks in the observed effective depth, was revised to a rational formulation and adopted in both standards.
2. The relevance of the plastic effective depth was found to be minimal in most cases. Additionally, since brittle failure is only relevant if its failure load is lower than the ductile capacity (obtained through the EYM), only the elastic effective depth from the original model has been retained in the standards.

The re-evaluation of the original design models using an extended database shows how the modifications introduced in the models for their inclusion in the standards led to conservative estimates of the connection capacities. Despite some differences in the implementation in the standards, relatively similar predictions are observed in both standards when compared to the experimental database from literature.

Despite extensive exchange between working groups from Europe and Canada, differences remain between the two standards, which require further harmonisation:

1. Differences between bolts/dowels and STS in CSA O86;
2. The calculation of the parallel-to-grain length of the shear planes;
3. Pre-factors used for tensile and shear strength;
4. The calculation of the block shear (group tear-out) resistance of unreinforced connections;
5. The lack of consideration in Eurocode 5 of step shear and row shear failure modes for partially penetrating fasteners; and
6. Block shear check of internal member partially penetrated from both sides.

## Acknowledgments

The Spanish authors would like to acknowledge the financial support provided by the Spanish Ministerio de Ciencia e Innovación and Fondo Europeo de Desarrollo Regional under contract PID2020-118569GB-C21 MINECO/FEDER UE. The Canadian test programs were supported by the Natural Sciences and Engineering Research Council (NSERC) of Canada and FPIInnovations.



## References

- [1] Johansen, K.W., Theory of timber connections. *Int Assoc Bridge Struct Eng* 9 (1949), 249–262,
- [2] EN 1995-1-1 (2004) Eurocode 5. Design of timber structures - Part 1–1: General - Common rules and rules for buildings. Comité Européen de Normalisation (CEN), Brussels, Belgium.
- [3] CSA. (2009) Engineering design in wood. CSA O86 – 2019. Canadian Standards Association, Mississauga, Ontario, Canada.
- [4] Hossain A et al. (2018) Group-effect of self-tapping screws in cross-laminated timber shear connections. INTER 51-07-11.
- [5] Mohammad, M., Quenneville, J. H. P. (2001). Bolted wood-steel and wood-steel-wood connections: Verification of a new design approach. *Canadian Journal of Civil Engineering*, 28(2), 254–263.
- [6] Quenneville, J., Mohammad, M. (2000). On the failure modes and strength of steel-wood-steel bolted timber connections loaded parallel-to-grain. *Canadian Journal of Civil Engineering*, 27, 761–773.
- [7] CSA (2024) Engineering design in wood. CSA O86 – 2024. CSA Group, Toronto, ON, Canada.
- [8] CEN/TC250/SC5/WG5 (ed.) (2024) (unpublished) N619 prEN 1995-1-1 v0 to v1A. Connections, in Eurocode 5: Design of timber structures – Part 1-1: General rules – General rules and rules for buildings. Comité Européen de Normalisation, Brussels, Belgium. Status: 18-7-2024
- [9] Yurrita M., Cabrero J. M. (2019) Effective Thickness of the Wood Member in a Timber-to-steel Connection with Large Diameter under Brittle Failure. INTER 52-7-5.
- [10] Yurrita, M., Cabrero J. M. (2019) New Analytical Model for Brittle Failure in the Parallel-to-grain Direction of Timber Connections with Large Diameter Fasteners. INTER 52-7-7.
- [11] Yurrita M., Cabrero J. M. (2021) New Analytical Model for Plug Shear of Timber Connections with Small Diameter Dowel-Type Fasteners in the Parallel-to-Grain Direction. INTER 54-7 10.
- [12] Teichmann S. (2023) Summary of the main results of the Master's thesis: Brittle failure modes in timber connections with laterally loaded fasteners. A comparison of design proposals. KIT.
- [13] Teichmann, S. (2024) Analysis of the corrected Draft: Brittle failure modes in timber connections with laterally loaded fasteners. Comparison of the EC5, the Draft and the corrected Draft.

- [14] CEN (2023) prEN 1995-1-1 Eurocode 5 for Formal CEN enquiry. Eurocode 5: Design of timber structures – Part 1-1: General rules – General rules and rules for buildings. Comité Européen de Normalisation, Brussels, Belgium.
- [15] Ni C., Niederwestberg J. (2022) Investigation of brittle failure modes in self-tapping screw steel to wood connections parallel to the grain. Project Number 301014606 Report. FPInnovations, Vancouver, Canada.
- [16] Ni C., Niederwestberg J. (2022) Investigation of brittle failure modes in self-tapping screw steel to wood connections parallel to the grain – Part 2. Project Number 301015178 Report. FPInnovations, Vancouver, Canada.
- [17] Cabrero, J.M., Honfi, D., Jockwer, R., Yurrita, M. (2019) A probabilistic study of brittle failure in dowel-type timber connections with steel plates loaded parallel to the grain. *Wood Material Science and Engineering*, 14 (5), pp.298-311.
- [18] Cabrero, J.M., Yurrita, M. (2018) Performance assessment of existing models to predict brittle failure modes of steel-to-timber connections loaded parallel-to-grain with dowel-type fasteners. *Engineering Structures*, 171, pp. 895-910.
- [19] Anderson, G. T. (2001). Experimental investigation of group action factor for bolted wood connections. Virginia Polytechnic Institute and State University.
- [20] Baird, Z., Woods, J. E., Viau, C., Doudak, G. (2024). Cyclic Behavior of Bolted Glued-Laminated Timber Brace Connections with Slotted-In Steel Plates. *Journal of Structural Engineering*, 150(7).
- [21] Bocquet, J. F. (2022). Campagne d'essais visant à caractériser la raideur d'assemblages courants de structures en bois. Private communication.
- [22] Breijinck, T., Woods, J. E., MacDougall, C. (2023). Behaviour of small-scale glulam timber connections with slotted-in steel plates and dowel-type fasteners reinforced with self-tapping screws. *Construction and Building Materials*, 402.
- [23] Danielsson, H., Crocetti, R., Gustafsson, P. J., Serrano, E. (2016). Brittle failure modes in nailed steel plate connections. *World Conference Timber Engineering*.
- [24] Dodson, M. A. (2003). The effects of row spacing and bolt spacing in 6-bolt and 4-bolt wood-to-steel connections. Washington State University.
- [25] Ehlbeck, J., Werner, H. (1989). Tragverhalten von Stabdübeln in Brettschichtholz und Vollholz verschiedener Holzarten bei unterschiedlichen Rißlinienanordnungen.
- [26] Ehlbeck, J., Werner, H. (1992). Tragfähigkeit von Laubholzverbindungen mit stabförmigen Verbindungsmitteln.
- [27] Hanhijarvie, A., Kevarinmaki, A. (2008). Timber failure mechanisms in high-capacity dowelled connections of timber to steel. VTT Technical Research Centre of Finland.
- [28] Hübner, U. (2013). Mechanische Kenngrößen von Buchen-, Eschen- und Robinienholz für lastabtragende Bauteile. Technische Universität Graz.

- [29] Iraola, B. (2016). Simulación del comportamiento mecánico de la madera en uniones estructurales y su aplicación mediante modelos tridimensionales de elementos finitos. Universidad de Navarra.
- [30] Jensen, J. L., Quenneville, P. (2011). Experimental investigations on row shear and splitting in bolted connections. *Construction and Building Materials*, 25(5), 2420–2425.
- [31] Johnsson, H. (2004). Plug shear failure in nailed timber connections: Experimental studies [Lulea University of Technology]. In International Council for Research and Innovation in Building and Construction.
- [32] Jorissen, A. (1998). Double shear timber connections with dowel type fasteners. Technische Universiteit Delft.
- [33] Kevarinmäki, A. (2009). Design method for timber failure capacity of dowelled and bolted glulam connections.
- [34] Massé, D. I., Salinas, J. J., Turnbull, J. E. (1988). Lateral strength and stiffness of single and multiple bolts in glued-laminated timber loaded parallel to grain.
- [35] Mischler, A. (1998). Bedeutung der Duktilität für das Tragverhalten von Stahl-holz-bolzenverbindungen. ETH Zürich.
- [36] Misconel, A., Ballerini, M., Van De Kuilen, J.-W. (2016). Steel-to-timber joints of beech-LVL with very high strength steel dowels. World Conference on Timber Engineering.
- [37] Sjödin, J., Johansson, C. J. (2007). Influence of initial moisture induced stresses in multiple steel-to-timber dowel joints. *Holz Als Roh - Und Werkstoff*, 65(1), 71–77.
- [38] Yurrita, M., Cabrero, J. M. (2021). Experimental analysis of plug shear failure in timber connections with small diameter fasteners loaded parallel-to-grain. *Engineering Structures*, 238.
- [39] Yurrita, M., Cabrero, J. M., Quenneville, P. (2019). Brittle failure in the parallel-to-grain direction of multiple shear softwood timber connections with slotted-in steel plates and dowel-type fasteners. *Construction and Building Materials*, 216, 296–313.
- [40] Zarnani, P., Quenneville, P. (2015). Group tear-out in small-dowel-type timber connections: Brittle and mixed failure modes of multinail joints. *Journal of Structural Engineering*, 141(2).

## DISCUSSION

The paper was presented by J M Cabrero

*C Sandhaas commented that since the presented approach would be intended as the main model for EC5 one should carefully scrutinize the approach. The model would only be as good as its validation. C Sandhaas questioned how the experimental data was evaluated to calibrate the proposed model as in most resources either necessary information is missing or the evaluation was done on different levels of deformation. She questioned that the failure modes stated in the paper could be properly differentiated from the information in the original reports. C Sandhaas pointed out a range of issues including the use of reinforced connections to validate the approach, how splitting was considered, about factors such as the  $k_t$ -factor being fiddle factors, why some data were culled and how mixed failure types between beginning fastener yielding and brittle failure were treated. C Sandhaas received confirmation that there was no model verification.*

*P Dietsch commented that a collaborative approach would be needed.*

*H Blass questioned the robustness of the approach to achieve desired safety for all cases. He has little trust in some of the used references. He stated that an upper bound should not be introduced but a lower bound should be used in Eurocode 5.*

*T Tannert said that the Canadian code was set based on 30 tests or so. Here 400 data points were considered with relatively comparable design models.*

*U Hübner commented about the project team and working group contributing to this work and urged for collaboration.*

*H Blass commented that some tests were not appropriate and collaboration on this basis would not make sense.*







# Reinforcements for compression perpendicular to grain of CLT elements with fully threaded screws: experimental validation of the design model

Roland Maderebner, University of Innsbruck, Unit of Timber Engineering

Thomas Stieb, University of Innsbruck, Unit of Timber Engineering

Linda Rathiens, University of Innsbruck, Unit of Timber Engineering

Roberto Tomasi, Norwegian University of Life Science

Keywords: Cross laminated timber, point loading, compression perpendicular to grain, reinforcement with screws

## 1 Introduction

In principle, cross laminated timber (CLT) allows the realization of large-area panels with point supports, using a concept similar to that of reinforced concrete pilotis constructions (e.g. the Dom-INO house concept proposed by Le Corbusier). In addition to the increased stresses around the point support, the column loads may also need to be transferred through the slab in multi-storey buildings (cf. Figure 1).

However, with this technological solution, a punching failure mechanism could occur due to concentrated loads at the end grain of the columns. This mechanism is related to the compression perpendicular to the grain (abbreviation in this article: CPG) and rolling shear. In this case, it may be necessary to use appropriate reinforcement systems to avoid excessive deformation due to the crushing of the wood fibres.

*Bejtka & Blass* (2006) have shown a way to significantly increase the resistance of the wood perpendicular to the grain by using fully threaded screws as a reinforcement. This approach was extended in the technical approval Z-9.1-519 (2014) to transfer loads through timber elements by using screws on the two opposite face sides in timber elements with an overlapping length of at least  $10 d$ . The findings of *Rodemeier* (2018) and *Dietsch et al.* (2019) to transfer loads via fully threaded screws for solid timber and glulam were further included within the prEN 1995-1-1 (2024). The experimental study presented in the following demonstrates that the corresponding model can also be used to transfer loads perpendicularly through CLT members.



In addition, it illustrates how the arrangement and spacing of screws influence the overall load-bearing capacity and how stiffness can be enhanced through this type of reinforcement.

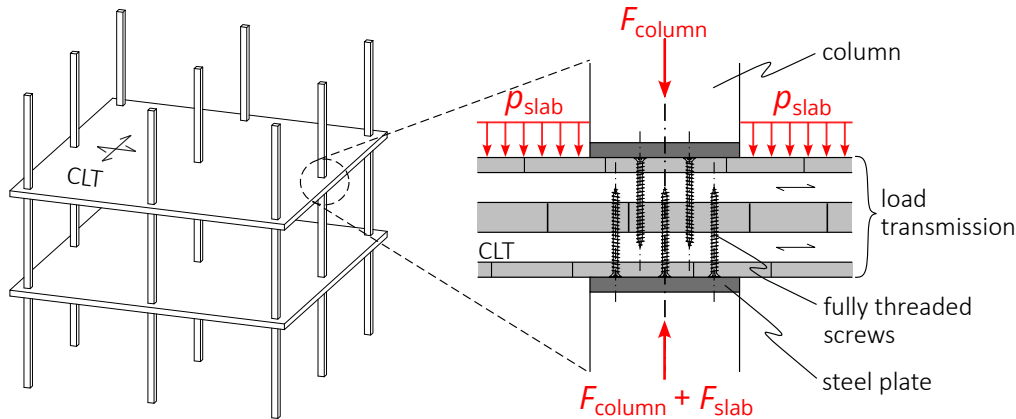


Figure 1. Load transmission in point-supported CLT slabs – reinforcement using self-tapping screws

## 2 Analytical model according to prEN 1995:2024

By the specifications in prEN 1995-1-1 (2024), the resistance of softwood members under compression perpendicular to the grain can be increased by using reinforcements. In the design concept to determine the resistance, three different failure mechanisms, according to *Bejtka & Blaß* (2004) (cf. Figure 2), must be taken into account:

- Failure at the level of the screw head, pushing of screws into the wood – mode I
- Failure at the level of the screw head, buckling of screws – mode II
- Failure at the level of the screw tip, CPG of the wood – mode III

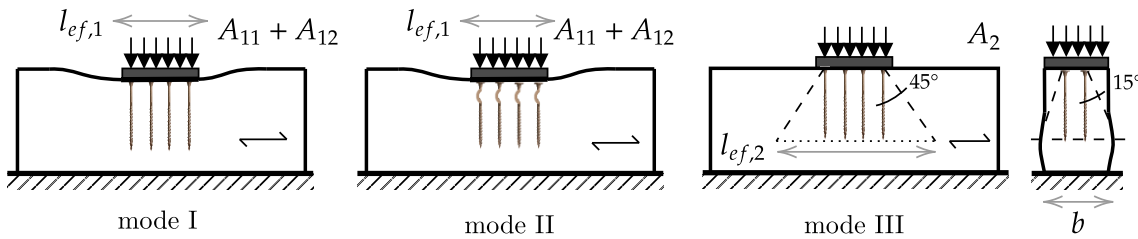


Figure 2. Failure modes for CPG reinforced solid timber and glulam with fully threaded self-tapping screws

The current draft of Eurocode 5 (prEN 1995-1-1, 2024) provides the capacity model for solid wood products under CPG with screw reinforcement based on the model of *Bejtka* (cf. equation (1)). The main differences from the proposal in *Bejtka* (2005) are the simplified consideration of an indirect load introduction and the modified calculation models for the axial screw load-bearing capacities.

$$F_{c,90,Rk} = \min \begin{cases} k_{mat} \cdot b_{c,90} \cdot l_{ef,1} \cdot f_{c,90,k} + n \cdot \min\{F_{w,k}, F_{c,k}\} = A_{11} + n \cdot A_{12} = A_1 \\ b \cdot l_{ef,2} \cdot f_{c,90,k} = A_2 \end{cases} \quad (1)$$

To realize a load transfer using this method, it is obvious to arrange the screws on both sides of the member with a certain overlap. This application is already included in the technical approval Z-9.1-519 (2014). *Rodemeier* (2018) carried out experimental and numerical investigations on glulam beams for applications of such reinforcements. Based on this work and further investigations in *Dietsch et al.* (2019) the reinforcement method with fully threaded screws from both sides for load transmission is included in prEN 1995-1-1 (2024) for use in solid wood (ST) and glued laminated timber (GL) members. The load bearing capacity of a component reinforced on both sides can be calculated in the same way as in the reinforced ones with only one side. However, the failure mode  $A_2$  acc. to equation (1) can be omitted if the load is transferred successfully via the overlapping area of the screws. To ensure this transfer, some geometric boundary conditions are defined in prEN 1995-1-1 (2024) (cf. Figure 3, left). Thus, the contact areas and the screws should be arranged axially symmetric on both opposite sides, the screws overlap at least  $10 d$ , and the distance between the screw tip and the opposite contact area should be at least  $15 d$ . In addition, a minimum spacing of screws of  $5 d$  is recommended.

*Mayer* (2023) extended the application of two-sided reinforcement for CPG through experimental investigations to CLT. However, the recommended minimum values for the height of the wood component (residual length together with the overlap length) of  $h_{\min} = 40 d$  are practically hard to meet with CLT. Therefore, *Mayer* (2023) defined geometric boundary conditions depending on the CLT height and minimum screw diameters based on experimental findings. According to this work, the overlap length  $l_{\text{lap}}$  should be at least  $0,5 \cdot t_{\text{CLT}}$  and the residual length at least  $0,1 \cdot t_{\text{CLT}}$  (cf. Figure 3, right) which also considers the allowed maximum deformations in the ultimate limit state according to Table 8.1 prEN 1995-1-1 (2024). Furthermore, it can be assumed that the effective contact length  $l_{\text{ef},1}$  is similar to an unreinforced cross laminated wood element. It has been shown that increasing the overlap length results in higher load capacities, and failure mode II (screw buckling) consistently happens in the first or second layer of the CLT element perpendicular to the grain direction.

### 3 Experimental campaign

The test setups and specimens were chosen to investigate the influence of screw diameter, screw number, and spacing on load bearing capacity and the stiffness of the connection. Furthermore, the increase in stiffness of the CLT element perpendicular to the plane is also investigated as a result of the reinforcement.

Due to the work of *Mayer* (2023) on the influence of the overlap length, residual length, and CLT-layup, these parameters were assumed constant for the presented investigations. For the tests, we used CLT according to ETA-20/0843 (2020) made from European Spruce with a thickness of  $t_{\text{CLT}} = 160$  mm with edge glue and without relief grooves. The CLT layout was fixed to 5 layers (40 | 20 | 40 | 20 | 40). When the test samples were

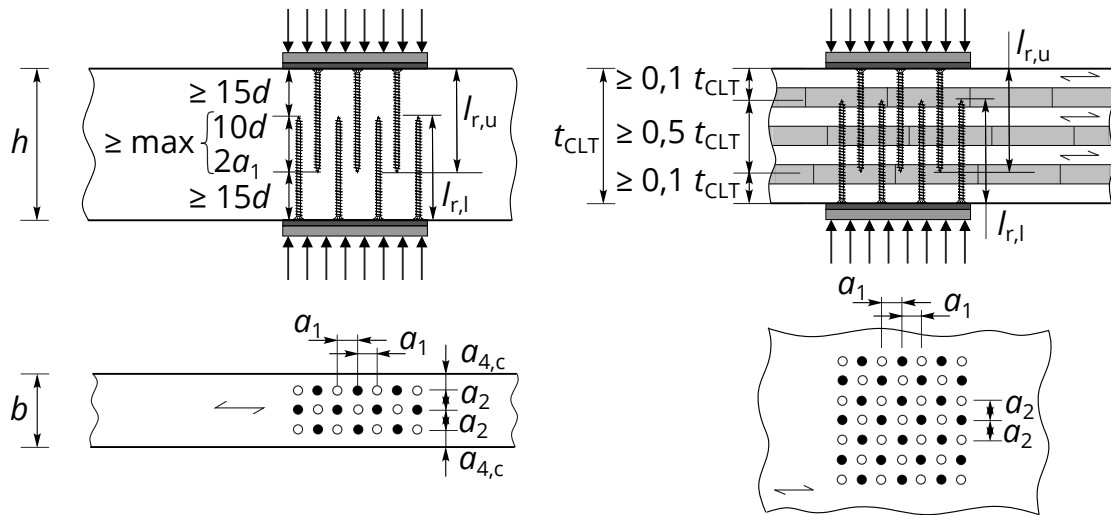


Figure 3. Geometric requirements for ST, FST, GST, GL and BGL (prEN 1995-1-1 (2024)) (left) and a proposal for CLT Mayer (2023) (right)

selected, it was ensured that the effects of knots and cracks were minimized. The CLT was conditioned in a climate chamber under standard conditions (20 °C and 65 % relative humidity EN 408 (2012)) before and after cutting the samples. Before the screws were driven-in, the gross density of each specimen was determined. The moisture content of the CLT samples was measured after tests on the entire test sample using the oven drying method EN 13183-1 (2003).

To reinforce the CLT specimens we use fully threaded screws according to ETA-21/0751 (2022) with a nominal diameter of  $d = \{8; 10\}$  mm and a length of  $l = 120$  mm. This allowed us to fulfill the geometric requirements according to Mayer (2023) (Figure 3, right) and to exclude buckling failure (failure mode II, cf. Figure 2) due to the low slenderness of the screws.

The edge distance  $a_{3,c}$  was set to  $6d$  according to prEN 1995-1-1 (2024) and ETA-21/0751 (2022). To prevent lamellae from splitting in samples with  $d = 10$  mm even without predrilling, the minimum edge distance  $a_{4,c}$  was increased from  $2,5d$  (acc. to prEN 1995-1-1 (2024) and ETA-21/0751 (2022)) to  $3,5d$  for all test specimens. The distances between the screws ( $a_1$  and  $a_2$ ) were varied between  $2d$ ,  $4d$  and  $8d$ . In contrast to the specifications in prEN 1995-1-1 (2024), the values for  $a_1$  and  $a_2$  were not distinguished and identical values were used for all CLT samples. This determination was chosen because computer tomography images of the test specimens in Rathiens (2023) showed that damage to the wood matrix in the grain direction occurred in all layers when the screws are inserted.

The test setups used can be divided into two main types (see Figure 4). In the so-called »Torx tests«, the load is applied directly to the screw head by a Torx bit. The bitholder, a steel cylinder, is equipped with a complete bridge strain gauge to determine the load on each of the individual screws. In addition, inductive displacement transducers (LVDTs) are placed on the top of the test specimen to measure the relative displacement

between the screw head and the wood surface. Due to the pure loading of the screw within this test setup, the first part of equation (1)  $A_{11}$  could be neglected (Tomasi et al., 2023).

The second type of test is the plate test. In these tests, the load is applied to the entire surface of the specimen via a steel plate. The deformation of the test samples is determined using a 2D optical measuring system (digital image correlation (DIC)) on the edge surfaces of the samples. Due to the loading of the entire test specimen by the steel plate in this set-up, the wood also acts in addition to the screws ( $A_{11} + n \cdot A_{12}$ , according to equation (1)).

A steel plate and a spherical calotte are arranged on the bottom of the test specimen in both setups. The calotte is fixed with four adjustment screws after applying a preload to compensate for any unevenness of the test specimens.

These specifications lead to the series summarized in Table 1 and shown in Figure 5.

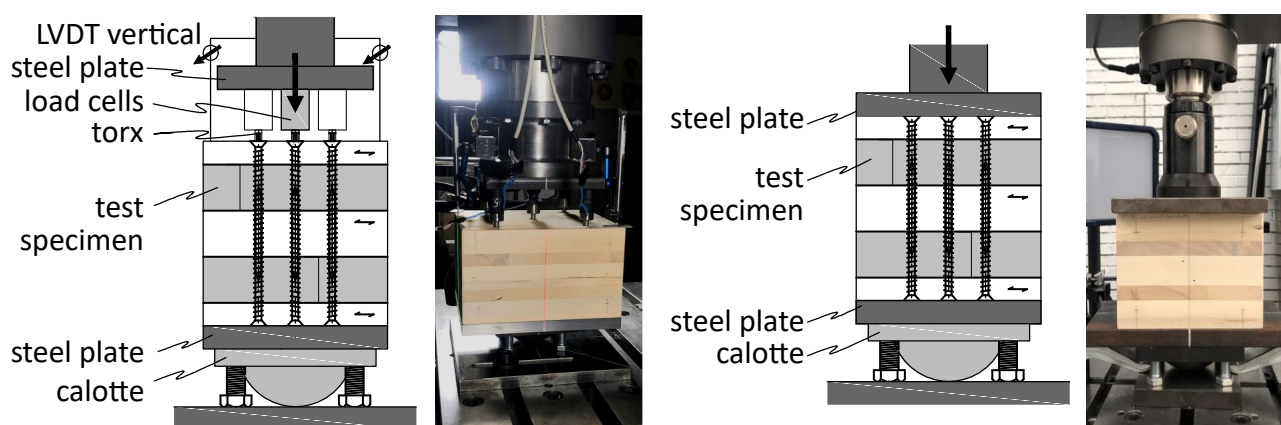


Figure 4. Torx type test for single screw or group of screws (left), plate type test for a group of screws (right)

Table 1. Overview of the different test series and the number of specimens. Each »series«, has a certain number of »subseries« with a variation of the reinforcement. Some specimens were tested twice (first stiffness (non destructive) then resistance, number of specimens in total 264 and amount of tests 398.

Series	Subseries	Number	Test type	Parameter	Factor considered
S1-○	2	17	Torx	resistance	reference test (single screw)
S2-○	6	55	Torx	resistance	influence spacing $a_1$ (2,4,8) $d$
S3-○	6	60	Torx	resistance	influence of spacing $a_2$ (2,4,8) $d$
S4-	6	62	Torx	resistance	influence of screw number and arrangement
S5-x-a	6	68	Plate	stiffness	MOE unreinforced
S5-x-b	6	68	Torx	stiffness	MOE reinforced
S5-x-c	6	32	Torx	resistance	influence of screw number and arrangement
S5-x-d	6	36	Plate	resistance	influence of screw number and arrangement

The S1-○ series is a reference test where a single screw is pressed into the CLT. In the S2-○ and S3-○ series, also only one screw is loaded via a Torx test, also reinforced with two screws inserted from the underside of the sample. The difference between these series is the orientation of the lamellas, which are rotated by 90 degrees. In the

S4-| series, two adjacent screws are loaded via the Torx test set-up, with two screw rows inserted from the bottom as reinforcement. The test procedure for the series S5-x consists of several investigations. In the first step of this series, the stiffness of the unreinforced CLT specimen was determined using plate tests, followed by the stiffness of the reinforced test body. *Rathiens* (2023) then determined the load carrying capacity in one part of the respective series using Torx tests and in the second part of the series using plate tests. In this series, the screws were inserted alternately from top and from bottom in a grid of 3 × 3 (5 screws from top, 4 screws from bottom). The number of different »subseries« (test specimens) (cf. Table 1) then results from the variation of the screw diameters ( $d = \{8; 10\}$  mm) – in all series – and the variation of the screw spacing among each other ( $a = \{2; 4; 8\} \cdot d$ ) – in all series with the exception of S1-○.

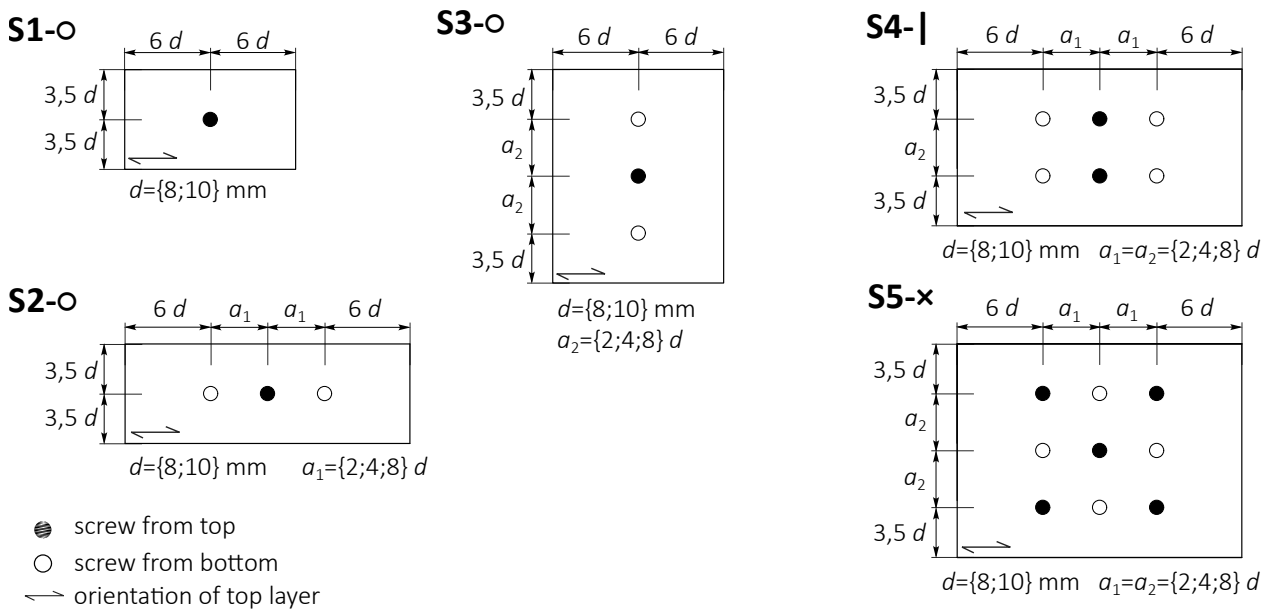


Figure 5. Series of the experimental campaign, top view

Due to the plastic failure of the wood under compression perpendicular to the grain direction, very large deformations can be achieved in the tests until a maximum load is reached. For this reason, a procedure based on EN 408 (2012) is used to determine the maximum load  $F_{max}$ . Here, an estimated maximum load  $F_{max,est}$  is used to calculate the gradient in the load-deformation curve between 10 % and 40 % of  $F_{max,est}$ . The slope is then shifted by 1 % of the reference height  $t_{CLT}$  and the point of intersection with the force displacement curve is taken as the maximum deformation. The maximum load  $F_{max}$  is then taken as the maximum value until this point. If the deviation between  $F_{max,est}$  and  $F_{max}$  is greater than  $\pm 5\%$ ,  $F_{max,est}$  is adjusted until this limit is reached. If not sufficiently large deformations occur due to a brittle failure, the maximum applied load is used  $F_{max,tot}$ .

The stiffness of the reinforcement in the Torx tests (cf. Figure 4) is determined on the basis of a linear regression in the load–deformation curve of the attached LVDTs between

10– and 40 % of the applied maximum load  $F_{\max}$ . In tests to determine the stiffness of the unreinforced (series S5–x–a) and reinforced (series S5–x–b) specimens, a two-dimensional optical measurement system was used on the two sides of the samples instead of the LVDT s. To ensure a non-destructive test method, the load was only applied up to a force of  $0,4 \cdot f_{c,90,k}$  (with  $f_{c,90,k} = 3,0$  MPa according to Annex K in OENORM B 1995-1-1 (2023)). To determine the stiffness, a linear regression of the entire load-displacement curve is then carried out according to the specifications given in EN 408 (2012).

## 4 Results and discussion

The main results of all studied series are summarized in Table 2. The determined wood moisture content  $u$  in all test specimens ( $u_{\text{mean}} = 11,5$  %;  $\text{COV} = 3,6$  %;  $u_{\text{min}} = 10,5$  %;  $u_{\text{max}} = 12,8$  %) as well as the achieved gross densities ( $\rho_{\text{mean}} = 440$  kg/m<sup>3</sup>;  $\text{COV} = 4,9$  %;  $\rho_{\text{min}} = 383$  kg/m<sup>3</sup>;  $\rho_{\text{max}} = 502$  kg/m<sup>3</sup>) vary only slightly between the individual series. However, to ensure comparability between the series, the results are adjusted to a gross reference density  $\rho_{\text{ref}}$  according to equation (2), with  $k = 0,8$ . The same procedure is chosen for the axial stiffness parameters  $K_{\text{ser}}$  of the screws, assuming a linear influence of the gross density (exponent  $k = 1,0$ ). Basically, the mean value from all test specimens ( $\rho_{\text{mean}} = 440$  kg/m<sup>3</sup>) is used as the reference gross density. For comparison of test data with the model (see Table 3), a reference gross density is used according to the characteristic density of the strength class CL24 (prEN 1995-1-1, 2024) ( $\rho_{12,\text{ref}} = 385$  kg/m<sup>3</sup>).

$$F_{\max,\text{ref}} = F_{\max} \cdot \left( \frac{\rho_{12,\text{specimen}}}{\rho_{12,\text{ref}}} \right)^k \quad (2)$$

In the S1–○ series, where a single screw was inserted into the test sample (Torx tests), the findings in Table 2 indicate a notably lower variance for the tests with a diameter of  $d = 10$  mm. This reduction in variance can be explained by the use of a drilling tip for that specific diameter, resulting in significantly reduced splitting forces.

Figure 6 presents the results of the series S1–○, S2–○ and S3–○ with one single loaded screw. The effects of distances  $a_1$  and  $a_2$  were analyzed based on these results. It was determined that there is no statistically significant influence of spacing on the load-bearing capacity of screws or on the orientation of the outer layers (Rathiens, 2023). Thus, a differentiation of screw distances depending on the grain orientation of the top layer is not necessary for this method of reinforcement.

Table 2. Summary of the main results of the test series. Where  $d$  is the nominal diameter of the screw;  $a$  is the spacing between the screws and  $n_{test}$  is the number of specimens for each series

Series	$d$ [mm]	$a_1, a_2$ [mm]	Test	$n_{test}$ [-]	$u_{mean}$ (COV) [%] (in %)	$\rho_{12,mean}$ (COV) [kg/m <sup>3</sup> ] (in %)	$F_{max,mean}$ (COV) [kN] (in %)	$K_{ax,mean}$ (COV) [kN/mm] (in %)
S1-○	8	-	Torx	10	11,2 (2,3)	423 (3,9)	18,5 ( 7,3)	23,6 (12,6)
	10	-		7	11,0 (1,5)	472 (3,7)	27,1 ( 3,8)	30,5 (12,7)
S2-○	8	$2 \cdot d$	Torx	10	11,6 (1,3)	407 (2,4)	19,1 (11,1)	22,4 ( 8,6)
		$4 \cdot d$		10	11,4 (1,5)	437 (4,8)	21,5 (13,2)	20,9 (12,2)
		$8 \cdot d$		10	11,5 (1,4)	436 (2,5)	22,3 ( 8,1)	20,6 (10,2)
	10	$2 \cdot d$	10	11,4 (3,1)	464 (2,9)	27,9 (14,9)	31,8 ( 5,5)	
		$4 \cdot d$	7	10,7 (2,3)	473 (4,1)	26,2 (12,5)	27,3 (14,5)	
		$8 \cdot d$	10	11,2 (2,9)	460 (3,6)	26,3 ( 9,6)	24,3 ( 6,4)	
S3-○	8	$2 \cdot d$	Torx	10	11,3 (2,7)	448 (2,6)	21,3 ( 7,4)	23,8 ( 7,6)
		$4 \cdot d$		10	11,7 (1,6)	450 (4,4)	22,0 ( 8,8)	21,1 ( 9,9)
		$8 \cdot d$		10	11,5 (1,4)	436 (2,2)	21,8 ( 5,7)	19,1 ( 7,9)
	10	$2 \cdot d$	10	11,5 (0,9)	430 (2,9)	26,3 ( 9,3)	30,3 (13,5)	
		$4 \cdot d$	10	11,9 (1,3)	451 (3,2)	26,8 ( 5,6)	25,9 ( 5,7)	
		$8 \cdot d$	10	12,0 (0,9)	446 (4,0)	27,2 (11,4)	23,3 (10,4)	
S4-	8	$2 \cdot d$	Torx	11	11,6 (0,7)	441 (5,1)	41,5 (10,4)	49,2 (15,6)
		$4 \cdot d$		11	11,3 (1,3)	451 (4,9)	47,6 (18,1)	52,0 (17,6)
		$8 \cdot d$		10	11,6 (1,1)	431 (4,0)	42,7 ( 5,5)	49,3 ( 7,0)
	10	$2 \cdot d$	9	12,5 (2,5)	427 (2,9)	49,2 ( 6,8)	56,0 (10,2)	
		$4 \cdot d$	9	11,9 (1,4)	427 (3,5)	47,8 ( 5,4)	51,2 ( 6,4)	
		$8 \cdot d$	12	12,1 (2,4)	432 (5,1)	49,4 ( 9,0)	51,8 (17,3)	
S5-x-c	8	$2 \cdot d$	Torx	6	10,8 (2,8)	431 (4,5)	97,0 ( 7,3)	135,6 (13,0)
		$4 \cdot d$		6	11,6 (3,5)	436 (7,5)	107,9 ( 5,7)	110,3 (12,1)
		$8 \cdot d$		6	11,3 (0,6)	452 (4,2)	107,2 ( 5,0)	125,9 ( 8,2)
	10	$2 \cdot d$	6	11,7 (1,2)	449 (1,4)	112,3 ( 8,3)	117,0 (23,5)	
		$4 \cdot d$	6	11,5 (1,6)	431 (4,0)	115,1 ( 6,0)	136,1 ( 7,4)	
		$8 \cdot d$	6	11,4 (1,3)	423 (2,8)	123,9 ( 3,6)	150,5 (13,2)	
S5-x-d	8	$2 \cdot d$	Plate	6	11,0 (0,9)	456 (3,7)	86,6 ( 8,1)	77,7 (17,3)
		$4 \cdot d$		5	11,8 (3,4)	436 (3,1)	115,8 (10,3)	116,4 (26,8)
		$8 \cdot d$		6	11,1 (0,4)	434 (3,1)	233,6 (10,2)	268,8 (13,7)
	10	$2 \cdot d$	5	11,7 (2,2)	432 (6,0)	125,6 ( 6,4)	143,5 ( 5,6)	
		$4 \cdot d$	5	11,9 (1,8)	428 (3,7)	159,3 ( 6,8)	181,8 (13,5)	
		$8 \cdot d$	5	11,4 (3,0)	443 (1,2)	283,0 ( 8,0)	399,3 (11,0)	
all specimens:				264	11,5 (3,6)	440 (4,9)		

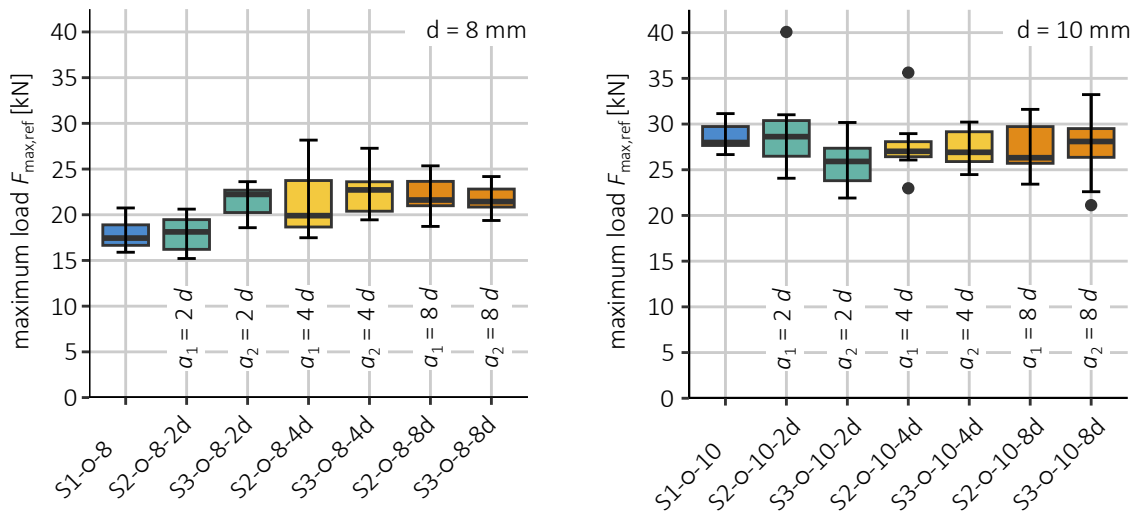


Figure 6. Results for series S1-O, S2-O and S3-O – Axial compressive resistance  $F_{\max, \text{ref}}$  –  $d = 8 \text{ mm}$  (left),  $d = 10 \text{ mm}$  (right),

To explore the effects of screw spacing and the quantity of loaded screws, Figure 7 presents the outcomes of the Torx tests from series S2-O, S3-O, and S4-|. In this scenario, the individual test load-bearing capacities  $F_{\text{test}, \text{max}, \text{ref}}$  are graphed relative to the factor  $n \cdot A_{12}$  as defined by Equation (1). To determine the factor  $n \cdot A_{12}$ , the outcomes of tests on a single screw in the non-reinforced specimen from series S1-O are utilized. Based on a mean density of  $\rho_{\text{mean}} = 440 \text{ kg/m}^3$ , average load-carrying capacities  $F_{S1-O, \text{mean}, \text{ref}}$  of 17,9 kN ( $d = 8 \text{ mm}$ ) and 28,6 kN ( $d = 10 \text{ mm}$ ) are obtained. These load-bearing capacities are then multiplied by the number of loaded screws  $n$ . Across all experiments, neither the distances ( $a_1$  and  $a_2$ ) nor the quantity of loaded screws appear to impact the results. In experiments involving five loaded screws, the variability of the results decreases considerably. This reduction is attributed to the homogenization effects caused by the higher number of loaded screws.

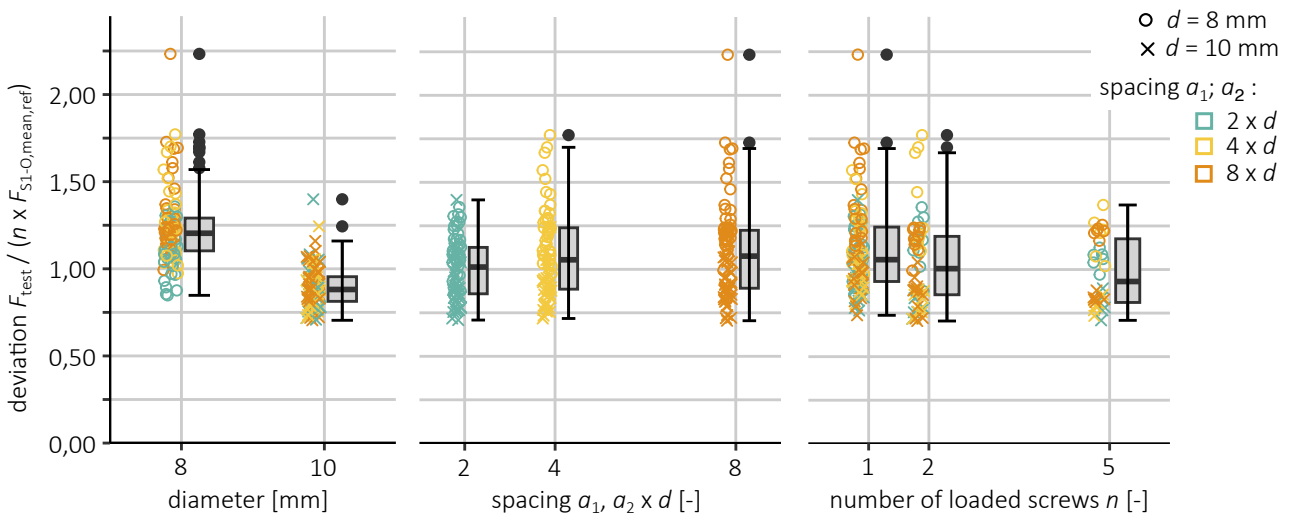


Figure 7. Comparison between  $F_{\text{test}, \text{max}, \text{ref}}$  and results from series S1-O ( $F_{S1-O, \text{mean}, \text{ref}}$ ) multiplied by number of loaded screws ( $n$ )



Although no influence of the number of loaded screws can be determined based on the results in Figure 7, the results of the load cells in the individual screws show varying loads (see Figure 8). After an initial alignment of the loading apparatus in the range of up to 1 mm deformation, a relatively constant load distribution is observed between the individual screws. However, in the range of maximum load, between 2 and 3 mm, the forces of the individual screws deviate by up to 30 % from each other. These deviations are attributed to different axial stiffnesses of the screws in the test specimen. However, due to the highly ductile behavior of the screws under compression, it is not necessary to consider an effective number of fasteners.

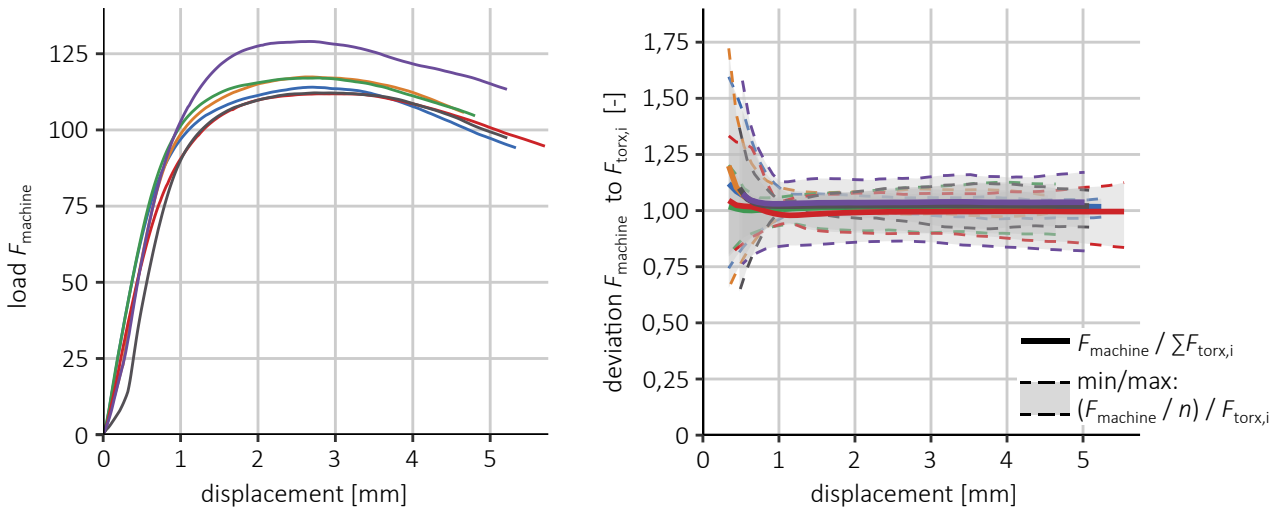


Figure 8. Series S5-x-c ( $d = 10 \text{ mm}$ ,  $a = 4 \cdot d$ ) – load deformation curve for the corresponding series (left) – deviation between the individual load of the screws  $F_{\text{torx},i}$  and the theoretical approach by  $F_{\text{machine}}/n$ , where  $n$  is the number of Torx-loaded screws (right)

To validate the design approach according to prEN 1995-1-1 (2024), the load-bearing capacities of series S5-x-d, plate tests are used, as these tests align with the subsequent application. The results of this validation are presented in Table 3. The characteristic load capacity  $F_{Rk, \text{test}}$  of the respective subseries was calculated according to the specifications outlined in EN 14358 (2016). To calculate the model, the factor  $k_{\text{mat}}$  was set at 1,0 and the dimensions  $l_{\text{ef},1}$  and  $b_{c,90}$  were selected according to the shape of the sample, which is that of a cube. This corresponds to the external dimensions of the CLT specimen. The relevant ETA document defines the characteristic compressive strength as  $f_{c,90,k} = 2,5 \text{ MPa}$ . The screw load bearing capacity for the failure mode designated as  $A_{12}$  was designed according to the specifications outlined in the associated ETA of the screws. The load-bearing capacities calculated by the design model are in good agreement with the experimental results. However, if the failure mode  $A_2$  were taken into account, the load-bearing capacities achieved with the model would be significantly underestimated. Thus, it can be inferred that the existing design method from prEN 1995-1-1, 2024 suggested for solid wood, which omits this mode when certain geometric criteria are fulfilled, is also applicable to CLT.

Table 3. Comparison of the characteristic load-carrying capacities of the experimental characterisation of series S5-x-d (plate tests) with the model according to prEN 1995-1-1 (2024). Where  $d$  is the nominal diameter of the screw;  $a$  is the spacing between the screws and SF is the safety factor

Series	$d$ [mm]	$a_1, a_2$ [mm]	$F_{k,test}$ [kN]	$A_{11}$ [kN]	$n \cdot A_{12}$ [kN]	$F_{k,prEN 1995}$ [kN]	$SF(A_1)$ [-]	$A_2$ [kN]	$SF(A_2)$ [-]
S5-x-d	8	$2 \cdot d$	82,2	28,2	48,9	77,1	1,07	28,2	2,92
		$4 \cdot d$	97,2	48,0	48,9	96,9	1,00	48,0	2,02
		$8 \cdot d$	198,1	103,0	48,9	151,9	1,30	103,0	1,92
	10	$2 \cdot d$	114,9	44,0	58,0	102,0	1,13	44,0	2,61
		$4 \cdot d$	141,9	75,0	58,0	133,0	1,07	75,0	1,89
		$8 \cdot d$	264,9	161,0	58,0	219,0	1,21	161,0	1,65

It can be observed that the spacing of the fasteners in the Torx tests does not influence the load-bearing capacity of the reinforcement (cf. Figure 6). However, according to *Rathiens* (2023), there is a statistically significant effect on the stiffness of the connection (refer to Figure 9). The stiffness decreases by up to 30 % with increasing spacing of the screws. The results of the series with two loaded screws in series S4-|, also show a similar result. However, the effect is much more pronounced for screws with  $d = 10,mm$ . In a similar manner to the load-bearing capacity, no significant impact of the top layer's orientation is observed.

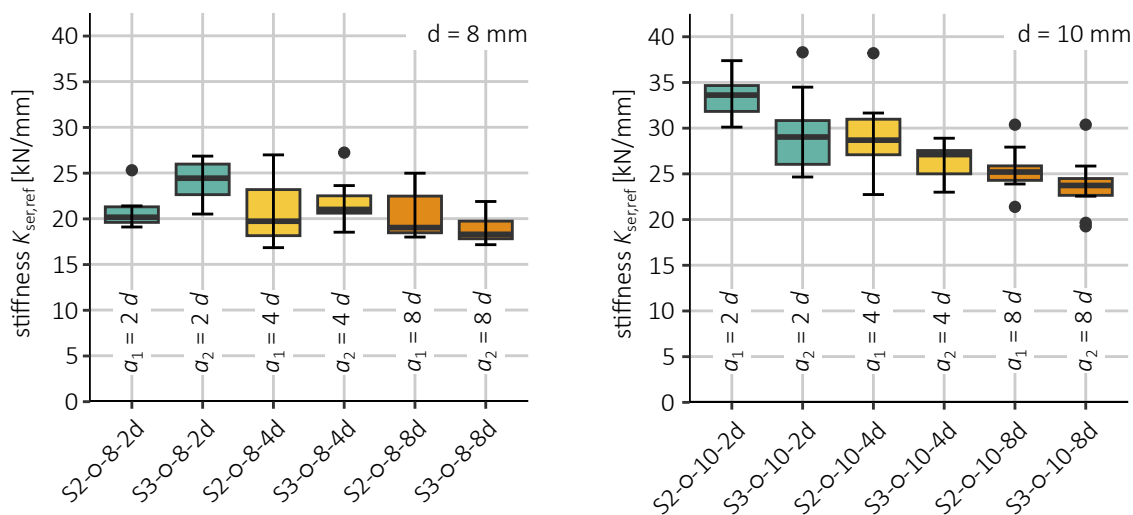


Figure 9. Results for series S1-O, S2-O and S3-O – stiffness in compression  $K_{ax}$  –  $d = 8 \text{ mm}$  (left),  $d = 10 \text{ mm}$  (right)

Before testing the load-bearing capacity, the increase in stiffness resulting from the reinforcement measure was investigated in the tests of series S5-x. The results of these tests are presented in Figure 10 and are summarized below. The increase in stiffness depends on the dimensions of the test specimen. As the dimensions of the test sample increase, the increase in stiffness decreases. From a fastener spacing of  $4d$ , the

increase due to the fasteners used here is, on average, approximately 50 % compared to unreinforced CLT test sample.

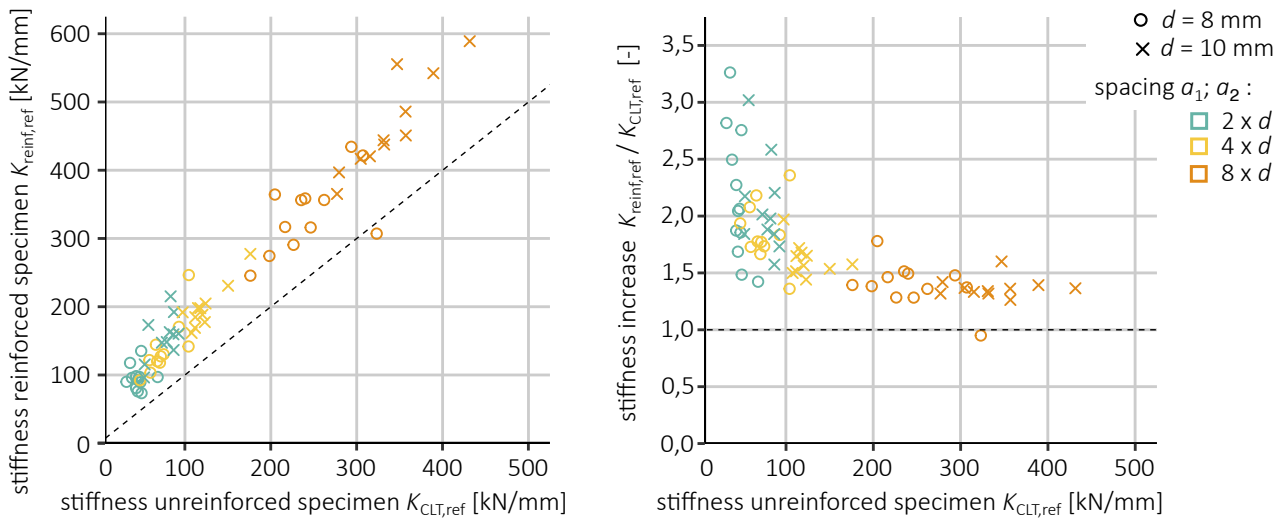


Figure 10. Increase in stiffness due to the reinforcement – comparison between the unreinforced specimens (series S5-x-a) and the reinforced specimens (series S5-x-b)

## 5 Conclusions and recommendations

Based on the experimental validation, it can be stated that the design approach according to prEN 1995-1-1 (2024) can also be applied to CLT to reinforce the resistance of CPG using fully threaded screws. The results show that the design approach agrees well with the experimental resistance values. Nevertheless, the specimens examined in this research were solely those with dimensions matching the steel plate used for load application. Investigations by *Hagen* (2024) and *Mayer* (2023), using the same screws and arrangement, but with a larger edge distance of CLT plates ( $t_{CLT}/2$ ), indicate that significantly higher load-bearing capacities could be achieved. Consequently, the influence of the position of the reinforcement in the slab (edge, corner, center) will be analyzed in more detail in future investigations to provide  $k_{c,90}$  values.

Based on the investigations carried out, the following recommendations should be considered for the reinforcement of CLT. The geometric requirements of prEN 1995-1-1 (2024) should be adapted for CLT to allow efficient application. Therefore, the boundary conditions suggested by *Mayer* (2023) which were also considered in the tests of *Rathiens* (2023) should be adopted. An overlap length of at least  $0,5 \cdot t_{CLT}$  should be ensured, with  $10d$  and  $8d$  being the values adopted in this research. A residual screw length of at least  $15d$  between the screw tip and the opposite contact surface is not required for CLT. Based on the investigations, the minimum thickness of the CLT elements ( $t_{CLT}$ ) should be limited to 160 mm. The minimum diameter of the screws should be 8 mm. A minimum distance of  $4d$  should be maintained between the screws, without the need to differentiate between the spacing  $a_1$  and  $a_2$ . The proposals resulting from this study are summarized in Figure 11.

In addition to the investigations presented, it is advisable to set the effective contact length  $l_{ef,1}$  equal to  $l_{c,90}$  in the model for simplicity.

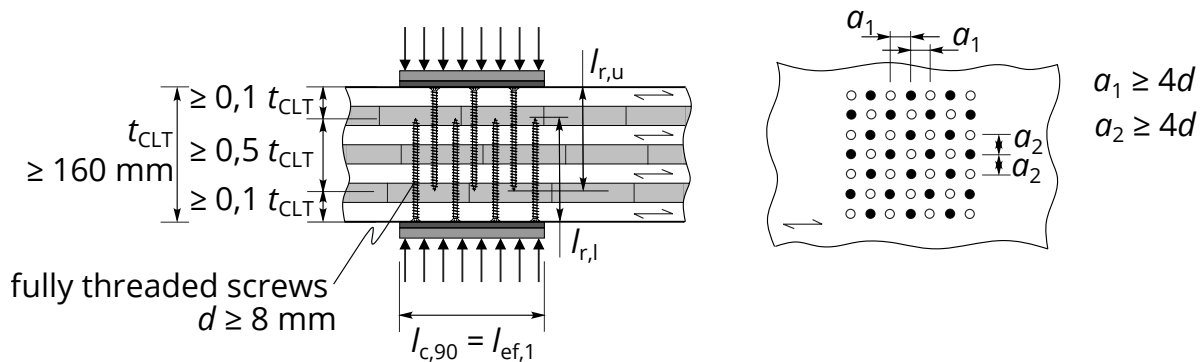


Figure 11. Proposal for reinforcement for CPG of CLT elements with fully threaded screws

## 6 References

- Bejtka, I. (2005). "Verstärkung von Bauteilen aus Holz mit Vollgewindeschrauben." PhD thesis. Karlsruher Institut für Technologie (KIT).
- Bejtka, I. & H. Blass (2006). "Self-tapping screws as reinforcements in beam supports." In: *Self-tapping Screws As Reinforcements in Beam Supports*, pp. 1–13.
- Bejtka, I. & H. J. Blaß (2004). "Reinforcements perpendicular to the grain using self-tapping screws." In: *Proceedings, 8th World Conference on Timber Engineering*. Lahti, Finland.
- Dietsch, P.; S. Rodemeier & H.-J. Blaß (2019). "Transmission of perpendicular to grain forces using self-tapping screws." In: *Proceedings of the International Network on Timber Engineering Research INTER, Meeting 52*. Tacoma WA, USA, INTER / 52–7–10.
- EN 13183-1 (2003). *Moisture content of a piece of sawn timber – Part 1: Determination by oven dry method*. EN 13183-1. Brussels, Belgium: European Committee for Standardization.
- EN 14358 (2016). *Timber structures - Calculation and verification of characteristic values*. Brussels, Belgium: European Committee for Standardization.
- EN 408 (2012). *Timber structures - Structural timber and glued laminated timber - Determination of some physical and mechanical properties*. EN 408. Brussels, Belgium: European Committee for Standardization.
- ETA-20/0843 (2020). *Theurl CLTPLUS*. Vienna, Austria: Österreichisches Institut für Bautechnik (OiB).
- ETA-21/0751 (2022). *fischer PowerFull II Schrauben*. Nordhavn, Denmark: ETA-Danmark A/S.
- Hagen, K. M. (2024). "Two-sided reinforcement of CLT and push-in capacity of fully threaded screws." MA thesis. Norwegian University of Life Sciences.
- Mayer, J. (2023). "Verstärkungsmaßnahmen mittels Vollgewindeschrauben für die Lastdurchleitung bei Brettsperholz und Brettschichtholz." MA thesis. University of Innsbruck.

- OENORM B 1995-1-1 (2023). *Eurocode 5: Bemessung und Konstruktion von Holzbauten - Teil 1-1: Allgemeines - Allgemeine Regeln und Regeln für den Hochbau - Konsolidierte Version mit nationalen Festlegungen, nationalen Erläuterungen und nationalen Ergänzungen zur Umsetzung der ÖNORM EN 1995-1-1*. Vienna, Austria: Austrian Standards Institute.
- prEN 1995-1-1 (2024). *Eurocode 5: Design of timber structures – Part 1-1: General and rules for buildings*. EN 1995-1-1. Brussels, Belgium: European Committee for Standardization.
- Rathiens, L. (2023). “Maßnahmen zur Querdruckverstärkung zur Lastdurchleitung im Ingenieurholzbau.” MA thesis. University of Innsbruck.
- Rodemeier, S. (2018). “Querdruckverstärkung von Holzbauteilen bei beidseitiger Druckkrafteinleitung.” MA thesis. Technische Universität München.
- Tomasi, R.; A. Aloisio; E. Hånde; K. Thunberg & E. Ussher (2023). “Experimental investigation on screw reinforcement of timber members under compression perpendicular to the grain.” In: *Engineering Structures* 275, p. 115163. ISSN: 0141-0296.
- Z-9.1-519 (2014). *SPAX-S Schrauben mit Vollgewinde als Holzverbindungsmittel*. Berlin, Germany: Deutsches Institut für Bautechnik (DIBt).

## DISCUSSION

**The paper was presented by R Tomasi**

*P Dietsch received clarification that the screw tip distance was at least  $0.1t_{CLT}$  but recommended to discuss the results of the underlying Master thesis in the community.*

*P Dietsch commented that failure mode  $a_2$  is related to horizontal elongation of the wood which for CLT is hindered by the orthogonal arrangement.*

*A comparison to the results of the unreinforced situation would have been helpful.*

*Finally the Torx tests fixed the screw head against rotation which might not be realistic and lead to overestimation of results compared to practical situations, where screw heads could feature small horizontal movement.*

*F Lam inquired about distance requirements and long-term effects in these situations.*



# Punching-shear resistance of point-supported CLT panels

Houman Ganjali, PhD candidate, University of Northern British Columbia (UNBC), Prince George, Canada; ganjali@unbc.ca

Thomas Tannert, UNBC, Prince George, Canada; thomas.tannert@unbc.ca

Md Shahnewaz, Fast + Epp, Vancouver, Canada; mshahnewaz@fastepp.com

Carla Dickof, Fast + Epp, Vancouver, Canada; cdickof@fastepp.com

Marjan Popovski, FPInnovations, Vancouver, Canada; marjan.popovski@fpinnovations.ca

Keywords: Floor systems, experimental investigation, shear analogy

## 1 Introduction

### 1.1 Background

Cross-laminated timber (CLT) has gained popularity in recent years as a sustainable and cost-effective alternative to traditional construction materials, particularly for floor applications (Karacabeyli & Gagnon, 2019). This includes point-supported flat-slabs, where the panels are supported directly by columns, without the need for beams and their connections (Popovski et al., 2016). One of the key properties in these applications is the CLT punching shear resistance, which refers to its ability to resist concentrated loads or "punching" through the material. The factors influencing CLT punching shear resistance are either material-strength-related or support-condition-related and should be accounted for in design.

### 1.2 CLT punching shear resistance

CLT punching shear resistance,  $R_{pu}$ , is directly related to the rolling shear strength,  $f_s$ , and impacted by the confinement of lamellas from adjacent layers and the presence of concurrent compression forces. These effects are accounted for in design by the rolling shear resistance in punching shear adjustment factor,  $K_{r,pu}$ , (Mestek, 2011; Bogensperger & Jöbstl, 2015; Muster, 2020). Mestek & Dietsch (2013) proposed an adjustment factor of 1.2; in Annex D of prEN1995 (2023) a  $K_{r,pu}$  of 1.6 is recommended; and Muster (2020) proposed  $K_{r,pu}$  of 1.6 and 1.3 for centre and corner columns.

While the Canadian Standard for Engineering Design in Wood CSA O86 (2024) provides specified  $f_s$  strength values of 0.5-0.66 MPa, the characteristic 5<sup>th</sup>%  $f_s$  values of CLT panels from major Canadian providers (adjusted for normal duration of load) were reported to range from 0.54 MPa to 1.08 MPa (Ganjali et al., 2023).



Adopting an appropriate shear stress distribution model to estimate the actual stresses close to point-supports is crucial. prEN1995 (2023) recommends checking the rolling shear stress at an effective perimeter of the loaded area defined at 35° to the centre line of the CLT thickness. However, this provision lacks a clear analytical basis and does not provide any adjustment factors for support-condition, i.e. the effect of column location and geometry, which are required for efficient CLT punching shear design.

The Shear Analogy (SA) method is capable of accounting for the effect of transverse layers on the shear stress profile in CLT. In this method, based on the parallel axis theorem for determining the moment of inertia of a body about a given axis, the CLT panel is separated into two virtual beams, A and B, linked with infinitely rigid web (see Figure 1). The bending stiffness of beam A, ( $B_A$ ), is the sum of the flexural stiffness of the individual layers along their own neutral axes Eq. 1, while beam B ( $B_B$ ) provides the “Steiner” contribution to the effective flexural stiffness Eq. 2 (Kreuzinger 1999; Karacabeyli & Gagnon, 2019). Mestek (2011) proposed a simplified approach to determine the internal forces of the ideal beams without using a statics program.

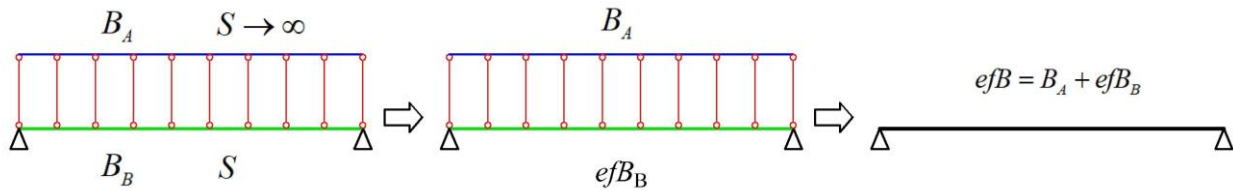


Figure 1. SA method representation of CLT panel as beam A and beam B.

$$B_A = \sum_{i=1}^n E_i \cdot I_i = \sum_{i=1}^n E_i \cdot b_i \cdot \frac{h_i^3}{12} \tag{Eq. 1}$$

$$B_B = \sum_{i=1}^n E_i \cdot A_i \cdot z_i^2 \tag{Eq. 2}$$

Where  $B_A$  is  $(EI)_A$ ;  $b_i$  is the layer width;  $h_i$  is the layer thickness;  $B_B$  is  $(EI)_B$ , and  $z_i$  is the distance between the layer centre point and the panel neutral axis.

In the ideal rigid system in SA, the share of the internal shear forces ( $V_A$  and  $V_B$ ) can thus be determined and assigned to beam A and B via the ratio of the bending stiffnesses:

$$V_A = V \cdot \frac{B_A}{efB} \tag{Eq. 3}$$

$$V_B = V \cdot \frac{efB_B}{efB} \tag{Eq. 4}$$

Where,  $V$  is the maximum external shear force on CLT from force analysis; and  $efB_B$  and  $efB$  are the effective bending stiffnesses of beam B and CLT (Mestek, 2011):

$$efB = B_A + efB_B \quad \text{Eq. 5}$$

$$efB_B = B_B \cdot \frac{1}{1 + \frac{B_B \cdot \pi^2}{S \cdot l^2}} \quad \text{Eq. 6}$$

where  $S$  is section modulus; and  $l$  is the length of the beam.

The rolling shear stress ( $\tau_s$ ) in each beam is calculated:

$$\tau_{s,A,i} = \frac{V_A \cdot E_i \cdot h_i^2}{8 \cdot B_A} \quad \text{Eq. 7}$$

$$\tau_{s,B,i} = \frac{V_B}{B_B} \cdot \sum_1^{i-1} E_i \cdot h_i \cdot z_i \quad \text{Eq. 8}$$

The rolling shear stress in the  $i^{\text{th}}$  layer of CLT panel,  $\tau_{s,i}$ , then is:

$$\tau_{s,i} = \tau_{s,B,i} + \tau_{s,A,i} \quad \text{Eq. 9}$$

While the SA method can be deemed adequate for estimating the bending stiffness, the transformed-section method (Dunham, 1944) can be more readily adopted to determine the stress distributions in composite materials. In this method, originally developed for reinforced concrete, the steel rebars are replaced by an equivalent area of concrete,  $A_{\text{trans.}}$ , (reference material), Eq. 10, through the ratio ( $n$ ) of modulus of elasticity ( $E_{\text{ref.}}$ ) of concrete to  $E_{\text{steel}}$ , Eq. 11; this approach results in an imaginary transformed beam made of the reference material that can be used thereafter to calculate the geometry properties of the section and determine shear and bending stresses (Eq. 12 and Eq. 13). This method is simpler than SA method and can be used for CLT, however its efficiency in terms of shear stress distribution in CLT needs to be investigated.

$$A_{\text{trans}} = \frac{A_{\text{steel}}}{n} \quad \text{Eq. 10}$$

$$n = \frac{E_{\text{ref}}}{E_{\text{steel}}} \quad \text{Eq. 11}$$

$$\tau = \frac{V \cdot Q}{I \cdot b} \quad \text{Eq. 12}$$

$$\sigma = \frac{M \cdot y}{I} \quad \text{Eq. 13}$$

Once a 2D finite element analysis (FEA) method is adopted to obtain internal shear forces and design shear stresses in the major and minor strength directions, CLT point supports should be modelled as surface supports. The elastic support stiffness ( $C_{u,z}$ ) is a key modelling parameter (Muster, 2020) because it has a significant impact on the predicted forces and stresses on each column face (Slotboom et al., 2023). Muster (2020) proposed an equation for  $C_{u,z}$  as a function of CLT thickness (Eq. 14). However, this model needs to be verified with experimental results.

$$C_{u,z,Muster} = 10^{13} \cdot t_{CLT}^{-3.15} \text{ [kN/m}^3\text{]} \tag{Eq. 14}$$

### 1.3 Objectives

While limited design provision for point-supported CLT floors is provided in prEN1995 (2023), the current North American standards (CSA O86, 2024; NDS, 2024) do not include such guidance. To close this gap, a research project is being conducted by Fast + Epp structural engineers in collaboration with UNBC, consisting of four phases. The focus of this contribution is on phase (iii) with the objective to: a) investigate the effect of various support-condition-related parameters on CLT punching shear and ii) propose a more detailed CLT punching shear design provision.

## 2 Materials and Methods

### 2.1 Experimental investigation

The punching-shear resistance of 164 CLT panels from four Canadian manufacturers was evaluated to study the impact of: i) column location (edge, centre, corner, and perimeter, Figure 2, ii) grade (E1, V2), species (Spruce-Pine-Fir (SPF), Douglas Fir, and Hemlock), and layup (5-ply 175 mm thick and 7-ply 245 mm thick); and iii) column geometry and size (square, rectangle, round), see Figure 3. The E1 series had 1950 Fb-1.7E SPF and No.3 SPF in longitudinal and transverse layers, respectively. The V2 series had No.1/2 SPF and No.3/Stud SPF in longitudinal and transverse layers, respectively, produced in accordance with ANSI/APA PRG 320. Series S4, S5, and S6 panels were edge glued. The panels were sized 1.7 m × 1.8 m, 1.5 m × 1.8 m, and 1.5 m × 1.5 m.

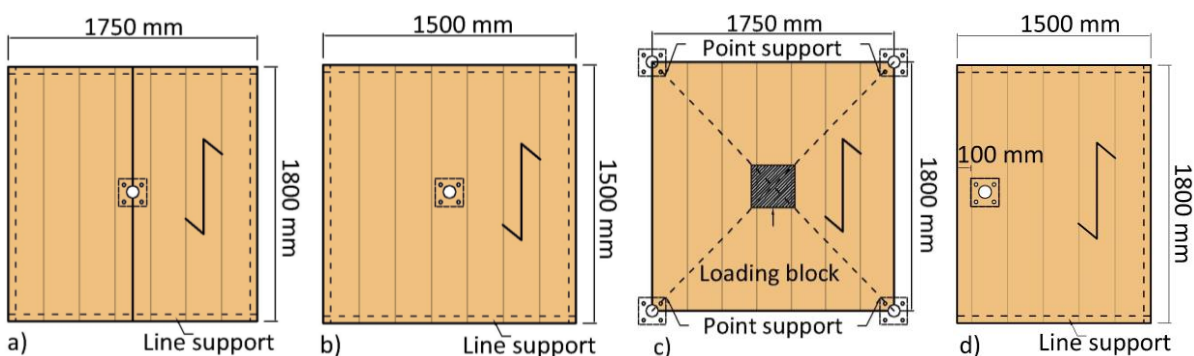


Figure 2. Punching shear test support locations: a) edge; b) centre; c) corner; and d) perimeter.

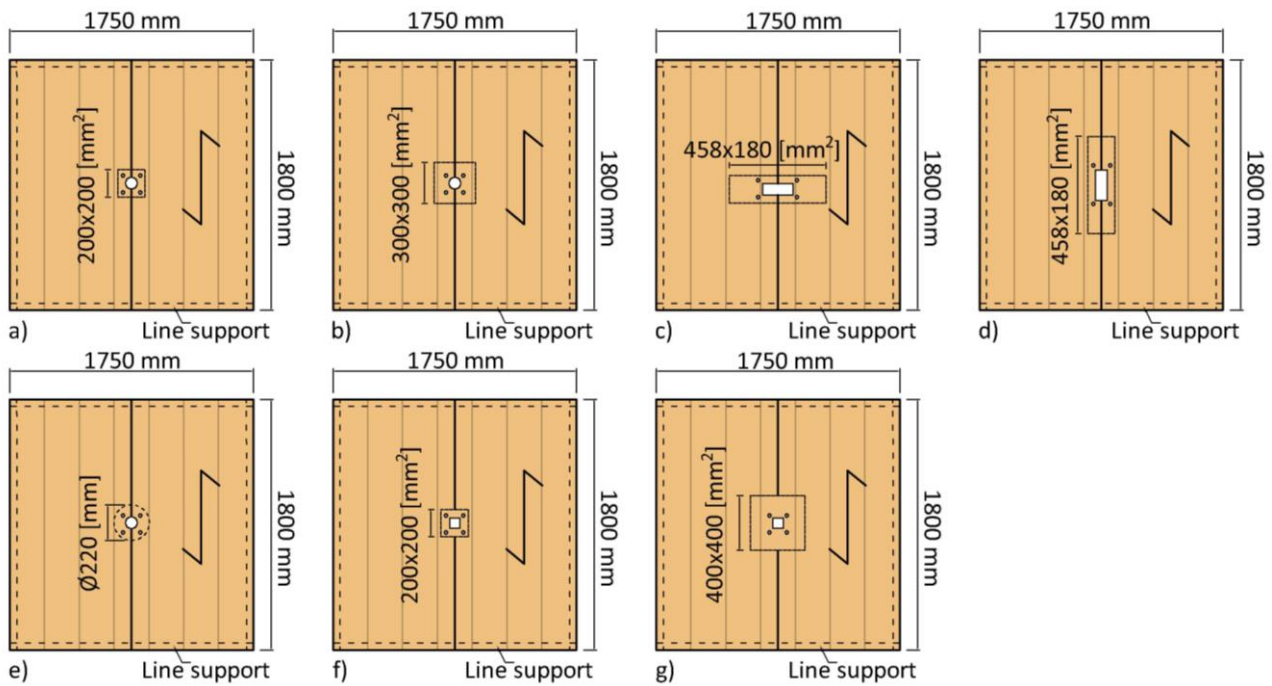


Figure 3. Different column geometries: a) square plate with stub (S1-S4, S6-S9, S15-S16); b) square plate with wood stub (S5); c) rectangular plate with wood stub (S10); d) rectangular plate with wood stub (S11); e) round column (S12); f) square plate and HSS (S13); and g) square plate and HSS (S14).

The edge and centre specimens were line-supported on four edges along the length, while the perimeter condition specimens were line-supported on three edges. The corner condition specimens were point-supported on four corners having the same bearing area, ensuring an equal possibility of failure for all corners. The test series overview is shown in Table 1. The tests were conducted according to ISO 6891 (1983) using a hydraulic actuator at a monotonic loading rate of 5 mm/min. The displacement of the tension side of the panels (underside for the edge, centre, and perimeter series and top for corner series) was recorded using string pots at various points throughout the tests. The typical test setup of each column condition is shown in Figure 4.

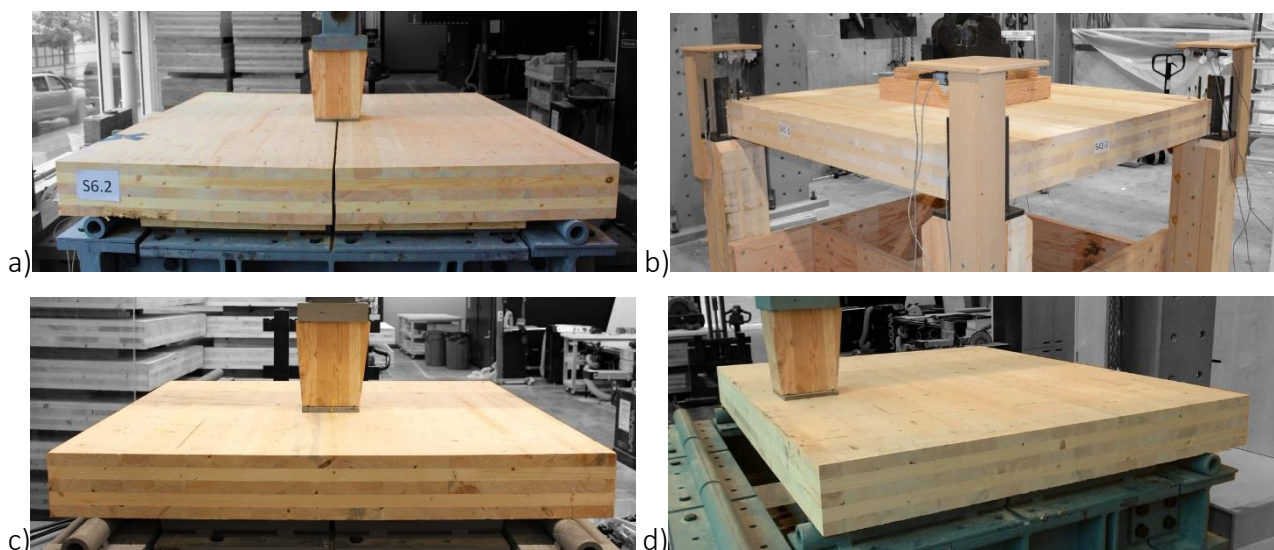


Figure 4. Typical a) edge; b) corner; c) centre; and d) perimeter setups.

Table 1. Overview of punching shear test series.

Series	Producer	Grade	CLT thick- ness [mm]	Species	Support dimen- sion [mm]	Column location
S1	D	V2	175	SPF	200 × 200	Edge
S2	D	E1	175	SPF	200 × 200	Edge
S3	A	E1	175	Spruce	200 × 200	Edge
S4	B	E1	175	SPF	200 × 200	Edge
S5	B	E1	175	SPF	300 × 300	Edge
S6	F	V2	175	SPF	200 × 200	Edge
S7	F	E1	175	SPF	200 × 200	Edge
S8	F	E1	175	D Fir	200 × 200	Edge
S9	F	E1	175	Hem	200 × 200	Edge
S10	F	E1	175	SPF	460 × 180	Edge
S11	F	E1	175	SPF	180 × 460	Edge
S12	F	E1	175	SPF	∅ 219	Edge
S13	F	E1	175	SPF	200 × 200	Edge
S14	F	E1	175	SPF	400 × 400	Edge
S15	F	E1	175	SPF	300 × 300	Edge
S16	F	E1	175	SPF	200 × 200	Edge
S17	F	E1	245	SPF	300 × 300	Edge
S23	F	E1	175	SPF	200 × 200	Edge
S24	F	E1	175	SPF	200 × 200	Centre
S25	F	E1	175	SPF	∅ 219	Centre
S26	F	E1	175	SPF	300 × 300	Centre
S27	F	E1	175	SPF	200 × 200	Centre
S28	F	E1	175	SPF	200 × 200	Centre
S29	F	E1	245	SPF	300 × 300	Centre
S30	F	E1	175	SPF	200 × 200	Perimeter
S41	F	E1	175	SPF	200 × 200	Corner
S42	F	E1	245	SPF	200 × 200	Corner

## 2.2 Analytical work

Two approaches were used to estimate the maximum rolling shear stress,  $\tau_{r,max}$  at the ultimate load in the tests. First, Eq. 15 as proposed by Muster (2020) was used:

$$\tau_{r,max,i} = \frac{1.5 \cdot V_i \cdot K_A \cdot K_{edge}}{b_{eff,i} \cdot t_{CLT}} \quad \text{Eq. 15}$$

Where  $V_i$  is the shear force in each direction, determined by a FE model in RFEM, using the experimentally observed punching shear resistance as input;  $K_A$  is the shear stress

distribution adjustment factor (Table 2);  $K_{edge}$  is the edge column at opening adjustment factor, computed using Eq. 17;  $b_{eff}$  is effective support width, computed using Eq. 16, as shown in Figure 5, and  $t_{CLT}$  is the thickness of the CLT.

$$b_{eff,i} = b_{A,i} + t_{CLT} \cdot \tan 35^\circ \tag{Eq. 16}$$

$$K_{edge} = 1 + \frac{w_o}{3 \cdot b_{A,i}} \tag{Eq. 17}$$

where  $b_{A,i}$  is point-support dimension in each direction.

Table 2. Shear stress distribution adjustment factor ( $K_A$ ).

Ratio of $b_{A,i}/t_{CLT}$	$\leq 1$	$\leq 1.5$	$\leq 2$
$K_{A, \text{corner/edge columns}}$	1.35	1.5	1.65
$K_{A, \text{centre columns}}$	1.0	1.0	1.0

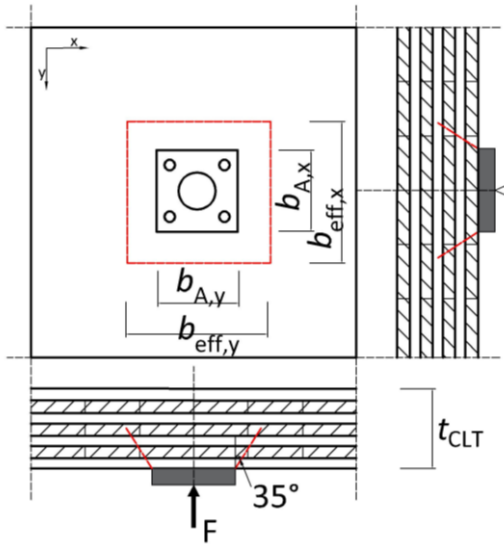


Figure 5. Geometric parameters in Muster (2020) model.

In addition, the  $\tau_{r,max}$  was also calculated with the shear analogy (SA) method (Kreuzinger 1999; Mestek, 2011; Karacabeyli & Gagnon, 2019). The adjustment factor of rolling shear resistance in punching ( $k_{r,pu}$ ) was calculated as the ratio of the maximum rolling shear stress from punching shear tests to the average of the RS strength from in-plane shear tests (Ganjali et al., 2023):

$$K_{r,pu} = \frac{\tau_{r,max}}{f_{s,mean}} \tag{Eq. 18}$$

The experimental elastic support stiffness ( $C_{u,z,exp}$ ) values were calculated as the ratio of a reference compressive stress at the load level ( $F$ ) that ensured the CLT to remain in the elastic region, to support deformation using Eq. 19:



$$C_{u,z,exp} = \frac{\sigma_{\perp}}{\Delta z} = \frac{F}{A_{net} \cdot \Delta z} \tag{Eq. 19}$$

where  $A_{net}$  is net support area and  $\Delta z$  is vertical displacement (indentation depth).

### 2.3 Numerical modelling

To determine the shear stresses through FE analysis (FEA), the panels were modelled as 2D plates in Dlubal’s RFEM adopting RF-Laminate. The panel geometry was defined as a rectangular surface in accordance with the experimental setups. All loaded areas and the point-supports (corner series only) were modeled as separate surface elements integrated with the rest of the panel. The boundary conditions of edge, centre, and perimeter supports was modelled as roller line-supports with locked in-plane displacement in accordance with Figure 2. The supports in the corner-series, however, were modelled as surface supports (Figure 6a) having the effective bearing areas calculated with Eq. 16 and adopting a support stiffness,  $C_{u,z}$ , of 1.7 N/mm<sup>3</sup>, determined from the experimental results of the present study. Test loads of edge, centre, and perimeter condition series were applied on a surface equal to the effective bearing area of point supports calculated with Eq. 16 as shown in Figure 2. For the edge series, due to symmetry only a half panel was modeled (Figure 6b). The test load of the corner series was applied on a 600 mm × 600 mm surface in the centre of the panel. The material properties were assigned using RF-Laminate modules by entering the layers’ thickness and their manufacturer-provided material properties. In RF-Laminate, details of composites, the option for considering coupling effect was selected for all series, and cross laminated timber without glue at narrow sides was unchecked for series S4, S5, and S6. The local X-axis was set to be parallel to the major direction of the panels. The mesh size was 30 mm with refinements around point supports.

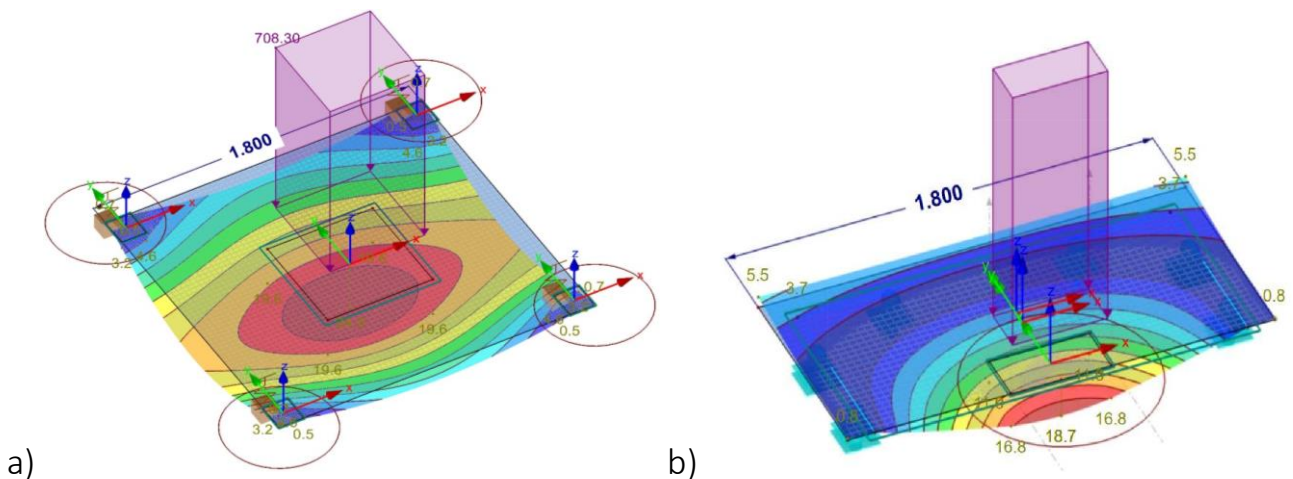


Figure 6. RFEM model of a corner-column panel (a) and an edge-column panel (b)

### 3 Results and discussion

#### 3.1 Load-displacement behaviour and failure modes

Figure 7 shows representative load-displacement curves obtained from testing. All specimens exhibited a quasi-linear behaviour up to the ultimate load. Typically, the tests were stopped after a 10% drop in the load. This was done because in a gravity load system and for the objectives of this study, observing further load drops was of no interest. However, for a few series, one specimen was pushed to the full actuator stroke to investigate the point-supported panel's ability to develop large displacement and disproportionate collapse mechanism.

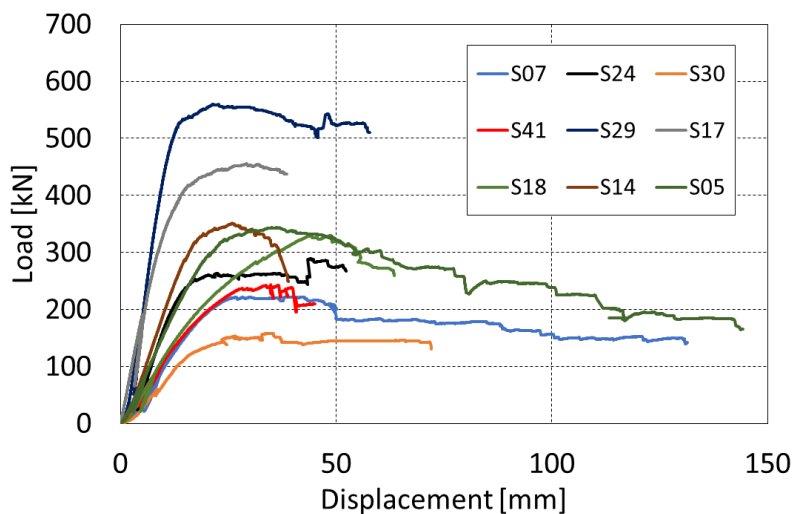


Figure 7. Representative load-displacement curves.

Local failure always initiated with minor audible rolling shear cracks (not visible), followed by rolling shear failure of lamellas near the loaded area (Figure 8a). The load was redistributed multiple times before and after the major load drop. As the displacement increased, the tension face lamellas of the panel close to the support failed in bending (Figure 8b); at larger displacements, global panel failure was observed (Figure 8c).

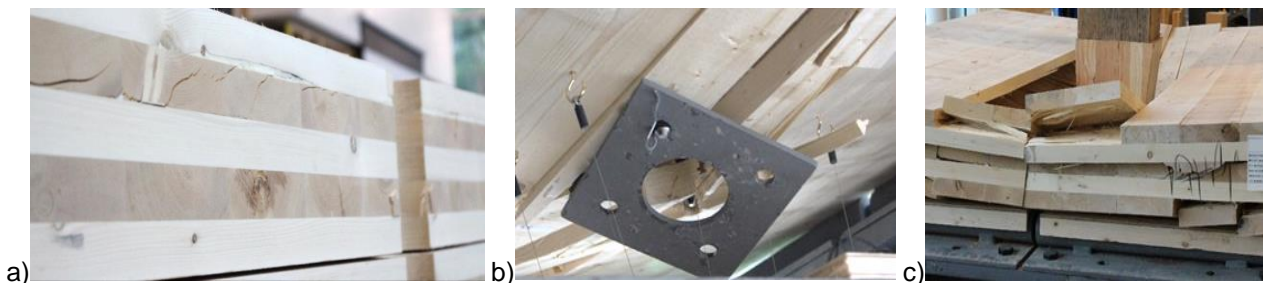


Figure 8. Failure modes under punching shear: a) rolling shear failure close to the point support; b) tensile failure of the underside boards; c) delamination at large displacement.



### 3.2 Punching shear resistance

The average punching shear resistance,  $R_{pu,avg}$ , of each series and the corresponding COV are summarized in Table 3. The results show CLT panels having the same CLT thickness, grade, species, and manufacturer, supported on different locations had substantially different resistances.

Table 3. Punching shear resistance obtained from testing along with the analytical and numerical maximum shear stresses.

Series	$R_{pu,avg}$ [kN]	COV [%]	$f_{s,avg}$ [MPa]	$\tau_{r,ult,Muster}$ [MPa]	$\tau_{r,max,FEA}$ [MPa]	$K_{r,pu,FEA}$ [-]	$K_{TW,FEA}$ [-]
S01	259.8	3.9	1.12	3.40	2.99	2.7	1.5
S02	273.9	5.5	1.48	3.59	3.12	2.1	1.5
S03	262.3	9.4	1.06	3.44	2.95	2.8	1.5
S04	321.1	2.1	1.51	4.20	3.66	2.4	1.5
S05	347.6	2.2	1.51	3.89	2.61	1.7	1.4
S06	221.2	12.3	1.14	2.89	2.54	2.2	1.5
S07	231.2	6.8	1.62	3.02	2.64	1.6	1.5
S08	322.2	3.2	1.44	4.21	3.70	2.6	1.5
S09	243.7	4.8	1.06	3.19	2.80	2.6	1.5
S10	335	3.9	1.62	3.17	2.06	1.3	1.2
S11	324	3.9	1.62	4.08	3.37	2.1	1.5
S12	259.4	5.0	1.62	[-]	2.73	1.7	[-]
S13	265.8	5.1	1.62	3.44	2.67	1.6	1.4
S14	352.5	6.3	1.62	2.74	2.27	1.4	1.3
S15	209.2	6.1	1.62	2.71	2.39	1.5	1.6
S16	259.2	3.6	1.62	3.36	2.96	1.8	1.5
S17	463.2	7.3	1.62	3.02	2.46	1.5	1.2
S23	217.8	7.5	1.62	2.82	2.48	1.5	1.5
S24	268	7.3	1.62	1.98	2.50	1.5	1.1
S25	271.5	2.4	1.62	[-]	2.75	1.7	1.1
S26	363	7.7	1.62	1.71	2.44	1.5	1.1
S27	307.4	6.6	1.62	2.27	2.78	1.7	1.1
S28	288.5	3.5	1.62	2.13	2.61	1.6	1.1
S29	566.5	3.8	1.62	2.35	2.42	1.5	1.1
S30	151.8	12.5	1.62	1.87	1.40	0.9	1.0
S30.7*	175	[-]	1.47	2.38	1.74	1.2	1.1
S30.8*	215	[-]	1.48	2.93	2.14	1.4	1.1
S41	255	5.6	1.62	2.38	4.20	2.6	1.7
S42	387.8	8.9	1.62	2.28	2.97	1.8	1.5

Figure 9a shows the effect of column location on the punching shear resistance of the series, highlighting the necessity of a proper shear stress distribution adjustment factor. The setup used for series S30 with perimeter support did not result in punching

shear failure. Therefore, two additional panels were tested with clamped ends at the line support in the minor direction; denoted with \* in Table 3. That change helped activate two-way load distribution and better represent this column condition.

The impact of CLT manufacturer, grade and species is illustrated in Figure 9b. Among the 175 mm SPF edge column series, S05 (manufacturer B) had a 40% larger resistance than S07 (manufacturer F). This could be attributed to the effect of manufacturing process pressure on the RS strength as Yawalata and Lam (2011) described. Grade E1 series was 5% stronger than grade V2 series (S06 vs. S07) since punching shear failure is accompanied by the tensile failure, and E1 grade has boards with higher tensile strength in the longitudinal layers. D Fir series (S08) outperformed most SPF series; the average punching shear resistance of S08 was 40% higher when compared to the SPF series of the same manufacturer. This difference was 10% for the Hemlock series (compare S09 with S07).

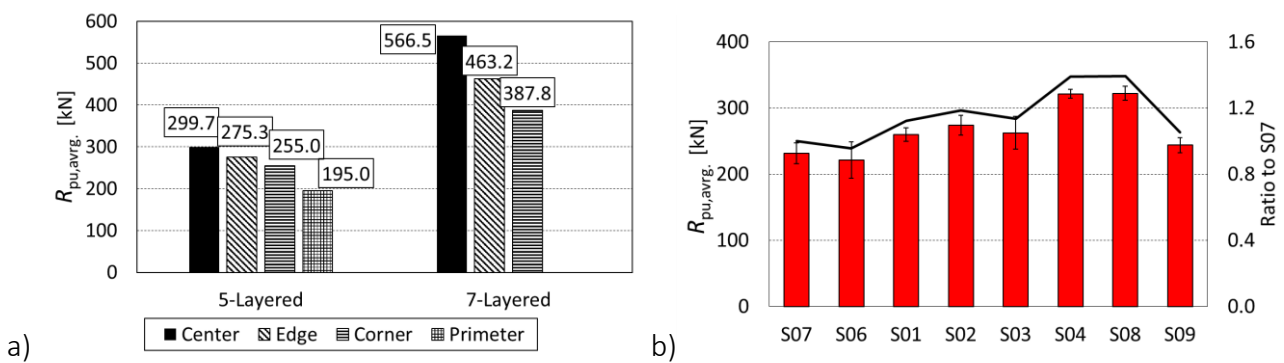


Figure 9. Impact of support condition (a); and provider, wood species, and stress grade on  $R_{pu}$  (b).

The effect of column geometry on the load-carrying capacity is shown in Figure 10. A 45% and 40% increase was attained when X- and Y-oriented rectangular columns (Figure 3c and d) were adopted. The softer (thinner) load distribution plate in S13 resulted in a 13% increase in  $R_{pu,avg}$ ; this can be attributed to the reduced stress concentration, Figure 10a. In the edge column series, using a round column increased the capacity by 12%. However, the results of the round column series with center column condition, S25, Figure 10b showed no increase when compared to S24 with a square load distribution plate.

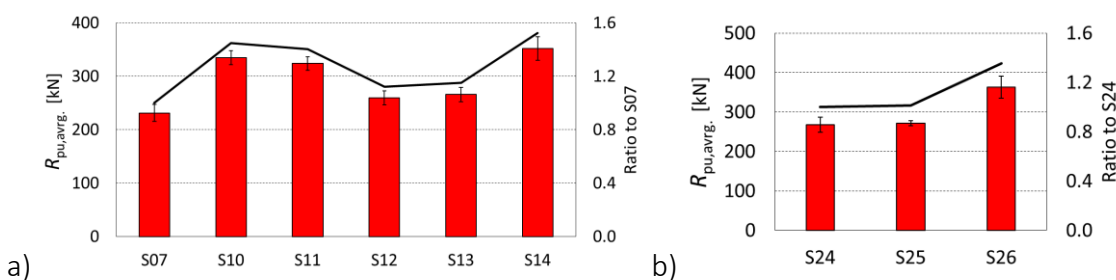


Figure 10. Column shape and size impact in edge column series (a); and centre column series (b).

Figure 11a shows that a bigger support width in the governing direction did not necessarily result in a higher capacity, but a larger support area, regardless of geometry, predicted up to 50% higher punching shear resistance (Figure 11b).

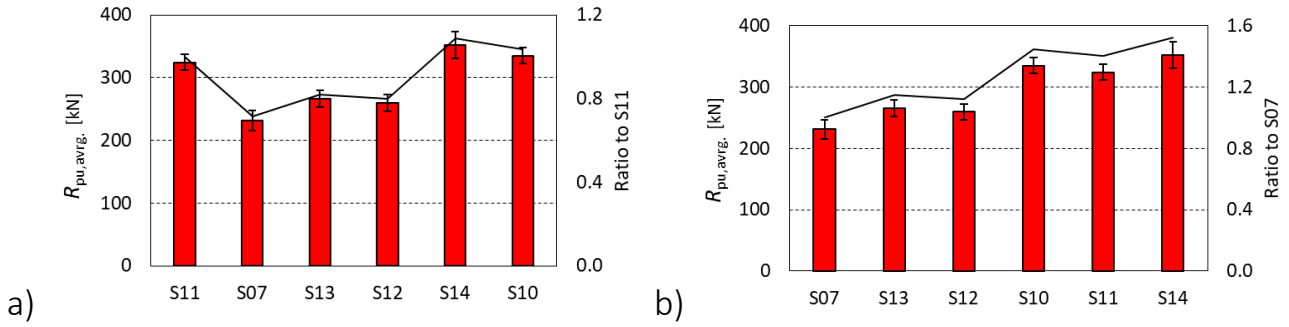


Figure 11. Impact of support width (a); and support area (b) on CLT punching shear resistance.

### 3.3 Magnitude and distribution of rolling shear stresses

The maximum rolling shear stress ( $\tau_{s,max,Muster}$ ) values calculated with Muster (2020) equation, those determined through FEA ( $\tau_{s,max,FEA}$ ), and the adjustment factor for rolling shear resistance in punching from FEA ( $k_{r,pu,FEA}$ ) are reported in Table 3. The values of  $\tau_{s,max,FEA}$  were considerably higher than those reported in Ganjali et al. (2023). The  $k_{r,pu,FEA}$  values for the edge-column series averaged 2.0; for the centre column series 1.6; for the perimeter and perimeter\* series 1.0 and 1.3; and for the corner series 2.2.

All shear stress distribution models discussed before give the shear stress profile across the thickness while assuming a constant profile along the width. This assumption only holds true in a one-way bending problem such as when CLT panels are supported by walls. In a point supported CLT, the two-way bending of the panel leads to a different shear stress profile along the support dimensions. Therefore, an adjustment factor for shear stress distribution in two-way bending ( $K_{TW}$ ) was defined as the ratio of  $\tau_{r,max,FEA}$  to  $\bar{\tau}_{r,FEA}$ :

$$K_{TW} = \frac{\tau_{r,max,FEA}}{\bar{\tau}_{r,FEA}} \tag{Eq. 20}$$

The  $K_{TW,FEA}$  of the tested series are reported in Table 3.  $K_{TW,FEA}$  for the edge-column series averaged 1.5; for the centre column series averaged 1.1; for the perimeter\* series averaged 1.1; and for the corner series 1.6. Using the proposed  $K_{TW}$  is contingent on the ability of adopted stress distribution model in giving the same  $\bar{\tau}_r$  as those of from FEA.

The model proposed by Muster (2020) assumes a parabolic shear profile across CLT thickness and was developed for asymmetrical CLT layup meaning that it does not differentiate between the CLT thickness contributing to shear resistance in major and minor directions of a symmetric CLT layup. As shown in Table 3, This model resulted in

overestimating the  $\bar{\tau}_r$  values and when its adjustment factors were applied overestimated the  $\tau_{r,max}$  values, especially for the edge column series. SA method, however, accounts for the effect of transverse layers and predicted the same  $\bar{\tau}_{r,max}$  values as the FE model; as an example,  $\bar{\tau}_r$  through SA method and Muster (2020) in major and minor directions of S20 are compared in Figure 12a and b. Nevertheless, SA method has many steps and could make the design process laborious.

Therefore, herein, adopting the Transformed Composite Section (TCS), Figure 12e, is proposed which can be easily adopted through the following steps: 1) calculate the ratio of the longitudinal layers' modulus of elasticity ( $E$ ) to the transverse layers'  $E$ ; 2) determine the transformed width of the transverse layers ( $b_{trans.}$ ) through dividing the effective width of the shear plane by the ratio calculated in step 1; 3) calculate the first moment of area of the transformed section ( $Q_{trans.}$ ) at the desired CLT depth, excluding the outermost layers for the minor direction; 4) calculate the second moment of area of the transformed section ( $I_{trans.}$ ), excluding the outermost layers for the minor direction; 5) calculate the rolling shear stress ( $\tau_r$ ) by Eq. 21:

$$\tau_r = \frac{V_i \cdot Q_{trans}}{I_{trans} \cdot b_{eff}} \tag{Eq. 21}$$

Where  $V_i$  is the shear force from force analysis;  $Q_{trans}$  is the first moment of inertia of the transformed section,  $I_{trans}$  is the moment of inertia of the transformed section; and  $b_{eff}$  is the effective width of the shear plane.

The shear stress distribution of S29 in both directions through SA and TCS methods are compared in Figure 12c and d; where the simpler method, TCS, is shown to result in the same shear profile and the ultimate shear stress as SA method.

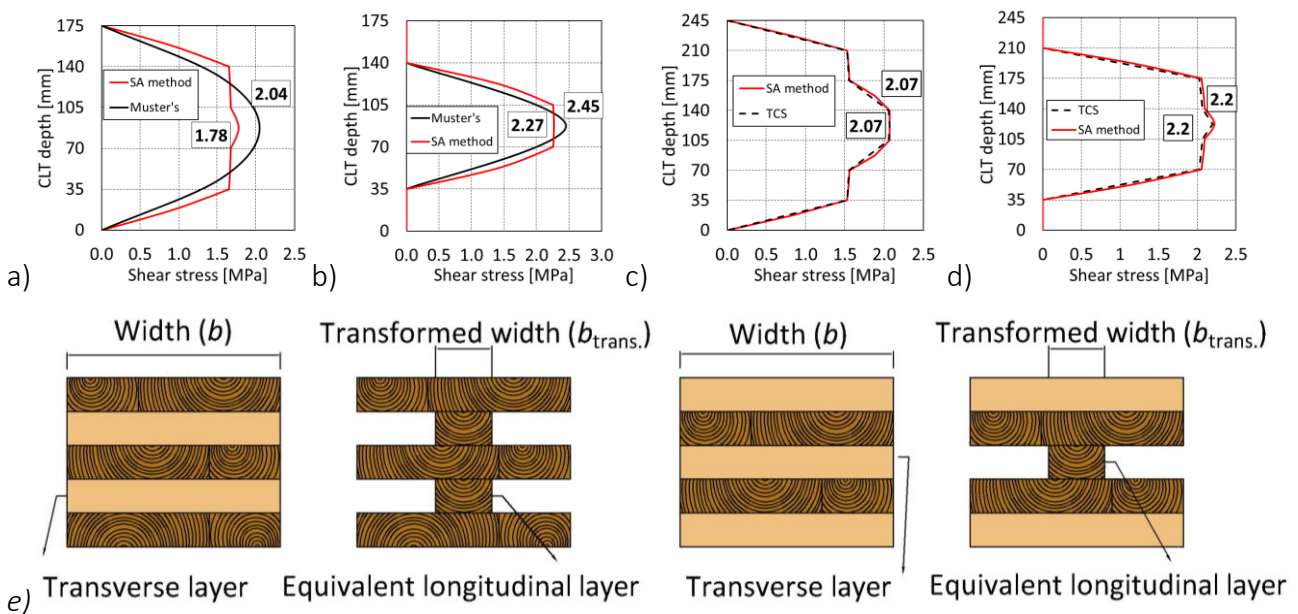


Figure 12. SA vs. Muster (2020) method in major (a) and minor (b) directions; SA vs. TCS in major (c) and minor (d) directions; TCS method description (e).

### 3.4 Point-support stiffness

The average  $C_{u,z,exp}$  values at a reference compressive stress level of 3.6 MPa are compared with those proposed by Muster (2020) in Table 4. The average  $C_{u,z,exp}$  for 175 mm thick and 245 mm thick panels were 1.69 N/mm<sup>3</sup> and 1.73 N/mm<sup>3</sup> respectively. These experimentally determined values do not confirm Muster (2020) values for different CLT thicknesses. The performed one-way ANOVA test with a P-value of 0.78 showed no statistically significant difference between the  $C_{u,z,exp}$  of 5- and 7-layered panels, suggesting on average a  $C_{u,z}$  of 1.71 N/mm<sup>3</sup> for SPF CLT panels having E1 stress grade regardless of thickness. The experimentally determined  $C_{u,z}$  in this study can be adopted for a FEA based design of point supported CLT floors.

Table 4. Elastic support stiffness values.

CLT thickness [mm]	$C_{u,z,Muster}$ [N/mm <sup>3</sup> ]	$C_{u,z,exp}$ [N/mm <sup>3</sup> ]	Specimen count	COV [%]
175	0.3	1.69	30	24
245	0.86	1.73	24	31

### 3.5 Proposed analytical model

For punching shear design of point supported CLT, the simple yet accurate TCS stress distribution model is used along with the required material-strength related, and column-condition related adjustment factors. The TCS method results in the same shear stress profile as the SA method but is easier to implement. The experimentally determined punching shear adjustment factor,  $k_{r,pu}$ , for the rolling shear resistance for different column conditions (Table 5) are higher than the  $k_{r,pu}$  of 1.6 recommended in prEN1995 (2023) for all column conditions, except for perimeter column condition. therefore, prEN1995 (2023) seems overly conservative for centre, edge, and corner columns. The proposed adjustment factor for shear stress distribution in two-way bending ( $K_{TW}$ ) for different column conditions can be adopted for both TCS and SA methods resulting in the same maximum rolling shear stress from 2D FEA in RFEM. Thus, when designing point supported CLT, Eq. 22 should be satisfied:

$$\tau_{r,d} \geq \tau_{r,max} \tag{Eq. 22}$$

$$\tau_{r,d} = K_{r,pu} \cdot f_s \tag{Eq. 23}$$

Where  $\tau_{r,d}$  is the design rolling shear stress;  $f_s$  is rolling shear strength of CLT; and  $k_{r,pu}$  is based on Table 5.

Table 5. Rolling shear resistance in punching shear adjustment factor ( $k_{r,pu}$ ).

Column location	Centre	Edge	Corner	Perimeter
$k_{r,pu}$	1.6	2	2.2	1.3

The maximum rolling shear stress ( $\tau_{r,max}$ ) in the decisive layer can be calculated by:

$$\tau_{r,max} = \frac{V_i \cdot Q_{trans} \cdot K_{TW}}{I_{trans} \cdot b_{eff}} \quad \text{Eq. 24}$$

Where  $b_{eff,i}$  is determined with Eq. 25 and Eq. 26 according to Figure 13 for the cases where the panel is continuous on the both sides of the point support and when it is not, respectively; and  $K_{TW}$  is based on Table 6.

$$b_{eff,1} = b_{A,i} + t_{CLT} \cdot \tan 35^\circ \quad \text{Eq. 25}$$

$$b_{eff,2} = b_{A,i} + 0.5 \cdot t_{CLT} \cdot \tan 35^\circ \quad \text{Eq. 26}$$

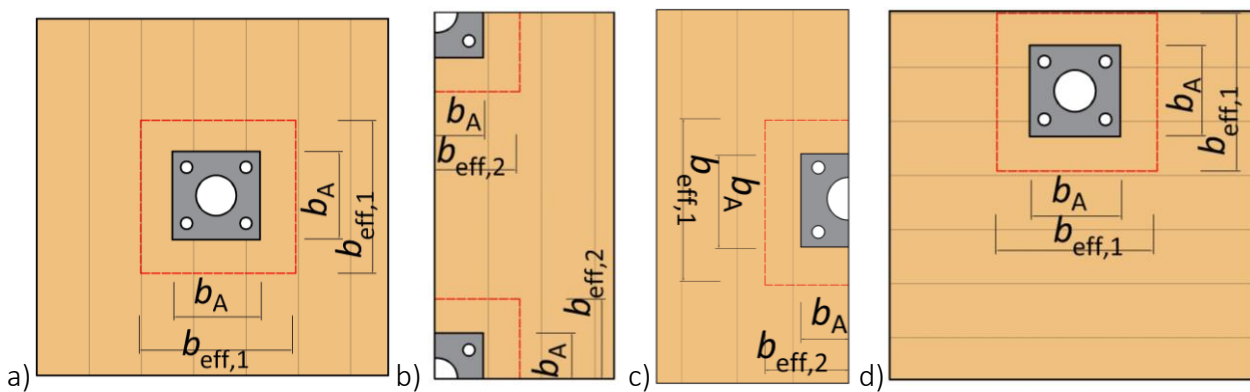


Figure 13. Determination of  $b_{eff}$  in centre (a); corner (b); edge (c); and perimeter (d) columns.

Table 6. Adjustment factor for shear stress distribution in two-way bending ( $K_{TW}$ ).

Column type	Centre	Edge	Corner	Perimeter
$K_{TW}$	1.1	1.5	1.6	1.1

## 4 Conclusions and outlook

Based on the punching shear tests on 164 full-scale CLT panels, and subsequent analytical and numerical analyses, the following conclusions can be drawn:

- Column location impacted the punching shear resistance,  $R_{pu}$ , highlighting the need for incorporating a shear stress distribution adjustment factor in CLT punching shear design.
- Douglas Fir and Hemlock series were 40% and 10% stronger than SPF panels from the same provider, respectively. Panels from different manufacturers with the same grade and species were up to 40% stronger.
- A larger support area (regardless of geometry) and softer (thinner) load distribution plate increased the resistance by 50% and 13%, respectively. Overall, the E1 series were slightly (5%) stronger than V2 series.

- Round column geometry increased the resistance of the edge column panels while it had no effect on the punching shear resistance  $R_{pu,avrg}$  of the centre column series.
- The adjustment factor for rolling shear resistance in punching shear,  $k_{r,pu,FEA}$ , for the edge-column series averaged at 2.0; for the centre column series it averaged at 1.6; for the perimeter and perimeter\* series averaged at 1.0 and 1.3; for the corner series it was 2.2 and in total averaged at 1.8.
- An adjustment factor for shear stress distribution in two-way bending ( $K_{TW}$ ) was introduced. Based on the tests,  $K_{TW}$  should be 1.5 for the edge-column series; 1.1 for the centre column series; 1.1 for the perimeter\* series; and 1.6 for the corner series.
- Simple beam bending model overestimated the shear stresses in CLT, whereas adopting the SA method resulted in more accurate shear stress profile across CLT thickness. To avoid the laborious SA method, the TCS method is proposed that leads to the same shear stress profile as the SA method.
- The average experimentally determined elastic support stiffness,  $C_{u,z,exp}$ , for 175 mm thick and 245 mm thick CLT panels were 1.69 N/mm<sup>3</sup> and 1.73 N/mm<sup>3</sup>; this does not confirm Muster (2020) equation values.
- A model for punching shear design of CLT based on TCS method is proposed with the required adjustment factors accounting for the effect of concurrent RS and compression perpendicular stresses as well as the effect of two-way bending on the maximum RS shear.
- Even with the proposed analytical model and the required support-condition and material-strength related adjustment factors, point supported CLT design requires a FE force-analysis. Therefore, a simple force analysis method will be developed in the next phase of this project.

## Acknowledgments

The project was supported by the Province of British Columbia's 'Green Construction Through Wood' program and the Natural Sciences and Engineering Research Council of Canada through an Alliance grant. The support by the UNBC laboratory technicians James Andal, Nathan Downie, and Ryan Stern, as well as Fast + Epp Concept Lab manager Brandon Sullivan and Concept Lab technician Bernhard Zarnitz is appreciated.

## References

- Bogensperger T, Jöbstl R A (2015) Concentrated Load Introduction in CLT Elements perpendicular to Plane. In proc. INTER, Šibenik, Croatia.
- CSA-O86 (2024) Engineering Design in Wood. Canadian Standards Association, Mississauga, Canada.

- Dunham, C W (1944) The theory and practice of reinforced concrete, 2nd edition McGraw-Hill Book Co., Inc, New York, USA.
- Ganjali, H et al. (2023) Punching-shear strength of point-supported CLT floor panels. In proc. INTER, Biel, Switzerland.
- ISO 6891 (1983) Timber structures, Joints made with mechanical fasteners, General principles for the determination of strength and deformation characteristics, International Organization for Standardization (ISO).
- Karacabeyli, E, & Gagnon, S (2019) Canadian CLT Handbook, 2019 Edition. FPInnovations, Canada.
- Kreuzinger, H (1999) Platten, Scheiben und Schalen—ein Berechnungsmodell für gängige static program. Bauen Mit Holz 1: 34–39.
- Mestek, P & Dietsch, P (2013) Design concept for CLT-reinforced with self-tapping screws. In Focus Solid Timber Solutions-European Conference on Cross Laminated Timber (CLT). Graz, Austria
- Mestek, P (2011) Punktgestützte Flächentragwerke aus Brettsperrholz – Schubmessung unter Berücksichtigung von Schubverstärkungen (in German). Technical University, Munich (Doctoral Thesis).
- Muster, M (2020) Column-Slab Connection in Timber Flat Slabs. ETH, Zurich (Doctoral Thesis).
- NDS (2024) National Design Specification for Wood Construction. American Wood Council.
- Popovski, M et al. (2016) Structural behaviour of Point-supported CLT floor Systems. In proc. WCTE. Vienna, Austria
- prEN 1995-1-1 (2023) Eurocode 5 for CEN enquiry - Design of timber structures - part 1-1: General rules and rules for buildings. European Committee for Standardization, Brussels, Belgium.
- Slotboom, C et al. (2023) A Comparison of Punching Shear Design Approaches for Point Supported CLT Panels. In proc. WCTE.
- Yawalata D, Lam F (2011) Development of technology for cross laminated timber building systems. Research report submitted to Forestry Innovation Investment Ltd. Vancouver, BC, Canada: University of British Columbia.



DISCUSSION

**The paper was presented by H Ganjali**

*P Dietsch commented that experimental work indicated premature delamination failure of some specimens. These results should be culled. P Dietsch questioned the claim that shear analogy method being cumbersome and asked whether the transformed section method can take into account the other issues offered by shear analogy method. H Ganjali claimed that the middle layer showed similar longitudinal shear stresses between the two methods. P Dietsch stated that the rolling shear stresses in the inner cross layers are more important than the longitudinal shear stresses in the middle layer. H Ganjali agreed.*

*H Blass questioned the use of transformed section method. He asked where was the consideration of the shear modulus as the transformed section method was based on bending stresses only. As  $G_{RS}/G_{long}$  was not considered the results are inappropriate. T Tannert suggested that the transformed section approach allowed longitudinal shear stress distributions to be calculated even though the rolling shear stresses were not accurate. P Dietsch stated that differences in the shear stiffness must be considered.*

*R Brandner stated that short spans were tested in a past work (last year INTER meeting) on the topic and it should be cited. T Tannert responded that in long span floors rolling shear and punching shear failures would not be a problem. P Dietsch mentioned that the work of Bogensberger should be taken into account.*

*JW van de Kuilen stated that the creep factor seemed high and received confirmation that the loading was based on 55% of the fifth percentile of the short-term capacity.*

*J Töpler and H Ganjali discussed how to consider the influence of the rotational stiffness (clamping situation) at the support which would be related to the span under consideration.*

*S Aicher questioned the statement attributing the difference in results to uncertainties from different manufacturers. The high variability in rolling shear strength would more likely to be the cause. H Ganjali said statistical work not reported supported the claim.*





# Comparison of Calculation Methods for Application on Veneer-Reinforced Timber with Standard Lamella

Niklas Kainz, Chair of Timber Structures and Building Construction, Technical University of Munich, Germany

Patrik Aondio, Timber Construction Engineering, Biberach University of Applied Sciences, Germany

Martin Danzer, Chair of Timber Structures and Building Construction, Technical University of Munich, Germany

Stefan Winter, Chair of Timber Structures and Building Construction, Technical University of Munich, Germany

Keywords: Veneer Reinforced Timber, Standard Lamella, Softwood, Hardwood, Finite Element Method, Simulation, Wood, Solid, Shell

## 1 Introduction

Veneer-reinforced timber (VRT) with standard lamella is a composite beam of glued laminated timber (GLT) made of softwood and laminated veneer lumber with variably oriented fiber directions in the individual layers (LVLV) made of hardwood. The LVLV is mainly intended to strengthen the weaker properties of the GLT, which is the transverse direction and shear. Using a standard lamella, the LVLV has the same structure along the length and height of the beam. Figure 1 schematically shows one possible structure of VRT with the standard lamella as reinforcement. Internal hardwood reinforcements in GLT have been investigated by *Lechner et al. (2021)* and *Aicher & Tapia (2018)*. *Lechner (2021)* determined the first basic principles of VRT with variably oriented fiber direction in the individual layers of the LVLV. In the case of shear loading, it was observed that the maximum shear load capacity in VRT increased by 67% compared to the mean value of the GLT test specimens. Furthermore, the shear tests showed that the mean value of the shear modulus in the VRT cross-sections increased between 20% and 50%, depending on the structure. In the tests on the tensile and compressive strength perpendicular to

the beam axis of VRT, *Lechner* (2021) came to the conclusion that the LVLV significantly reduces tensile and compressive stresses perpendicular to the grain in the GLT partial cross-sections, which increased the respective load capacity. The maximum load could be increased by a factor of 2.3 to 4.7 for tension perpendicular to the beam axis and on average by a factor of 2.0 to 2.9 for compression perpendicular to the beam axis, with the selected test setup and depending on the LVLV structure. For notches, openings and transverse connections, it was determined that the VRT could achieve load increase factors between 4.1 and 5.4 for notches, between 1.9 and 2.1 for openings and between 3.1 and 3.6 for transverse connections compared to the GLT specimen. The use of the standard lamella, which was mainly designed to reinforce shear and the transverse direction, showed a reduction of 10% in bending capacity compared to GLT, because of the reduction of fibers in longitudinal beam direction through the LVLV reinforcement.

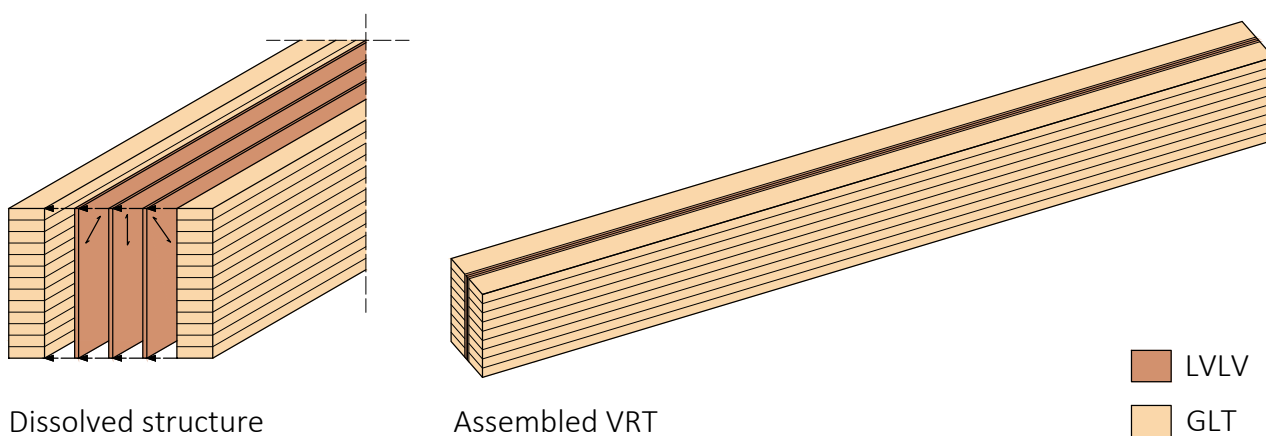


Figure 1. Schematic representation of one possible structure of VRT with standard LVLV lamella

The experimental investigations, carried out in *Lechner* (2021), were mainly verified by means of three-dimensional (3D) solid element simulations. The comparison of experimental results and FEM results was carried out on basis of deformation and stresses. The stresses in the experiments were analytically determined for the gross VRT cross-section as well as for the net GLT cross-section using the bending moment and the elastic section modulus. A comparison of the bending stresses derived from the experiment (net GLT stresses) with the results of the FEM calculation showed a maximum deviation of 2%. Furthermore, the comparison of the global deflections in the center of the beam also showed good agreements, which is shown in Figure 2. According to *Lechner* the deformations in the middle of the span in the bending tests are mainly dependent on the stiffness of the GLT partial cross-sections and not on the veneer layers. In the shear tests, good agreement was again achieved between the experimental test and the FEM calculation for the global deformation at selected points. In addition, strain gauges were applied between the LVLV layers of selected test specimens for the shear tests. The result of the strain achieved in the test compared with that of the numerical calculation showed very good agreement for one test specimen, but a clear deviation for the other (see Figure 3).

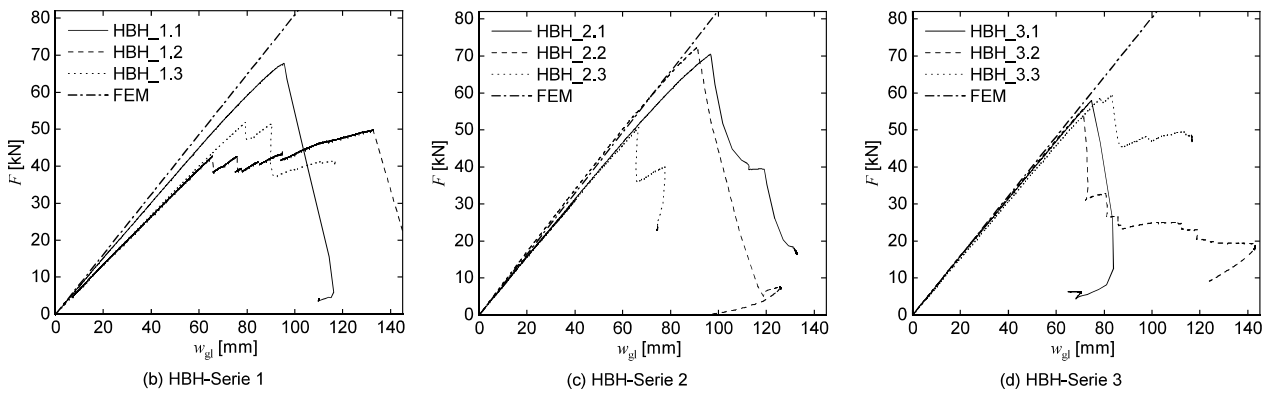


Figure 2. Comparison of the deformation in the center of the beam from the FEM calculation with the experimental results from the bending test (partial sections of a figure from Lechner (2021) rearranged)

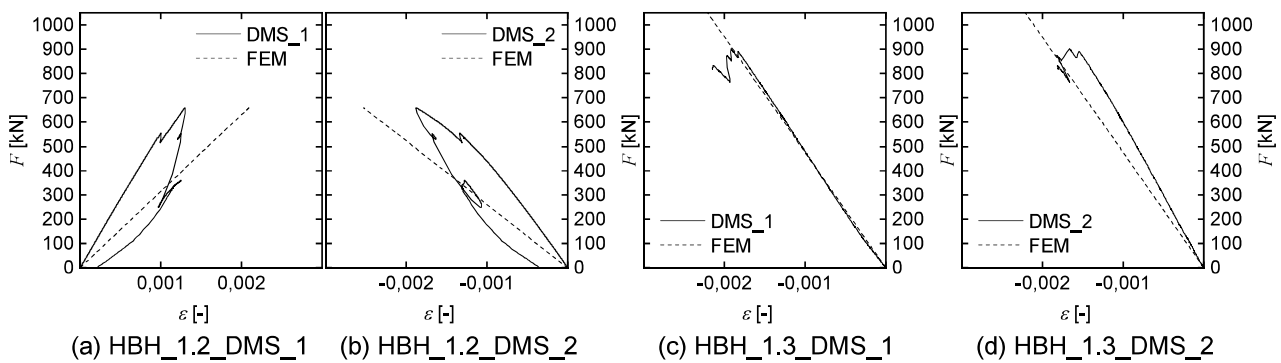


Figure 3. Strain achieved in the shear test compared with that of the numerical calculation from Lechner (2021)

Furthermore, for one beam with two cross-section variants, a comparison of the analytical solution based on the constructive anisotropy approach and the results obtained from the solid model has been done by *Lechner (2021)*. This comparison showed good agreement in selected positions for vertical loading. However, these positions do not cover the whole cross-section results. In addition, design equations have been derived by *Lechner (2021)* from the test results that allow an analytical dimensioning of the beams. These equations are not compared with the FEM results in this paper.

In this paper, the differences in the results of a shell model and those of the solid model are examined. For this purpose, a parameter study with different VRT structures is carried out and the results are compared. Both the main load-bearing direction (vertical load) and the secondary load-bearing direction (horizontal load) are examined. A linear-elastic computation is performed, where deformations and stresses are compared. The aim is to identify special features in the modeling of VRT with a shell model and to check whether it is suitable for modeling VRT, since shell models are easier to create and require less computational time than the solid ones.

## 2 Materials and Methods

### 2.1 Materials

For the investigation in this paper, the material properties of GL24h according to DIN EN 14080:2013-09 (2013) are used for the GLT partial cross-sections. The material properties for the hardwood LVLV layers are assumed to be the same as Pollmeier Baubuche S according to aBG Z-9.1-838 (2023). The Poisson ratios for GLT and LVLV layers are neglected (zero). The material values are listed in Table 1. However, no strength values are listed because no strength verification is performed in this work.

Table 1. Stiffness and strength values of the used materials in [N/mm<sup>2</sup>]

Parameter	GL 24 h	Baubuche S
$E_{0,mean}$	11500	16800
$E_{90,mean}$	300	470
$G_{mean}$	650	760
$G_{R,mean}$ *	65	76

\*  $G_{R,mean}$  is assumed to be 10% of  $G_{mean}$ .

### 2.2 Cross-Sections

The cross-sections are divided into four categories (1 to 4) to investigate and compare different setups. In addition, different cross-section heights with labels (A to C) are used to evaluate the influence of the cross-section geometry on the result. Figure 4 contains the height-neutral representation of all cross-section types, with the classification of the cross-sections in combination with the different heights.

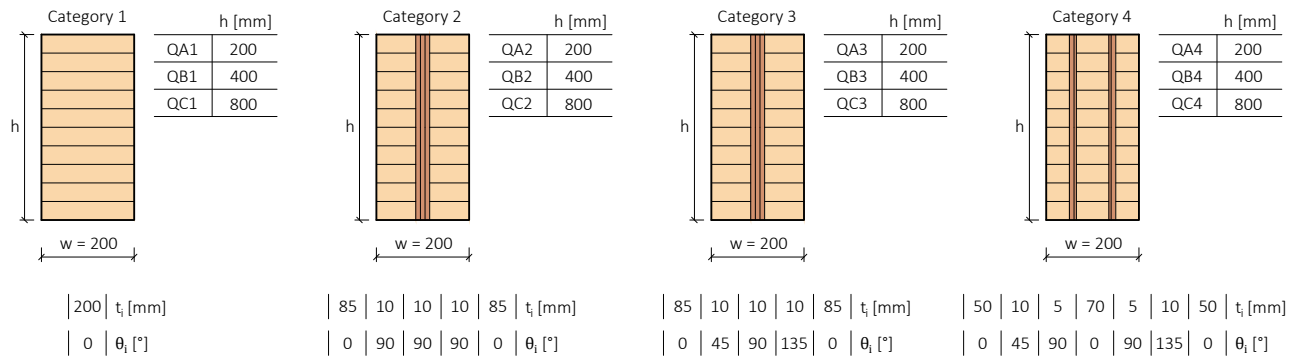


Figure 4. Cross-sections classification with  $\theta_i$  as the fiber orientation located in the  $xz$ -plane and indicated in relation to the  $x$ -axis (see Figures 6 and 7) and  $t_i$  as the width of the partial cross-section.

### 2.3 System Geometry

#### 2.3.1 General

In this work, a distinction is made between the two load cases, "vertical loading- plate in membrane action" and "horizontal loading- plate in bending". The load acts parallel to the layers in the case of "plate in membrane action" and transverse to the layers in the case of "plate in bending action" (see Figures 5, 6 and 7). However, the partially

asymmetrical cross-sections result in a combined state (membrane + bending action) due to coupling effects, which is neglected in the designation of the load cases. The dead weight of the beams is not taken into account in the analysis.

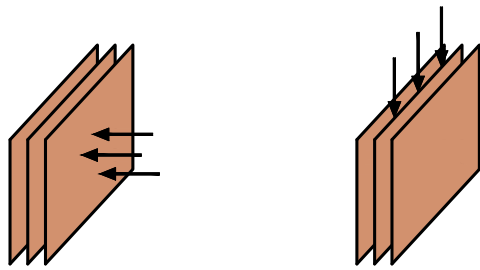


Plate in Bending Action

Plate in Membrane Action

Figure 5. Definition of plate in membrane action and plate in bending with respect to the LVLV layers

### 2.3.2 Vertical Loading - Plate in Membrane Action

The static system is defined as a function of the beam height  $h$ . This results in different static systems for different heights, which aims to investigate the influence of the beam height  $h$  to width  $w$  ratio. By using steel plates in the support and the load application area, the support forces and the load are applied to the individual layers of the composite cross-section based on their stiffness. The magnitude of the load  $F_V$  [MN] =  $0.213 \cdot h$  [m] is also linked to the height of the beam to obtain comparable results. Figure 6 shows the static system for the load case "vertical loading- plate in membrane action".

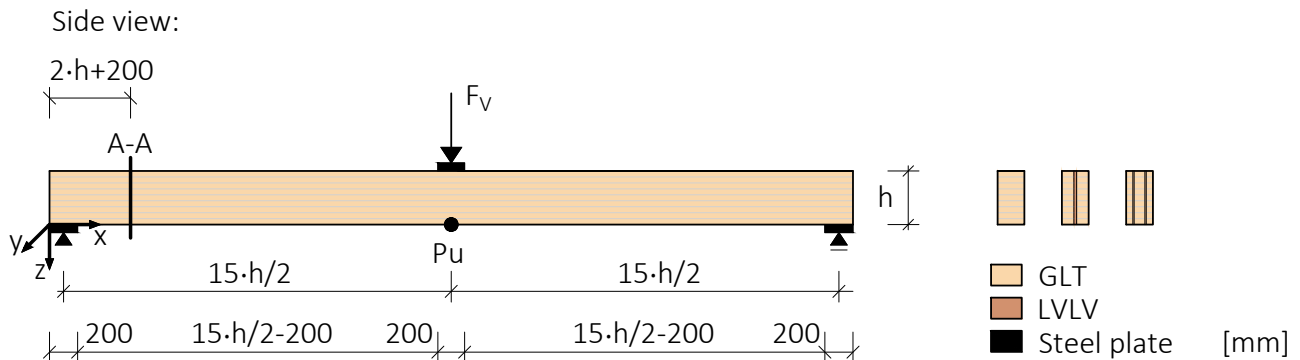


Figure 6. System for the "vertical loading - plate in membrane action" situation with section A-A for the evaluation of the stresses and point  $P_u$  for the evaluation of the beam deformations

### 2.3.3 Horizontal Loading - Plate in Bending

For the horizontal loading, investigations are only carried out for the cross-section height  $h = 400$  mm. The load is distributed as a line load over the cross-section height and totals 0.0426 MN. The steel plates at the supports and the load application point are added only for the solid models since the plane stress problem appears for the shell model. The GLT is divided into several layers during shell-modeling to ensure a better evaluation. Figure 7 shows the static system for the load case "horizontal loading- plate in bending action".



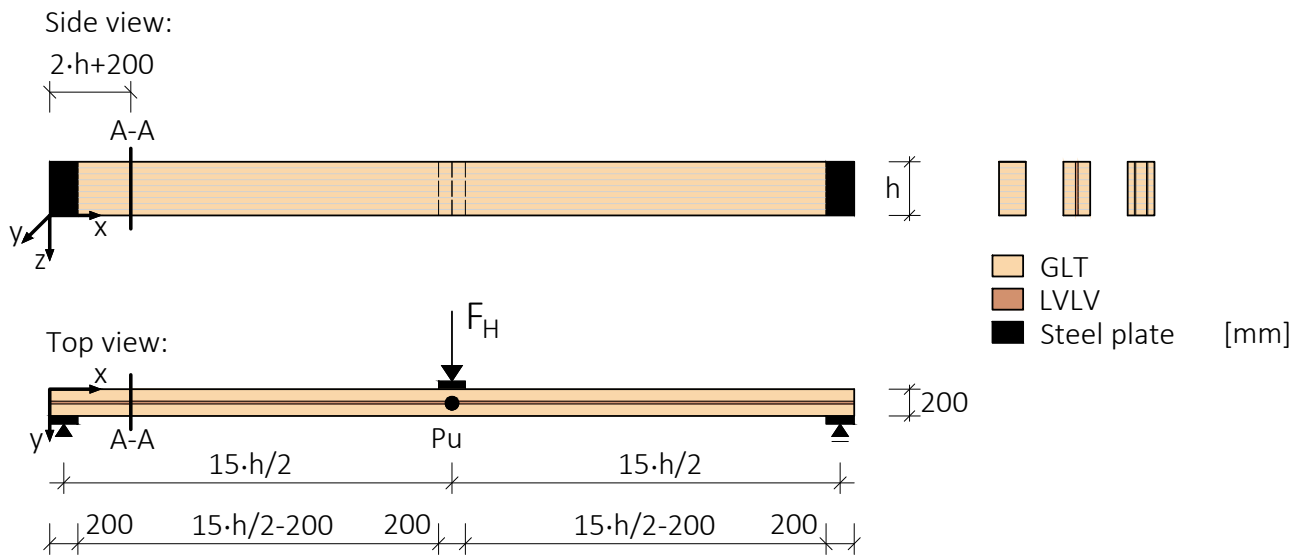


Figure 7. System for the "horizontal loading - plate in bending" situation with section A-A for the evaluation of the stresses and point  $P_u$  for the evaluation of the beam deformations

## 2.4 Mechanical Basics

### 2.4.1 Material Modeling

The material model for both the GLT and the LVLV is considered to be transversely isotropic for the solid model as well as for the shell model. The transversal isotropy combines the radial and tangential properties into ones transverse to the grain. An orthotropic material model with a cylindrical element coordinate system for the GLT partial cross-sections was additionally examined as an example. The differences in the results compared to the transversely isotropic material model were only slight, which is why the transversely isotropic material model is used in this work.

### 2.4.2 Finite Elements

Shell-elements and solid-elements are used for the investigation. While the shell-model reduces the cross-section to a surface plane, the solid-model recreates it with volumes. Figure 8 highlights the difference between the two systems in the modeling. When modeling VRT as a solid model, the element type "SOLID186" from Ansys is used. The SOLID186 element is a higher order 3-D 20-node solid element that exhibits quadratic displacement behavior. It is defined by 20 nodes having three degrees of freedom per node, which are the translations in the nodal x, y, and z directions. For the modeling of VRT as a shell, the composite cross-section is modeled as one with rigidly interconnected layers using laminate theory. The element type used is a shell element with both an in-plane and an out-of-plane load-bearing effect and whose cross-sectional structure is possible with rigidly interconnected layers. The element "SHELL181" was selected for this purpose. The element is based on the first-order shear deformation theory, known as the Reissner-Mindlin plate theory. Ansys (2023)

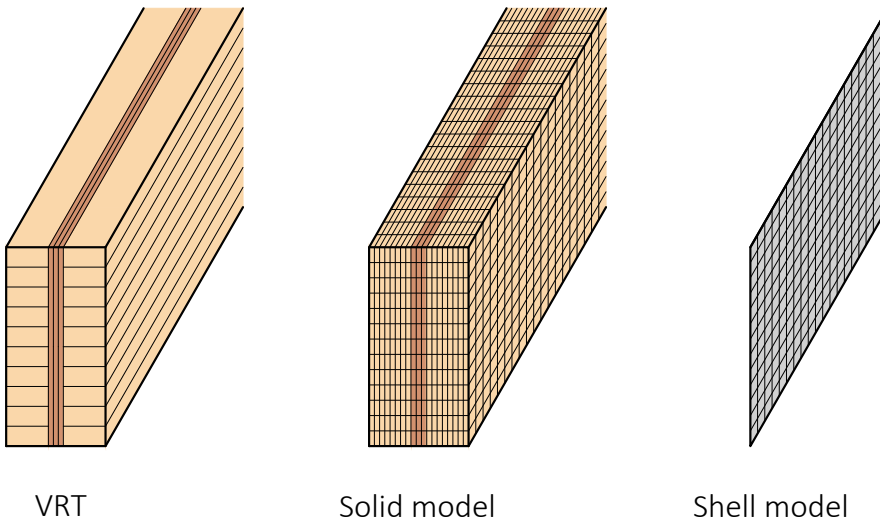


Figure 8. Schematic representation of the solid and shell model

## 3 Results and Discussion

### 3.1 Vertical Loading - Plate in Membrane Action

#### 3.1.1 General

The results are evaluated separately for the individual cross-section types. Both deformations and stresses are compared for the respective calculation methods. The position of the stress evaluation is shown in Figure 6. The stresses are always referred to the global coordinate system in evaluating the results. A transformation to the local coordinate system is not performed since comparing global stresses appears to be sufficient. In the solid model, the stresses are calculated as the average of the stresses at the element nodes. For the stresses in the shell model, the layers' average value in the center of the layer is used. The difference stress results from subtracting the stresses of the shell model from those of the solid.

#### 3.1.2 Vertical Loading - Results of cross-sections QA1, QB1 and QC1 (Figure 4)

The deformation of the solid model is greater than that of the shell model. For the pure GLT cross-section, the difference of deformation between the solid and shell model are 0.8% for QA1, 0.3% for QB1 and 0.1% for QC1. It is observed, that the difference in deformation decreases with increasing cross-section height. The absolute and percentage difference in deformation along the beam length are shown in Figure 9, where the different beam lengths are normalized to the width of the diagram.

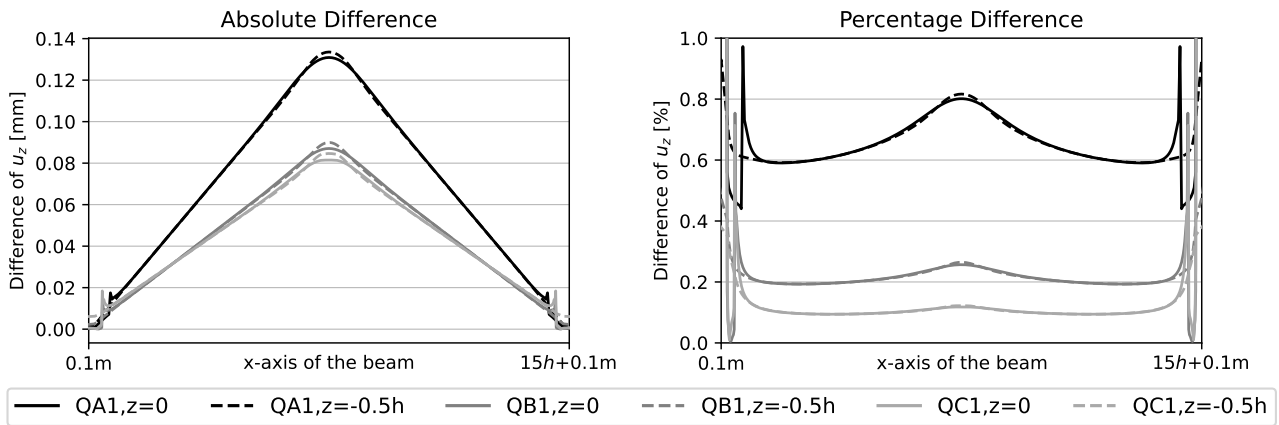


Figure 9. Difference of deformation for QA1, QB1 and QC1 over the x-axis of the beam (see Figure 6)

As expected for QA1, QB1, and QC1, the stresses differ little to not at all when comparing the solid and the shell model (see Figures 10 and 11).

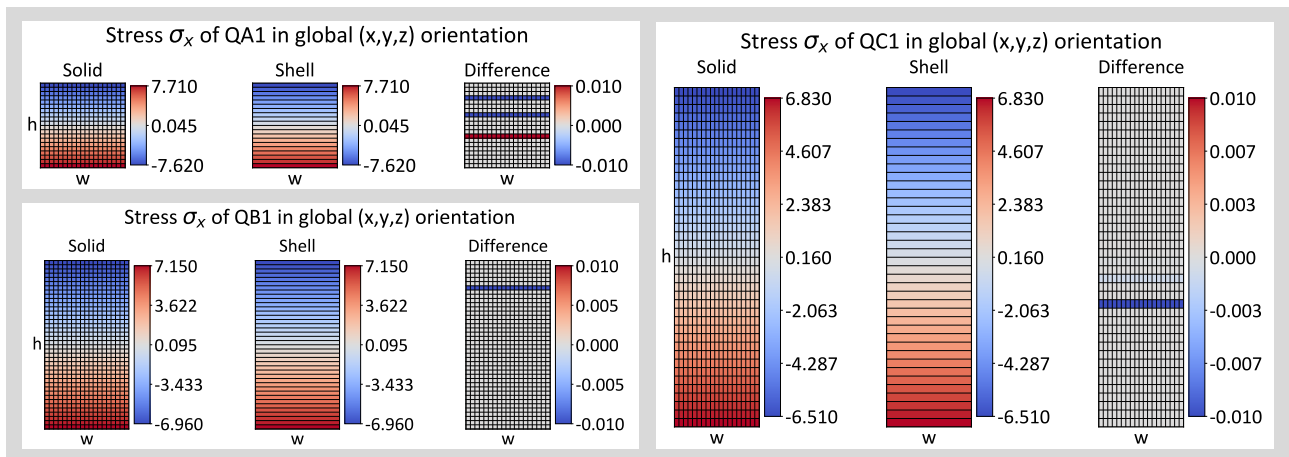


Figure 10. Evaluation of stress  $\sigma_x$  on section A-A (see Figure 6) for QA1, QB1 and QC1 [N/mm<sup>2</sup>]

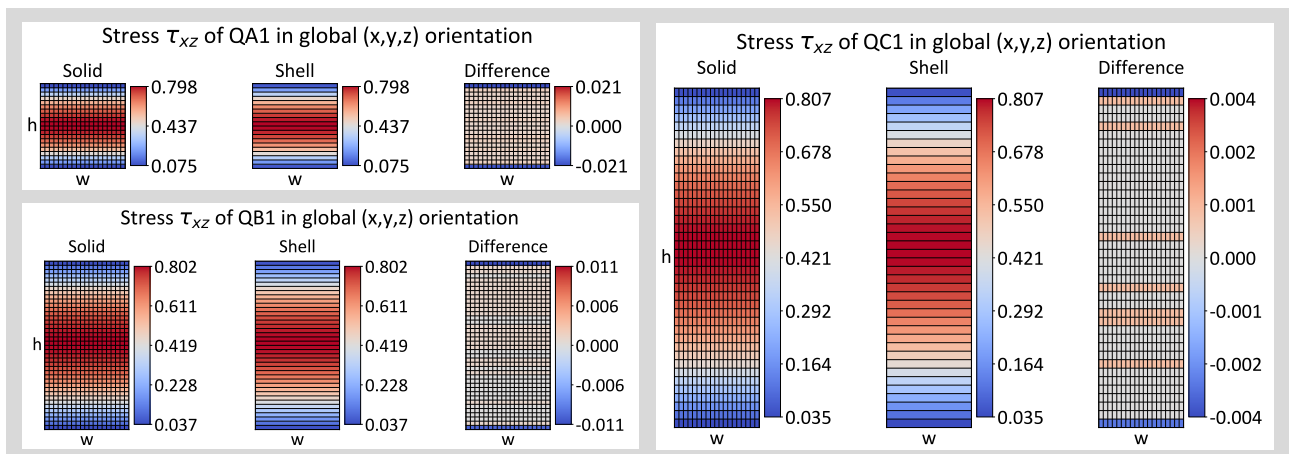


Figure 11. Evaluation of stress  $\tau_{xz}$  on section A-A (see Figure 6) for QA1, QB1 and QC1 [N/mm<sup>2</sup>]

### 3.1.3 Vertical Loading - Results of cross-sections QA2, QB2 and QC2 (Figure 4)

When comparing the difference between the deformation of the shell and the solid model, it is noticeable that the differences are slightly higher than for cross-section

category 1. The difference of deformations between the solid and shell model are 1.4% for QA2, 0.5% for QB2 and 0.2% for QC2. Again the deformation in the center of the beam of the solid model is higher than the shell one.

The comparison of the stresses for the cross-sections QA2, QB2 and QC2 shows that the stresses in the longitudinal direction  $\sigma_x$  differ only slightly between the solid and the shell model (see Figure 12). However, due to the low stiffness of the LVLV in the longitudinal direction of the beam, the stresses in this direction are very low for the LVLV layers.

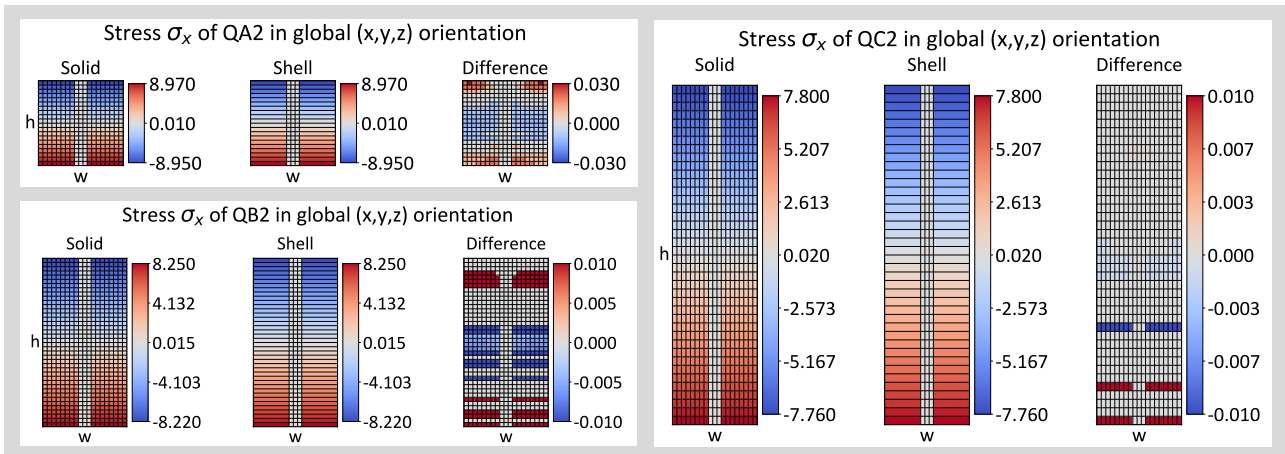


Figure 12. Evaluation of stress  $\sigma_x$  on section A-A (see Figure 6) for QA2, QB2 and QC2 [N/mm<sup>2</sup>]

Figure 13 contains the shear stress  $\tau_{xz}$  for cross-section QA2, QB2 and QC2. It can be observed, that the shear stress distribution in the cross-section of the solid model is not constant along the width. For the GLT partial cross-sections, the outer edge shows higher stresses than the edge adjacent to the LVLV. Compared to the shell model, the solid model results in higher stresses for the GLT partial cross-sections. In the LVLV, it can be seen that the outer layers exhibit higher stresses than the inner layers. In the solid model, the LVLV partial cross-section shows lower stresses compared to the shell model.

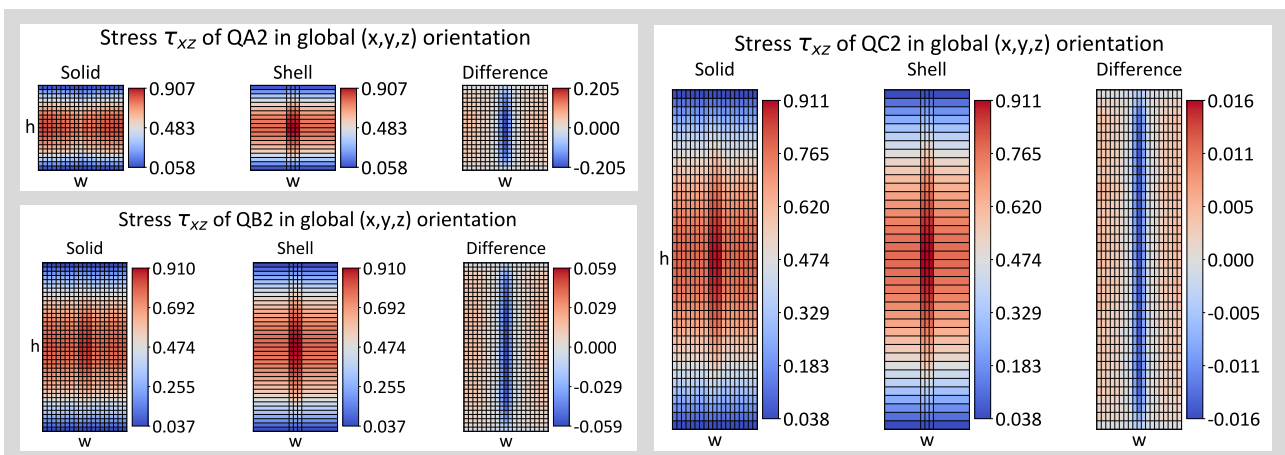


Figure 13. Evaluation of stress  $\tau_{xz}$  on section A-A (see Figure 6) for QA2, QB2 and QC2 [N/mm<sup>2</sup>]

3.1.4 Vertical Loading - Results of cross-sections QA3, QB3 and QC3 (Figure 4)

Again the deformation in the center of the beam of the solid model is higher than the shell one. When comparing the deformations in the center of the beam, a difference of 4.2% for QA3, 2.2% for QB3 and 1.1% for QC3 could be determined. Compared to the deformation differences of cross-section category 1 and 2, larger differences prevail here.

The comparison of the stresses  $\sigma_x$  in longitudinal direction of the beam are shown in Figure 14, for the cross-section variants QA3, QB3 and QC3. In LVLV inclined layers, higher stresses occur in the shell model compared to the solid one. The differences in stresses between solid and shell at the 45° and the 135° layers are mainly evident in the top and bottom region of the cross-section. It is observed that the differences are greater for the low cross-sectional height than for the large one. For the GLT partial cross-sections, slightly higher stresses result in the solid model than in the shell model.

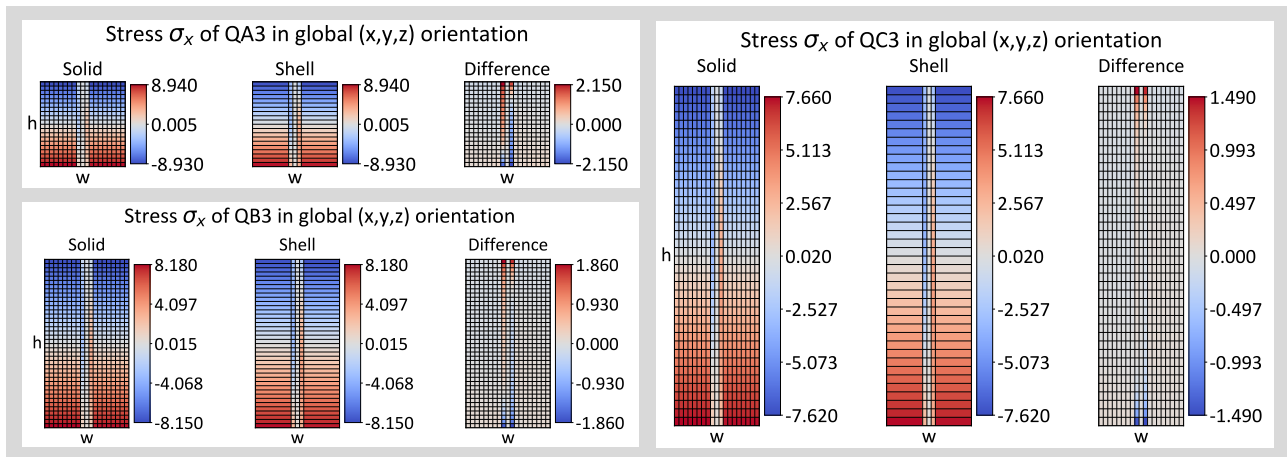


Figure 14. Evaluation of stress  $\sigma_x$  on section A-A (see Figure 6) for QA3, QB3 and QC3 [N/mm<sup>2</sup>]

For the stresses in the z-direction, again the differences occur predominantly in the LVLV layers. The GLT partial cross-sections exhibit only low stresses due to the low stiffness in the z-direction.

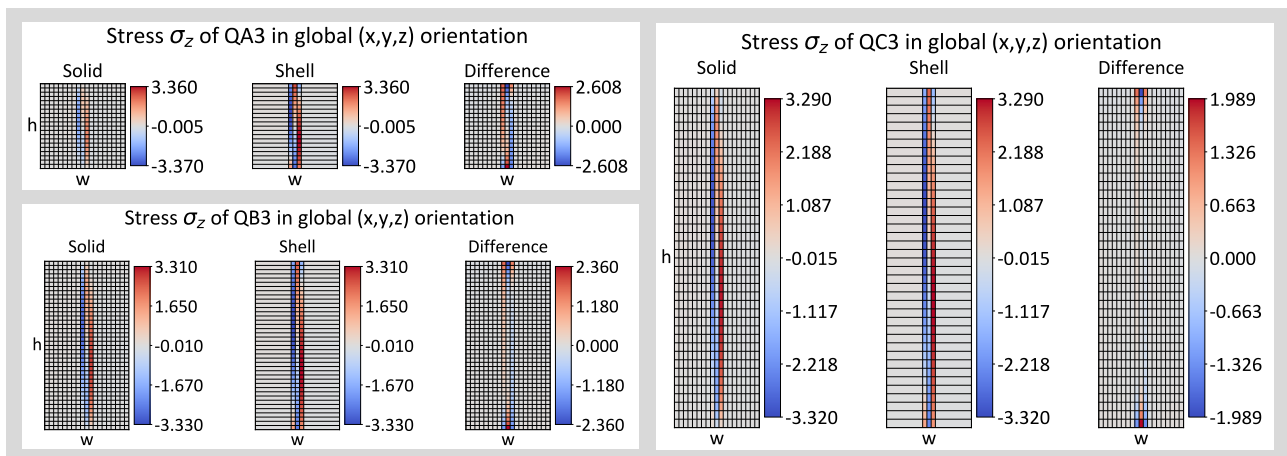


Figure 15. Evaluation of stress  $\sigma_z$  on section A-A (see Figure 6) for QA3, QB3 and QC3 [N/mm<sup>2</sup>]

Comparing the shear stresses for cross-section category 3, differences occur between the calculation methods, especially in the top and bottom regions (see Figure 16). Again, it is observed that the differences are greater for the low cross-sectional height than for the large one.

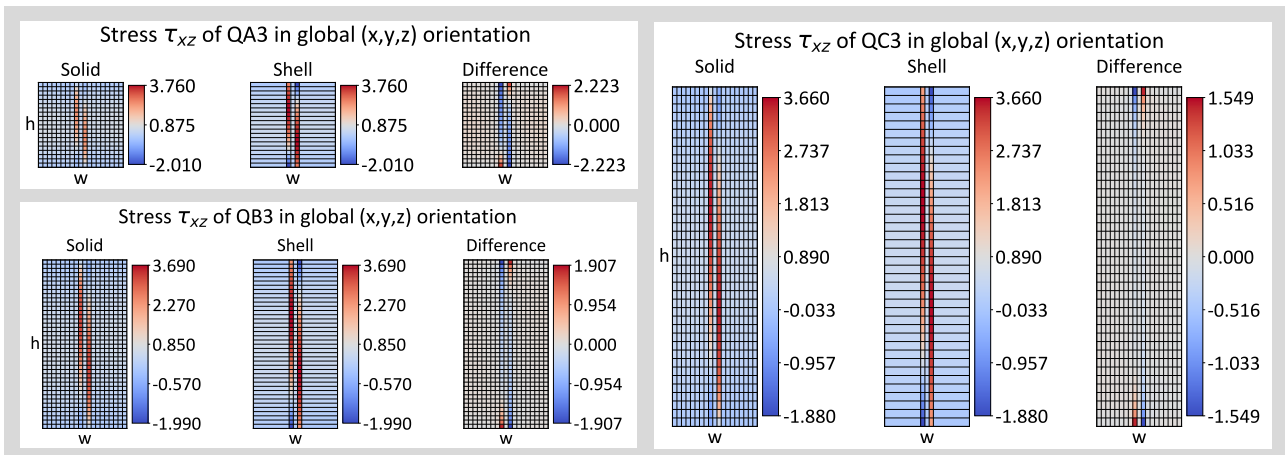


Figure 16. Evaluation of stress  $\tau_{xz}$  on section A-A (see Figure 6) for QA3, QB3 and QC3 [N/mm<sup>2</sup>]

### 3.1.5 Vertical Loading - Results of cross-sections QA4, QB4 and QC4 (Figure 4)

The difference of deformations between the solid and shell model are 2.9% for QA4, 1.4% for QB4 and 0.8% for QC4. Again the deformation in the center of the beam of the solid model is higher than the shell one.

The stresses in longitudinal direction of the beam  $\sigma_x$  are shown in Figure 17. As with the previous cross-section category, there is a difference between the two models in the inclined layers of the LVLV in the top and bottom region of the cross-section. The stress of the LVLV in the shell model is higher than in the solid model. The difference in stresses decreases from the top and bottom to the center of the cross-section. Due to the higher coupling stiffness compared to the other cross-section categories, there is a bending in the transverse direction, which results in a deviation of the stresses in the GLT partial cross-sections due to the coarse discretization of the shell model in the beam width.

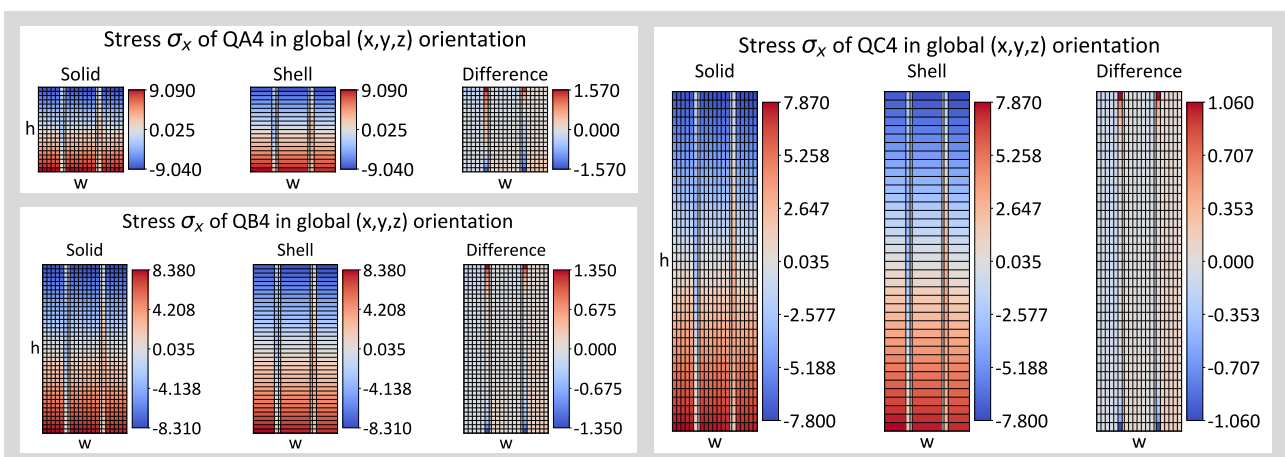


Figure 17. Evaluation of stress  $\sigma_x$  on section A-A (see Figure 6) for QA4, QB4 and QC4 [N/mm<sup>2</sup>]



The stresses in transverse direction of the beam  $\sigma_z$  are shown in Figure 18. The differences in stresses between solid and shell are mainly evident in the LVLV layers in the top and bottom region of the cross-section. Again, the stress differences decrease as the height of the cross-section increases. In addition, it can be seen that the differences become smaller towards the center of the cross-section.

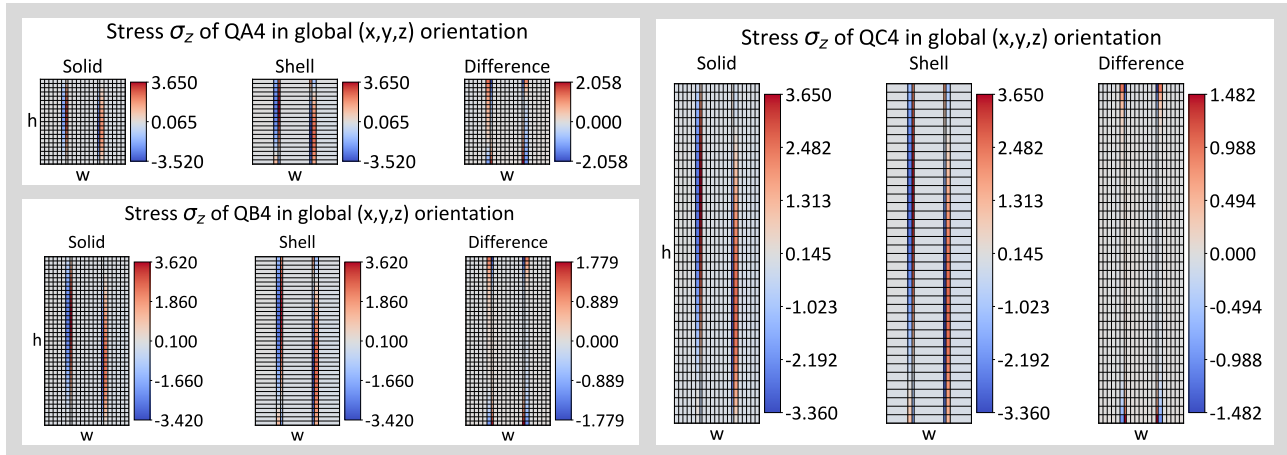


Figure 18. Evaluation of stress  $\sigma_z$  on section A-A (see Figure 6) for QA4, QB4 and QC4 [N/mm<sup>2</sup>]

Based on the shear stresses  $\tau_{xz}$ , shown in Figure 19, it can be observed that the 45° and 135° inclined LVLV layers experience the most shear stresses, as they also have a much higher shear stiffness than the other partial cross-sections due to the inclination. Again, the largest stress differences are found in the LVLV layers at the top and bottom of the cross-section.

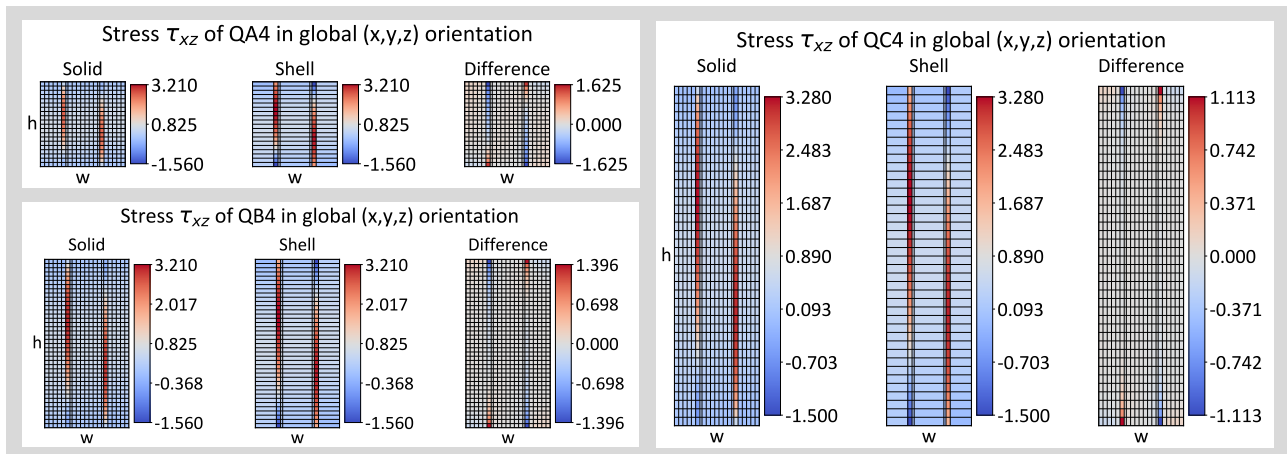


Figure 19. Evaluation of stress  $\tau_{xz}$  on section A-A (see Figure 6) for QA4, QB4 and QC4 [N/mm<sup>2</sup>]

### 3.2 Horizontal Loading - Plate in Bending Action

#### 3.2.1 General

As described in Chapter 2.3, only investigations for the cross-section height  $h = 400$  mm are carried out. The evaluation is performed analogously to the evaluation of the plate in membrane action. The deformations are evaluated in the  $y$ -direction. The average of all nodes in the height is therefore used as the value for comparison.

### 3.2.2 Horizontal Loading - Results of cross-section QB1 (Figure 4)

The deformation of the structure in the shell model is higher than the solid one. Comparing the deformation of the two models, a deviation of about 2.4% is observed. The comparison of the stresses shows little to no differences (see Figure 20).

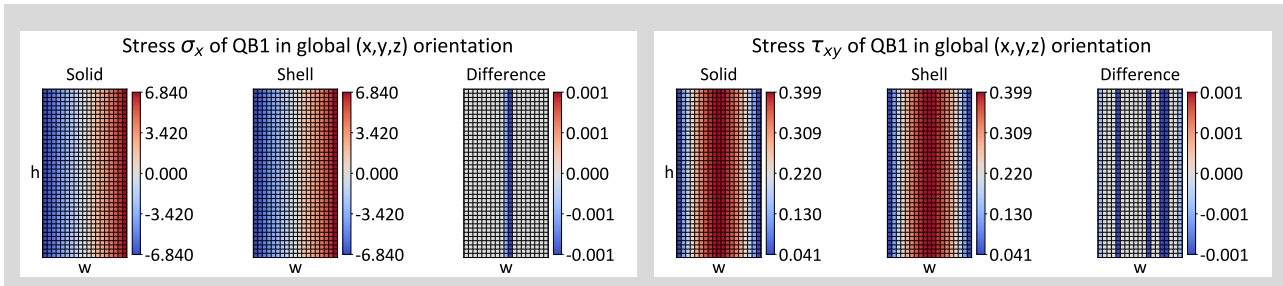


Figure 20. Evaluation of stresses  $\sigma_x$  and  $\tau_{xy}$  on section A-A (see Figure 7) for QB1 [N/mm<sup>2</sup>]

### 3.2.3 Horizontal Loading - Results of cross-section QB2 (Figure 4)

Comparing the deformation of the solid and the shell model, a deviation of approx. 2.9% results. The deformation of the structure in the shell model is higher than the solid one. The comparison of the stresses exhibits minor differences for the stress in the longitudinal direction of the beam  $\sigma_x$  and for the shear stress  $\tau_{xy}$  (see Figure 21).

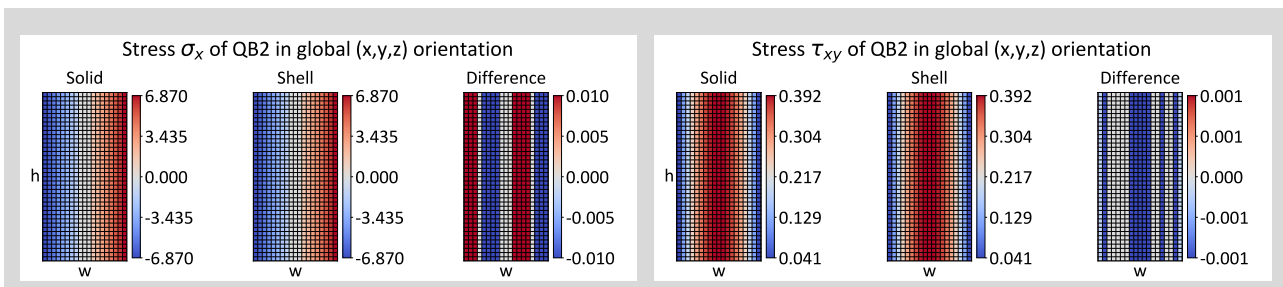


Figure 21. Evaluation of stresses  $\sigma_x$  and  $\tau_{xy}$  on section A-A (see Figure 7) for QB2 [N/mm<sup>2</sup>]

### 3.2.4 Horizontal Loading - Results of cross-section QB3 (Figure 4)

Comparing the deformation of the two models, a deviation of about 2.5% is observed. The deformation of the structure in the shell model is higher than the solid one.

The stress evaluation is shown in Figure 22. Especially in the top and bottom regions of the cross-section, little differences appear in  $\sigma_x$  for the LVLV layers. The deviation of  $\sigma_x$  in the GLT partial cross-sections is small and no pattern is recognizable. The difference of the stresses in z-direction  $\sigma_z$  exhibits mainly differences in the LVLV layers at the top and bottom region of the cross-section. The 90° LVLV layer as well as the GLT partial cross-sections are hardly stressed in the z-direction. In the case of transverse shear stresses  $\tau_{xy}$ , stress peaks appear in the solid model next to the LVLV at the top and bottom region of the cross-section.



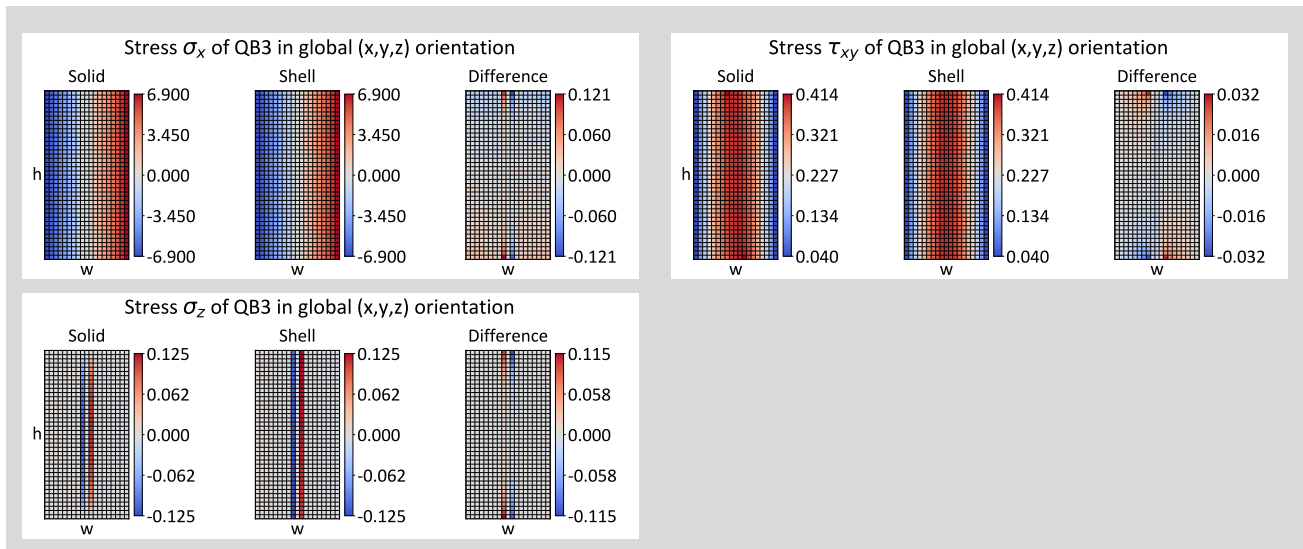


Figure 22. Evaluation of stresses  $\sigma_x$ ,  $\sigma_z$  and  $\tau_{xy}$  on section A-A (see Figure 7) for QB3 [N/mm<sup>2</sup>]

### 3.2.5 Horizontal Loading - Results of cross-section QB4 (Figure 4)

Comparing the deformation of the two models, a deviation of about 2.4% is observed. The deformation of the structure in the shell model is higher than the solid one.

Figure 23 shows the stresses of QB4. The stresses  $\sigma_x$  mainly show differences in the top and bottom region of the cross-section for the 45° and 135° inclined LVLV layers. The deviation of  $\sigma_x$  in the GLT partial cross-sections is small. It can further be observed that differences in the stresses in the z-direction  $\sigma_z$  are also only to be found in the upper and lower region of the cross-section in the LVLV layers. In contrast to QB3, the 90° inclined layer of the LVLV in QB4 has a tension in the z-direction. The GLT partial cross-sections are hardly stressed in the z-direction. In the case of transverse shear stresses  $\tau_{xy}$ , peaks of stress difference appear in the solid model next to the LVLV at the upper and lower ends of the cross-section.

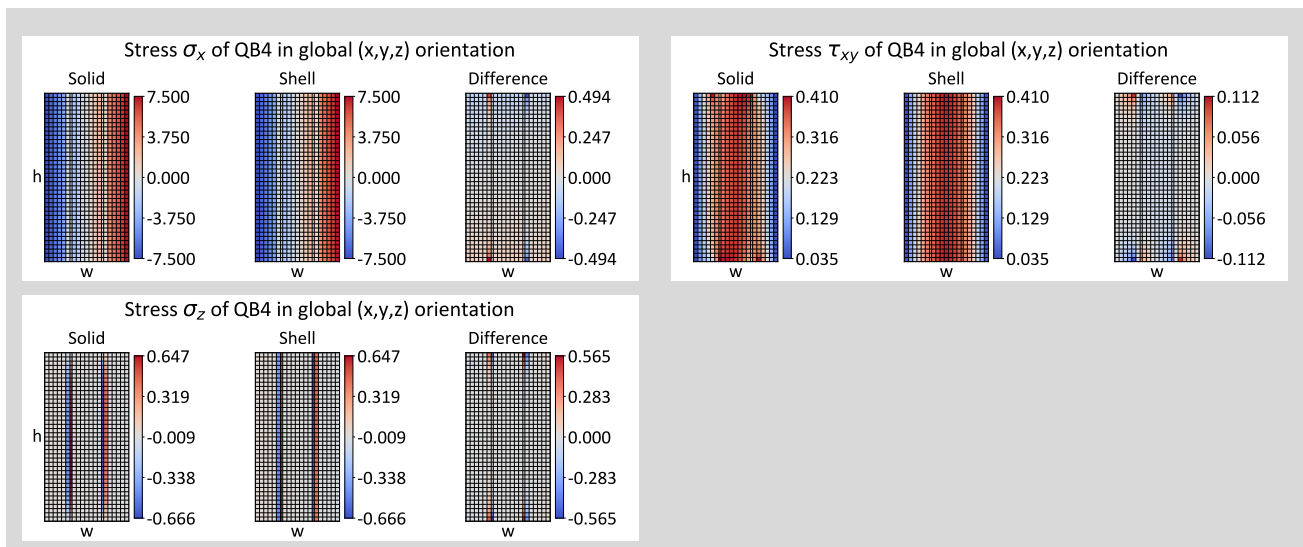
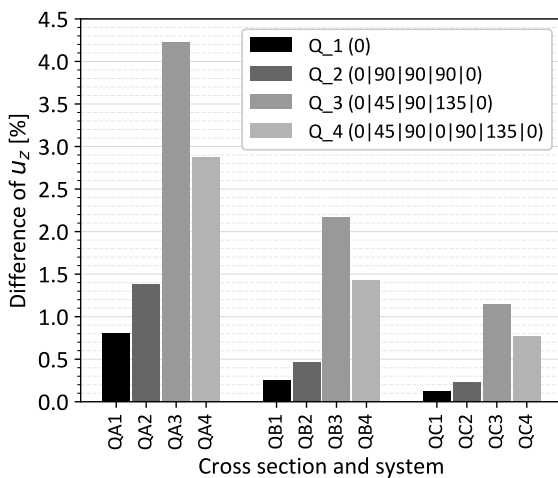


Figure 23. Evaluation of stresses  $\sigma_x$ ,  $\sigma_z$  and  $\tau_{xy}$  on section A-A (see Figure 7) for QB4 [N/mm<sup>2</sup>]

### 3.3 Summary

#### 3.3.1 Vertical Loading - Plate in Membrane Action

The differences in the deformation are listed and visualized in Figure 24. The deformations under vertical loading were higher in the solid model than in the shell model. It is noticeable that the difference is smaller for the pure GLT cross-section (category 1) than for the other cross-section variants. This can be attributed to the fact that this variant had the least disturbance effects, such as the limited deformation of the individual layers at the top and bottom region of the cross-section relative to each other in the shell model. Furthermore, it is observed that differences of the cross-section and systems with only 90° LVLV layers (category 2) are lower than those with 45° and 135° layers, respectively (category 3 and 4). Additionally it could be examined that with increasing  $h/w$  ratio, the difference in deformation deviates. However, this is not due to the  $h/w$  ratio, but rather to the shear stiffness of the beam in the different models, as revealed by the evaluation of the difference in deformation of QA1, QB1 and QC1 (see Figure 9). The linear deviation of the absolute difference in deformation indicates a difference in shear deformation and has a greater effect on the percentage deviation for the short span than for the larger spans.



C-S	$u_z$ -Solid [m]	$u_z$ -Shell [m]	Difference [%]
QA1	0.016337	0.016206	0.8
QA2	0.018769	0.018509	1.4
QA3	0.018128	0.017362	4.2
QA4	0.018081	0.017561	2.9
QB1	0.033910	0.033823	0.3
QB2	0.038846	0.038664	0.5
QB3	0.037120	0.036316	2.2
QB4	0.037225	0.036692	1.4
QC1	0.069059	0.068978	0.1
QC2	0.078525	0.078348	0.2
QC3	0.074515	0.073664	1.1
QC4	0.074860	0.074281	0.8

Figure 24. Difference of the deformation between the solid model and the shell model in the center of the beam under vertical loading (C-S: cross-section)

In the stress evaluation, differences of a magnitude that cannot be neglected appeared mainly at the top and bottom region of the cross-section in the LVLV layers. In contrast to the solid model, the shell model showed higher stresses in the LVLV layers under vertical loading, while the GLT areas were less stressed. During the evaluation, it was noticed that the differences were present to a greater extent for the smaller cross-section heights than for the larger ones. One explanation for this is the blocking effect of the layers at the edge of the cross-section with the laminate theory, which spreads into the center of the cross-section. Compared to the differences in the LVLV layers, the differences in the GLT partial cross-sections were only small.

### 3.3.2 Horizontal Loading - Plate in Bending

The differences in the deformation are listed in Table 2. The differences in deformation between the models are low and in a similar range for all cross-section types.

Table 2. Difference of the deformation between the solid model and the shell model in the center of the beam under horizontal loading (C-S: cross-section)

C-S	$u_y$ -Solid [m]	$u_y$ -Shell [m]	Difference [%]
QB1	0.062621	0.064148	2.4%
QB2	0.065470	0.067400	2.9%
QB3	0.064546	0.066170	2.5%
QB4	0.068101	0.069759	2.4%

A comparison of the stresses reveals similar findings to the vertical loading. The LVLV layers are stressed more in the shell model than in the solid model, particularly in the top and bottom region of the cross-section. The reasons for this have already been mentioned. The differences in the stresses in the GLT partial cross-sections are mostly minor. Only the shear stresses around the LVLV layer show greater deviations in the stresses in the GLT partial cross-sections.

## 4 Conclusion

The calculation results of the shell model and those of the solid model agree to a large extent, especially for larger  $h/w$  ratios. While the deformation between the models agrees very well, considerable differences can be observed in the stresses in some areas. The problem here is that the stresses in the shell model are not always on the safe side, as they are often lower in the GLT partial cross-sections than those of the solid model. It can therefore be concluded that the shell model provides a good approximation to the solid model, but has some uncertainties for the design.

Working Group 11 of the European standardisation Sub-Committee CEN/TC250/SC5 Eurocode 5 for Finite Element Based Design was recently founded, which emphasizes the importance of numerical modeling for practitioners. This work should contribute to the creation of guidelines and recommendations for the modeling of VRT using FEM. Further research could lead to the derivation of a global modeling safety factor in the future, which could make it possible to calculate and dimension VRT using shell elements. However, this would require a review of various load-bearing systems, types of loading and geometries.

## 5 References

aBG Z-9.1-838 (2023). *Furnierschichtholz aus Buche zur Ausbildung stabförmiger und flächiger Tragwerke "Platte BauBuche S" und "Platte BauBuche Q": Pollmeier Furnierwerkstoffe GmbH.*

- Aicher, S. & Tapia, C. (2018). “Novel internally LVL-reinforced glued laminated timber beams with large holes”. In: *Construction and Building Materials* 169, pp. 662–677. DOI: 10.1016/j.conbuildmat.2018.02.178.
- Ansys (2023). *Element Reference: Release 2023 R1*.
- DIN EN 14080:2013-09 (2013). *DIN EN 14080:2013-09, Holzbauwerke - Brettschichtholz und Balkenschichtholz - Anforderungen; Deutsche Fassung EN 14080:2013: DIN Deutsches Institut für Normung e.V. Berlin*. DOI: 10.31030/1936211.
- Lechner, M. (2021). “Holzbewehrtes Holz: Entwicklung eines furnierverstärkten stabförmigen Holzprodukts für tragende Zwecke”. Dissertation. München: Technische Universität München.
- Lechner, M.; Dietsch, P. & Winter, S. (2021). “Veneer-reinforced timber – Numerical and experimental studies on a novel hybrid timber product”. In: *Construction and Building Materials* 298, p. 123880. DOI: 10.1016/j.conbuildmat.2021.123880.

## Acknowledgement

Gefördert durch:



aufgrund eines Beschlusses  
des Deutschen Bundestages

DISCUSSION

**The paper was presented by N Kainz**

*U Kuhlmann mentioned the necessity to vary the span to change the ratio between bending and shear stresses.*

*W Seim stated that comparisons between model and test results should be based on deformations and not stresses. He commented more detailed information on shell elements was missing in the paper. JW van de Kuilen agreed with W Seim's comments.*

*S Aicher stated the paper missed analytical results for engineers. He echoed the comment that one cannot measure stresses which would be obtained via strain measurements with knowledge of the elasticity constants. These issues should be addressed in the final paper submission.*

*J Töpler and N Kainz discussed model uncertainties. J Töpler mentioned the WG11 procedures to verify the model.*

*P Dietsch stated the results would depend on  $E_{90}$  which would be dependent on annual ring orientation; hence, using polar approach might be more appropriate. N Kainz responded that he would not expect not much effect. P Dietsch stated a lot of the cited reference are in German language. One should consider giving English reference and expand the reference list.*

*C Tapia Camu commented that one advantage of this veneer reinforcement method would be the reinforcement against stress concentration for holes etc. He questioned the use of such simplified models as they would render worse results compared to a solid model.*





# Strength and stiffness of adhesively bonded timber-steel composite beams

Simon Aurand<sup>1)</sup>, Peter Haase<sup>2)</sup>, Jakob Boretzki<sup>2)</sup>, Matthias Albiez<sup>2)</sup>, Philipp Dietsch<sup>1)</sup>, Thomas Ummenhofer<sup>2)</sup>

<sup>1)</sup> KIT Timber Structures and Building Construction, Karlsruhe

<sup>2)</sup> KIT Steel and Lightweight Structures, Karlsruhe

Keywords: timber, steel, adhesive bonding, timber-steel composite

## 1 Introduction

### 1.1 Background

As a sustainable building material, timber can help replace conventional CO<sub>2</sub>-intensive construction materials. To further establish timber structures in the sector of e.g. office buildings, appropriate cross-sections for large spans are required. These could be realized as composite cross-sections consisting of different materials. The materials timber and steel can complement each other in composite cross-sections and compensate for the weaknesses of the other bonding partner (*Riola Parada (2016)*). Advantages include the use of slender steel profiles, as they are embedded in the timber and local stability failure is prevented. Also, the fire resistance is increased by the embedment in the timber. Finally, the composite beams allow for typical bolted steel connections with high load-carrying capacity and stiffness, as is usual in steel construction.

### 1.2 State of the art

Numerous research projects have studied the potential of composite timber beams by adding a composite partner horizontally either in the tensile zone (of bending beams) or in both, the tensile and compressive zone. *Blaß & Romani (2000)* and *Blaß et al. (2003)* adhesively bonded carbon-fibre-reinforced polymers (CFRP) to GLT beams and performed 4-point bending tests. The area ratio of CFRP to timber was merely 0.4 to 3.0%. They determined an increase of 25 to 100% in load-carrying capacity and of 10 to 110% in bending stiffness. The test data showed that a significant increase in bending stiffness of  $\geq 100\%$  was only possible with the highest tested area ratio of 3.0%. *Shekarchi et al. (2020)* adhesively bonded pultruded GFRP profiles to timber beams. The results showed an increase of the bending stiffness of only 20 to 60%, although the area ratios were quite high with 5% to 17%. In these, the moduli of elasticity (*MOE*) of the used materials were almost equal, with a ratio ( $E_{\text{Timber}}/E_{\text{GFRP}}$ ) of 0.77. *Fukutomi &*



*Shioya* (2018) and *Mori & Shioya* (2021) adhesively bonded steel rebars in the tensile and compressive zone of timber beams, and also performed 4-point bending tests. The results are quite promising, with an increase in load-carrying capacity of 25 to 100% and a significant increase in bending stiffness of 130 to 280%. The higher increases (180 to 280%) are due to an area ratio of 3.6 to 11%, a ratio of the *MOEs* ( $E_{\text{Timber}}/E_{\text{Steel}}$ ) of approx. 0.05, and a ratio of timber bending strength to steel tensile strength of approx. 0.15.

The following research projects inserted a flatwise arranged joining partner in horizontal orientation: *Alam* (2004) investigated internally reinforced LVL, by joining steel and LVL either with nails or adhesive bonding. The evaluation of the results showed an increase in load-carrying capacity of max. 50% and an increase of bending stiffness of 170% (both for the adhesively bonded specimens). *Riola Parada* (2016) embedded steel I-profiles in GLT and CLT and joined the hybrid partners with bolts. The tests showed an increase in bending stiffness of 50%, when the profile was arranged symmetrically, and of 110%, when the profile was arranged asymmetrically. For both research projects with vertically arranged steel profiles, the area ratio ( $A_{\text{steel}}/A_{\text{timber}}$ ), the ratio of the *MOEs* ( $E_{\text{timber}}/E_{\text{steel}}$ ), and the ratio of bending to tensile strength ( $f_m/f_u$ ) were quite similar, with values of approx. 0.05, 0.06, and 0.12, respectively.

Concluding from the evaluation of the cited literature it can be stated that the area ratio of the two joined materials needs to be high enough (>0.03). The ratio of the *MOEs*, however, needs to be low enough (approx. 0.05), while on the other side, the ratio of bending to tensile strength should not be too low (>0.05) whilst simultaneously not too high either (<0.3). Furthermore, the bond between the two composite partners has to be sufficient. This is highlighted by the results of the vertical reinforcement, where the ratios all fit the aforementioned requirements, but the max. increase in stiffness was still 100%. Here, the bond was realized with nails or bolts and did, therefore, not have sufficient stiffness. Table 1 summarises the evaluated results from the cited literature and the corresponding ratios of the specimens' properties.

Table 1. Results from literature: increase in load-carrying capacity  $F_{\text{max}}$ ; increase in bending stiffness  $EI$ ; area ratio of joined material 1 to timber; ratio of MOE of timber to material 1; ratio of bending to tensile strength of timber to material 1.

		Mat.	$\Delta F_{\text{max}}$	$\Delta EI$	Area ratio	Ratio MOE	Ratio $f_m/f_u$
Horizontal	<i>Blaß &amp; Romani</i> (2000)	CFRP	25–100%	10–110%	0.4–3.1%	7–16%	1.5–4.6%
	<i>Blaß et al.</i> (2003)	CFRP	40–75%	10–35%	0.4–0.9%	6–15%	1.5–3.5%
	<i>Shekarchi et al.</i> (2020)	GFRP	-	20–60%	5.0–17%	77%	29%
	<i>Fukutomi &amp; Shioya</i> (2018)	Steel	25-95%	130–280%	2.6–11%	4%	15%
	<i>Mori &amp; Shioya</i> (2021)	Steel	-	180–250%	3.6–5.5%	4%	14%
Vertical	<i>Alam</i> (2004)	Steel	50%	70*–170%	5.4%	6%	12%
	<i>Riola Parada</i> (2016)	Steel	-	50–100%	4.6–5.4%	6%	13%

\* nailed specimens

To investigate the bond of different state of the art and recently developed joining techniques, *Haase et al. (2024a)* conducted small-scale tensile tests on double-shear, steel-to-timber specimens with dowel-type fasteners, punched metal plate fasteners (PMPF), and adhesive bonds. The results demonstrated that the stiffness of the adhesively bonded specimens was 93 times higher than that of the dowel-type fasteners, and 5.5 times higher than that of the PMPFs.

### 1.3 Objective and investigated geometries

The aim of the research project was to develop, systematically investigate, and optimize the structural design of timber-steel composite beams. Specifically, the project sought to achieve the following scientific and technical research results: selecting and characterizing suitable wood and steel materials and profile cross-sections; designing and optimizing suitable timber-steel composite cross-sections and their manufacturing processes; experimentally investigating the composite load-carrying and failure behaviour using different composite methods; experimentally investigating the bending and shear load-carrying capacity, resistance, and long-term load-carrying behaviour of composite timber-steel beams; and developing a near-standard design model for designing the composite cross-sections.

This paper is an excerpt of the research project and contains the experimental investigations determining the load-carrying capacity and stiffness under governing bending and shear load.

The investigated geometries included Glulam GL 24h reference beams, laminated veneer lumber LVL 48p reference beams, and composite beams with two different geometry combinations (see Figure 1.1) and two different material combinations. A combination of steel S355 and GL 24h was analysed for both geometry variants (regular strength – RS). Additionally, steel S420 was tested in the vertical geometry in combination with LVL 48p and the horizontal geometry with beech LVL 80p (higher strength – HS). This paper summarises the results of the 4-point bending tests, which are fully detailed in *Haase et al. (2024b)*, and supplements these with the results of the 3-point bending tests. The experimentally determined load-carrying capacities and stiffness values are compared with analytically determined values.

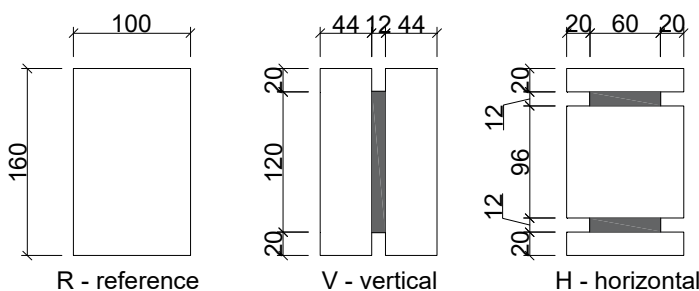


Figure 1.1. Geometries of tested specimens for all material combinations (all dimensions in mm).

## 2 Materials and methods

### 2.1 Materials

#### 2.1.1 Timber and steel

The specimens analysed were made of glulam GL 24h, softwood LVL 48p and beech LVL 80p (BauBuche). The mechanical properties bending strength  $f_m$ , shear strength  $f_v$  and  $MOE$  of GL 24h and LVL 48p were determined according to EN 408 (2010). The mechanical properties of LVL 80p were taken from the LVL Handbook Europe (2020). A coefficient of variation of 5% was assumed for LVL 80p, to convert the characteristic values to mean values. For the steel plates, two steel grades were used, i.e. a mild steel S355 and higher strength steel S420. The ratio of  $MOE$  of timber to steel was 5.3% for GL 24h, 6.0% for LVL 48p, and 8.0% for LVL 80p. Tensile tests were performed to determine the yield and tensile strength of the steel plates in accordance with EN ISO 6892-1 (2020). The ratio of the bending strength  $f_m$  of the timber to the tensile strength  $f_u$  of the steel was 6.6% for GL 24h+S355, 10% for LVL 48p+S420 and 17% for LVL 80p+S420. All material properties are given in Table 2.

#### 2.1.2 Adhesives

Three different adhesives were used to bond timber and steel. Two two-component epoxy adhesives (EP1 and EP2), and a polyurethane (PUR) system were compared. The material values of EP1 were determined in *Grunwald et al.* (2019). Tensile tests according to EN ISO 527-2 (2012) were performed to determine the material properties of the EP2 and PUR adhesives (*Haase et al.* (2024a)). The mechanical properties are given in Table 2.

Table 2. Material properties (mean values).

Material		$MOE$ in [N/mm <sup>2</sup> ]	Bending strength $f_m$ in [N/mm <sup>2</sup> ]	Shear strength $f_v$ in [N/mm <sup>2</sup> ]	Density $\rho$ in [kg/m <sup>3</sup> ]	Moisture content in [%]
Timber	GL 24h ( $n = 8$ )	11,100±1400	35.0±5.2	4.86±0.7	443±23	11.5±0.7
	LVL 48p ( $n = 5$ )	12,600±260	51.7±1.3	5.99±0.2	493±5.3	9.6±0.2
	LVL 80p*	16,800*	81.7*	8.72*	841±17**	7.2±0.6**
Steel			Yield strength $f_y$ in [N/mm <sup>2</sup> ]	Tensile strength $f_u$ in [N/mm <sup>2</sup> ]		
	S355	210,000	380±15	537±14	-	-
	S420	210,000	449±20	483±0.6	-	-
Adhesive			Tensile strength $f_t$ in [N/mm <sup>2</sup> ]			
	EP1	6,300	24.6±6.8	-	-	-
	EP2	5,400±110	45.0±1.4	-	-	-
	PUR	5,000±490	45.5±0.7	-	-	-

\* properties derived from literature and determined from 5%-quantiles with COV = 5% and  $k_s(n) = 1.645$

\*\* properties determined in tests

## 2.2 Methods

### 2.2.1 Specimen geometry and test programme

The tested specimens and investigated geometries are given in Figure 1.1. Geometry V was tested with mild steel S355 + GL 24h (RS – regular strength) and higher strength steel S420 + LVL 48p (HS – higher strength). Geometry V used LVL 80p for the HS combination. The area ratio of steel to timber was 10%. Table 3 gives an overview of the test campaign with composite beams under governing bending loading (4-point bending) and governing shear loading (3-point bending). The steel plates were either corundum blasted or galvanised, however, results showed no significant difference between the different surface preparations. Therefore, no further distinction was made. The naming of the specimens follows a simple code: The first letter represents the orientation of the steel sheet (V-vertical and H-horizontal). The next two letters identify the material combination (RS-regular strength and HS-higher strength). The last three letters identify the adhesive (EP1, EP2 and PUR), followed by a sequential number of the specimens in each series.

Table 3. Overview of the test campaign with number of tests for 3-point and 4-point bending setup.

Geometry	Material	3-point bending			4-point bending		
		EP1	EP2	PUR	EP1	EP2	PUR
V (vertical steel plate)	GL 24h + S355	2	2	1	2	3	1
	LVL 48p + S420	4	-	1	4	-	1
H (horizontal steel plates)	GL 24h + S355	-	-	-	2	4	1
	LVL 80p + S420	4	-	-	4	-	-

### 2.2.2 Manufacturing of specimens

For the manufacturing of the test specimens, all steel parts were either blasted or galvanised. Prior to bonding, the parts were degreased with methyl ethyl ketone (MEK). For the PUR adhesive, a primer was required to prepare the steel surface. The timber surface was planed within 24 hours prior to bonding. The specimens with the RS materials for the Geometry H (only for 4-point bending), were reinforced with inclined fully threaded screws ( $d = 8$  mm and  $\ell = 200$  mm), to increase the shear strength. The manufacturing and the reinforcement of the specimens for the 4-point bending tests is described in more detail in *Haase et al. (2024b)*. The manufacture of the 3-point bending tests was analogous.

### 2.2.3 Experimental testing

4-point bending tests according to EN 408 (2010) were carried out on the composite beams with two different geometry and material combinations. Figure 2.1a shows the test set-up. All specimens had a height of 160 mm. To avoid local compression failure perpendicular to the grain of the wood, the load was applied directly to the steel sections via steel inlets. All specimens were tested with a span of  $\ell = 2400$  mm.

In addition, 3-point bending tests, following the proposal of *Gehri* (2010), were carried out on composite beams with a much shorter span of  $\ell = 740$  mm, to enforce shear failure of the beams. For Geometry V, the same material combinations were tested. For Geometry H, only tests with the higher strength combination were carried out. Figure 2.1b shows the test set-up.

For comparative reasons, reference beams of GL 24h, and LVL 48p were tested with both test setups. The results were used to determine reference values (and also the material properties given in Table 2) and to highlight the performance of the various composite beams.

To evaluate the shear stiffness, the deformations of the shear fields were measured on the front of each beam with digital image correlation (DIC). With the DIC system, the displacement of the markers at the corners of the shear fields were measured. The shear stiffness  $GA$  was analysed for each specimen in the range of 10–40% of the ultimate load. Only the global displacement of the machine head was measured. Additionally, the steel stresses were measured using strain gauges. The location of the strain gauges was at the top and bottom fibres of the steel plate for Geometry V, and in the neutral axis of the steel plates for Geometry H. All specimens were tested with a constant loading rate of 5 mm/min. The loading was continuously increased, until failure of the beams occurred.

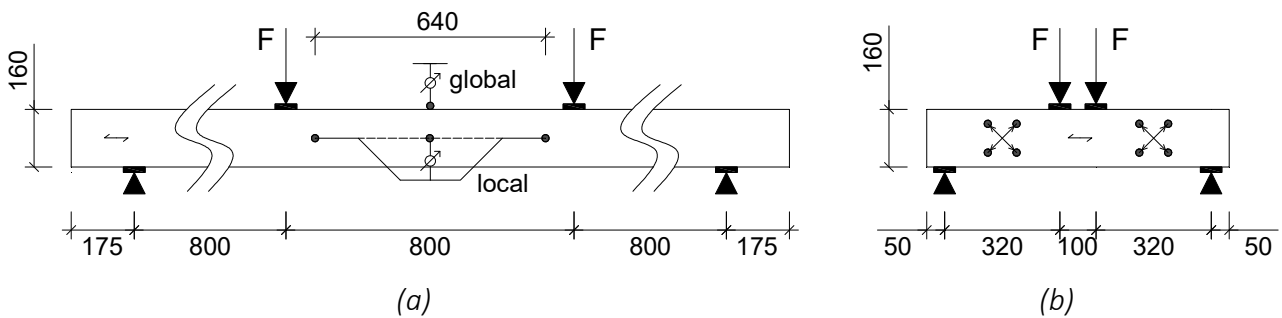


Figure 2.1. Test setup and location of measured deformations for (a) 4-point-bending tests and (b) 3-point bending tests.

## 2.2.4 Analytical load-carrying capacity and stiffness

Full bond between timber and steel was assumed for the analytical determination of the load-carrying capacity (as shown in *Aurand et al.* (2023)). Using the ratio of the *MOEs* of timber and steel, cross-sectional values were calculated for both steel (index S) and timber (index T). The second moment of inertia was calculated using Equation (1), and given here exemplarily related to the timber material. The bending stiffness of the composite section  $EI_{comp}$  was calculated using Equation (2):

$$I_{y,rel,T} = \sum I_{y,T,i} + \frac{E_S}{E_T} \cdot \sum I_{y,S,i} \quad (1)$$

$$EI_{comp} = E_T \cdot I_{y,rel,T} = E_S \cdot I_{y,rel,S} \quad (2)$$

The shear stresses were calculated with the first moment of inertia. Since the width of the cross-section was not constant, different locations were relevant for the evaluation of the shear stresses. For Geometry V, two locations, and Geometry H, three locations were analysed (see Figure 2.2). Since shear failure in the timber was decisive, the first moment of inertia was only analysed in relation to the timber material, see Equation (3):

$$S_{y,rel,T} = \sum S_{y,T,i} + \frac{E_S}{E_T} \cdot \sum S_{y,S,i} \quad (3)$$

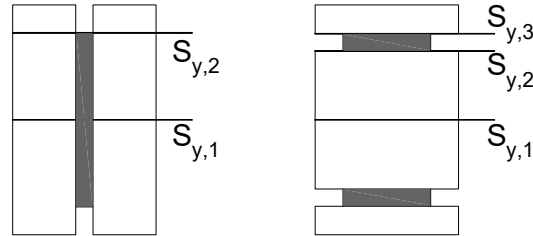


Figure 2.2. Locations for evaluating the shear stress.

The bending and shear stresses were calculated according to the mechanics of materials, using equations (4) to (6). Depending on whether the stresses were determined in the timber or in the steel, the corresponding related properties were used. With the determined mean values of the bending strength, the yield strength and the shear strength (see Table 2), the expected load-carrying capacities were calculated, using equations (7)–(9):

$$\sigma_{m,T} = \frac{M_{Ed}}{I_{y,rel,T}} \cdot z_T \quad (4)$$

$$F_{m,exp,T} = \frac{f_m \cdot I_{y,rel,T}}{a \cdot z_T} \quad (7)$$

$$\sigma_{y,S} = \frac{M_{Ed}}{I_{y,rel,S}} \cdot z_S \quad (5)$$

$$F_{y,exp,S} = \frac{f_y \cdot I_{y,rel,S}}{a \cdot z_S} \quad (8)$$

$$\tau_T = \frac{V \cdot S_{Y,i}}{I_{Y,T} \cdot \left( b_{T,i} + \frac{E_S}{E_T} \cdot b_{S,i} \right)} \quad (6)$$

$$F_{v,exp,T} = \frac{f_v \cdot I_{y,rel,T} \cdot b_i}{S_y} \quad (9)$$

## 3 Results and discussion

### 3.1 4-point-bending tests (governing bending load)

#### 3.1.1 Geometry V (vertical steel plate)

At first, tests with vertical steel plate and the RS material combination of GL 24h and S355 were performed. Figure 3.1a shows the global load-displacement curves of all specimens. All specimens showed a very similar load-displacement behaviour, independent of the surface finish of the steel plate, and independent of the used adhesive. Therefore, they are grouped together as “vertical – regular strength” (V-RS). The average load-carrying capacity of this group was  $F_{max} = 75.7$  kN (COV = 9.8%) (see dashed, horizontal line in Figure 3.1a). The average bending stiffness  $EI$ , evaluated in the range of 10–40% of the ultimate load, was  $74.8 \cdot 10^{10}$  Nmm<sup>2</sup> (COV = 5.9%). The

average ultimate load and the average bending stiffness both correspond to an increase of 100%, compared to the GLT reference beams. This means that a reference timber beam with the same width would have to be 25% higher to achieve the same stiffness value.

The global load-displacement behaviour of all tested specimens with vertical steel plates and the material combination of LVL 48p and S420 is illustrated in Figure 3.1b. The global behaviour was very similar for all specimens with higher strength materials. Again, no significant difference was detected between the different surface conditions of the steel plate, and between the different adhesives. Therefore, all specimens are grouped as “vertical – higher strength” (V-HS). On average, the load-carrying capacity increased by 20% (compared to V-RS) to  $F_{max} = 91.1$  kN (COV = 2.5%). The average bending stiffness  $EI$ , evaluated in the range of 10–40% of the ultimate load, is similar to the V-RS tests with  $76.9 \cdot 10^{10}$  Nmm<sup>2</sup> (COV = 3.5%). The significantly lower COV confirms the homogenisation effect of the LVL in combination with the steel, which enables load redistribution into the steel, in the event of local failure of the timber. A further homogenisation of the composite beam with LVL, compared to the reference LVL beam (COV = 2.7%), was not detected. The average ultimate load corresponds to an increase of 60% and the average bending stiffness corresponds to an increase of 80%, both compared to the LVL reference beams. A reference timber beam with the same width would have to be 20% higher, to achieve the same stiffness value.

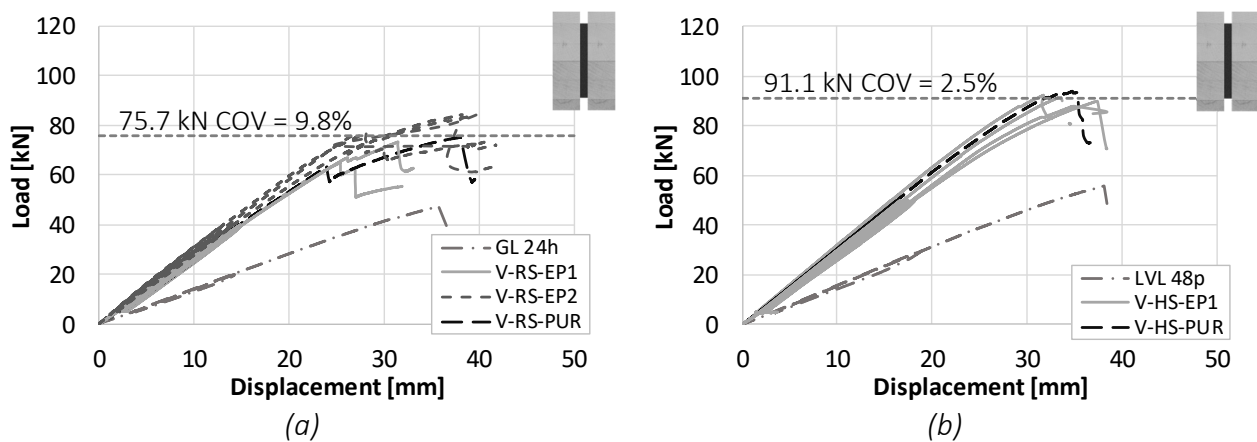


Figure 3.1. Global load-displacement curves for Geometry V: (a) GL 24h + S355 (RS) and (b) LVL 48p + S420 (HS).

### 3.1.2 Geometry H (horizontal steel plate)

For the regular strength specimens with GL 24h and S355, the global load-displacement behaviour is shown in Figure 3.2a. A linear load increase was observed, without any influence from the unloading loop. The specimens failed brittle due to shear failure of the timber member. Due to similar behaviour, all specimens are grouped as “horizontal – regular strength” (H-RS). On average, the ultimate load was  $F_{max} = 82.9$  kN (COV = 12.7%), which is similar to Geometry V. However, the average bending stiffness  $EI$ , evaluated in the range of 10–40% of the ultimate load, significantly

increased to  $129 \cdot 10^{10} \text{ Nmm}^2$  (COV = 5.5%). The failure mode of all specimens was shear failure in the timber member, which explains the larger scatter of the load-carrying capacity (as compared to Geometry V). The average ultimate load corresponds to an increase of 120% and the average bending stiffness to an increase of 250%, both compared to a GLT reference beam. A reference timber beam with the same width would have to be 50% higher, to achieve the same stiffness value.

For the timber section of the specimens with the higher strength material combination, beech LVL 80p was selected, rather than LVL 48p, because of its higher shear strength. Their global load-displacement behaviour is shown in Figure 3.2b. Here, no reinforcement screws were added to the timber member. The specimens were grouped as “horizontal – higher strength” (H-HS). As it was expected, the failure mode was shear failure in the central timber member. On average, the ultimate load increased by 44% to  $F_{\max} = 119 \text{ kN}$  (COV = 0.6%), compared to the RS specimens. However, the average bending stiffness  $EI$ , evaluated in the range of 10–40% of the ultimate load, did not further increase with  $128 \cdot 10^{10} \text{ Nmm}^2$  (COV = 3.3%). The average ultimate load corresponds to an increase of 30% compared to the analytically determined load-carrying capacity of the LVL 80p. The average bending stiffness corresponds to an increase of 120%, compared to the analytical calculation. This means that a reference timber beam with the same width would have to be 30% higher, to achieve the same stiffness value.

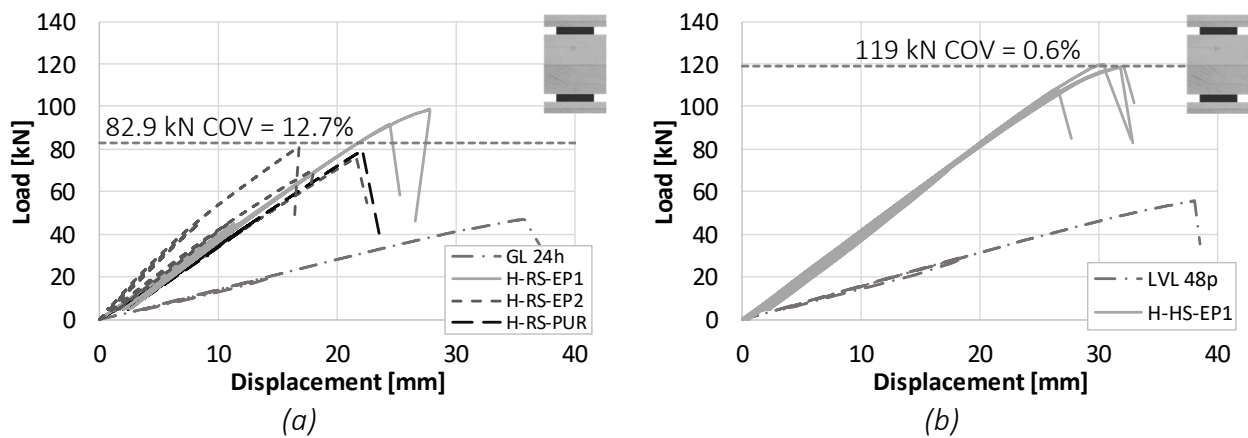


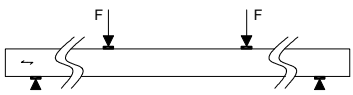
Figure 3.2. Global load-displacement curves for Geometry H: (a) GL 24h + S355 (RS) and (b) LVL 80p + S420 (HS).

The comparison of the test results to the analytical determined values shows a deviation of 14% of the expected load for H-RS. This deviation is due to the reinforcement screws in the inner timber part, which increased the shear strength.

Table 4 summarizes all results of the 4-point bending tests. In contrast to the 3-point bending tests, the span of the specimens was 2.4 m and the specimens were primarily under bending load. Additionally to the ultimate load and the bending stiffness, an equivalent bending strength  $f_m$  and an equivalent Young's modulus  $E$  were determined. Both values refer to the reference cross section of 100 x 160 mm.



Table 4. Test results of all 4-point-bending tests.



		Ultimate load	Bending stiffness	Equivalent bending strength $f_m$	Equiv. Young's modulus $E$
		$F_{max}$	$EI$		
		[kN]	[ $\cdot 10^{10}$ Nmm <sup>2</sup> ]	[N/mm <sup>2</sup> ]	[N/mm <sup>2</sup> ]
Reference	GL 24h	37.3 ± 5.6	37.7 ± 4.7	35.0 ± 5.2	11,058 ± 1,370
	LVL 48p	55.1 ± 1.4	43.0 ± 0.9	51.7 ± 1.3	12,602 ± 262
	LVL 80p <sup>*/**</sup>	86.8 <sup>**</sup>	57.3 <sup>**</sup>	81.7 <sup>*</sup>	16,800 <sup>*</sup>
Vertical	GL 24h + S355	75.7 ± 7.4	74.8 ± 4.4	70.8 ± 7.0	22,000 ± 1,400
	LVL 48p + S420	91.1 ± 2.3	76.9 ± 2.7	85.4 ± 2.2	22,500 ± 800
Horizontal	GL 24h + S355	82.9 ± 10.5	129 ± 7.1	77.8 ± 2.2	37,800 ± 1,900
	LVL 80p + S420	119 ± 0.7	128 ± 4.2	112 ± 0.7	37,370 ± 1,200

\* derived from literature and determined from 5%-quantile with COV = 5% and  $k_s(n) = 1.645$

\*\* analytically determined values with derived properties of  $f_m$  and  $MOE$

### 3.1.3 Analytical calculations

The comparison of the analytical load-carrying capacity to the test results can be seen in Figure 3.3. The minimum value of Equations (7)–(9) was the decisive, expected load-carrying capacity. For Geometry V, this was governed by the yield strength of the steel. The test results, however, showed plastic utilization of the steel profiles, exceeding the yield strength. Therefore, the deflection could be further increased, until the bending strength of the timber was reached. The tests showed bending failure of the timber and plastification of the steel, which is congruent to the analytic calculation ( $\pm 10\%$  deviation for V-RS and V-HS). The deviation of the test results of the bending stiffness to the calculated stiffness is small with 5–8%.

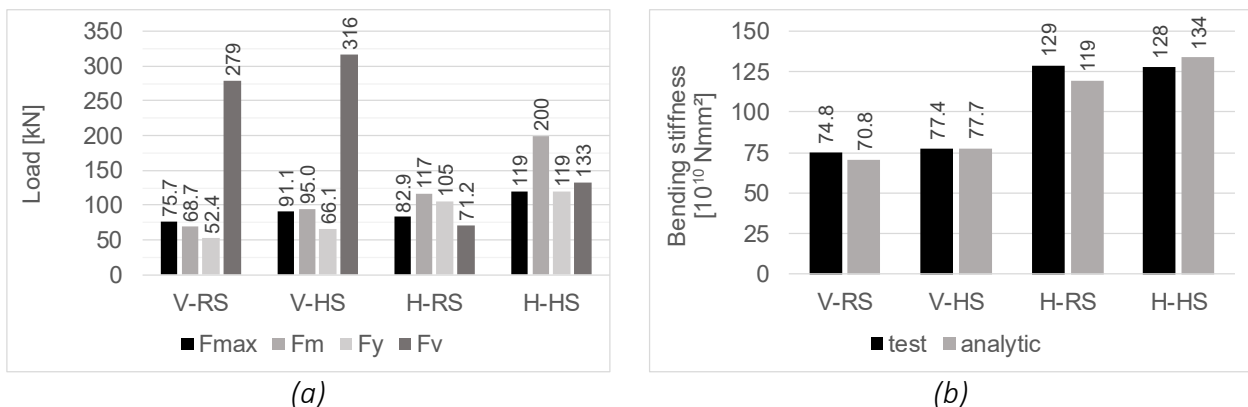


Figure 3.3. Comparison of test results to analytical results: (a) load-carrying capacity and (b) bending stiffness of 4-point bending tests.

## 3.2 3-point-bending tests (governing shear load)

### 3.2.1 Geometry V (vertical steel plate)

In this section, the results of all specimens with a vertical steel plate and the material combination of GL 24h and S355 are presented and discussed. Figure 3.4a shows the global load-displacement curves. During the tests, the deformation of the shear field and the global machine deformation were continuously measured. Therefore, all

following graphs show the displacement of the machine head. Clearly visible is some slip at the beginning of the tests. All specimens showed a very similar load-displacement behaviour, i.e. a linear increase in load and stiffness. With increasing displacement, the stiffness slightly reduces until failure occurs. The load drops by approx. 25% before remaining more or less constant as the deformation increases. Therefore, all specimens were grouped as “vertical – regular strength” (V-RS). The average load-carrying capacity of this group was  $F_{\max} = 199 \text{ kN}$  (COV = 5.7%). As the specimens were primarily under shear load, the shear stiffness  $GA$  was evaluated instead of the bending stiffness  $EI$ . Analogously, the shear stiffness  $GA$  was evaluated in the range of 10–40% of the ultimate load, and was on average  $10.7 \cdot 10^7 \text{ Nmm}^2$  (COV = 35%). The average ultimate load corresponds to an increase of 90%, compared to the GLT reference beams. This increase is congruent to the results from the 4-point bending tests. The average shear stiffness corresponds to an increase of 430%.

To further increase the load and stiffness, tests with a vertical steel plate and the higher strength material combination of LVL 48p and S420 were performed. The global load-displacement curves of all specimens is shown in Figure 3.4b. Again, the displayed displacement is of the machine head, which explains the visible slip at the beginning of the tests. All specimens showed a very similar load-displacement behaviour, and were, therefore, grouped as “vertical – higher strength” (V-HS). The load-displacement behaviour is similar to that of the RS specimens. The average load-carrying capacity of this group increased by 13% to  $F_{\max} = 224 \text{ kN}$  (COV = 3.4%). The shear stiffness  $GA$ , evaluated in the range of 10–40% of the ultimate load, was on average  $7.6 \cdot 10^7 \text{ Nmm}^2$  (COV = 39%), which is lower than for the RS specimens. But also, the shear stiffness of the LVL reference beams was lower than for the GLT reference beams. This shows that the existing differences in the shear modulus for GLT and LVL are transferred to the composite beams, and that even the use of higher strength steel cannot contribute to an increase in shear stiffness (due to the constant shear moduli of different steel grades). The average ultimate load corresponds to an increase of 75%, compared to the LVL reference beam. This is congruent to the results from the 4-point bending tests. The average shear stiffness corresponds to an increase of 380%.

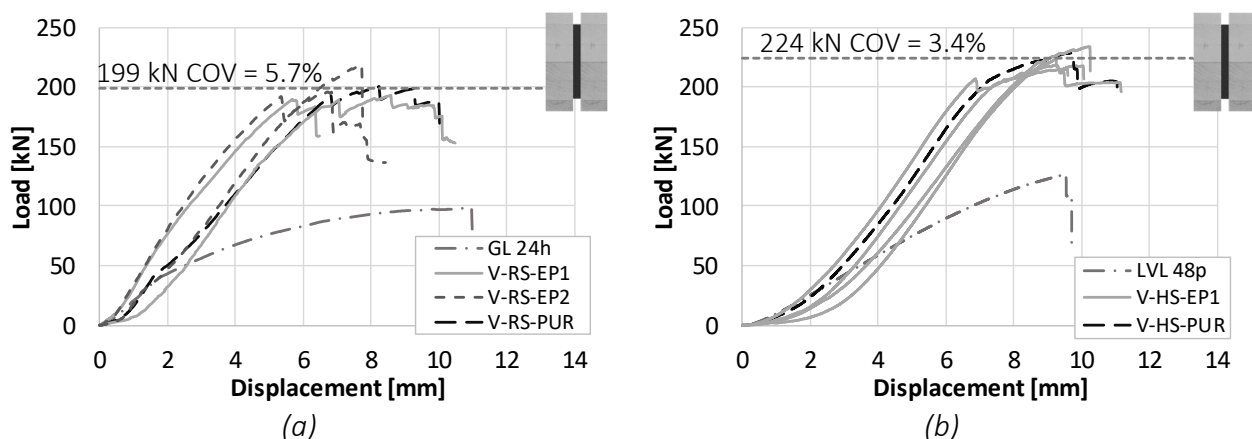


Figure 3.4. Global load-displacement (machine head) curves for Geometry V: (a) GL 24h + S355 (RS) and (b) LVL 48p + S420 (HS).

The failure of the specimens was bending-tensile failure, accompanied by secondary shear failure. Figure 3.5a shows bending-tensile failure, and Figure 3.5b+c show shear failure of a RS specimen. The bond line between steel and timber can be described as uncritical for this material combination as no failure was observed in all tests.

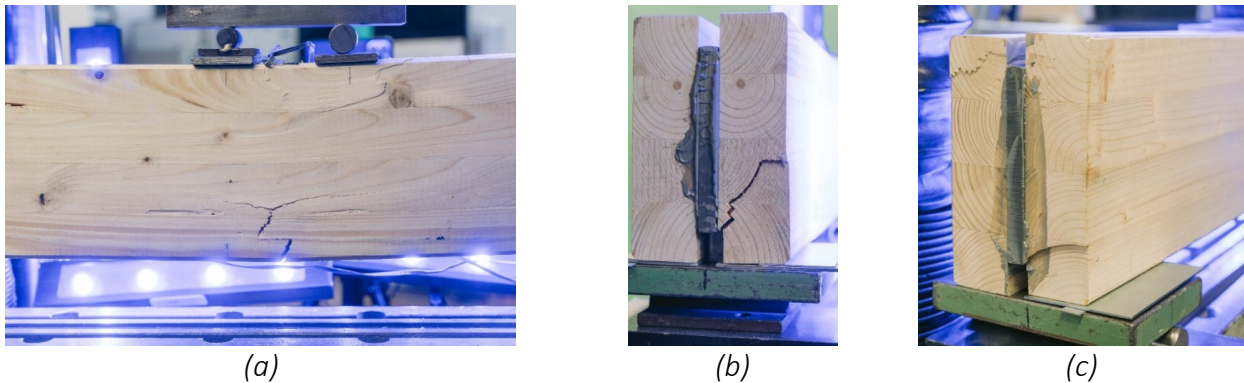


Figure 3.5. Bending tension failure (a) and shear failure of (b+c).

Figure 3.6a shows the top edge of a HS specimen. Clearly visible are kink bands that have formed in the compressive zone. This shows a full utilization of the timber section across its height. Figure 3.6b+c show secondary shear failure of the timber part that occurred with the first load drop.

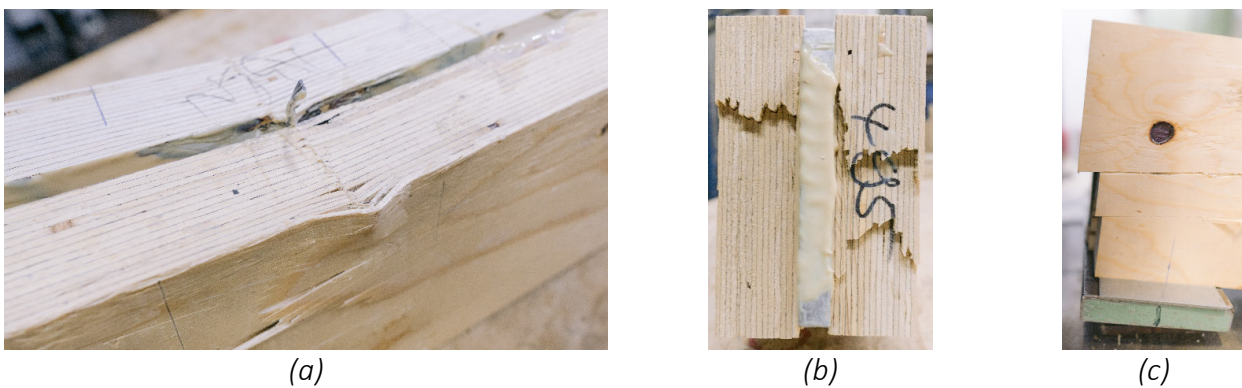


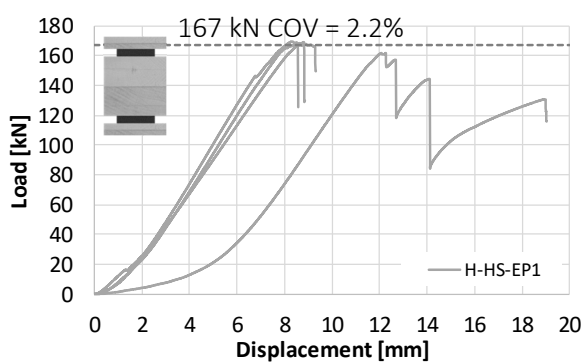
Figure 3.6. Compression kink bands at top of specimen (a) and shear failure of LVL (b+c).

After the tests, the strain gauges, attached to the edge fibres of the steel plate, were evaluated. For both material combinations, the yield strength of the steel ( $f_y = 380$  and  $448 \text{ N/mm}^2$ ) was reached well before the ultimate load was achieved. This led to plastic deformation of the steel until the bending-tensile strength of the timber was reached. After brittle failure of the timber parts accompanied with a load drop, the displacement was further increased without a decrease of load-carrying capacity.

### 3.2.2 Geometry H (horizontal steel plate)

For the Geometry H with horizontal steel plates, only the higher strength material combination was tested, because of the predicted shear failure. Contrary to the tests before, beech LVL 80p was chosen, instead of softwood LVL. This can be explained by the higher shear strength of LVL 80p compared to LVL 48p. Timber and steel parts were bonded with the adhesive EP1. This was analogous to the 4-point bending tests. Figure 3.7a shows the load-displacement curve, with the displacement of the machine

head. Clearly visible is the large slip of one specimen at the beginning of the tests. This was assumed to result from the design of the support, where excess adhesive might have an influence. Still, all four specimens showed a very similar load-displacement behaviour, and were, therefore, grouped as “horizontal – higher strength” (V-HS). The load increases linearly up to the brittle shear failure of the specimens. The load drops by approx. 50% before it can be increased again with further displacement (shown exemplarily for one specimen in Figure 3.7a). However, the ultimate load is not reached again by any specimen. The average load-carrying capacity of all four specimens in this group, decreased to  $F_{\max} = 167 \text{ kN}$  (COV 2.2%). The shear stiffness  $GA$ , evaluated in the range of 10–40% of the ultimate load, was on average  $2.6 \cdot 10^7 \text{ Nmm}^2$  (COV = 5.7%). Both, the decrease in load-carrying capacity and shear stiffness (compared to Geometry V) can be explained by the failure mode of shear failure, which was completely dependent on the timber properties and not influenced by the bonded steel plates. Here, the reduced COV, especially for the shear stiffness shows the homogenized properties of the LVL. The average ultimate load shows no increase when compared to the analytically determined load-carrying capacity of a beech LVL reference beam. The average shear stiffness however, corresponds to an increase of 110%.



(a)



(b)

(c)

Figure 3.7. Load-displacement (machine head) curves (a) and brittle shear failure of the timber part (b+c) for Geometry H and LVL 80p + S420 (HS).

The evaluation of the strain gauges showed that the stress in the steel was at all times below the yield strength. Therefore, no plastification of the steel plates occurred. The analytical evaluation of the shear stresses across the height of the cross section (see Figure 3.8b) show shear stresses of  $10.6 \text{ N/mm}^2$  (and therefore greater than the shear strength of LVL 80p) close to the bond line between the steel and the inner timber part, where the width of the specimen suddenly increases. Shear stresses of  $7.50 \text{ N/mm}^2$ , at half the specimen's height, were less than the shear strength of LVL 80p. That the failure occurred close to the bond line is clearly visible in Figure 3.7b+c.

Figure 3.8a shows that the analytical equations also predict the load-carrying capacity quite well for specimens primarily loaded in shear. Here, the deviation of experimental and analytical results is 6–14% for Geometry V and 20% for Geometry H.

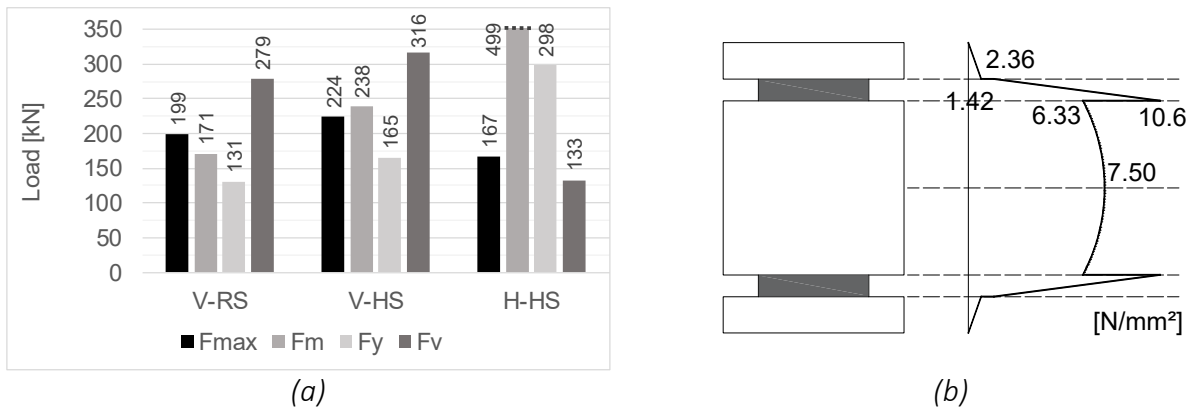
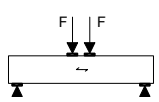


Figure 3.8. Comparison of test results to analytical results for 3-point bending tests (a) and shear stresses at  $F_{max}$  for Geometry H (b).

Table 5 summarizes all results of the 3-point bending tests. In contrast to the 4-point bending tests, the span of the specimens was reduced to 0.74 m and the specimens were primarily under shear load. Additionally to the ultimate load and the shear stiffness, an equivalent shear strength  $f_v$  and an equivalent shear modulus  $G$  were determined. Both values refer to the reference cross section of 100 x 160 mm.

Table 5. Test results of all 3-point-bending tests.

		Ultimate load $F_{max}$ [kN]	Shear stiffness $GA$ [ $\cdot 10^7$ Nmm <sup>2</sup> ]	Equivalent shear strength $f_v$ [N/mm <sup>2</sup> ]	Equiv. shear modulus $G$ [N/mm <sup>2</sup> ]
Reference	GL 24h	104 ± 15	2.07 ± 0.7	4.86 ± 0.7	1,200 ± 440
	LVL 48p	128 ± 4	1.59 ± 0.2	5.99 ± 0.2	1,200 ± 140
	LVL 80p*/**	186**	1.22**	8.72*	760*
Vertical	GL 24h + S355	199 ± 11	10.7 ± 3.7	9.35 ± 0.5	6,700 ± 3100
	LVL 48p + S420	224 ± 8	7.61 ± 2.6	10.5 ± 0.4	4,700 ± 1600
Horizontal	LVL 80p + S420	167 ± 4	2.7 ± 0.2	7.83 ± 0.2	1,700 ± 120

\* derived from literature and determined from 5%-quantile with COV = 5% and  $k_s(n) = 1.645$

\*\* analytically determined values with derived properties  $f_v$  and  $G$

## 4 Conclusion

The most important results are summarised below; all comparisons refer to the corresponding timber reference specimens:

- Geometry V (vertical combination) with regular-strength (RS) materials increased the load-carrying capacity by 90–100%, the bending stiffness by 100% and the shear stiffness by 430%. With higher-strength (HS) materials the load-carrying capacity was increased by 6 to 75%, the bending stiffness by 80% and the shear stiffness by



380%. Consequently, beams with Geometry V are suitable for use under high shear load.

- All specimens of Geometry V failed due to bending tensile failure in the timber part with a ductile behaviour after reaching  $F_{max}$ . The steel parts could be partially plastically utilized.
- Geometry H (horizontal combination) with regular-strength (RS) materials increased the load-carrying capacity by 120% and the bending stiffness by 250%. With higher-strength (HS) materials the load-carrying capacity was increased by up to 30%, the bending stiffness by 120% and the shear stiffness by 110%. Consequently, beams with Geometry H are suitable for use under high bending load.
- All specimens of Geometry H failed due to shear in the middle timber part. The RS material specimens could not reach the yield strength of the steel. With the HS materials, the steel was fully plastically utilised before shear failure occurred.
- For both geometry combinations, the bending and shear stiffness could not be further increased when using HS materials compared to RS materials.
- Full bond between timber and steel is confirmed by the comparison between the analytical calculations and the experimental investigations. Both the bending stiffness and the stress distribution in the cross-section could be reliably calculated analytically.

The results demonstrate the high potential of timber-steel composite beams. The geometry combination can be chosen accordingly to the governing loading mode. While the horizontal combination is ideal for structures subjected to bending loads (deflection), the vertical combination is ideal for components subjected to high shear loads. The tests have also shown that slender steel profiles, at risk of stability failure, can be used. The small deviations of test results to analytical results, however, only apply to the analysed geometry combinations. Therefore, in further numerical and experimental investigations, other material and geometry combinations must be investigated, in order to determine e.g. geometrical boundary conditions for the use of the analytical equations.

## 5 Acknowledgements

The research project IFG 21722 N/P 1537 “Timber-steel hybrid construction methods using the example of load-bearing elements subject to bending stress—HoStaBau” from the Research Association for steel Application (FOSTA), Düsseldorf, was supported by the Federal Ministry of Economic Affairs and Climate Action through the German Federation of Industrial Research Associations (AiF) as part of the program for promoting industrial cooperative research (IGF) on the basis of a decision by the German Bundestag. These supports are gratefully acknowledged.

## 6 References

- Alam P (2004): The reinforcement of timber for structural applications and repair [PhD thesis]. Department of Mechanical Engineering, University of Bath.
- Aurand S, Boretzki J, Haase P, Ummenhofer T, Dietsch P (2023): Structural behavior of timber-steel-joints with either dowel-type fasteners or continuous joints. In: World Conference on Timber Engineering (WCTE 2023). Oslo, Norway.
- Blaß HJ, Romani M (2000): Trag- und Verformungsverhalten von Verbundträgern aus Brettschichtholz und faserverstärkten Kunststoffen. Versuchsanst. für Stahl, Holz und Steine, Abt. Ingenieurholzbau, Univ. (TH): Karlsruhe.
- Blaß HJ, Romani M, Schmid M (2003): Optimierung von Verbundträgern aus Brettschichtholz mit Verstärkungen aus Faserverbundkunststoffen. Versuchsanst. für Stahl, Holz und Steine, Abt. Ingenieurholzbau, Univ. (TH): Karlsruhe.
- EN 408 (2010): Timber structures – Structural timber and glued laminated timber – Determination of some physical and mechanical properties. CEN: Brussels, Belgium.
- EN ISO 527-2 (2012): Plastics – Determination of tensile properties – Part 2: Test conditions for moulding and extrusion plastics (ISO 527-2:2012). CEN: Brussels, Belgium.
- EN ISO 6892-1 (2020): Metallic materials – Tensile testing – Part 1: Method of test at room temperature (ISO 6892-1:2019). CEN: Brussels, Belgium.
- Fukutomi N, Shioya S (2018): Design method to estimate stiffness and strength of hybrid timber-steel bar beams. In: World Conference on Timber Engineering (WCTE 2018). Seoul, Korea.
- Gehri E (2010): Shear problems in timber engineering – Analysis and solutions. In: World Conference on Timber Engineering (WCTE 2010). Riva del Garda, Italy.
- Grunwald C, Vallée T, Fecht S, Bletz-Mühldorfer O, Diehl F, Bathon L, Myslicki S, Scholz R, Walther F (2019): Rods glued in engineered hardwood products part I: Experimental results under quasi-static loading. *International Journal of Adhesion and Adhesives*. 90:163–181. doi:10.1016/j.ijadhadh.2018.05.003.
- Haase P, Aurand S, Boretzki J, Albiez M, Sandhaas C, Ummenhofer T, Dietsch P (2024): Bending Behavior of Hybrid Timber–Steel Beams. *Materials*. 17(5):1164. doi:10.3390/ma17051164.
- Haase P, Boretzki J, Aurand S, Sandhaas C, Ummenhofer T, Albiez M (2024): Influence of the joining technique on the structural behaviour of hybrid timber-steel cross-sections. *The Journal of Adhesion*. doi:10.1080/00218464.2024.2360498.
- LVL Handbook Europe (2020): 2nd ed., Federation of the Finnish Woodworking Industries: Helsinki, Finland.
- Mori K, Shioya S (2021): Stiffness and strength of full-scale steel bar-timber composite beams with comparative small depth. In: World Conference on Timber Engineering (WCTE 2021). Santiago, Chile.
- Riola Parada F (2016): Timber-Steel Hybrid Beams for Multi-Storey Buildings [PhD thesis]. Institut für Architekturwissenschaften, Technische Universität Wien.
- Shekarchi M, Vatani Oskouei A, Raftery GM (2020): Flexural behavior of timber beams strengthened with pultruded glass fiber reinforced polymer profiles. *Composite Structures*. 241:112062. doi:10.1016/j.compstruct.2020.112062.

## DISCUSSION

**The paper was presented by S Aurand**

*R Brandner commented that he would not recommend changing the partial safety factor and that the Eurocode has a system effect approach. S Aurand responded that this was not considered in this study. P Dietsch added that the system effect approach might work.*

*G Doudak received confirmation that only one geometry was considered in the experiment and residual load capacity was available in the vertical case after the first load drop off.*

*U Hübner commented about the relationship between mechanical performance, cost and ecological assessment of European products. Reuse of beams might not be easy as 1:1 replacement because every building would be slightly different.*

*A Frangi suggested some optimization should be performed in terms of arrangement.*

*T Ehrhart discussed about shrinkage. S Aurand responded that this should not be critical because the steel could take up the load. T Ehrhart commented about the shear stress calculations in relation to the location of the failure plane.*

*S Winter commented about the partial safety factor. System effect approach might be preferred and fire protection of the steel should work. He discussed moisture change effect in the vertical reinforced beam needing tests with varying climatic conditions. He received confirmation that comparisons at the mean level were made.*

*W Seim stated that he is not sure about standardization with these hybrid materials of timber and steel with such long bonding length. He commented about vertical reinforcement case with using 4 timber parts rather than 2 timber parts.*

*F Lam commented that the stressed volume effect in shear might need to be considered.*





# OSB sheathed timber-framed shear walls with optimized performance for horizontal loading

Nadja Manser, Empa - Swiss Federal Laboratories for Materials Science & Technology, Structural Engineering Research Laboratory; Dübendorf, Switzerland and ETH Zürich - Swiss Federal Institute of Technology, Institute of Structural Engineering; Zürich, Switzerland

René Steiger, Empa - Swiss Federal Laboratories for Materials Science & Technology, Structural Engineering Research Laboratory; Dübendorf, Switzerland

Martin Geiser, BFH – Bern, Bern University of Applied Sciences Architecture, Wood and Civil Engineering, Biel, Switzerland

Andrea Frangi, ETH Zürich - Swiss Federal Institute of Technology, Institute of Structural Engineering; Zürich, Switzerland

Keywords: Eurocode 5, Timber-framed shear walls, sheathing, OSB/3, shear strength

## 1 Introduction

Timber-framed buildings are a common type of wooden construction because they provide several advantages both during construction and in use. These advantages include simplicity, efficient use of materials, prefabrication in a controlled environment, quick assembly, and the ability to dissipate energy during seismic events, when properly designed. In the past, various factors influencing the performance of this wall type have been studied, targeting the effects of anchorage, the choice of sheathing material, the differences in behavior under static and cyclic loading, the impact of openings, different loading scenarios, and numerical modeling (Filiatrault (1990), Källsner & Girhammar (2009)a, Källsner & Girhammar (2009)b, Sartori & Tomasi (2013), Seim et al. (2016), Grossi et al. (2015), Steiger & Marzaleh (2021), Kuai et al. (2022), Kuai et al. (2024).

The materials commonly applied for assembling timber-framed wall elements are:

- Sheathing panels: Oriented strand board (OSB), gypsum fibre board, plywood
- Framing members: Glued laminated timber (GLT), glued solid timber, solid timber
- Sheathing-to-framing connection: Nails, staples, screws.

Since the investigations presented in this paper are part of an ongoing research project in Switzerland, the focus is on the type of timber-framed shear walls prevalently used in Switzerland and Europe and the materials subjected to investigation were chosen accordingly. In Europe, the dimensions of the framing members and the thickness of the sheathing panels are generally larger compared to e.g. North-America. In Switzerland, it is common practice to use resined staples to connect sheathing panels to framing elements. In other European countries, staples are rarely used as they result in limited ductility. This means that walls using staples can only achieve ductility class 1 or 2. To reach ductility class 3, nails are required. (prEN 1995-1-1 (2023)).

In case of an earthquake, even buildings located in regions with low to moderate seismicity might experience significant horizontal forces (Geiser et al. (2018)), and hence require a high lateral load-carrying capacity of the shear walls. There are different ways to reach a high load-carrying capacity. The easiest way is to design a strong sheathing-to-framing connection by applying a higher amount of fasteners. This can be achieved by arranging the fasteners with a smaller distance between the fasteners, or in multiple rows. Arranging more than one row of fasteners is a quite common practice in Switzerland and is matter of an ongoing research project in Canada as well (Qiang et al. (2022)).

In general, the shear resistance of a timber-framed wall element is determined as the minimum of the resistance of the sheathing-to-framing connection and the shear resistance of the sheathing. When applying a strong sheathing-to-framing connection, the shear resistance of the sheathing can become the governing factor in design. The shear resistance of a sheathing panel, when applied in a timber-framed shear wall, is reduced compared to the shear strength of the panel. The reason for this reduction are additional stresses in the sheathing panel (see Chapter 2). This reduction in strength is accounted for in design by means of a reduction factor (e.g. in DIN EN 1995-1-1/NA (2013) or in prEN 1995-1-1 (2023)). However, to the best knowledge of the authors of this study, these reduction factors have never been experimentally investigated. Therefore, the design standards likely use rules of thumb, resulting in conservative designs. This conservatism in defining reduction factors for calculating the shear resistance of sheathing panels limits the design lateral stiffness and the design load-carrying capacity of timber-framed shear wall elements. Consequently, this leads to uneconomical solutions where the full capacity of the sheathing material is not fully utilized.

The objective of the presented study was to experimentally investigate the reduction factors applied in the calculation of the shear resistance of a timber-framed wall element (DIN EN 1995-1-1/NA (2013) or prEN 1995-1-1 (2023)). Reducing the conservatism of these reduction factors will maximize the overall performance of timber-framed shear wall elements for lateral loading. The results of these investigations help determine the best combination of sheathing thickness and fastener layout. This is an important step towards designing high-performance timber-framed shear wall elements with optimized load-carrying capacity, leading to more efficient designs for timber-framed buildings.

The presented study is part of an ongoing research project in Switzerland. The overall goal is to develop a design method for timber-framed shear walls with large openings contributing to the lateral force-resisting system of timber buildings. When aiming at maximizing the contribution of wall elements with openings in the design of the lateral force-resisting system, the optimization of the sheathing-to-framing connection layout is crucial.

## 2 Shear resistance of timber-framed shear walls

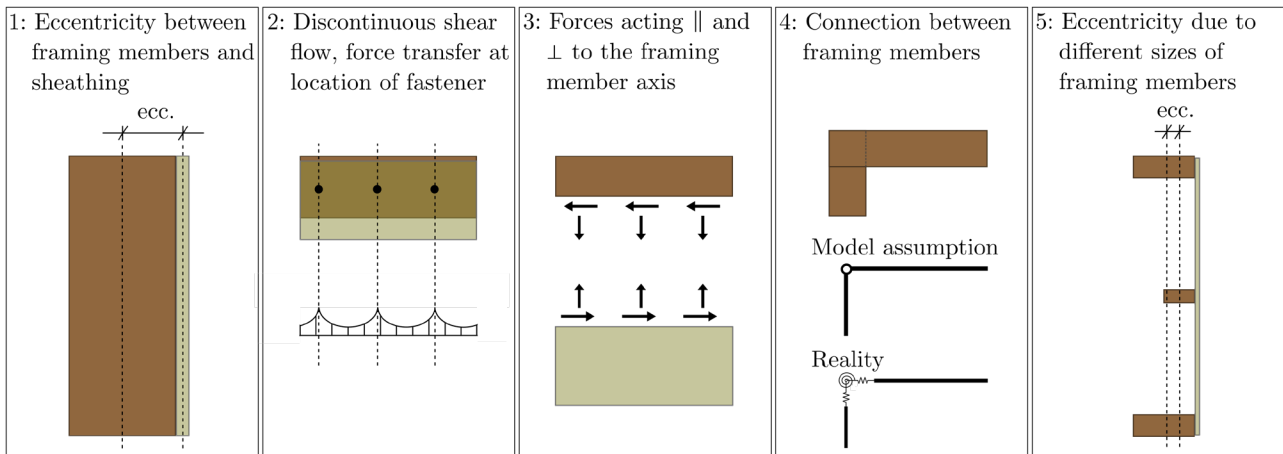
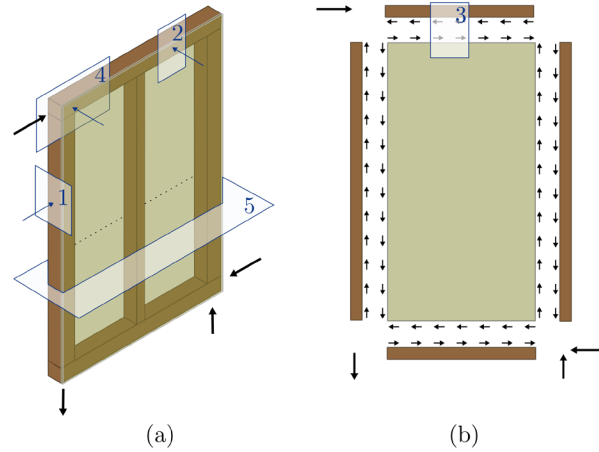
The shear resistance of a timber-framed wall element is given as the minimum of the resistance of the sheathing-to-framing connection and the shear resistance of the sheathing. In addition to the evaluation of the shear resistance of the wall element, corresponding verification of the anchoring and the framing members must be carried out. Respective design approaches are given in earlier German standards DIN 1052 (2008), in the German National Annex to Eurocode 5 DIN EN 1995-1-1/NA (2013), in the current version of Eurocode 5 EN 1995-1-1 (2008) and in the CEN Enquiry (ENQ) draft of Eurocode 5 prEN 1995-1-1 (2023).

The design approach in DIN EN 1995-1-1/NA (2013) was adopted from DIN 1052 (2008) (Eq. (1)) and is based on the shear field theory (Figure 1 (a) and (b)) (Colling & Janssen (2021), Hertel (1960)).

$$f_{v,0,d} = \min \begin{cases} k_{v,1} \cdot R_d / a_v \\ k_{v,1} \cdot k_{v,2} \cdot f_{v,d} \cdot t \\ k_{v,1} \cdot k_{v,2} \cdot f_{v,d} \cdot 35 \cdot t^2 / a_r \end{cases} \quad (1)$$

The first line in Eq. (1) accounts for the limit given by the resistance of the sheathing-to-framing connection, the second line for the limit given by the shear resistance of the sheathing panels, and the third line for the limit given by the buckling resistance of the sheathing panels. The shear resistance of the panels in the application as sheathing material of timber-framed shear walls does not reach the shear strength of the panel, because the shear resistance is reduced due to additional stresses in the panel. According to DIN EN 1995-1-1/NA (2013), the reduction factor  $k_{v,2}$  covers additional stresses arising from:

- the distance between the axis of the sheathing panel and the framing members (Figure 1 (c) 1.);
- a discontinuous shear flow (Figure 1 (c) 2.);
- forces acting perpendicular to the axes of the framing members (Figure 1 (c) 3.).



(c)

Figure 1. Timber-framed shear wall element (a), shear flow distribution in the framing members and in the sheathing panel (b) and reasons for additional stresses in the sheathing panel and hence, reduce the shear resistance of the sheathing compared to the shear strength of the sheathing panels. (c) (1. to 5.)

In DIN EN 1995-1-1/NA (2013), the factor  $k_{v,2}$  is set to 0.33 for the design of timber-framed wall elements with one-sided sheathing and to 0.50 for sheathings placed on two sides (Hall (2012), Vogt (2015)). In the background document of DIN 1052 (Blass et al. (2005)), reference is made to Kessel & Sandau-Wietfeldt (2003) as a source containing information about the reduction factor  $k_{v,2}$ . However, no particular information can be found there.

The design rules in the European standard EN 1995-1-1 (2008) are based on the design rules in DIN 1052 (2008). In EN 1995-1-1 (2008) it is assumed that the resistance of the sheathing-to-framing connection is governing for any wall geometry. This corresponds to the assumption that the resistance of the sheathing-to-framing connection is always

lower than the resistance of the sheathing panel. This assumption may not be valid when a strong (e.g. multiple row) sheathing-to-framing connection is applied.

The rules for the design of timber-framed shear walls in prEN 1995-1-1 (2023), are based on the design rules specified in DIN EN 1995-1-1/NA (2013) (Eq. (1)). The  $k_{v,2}$  factor was renamed to  $k_{p,model}$  and increased to 0.50 for one-sided and to 0.67 for two-sided sheathings. In this paper, the term "reduction factor" will be used for both factors  $k_{v,2}$  and  $k_{p,model}$ . The applicability of the design formulae is limited to wall elements, where the sheathing panels are connected to the framing members along all edges in a sufficiently stiff manner in terms of transferring shear stresses, meaning that the factor  $k_{v,1}$  in Eq.(1) is equal to 1.0. In addition to the three factors inducing additional stresses and reducing the panel shear resistance listed in DIN 1052 (2008), in prEN 1995-1-1 (2023) two additional factors are mentioned:

- The design model was developed assuming pinned connections between the studs while in reality these connections are often weaker (Figure 1 (c) 4.).
- If the framing members are of different depth in cross-section (Figure 1 (c) 5.), there results an eccentricity leading to additional stresses in the panel.

The first parameter, i.e. the influence of the stiffness of the connection between the framing members is somewhat misleadingly formulated. In reality, the framing members are not perfectly hinged as assumed in the model. Whether the flexural and rotational stiffness is weaker or stronger than the underlying assumption of perfect hinges depends on the constructional detailing. In the presented study, where framing members with large cross-sections were used, the connections are stronger than the assumed pinned connection in the model.

### 3 Materials

The sheathing panels investigated were of type OSB/3 with thicknesses of 12 mm, 15 mm, 18 mm and 25 mm and dimensions (width x height) of 1250 mm x 2500 mm. For each panel thickness, the sheathing panels originated from one single production batch and from one single producer. For the framing members, Swiss-grown Norway spruce (*Picea abies* (L.) H. Karst) glued-laminated timber GLT of strength class GL24h (EN 14080 (2013)) was used and two types of fasteners were applied as sheathing-to-framing connection:

- resined staples (Haubold, KG 700) with a nominal diameter of 1.53 mm, a length of 50 mm and a tensile strength of  $f_u \geq 800 \text{ N/mm}^2$
- threaded nails (Haubold 3.10 x 90 Ring Wire Weld) with a nominal diameter of 3.10 mm, a length of 90 mm and a tensile strength of  $f_u \geq 600 \text{ N/mm}^2$

## 4 Methods

### 4.1 Specimens

To determine the reduction of the shear resistance of OSB/3 sheathings and the shear strength of OSB/3 panels, large size wall elements were investigated. The specimens were designed for a failure in the sheathing. To achieve this specific failure, the framing members, the fasteners, and the anchorage were over-designed compared to the resistance of the sheathing panels. This led to a very strong sheathing-to-framing connection layout with up to 10 rows of fasteners. In total nine wall element types were tested, each type in three runs. Five wall element types were of quadratic and four of rectangular shape. A summary of the materials used and the geometrical properties of all investigated wall elements is provided in the Annex (Table 3).

Four rectangular-shaped (R) wall configurations were tested applying a one-sided sheathing. The OSB/3 panels with thicknesses of 12 mm, 15 mm, and 18 mm were fastened to the framing members using resined staples (S). For the 25 mm thick OSB/3 panels, threaded nails (N) were used, since the penetration depth in the framing members would be critically low and the staples typically used would be difficult to penetrate into the 25 mm thick OSB/3 panel. Another five quadratic specimens (Q) were tested. The influence of the arrangement of the sheathing, whether on one side or both sides, was investigated on two types of walls with 12 mm thick sheathing using resined staples as fasteners. To investigate the influence of the thickness of the framing members, one wall configuration with a 12 mm thick sheathing fastened using resined staples was examined, in which the thickness of the framing members was reduced by 50% compared to all other investigated wall configurations. The last two quadratic configurations were both sheathed on one sided with 18 mm thick panels, using once resined staples and once threaded nails for the sheathing-to-framing connection.

The size of the specimen was governed by the dimensions of the OSB/3 panels (2.50 m and 1.25 m) with an offset of 20 mm at the panel edges, to avoid local crushing of the sheathing panel due to large displacements during testing. To avoid compression perpendicular to the grain, the edge studs were connected by mortise and tenon joints. For all framing connections, fully-threaded screws were added to hold the elements in place during manufacturing. The dimensions (width x height) of the specimens were 1.29 m x 1.29 m (quadratic) and 1.29 m x 2.54 m (rectangular).

The specimens are named using the following scheme:

- Letter Q or R: Shape of the specimen, Q for quadratic, R for rectangular
- Number 12, 15, 18 or 25: Thickness of the OSB/3 sheathing panel
- Letter S or N: Fastener type used, S for resined staples, N for threaded nails
- Letters TF or 2S: TF for thin framing members, 2S for sheathing on two sides

## 4.2 Experimental setup

The experiments on the wall elements tests were conducted following the specifications in ISO 21581 (2010). The maximum force was estimated based on the induced shear flow in a timber-framed shear wall element at the mean level, calculated according to DIN EN 1995-1-1/NA (2013) (Eq. 1) using the following parameters:

- $k_{v,1} = 1.0$ ;
- $k_{v,2} = 1.0$ , which is a conservative assumption for the investigated reduction factor;
- $f_{v,mean,est} = 9.4 \text{ N/mm}^2$  (Schick (2017));
- $t$ : nominal thickness of the sheathing.

The wall elements were tested in a position rotated by  $90^\circ$  (Figure 2) compared to the situation in reality, leading to a 50% reduction of the vertical reaction forces. The static system and the internal force flow in the wall element remain unchanged. The horizontal force was applied using a 1000 kN hydraulic jack with a load cell of precision class 1. For wall elements with one-sided sheathing, out-of-plane forces arise when loaded horizontally. To prevent out-of-plane displacements, a steel bracket was attached to the top edge of the wall element. By placing a 50 kN hydraulic jack and controlling the stroke of it to a displacement of 0 mm, the upper longitudinal framing member of the wall element was stabilized against lateral displacement. The vertical reaction forces were transferred to the test rig through a steel plate at the top and four steel rods along the top rail, on the side of force application. The shear anchoring consisted of a steel angle bracket at the end of the wall element. The horizontal displacements were measured in the centre of the top edge using a laser distance sensor with a precision of 0.11 mm and in the centre of the bottom edge with a linear variable differential transducer (LVDT) with a measuring range of 10 mm and a precision of 0.04 mm.

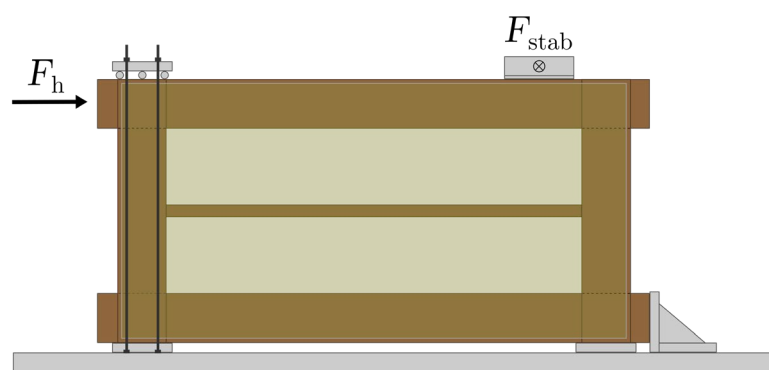


Figure 2. Timber-framed wall element mounted on the test rig for investigating the shear resistance.



## 5 Results and discussion

### 5.1 Introduction

Table 1 provides the estimated maximum forces  $F_{max,est}$ , calculated as described in Chapter 4.2, the maximum forces measured when failure occurred in the experiment  $F_{max,exp}$  and the failure modes for all 27 investigated wall elements. In all experiments, the OSB/3 sheathing panels failed in a brittle manner. The initial failure occurred in the direction of the force flow between the point of force application and the point of the shear anchoring, either diagonally in the sheathing (SF), along a row of fasteners (FR), or as a combination of these two failure types (CF) (Figure 3). In all tests, there were minimal to zero plastic deformations observed.

Table 1. Failure modes (FM), measured maximum forces when failure occurred in the experiment ( $F_{max,exp}$ ) and estimated maximum forces ( $F_{max,est}$ ). (Manser et al. (2024))

Quadratic specimens					Rectangular specimens				
		FM <sup>1</sup>	$F_{max,exp}$ [kN]	$F_{max,est}$ [kN]			FM <sup>1</sup>	$F_{max,exp}$ [kN]	$F_{max,est}$ [kN]
Q-18-N	1	FR	163	218	R-25-N	1	FR	394	597
	2	FR	159	218		2	FR	405	597
	3	?	155	218		3	?	379	597
Q-18-S	1	FR	135	218	R-18-S	1	?	299	430
	2	FR	144	218		2	FR	290	430
	3	FR	157	218		3	CF	305	430
Q-12-S	1	FR	98	146	R-15-S	1	?	241	358
	2	FR	101	146		2	CF	221	358
	3	FR	100	146		3	SF	229	358
Q-12-S-TF	1	FR	92	146	R-12-S	1	SF	181	287
	2	FR	95	146		2	SF	186	287
	3	SF	101	146		3	SF	178	287
Q-12-S-2S	1	SF	185	291					
	2	SF	185	291					
	3	?	179	291					

<sup>1</sup> SF: initial failure diagonally in the sheathing; FR: initial failure occurred along a row of fasteners; CF: initial failure is a combination of FR and SF; ?: initial failure remains unclear

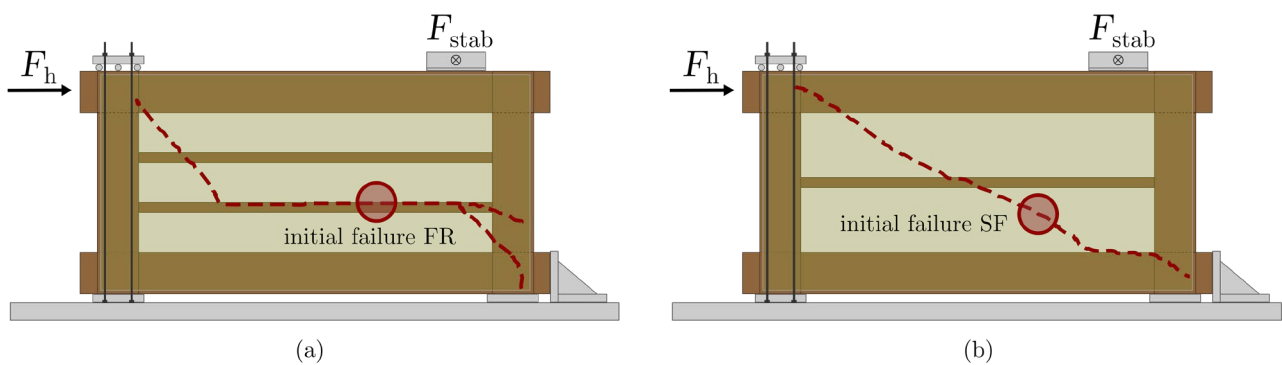


Figure 3. Example of a failure pattern, (a) where the initial failure of the OSB/3 sheathing panel occurred along the row of staples (R-15-S-2) and (b), where the initial failure of the OSB/3 sheathing panel occurred diagonally in the sheathing (R-25-N-3).

## 5.2 Evaluation of the reduction factor

The reduction factor investigated in this study (specified in DIN EN 1995-1-1/NA (2013) and prEN 1995-1-1 (2023)) corresponds to the ratio between the shear resistance of the OSB/3 sheathing reached in the experiments  $f_{v,SW}$  and the mean value of the shear strength of the OSB/3 panel  $f_{v,mean}$ . The shear resistance of the OSB/3 sheathing  $f_{v,SW}$  is calculated by dividing the maximum force reached in the tests by the length of the wall element and by the thickness of the panel.

The thickness and the mean shear strength of the panel both involve a degree of uncertainty. Both values were investigated in additional experiments according to EN 789 (2005), which are not presented in this paper. For details of those test results, see Manser et al. (2024). In order to investigate the impact of the uncertainties of these two parameters on the estimation of the reduction factor, two different evaluation approaches (A and B) were applied.

### 5.2.1 Evaluation approach A

In evaluation approach A, the nominal thickness of the OSB/3 panels was used to calculate the reduction factor. The mean value of the shear strength of the OSB/3 panel  $f_{v,mean}$  was estimated starting from the characteristic shear strength of the OSB/3 panels specified in EN 1995-1-1:2008 (i.e.  $f_{v,k} = 6.8 \text{ N/mm}^2$ ), and assuming a log-normal distribution (JCSS (2024)). For this estimation, an assumption for the coefficient of variation (CoV) of the shear resistance of OSB/3 panels needs to be made.

Since the JCSS Probabilistic Model Code does not provide information on the CoV of the shear resistance of OSB/3 panels, a CoV of 15% was set as the upper limit for the evaluation. This value is specified in the JCSS Probabilistic Model Code for the shear strength of GLT. The mean CoV determined from the shear tests on the OSB/3 panels was 6%. This low value can be attributed to all the OSB/3 panels originating from a single production batch for each thickness and from one producer. Therefore, a CoV value of 6% was chosen as the lower limit for calculating the reduction factors. Additional calculations were performed using a CoV of 11%.

The average reduction factors calculated with this approach ranged between 0.69 and 0.91 for the different wall configurations and panel thicknesses (Figure 4).

### 5.2.2 Evaluation approach B

In evaluation approach B, the actually measured panel thickness and the panel shear resistance determined from the shear tests on the OSB/3 panels were used to calculate the reduction factors. To obtain the most conservative reduction factor, the higher value of shear strength, whether parallel or perpendicular to the strand orientation of the top layer, was used.

To account for the limited sample size, confidence intervals (CIs) were calculated. These CIs define the range where the true mean value of shear resistance is expected

to lie with a certain level of confidence. It was assumed that shear strength is log-normally distributed. Reduction factors were calculated for a 75% CI, as prescribed in EN 1990 (2021) for the statistical determination of individual properties, and for a 95% CI, which is a very conservative assumption. To obtain the most conservative result for the reduction factor, the upper bound of the CI was applied.

The average reduction factors calculated applying this approach lie between 0.78 and 0.99 (Figure 4) for the different wall configurations and panel thicknesses.

### 5.3 Calculated reduction factors

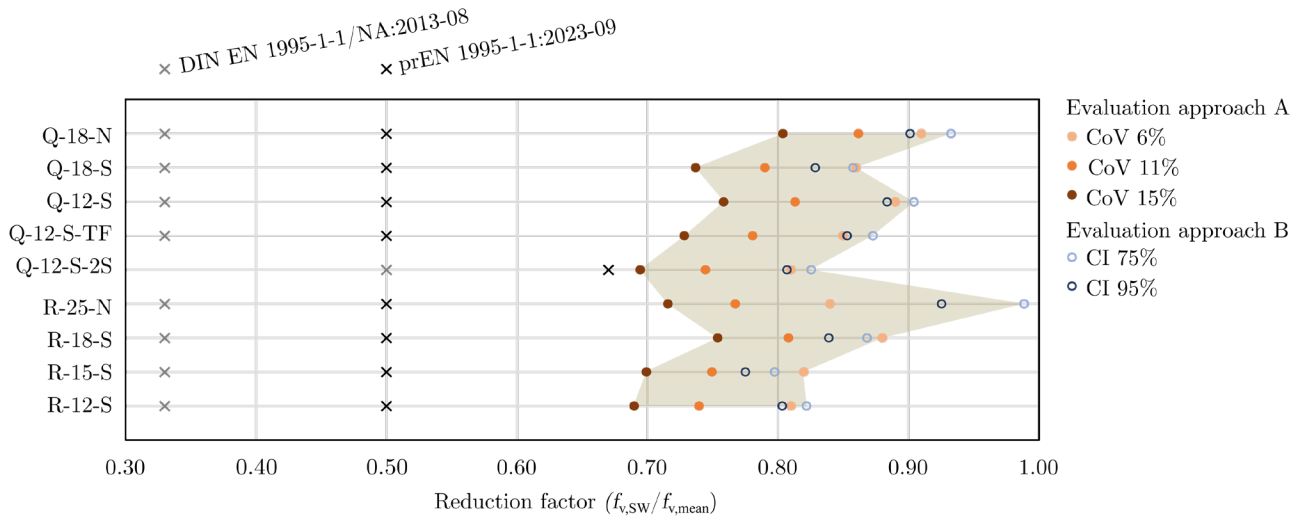


Figure 4. Reduction factors for 12 mm, 15 mm, 18 mm and 25 mm thick OSB/3 panels. Comparison of values specified in DIN EN 1995-1-1/NA:2013-08 and prEN 1995-1-1:2023-09 with the values obtained from the experiments. The filled dots represent the results obtained by applying the evaluation approach A, the empty dots the results obtained by applying the evaluation approach B.

Comparing the two evaluation approaches for determining the reduction factor shows that both result in values of similar magnitude. The reduction factors specified in DIN EN 1995-1-1/NA (2013), which account for additional stresses reducing panel shear strength (0.33 for one-sided and 0.50 for two-sided sheathing), seem very conservative compared to this study's results. Increasing these reduction factors would result in higher calculated shear resistance for the sheathing panel, allowing for a stronger sheathing-to-framing connection and more economical timber-framed wall elements.

The reduction factors determined from the experimental investigations (Figure 4) in this study range from 0.69 to 0.99, depending on the evaluation approach, wall element configuration, and panel thickness. For timber-framed wall elements sheathed with OSB/3 panels on one side, the reduction factor of 0.50 specified in prEN 1995-1-1 (2023) ( $k_{p,model}$ ) was confirmed in the experiments. However, the reduction factor of 0.67 for two-sided OSB/3 sheathing could not be confirmed. The respective experimental results are almost equal to the value given in prEN 1995-1-1 (2023).

Both design standards, DIN EN 1995-1-1/NA (2013) and prEN 1995-1-1 (2023), specify a higher reduction factor for the design of wall elements with two-sided sheathing compared to one-sided sheathing, which was not observed in the experiments. In fact,

the reduction factor for wall elements with two-sided sheathing (Q-12-S-2S) was even lower than for those with one-sided sheathing (Q-12-S). This raises the question whether differentiating between one-sided and two-sided sheathing is justified.

The small difference in reduction factors for one-sided and two-sided sheathing suggests that the distance between the stud axis and the sheathing axis (Figure 1 (c) 1.) has minimal impact on additional stresses in the sheathing panel. Investigations on wall elements with different stud widths (Q-12-S and Q-12-S-TF) support this hypothesis, showing little difference in reduction factors. However, it should be noted that the framing members had large cross-sections, making the overall framing very stiff and potentially reducing the impact of one-sided versus two-sided sheathing.

The use of very stiff framing members results in a timber-framed shear wall that differs from what is typically constructed in low-rise buildings. When framing members with smaller cross-sections are used, deformations can occur in the framing members, leading to additional effects that were not considered in the experimental study presented in this paper. However, with small cross-section framing members, it is not possible to arrange a strong sheathing-to-framing connection, because there is not enough space on the framing member to place multiple rows of fasteners while still keeping the minimal distances between the fastener rows. In cases where the sheathing-to-framing connection is not strong, the reduction factor becomes irrelevant, because the sheathing-to-framing connection is the weakest link.

#### 5.4 Application example

Following, the influence of the choice of the reduction factor on the number of fastener rows that can be arranged is shown. The two design approaches ductile and non-ductile will be discussed, whereby ductile means that a building is designed for a ductile failure, to ensure buildings can withstand unexpected and extreme loads and dissipate energy in case of an earthquake. In Switzerland, the minimal distances between two staples within one row are 25 mm for a non-ductile design and 35 mm for a ductile design. Setting the limit given by the resistance of the sheathing-to-framing connection and the limit given by the shear resistance of the OSB/3 sheathing panel (first two lines in Eq. 1) equal, the minimum distance between the fasteners can be calculated. When the calculated distance is smaller than the minimal distance, fastener need to be arranged in multiple rows. Calculated using the design rules specified in Switzerland (SIA 265 (2021) and SIA 265/1 (2018)), the number of rows of fasteners in a 15 mm or a 18 mm thick OSB/3 panel for different reduction factors are summarized in Table 2.

Table 2. Influence of the choice of the reduction factor on the maximum number of rows of staples for a 15 mm and a 18 mm thick OSB/3 sheathing.

Sheathing thickness	Design approach	Minimal distance between staples	Reduction factor					
			0.3	0.4	0.5	0.6	0.7	0.8
15 mm	Non-ductile	$a_{v,min} = 25$ mm	1	1	2	2	3	3
	Ductile	$a_{v,min} = 35$ mm	1	1	2	2	3	3
18 mm	Non-ductile	$a_{v,min} = 25$ mm	1	2	2	3	4	4
	Ductile	$a_{v,min} = 35$ mm	1	2	2	3	3	4

A sheathing-to-framing connection arranged in 2 or 3 rows of fasteners, separated with minimal distances is considered a strong connection. In most application, not more than 2 to 3 rows of staples will be applied. Table 2 shows that a reduction factor of 0.6 already allows for the application of a strong (2-3 rows) sheathing-to-framing connection in timber-framed shear walls.

## 6 Conclusions

The shear resistance of timber-framed shear walls is calculated as the minimum of the resistance of the sheathing-to-framing connection and the resistance of the sheathing. When applied as sheathing material, the panel shear resistance is reduced due to additional stresses in the panel. This reduction has never been experimentally investigated and the values in current design standards had likely been set as rules of thumb. Based on the presented investigations on timber-framed wall elements with OSB/3 sheathing, the following statements about the reduction factor can be formulated:

- The reduction factors specified in DIN EN 1995-1-1/NA (2013), 0.33 for one-sided sheathing and 0.50 for two-sided sheathing are substantially lower than those resulting from the presented experiments.
- For one-sided sheathing, the reduction factors resulting from the presented experiments lie above the value specified in prEN 1995-1-1 (2023) ( $k_{p,model} = 0.50$ ).
- For two-sided sheathing, the reduction factors resulting from the presented experiments lie close to the value specified in prEN 1995-1-1 (2023) ( $k_{p,model} = 0.67$ ).
- The experimental results on OSB/3 sheathed timber-framed shear wall elements did not reveal a difference in the reduction factor for assemblies with one-sided sheathing and such with two-sided sheathing.
- Based on the experimental investigations presented in this study, a reduction factor of 0.60 for both cases, sheathing on one and on two sides, is suggested for sheathed timber-framed shear walls with stiff timber frames.

## 7 References

- Blass, H. J., Ehlbeck, J., Kreuzinger, H., Steck, G. (2005): Explanations to DIN 1052 (in German). Informationsdienst Holz, DGfH, Munich, Germany.
- Colling, F., Janssen, P. (2021): Bracing of buildings consisting of timber frame wall panels – According to shear field theory and extended shear field beam model (in German).
- DIN EN 1995-1-1/NA (2013): German National Annex - Nationally determined parameters – Eurocode 5: Design of timber structures - Part 1-1: General - Common rules and rules for buildings (in German). DIN.
- DIN 1052 (2008): Design, calculation, and dimensioning of timber structures - general dimensioning rules and dimensioning rules for building construction (in German). DIN.
- EN 14080 (2013): Timber structures - Glued laminated timber and glued solid timber. CEN.
- EN 1990 (2021), Basis of structural design. CEN.
- EN 1995-1-1/A1 (2008): Design of timber structures - Part 1-1: General - Common rules and rules for buildings. CEN.
- EN 789 (2005): Timber structures - Test methods - Determination of mechanical properties of wood based panels. CEN.
- Filiatrault, A. (1990): Static and dynamic analysis of timber shear walls. *Canadian Journal of Civil Engineering*, vol. 17, no. 4, pp. 643-651, 1990, doi: 10.1139/l90-073.
- Geiser, M., Meier, S., Ratsch, R., Vogel, M. (2018): Ductile seismic design - Considerations for the seismic design of timber structures according to the concept of ductile structural behavior (in German). Bern University of Applied Sciences, Switzerland.
- Grossi, P., Sartori, T., and Tomasi, R. (2015): Tests on timber frame walls under in-plane forces: part 1. *Proceedings of the Institution of Civil Engineers-Structures and Buildings*, vol. 168, no. 11, pp. 826-839, doi: 10.1680/stbu.13.00107.
- Grossi, P., Sartori, T., and Tomasi, R. (2015): Tests on timber frame walls under in-plane forces: part 2. *Proceedings of the Institution of Civil Engineers-Structures and Buildings*, vol. 168, no. 11, pp. 840-852, doi: 10.1680/stbu.13.00108.
- ISO 21581 (2010): Timber structures - Static and cyclic lateral load test methods for shear walls. ISO.
- Hall, C. (2021): Methods for elastic and plastic modeling of timber-framed walls loaded in shear (in German). University of Braunschweig, Germany.
- Hertel, H. (2021): Lightweight construction: components, dimensioning, and constructions of aircraft and other lightweight structures (in German).
- JCSS (2024): Probabilistic Model Code. Joint Committee on Structural Safety JCSS. <http://www.jcss.byg.dtu.dk/> (accessed 08.07.2024)

- Källsner, B. and Girhammar, U. A. (2009): Plastic models for analysis of fully anchored light-frame timber shear walls. *Engineering Structures*, vol. 31, no. 9, pp. 2171-2181, doi: 10.1016/j.engstruct.2009.03.023.
- Källsner, B. and Girhammar, U. A. (2009): Analysis of fully anchored light-frame timber shear walls-elastic model. *Materials and Structures*, vol. 42, no. 3, pp. 301-320, doi: DOI 10.1617/s11527-008-9463-x.
- Kessel, M. H., Sandau-Wietfeldt, M. (2003): Extension of the applications of thin, adhesive- and binder-free wood composite panels for timber construction (in German). University of Braunschweig, Germany.
- Kuai, L., Ormarsson, S., Vessby, J., Maharjan, R. (2022): A numerical and experimental investigation of non-linear deformation behaviours in light-frame timber walls. *Engineering Structures*, vol. 252, doi: 10.1016/j.engstruct.2021.113599.
- Kuai, L., Ormarsson, S., Vessby, J. (2023): Nonlinear FE-analysis and testing of light-frame timber shear walls subjected to cyclic loading. *Construction and Building Materials*, vol. 362, doi: 10.1016/j.conbuildmat.2022.129646.
- Manser, N., Steiger, R., Geiser, M., Otti, M., Frangi, A. (2024): Shear resistance of Oriented Strand Board panel sheathings in timber-framed shear walls. *Engineering Structures*, vol. 316, doi: 10.1016/j.engstruct.2024.118461.
- Sartori, T. and Tomasi, R. (2013): Experimental investigation on sheathing-to-framing connections in wood shear walls. *Engineering Structures*, vol. 56, pp. 2197-2205, doi: 10.1016/j.engstruct.2013.08.039.
- Seim, W., Kramar, M., Pazlar, T., and Vogt, T. (2016): OSB and GFB As Sheathing Materials for Timber-Framed Shear Walls: Comparative Study of Seismic Resistance. *Journal of Structural Engineering*, vol. 142, no. 4, doi: Artn E4015004 10.1061/(Asce)St.1943-541x.0001293.
- prEN 1995-1-1 (2023): Design of timber structures - Part 1-1: General - Common rules and rules for buildings. CEN.
- Qiang, R. T, Zhou, L. N., Ni, C., Huang, D. S. (2022): Seismic performance of high-capacity light wood frame shear walls with three rows of nails. *Engineering Structures*, vol. 268, doi: 10.1016/j.engstruct.2022.114767.
- Schick, M. (2017): Probabilistic investigations on overstrength of nailed timber-framed wall elements (in German). University of Kassel, Germany.
- SIA 265 (2021): Timber Structures (in German). SIA.
- SIA 265/1 (2018): Timber Structures - Additional provisions (in German). SIA.
- Steiger, R., Marzaleh, A. S. (2021): Experimental investigation of OSB sheathed timber frame shear walls with strong anchorage subjected to cyclic lateral loading. *Engineering Structures*. *Engineering Structures*, vol. 226, doi: 10.1016/j.engstruct.2020.111328

Vogt, T. (2015): Development of a calculation model to describe the load-carrying and the deformation behavior of timber-framed walls considering local effects (in German). University of Kassel, Germany.



# Annex

Table 3. Overview of the geometric properties of the tested wall elements. (Manser et al. (2024))

	Rectangular wall elements						Quadratic wall elements					
	R-12-S	R-15-S	R-18-S	R-25-N	Q-12-S	Q-12-S-DS <sup>2</sup>	Q-12-S-BB <sup>2</sup>	Q-18-S	Q-18-N			
<b>Sheathing</b>												
Thickness	[mm]	12	15	18	25	12	12	12	18			
One- or two sided	one	one	one	one	one	one	two	one	one			
<b>Framing</b>												
Top- and bottom rail (width x height) <sup>1</sup>	[mm]	200 x 240	200 x 240	200 x 240	200 x 280	200 x 240	200 x 240	200 x 240	200 x 240			
Edge stud (width x height)	[mm]	240 x 200	240 x 200	240 x 200	280 x 200	240 x 200	240 x 200	240 x 200	240 x 200			
Interm. stud (width x height) <sup>1</sup>	[mm]	200 x 60	200 x 60	200 x 60	200 x 100	200 x 60	200 x 60	200 x 60	200 x 60			
Interm. stud	[-]	2	2	2	1	2	2	2	2			
<b>Fasteners</b>												
Type	[-]	staples	staples	staples	nails	staples	staples	staples	nails			
Rows at sheathing edge	[-]	8	8	8	10	8	8	8	8			
Rows on interm. studs	[-]	2	2	2	2	2	2	2	2			
d <sub>1</sub> : Offset of the sheathing panel to the wall edge	[mm]	20	20	20	20	20	20	20	20			
d <sub>2</sub> : Fastener edge distance on the panel edge	[mm]	20	20	20	30	20	20	20	22			
d <sub>3</sub> : Distance between fastener rows on the bottom rail, the top rail and the edge studs	[mm]	25	25	25	20	25	25	25	24			
d <sub>4</sub> : Fastener edge distance on the inner edge of the bottom rail, the top rail and the edge studs	[mm]	25	25	25	50	25	25	25	30			
d <sub>5</sub> : Fastener edge distance on the inner studs	[mm]	20	20	20	35	20	20	20	20			
d <sub>6</sub> : Distance between fastener rows on the inner studs	[mm]	20	20	20	30	20	20	20	30			
a <sub>v</sub> : Spacing between the fasteners within a row	[mm]	23	23	23	40	23	23	23	40			

<sup>1</sup> Lamellas arranged edge-wise.; <sup>2</sup> TF: Thinner timber framing members, 2S: Sheathing placed on two sides.

## DISCUSSION

**The paper was presented by N Manser**

*F Lam received clarification that the objective is to establish the shear strength capacity of the OSB panel as this failure mode cannot be avoided in design of the timber frame shear wall.*

*H Blass asked as the shear strength of OSB is of interest why not just test the shear strength of the OSB. N Manser said that was also done. H Blass asked whether the tested OSB/3 is representative. N Manser said the producers do not control shear strength of the OSB; therefore, this is a problem.*

*R Jockwer and N Manser discussed the differences in failure modes of OSB in full scale wall tests versus panel tests. Also the factors in EC5 may be an issue.*

*S Winter commented that the full-scale tests indicated tensile failure mode of the OSB and not the shear failure of OSB so evaluation of the tension strength of OSB panels should be considered. N Manser said that although tensile failure of OSB existed, the limit for nailed connection is clearly shown in the test. S Winter commented that more realistic design might lead to more deformation leading to differences in observed behaviour.*

*G Doudak asked about differences in failure mode in two side sheathed versus one side sheathed wall. N Manser said they are similar. G Doudak asked if there are more staples on top versus the bottom. N Manser said they are the same.*

*A Salenikovich commented that some of the factors are not available in the Canadian code and asked about the background of the reduction factors. N Manser said that the background was not available. They further discussed the loading configurations and the influence of hold downs on lateral resistance.*



# Proposal for an Analytical Model of Light Timber-Framed Shear Walls with additional Cladding

Lukas Rauber, RWTH Aachen University (Germany)

Benno Hoffmeister, RWTH Aachen University (Germany)

Keywords: light timber-framed walls, cladding, lateral resistance, analytical model

## 1 Introduction

Light timber-framed shear walls (LTFWs) are used to provide lateral resistance and stiffness in timber buildings – with increasing demand for multi-storey structures. According to *EN 1995-1-1* (2004) the lateral load-carrying capacity and stiffness of LTFWs are governed by their components (fasteners, sheathing, framing and anchorages). For multi-storey timber buildings European regulations require additional fire protection, which is usually applied by means of additional cladding with gypsum board or gypsum fibre board (GFB). Claddings are generally attached by fasteners to the framing through the structurally considered sheathing. These fasteners lead to additional sheathing-to-framing connections (Figure 1). The contribution of cladding and its fasteners is neglected in the calculation of the resistance according to European standards – *EN 1995-1-1* (2004) and also in the new draft *prEN 1995-1-1* (2023).

Neglecting cladding and their sheathing-to-framing connections is unfavourable in two respects: (i) economic potential, as higher stiffness and resistance of the structure is *not* exploited for quasi-static loads, e.g. wind loading, and (ii) safety concerns in seismic design, as the structural model requires a realistic assessment of the structural properties (i.e. stiffness, load-carrying capacity and ductility) of all structurally relevant components.

In this contribution an analytical model for the horizontal load-carrying capacity of LTFWs with cladding is presented and validated by experimental data. To investigate the influence of claddings, 62 tests on LTFW elements were performed. The proposed analytical model for the lateral resistance of LTFWs with cladding considers the additional cladding fasteners in the sheathing-to-framing connection.

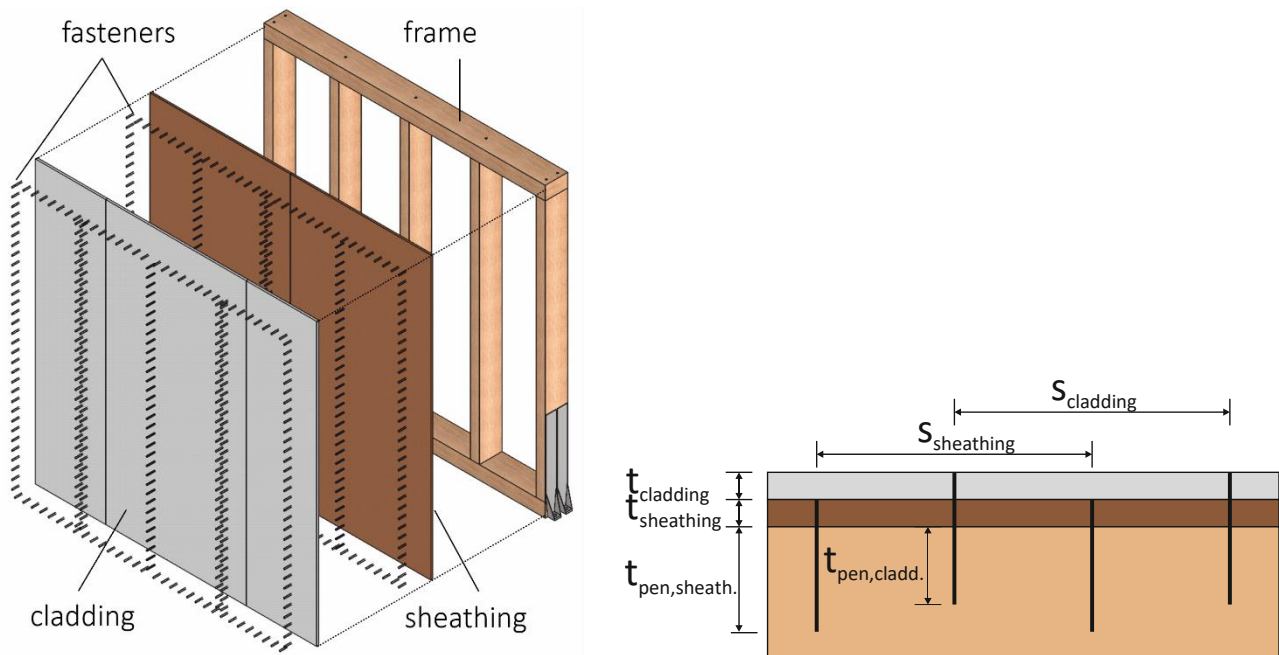


Figure 1. Components of a LTFW with cladding (left) and sheathing-to-framing connection (right).

## 2 State of the Art

First tests on LTFWs with cladding were performed by *Glos et al.* (1985). The international literature includes tests by *Chen et al.* (2016) and *Valdivieso et al.* (2023). The results of 24 own tests on LTFWs with cladding were already presented in *Rauber and Hoffmeister* (2024). All test results showed a significant increase in load-carrying capacity as well as stiffness for LTFWs with additional cladding.

An analytical model to determine the load-carrying capacity of LTFWs with cladding is *not* available so far – only a model for the calculation of the load-carrying capacity of fasteners with interlayers was presented by *Blaß and Laskewitz* (2003) and a model to modify the European Yield Model (EYM) according to *EN 1995-1-1* (2004) by the embedment strength of an additional outer layer was presented by *Gebhardt* (2012).

## 3 Materials and Methods

### 3.1 Proposed Analytical Model

The proposed analytical model for the calculation of LTFWs with claddings supplements the given model of *EN 1995-1-1* (2004) by two parts: (i) the capacity of the sheathing-to-framing connection is calculated by the EYM for sheathing fasteners and the model by *Gebhardt* (2012) for cladding fasteners; (ii) the load-carrying capacity at wall scale is calculated according to *EN 1995-1-1* (2004) using both these capacities.

#### 3.1.1 Load-Carrying Capacity of Sheathing Fasteners

The load-carrying capacity of the sheathing-to-framing connection created by the sheathing fasteners is calculated by the EYM from *EN 1995-1-1* (2004) formula (8.6). The possible failure modes are shown in Figure 2.

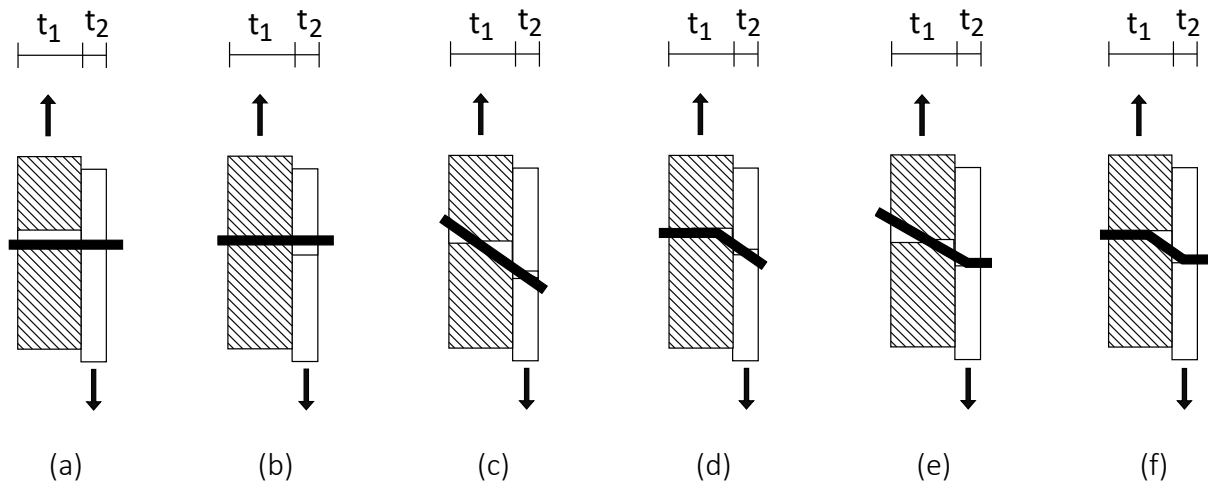


Figure 2. Modes of the EYM used to calculate the load-carrying capacity of sheathing fasteners.

### 3.1.2 Load-Carrying Capacity of Cladding Fasteners

To calculate the load-carrying capacity of the sheathing-to-framing connection created by cladding fasteners, the following assumption based on the test results was made: The internal forces due to lateral loading of LTFWs is fully transferred through the shear plane of the sheathing-to-framing connection. That leads to the condition that the failure mode always occurs between the sheathing-to-framing connection. The cladding only contributes with its embedment strength. The considered failure modes are shown in Figure 3. A comparison with the EYM failure modes (Figure 2) shows, that only mode (c) and mode (d) of the EYM according to formula (8.6) of *EN 1995-1-1* (2004) need to be modified.

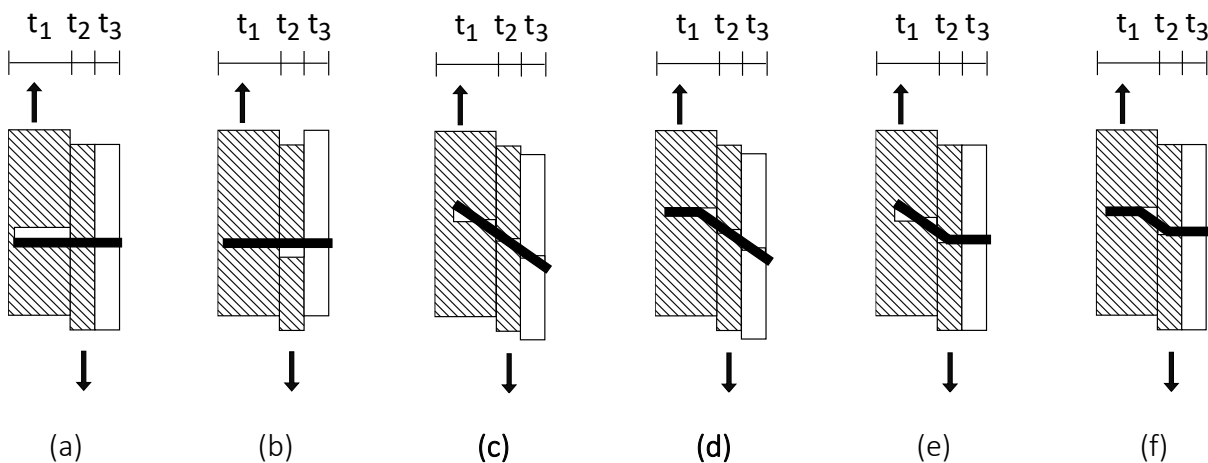


Figure 3. Extended modes used to calculate the load-carrying capacity of cladding fasteners.

In *Gebhardt* (2012) this modification of the EYM is presented for wood fibre board to timber connections with additional timber counter-battening. This approach is used for the proposed analytical model. The resistances of the two modified modes can be calculated by formula (1) for mode (c) and by formula (2) for mode (d):

$$R_c = \frac{f_{h,1} \cdot t_1 \cdot d}{1 + \beta_2} \left[ \sqrt{\beta_2 + 2\beta_2^2 \left[ 1 + \left(\frac{t_2}{t_1}\right) + \left(\frac{t_2}{t_1}\right)^2 \right] + \beta_2^3 \left(\frac{t_2}{t_1}\right) + \beta_2 \cdot \beta_3 (\beta_2 + 1) \left(\frac{t_3}{t_1}\right)^2} - \beta_2 \left( 1 + \frac{t_2}{t_1} \right) \right] \quad (1)$$

$$R_d = \frac{f_{h,1} \cdot t_1 \cdot d}{2 + \beta_2} \left[ \sqrt{2\beta_2(1 + \beta_2) + \frac{4\beta_2(2 + \beta_2) M_y}{f_{h,1} \cdot d \cdot t_1^2} + \beta_2 \cdot \beta_3 (\beta_2 + 2) \left(\frac{t_3}{t_1}\right)^2} - \beta_2 \right] \quad (2)$$

where  $\beta_2 = f_{h,2}/f_{h,1}$  and  $\beta_3 = f_{h,3}/f_{h,1}$ .

### 3.1.3 Load-Carrying Capacity of LTFWs with Cladding

The lateral resistance of LTFWs is governed by the resistance of their components (fasteners, sheathing, frame and anchorage). The fastener resistance  $F_{i,v,R}$  at wall scale considers the individual shear resistance of the fasteners as well as the wall width  $b_i$  and a height factor  $c_i$ . The proposed model modifies the formula (9.21) of *EN 1995-1-1* (2004) by the following formulation:

$$F_{i,v,R} = \left( \frac{F_{f,R,sheathing}}{S_{sheathing}} + \frac{F_{f,R,cladding}}{S_{cladding}} \right) \cdot b_i \cdot c_i \quad (3)$$

where  $F_{i,v,R}$  is the lateral load-carrying capacity of the fasteners at wall element scale,  $F_{f,R,i}$  is the load-carrying capacity of one fastener ( $i = \text{sheathing or cladding}$ ),  $s$  is the fastener spacing,  $b_i$  is the width of a single wall element and  $c_i$  is the height factor of the wall with  $c_i = 1.0$  if  $b_i \geq b_0$  and  $c_i = b_i/b_0$  if  $b_i < b_0$ , where  $b_0 = h/2$  and  $h$  is the height of the wall element.

In case of board-to-board connection (cladding-to-sheathing) using short staples, it was assumed that these fasteners do *not* contribute to the sheathing-to-framing connection. They were neglected in this case.

According to *DIN EN 1995-1-1/NA* (2013) also the shear resistance of the sheathing needs to be verified. This resistance can be determined using formula (4):

$$F_{i,v,R} = k_v \cdot k_B \cdot f_v \cdot t \cdot b_i \quad (4)$$

where  $F_{i,v,R}$  is the in-plane resistance of the sheathing,  $k_v$  is the factor to account for additional stresses in the sheathing,  $k_B$  is the buckling factor (with  $k_B = \min(1; 35 \cdot t_i/b_{net})$ ),  $b_{net}$  is the net stud spacing,  $f_v$  is the shear strength of the sheathing,  $t$  is the thickness of the sheathing,  $b_i$  is the width of the wall element.

The capacities of the remaining LTFW components (framing and anchorages) may be calculated according to *EN 1995-1-1* (2004) or technical approvals.

### 3.1.4 Input Values for Validation

To compare the analytical model with the test results, mean values of the material properties as well as the measured raw density  $\rho$  of each test specimen were used.

The following formulas for calculating the mean embedment strength  $f_{h,m}$  were used according to Schick (2017):

$$f_{h,m} = 0.082 \cdot \rho_m \cdot d^{-0,3} \text{ for structural timber} \quad (5)$$

$$f_{h,m} = 131.8 \cdot d^{-0,779} \cdot t^{0,1} \text{ for OSB} \quad (6)$$

$$f_{h,m} = 8.0724 \cdot d^{-0,463} \cdot t^{0,9} \text{ for GFB} \quad (7)$$

where  $f_{h,m}$  is the mean embedment strength of the material,  $\rho_m$  is the measured raw density of the framing material,  $d$  is the diameter of the fastener shaft and  $t$  is the board thickness.

For the fasteners the mean yield moment was taken from internal documentation of the manufacturer. The values for the staples of diameter 1.8 mm were taken to  $M_{y,m,1.8} = 1143 \text{ Nmm}$  and for diameter 1.53 mm taken to  $M_{y,m,1.53} = 737 \text{ Nmm}$ .

The factor  $k_v$ , considering the additional stresses in the sheathing was investigated experimentally by Manser *et al.* (2023) for OSB and by Kramer *et al.* (2023) for a specific GFB product. From Manser *et al.* (2023),  $k_{v,OSB} = 0,75$  was selected for the calculations. The investigations by Kramer *et al.* (2023) considered only a specific GFB type. Since GFB shear failure was partly observed in the own tests, the  $k_{v,GFB}$ -factor was calculated for each specimen type with GFB sheathing failure by:

$$k_{v,GFB,i} = \frac{F_{max,i}}{k_B \cdot f_{v,m} \cdot t \cdot b_i} \quad (8)$$

where the  $F_{max}$  is the maximum lateral force resisted by the tested wall  $i$  and  $f_{v,m}$  is the mean value of the sheathing shear strength. Mean values found in the current literature were used for the shear strength  $f_v$ . The mean shear strength of OSB  $f_{v,m,OSB} = 7.4 \text{ N/mm}^2$  was taken from Manser *et al.* (2023). The mean shear strength of GFB was considered to be  $f_{v,m,GFB} = 3.96 \text{ N/mm}^2$  based on internal documentation of the manufacturer. The used value is slightly lower than the value that was shown by Schick (2017), who used  $f_{v,m,GFB} = 4.35 \text{ N/mm}^2$ .

The rope effect was considered for modes (c) to (f) for sheathing fasteners (Figure 2) as well as cladding fasteners (Figure 3). The mean values for the rope effect were based on internal documentation by the manufacturer of the staples. The values used for the pull-out strengths were  $f_{ax,m,1.8} = 7.25 \text{ N/mm}^2$  for staples with diameter of 1.80 mm and  $f_{ax,m,1.53} = 8.12 \text{ N/mm}^2$  for staples with diameter of 1.53 mm. The used pull-through strengths were  $f_{head,m,1.8} = 56.5 \text{ N/mm}^2$  and  $f_{head,m,1.53} = 52.3 \text{ N/mm}^2$ . For the own calculations of the rope effect the coefficient of friction was set to  $\mu = 0.40$  (not 0.25 according to EN 1995-1-1 (2004)) and the rope effect was not limited to a fraction of the shear resistance of the fastener.



Partial (safety) factors for mode (d) to (f) of EYM (1.05 or 1.15), required by *EN 1995-1-1* (2004) for design, were omitted in the calculations.

The increase factor of 1.2 for the sheathing-to-framing connection according to *EN 1995-1-1* (2004) section 9.2.4.2 (5) was not used for the calculations.

### 3.2 Experimental Investigations

As a basis for the model validation, 62 experimental tests on LTFWs ( $2.50 \times 2.50$  m) were performed. Shear walls with additional cladding made of GFB and reference walls with sheathing only (OSB or GFB) were tested. The tests were performed using monotonic or cyclic loading according to *ISO 21581* (2010).

The horizontal load was applied by a hydraulic cylinder and transferred to the ends of the top rails of each wall by two steel profiles connected with threaded rods. The top rails of the LTFWs were held against stability failure out of plane with rollers but *not* against uplift. The horizontal wall supports were realised using steel profiles. Two Simpson StrongTie HTT31 were used as vertical anchorages at each perimeter stud.

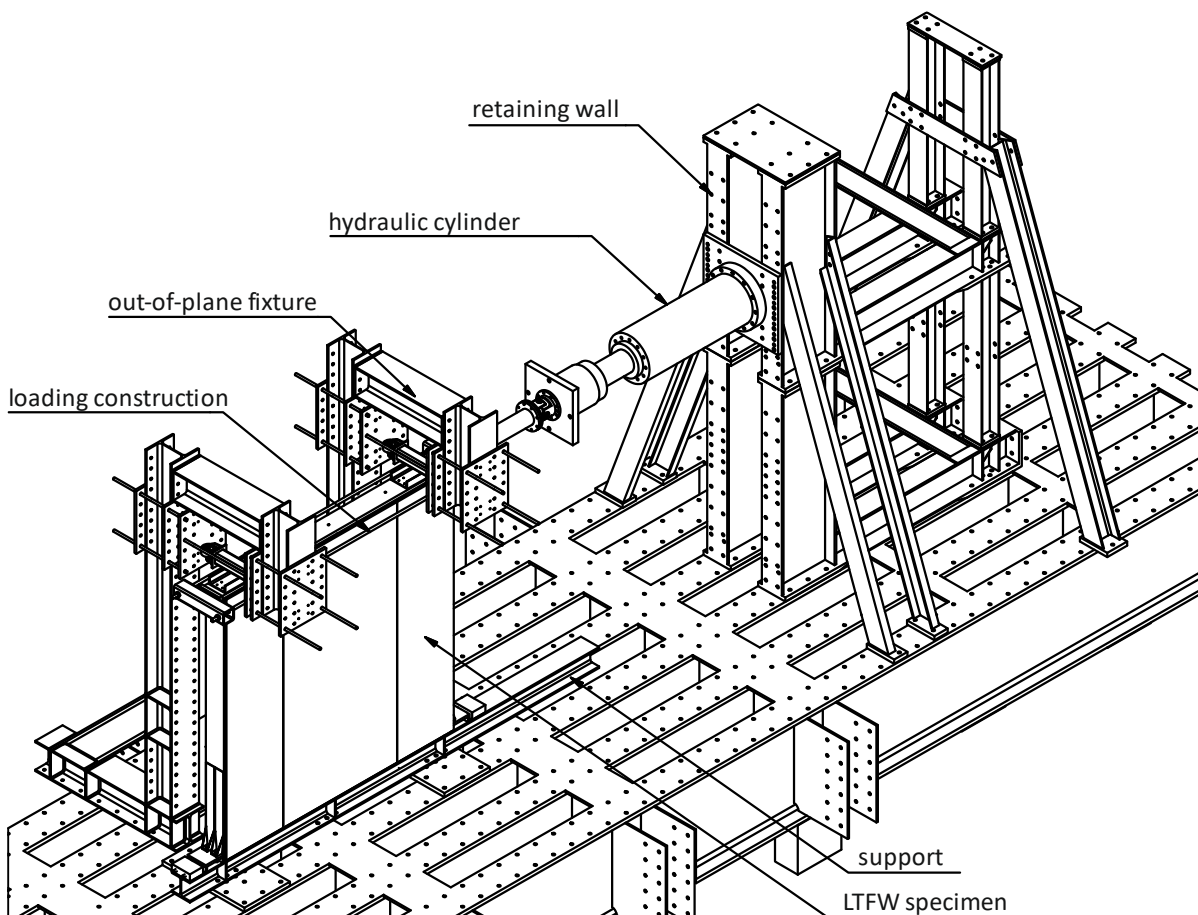


Figure 4. Used test setup for the LTFW tests.

#### 3.2.1 Materials

Structural timber of strength class C24 was used for the framing. The top and bottom rails had a cross-section of  $120 \times 200$  mm; the studs had a cross-section of  $80 \times 200$  mm. The moisture content of the timber framing was determined after each test using the resistance measurement method in accordance with *EN 13183-2* (2002).

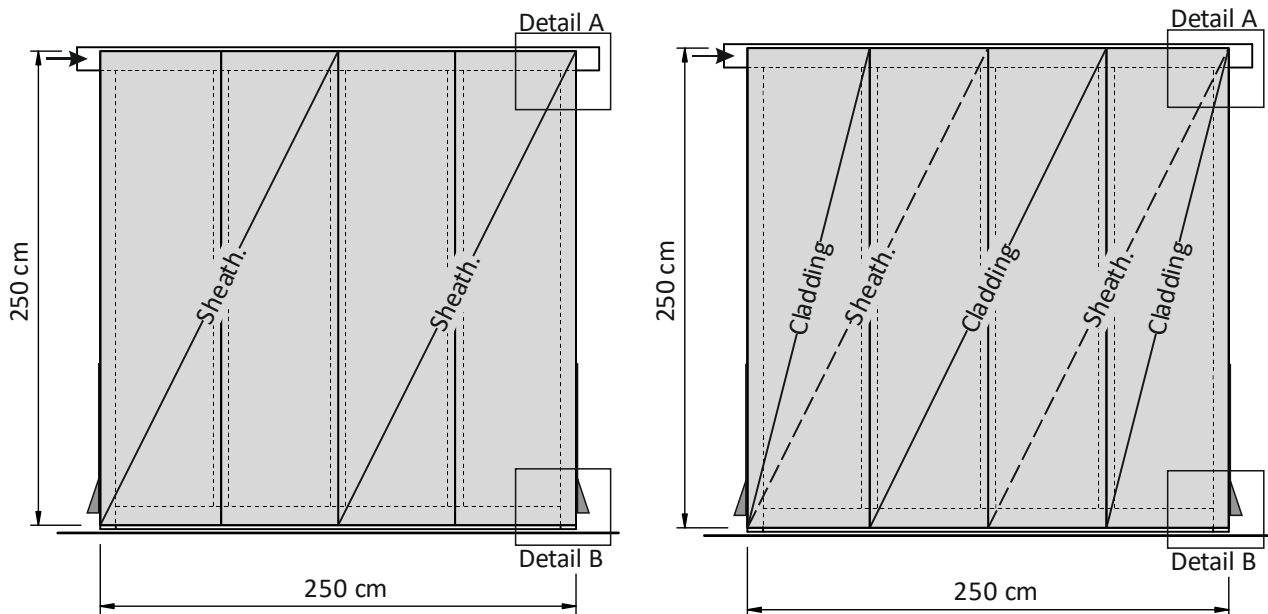
The sheathing consisted of OSB/3 boards ( $t = 15$  mm), provided by Egger Holzwerkstoffe Wismar GmbH & Co. KG, or gypsum fibre boards (GFB) with a thickness of  $t = 12.5$  or  $18$  mm, provided by James Hardie Europe GmbH (fermacell®). The cladding consisted of the same GFB boards. Boards of the same thickness were each from the same production batch. The board dimensions were  $1250 \times 2500$  mm.

The fasteners used were resin-coated staples, provided by ITW Befestigungssysteme GmbH (Haubold). Two types of staples were used: (i) HD 7900 with a diameter of  $\varnothing = 1.80$  mm and a length of  $L = 65$  mm (or  $L = 75$  mm for the second GFB layer in wall type 07); (ii) KG 700 CDNK (divergent staples), with  $\varnothing = 1.53$  mm and  $L = 35$  mm for the board-to-board connection of wall type 10.

Two Simpson Strong-Tie HTT31 anchors were fully attached to each side of the wall using 41 nails (TJEP KA 40/60 mm) and four screws (CSA5.0 $\times$ 80).

### 3.3 Test Specimens

All test specimens had a sheathing area of  $2.50 \times 2.50$  m (Figure 5) and a fastener spacing of  $s = 75$  mm (if not stated otherwise). The cladding was offset by half the sheathing width and the cladding fasteners were offset by  $s/2$  to the sheathing ones (if not stated otherwise). The LTFW specimens were manufactured at the facilities of Adams Holzbau-Fertigbau GmbH and taken to the lab at RWTH Aachen, where the experimental tests were performed and the material measurements were carried out.



(a) Reference specimens without cladding

(b) Specimens with one cladding layer

Figure 5. Dimensions and sheathing arrangement of the LTFW test specimens.

Type 02 from test series 0 and the walls with double-sided boarding differed from the other test specimens in that the framing was *not* notched as it is usually done in production by the manufacturer (Figure 6 (b)).

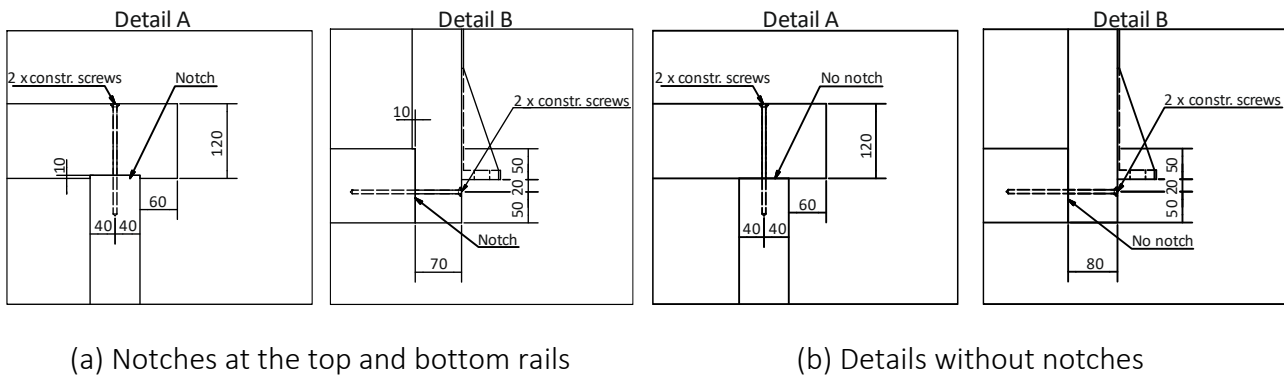


Figure 6. Notch details of the timber frames.

The fasteners of the reference tests without cladding are shown in Figure 7 (a). Claddings were fastened through the sheathing into the framing (Figure 7 (b)). Specimen type 10 was fastened board-to-board with short staples (Figure 7 (d)).

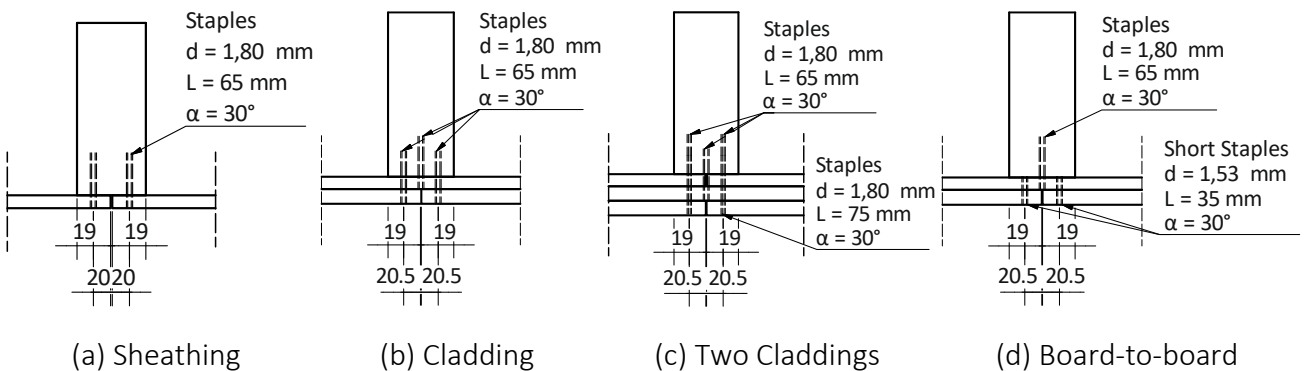


Figure 7. Fastening details of the test specimens at the connection to the studs.

### 3.3.1 Tests on LTFWs with single-sided sheathing

Within the first test series the lateral load-carrying capacities of LTFWs with and without cladding were tested with single-sided sheathing. The sheathing and cladding arrangement is shown in Figure 8.

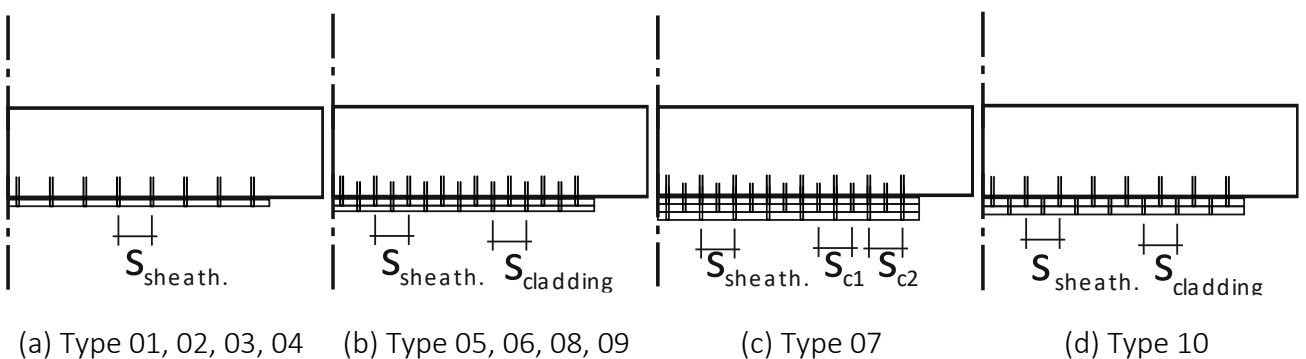


Figure 8. Fastener details in top rail of the test specimens with single-sided sheathing.

The mean value of the moisture measurements of these test series was  $13.8 \pm 0.91\%$ . Table 1 shows the test series.

Three wall types differed from the regular wall structure:

- Type 02 had *no* constructive frame notches (Figure 6 (b)).
- For type 07 a double layer of cladding was used. The second cladding was stapled above sheathing fasteners, leaving *no* minimum distances between the fasteners of the sheathing and the second cladding in the sheathing-to-framing connection.
- The cladding of type 10 was fastened board-to-board with divergent staples.

Table 1. Experimental series of LTFWs with single-sided sheathing.

Series	Type	Number	Sheathing	Cladding	Staples	Notes
[-]	[-]	m* c*	t [mm]	t [mm]	∅ - L [mm]	[-]
0	01	2 1	OSB 15	-	1.80 - 65	
	02	1 1	OSB 15	-	1.80 - 65	frame <i>not</i> notched (Figure 6 (b))
	03	2 1	GFB 12.5	-	1.80 - 65	
	04	1 1	GFB 18	-	1.80 - 65	
1	05	2 1	OSB 15	GFB 12.5	1.80 - 65	
	06	1 1	OSB 15	GFB 18	1.80 - 65	
	07	1 1	OSB 15	2 × GFB 18	1.80 - 65	2nd clad. with st. 1.80-75 (Fig. 6 (c))
2	08	2 1	GFB 12.5	GFB 12.5	1.80 - 65	
	09	1 1	GFB 18	GFB 18	1.80 - 65	
	10	1 1	GFB 18	GFB 18	1.53 - 35	fastened board-to-board (Fig. 6 (d))

\*monotonic (m) or cyclic (c) according to ISO 21581 (2010)

### 3.3.2 Tests on LTFWs with double-sided sheathing

Within the second test series the lateral load-carrying capacity of LTFWs with and without cladding were tested with double-sided sheathing (Figure 9).

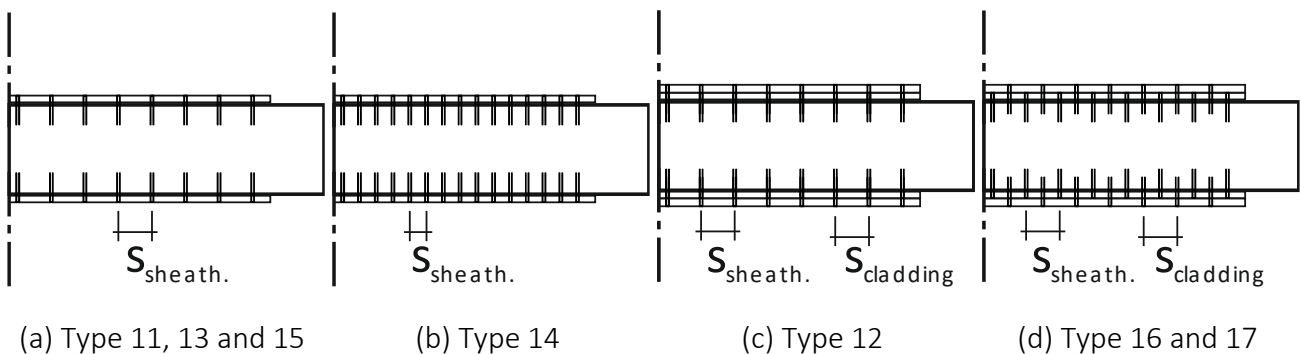


Figure 9. Fastener details in the top rail of the test specimens with double-sided sheathing.

The mean value of the moisture measurements of these test series was  $14.3 \pm 1.05\%$ . The experimental series with double-sided sheathing are shown in Table 2. Two wall types differed from the other wall structures:

- Type 12, where the cladding staples were fastened right above the sheathing fasteners leading to zero distance (*s*) in the sheathing-to-framing connection.

- Type 14 had the same wall arrangement as type 13, but with double the number of staples by using  $s = 37.5 \text{ mm}$  (halved fastener spacing).

Table 2. Experimental series of LTFWs with double-sided sheathing.

Series	Type	Number		Sheathing	Cladding	Staples	Spacing	Notes
[-]	[-]	m*	c*	t [mm]	t [mm]	∅ - L [mm]	s [mm]	[-]
3	11	2	0	OSB 15	-	1.80 - 65	75	
	12	2	0	OSB 15	GFB 12.5	1.80 - 65	75	without min. spacings
4	13	4	3	OSB 15	-	1.80 - 65	75	
	14	2	1	OSB 15	-	1.80 - 65	37.5	doubled no. of staples
	15	5	3	GFB 18	-	1.80 - 65	86.6	
5	16	5	3	OSB 15	GFB 18	1.80 - 65	75	
	17	5	3	GFB 18	GFB 18	1.80 - 65	86.6	

\*monotonic (m) or cyclic (c) according to ISO 21581 (2010)

## 4 Results

### 4.1 Experimental Results

The observed initial failure mode of the test specimens was always plastification of the fasteners. One or two plastic hinges formed in the staple shafts before secondary failure modes occurred. The secondary failure modes were either (i) detaching of the sheathing from the frame due to fastener pull-through (Figure 10 (a)) or pull-out (Figure 10 (b)) or (ii) failure of the sheathing, which did only occur for some wall specimens with GFB sheathing. If the GFB sheathing failed and an additional cladding was present, the crack was usually transferred to the cladding and also propagated there with the same pattern (Figure 10 (c)). GFB sheathing failure only occurred in the monotonic tests, with the exception of the cyclic test of wall type 03.



(a) staple pull-through

(b) staple pull-out

(c) sheathing failure

Figure 10. Observed failure modes during the LTFW tests.

Figure 11 shows a bar chart comparing the load-carrying capacities of the experimental test results. The load-carrying capacities of the monotonic (dark) and cyclic (light) tests are shown with the standard deviation (where applicable). Tests with GFB sheathing failure are marked by a superscript number (<sup>1</sup> for failure in some monotonic tests and <sup>2</sup> for failure in all monotonic tests).

The results show an increase in load-carrying capacity for LTFWs with cladding compared to the reference walls. Wall type 05 (with additional GFB cladding of 12.5 mm) had an increased resistance of over 100% compared to wall type 01 (with only OSB sheathing). Wall type 10 with divergent staples (fastened board-to-board) showed no increase in resistance compared to type 04.

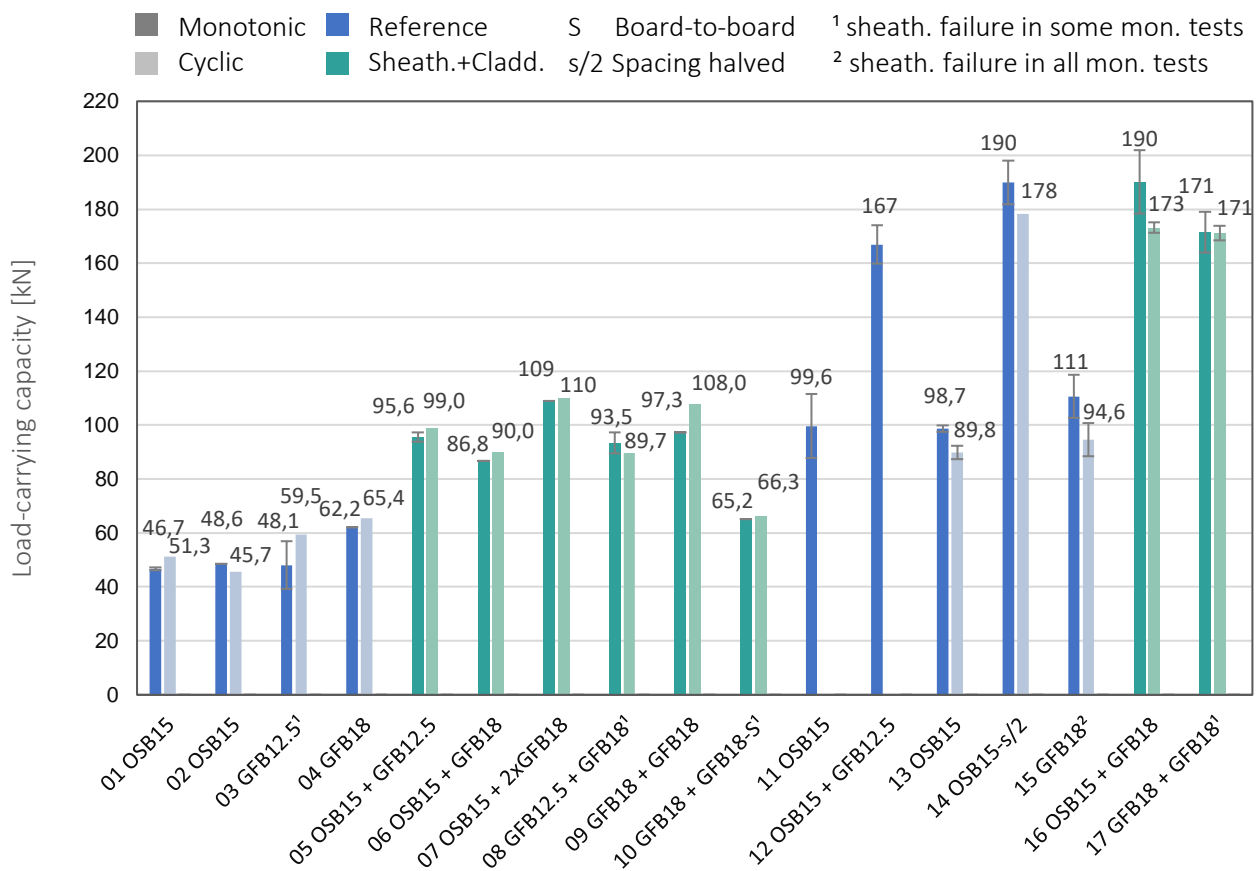


Figure 11. Bar chart of experimental load-carrying capacities for monotonic and cyclic tests.

#### 4.2 Comparison of analytical model and test results

Figure 12 shows a comparison of the analytical model and the monotonic test results. The model results (light) are shown next to the test results (dark). The model results are close to the test results for OSB-sheathed wall types. The test results are usually underestimated by the analytical model, except for wall type 12.

The decisive failure mode calculated for the cladding fasteners by the analytical model was also evaluated. The results showed that mode (f) from Figure 3 was always the decisive failure mode.

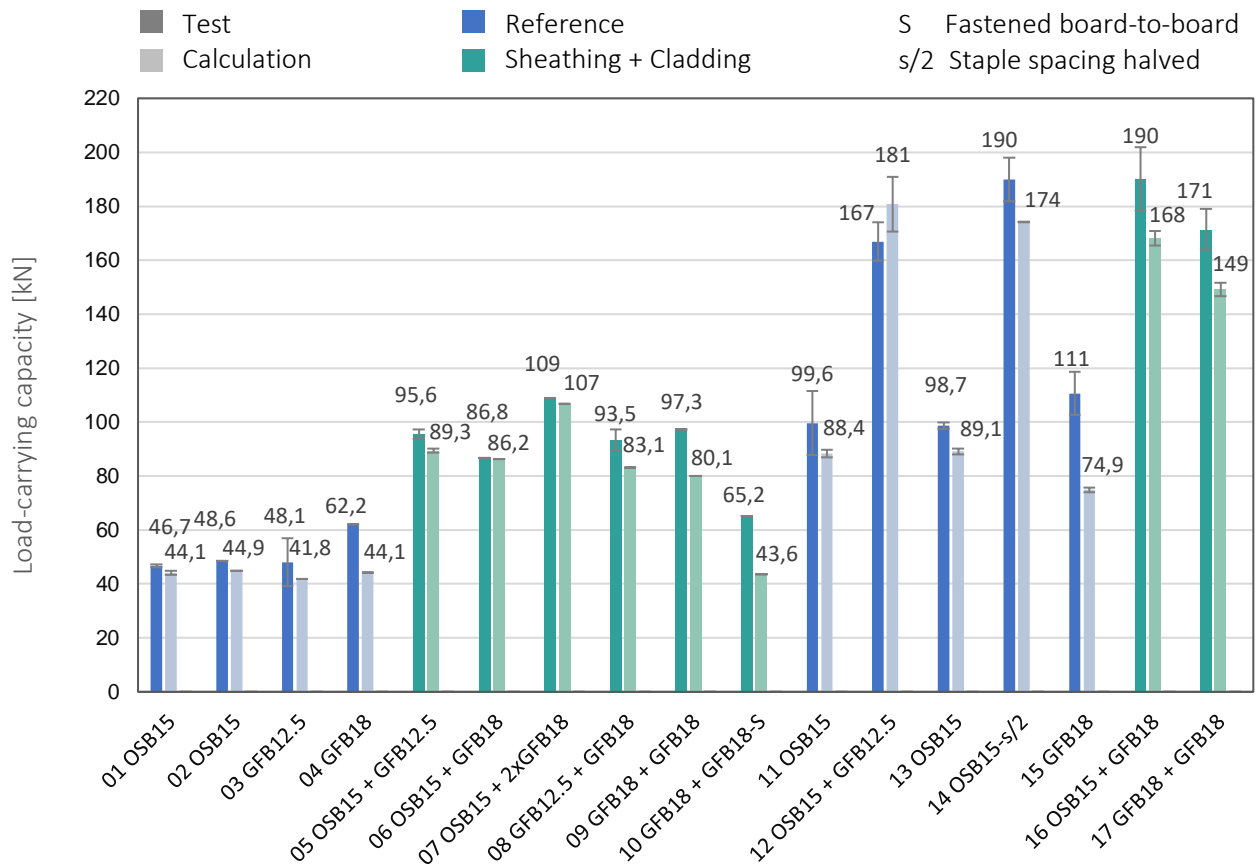


Figure 12. Comparison of calculated capacities versus experimental capacities (monotonic).

## 5 Discussion

The **experimental results** on LTFWs show a strong increase (up to 2-times) of the horizontal load-carrying capacity by additional claddings. This very significant increase should be considered in design rules provided by standards. The influence is only observed for cladding-staples fastened through the sheathing to the timber frame, which leads to increased resistance of the sheathing-to-framing connection. These observations are in accordance with the literature mentioned in the state of the art.

The test results for claddings with board-to-board connections to the sheathing with divergent staples show *no* increase in load-carrying capacity. It is therefore proposed to neglect this connection in calculation models for the load-carrying capacity.

The load-carrying capacities of LTFWs with OSB sheathing (and additional cladding) calculated by the **analytical model** are in good agreement with the experimental results. The model fits less for LTFWs with GFB sheathing (and additional cladding) – it underestimates their load-carrying capacity more. The underestimation is supposed to be related to the specific material behaviour of GFB. The EYM was originally developed for timber-(or timber engineered products)-to-timber connections and seems less reliable for GFB. The overestimation of the model for wall type 12 could be explained by the *non-existing* fastener spacings between sheathing and cladding staples (Figure 9 (c)). The model did not consider a reduction for this special fastener arrangement.



The fastener failure modes present in the experimental tests were always in the sheathing-to-framing connection. This shows that the proposed modelling approach, which only accounts for the sheathing-to-framing connection, was correct. The failure modes (a) to (f) of Figure 3 are suitable – the analytical approach to account for interlayers in the EYM according to *Blaß and Laskewitz* (2003) is not applicable.

The calculated failure modes of the cladding fasteners by the analytical model were always mode (f). For shorter embedment depth of shafts into the framing, mode (e) could also become decisive for the investigated materials OSB and GFB. Formula (1) and formula (2) do not seem to affect the outcome of the calculations for the investigated stapled connections of claddings – in this case the EYM would lead to the same results. Therefore, it could be considered to just use the EYM on the safe side to calculate cladding fasteners in sheathing-to-framing connections.

## 6 Conclusions

The following conclusions can be drawn from the **experimental tests**:

- The influence onto the load-carrying capacity of LTFWs is significant, if cladding fasteners contribute to the sheathing-to-framing connection.
- Board-to-board connection of cladding to sheathing by short divergent staples does not affect the load-carrying capacity of LTFWs.
- Fastening the cladding by staples right above the staples of the sheathing (without min. spacing) still leads to a significant increase in load-carrying capacity of LTFWs. For a predictable behaviour, the required minimum distances between all fasteners in the sheathing-to-framing connection should still be considered and ensured.

For the proposed **analytical model**, the following conclusions can be drawn:

- All fasteners providing additional resistance to the sheathing-to-framing connection should be taken into account to determine the load-carrying capacity.
- The proposed analytical model is in good agreement with the test results and predicts the load-carrying capacity more realistically than Eurocode 5.

## 7 Summary and Outlook

In this paper the influence of claddings on the load-carrying capacity of LTFWs was investigated and an analytical model was proposed. A significant influence of cladding fasteners on the load-carrying capacity of LTFWs was confirmed by full scale shear wall tests. However, this only applied to cladding fasteners reaching into the framing and thus adding resistance to the sheathing-to-framing connection.

For quasi-static lateral loading the existing calculation model of Eurocode 5 and its new draft are shown to be very safe sided for LTFWs with cladding – this leads to a neglect of the full load-carrying potential. The proposed analytical model utilises the EYM modification of *Gebhardt* (2012) with additional outer layers to calculate the



lateral load-carrying capacity of LTFWs with cladding. This analytical model was validated with good agreement against the experimental results.

The additional resistance should be considered in future code provisions. To this end a simplified model could be implemented into Eurocode 5 – without extending the EYM modes – by introducing formula (9) for the sheathing-to-framing connection:

$$F_{i,v,R} = \sum \frac{F_{f,R,j}}{s_j} \cdot b_i \cdot c_i \quad (9)$$

where  $F_{i,v,R}$  is the load-carrying capacity of the sheathing-to-framing connection,  $F_{f,R,j}$  is the shear resistance of one fastener of board  $j$  according to the EYM,  $s_j$  is the spacing of the fasteners in board  $j$ ,  $b_i$  is the width of the wall element and  $c_i$  is the height factor of the wall.

The calculation of the additional resistance of cladding fasteners may neglect the cladding embedment strength on the safe side. Using this approach, the contribution of claddings and their fasteners to the load-carrying capacity of LTFWs could be implemented with minimum changes to the current draft version of Eurocode 5.

It should be noted that the proposed changes are valid only for static design situations. Seismic design of timber buildings with LTFWs and additional cladding also requires consideration of the increased stiffness. The realistic determination of wall stiffnesses is crucial for the application of the response spectrum method. A significant influence of claddings on stiffness was observed in the tests but was not yet addressed in analytic formulations.

Additionally, the observed “overstrength” has an impact on capacity design rules, in particular of the frame, sheathing, anchorages and inter-storey connections. Here a new concept needs to be developed. *Not* considering both effects – stiffness and overstrength – may lead to unsafe seismic design results for LTFWs with cladding.

## 8 Acknowledgements

The authors gratefully acknowledge the financial support of the FNR research project HELEPOLIS funded by BMEL and the effective cooperation with the project partners Walter + Reif Ingenieurgesellschaft mbH and Adams Holzbau-Fertigbau GmbH.

## 9 References

- Blaß H. J.; Laskewitz, B. (2003): Tragfähigkeit von Verbindungen mit stiftförmigen Verbindungsmitteln und Zwischenschichten. In: Bauen mit Holz 105, Heft 1-2, S. 26-35.
- Chen, Z.; Chui, Y.-H.; Doudak, G. et al. (2016): Contribution of Type-X Gypsum Wall Board to the Racking Performance of Light-Frame Wood Shear Walls. In: Journal of Structural Engineering 142, Issue 5.

- EN 13183-2 (2002): Moisture content of a piece of sawn timber - Part 2: Estimation by electrical resistance method. CEN.
- DIN EN 1995-1-1/NA (2013): Nationaler Anhang - National festgelegte Parameter - Eurocode 5: Bemessung und Konstruktion von Holzbauten - Teil 1-1: Allgemeines - Allgemeine Regeln und Regeln für den Hochbau. DIN.
- Eurocode 5 (2004): Design of timber structures - Part 1-1: General – Common rules and rules for buildings. CEN. (EN 1995-1-1).
- Gebhardt, G. (2012): Holzfaserdämmplatten als aussteifende Beplankung von Holztafeln. Dissertation. Karlsruher Berichte zum Ingenieurholzbau, Heft 23, Universitätsverlag Karlsruhe, Karlsruhe, Germany.
- Glos, P.; Henrici, D.; Schmelmer, B. (1987): Festigkeit von ein- und zweiseitig beplankten Wandelementen. In: Holz als Roh- und Werkstoff 45, page 41-48.
- ISO 21581 (2010): Timber structures - Static and cyclic lateral load test methods for shear walls. International Organization for Standardization.
- Kramer, L.; Furrer, L.; Geiser, M. (2023): Bemessung von Holzrahmenbau-Wänden mit Gipsfaserbeplankung. Tagungsband Von der Forschung zur Praxis. Neue Erkenntnisse für die Bemessung im Holzbau. S-win. Berner Fachhochschule. page 14-21.
- Manser, N.; Steiger, R.; Geiser, M.; Kramer, L.; Frangi, A. (2023): TIMBER-FRAMED SHEAR WALLS WITH LARGE OPENINGS AS PART OF THE LATERAL FORCE-RESISTING SYSTEM - OPTIMIZATION OF THE SHEATHING-TO-FRAMING CONNECTION LAYOUT. World Conference on Timber Engineering 2023.
- prEN 1995-1-1 (2023): Eurocode 5 - Design of timber structures - Part 1-1. CEN.
- Rauber, L.; Hoffmeister, B. (2024): Experimentelle Untersuchungen zum Einfluss von Bekleidungen auf das Tragverhalten von Holztafelwänden. Doktorandenkolloquium Holzbau "Forschung und Praxis" 18.+19. März 2024, Stuttgart , Germany.
- Schick, M. (2017): Probabilistische Untersuchungen zu Überfestigkeiten von genagelten Wandelementen in Holztafelbauweise. Dissertation. Kassel University Press GmbH, Kassel, Germany.
- Valdivieso, D.; Guindos, P.; Montaña, J. et al. (2023): Experimental investigation of multi-layered strong wood-frame shear walls with nonstructural Type X gypsum wallboard layers under cyclic load. In: Engineering Structures 282.

DISCUSSION

**The paper was presented by L Rauber**

*G Doudak received clarification on the difference in the ductility ratio between the cases with and without cladding. Also the influence of difference in failure mode on added capacity from both sheathing types.*

*P Dietsch commented on the formulation of conclusions needing to clarify the failure of fasteners versus influence of cladding. Extra capacity from additional number of fasteners versus contribution of cladding was not clear in the paper and presentation.*

*M Fragiacommo commented that the overstrength factor did not seem right and the delay of brittle failure via the use of staples. L Rauber and M Fragiacommo discussed the load path between connections, OSB sheathing and cladding.*

*C Sandhaas commented on the load set up in relation to the vertical loading.*

*R Tomasi also commented that full anchorage was provided without vertical load.*

*R Jockwer asked about the error if only EYM was used. L Rauber responded that there was no issue if EYM was used.*

*H Blass discussed the load transfer mechanism and change in failure mode in the fasteners when cladding was introduced.*

*F Lam commented there was large volume of work on stucco cladded light wood frame shear wall from UBC and CUREE project in the 2000's. Although the contribution of stucco is clear, it was not included in NA code because of difficulties in quality control of onsite applied stucco. Also in N.A. staples are not considered in shear wall designs.*

*D Casagrande commented on spacing requirements of staples as related to fire resistance issues.*

*A Ceccotti received clarification that ISO21581 was followed. He mentioned that between ISO and European rules, implications on seismic design are different. He commented that dynamic response of cladded structures should be considered as seismic mass would increase and period would decrease.*





# Seismic performance of braced timber frames

Marjan Popovski, FPInnovations, Canada, marjan.popovski@fpinnovations.ca

Zhiyong Chen, FPInnovations, Canada, zhiyong.chen@fpinnovations.ca

Keywords: Braced Timber Frames, R-factors, Seismic performance

## 1 Introduction

Braced timber frames (BTFs) are one of the most efficient mass timber (MT) structural systems to resist lateral loads induced by earthquakes or high winds. Because of their inherent high lateral stiffness, they have been used as a Lateral Load Resisting System (LLRS) in many MT buildings and can easily meet the specified building drift limits. Example of a chevron-type BTF as LLRS used in the John W. Oliver Design Building, at the University of Massachusetts in Amherst is shown in Figure 1.



*Figure 1. A chevron-type BTF: during construction (left) and in a finished building at night (right). (Photos courtesy of Nordic Structures).*

Centrally braced frames (CBFs) resist lateral loads through a vertical concentric truss system where the longitudinal axes of the members align concentrically at the joints. There are many different configurations of CBFs with some of the most used been presented in Figure 2. The research presented in this paper is related to single diagonally braced timber frames, such as those shown in Figure 2(a) and (b).

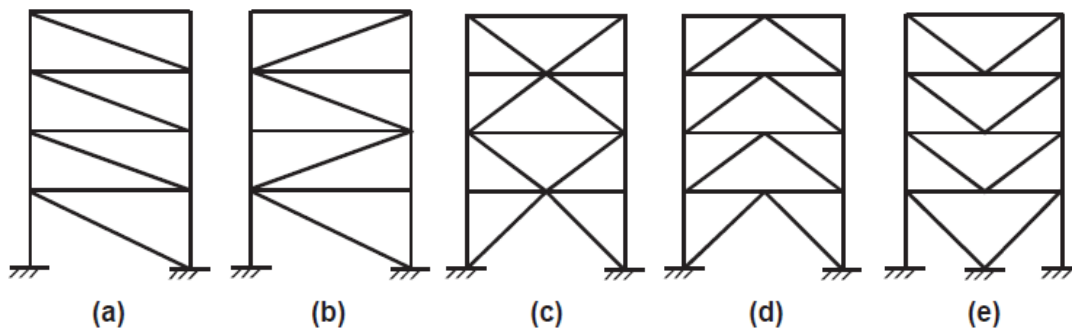


Figure 2. CBF configurations: single diagonally braced (a and b); X-braced (c); chevron (d); inverted chevron (e).

## 2 Research needs and objectives

In the National Building Code (NBC) of Canada (NRC, 2022), BTFs are included as a seismic force resisting system (SFRS) with two ductility categories: moderately ductile and with limited ductility. Moderately ductile BTFs can be designed using the equivalent static force procedure by reducing the elastic base shear force by a ductility-related force modification factor,  $R_d = 2.0$  and an overstrength-related force modification factor,  $R_o = 1.5$ . The BTFs with limited ductility can be designed using  $R_d = 1.5$  and  $R_o = 1.5$ . For design details on BTFs with different  $R_d$ -factors, NBC references CSA O86, the Canadian Standard for Engineering Design in Wood (CSA, 2024). No design guidelines for BTFs, however, currently exist in CSA O86, making the system out of reach of the average designer. To remedy the situation, FPInnovations is leading a multi-year research project to study the seismic behaviour of BTFs as SFRSs and generate the technical information needed for the development of design guidelines for BTFs. The main objectives of this multi-year project are to:

- Develop design guidelines for concentrically BTFs subjected to lateral loads (wind and seismic) for implementation in the supplement to the 2024 CSA O86;
- Identify if braced frames with bolted and riveted connections are able to achieve moderately ductile ( $R_d = 2.0$ ) or limited ductility ( $R_d = 1.5$ ) performance as specified in NBC;
- Determine the height limits for single- and multi-storey BTFs with different ductility for moderate and high seismic zones.

To fulfil the objectives, the research process includes significant experimental and analytical work. This paper summarizes some of the work conducted to date.

## 3 Background information

Seismic response of BTFs depends on several interacting factors that need to be investigated and quantified. Overall ductility and energy absorption capacity are the two critical parameters for adequate seismic behaviour. It was found that the two parameters are almost completely controlled by the diagonal brace connections

(Buchanan et al. 1989; Chen and Popovski 2020; Popovski 2000). Various types of timber connections can be used to connect the braces to the columns. Nail-plate connections were found to be more ductile than tooth-plate connections and bolted connections (Buchanan et al. 1989). Timber riveted connections exhibited excellent seismic performance, with respect to strength deterioration, deformation, ductility, and energy dissipation, compared with bolted connections at the comparable design loads (Popovski 2000; Popovski, Prion and Karacabeyli 2002, 2003). For BTFs with bolted connections, the behaviour was reliant on the bolt slenderness which is a ratio between bolt effective length (i.e., brace thickness) and bolt diameter. The energy dissipation and ductility in bolted connections using slender bolts were greater than in connections using stubby bolts (Chen et al. 2019; Popovski et al. 2002). Diagonal braces may rotate at the end connections, suggesting that potential stresses perpendicular to grain at the end brace connections have to be prevented or minimized (Popovski et al. 2003).

Based on dynamic time history analyses with three different ground motions conducted by Yasumura (1990), the ductility-based force modification factor was assessed to be 1.5 for non-ductile BTFs and 2.0 for ductile BTFs. Popovski (2000) suggested that BTFs with different connections should be assigned different  $R_d$ -factors. An  $R_d$  factor of 1.5 and 2.0 was suggested for BTFs with slender bolted connections and riveted connections, respectively. Results from time history analyses by Popovski (2004) showed that BTFs using riveted connections in LVL, glulam, and PSL, designed to fail in rivet yielding mode, can be assigned an  $R_d$  factor of 2.0. Popovski and Karacabeyli (2008), and Popovski (2009) also carried out analytical studies on the seismic performance of BTF to assess their  $R_d$  factors according to the 2005 NBC, using simplified nonlinear dynamic analysis method. The results showed that an  $R_d = 2.0$  was appropriate for braced frames with riveted connections. It should be noted, however, that all these studies that dealt with determining the  $R_d$ -factors were conducted prior to introduction of comprehensive methodologies for determining of the R-factors such as the FEMA P-695 (ATC 2009) in the US, the CCMC Procedure (De Vall et al. 2022), and the Unified Procedure (Fazileh et al. 2023) in Canada. Also, the studies used limited number of archetypes, while the ground motions used are not compatible to the current seismic hazard in Canada. Finally, Chen and Popovski (2021) conducted a study to investigate the seismic response of 30 BTFs with riveted connections designed with  $R_d=2.0$  and  $R_o=1.5$  using a pushover analysis following the coefficient evaluation method. It was found that single- and multistorey BTFs with wider frame bays had lower ductility and collapse margin ratio (CMR). The response of the investigated BTFs proved again that  $R_d=2.0$  and  $R_o=1.5$  were appropriate for the seismic design of BTFs with riveted connections.



## 4 Testing of braces with bolted connections

As the seismic response of single diagonal BTFs is highly influenced by the performance of the brace connections that connect it to the rest of the frame, a series of tests on braces with bolted connections was conducted.

### 4.1 Materials and methods

A variety of different configurations of brace specimens with bolted connections were tested for a total number of 68 tests. The details of the test matrix are not presented here due to space limitation, but more information can be found in Popovski et al. (2024). Each brace configuration consisted of a glulam brace and a bolted connection at both ends, top and bottom (Figure 3). The brace members were made of either 16c-E grade Douglas Fir (D-Fir) glulam ( $E=12400$  MPa), or 12c-E grade Spruce Pine (SP) glulam ( $E=9700$  MPa). The bolts were zinc plated ASTM A 307 with hexagonal head and a tensile strength of 400MPa (60,000 psi), as per CSA O86 (CSA, 2024). Braces had bolted connections with different number of rows and columns (2x2, 3x3, 2x4, 3x5), with either 9.5 mm (3/8"), 12.7 mm (1/2"), or 15.9 mm (5/8") diameter bolts. The slenderness ratio ( $t/d_F$ , where  $t$  is the thickness of the glulam and  $d_F$  is the bolt diameter) of the bolts in the connections was 7.5, 8.0, or 10.0.



Figure 3. The test setup with a brace specimen ready for testing (left); Example of a top reinforced connection (top right) and a bottom unreinforced connection (bottom right)

To lower the chance for any brittle behaviour of the connections, the spacing between fasteners parallel to grain  $S_p$  for most connections was chosen to be  $8d_F$  at least twice that of the minimum one specified in CSA O86, which is  $4d_F$ . Similarly, the spacing perpendicular to the grain  $S_q$  was taken to be a minimum of  $6d_F$  which is 1.5

times the minimum value of  $3d_F$  specified in O86. For the same reasons, the loaded end distance  $a_L$  was taken to be  $10d_F$ , which is close to twice the minimum allowed value of  $5d_F$  for most of the connections. Although all connections were designed to fail in yielding mode (g) per CSA O86 with three plastic hinges occurring in each bolt, a number of connection configurations were also reinforced with Self Tapping Screws (STS) to prevent potential splitting to occur. Two STS were placed halfway between bolt rows and halfway to the end of the connection (Figure 3 top right showing two STS and another two were on the back side). The STSs were fully threaded ASSY VG CSK screws with a diameter of 8mm and a length slightly shorter than the member width. It should be noted that the use of STS for reinforcement purposes is not currently codified in CSAO86, so the design of the STS was conducted using a simplified methodology. The average apparent density of the D-fir specimens was  $557.0 \text{ kg/m}^3$  with a COV of 4.2%. The average density of the Spruce Pine (SP) specimens was  $376.0 \text{ kg/m}^3$  with a COV of 3.7%.

All specimens were subjected to reversed cyclic tests using the protocol B in ASTM E2126 standard (ASTM, 2019). Slight modifications to the protocol were made by eliminating the first four low amplitude cycles at the beginning. Although in most standards a failure of a connection is defined as the point when the load drops to 80% of the maximum load, the testing continued until the load dropped to approximately 25% of the maximum load. This was done to determine the brace behaviour at large deformation levels so that the response can be accurately modelled.

## 4.2 Main results and discussion

All specimens throughout the testing program exhibited typical pinched hysteretic curves that are characteristic for timber connections with doweled fasteners (Figure 4). The response was characterized by an initial slip because the bolt holes had a 1mm to 1.5mm larger diameter than the bolts. In all unreinforced connections, different deformation levels were observed between the top and the bottom connections (Figure 4). Local variability in wood properties around the fasteners, connection fabrication precision, and tolerance, among others, contribute to this phenomenon.

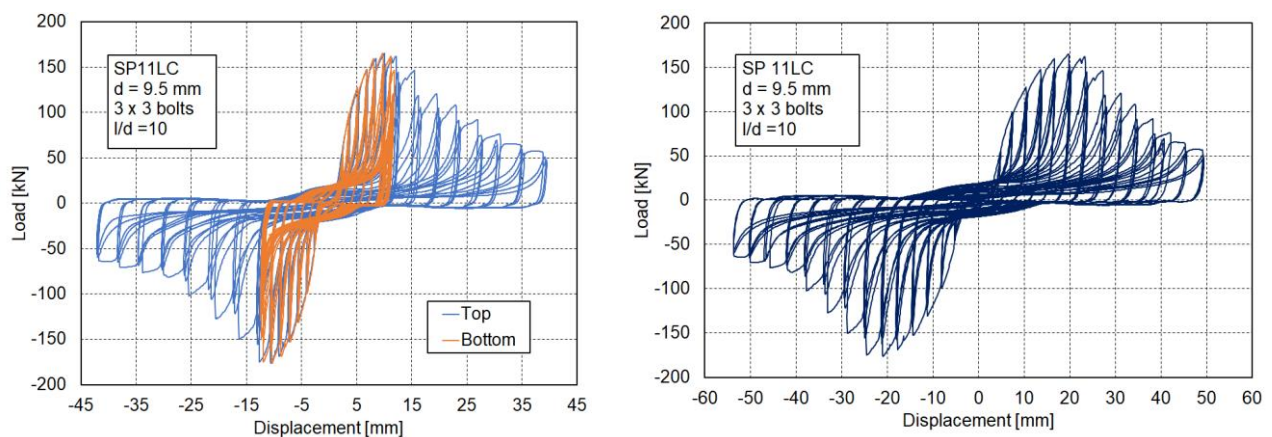


Figure 4. Typical hysteretic curves of the top and the bottom connection of a brace in Spruce Pine: specimen SP11LC (left); Combined hysteretic curve of both connections of the same specimen (right).

The connection that experienced larger displacements was the one where the bolts experienced more significant bending followed by rupture of some bolts and then partial wood splitting. As the testing progressed to large deformation levels, the splitting length increased that caused more bolts to fail. Because of the large deformations, significant splitting of the braces was observed at the end of the testing (Figure 5 left). Such significant splitting would have not been observed if the testing was stopped at a level when the load dropped to 80% of the maximum load. The bolts showed significant bending deformations with pronounced necking. This was followed by bolt rupture in one or two places (Figure 5 right).



Figure 5. Typical wood crushing followed by splitting of a typical brace with non-reinforced connections (left) (15  $d_F=9.5\text{mm}$  bolts;  $S_p=9.4d_F$ ); Bolt rupture in the shank near the head (right).

Bolted connections reinforced with STS were able to sustain significantly larger proportion of the maximum load at higher deformation levels, thus significantly improving the connection (brace) performance (Figure 6 right). Also, splitting failure mode was completely eliminated in all reinforced connections. The failure mode consisted of a combination of wood crushing with bolt deformation and finally a bolt rupture.

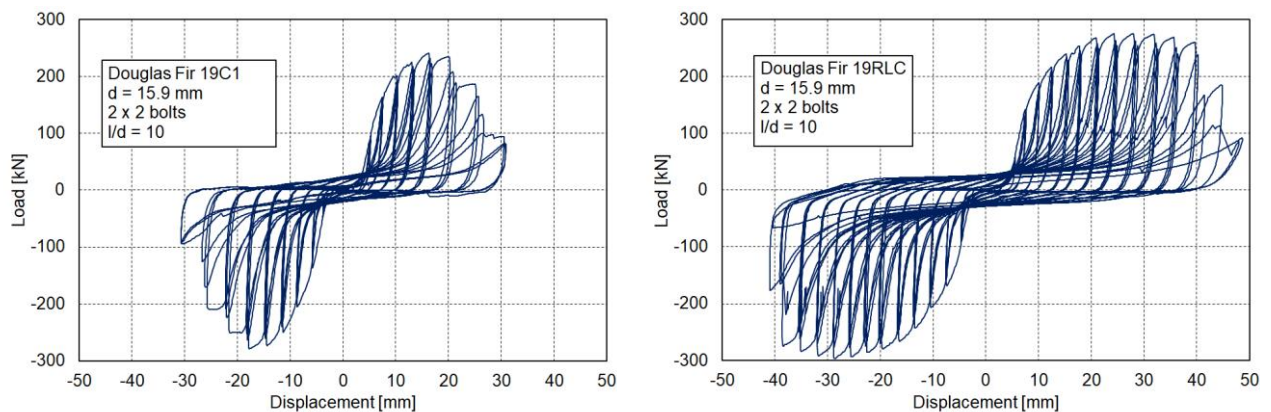


Figure 6. Typical hysteretic behaviour of a brace in D-fir with non-reinforced connections (left); Typical behaviour of the same brace with reinforced connections (right).

Use of reinforcement also allowed for deformations to be much better balanced between the top and the bottom connection. While there was still difference between the maximum deformation in the top and the bottom connection (Figure 7), it was much smaller than in the case of non-reinforced connections (Figure 4 left). Because



of their improved performance characteristics, bolted connections reinforced with STS were used in the numerical part of the study presented in Section 6.

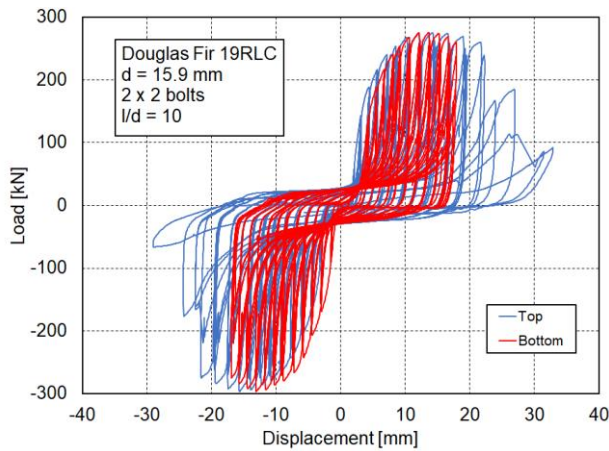


Figure 7. Typical hysteretic curves of the top and the bottom reinforced connection of a brace in D-fir specimen 19RLC.

## 5 Draft design guidelines for braced frames

To quantify the  $R_d$ -factors for seismic design of BTFs, a series of building archetypes were designed and subjected to a series of incremental dynamic analyses using representative ground motions. Draft seismic design provisions were developed for design of these archetypes. The final design rules can be modified later based on the findings from the analyses and the input from the CSAO86 Technical Committee. This section covers the main aspects of the draft design provisions.

### 5.1 General design

CBTFs should have all members triangularly connected with the diagonal braces been within  $30^\circ$  to  $60^\circ$  from the horizontal beam (strut). Diagonal braces inclined at  $45^\circ$  or smaller are recommended, as in most cases this provides more efficient system compared to other arrangements. Narrower frames with steeply inclined braces have lower stiffness and are more sensitive to bending-type deformations. They also develop larger overturning forces that are taken by the columns and the anchoring connections. Wider braced frames (with smaller brace angle) on the other hand provide stiffer system with lower overturning forces and result in more shear-type response under lateral loads. It is sometimes convenient to use several braced bays rather than a single bay frames to reduce the overturning demands (Chen & Popovski, 2021). It is the most efficient to place the frames at the perimeter of the building to provide large box effect and torsional resistance. Frames should be arranged symmetrically in the floor plan, to lower the effects of the of torsional moments.

Depending on the design, the CBTFs as a SFRS can also be designed to be part of the Gravity Load Resisting System (GLRS). Whether or not a BTF belongs to the GLRS will affect the design of the frame elements. If the CBTF is not part of the GLRS, the

components and connections of the CBTF can be designed based on the corresponding internal forces developed from the lateral loads; else, the components and connections should be designed based on the internal forces induced by gravity and lateral loads combined. The effects of the deformed geometry of the structure (second order effects) need to be considered if the deformations during the response significantly increase the forces in the structure, or if the deformations significantly modify the structural behaviour. Where second order effects are significant and need to be included, the most common method used during the design is by amplification of a first order elastic analysis using the initial geometry of the structure.

## 5.2 Seismic design considerations

CBTFs should be designed according to the capacity-based design provisions. Inelastic deformations and energy dissipation should only occur in the connections between the diagonal braces and the rest of the frame (called brace connections). Brace connections should be the only dissipative connections in the system and should be able to yield by combination of wood crushing and fastener yielding. All other connections should be designed as non-dissipative ones. Dissipative connections should possess sufficient deformation capacity to allow the frame to attain its target lateral deflection. A sufficient gap should be left between the end of the diagonal brace and the rest of the frame to ensure that the brace connection is able to develop the deformation needed. To ensure ductile behaviour, the lowest brittle failure mode resistance of the brace connections should be at least 60% higher than that of their governing yielding failure mode. In addition, moderately ductile dissipative connections should have their resistance of the most ductile modes (d) or (g) be at least 30% lower than that of the other less ductile failure modes. Finally, dissipative connections should be designed not to buckle in-plane or out-of-plane.

Non-dissipative connections should be designed to resist the force and displacement demands that are induced in them when the brace connections reach the 95<sup>th</sup> percentile of their ultimate resistance, or their target displacement. Based on the fastener type used, this can be achieved by designing the connections with an overstrength factor in the range of 1.6 to 2.0. Similarly, frame members (columns, diagonal braces, and beams) should be designed for seismic forces that are developed when ductile brace connections reach the 95<sup>th</sup> percentile of their ultimate resistance. This can also be considered to be achieved if they are designed using an overstrength factor in the range of 1.6 to 2.0. Columns should be designed to be continuous along the entire height of the frame with adequate strength and stiffness to spread the yielding in all brace connections along the height of the frame. This can be achieved by using either the so-called “column tree design method” proposed by Goel and Chao (2008) for steel structures or the worst soft-storey scenario with the removal of a diagonal brace (Chen et al., 2023).

According to the column tree design method (Figure 8), each of the columns is designed as a self-standing structure. The lateral forces on each storey of the columns

are defined as  $C_i F_L$  for the left column, and  $C_i F_R$  for the right column, for each storey  $i$ . The  $C_i$  coefficients are related to the distribution of the seismic forces along the height of the building determined either using the equivalent static force procedure or the response spectrum analysis. For example, if the equivalent static procedure was used for the example shown in Figure 8, the inverse triangular distribution will define the values for the coefficients as:  $C_1=0.334$ ,  $C_2=0.667$ , and  $C_3 = 1.0$ . The Forces  $P_i$  on the columns are the forces that are obtained from the static analysis of the braced frame subjected to the design lateral loads. Using moment equilibrium about the bottom of each column, the force  $F_L$  acting on the left column and the force  $F_R$  on the right one can be determined. The columns are then designed to withstand the forces that act on them. Preliminary non-linear dynamic analyses have shown that this method results in column sizes that are able to adequately transfer the forces along the height of the structure and prevent soft storey mechanism from occurring.

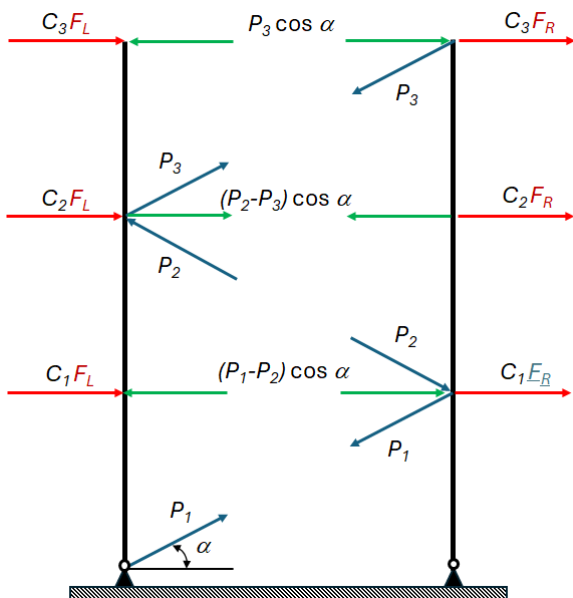


Figure 8. Forces on the left and the right column of a typical braced frame according to the column tree design

Splice connections in the columns should be designed as non-dissipative connections with adequate strength and stiffness. Splices should be placed on the columns where bending moments are at their minimum. Reduction of column cross section along the height is allowed according to the design and stiffness requirements. Columns should not buckle either in-plane or out-of-plane. All members of the frame should be designed to be concentric to avoid development of bending moments in the connections between the braces and the rest of the frame and between the beams and the columns. Influence of the brace rotation on the performance of the brace connections should be minimized. Connections anchoring the frame to the foundation should be designed and detailed as pinned to allow for the column rotation.

## 6 Design and analysis tools for the archetypes

A new module was developed in Altair S-TIMBER computer program in collaboration with Altair staff, to automatize the seismic design of different BTF archetype buildings that will need to be analysed. The module consists of three main parts, and they are shown in Figure 9. The output of the module was detailed information of the designed archetypes that can be used for development of the non-linear models of BTF archetypes that were used for seismic evaluation.

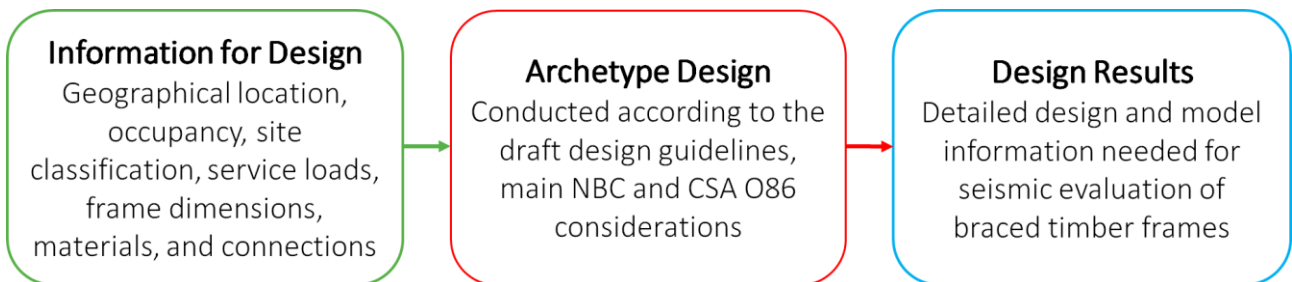


Figure 9. Main parts of the developed seismic design module for BTFs in Altair S-Timber.

The seismic behaviour of BTFs was evaluated using the OpenSees computer software (McKenna et al. 2010). The non-linear properties of the connections were modelled using the Pinching4 model. This model (Figure 10 left) has 39 different parameters that define the connection performance. Parameters for this model for various connections were derived by fitting the hysteresis loops obtained from the cyclic tests. Example of the modelled behaviour vs. the behaviour obtained from testing for a typical brace is shown in Figure 10 right.

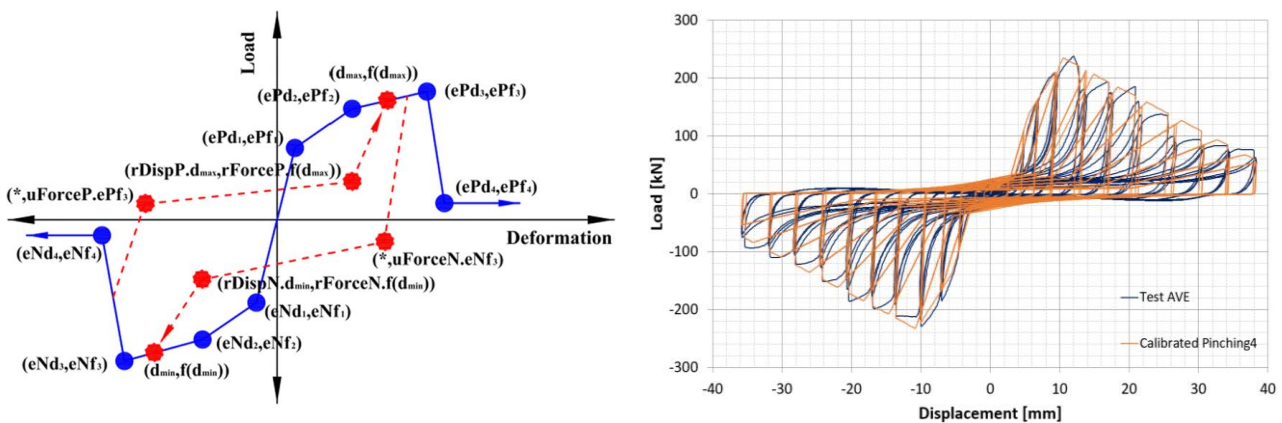


Figure 10. The Pinching4 model in OpenSees used for modeling of the braces (left); Use of the model to predict a hysteretic response of a tested brace with bolted connections (right).

In addition, connection model updating rules were developed. The updating rules established the relationship between the model parameters and some of the most important connection properties such as the material of the brace, number and diameter of the bolts used, different bolt slenderness ratios, connections with and without STS reinforcement, etc. The developed updating rules were then used for development of the nonlinear braced timber frame models in OpenSees to investigate the seismic response of BTFs.

The seismic response of the BTFs with different connections and different  $R_d$ -factors was evaluated using a series of incremental dynamic analyses (IDAs) with different earthquake motions. Three locations for the building archetypes were chosen for this study: Vancouver, BC, Victoria, BC, and Montreal, QC. These three locations represent large part of the spectrum of seismic hazards across Canada. A set of eleven ground motions for Vancouver and Victoria were developed for each of the crustal, subcrustal and subduction earthquakes, for a total of 33 records per location. One set of eleven ground motions was also developed for Montreal. A new engine was developed in MATLAB (MathWorks Inc. 2024), to automatize the modelling and non-linear dynamic analyses of different archetypes (Figure 11).

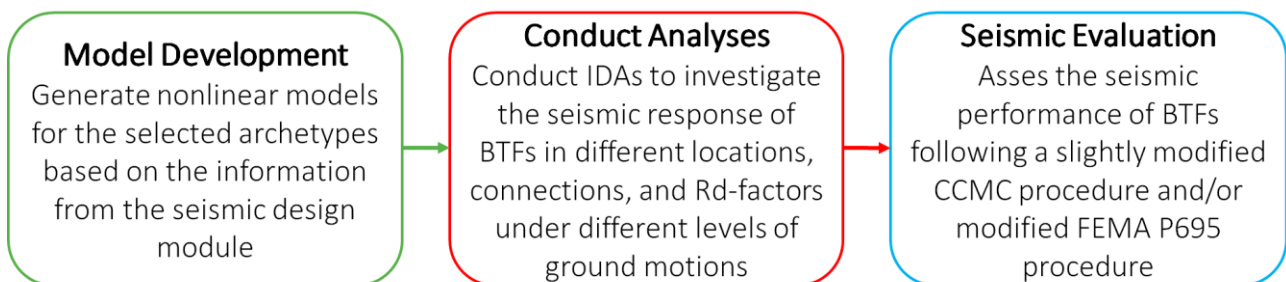


Figure 11. Main parts of the engine developed for seismic evaluation of various BTF archetypes.

## 7 Acceptable $R_d$ -factors for selected BTFs in Montreal

To determine the suitable  $R_d$  factors for seismic design of selected BTFs, a series of building archetypes were designed and analysed using the design and analysis tools developed in Section 6. This section covers some of the main aspects related to the design and analysis of BTFs that use brace connections with steel side plates and 15.9mm bolts (15.9mm bolted connections) located in Montreal. Results presented in this section should still be treated as preliminary. Analyses and results for BTFs with different connections and in other locations will be presented in the future.

### 7.1 Design archetypes and numerical models

A total of 34 multi-storey commercial building archetypes with various number of storeys, aspect ratios of the brace tiers, and  $R_d$  factors were designed for the seismic assessment of BTFs (Table 1). Twelve archetypes with different number of storeys and tier aspect ratios (height/width) were designed with an  $R_d$  factor of 1.5, while 22 archetypes with different number of storeys and a tier aspect ratio of 1:1, were designed with different  $R_d$  factors, from 2.0 to 4.5.



Table 1. Archetype matrix for BTFs with 15.9mm bolted connections reinforced with STS in terms of the tier aspect ratio, number of storeys, and  $R_d$  factors.

No. of storeys	$R_d$ factor								
	1.5	2.0	2.5	3.0	3.5	4.0	4.5		
2	2:3	1:1	3:2	1:1	1:1	1:1	1:1	N/A	N/A
4	2:3	1:1	3:2	1:1	1:1	1:1	1:1	1:1	1:1
5	2:3	1:1	3:2	1:1	1:1	1:1	1:1	1:1	1:1
7	2:3	1:1	3:2	1:1	1:1	1:1	1:1	1:1	1:1

All building archetypes were assumed to have an identical floor plan with a length of 31.2 m, width of 18.0 m, and a storey height of 3 m. The SFRS consisted of nine (9) BTFs with bolted connections in each direction. All archetypes were located in Montreal (City Hall area) on a Site Class D ( $V_{s30} = 290$  m/s). According to NBC 2020, the design spectral accelerations at different periods are:  $S_a(0.2) = 0.744$ ,  $S_a(0.5) = 0.542$ ,  $S_a(1.0) = 0.294$ ,  $S_a(2.0) = 0.134$ ,  $S_a(5.0) = 0.035$ . The 1-in-50-year ground snow load and associated rain load were taken as 2.6 kPa and 0.4 kPa, respectively. The dead loads on the roof and the floor were 1.4 kPa and 2.4 kPa, respectively, while the live load was 4.8 kPa for the floor and 1.0 kPa for the roof. Partition wall load of 0.4 kPa was also considered. The archetypes were designed automatically using the developed module in S-TIMBER, following the draft design guidelines proposed in Section 5. Douglas Fir 16c-E Glulam and 15.9 mm bolted connections were used for the design of all archetypes.

Since all BTFs in one single building were identical and placed symmetrically in the floor plan, a two-dimensional modelling approach (Chen et al., 2022) was adopted in this study. All archetypes were modelled and analysed using OpenSees. Figure 12 (left) shows the model of a four-storey BTF archetype. Columns were assumed to be continuous elements from the top to the bottom and were modelled using elastic beam-column elements. Elastic truss elements were used for the beams and diagonal braces, which were connected to the columns using semi-pin connections. Connections on both ends of diagonal braces were simulated using one zero-length Pinching4 element, which was added to one end of the brace. The columns were connected to the ground using pin connections. The MOE of glulam members was 12400 MPa according to CSA O86. The brace connections in 34 archetypes were modelled with the hysteresis loops of 15.9 mm bolted connections reinforced with STSs (see Section 4). As expected, the fundamental periods of the models were slightly different than those obtained using the NBC formula. For example, the code formula gives a period of  $T_a = 0.3s$  for a four-storey braced frame, while periods of 0.34s, 0.41s, and 0.47s were obtained from the models of braced frames with aspect ratios of 2:3, 1:1, and 3:2, respectively.

To investigate the influence of STS reinforcement on the  $R_d$  factor, 26 of the 34 archetypes were remodelled with the hysteresis loops of the 15.9 mm bolted connections without reinforcement. Only 1:1 aspect ratio from Table 1 was considered for

these additional models. Therefore, results from analyses on a total of 60 models are presented here. Eleven (11) ground motions were selected and scaled for analysis of the design archetypes according to NBC of Canada (NRC, 2022). The scaled spectra of selected ground motions are plotted in Figure 12 right, along with the design uniform hazard spectrum (UHS) for Montreal.

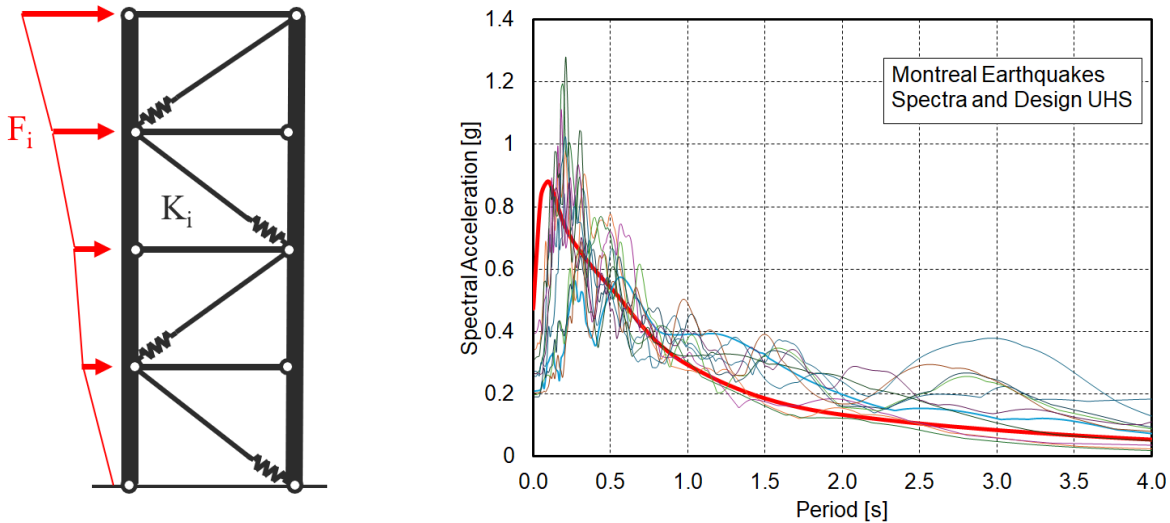


Figure 12. Schematics of a four-storey braced timber frame model (left); Spectral acceleration of the selected Ground Motions for 2%/50 years hazard level scaled between 0.2 and 1.5s.

## 7.2 Main results and discussion

The seismic response of BTFs was investigated by conducting incremental dynamics analyses (IDAs) in OpenSees. The 60 models were analysed under 11 motions at different intensity levels, from 0.5 to 3 times the design  $S_a$ . Maximum inter-storey drifts (ISDs) obtained from the analyses were considered as primary seismic performance indicator. Figures 13 (top) and bottom left show the maximum ISDs of four-storey archetypes with different tier aspect ratios at different  $S_a$  levels for the selected 11 motions, while Figure 13 (bottom right) shows the ISD curves for a seven-storey archetype with 1:1 tier aspect ratio. As expected, the ISDs increased with an increase in the intensity level and the aspect ratio. By comparing Figure 13 (top right) and (bottom right), the four- and seven-storey archetypes with the same tier aspect ratio of 1:1, it can be noticed that the ISDs decreased with an increase of number of storeys. Although this is a contra intuitive finding, it can be attributed to the predominant period of the motions with respect to the period of the building. Also, in many cases low-rise, short-period, buildings tend to have higher probability of failure when analysed numerically, while no such performance is observed during real earthquakes. This phenomenon is called “short period paradox” and is covered in detail in FEMA P-2139 documents (ATC 2020).

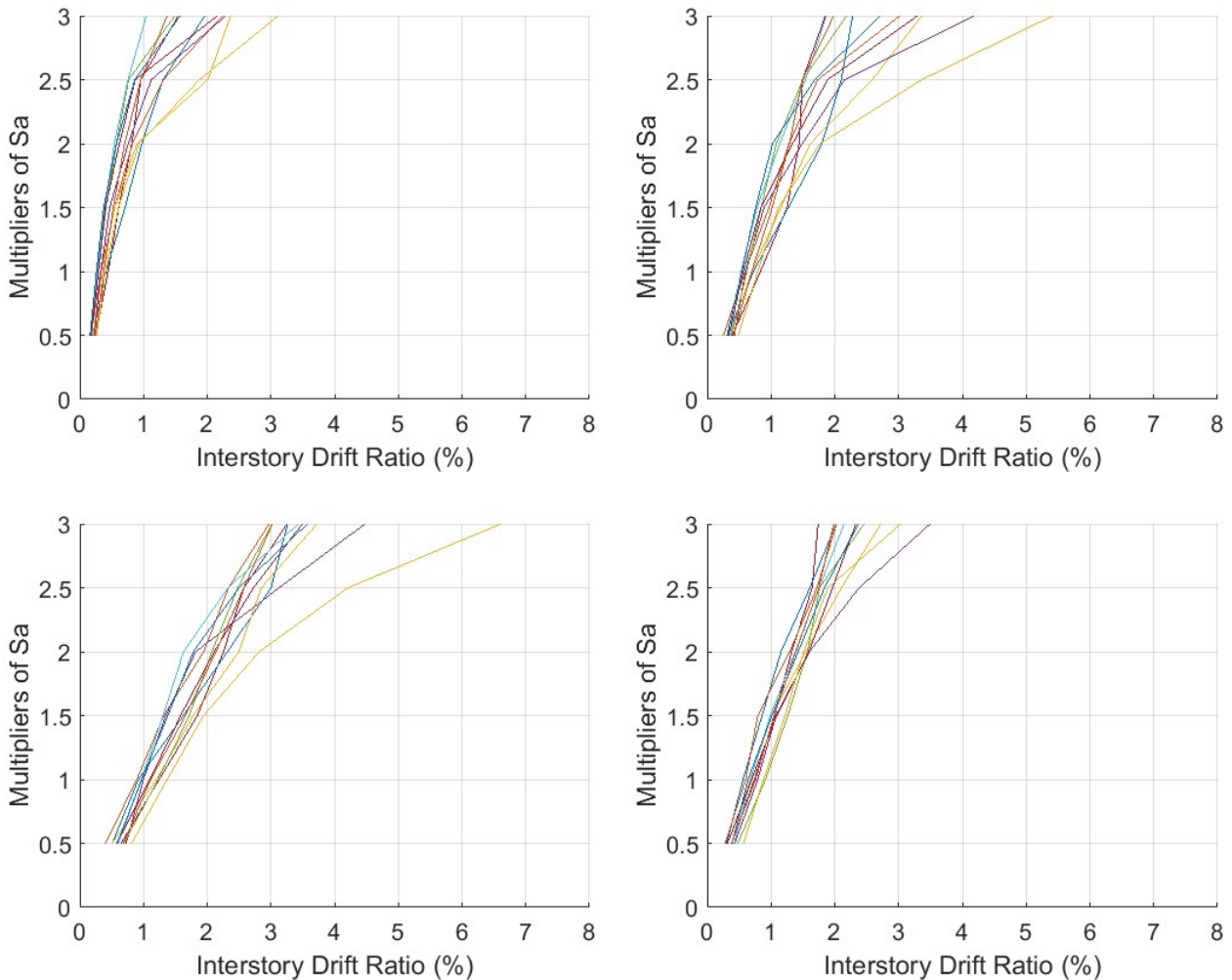


Figure 13. Maximum ISDs in 4-storey archetypes with different aspect ratios: 2:3 (top left), 1:1 (top right), and 3:2 (bottom left). ISDs in a 7-storey model with a tier aspect ratio of 1:1 (bottom right).

The CCMC guide (De Vall et al., 2022), is a much-simplified version of FEMA P-695 (ATC 2009), that was developed in Canada to assess the seismic performance of different building archetypes and determine the appropriate  $R_d$  factors. The Guide requires that ISDs under earthquake motions scaled to 100% of the UHS per NBC, should not exceed the 2.5% limit. For response to ground motions scaled at 200% of UHS, the absolute value of the maximum ISDs from the suite of analyses should not exceed 4.5% for more than 50% of the motions. Due to the stiff characteristics of BTFs their collapse occurs at a much lower ISD than 4.5%. The ISD limits differ depending on the connection deformability and the geometry of the tier (Chen et al., 2019). Table 2 lists the ISD limit criteria for BTFs with bolted connections and different aspect ratios that were used in the study, along with the necessary parameters for deriving the criteria. The seismic performance of BTFs with an aspect ratio of 2:3, 1:1, and 3:2 was evaluated using 1.0% (50% of 2.0%), 1.18% (50% of 2.36%), and 1.5% (50% of 3.0%) drift limit at 100% of UHS, respectively, while at 200% UHS the drift limits were 2.0%, 2.36%, and 3.0%.

Table 2. Inter-storey drift limit criteria at 200% of UHS used in the study.

Aspect Ratio	Storey Height [m]	Tier Width [m]	Brace Angle [°]	Connection Deformation Limit [mm]	Inter-storey Deformation Limit [mm]	ISD Limit at 200% UHS [%]
2:3	3	4.5	33.7	50	60.1	2.0
1:1	3	3	45.0	50	70.7	2.36
3:2	3	2	56.3	50	90.1	3.0

The ISDs of all analysed archetypes at 100% of UHS met their evaluation criteria. The probability of collapse of all archetypes at different levels of motions was then analysed to check if the second CCMC evaluation criterion was met. If the probability of collapse at 200% of UHS (i.e., 2Sa) is lower than 0.5, then the analysed archetype meets the 2<sup>nd</sup> criterion. Examples of some of the obtained probabilities of failure curves are shown in Figure 14. Figure 14 (left) shows the probability of collapse of a four-storey archetype with a tier aspect ratio of 1:1 using 15.9 mm bolted connections reinforced with STS and designed with  $R_d = 3.5$ . Figure 14 (right) shows the probability of failure of an archetype without STS reinforcement designed with  $R_d = 2.0$ .

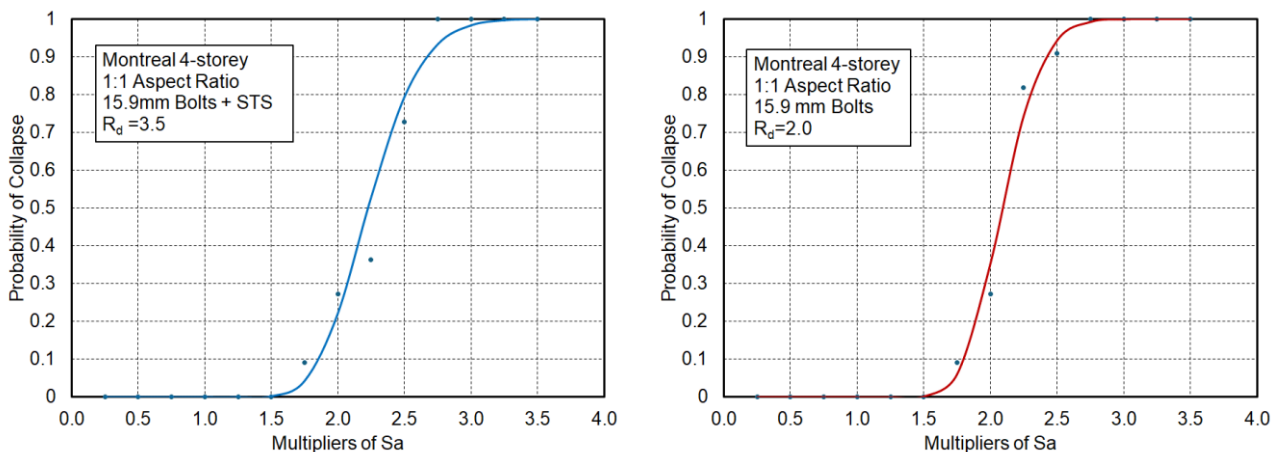


Figure 14. Probability of collapse for 4-storey models with 1:1 aspect ratio using 15.9 mm bolts + STS reinforcement designed with  $R_d = 3.5$  (left), and without reinforcement designed with  $R_d = 2.0$  (right).

Table 3 shows the acceptable  $R_d$  factors for the analysed BTF models with different number of storeys and a tier aspect ratio of 1:1 obtained from this study. The  $R_d$  factors in Montreal were governed by the archetypes with a lower building height. An  $R_d$  factor of 1.5 and 1.0 can be assigned to two-storey BTFs with 15.9mm bolted connections with and without STS reinforcement, respectively. If the BTFs have four storeys or more, an  $R_d$  factor of 3.5 and 2.0 can be used for frames with and without connection reinforcement. Since the ISD increases with an increase in the tier aspect ratio, the  $R_d$  factor is expected to decrease. Consequently, Table 3 indicates that higher  $R_d$  factors for BTFs with a lower aspect ratio (wider frames) are expected (not analysed), while lower  $R_d$  factors are expected for BTFs with a larger aspect ratio (narrower frames).

Table 3. Acceptable  $R_d$  factors for BTFs located in Montreal with 15.9 bolted connections.

# of Storey	Reinforced with STS			Without Reinforcement
	Aspect Ratio			Aspect Ratio
	2:3	1:1	3:2	1:1
2	$\geq 1.5$	1.5	$< 1.5$	1.0
4	$\geq 3.5$	3.5	$< 3.5$	2.0
5	$\geq 4.0$	4.0	$< 4.0$	2.5
7	$\geq 4.0$	4.0	$< 4.0$	2.0

## 8 Conclusions

FPIinnovations is leading a multi-year research project to study the seismic performance of BTFs as SFRSs and generate the technical information needed for the development of design guidelines for this system. Part of the guidelines should provide answers to the question which connections can provide moderately ductile ( $R_d = 2.0$ ) or limited ductility ( $R_d = 1.5$ ) seismic performance specified in NBC.

To evaluate the performance of Spruce Pine and D-fir glulam braces with bolted connections, a series of 68 tests were conducted. Bolted connections with steel side plates had different number of rows and columns (2x2, 3x3, 2x4, 3x5). They used 9.5 mm (3/8"), 12.7 mm (1/2"), or 15.9 mm (5/8") diameter bolts, with slenderness ratios of 7.5, 8.0, and 10.0, respectively. Different deformation levels were observed between the top and the bottom connection in all braces tested. Although all bolted connections were designed to fail in yielding mode (g), splitting of the wood eventually occurred at very high deformation levels. Connection reinforcement consisting of two STS placed between bolt rows and at the end of the connection was able to prevent the splitting entirely, thus allowing for higher portion of the load to be carried at higher deformation levels. Use of reinforcement also allowed for deformations to be much better balanced between the top and the bottom brace connection during the response. Since use of STS for reinforcement purposes is not currently codified in CSAO86, the design of the STS was conducted using a simplified methodology.

To quantify the preliminary  $R_d$ -factors for seismic design of BTFs with 15.9 mm bolted connections (slenderness of 10.0) with and without reinforcement in Eastern Canada, a series of 34 different BTF building archetypes were designed. The seismic response was evaluated using a series of incremental dynamic analyses (IDAs) using OpenSees under a suite of eleven earthquake motions developed for Montreal City Hall as a location. Draft seismic design provisions were developed for designing of these archetypes. Also, a new module was developed in Altair S-TIMBER computer program in collaboration with Altair staff, to automatize the seismic design of the archetypes. In addition, a new engine was developed in MATLAB to automatize the modelling and non-linear dynamic analyses of the archetypes.

It was found that the  $R_d$  factors for the analysed buildings in Montreal were governed by the archetypes with a lower building height. An  $R_d$  factor of 1.5 and 1.0 can be preliminary assigned to two-storey BTFs with 15.9mm bolted connections, with and without STS reinforcement, respectively. If the BTF buildings have four storeys or more,  $R_d$  factors of 3.5 and 2.0 can be used for frames with an aspect ratio of 1:1. Although higher acceptable  $R_d$ -factors for taller buildings is contra intuitive finding, this can be attributed to the predominant period of the motions been close to the fundamental period of the building. Since the ISDs increase with an increase in the tier aspect ratio, the  $R_d$  factors are expected to decrease. Consequently, higher  $R_d$  factors are expected for BTFs with a lower aspect ratio (wider frames), while lower  $R_d$  factors are expected for BTFs with a larger aspect ratio (narrower frames).

Additional analyses are needed to determine the  $R_d$ -factors for braced frames with different bolt diameters in Montreal. Also, additional series of analyses are needed for locations such as Vancouver and Victoria, that have the highest seismic hazard in the country. Results from these analyses as well as analysis with other bolted connections will be presented in the future.

## 9 References

- Applied Technology Council (ATC) (2009): Quantification of building seismic performance factors. ATC-63/FEMA P-695 Project Report, Redwood City, CA.
- ASTM (2019): Standard test methods for cyclic (reversed) load test for shear resistance of vertical elements of the lateral force resisting systems for buildings. ASTM E2126, West Conshohocken, PA.
- ATC (2020): Applied Technology Council ATC/FEMA P-2139 series on Short-Period Building Collapse Performance and Recommendations for Improving Seismic Design. Redwood City, CA.
- Buchanan, A. H., Deam, B. L., Dean, J. A., & Moss, P. J. (1989): Multi-storey timber buildings. In: Proceedings of Workshop on Structural Behaviour of Timber structures. Florence, Italy.
- Chen, Z., & Popovski M. (2021): Preliminary Structural Design Guidelines for Braced Timber Frames. FPInnovations Report. Vancouver, BC, Canada.
- Chen, Z., and Popovski, M. (2020): Connection and System Ductility Relationship for Braced Timber Frames. ASCE Journal of Structural Engineering. 146(12): 04020257.
- Chen, Z., and Popovski, M. (2021): Seismic Response of Braced Heavy Timber Frames with Riveted Connections. Journal of Performance of Constructed Facilities, volume 35, Issue 5.
- Chen, Z., Popovski M., & Tung, D. (2023): Expanding Wood Use Towards 2025: Seismic Performance of Braced Mass Timber Frames – Year 4. FPInnovations Report. Vancouver, BC, Canada.

- Chen, Z., Popovski, M., and Symons, P. (2019): Seismic Performance of Braced Mass Timber Frames Year 1. FPI Report Project 301013067. Vancouver, BC, Canada.
- Chen, Z., Tung, D., & Karacabeyli, E. (2022). Modelling Guide for Timber Structures. FPIInnovations Special Publication SP-544, Point-Claire, Canada.
- CSA (2024): CSA O86 2024 Engineering Design in Wood. Canadian Standards Association. Toronto, ON, Canada.
- De Vall, R., Popovski, M., McFadden, J. and Yang, T. (2022): Evaluation of Seismic Force Resisting Systems and Their Force Modification Factors for Use in the National Building Code of Canada with Concepts Illustrated using a Cantilevered Wood CLT Shear Wall Example. Canadian Construction Materials Centre (CCMC).
- Fazileh, F., Fathi-Fazl, R. & Huang, X. (2023): Performance-based unified procedure for determination of seismic force modification factors  $R_d$ ,  $R_o$  in NBC. National Research Council of Canada, Ottawa.
- MathWorks Inc. (2024): MATLAB version: R2024a, Natick, Massachusetts: The MathWorks Inc.
- McKenna, F., Scott, M. H., & Fenves, G. L. (2010): Nonlinear finite-element analysis software architecture using object composition. *Journal of Computing in Civil Engineering*, 24(1):95-107.
- NRC (2022): 2020 National Building Code of Canada. Canadian Commission on Building and Fire Codes and National Research Council of Canada, Ottawa, Canada.
- Popovski, M. & Karacabeyli, K. (2008): Force modification factors and capacity design procedures for braced timber frames. Proc. 14<sup>th</sup> WCEE, Beijing, China.
- Popovski, M. (2000): Seismic performance of braced timber frames. Ph.D. Dissertation, Department of Civil Engineering, University of British Columbia, Vancouver.
- Popovski, M., and Karacabeyli, E. (2004): Seismic performance of riveted connections in heavy timber construction. Proc. 13<sup>th</sup> WCEE, Vancouver, Canada.
- Popovski, M., Ni, C., Chen, Z., Lum, C., Cheng, V., and Tung, D. (2024): Expanding Wood Use Towards 2025 - Seismic Performance of Braced Mass Timber Frames Year 5. FPI Report Project 301015758. Vancouver, BC, Canada.
- Popovski, M., Prion, H., & Karacabeyli, E. (2003): Shake table tests on single-storey braced timber frames. *Can. J. Civ. Eng.*, 30: 1089-1100.
- Popovski, M., Prion, H., and Karacabeyli, E. (2002): Seismic performance of connections in heavy timber construction. *Can. J. Civ. Eng.*, 29: 389-399.
- Yasumura, M. (1990): Seismic behaviour of braced frames in timber construction. Proc., 23<sup>rd</sup> Meeting of the CIB W18, Karlsruhe, Germany.

## DISCUSSION

**The paper was presented by M Popovski**

*F Lam received confirmation that the GLT brace was C grade columns per recommendations of designers participating in the project. F Lam also received confirmation that the observed brittle failure occurred at high deformation after yielding of the fasteners.*

*P Dietsch asked as positive effects of reinforcement were observed why not make the reinforcements a requirement. M Popovski responded that yes this will be considered. T Tannert said Canadian standards do not provide design guidance on reinforcements but this needs to be developed. M Popovski responded that they will work on this.*

*M Fragiacommo commented on the 30% difference between ductile and non ductile cases. He questioned the Q factors for the unreinforced connections. M Popovski will coordinate for procedures for the reinforced connections.*

*A Ceccotti asked why use ASTM standards for cyclic testing. M Popovski said that ASTM standard B is related to the European approach. A Ceccotti asked how collapse was decided. M Popovski said that European approach consider 80% post peak load; however, in this study a lower load was considered.*

*G Doudak and M Popovski discussed Q factor in Eurocode versus RdRo in Canadian code. In this study Rd was referenced. They also discussed using larger spacing and end distances for seismic to guard against splitting failures. M Popovski reaffirmed that the splitting was caused by large deformations. M Popovski also confirmed that that building period calculated from code equations were compared with period of archetype but yielded little difference.*

*O Sisman commented that dowels will fail less.*

*H Blass commented that information on the reinforcement cases is given in ETAs and received clarification that the moisture content of the connections were 11.8 to 14.5%. He discussed moisture content of GLT in practice with higher moisture contents more issues with reinforcement could arise.*

*C Binck received clarification of the periods of the four and seven stories buildings.*





# Investigation on the performance of platform-type coupled-panel CLT shear walls under seismic conditions

Jianan Chen, Dept. of Wood Science, University of British Columbia, Canada

Frank Lam, Dept. of Wood Science, University of British Columbia, Canada

Minghao Li, Dept. of Wood Science, University of British Columbia, Canada

Marjan Popovski, FPInnovations, Canada

Keywords: CLT shear walls, Overstrength, Capacity protection factor, Seismic performance, Coupled-panel, yield hierarchy

## 1 Introduction

There are two general construction typologies of Cross-Laminated Timber (CLT) shear walls: platform-type and balloon-frame construction. In areas under Seismic Category (SC) 4 in Canada, such as Vancouver and Victoria, platform-type mass timber walls as seismic force resisting system (SFRS) are limited to 20 m in height, while the height limit is 30 m in other seismic categories. Within platform-type construction, the coupled-panel shear wall refers to the shear wall consisting of two or more panels. Each CLT wall was connected to the foundation or the floor diaphragm using two hold-downs and a certain number of angle brackets (Sun et al., 2019). Basically, two kinds of kinematic modes for a coupled-panel CLT shear wall can be achieved depending on the mechanical properties of connections and applied loads, as shown in Figure 1.1. The preferred kinematic modes of a coupled-panel CLT shear wall is called coupled-panel (CP) mode (Casagrande et al., 2019) in which each wall panel rocks around its own pivot point (Figure 1.1 (a)). Previous experimental investigations of the behaviour of CLT shear walls have revealed that CLT wall panels exhibit rigid body motion, due to their high in-plane rigidity, while non-linearity is mainly achieved in the connections (Masroor, 2023).

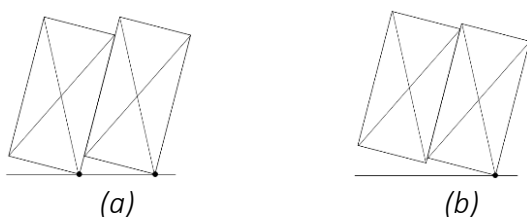


Figure 1.1. Coupled-panel CLT shear wall kinematic modes: (a) Coupled-panel mode; (b) Single-wall mode

To ensure rocking behaviour and satisfy the target ductility factor  $R_d$  and the over-strength factor  $R_o$  specified in the National Building Code of Canada (NRC, 2021), reasonable yielding hierarchy should be established based on the concept of capacity-based design (CBD). Three overstrength factors for connections are adopted in the process of CBD, as stated in the Canadian Standard for Engineering Design in Wood CSA O86 (Casagrande et al., 2021; CSA, 2024). The three overstrength factors are related to 15<sup>th</sup>, 30<sup>th</sup>, and 95<sup>th</sup> percentile of the peak resistance of one connection in vertical joint, respectively (More details in Section 3.1). According to O86, hold-downs are allowed to yield but after all the vertical joints have already yielded. At the same time, the wall strength is established at the point when the hold-down yields. A rational capacity protection factor for the design of hold-downs and other elements that need to be capacity-protected should be defined to satisfy the NBCC target of  $R_d = 2.0$  and  $R_d = 1.5$  for moderately ductile CLT shear walls.

This paper presents the evidence of cyclic performance of coupled-panel CLT shear walls, following the CBD procedure. Challenges of yield hierarchy and the influence of the capacity protection factors for hold-downs on the performance of the coupled-panel CLT shear walls are also discussed.

## 2 Experimental results of connections

### 2.1 Connection details

In this study, the experimental results of four types of CLT connections, previously tested at the University of British Columbia and the University of Canterbury, are selected for benchmark shear wall. Numerical models for these connections and structures are subsequently developed. The connection details are provided in Table 1 and Figure 2.1, where  $F_{exp}$  denotes the average of the peak load. The replicates of SP, N-HD, H-HD, and AB are 10, 15, 4, and 10, respectively. The experimental results are assumed to follow a normal distribution.

Table 1. Testing Results for connections

Connectors	Material details	$F_{exp}$ (kN)	COV (%)
Vertical spline joints (SP) (UBC, 2023)	19 mm (3/4 in) Douglas fir plywood connected to the CLT by washer head $\varnothing$ 6 mm self-tapping wood screws with a thread length of 50 mm and a total length of 80 mm (SWG 6x80/50 ASSY 4 SK screws Washer Head – RW 40)	18.4	9
Normal hold-downs (N-HD) (UBC, 2023)	Steel Plate: Simpson Strong-Tie HTT5 Nails: 76 mm common nail, 10D, 3.76 mm in diameter	20.3	11
High-stiffness hold-downs (H-HD) (Wright et al., 2023)	Inclined 45° Screws: twelve 12 × 260 partially threaded 90° Screws: eighteen 12 × 180 partially threaded	470	6.83
Angle brackets (AB) (UBC, 2023)	Steel Plate: Simpson Strong-Tie AE116-R Nails: 76 mm common nail, 10D, 3.76 mm in diameter	19.7	11

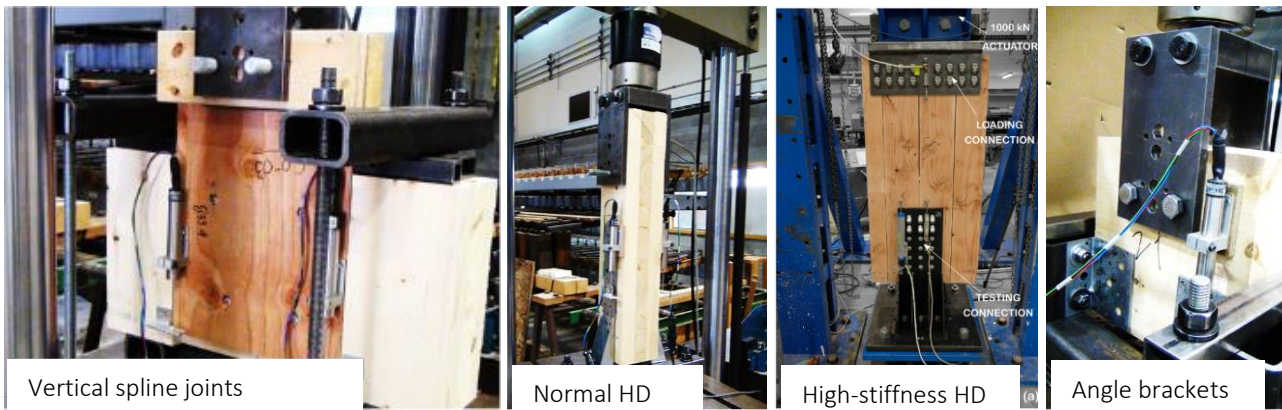


Figure 2.1. Tests of vertical splines, hold-down connections and angle brackets

Parameters calibrated of one representative results of each type of connection using the Equivalent Energy Elastic-Plastic (EEEP) method (ASTM E2126, 2019) are listed in Table 2 for future reference.

Table 2. EEEP method calibration

	SP	N-HD	H-HD	AB
Elastic stiffness $K_e$ (kN/mm)	3.15	2.76	335.46	1.36
$\Delta_{yield}$ (mm)	4.51	8.31	1.44	12.78
$P_{yield}$ (kN)	14.2	23.0	483.37	17.38
$\Delta_{peak}$ (mm)	17.78	11.61	26.67	18.62
$P_{peak}$ (kN)	18.53	24.86	559.80	20.27
$\Delta_u$ (mm)	31.28	21.30	38.40	27.25
$P_u$ (kN)	14.82	19.89	447.84	16.22
Ductility $\mu$	6.94	2.56	26.65	2.13

## 2.2 HYST calibration

The test results of the connections will be used to calibrate and verify the HYST connection model (Figure 2.2), a mechanics-based, protocol-independent connection subroutine (Li et al., 2012; Li & Lam, 2015). Backbone curves from cyclic loading were employed for the calibration. A search-based procedure was incorporated into the HYST program to calibrate the optimal parameters, simulate a complete hysteresis of the connection and validate it against full cyclic test results. The calibrated HYST models will subsequently be integrated into the CLT shear wall models to study the static performance of the walls.

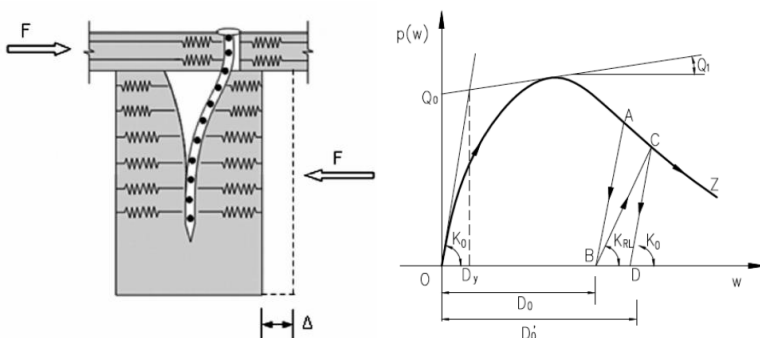


Figure 2.2. HYST subroutine

The force-deformation properties for embedment springs are described by Eq. (1). The calibrated HYST parameters from connection test data are shown in Table 3. The  $R^2$  (coefficient of determination) values (Fisher, 1925) were assessed in Table 3 to evaluate the fit for the HYST models, where the closer the  $R^2$  value is to 1, the more accurate the calibrated model is. In this study, all assessed  $R^2$  values exceeded 0.9, demonstrating the strong calibration capability of the HYST model. Figure 2.3 shows one representative case, that good agreement can be observed between model predictions and experimental results.

$$\begin{cases} p(w) = (Q_0 + Q_1 w) \left( 1 - e^{-\frac{K_0 w}{Q_0}} \right) & \text{if } w \leq D_{max} \\ p(w) = P_{max} e^{Q_3(w - D_{max})^2} & \text{if } w > D_{max} \end{cases} \quad (1)$$

Where  $P_{max} = (Q_0 + Q_1 D_{max}) \left( 1 - e^{-\frac{K_0 D_{max}}{Q_0}} \right)$  and  $Q_3 = \frac{\log(0.8)}{[(Q_2 - 1.0) D_{max}]^2}$

Table 3. HYST parameters calibrated by connection test data

HYST parameters		SP shear	SP separation	N-HD uplift	H-HD uplift	AB shear
Equivalent Fastener	$L$ (mm)	80	80	80	150	80
	$D$ (mm)	6	6	4	5.5	4
Embedment Properties $P(w)$	$Q_0$ (kN/mm)	10	10	97	800	100
	$Q_1$ (kN/mm <sup>2</sup> )	0.001	0.001	0.007	3	0.012
	$Q_2$	2	2	1.5	1.3	1.5
	$K_0$ (kN/mm <sup>2</sup> )	1	1	5	4000	2
	$D_{max}$ (mm)	11	11	4.6	15	7
	$\alpha$	0.2	0.2	0.2	0.2	0.2
$R^2$		0.93	0.93	0.97	0.96	0.96

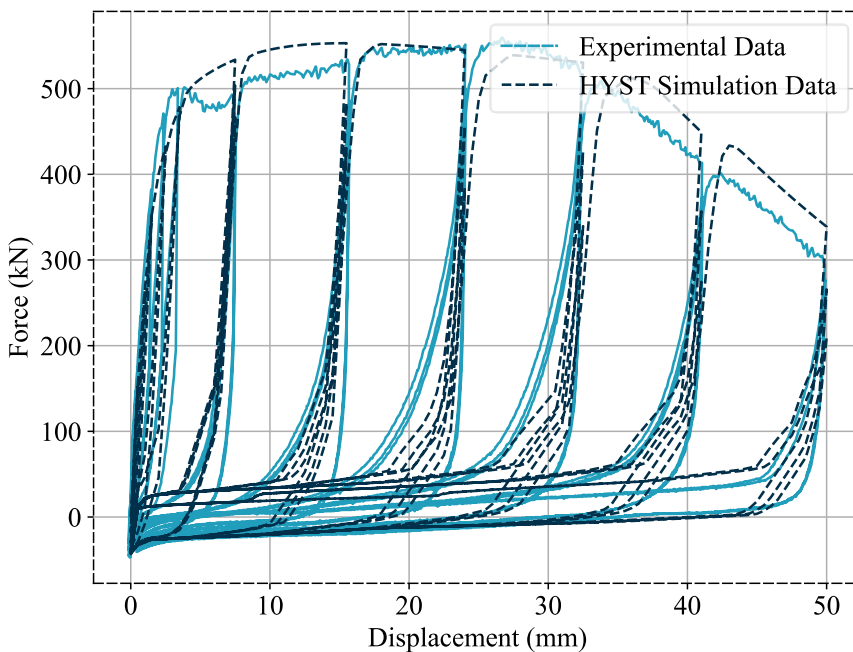


Figure 2.3. Comparison of experimental data and HYST simulation data

### 3 Capacity-based design

#### 3.1 Concept

The inception of capacity-based design (CBD) originated in New Zealand, introduced through a systematic procedure proposed by John P. Hollings to ensure adequate ductility in reinforced concrete building structures by guaranteeing that yielding occurs solely in selected ductile regions (Hollings, 1969). This concept was later adapted for timber structures and is now incorporated into Canadian codes. In the CBD of timber structures, ductile behaviour is ensured under seismic loading by detailing ductile connections as the weakest links along the load path and protecting all brittle timber elements from the overstrength of the ductile connections (Fardis, 2018).

The CBD concept is adopted in the new CSA O86.24 (CSA, 2024) by associating the design of connections and components with various percentiles of the primary energy-dissipative connections' peak resistance. Three overstrength factors for the design of connections and components can be employed in this context to:

- Ensure rocking behaviour and attain CP behaviour: The CLT shear wall strength is defined at the point where the hold-down yields. Yielding is prioritized in the panel-to-panel connections before the hold-down, achieved by using  $\gamma_{r,h}$  for the hold-down design, which corresponds to the 15<sup>th</sup> percentile of the spline (SP) connection peak resistance.
- Minimize the sliding mechanism: Shear connections in CLT shear walls are designed to remain elastic under the forces and displacement demands induced when connections in vertical joints reach the 30<sup>th</sup> percentile of their peak resistance or their target displacement.  $\gamma_{r,s}$  is used for designing the angle brackets to achieve this criterion.
- Prevent brittle failure and optimize the energy dissipation:  $\gamma_{r,ND}$  is employed in the design of non-dissipative elements (e.g., CLT panels) to ensure they are capacity-protected and remain elastic when connections in the vertical joints reach the 95<sup>th</sup> percentile of their peak resistance or their target displacement.

Extensive research on overstrength factors has been conducted by Jorissen & Fragiocomo (2011) and Ottenhaus et al. (2022). Their studies have informed the component-based concept of overstrength factors, illustrated in Figure 3.1. The commonly recognized equation for overstrength factors is provided in Eq. (2). Based on the test database in this study, the overstrength factors can be calculated based on the distribution of the peak resistance of the vertical spline joints. Results are listed in Table 4.

$$\gamma_r = \gamma_{sc} \cdot \gamma_{an} \cdot \gamma_M \quad (2)$$

Where:

$\gamma_{sc} = \frac{r_{f,x^{th}}}{r_{f,5^{th}}}$ , attributed to the variability of the connection strength properties. The different percentiles of the connection strength distribution are directly related to the variability of the timber material and steel fasteners within the specified material grade.

$\gamma_{an} = \frac{r_{f,sth}}{r_{f,an}}$ , assumed to be 1 in this study.

$\gamma_M = \frac{1}{\phi}$ , the partial material factor, typically represented by the resistance factor ( $\phi=0.8$ ) in Canadian design standard.

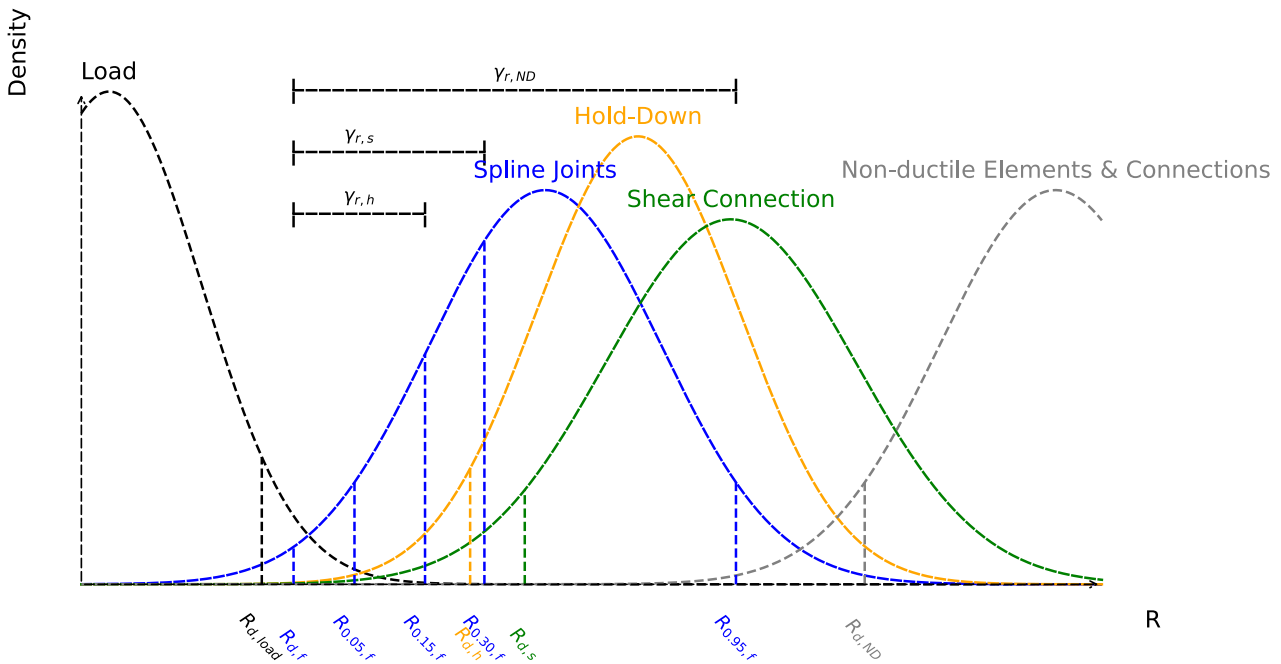


Figure 3.1. Theoretical overstrength factors (modified from Ottenhaus et al. (2022)).

Table 4. Calculation of overstrength factors

Element	Category	Behaviour	Related to x-percentile of SP's peak resistance	Overstrength factors
Vertical joints	Primary energy dissipative	Yield	/	/
Hold-downs	Other energy dissipative	Yield	15th	$\gamma_{r,h}$ 1.33
Angle brackets	Limited energy dissipative	Elastic	30th	$\gamma_{r,s}$ 1.40
CLT panels	Non-energy dissipative	Elastic	95th	$\gamma_{r,ND}$ 1.68

### 3.2 Case study archetype

The design framework is demonstrated for a six-storey platform-construction residential CLT shear wall structure. Each storey height is 3 meters. The archetype is situated in downtown Vancouver, Canada, which falls under seismic category 4. Considering the maximum lateral load-resisting capacity and avoiding dense wall distribution, the total floor area in this study is set to 30 meters by 28 meters, resembling a typical floor area for residential buildings. Figure 3.2 illustrates the typical floor plan.

A total of 24 two-panel CLT shear walls are placed in both the N-S and W-E directions. The contribution of other walls including partition walls was deemed insignificant and thus excluded from the structural models. One representative shear wall located at the cross section of axis A, and axis 3 and 4 on the ground floor, was selected for the case study.

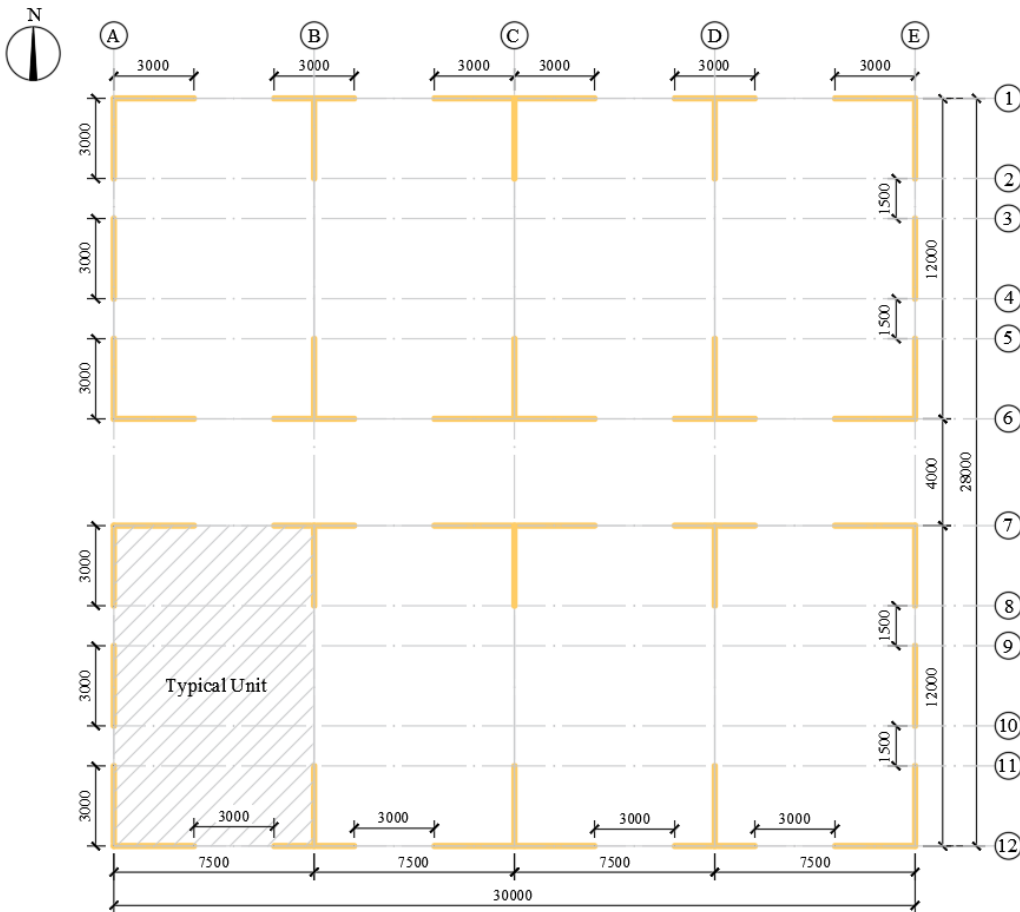


Figure 3.2. Configuration of the prototype CLT shear wall structures: plan view

### 3.3 Estimation and distribution of the base shear force

The design base shear force was calculated using Equivalent Static Force Procedure (ESFP) as per NBCC (NRC, 2021). A simplified approach for the loading and design of CLT shear walls has been adopted using free body diaphragms (Figure 3.3). The coupling effect between each set of two-panel CLT shear walls was neglected, and the shear force for each two-panel CLT shear wall at each storey was assumed to be uniform with rigid floor diaphragm assumption. Shear forces in walls were distributed linearly, with the shear force applied to each panel calculated as  $F_{panel} = \frac{F}{n} = \frac{F}{2}$ , given that the number of panels is two. Experimental investigations of CLT shear walls have demonstrated that the centers of rotation of the wall segments may not be located at the corner of each panel due to the presence of a compressive zone within the panel (Casagrande et al., 2016; Lukacs et al., 2019). This effect was incorporated into the proposed model by assuming a reduced panel length equal to  $b \cdot \beta$  in the coupled-panel behaviour, denoted as  $b_s$ . For simplicity in this study,  $\beta$  was set to 1.0.

In this study, the horizontal contribution of hold-downs and the vertical contribution of angle brackets are neglected. Hold-downs are designed to resist the overturning moment, while angle brackets, which connect the wall panels to the base, transfer the shear force only. By establishing the equilibrium equation for the system, the load demands shown in Figure 3.3 are calculated as follows:  $M_f = 1413 \text{ kN}\cdot\text{m}$ ,  $V_f = 236 \text{ kN}$ ,  $R_f = 113 \text{ kN}$ ,  $R_h = 583 \text{ kN}$ , and  $R_s = 118 \text{ kN}$ .



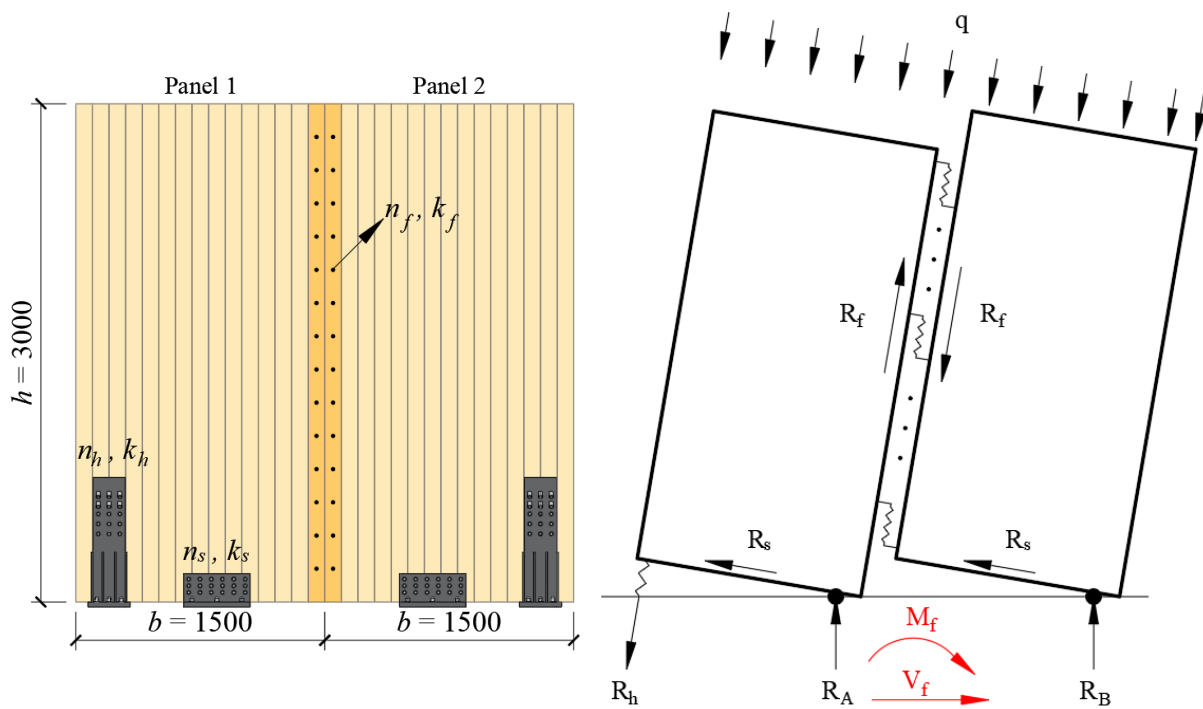


Figure 3.3. Schematic of adjacent CLT wall panels with CP behavior subjected to vertical and horizontal loads

### 3.4 Connections and components design according to CSA O86.24 provisions

The input parameters utilized in the models and the CBD procedure are summarized in Table 5.

Table 5. Input model parameters

Components	Properties	Values
Vertical joints	$k_f$ (kN/m)	3150
	$n_f$	9
	$r_f$ (kN) *	11.4
Normal hold-downs	$k_h$ (kN/m)	2760
	$n_h$	1
	$r_h$ (kN) *	18.4
High-stiffness hold-downs	$k_h$ (kN/m)	335460
	$n_h$	1
	$r_h$ (kN) *	386.7
Angle brackets	$k_s$ (kN/m)	1360
	$n_s$	1
	$r_s$ (kN) *	13.9
Length of a CLT panel within shearwall	$b_s$ (m)	1.5
Number of CLT panels in a shearwall	$m$	2
Total factored dead load applied at the top of shearwall	$q$ (kN/m)	164
Design shear load due to lateral load	$V_f$ (kN)	236
Design bending moment due to lateral load	$M_f$ (kN·m)	2119

\*  $r_f$ ,  $r_h$ , and  $r_s$  are factored resistance of vertical joints, hold-downs, and angle brackets, respectively.

### Step 1 – Ensure the coupled-panel kinematic mode

In the elastic region, the CP mode is characterized by all panels maintaining contact with the ground, thereby ensuring the vertical equilibrium of the panels (Casagrande et al., 2018). Eq.(3) must be satisfied for the kinematic mode to be considered as CP mode.

$$\tilde{k} \geq \frac{1 - \tilde{q} \frac{3m - 2}{m^2}}{1 - \tilde{q} \frac{m - 2}{m^2}} \quad (3)$$

In this case, with  $\tilde{q} = \frac{qm^2 b_s^2}{2Fh} = 1.0$ , the value of  $\tilde{k}$  must be greater than -0.04 to achieve the CP mode. This condition is inherently satisfied because  $\tilde{k} = \frac{k_h}{n_f k_f}$  is always positive.

### Step 2 – Design of vertical spline joints

The vertical spline joints are anticipated to yield first, serving as the primary energy-dissipative connections. Their shear strength  $n_f r_f$  must be equal to or greater than the corresponding action  $R_f$ , as determined by seismic analysis and free body diaphragm evaluations, as reported by Casagrande et al. (2021) and outlined in Eq. (4).

$$n_f \cdot r_f \geq R_f \quad (4)$$

Therefore,  $r_f$  should be equal or greater than 12.6 kN. Although future work will involve testing different configurations of vertical spline joints, the strength of the vertical spline joints used in this study does not fully comply with the requirements of the CBD procedure. Thus, scale factors must be applied to the vertical spline joints used in this study. The same rules will apply to other connection models, such as hold-downs and angle brackets.

### Step 3 – Design of hold-downs

According to the latest CSA O86.24, hold-downs are permitted to yield in uplift, but only after all vertical spline joints have yielded. The strength of the CLT shear wall is defined at the point where the hold-down yields, implying that the moment strength of the wall is equated to the bending moment strength associated with the yielding of the hold-down after the vertical joints have yielded, denoted as  $M_{s,r}$  in Eq. (5) (Masroor et al., 2022). This must be greater than or equal to the applied moment from lateral loads,  $M_f$ . Eq. (5) is equivalent to the free body diaphragm method, which necessitates  $r_h \geq R_h = 583$  kN. Although results from standard hold-down tests were utilized in this archetype due to limited test data, suitable commercial hold-downs from Simpson Strong-Tie can also be selected to meet the capacity and stiffness demands for real cases. Consequently, the final stiffness and factored resistance of the hold-down connection after scaling are 87,506 kN/m and 583 kN, respectively.

$$M_{s,r} \geq M_f \quad (5)$$

Where  $M_{s,r} = b_s \left[ r_h K_U + r_f (m - 1) n_f + \frac{q b_s m}{2} \right]$  is the factored rocking moment resistance of the shearwall under seismic loads.

To maintain the CP mode in the inelastic region, the bending moment resistance at the yield point of the vertical spline joints must not exceed that of the hold-downs. This yield hierarchy can be established using either Eq. (6) or (7), depending on the relative stiffness of the vertical joints and hold-downs. Given the design results based on Eq. (5), Eq. (6) is satisfied, thus confirming the yield hierarchy.

$$\text{When } k_h \geq n_f k_f, \text{ then } r_h \geq r_{f,15} \frac{k_h}{k_f} \quad (6)$$

$$\text{When } k_h < n_f k_f, \text{ then } r_h \geq \max \left( r_{f,15} \frac{k_h}{k_f}; n_f r_{f,15} - q b_s \right) \quad (7)$$

Where  $r_{f,15}$  is the 15<sup>th</sup> percentile of the peak resistance of one connection in vertical joint,  $r_{f,15} = \gamma_{r,h} \cdot r_{f,peak}$ .

It is important to note that the configuration of the hold-downs must be carefully selected and designed to satisfy the relevant equations. This challenge will be discussed in detail in Section 5.1.

#### Step 4 – Design of the angle brackets

To achieve rocking failure mode and limit sliding, the design of angle brackets should satisfy the condition in Eq. (8).

$$r_s \geq \frac{|M_{s,r,30}|}{|M_f|} F_{f,s} \quad (8)$$

Where  $M_{s,r,30}$  is the rocking moment resistance corresponding to  $r_{f,30}$  under seismic loads;  $r_{f,30}$  is the 30<sup>th</sup> percentile of the peak resistance of one connection in vertical joint,  $r_{f,30} = \gamma_{r,s} \cdot r_{f,peak}$ .

Despite achieving Eq. (8) by scaling the laboratory test results of angle brackets, the low stiffness of the angle brackets causes the sliding mode to dominate the wall's behaviour, which is undesirable for this study, especially when displacement-control loading protocols are used. Consequently, given the limited experimental database, the angle brackets are assumed to be sufficiently stiff to prevent sliding. Therefore, the value of one of the overstrength factors,  $\gamma_{r,s}$ , will not be the main focus of this paper.

#### Step 5 – Design of CLT panels

CLT panels shall be designed to resist seismic forces that are induced when connections in vertical joints of adjacent shear wall segments reach the 95<sup>th</sup> percentile of their peak resistance. The CLT panel used in this study was 9-ply E1, based on 35mm thick plies. The lamination materials were 1950 MSR and No. 3 SPF for the major and minor layers, respectively. Due to the high in-plane shear rigidity, the CLT panels are assumed to be rigid in this study.

## 4 CLTWALL2D modelling results

The static analysis was conducted using CLTWALL2D FE program (Li & Lam, 2015) (Figure 4.1). Model input parameters of critical connections such as hold-downs, angle

brackets, and vertical spline joints were calibrated based on the connection test database using HYST subroutine.

Three performance levels—immediate occupancy, life safety, and collapse prevention were defined using inter-storey drift ratios as the performance criteria, corresponding to drift ratios of 1.0%, 2.5%, and 4.5%, respectively. Reasonable inter-storey drift ratios will be helpful to control the compressive stress at the bottom corner of the wall panels. To study the static performance of coupled-panel CLT shear wall, the displacement-controlled loading protocols based on the building drift ratios were developed for both pushover and cyclic analysis. The loading protocols were applied at the top corner of the panels. The reversed cyclic loading protocol follows ASTM E2126 Method B (ASTM E2126, 2019), consisting of a series of cycle groups, each containing three identical cycles (Figure 4.1).

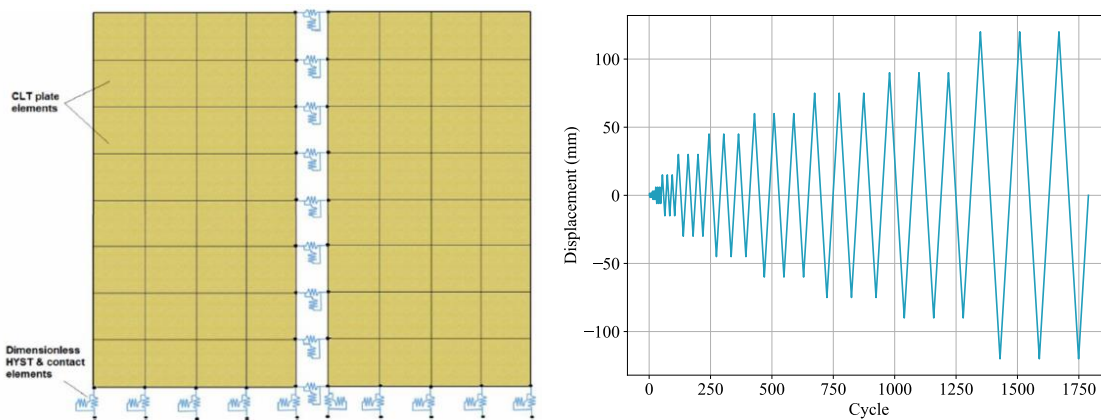


Figure 4.1. CLTWALL2D FE program(left) and Cyclic loading protocol(right)

The simulated cyclic behaviour obtained using the CLTWALL2D FE program (Li & Lam, 2015) is presented in Figure 4.2. The initial stiffness is 30810 kN/m, maximum capacity is 660 kN, with a ductility ratio of 4.36 and dissipated energy of 350 KJ, as calculated using the EEEP method. A moderate level of ductility and sufficient energy dissipation capacity are achieved. The simulation process reveals the CP mode, which validates the CBD procedure.

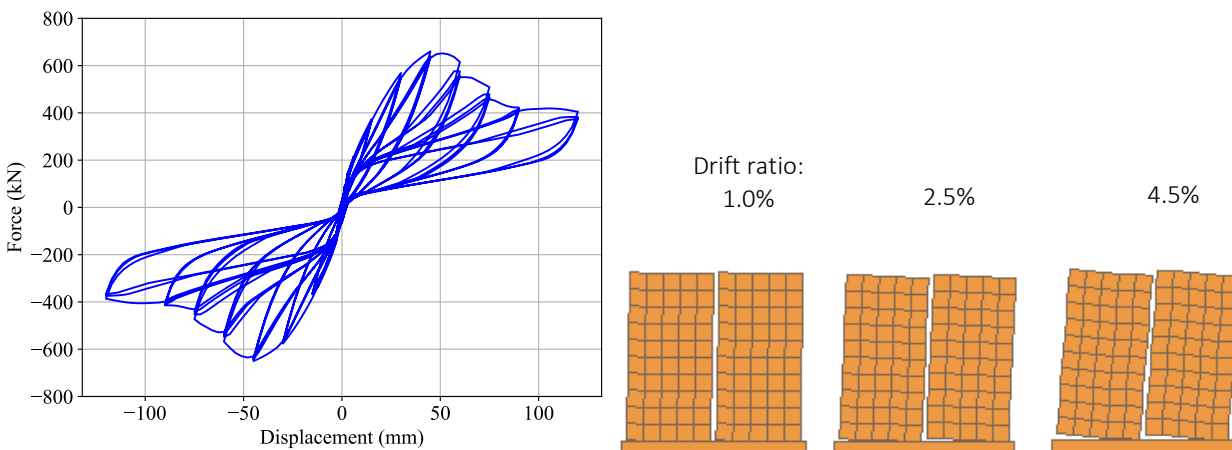


Figure 4.2. Simulated hysteretic behavior for the coupled-panel CLT shear wall (left), and wall deformation at different drifts (right)

## 5 Discussion

### 5.1 Yield hierarchy and challenges

In the process of designing hold-down connections, two requirements are considered. The first one is establishing the wall strength at the point when hold-down yields, in this case, Eq. (5) should be satisfied, which requires  $r_h \geq R_h$ . The second one is building the yield hierarchy between vertical joints and hold-downs according to either Eq. (6) or (7). The first condition is easy to meet as it considers the strength only, however, the second one could be tricky as it impedes the stiffness of connections.

Returning the definition of the yield hierarchy, if denoting the yield displacements of vertical joints and hold-downs as  $\Delta_{y,f}$  and  $\Delta_{y,h}$ , respectively, Eq. (6) can be rewritten as Eq. (9). Incorporating the peak resistance distribution of SP, rather than the factored resistance or yield strength distribution, enhances conservatism in establishing the yield hierarchy.

$$\text{When } k_h \geq n_f k_f, \text{ then } r_h \geq r_{f,15} \frac{k_h}{k_f} \Leftrightarrow \frac{r_h}{k_h} \geq \frac{r_{f,15}}{k_f} > \frac{\gamma_{r,h} r_f}{k_f} \Leftrightarrow \Delta_{y,h} > \gamma_{r,h} \Delta_{y,f} \quad (9)$$

However, this requirement is challenging because the design depends not solely on the strength or stiffness of hold-downs but on a reasonable combination of both. The ratio between yield strength and initial stiffness is inherently similar for a given type of connection when similar materials for fasteners and plates are used. This similarity arises because both yield strength and initial stiffness of hold-downs behave linearly with respect to the properties of a single fastener. Increasing the strength capacity will increase the stiffness at the same time.

Figure 5.1 presents the CLTWALL2D modelling results of CLT shear walls with two types of hold-downs introduced in Section 2: normal hold-down and high-stiffness hold-down. The normal hold-down and high-stiffness hold-down after scaling has the same factored resistance  $r_h$  of 583 kN, but different elastic stiffness  $k_h$  of 87506 kN/m and 506076 kN/m, respectively. The same type of vertical spline joints was used, with  $k_f$  of 3150 kN/m and  $r_f$  of 11.4 kN. It is evident that the high-stiffness hold-down does not satisfy Eq. (9). To meet the requirements of yield hierarchy with the existing high-stiffness hold-down would necessitate six times the original factored resistance, which is unrealistic. Therefore, for comparison purposes, the wall with high-stiffness hold-downs are designed by neglecting yield hierarchy requirements.

In the wall with normal hold-downs, the yielding of vertical spline joints was observed at step 117 ( $\Delta=24$  mm), followed by the yielding of hold-downs at step 242 ( $\Delta=39$  mm), thus validating the established yield hierarchy. In contrast, for the wall with high-stiffness hold-downs, the yielding of vertical spline joints was observed at step 117 ( $\Delta=24$  mm), and the yielding of hold-downs occurred at step 117 ( $\Delta=24$  mm), due to the neglect of considering the yield hierarchy in Eq. (9). The rocking ability, as indicated by the uplift displacement at the corner, was similar in both cases. Despite the absence of an established yield hierarchy, the wall with high-stiffness hold-downs

exhibited higher initial stiffness and ductility ratios but lower energy dissipation ability. This finding suggests that design of hold-down connections should not solely focus on achieving high stiffness or factored resistance; rather, a reasonable balance between stiffness and strength is essential.

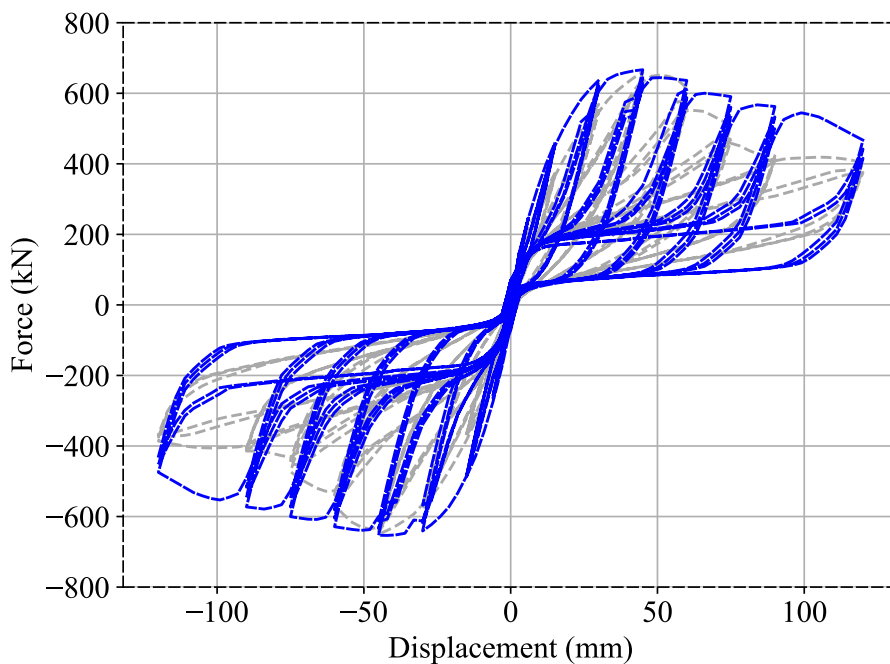


Figure 5.1. Simulation results of walls with normal hold-downs and high-stiffness hold-downs

Given the importance of establishing the yield hierarchy, several aspects require thorough investigation in the future:

- Accurately calculating the hold-down stiffness presents a significant challenge due to the limited information provided in the design standard.
- Balancing stiffness and strength of hold-downs across different systems, while simultaneously achieving the desired levels of ductility and energy dissipation, is crucial for the CBD procedure. These aspects require thorough investigation in the future.
- The coefficient of variation (COV) of the peak resistance of the vertical joints significantly influences the over-strength factors, thereby affecting the yield hierarchy requirements.

## 5.2 Capacity protection factors for hold-downs – Parametric study

According to Eq. (5), the wall strength can be established at the point when hold-down yields, which requires  $r_h \geq R_h$ . During the real design process, the hold-down capacity could be designed as  $\gamma_{CP,h} R_h$ , giving some redundancy in the hold-down connections with the intent of capacity protecting the hold-down elements.  $\gamma_{CP,h}$  is denoted as the capacity protection factors for hold-downs. If such a factor is set too large, rocking movements can be impeded which could in turn limit the system to dissipate energy through the assumed energy dissipating load-deformation behaviour of the vertical spline joints.

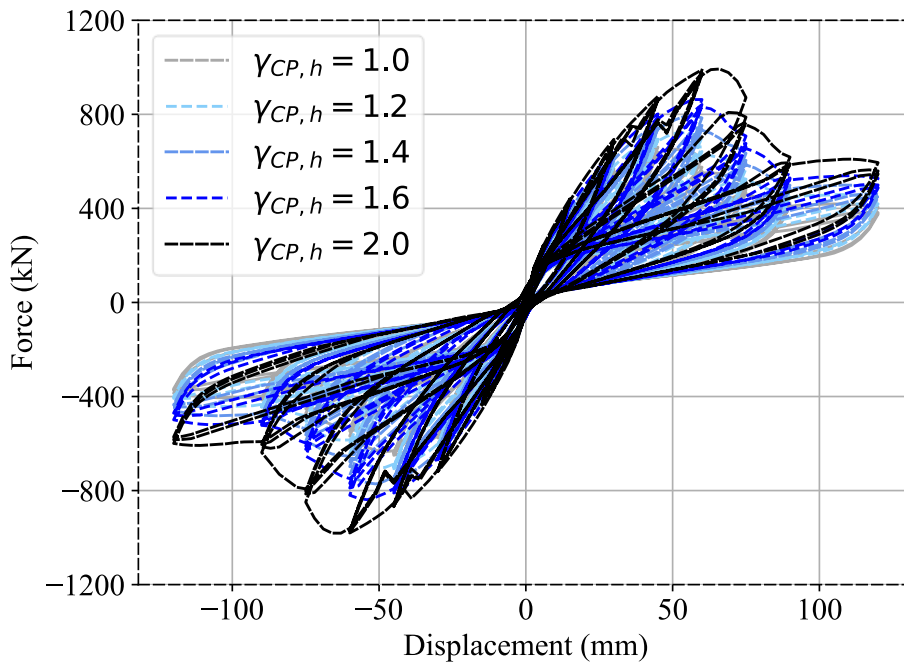


Figure 5.2. Cyclic results with different capacity protection factors for hold-down

Table 6. The influence of capacity protection factors for hold-down to wall performance

$\gamma_{CP,h}$	Maximum uplift displacement (mm)	$P_{max}$ (kN)	Ductility	Dissipated Energy (kJ)
1.0	58.069	660	4.4	350
1.2	58.017	722	4.1	375
1.4	57.967	793	3.9	398
1.6	57.906	863	3.6	420
2.0	55.672	993	3.2	480

Figure 5.2 and Table 6 summarize the cyclic performance of coupled-panel CLT shear walls utilizing different capacity protection factors for hold-downs. With the increase of  $\gamma_{CP,h}$ , the maximum uplift displacement decreases, indicating a reduction in rocking behaviour. The wall's maximum capacity and dissipated energy increase with higher capacity hold-downs. However, a notable decrease in ductility was observed. Therefore, an optimal capacity protection factor for hold-down design must be derived by balancing these aspects, ensuring the wall system has sufficient strength, can dissipate adequate energy, and maintains appropriate ductility levels.

### 5.3 Dynamic response – Future work

The degree of increase of the stiffness of the hold-downs as well as the whole system when capacity protection factors are applied must also be considered, as discussed in Section 5.2. The natural frequency of the system will change due to the alteration in stiffness, which will influence the dynamic behaviour of the system. Thus, determination of optimal capacity protection factors is pending further research of the dynamic response. Additionally, the nonlinear dynamic analysis will be conducted to calculate  $R_d$  and  $R_o$  and quantify the seismic performance.

## 6 Conclusions

This paper presents evidence on the cyclic performance of coupled-panel CLT shear walls used in platform-type construction and discusses the challenges encountered during the design process, in alignment with the new Canadian Standard on Engineering Design in Wood (CSA, 2024).

The following conclusions can be drawn from the results of the study conducted thus far:

- By designing the coupled-panel CLT shear walls following the CBD procedure per CSA O86.24, a moderate ductility level was achieved. The wall demonstrated sufficient energy dissipation capability via the primary energy-dissipative elements, the vertical spline joints and the secondary energy-dissipative elements, the hold-downs.
- Yield hierarchy can be established by designing the hold-downs and vertical joints with a rational ratio of yield strength to elastic stiffness. Establishing yield hierarchy can be challenging due to its dependence on both strength and stiffness of both primary and secondary energy dissipating elements.
- Parametric study on capacity protection factors for hold-downs was conducted, revealing their influence on rocking behaviour, ductility, and energy dissipation. The optimal capacity protection factor will be determined in the future pending further analysis of the dynamic performance of the system.

## 7 References

- ASTM E2126. (2019). Standard test methods for cyclic (reversed) load test for shear resistance of vertical elements of the lateral force resisting systems for buildings.
- Casagrande, D., Doudak, G., & Masroor, M. (2021). A proposal for capacity-based design of multi-storey CLT buildings. INTER Meeting 54-International Network on Timber Engineering Research [INTER/54-15-1].
- Casagrande, D., Doudak, G., Mauro, L., & Polastri, A. (2018). Analytical Approach to Establishing the Elastic Behavior of Multipanel CLT Shear Walls Subjected to Lateral Loads. *Journal of Structural Engineering*, 144(2), 04017193. [https://doi.org/10.1061/\(ASCE\)ST.1943-541X.0001948](https://doi.org/10.1061/(ASCE)ST.1943-541X.0001948)
- Casagrande, D., Doudak, G., & Polastri, A. (2019). A proposal for the capacity-design at wall- and building-level in light-frame and cross-laminated timber buildings.



Bulletin of Earthquake Engineering, 17(6), 3139–3167.

<https://doi.org/10.1007/s10518-019-00578-4>

Casagrande, D., Rossi, S., Sartori, T., & Tomasi, R. (2016). Proposal of an analytical procedure and a simplified numerical model for elastic response of single-storey timber shear-walls. *Construction and Building Materials*, 102, 1101–1112. <https://doi.org/10.1016/j.conbuildmat.2014.12.114>

CSA. (2024). Engineering design in wood. (CSA Standard No. O86:24).

<https://www.csagroup.org/>

Fardis, M. N. (2018). Capacity design: Early history. *Earthquake Engineering & Structural Dynamics*, 47(14), 2887–2896. <https://doi.org/10.1002/eqe.3110>

Fisher, R. A. (1925). *Statistical Methods for Research Workers*. Oliver and Boyd.

Hollings, J. P. (1969). Reinforced concrete seismic design. *Bulletin of the New Zealand Society for Earthquake Engineering*, 2(3), 217–250.

<https://doi.org/10.5459/bnzsee.2.3.217-250>

Jorissen, A., & Fragiacommo, M. (2011). General notes on ductility in timber structures. *Engineering Structures*, 33(11), 2987–2997. <https://doi.org/10.1016/j.engstruct.2011.07.024>

Li, M., Foschi, R. O., & Lam, F. (2012). Modeling Hysteretic Behavior of Wood Shear Walls with a Protocol-Independent Nail Connection Algorithm. *Journal of Structural Engineering*, 138(1), 99–108. [https://doi.org/10.1061/\(ASCE\)ST.1943-541X.0000438](https://doi.org/10.1061/(ASCE)ST.1943-541X.0000438)

Li, M., & Lam, F. (2015). Lateral Behaviour of Cross Laminated Timber Shear Walls under Reversed Cyclic Loads. *Proceedings of the Tenth Pacific Conference on Earthquake Engineering*.

Lukacs, I., Björnfot, A., & Tomasi, R. (2019). Strength and stiffness of cross-laminated timber (CLT) shear walls: State-of-the-art of analytical approaches. *Engineering Structures*, 178, 136–147. <https://doi.org/10.1016/j.engstruct.2018.05.126>

Masroor, M. (2023). *Multi-Panel CLT Shearwalls: Experimental Assessment, Analytical Development, and Design Considerations*. University of Ottawa.

- Masroor, M., Doudak, G., & Casagrande, D. (2022). Design of Multipanel CLT Shear Walls with Bidirectional Mechanical Anchors Following Capacity-Based Design Principle. *Journal of Performance of Constructed Facilities*, 36(1), 04021113. [https://doi.org/10.1061/\(ASCE\)CF.1943-5509.0001693](https://doi.org/10.1061/(ASCE)CF.1943-5509.0001693)
- NRC. (2021). National Building Code of Canada: 2020. <https://nrc-publications.canada.ca/eng/view/object/?id=515340b5-f4e0-4798-be69-692e4ec423e8>
- Ottenhaus, L.-M., Li, M., & Smith, T. (2022). Analytical Derivation and Experimental Verification of Overstrength Factors of Dowel-type Timber Connections for Capacity Design. *Journal of Earthquake Engineering*, 26(6), 2970–2984. <https://doi.org/10.1080/13632469.2020.1781711>
- Sun, X., He, M., Li, Z., & Lam, F. (2019). Seismic performance assessment of conventional CLT shear wall structures and post-tensioned CLT shear wall structures. *Engineering Structures*, 196, 109285. <https://doi.org/10.1016/j.eng-struct.2019.109285>
- UBC, T. E. and A. M. (TEAM) L. (2023). Establishing DOL factor of seismic load conditions for CLT connections (TEAM 2023-14). the University of British Columbia.
- Wright, T., Li, M., Moroder, D., Lim, H., & Carradine, D. (2023). Cyclic behaviour of CLT shear wall hold-down connections using mixed angle self-tapping screws. *Engineering Structures*, 286, 116123. <https://doi.org/10.1016/j.eng-struct.2023.116123>

DISCUSSION

**The paper was presented by J Chen**

*D Casagrande commented that similar approaches were taken in Eurocode and discussed the interactive behaviour of the hold downs and vertical joints. He asked for suggestions to make this less challenging. J Chen responded that commercial hold downs can work and the process could be simplified without considering hierarchy of yielding sequence. D Casagrande said if hold downs yielded much earlier then this might not work.*

*G Doudak received clarifications that two screws per connection were tested and inquired about the method for applying the results to computer model. He received confirmation that gamma-analytical was assumed to be 1 and discussed about this assumption. Also he received confirmation that the uplift in analysis showed 55 mm of displacement of the hold down which can be achieved as shown in experimental results.*

*H Ganjali asked about the performance of hold downs under biaxial loading. F. Lam responded that UBC test data on commercial hold downs and angle brackets for CLT systems were published in journals. The results showed hold down capacities were not influenced by biaxial loading while angle brackets capacities were.*





# Investigating the in-plane rigid diaphragm conditions of Cross-Laminated Timber floors for seismic design

Giuseppe D'Arenzo<sup>1</sup>, Valentino Nicolussi<sup>2,3</sup>, Pietro Rigo<sup>2,3</sup>, Luca Pozza<sup>3</sup>, Andrea Polastri<sup>2</sup>, Daniele Casagrande<sup>4</sup>

<sup>1</sup> Department of Civil and Architectural Engineering, Aarhus University, DK; <sup>2</sup> National Research Council of Italy (CNR-IBE), IT; <sup>3</sup> Department of Civil, Chemical, Environmental and Materials Engineering, University of Bologna, IT; <sup>4</sup> Department of Civil, Environmental and Mechanical Engineering, University of Trento, IT;

Keywords: Cross Laminated Timber, lateral load, seismic design, floor, shear-wall

## 1. Introduction

Floor diaphragms play a crucial role in the performance of seismic force resisting systems (SFERS) by transferring inertia forces to the vertical structural elements and ensuring that the entire structural system responds uniformly under seismic actions. For this reason, floor diaphragms are designed with sufficient in-plane stiffness and strength, and effective connections are realized between the floors and the vertical elements of the SFERS.

A high in-plane stiffness of floor diaphragms is essential to minimize the impact of in-plane deformations on the distribution of inertia forces to the vertical elements of the SFERS and to maintain in-plane regularity in the seismic response of the entire structure. When a floor diaphragm has significantly greater in-plane stiffness than the vertical elements, seismic forces are distributed to the vertical elements in proportion to their stiffness.

Simplifications in structural analysis and modelling of buildings can be made when floor diaphragms are considered rigid in their planes. In such cases, the masses and moments of inertia of each floor can be concentrated at the floor's centre of gravity, and a diaphragm constraint can be applied to connect the "master" node, representing the centre of gravity, to all other "slave" nodes of that floor. The constrained nodes move collectively as a planar diaphragm, eliminating in-plane deformation and significantly reducing the number of degrees of freedom, thereby decreasing computational effort.

International design codes and guidelines typically base rigid diaphragm conditions on the in-plane lateral displacements of floors. According to the European code for seismic design of structures, Eurocode 8 (EC8) (EN1998-1), a floor diaphragm is considered

rigid if its lateral displacements, accounting for its actual in-plane flexibility, do not exceed those from the rigid diaphragm assumption by more than 10%. According to ASCE 41-17 (ASCE 2017), a floor diaphragm is considered rigid when the lateral displacements of the floor are less than or equal to half of the average inter-storey drift of the floor directly below. Less stringent criteria are provided by the American International Building Code (IBC) (International Code Council (ICC) 2018), where a floor diaphragm can be assumed rigid for the distribution of shear forces and torsional moments when the lateral displacements of the floor are less than or equal to twice the average inter-storey drift of the floor below. Thus, the verification of rigid diaphragm assumptions requires the calculation of lateral displacements of floor diaphragms, taking into account their actual in-plane deformation. This process complicates structural analysis when the in-plane flexibility of floor diaphragms is included.

Some international codes, such as EC8, provide prescriptive provisions as an alternative to rigorous conditions based on numerical models. These provisions include structural details (e.g., minimum thickness of the topping layer in reinforced brick concrete slabs), geometrical limitations (e.g., maximum span between vertical supports), and design rules for rigid floor diaphragms.

For timber structures, Eurocode 8 includes prescriptive provisions and detailing rules for light-frame floors assembled with wood-based panels connected to timber beams by mechanical fasteners. For such floors, the rigid diaphragm condition can be assumed when transverse blocking elements are placed between the timber beams, ensuring the nailing of all sheathing edges, with no change of span direction over supports and minimal impact of openings on in-plane stiffness. However, there are currently no prescriptive provisions or design rules for Cross Laminated Timber (CLT) floor diaphragms. Consequently, the rigid diaphragm conditions for CLT floors must be verified through numerical analyses that consider their actual in-plane stiffness.

The lack of prescriptive rigid diaphragm conditions for CLT floors in international design codes, along with a review of existing literature, underscores the need for a better understanding of the conditions under which CLT floors can be considered rigid. No in-depth investigation has yet determined which structural and geometrical parameters should be considered to assume a rigid in-plane behaviour of CLT floors in the design process.

This paper presents the results of a parametric analysis aimed at defining the in-plane rigid conditions for CLT floor diaphragms. Through a comprehensive literature review and extensive numerical analyses, the conditions ensuring a rigid behaviour of CLT floor diaphragms in CLT platform-type buildings are identified and discussed. The study also examines the influence of geometrical and mechanical parameters used in designing CLT floor components (CLT panels and connections) on i) the distribution of elastic inertia forces among the vertical elements of the SFRS, ii) the relative in-plane deformation of CLT floor diaphragms, and iii) the natural period of CLT platform-type buildings.

## 2. State-of-the-art

Over the past decade, extensive research has focused on understanding the in-plane flexibility of Cross Laminated Timber (CLT) floor diaphragms. These studies include both full-scale floor diaphragms and the connections between CLT floor panels, as well as the connections between floor panels and the underlying walls. Popovski et al. (2023) provided a comprehensive review of the performance, analysis, and design of mass timber diaphragms, including CLT, synthesizing available literature and international building codes.

### 2.1. Studies at Floor Level

Several significant studies have been conducted to assess the behaviour of CLT floor diaphragms at the floor level. Kode et al. (2021) performed cyclic tests on two full-scale CLT floor diaphragms (5.00×4.27 m) under different layouts, namely simple-span and two-span continuous panels. The results indicated a rigid behaviour of the CLT panels and energy dissipation in the connections, underscoring the critical role of tension chords in internal force transmission. Similarly, Line et al. (2022) conducted monotonic tests on two full-scale CLT diaphragms (7.32×7.32 m) in a single-span configuration to validate design provisions in ANSI/AWC 202. Failures occurred in the panel-to-panel and panel-to-beam connections without significant deformations or failures in the CLT panels, confirming the adequacy of the ANSI/AWC 202 design provisions.

Popovski et al. (2023) analysed two configurations of CLT diaphragms (7.30×2.40 m) under a single-span test. This study examined both multi-panel and single-panel configurations, revealing that panel-to-panel connections significantly influence diaphragm behaviour, as evidenced by a 43% reduction in stiffness from the single- to the 3-panel configuration. Beirsto et al. (2022) conducted an extensive experimental campaign on twenty-eight full-scale CLT floor specimens (4.57×4.57 m) with different configurations of chord and panel-to-panel screw spacing and wood species. The results demonstrated that the flexibility and ductility of CLT floor diaphragms are primarily influenced by panel-to-panel connections.

Barbosa et al. (2018) performed a shake-table test on a two-storey timber building with a 6.10×17.7 m CLT floor diaphragm. The first-floor diaphragm, composed of sixteen panels with spline joints, showed a non-uniform response, whereas the CLT-concrete composite diaphragm at the roof level exhibited a more uniform acceleration pattern due to increased stiffness from the concrete top. Popovski and Gavric (2016) evaluated a two-storey full-scale platform-type CLT structure under cyclic loading. The floor diaphragms exhibited negligible in-plane deformations, behaving as rigid.

Loss and Frangi (2017) and Loss et al. (2018) investigated an innovative steel-timber hybrid floor diaphragm using modular prefabricated composite elements. The experimental tests and numerical analyses indicated that the main deformations occurred at



beam-to-beam steel joints, while steel-CLT hybrid elements remained elastic. Ashtari et al. (2014) utilized Finite Element (FE) models to analyse the in-plane behaviour of CLT floor diaphragms, conducting a parametric analysis to investigate the influence of geometrical and mechanical parameters. The lateral load distribution on shear walls was compared to theoretical distributions (tributary area and stiffness method), providing insights into the design for flexible and rigid floor diaphragms.

Moroder (2016) and Moroder et al. (2015) examined the influence of diaphragm stiffness on the dynamic behaviour of multi-storey timber buildings, demonstrating that the in-plane behaviour of CLT floor diaphragms can be accurately described through an Equivalent Truss Model. D'Arenzo et al. (2019) conducted a parametric numerical analysis to investigate the in-plane flexibility of CLT floor diaphragms, focusing on major deformation contributions. The study showed that panel-to-panel connections primarily govern in-plane flexibility, while CLT panels themselves have negligible influence, and floor-to-wall connections act as chord elements.

## 2.2. Studies at Connection Level

The in-plane behaviour of CLT floor diaphragms is significantly influenced by two types of connections: panel-to-panel connections and floor-to-wall connections. Four main types of joints are typically used to connect CLT panels: outer spline, inner spline, lap, and butt joints, utilizing nails, partially threaded screws (PTs), or fully threaded screws (FTs) (Figure 1).

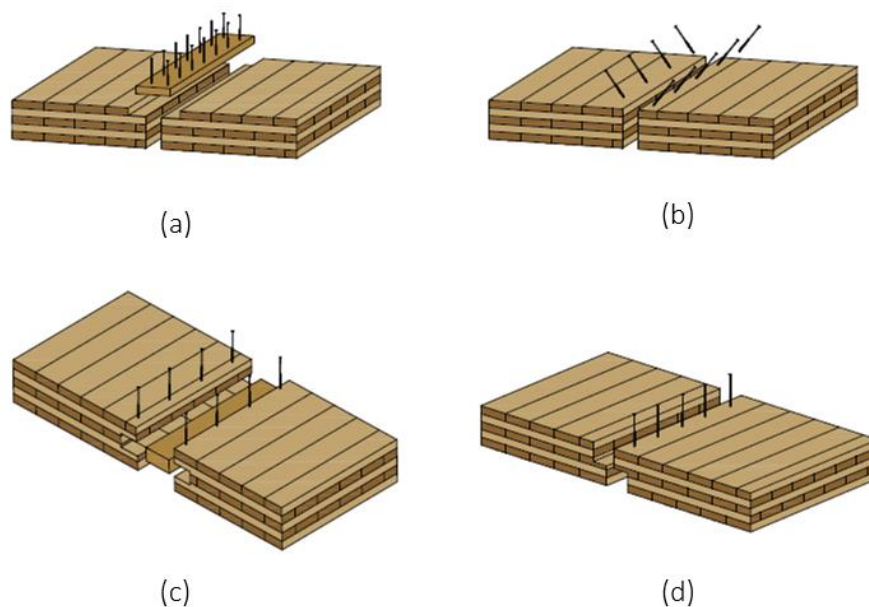


Figure 1: Examples of floor panel-to-panel connections: (a) outer spline-, (b) lap-, (c) inner spline- and (d) butt-joints.

Studies on lap joints with PTSs conducted by Flatscher (2017), Gavric et al. (2015), Hossain et al. (2019), and Yin et al. (2022) showed stiffness per fastener ranging from 0.19 to 1.27 kN/mm. Tests with FTs by Hossain et al. (2019) exhibited higher stiffness, between 2.70 and 4.70 kN/mm. Gavric et al. (2015) and Hossain et al. (2019) reported stiffness per fastener between 0.42 and 2.00 kN/mm for spline joints with PTSs. Investigations on butt joints by Loss et al. (2018a) and Hossain et al. (2019) using PTSs and FTs revealed a wide range of stiffness per fastener (0.40 to 7.50 kN/mm), influenced by screw length and insertion angle. Gavric et al. (2015) and Xiong and Huynh (2018) provided data on lap and spline joints under perpendicular loads, with stiffness values per fastener ranging from 0.83 to 2.66 kN/mm.

Screwed connections are commonly used to connect CLT floor panels to wall panels. Flatscher (2017) and Gavric et al. (2015) tested various PTSs, finding stiffness per fastener ranging from 0.46 to 1.49 kN/mm. Brown et al. (2021) and Xiong and Huynh (2018) reported a wider range of stiffness per fastener (0.80 to 11.25 kN/mm) in case of FTs, influenced by screw length and inclination.

In summary, current research indicates that the in-plane flexibility and rigidity of CLT floor diaphragms are primarily influenced by the type and configuration of the connections used. Although CLT panels exhibit limited in-plane deformation, the connections between panels, as well as those between panels and walls, are critical in determining the overall diaphragm behaviour. These findings underscore the importance of thoroughly considering connection properties in the design and analysis of CLT floor diaphragms to ensure accurate predictions of structural performance under seismic loading.

### 3. Parametric analysis: methodology

A parametric analysis to determine in-plane rigid diaphragm conditions through numerical simulations is conducted in the current study. The analysis focuses on a simplified CLT archetype to investigate the effects of geometrical and mechanical parameters of CLT floor components, such as panels and connections, on the elastic inertia force distribution among shear-walls, relative in-plane deformation between CLT floor diaphragms and shear-walls, and the natural period of the archetype.

#### 3.1. Archetype Description

A symmetric multi-storey CLT platform archetype with a rectangular plan (dimensions  $B \times L$ ) was selected for the parametric analysis. Each storey features three longitudinal and two transversal single-panel CLT shear-walls, with a height ( $h$ ), as shown in Figure 2 for a single-storey system. The two transversal walls (W1T and W2T) and two longitudinal walls (W1L and W3L) are on the perimeter, while the longitudinal wall W2L aligns along the symmetry axis. Each transversal and longitudinal wall has lengths  $B$  and  $L$ , respectively, and the distance between the central shear-wall W2L and each

outer longitudinal wall (W1L and W3L) is denoted by  $i$ . CLT floor panels aligned longitudinally are simply supported by the two transversal walls, with floor panel lengths and widths represented by  $L$  and  $b$ .

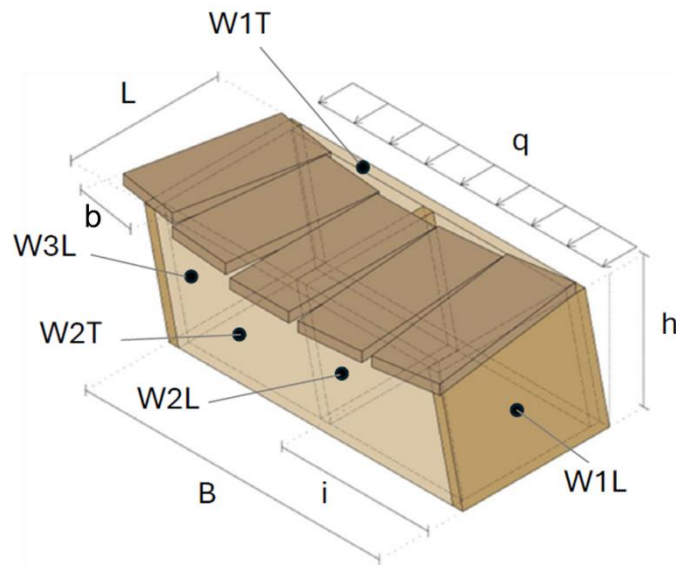


Figure 2: CLT platform archetype considered in the parametric analysis.

Five different storey configurations ( $N = 1$  to  $5$ ) with a constant inter-storey height ( $h = 3.18$  m) were analysed, each having three distances ( $i$ ) between the central and outer longitudinal walls (3, 5, and 7 m), resulting in total transversal lengths ( $B$ ) of 6, 10, and 14 m. The longitudinal length ( $L$ ) remained constant at 5 m. A uniformly distributed lateral load ( $q = 2.5$  kN/m) was applied along the longitudinal direction at each storey. The thickness and layout of CLT panels for shear-walls varied by storey height, with lower storey panels being thicker. Four types of 5-layers CLT panels were selected, with varying thicknesses: 100 mm, 124 mm, 137 mm, and 158 mm. Elastic modulus and shear modulus values were set at  $E_0 = 11.5$  GPa and  $G_0 = 0.69$  GPa. Floor panels of 5-layers 179 mm CLT were used, with elastic modulus and shear modulus values identical to the wall panels.

Angle brackets (AE116) connected with 25 4.0×60 mm annular ring nails and hold-down devices WHT 340, WHT440, WHT620 connected with 20, 35 and 55 4.0×60 mm annular ring nails were employed. The mechanical behaviour of these connections was varied to consider different wall stiffness values ( $S1$ ,  $S3$ ,  $S5$ ), increasing their stiffness for configurations  $S3$  and  $S5$  by factors of 3 and 5, respectively.

The types of screwed panel-to-panel and floor-to-wall connections were also varied, examining the influence on the rigid diaphragm conditions of CLT floors. The configurations for these connections were categorized into low (L), medium (M), and high (H) stiffness per unit length. Floor panel-to-panel connections were set with stiffness per unit length  $K_{f-f}$  values of 2, 8, and 20 kN/mm<sup>2</sup>, while floor-to-wall connections had  $K_{f-w}$  values of 3, 15, and 45 kN/mm<sup>2</sup>.

### 3.2. Finite Element Model

The finite element (FE) numerical analyses were carried out using the SAP2000 software package. Both wall and floor CLT panels were modelled with four-node quadrilateral homogeneous shell elements. A mesh size of 200 mm was selected following a mesh sensitivity analysis to balance computational efficiency and accuracy. The effective values of the modulus of elasticity in the vertical ( $E_{eff,v}$ ) and horizontal ( $E_{eff,h}$ ) directions, as well as the in-plane shear modulus ( $G_{eff}$ ), were calculated using Equations (1) to (3), which consider the orientation and lay-up of the CLT panels according to the methodologies proposed by Bogensperger et al. (2010) and Brandner et al. (2017).

$$E_{eff,v} = \frac{E_0 t_v + E_{90} t_h}{t_{CLT}} \quad (1)$$

$$E_{eff,h} = \frac{E_0 t_h + E_{90} t_v}{t_{CLT}} \quad (2)$$

$$G_{eff} = \frac{G_0}{1 + 6\alpha_T \left(\frac{t_{mean}}{w}\right)^2} \quad (3)$$

Here,  $E_0$  and  $E_{90}$  represent the moduli of elasticity parallel and perpendicular to the lamination,  $t_v$  and  $t_h$  are the total thicknesses of vertical and horizontal laminations,  $t_{CLT}$  is the total thickness of the CLT panel,  $G_0$  is the in-plane shear modulus of the lamination, and  $w$  is the width of the wooden lamellae. The mean thickness of the lamination ( $t_{mean}$ ) is defined in Equation (4), and the parameter  $\alpha_T$  is calculated using Equation (5).

$$t_{mean} = \frac{t_{CLT}}{n_{lay}} \quad (4)$$

$$\alpha_T = p \left(\frac{t_{mean}}{w}\right)^{-0.79} \quad (5)$$

In these equations,  $n_{lay}$  is the number of layers, and  $p$  equals 0.535 for three-layered CLT panels and 0.425 for five-layered CLT panels.

The hold-downs and angle brackets for the first and upper stories were modelled using one-joint and two-joint multi-linear link elements, respectively (Figure 3). The vertical mechanical behaviour of these components was represented by a bi-linear curve with tensile stiffness ( $k_h$  and  $k_{a,z}$ ) and rigid behaviour under compression. In the horizontal shear direction, angle brackets were modelled as linear with stiffness ( $k_{a,x}$ ). Vertical gap elements simulated contact along the base of the wall panels with the floor below or the foundation. Rigid translation restraints were added at the base of ground floor walls to prevent horizontal out-of-plane displacement.

Floor-to-wall connections were modelled with two-joint vertical link elements spaced equally, assuming linear elastic behaviour in both longitudinal and transverse directions. The stiffness of each link was calculated as the product of the chosen floor-to-wall connection stiffness per unit length and the mesh size.

Two-joint horizontal link elements were used to model floor panel-to-panel connections. A linear elastic behaviour was assumed parallel to the joint, while a bilinear elastic behaviour was used transversely to simulate panel separation and contact. Stiffness values were derived similarly to the floor-to-wall connections, assuming a rigid behaviour for transverse contact.

For models representing rigid diaphragms, rigid diaphragm constraints were applied to all joints at the same floor level, ensuring that the joints moved together as a planar diaphragm resistant to membrane deformations. Non-linear elastic static analyses were performed to account for non-linearities due to gap, hold-down, and angle bracket elements.

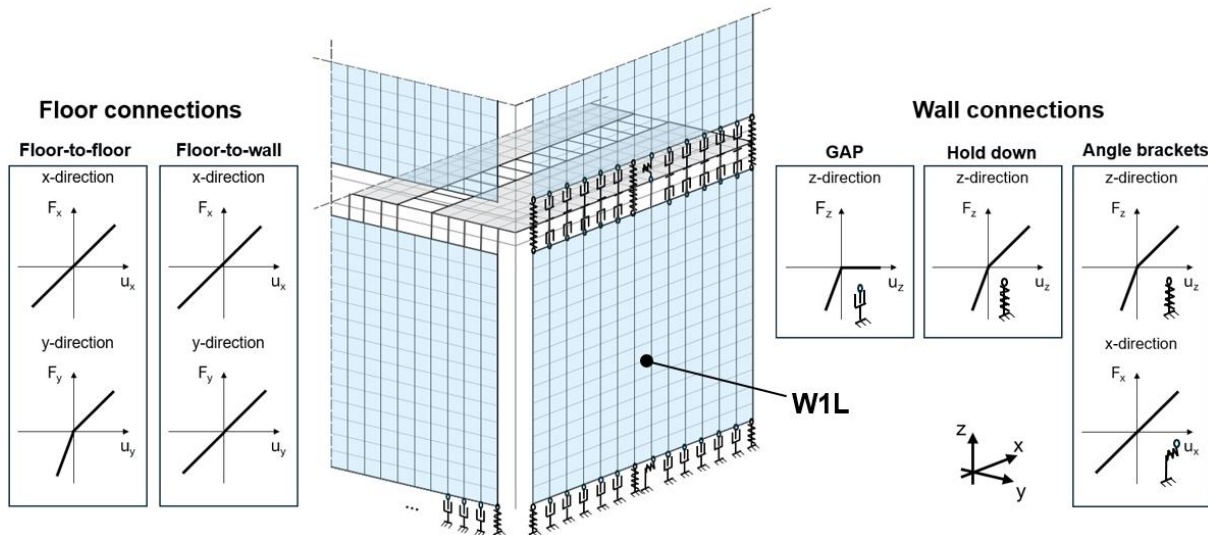


Figure 3: Numerical model of CLT archetype with non-rigid floors.

### 3.3. Method of Analysis

For each case study, models with actual floor diaphragm deformation (non-rigid) were compared with models incorporating rigid diaphragm constraints, with parameters related to in-plane behaviour being considered. The rigid diaphragm condition, as defined by Eurocode 8, was evaluated using the displacement increase parameter ( $\alpha_\delta$ ) (Equation (6)). Shear forces ( $V$ ) on the central shear wall (W2L) and the natural period of the archetype ( $T$ ) were also examined in the comparison, with discrepancies ( $\epsilon$ ) calculated for both parameters (Equation (7) and (8)).

$$\delta_{NR} = (1 + \alpha_\delta)\delta_R \tag{6}$$

$$\varepsilon_V = \frac{V_{NR} - V_R}{V_{NR}} \cdot 100 [\%] \quad (7)$$

$$\varepsilon_T = \frac{T_{NR} - T_R}{T_{NR}} \cdot 100 [\%] \quad (8)$$

In Equation (6) to (8) the subscripts NR and R refer to Non-Rigid and Rigid floor conditions, respectively.

Five key variable parameters were investigated in the analysis: the dimensionless distance between central and outer walls ( $i/L$ ), the number of storeys ( $N$ ), the stiffness per unit length of floor panel-to-panel connections ( $K_{f-f}$ ), the stiffness per unit length of floor-to-wall connections ( $K_{f-w}$ ), and the shear-wall stiffness configuration (S1, S3, S5). The parameter  $\alpha_\delta$  and discrepancies in shear force and natural period were analysed considering the ratio ( $\kappa$ ) between in-plane stiffness of the floor ( $K_{floor}$ ) and shear-walls ( $K_{wall}$ ). This ratio, describing the floor in-plane behaviour within the structural system, was calculated for a subsystem including the floor between two shear-walls.

The in-plane stiffness of the floor ( $K_{floor}$ ) was determined using Equation (9), considering shear deformation and neglecting bending deformation. The lateral stiffness of a single shear-wall ( $K_{wall}$ ) was calculated using Equation (10), accounting for sliding, rocking deformation, and shear panel deformation while ignoring bending contributions.

$$K_{floor} = \frac{q \cdot i}{\Delta_{floor}} = \left( \frac{\frac{i}{b} + \frac{b}{i} - 2}{8 \cdot K_{f-f} \cdot L} + \frac{i}{8 \cdot G_{ef, floor} \cdot t_f \cdot L} \right)^{-1} \quad (9)$$

$$K_{wall} = \frac{q \cdot i}{2 \cdot \Delta_{wall}} = \left( \frac{1}{K_{AB}} + \frac{h^2}{\sum_{i=1}^n K_{V,i} x_i^2} + \frac{h}{G_{ef, wall} \cdot t_w \cdot l} \right)^{-1} \quad (10)$$

## 4. Parametric analysis: results

Figure 4 shows the deformed configuration of the CLT platform archetype for single-storey, three-storey, and five-storey buildings under the conditions of shear-wall stiffness S1, floor panel-to-panel connection stiffness  $K_{f-f} = 2$  N/mm, and floor-to-wall connection stiffness  $K_{f-w} = 3$  N/mm. The archetype dimensions are 10 meters transversally and 5 meters longitudinally.

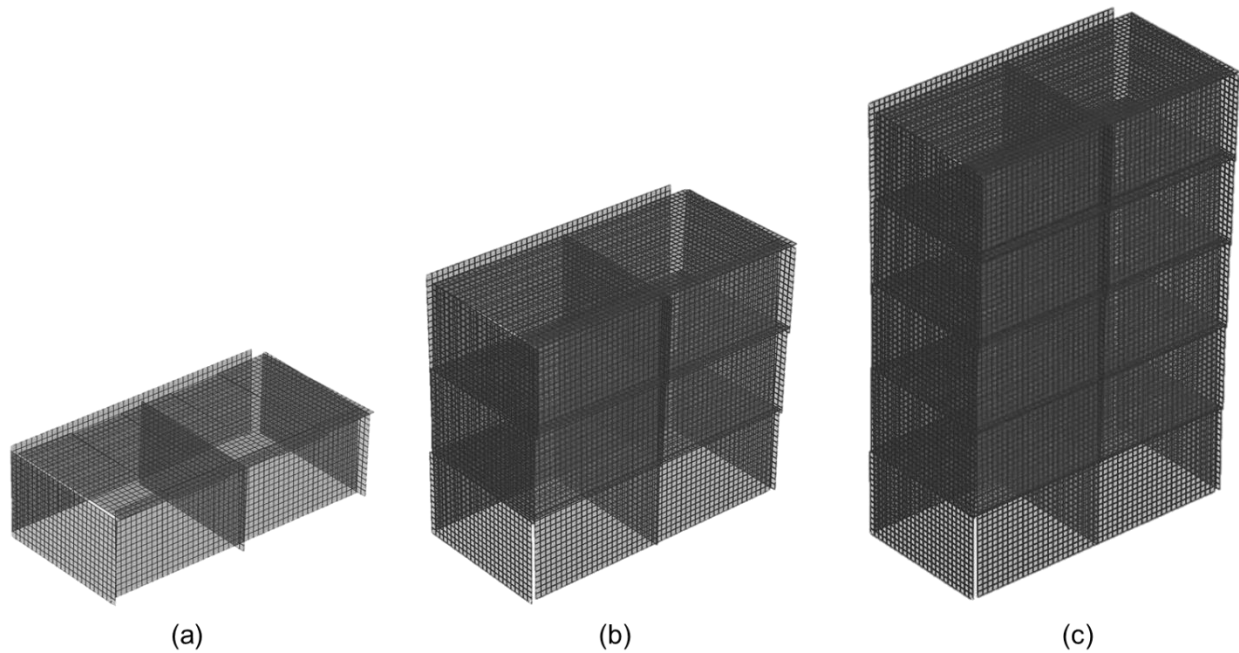


Figure 4: Deformed configuration of the numerical model of the CLT platform archetype: (a) single-storey, (b) three-storey, (c) five-storey.

Figure 5 plots  $\alpha_\delta$  as a function of the dimensionless distance ( $i/L$ ) between the central shear-wall and the two outer longitudinal shear-walls for floor-to-wall connection stiffnesses  $K_{f-w}$  of  $45 \text{ N/mm}^2$ . The cases with  $K_{f-w}$  of  $45 \text{ N/mm}^2$  are shown in the plot as they represent the cases with highest  $\alpha_\delta$  values, i.e., the cases where the floor's behaviour tends to flexible condition. The results reflect different combinations of floor panel-to-panel connection stiffnesses ( $K_{f-f}$ ) and shear-wall stiffnesses ( $S1, S5$ ). Within each graph, three curves are presented, corresponding to the number of storeys (one, three and five), focusing for each configuration on the storey with the greatest  $\alpha_\delta$  value.

An increasing trend of  $\alpha_\delta$  is observed with increasing  $i/L$  values, while  $\alpha_\delta$  decreases with increasing floor panel-to-panel connection stiffness ( $K_{f-f}$ ). Additionally,  $\alpha_\delta$  decreases as the number of storeys ( $N$ ) increases and rises with higher floor-to-wall connection stiffness ( $K_{f-w}$ ). For stiffness of the floor panel-to-panel connection  $K_{f-f} = 20 \text{ N/mm}^2$ , and number of storeys  $N > 1$ ,  $\varepsilon_V$  values below 10% are observed for  $K_{f-w} \leq 45 \text{ N/mm}^2$ ,  $i/L \geq 1.0$ , across all shear-wall stiffness.

The shear force discrepancy ( $\varepsilon_V$ ) on the central shear-wall is analysed, with results shown in Figure 6 for  $K_{f-w} = 45 \text{ N/mm}^2$ . The cases with  $K_{f-w}$  of  $45 \text{ N/mm}^2$  are shown in the plot as they represent the cases with highest  $\varepsilon_V$  values. The trends for  $\varepsilon_V$  are similar to those for  $\alpha_\delta$ , but the  $\varepsilon_V$  values are generally lower, ranging from 0 to 25%. For stiffness of the floor panel-to-panel connection  $K_{f-f} = 20 \text{ N/mm}^2$ , and number of storeys  $N > 1$ ,  $\varepsilon_V$  values below 10% are observed for  $K_{f-w} \leq 45 \text{ N/mm}^2$ ,  $i/L \geq 1.4$ , across all shear-wall stiffness.

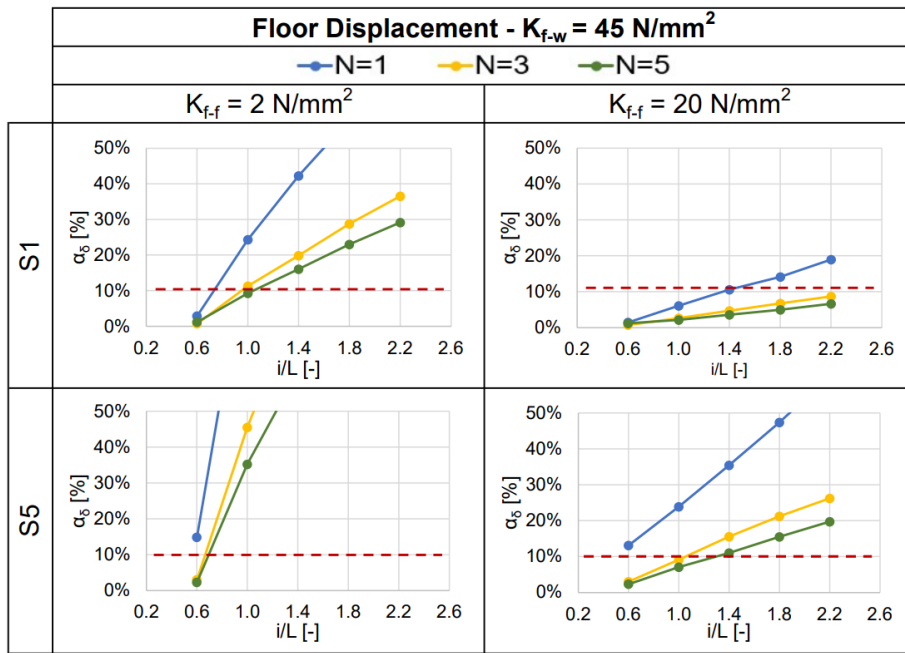


Figure 5: Maximum values of the parameter  $\alpha_\delta$ , plotted against the ratio  $i/L$ , in case of  $K_{f-w}=45$  N/mm<sup>2</sup>.

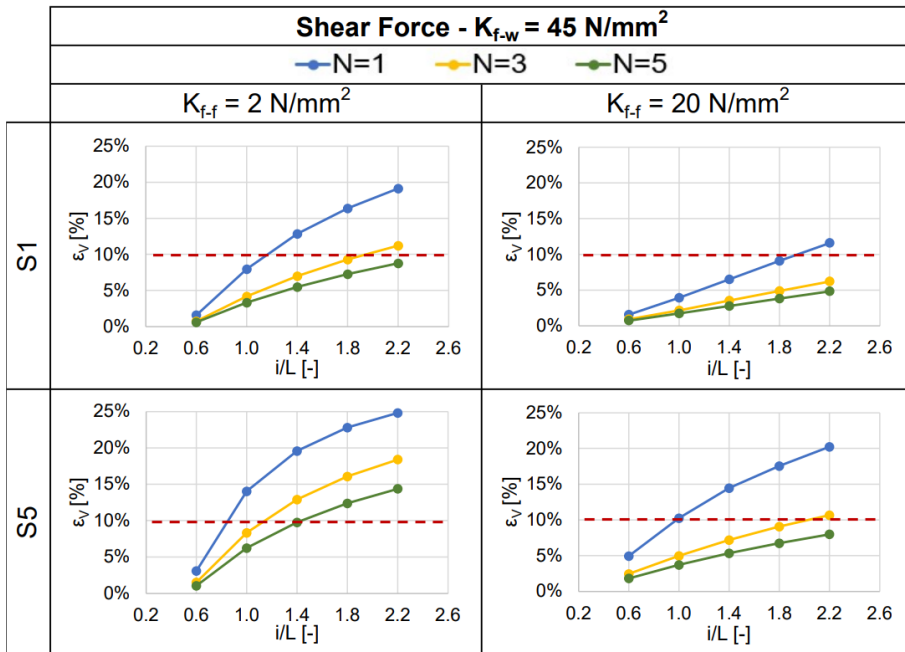


Figure 6: Maximum values of the parameter  $\epsilon_v$ , plotted against the ratio  $i/L$ , in case of  $K_{f-w}=45$  N/mm<sup>2</sup>.

The fundamental period discrepancy ( $\epsilon_T$ ) is thus examined, with results presented in Figure 7 as a function of  $i/L$  for  $K_{f-w} = 45$  N/mm<sup>2</sup>. The trends of  $\epsilon_T$  resemble those of  $\alpha_\delta$  and  $\epsilon_v$ . For  $K_{f-f} = 2$  N/mm<sup>2</sup>,  $\epsilon_T$  does not exceed 50%, while for  $K_{f-f} = 20$  N/mm<sup>2</sup>,  $\epsilon_T$  remains below 20%.  $\epsilon_T$  values under 10% are achieved for  $K_{f-f} \geq 20$  N/mm<sup>2</sup>,  $N > 1$ , and  $K_{f-w} \leq 45$  N/mm<sup>2</sup>, across all shear-wall stiffness and  $i/L$  values.  $\epsilon_T$  for  $K_{f-w} = 45$  N/mm<sup>2</sup> is consistently higher than for  $K_{f-w} = 3$  N/mm<sup>2</sup> and 15 N/mm<sup>2</sup>.



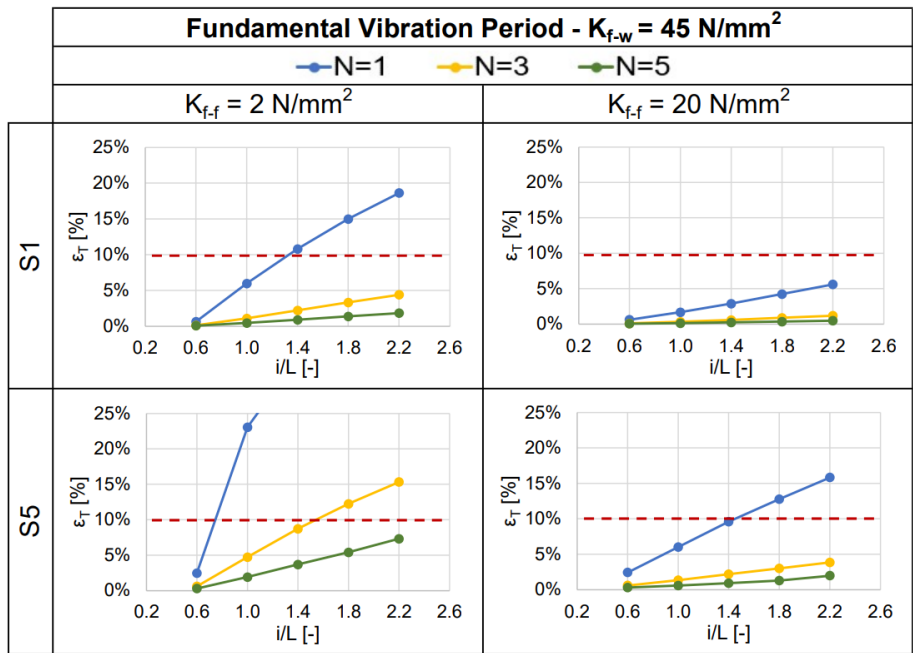


Figure 7: Maximum values of the parameter  $\epsilon_T$ , plotted against the ratio  $i/L$ , in case of  $K_{f-w}=45 \text{ N/mm}^2$ .

The influence of the stiffness ratio ( $\kappa$ ) between the floor and the shear-wall is also explored, with findings depicted in Figure 8, Figure 9 and Figure 10. The graphs show the results of the parametric analysis and regression equations that can be used to predict  $\alpha_\delta$ ,  $\epsilon_V$ , and  $\epsilon_T$  based on  $\kappa$  values.

The parameter  $\alpha_\delta$  shows a decreasing trend with increasing  $\kappa$ , as plotted in Figure 8. It can be observed that for  $\kappa \geq 10$ , and  $N > 1$ ,  $\alpha_\delta$  remains below 0.1 regardless of  $K_{f-w}$  values. A power regression equation ( $y = a \cdot \kappa^b$ ) was determined for these observations, with  $R^2$  values above 0.90 for  $K_{f-w} \geq 15 \text{ N/mm}^2$ , and around 0.8 for  $K_{f-w} = 3 \text{ N/mm}^2$ , indicating less accuracy due to the assumption of shear deformation dominating the floor stiffness (Equation (9)).

The shear force discrepancy ( $\epsilon_V$ ) shows a less pronounced decreasing trend with  $\kappa$ , as illustrated in Figure 9. The influence of  $K_{f-w}$  and building height (N) is significant, with  $\epsilon_V$  always below 10% for  $\kappa \geq 4$  and  $N > 1$ . The  $R^2$  values range from 0.55 to 0.80, indicating more data dispersion. The fundamental period discrepancy  $\epsilon_T$  exhibit trends similar to  $\epsilon_V$  but with less data dispersion, as shown in Figure 10. The  $R^2$  values range from 0.90 to 1.00. The discrepancies  $\epsilon_T$  remains below 10% for  $\kappa \geq 1$  and  $N > 1$ .

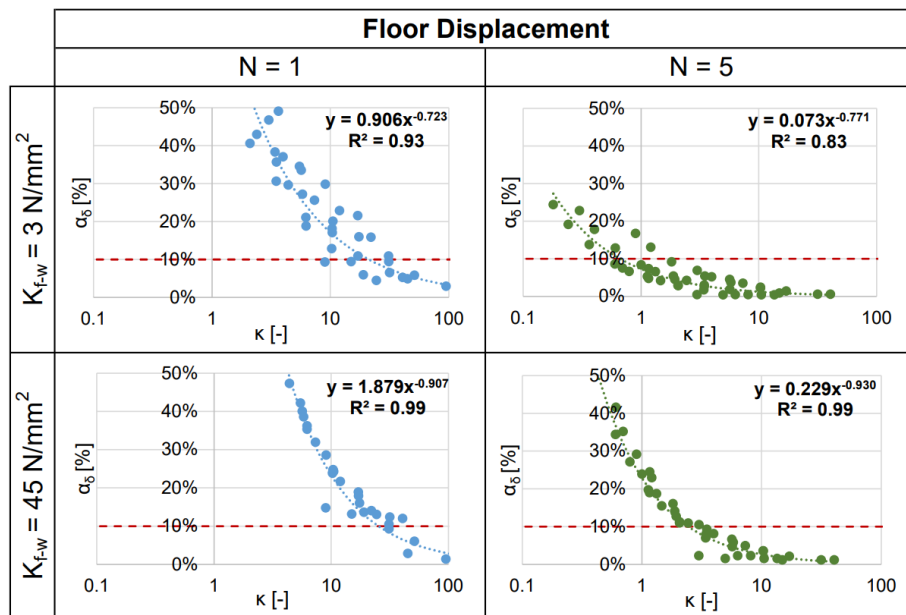


Figure 8: Maximum values of the parameter  $\alpha_\delta$ , plotted against the ratio  $\kappa$ .

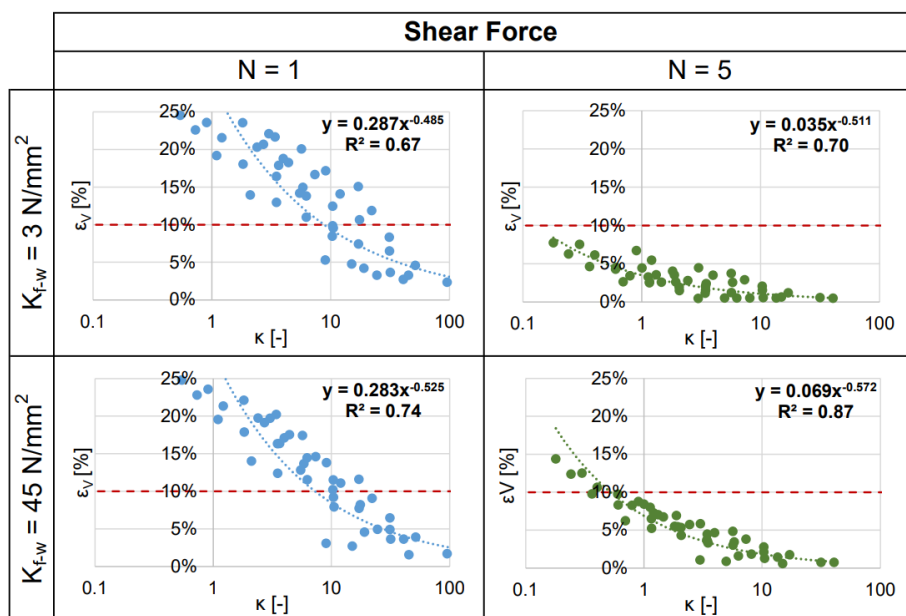


Figure 9: Maximum values of the parameter  $\epsilon_V$ , plotted against the ratio  $\kappa$ .

The results of the parametric analysis reveal that the structural behaviour of CLT floor diaphragms and shear walls is significantly influenced by the stiffness of floor-to-wall and panel-to-panel connections, building height, and the stiffness ratio between floors and walls. Increasing the stiffness of floor connections and the number of storeys generally reduces the displacement increase parameter ( $\alpha_\delta$ ) and discrepancies in shear force ( $\epsilon_V$ ) and fundamental period ( $\epsilon_T$ ). The stiffness ratio ( $\kappa$ ) is crucial, with in-plane behaviour towards the rigid condition observed for  $\kappa \geq 10$  and  $N > 1$ .

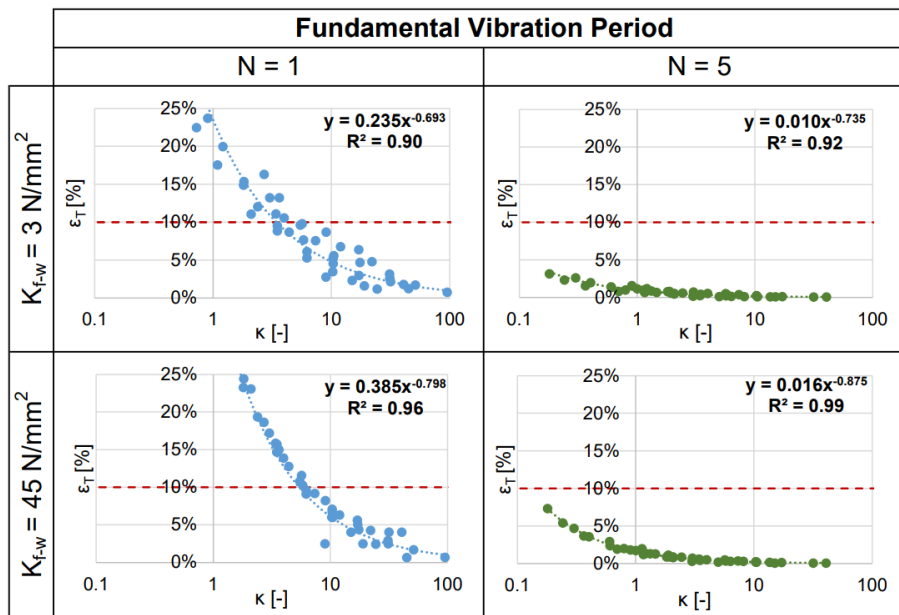


Figure 10: Maximum values of the parameter  $\epsilon_T$ , plotted against the ratio  $\kappa$ .

## 5. Rigid floor diaphragm conditions for the analysed archetypes

The results obtained from the parametric analysis enable to define the criteria under which CLT floors of the analysed archetypes can be considered rigid for linear seismic analyses.

Setting an upper limit for the floor displacement parameter  $\alpha_\delta$  at no more than 10%, according to Eurocode 8 (EN1998-1), and accepting maximum discrepancies of 10% for shear forces on the inner shear walls  $\epsilon_V$  and for the natural period of the archetype  $\epsilon_T$ , the conditions for rigid floor diaphragms can be expressed as reported below for single-storey and multi-storey archetypes.

For single-storey archetypes:

- $\epsilon_V \leq 10\%$ :  $K_{f-f} \geq 20 \text{ N/mm}^2$ ,  $K_{f-w} \leq 45 \text{ N/mm}^2$ , and  $i/L \leq 1.0$
- $\epsilon_T \leq 10\%$ :  $K_{f-f} \geq 20 \text{ N/mm}^2$ ,  $K_{f-w} \leq 45 \text{ N/mm}^2$ , and  $i/L < 1.4$
- $\alpha_\delta \leq 10\%$ :  $K_{f-f} \geq 20 \text{ N/mm}^2$ ,  $K_{f-w} \leq 45 \text{ N/mm}^2$ , and  $i/L < 0.6$

For multi-storey archetypes:

- $\epsilon_V \leq 10\%$ :  $K_{f-f} \geq 20 \text{ N/mm}^2$ ,  $K_{f-w} \leq 45 \text{ N/mm}^2$ , and  $i/L \leq 1.4$
- $\epsilon_T \leq 10\%$ :  $K_{f-f} \geq 20 \text{ N/mm}^2$ ,  $K_{f-w} \leq 45 \text{ N/mm}^2$ , and  $i/L \leq 2.2$
- $\alpha_\delta \leq 10\%$ :  $K_{f-f} \geq 20 \text{ N/mm}^2$ ,  $K_{f-w} \leq 45 \text{ N/mm}^2$ , and  $i/L \leq 1.0$ ;

The ratio ( $\kappa$ ) between floor stiffness ( $K_{\text{floor}}$ ) and shear-wall stiffness ( $K_{\text{wall}}$ ) further illustrates that, in multi-storey structures, when  $\kappa$  is greater than or equal to 10, both  $\alpha_\delta$  and discrepancies  $\epsilon_V$  and  $\epsilon_T$  remain under 10%. Therefore, the rigid floor condition for multi-storey structures can be expressed as  $\kappa = K_{\text{floor}}/K_{\text{wall}} \geq 10$ .

## 6. Conclusions

This paper presented a comprehensive numerical study on the in-plane stiffness of CLT floor diaphragms within CLT platform-type buildings, particularly under linear seismic analysis conditions. The study is based on the provisions from various international design codes, with a primary focus on Eurocode 8 (EN1998-1). A parametric analysis of a CLT platform archetype with regular geometry was conducted to identify critical geometrical and mechanical properties influencing the in-plane behaviour of CLT floor diaphragms.

In the analysis parameters such as the ratio between the distance of consecutive shear-walls and the floor span ( $i/L$ ), stiffness of floor panel-to-panel connections ( $K_{f-f}$ ), stiffness of floor-to-wall connections ( $K_{f-w}$ ), lateral stiffness of shear-walls ( $K_{wall}$ ), and the number of storeys ( $N$ ) were varied. The values of these parameters were chosen to reflect typical construction practices and were based on a state-of-the-art review. A significant focus was placed on the ratio ( $\kappa$ ) between the in-plane stiffness of the floor ( $K_{floor}$ ) and the lateral stiffness of the shear-wall ( $K_{wall}$ ).

The in-plane behaviour of CLT floors was evaluated by comparing numerical models where the floor was considered both with its actual in-plane deformability and rigid. The discrepancies in floor displacements ( $\alpha_\delta$ ), shear force distribution in shear-walls ( $\epsilon_V$ ), and the natural period of the structure ( $\epsilon_T$ ) were compared against threshold values from Eurocode 8.

It was found that the in-plane behaviour of the floor tends towards a rigid diaphragm condition with increasing  $K_{f-f}$  and the number of storeys  $N$ , and decreasing  $K_{f-w}$ ,  $i/L$ , and  $K_{wall}$ . An in-plane rigid behaviour with discrepancies in floor displacements below 10%, and shear force distribution and fundamental period discrepancies below 10%, was observed for  $K_{f-f} \geq 20 \text{ N/mm}^2$ ,  $K_{f-w} \leq 45 \text{ N/mm}^2$ ,  $i/L \leq 1.0$ , and  $N > 1$ .

The ratio  $\kappa = K_{floor}/K_{wall}$  proved to be an effective indicator of in-plane behaviour. The parametric analysis showed that an in-plane rigid behaviour, with all discrepancies below 10%, was consistently achieved when  $\kappa \geq 10$  and  $N > 1$ . This provides a straightforward condition for evaluating the in-plane behaviour of CLT floors in platform-type structures.

## 7. References

- ASCE (2017) American Society of Civil Engineers. ASCE/SEI 41-17: Seismic Evaluation and Retrofit of Existing Buildings.
- Ashtari S, Haukaas T, Lam F (2014) In-Plane Stiffness of Cross-Laminated Timber Floors. World Conf Timber Eng 1–10
- Barbosa AR, Rodrigues L, Sinha A, et al (2018) Numerical modeling of CLT diaphragms tested on a shake-table experiment. WCTE 2018 - World Conf Timber Eng
- Beirsto C, Gupta R, Miller TH (2022) Monotonic and Cyclic Behavior of CLT Diaphragms. Pract Period

- Struct Des Constr 27:1–14. [https://doi.org/10.1061/\(asce\)sc.1943-5576.0000658](https://doi.org/10.1061/(asce)sc.1943-5576.0000658)
- Bogensperger T, Moosbrugger T, Silly G (2010) Verification of CLT-plates under loads in plane. 11th World Conf Timber Eng 2010, WCTE 2010 1:231–240
- Brandner R, Dietsch P, Dröscher J, et al (2017) Cross laminated timber (CLT) diaphragms under shear : Test configuration, properties and design. Constr Build Mater 147:312–327. <https://doi.org/10.1016/j.conbuildmat.2017.04.153>
- D’Arenzo G, Casagrande D, Reynolds T, Fossetti M (2019) In-plane elastic flexibility of cross laminated timber floor diaphragms. Constr Build Mater 209:709–724. <https://doi.org/10.1016/j.conbuildmat.2019.03.060>
- EN1998-1 Eurocode 8 : Design of structures for earthquake resistance - Part 1: General rules, seismic actions and rules for buildings, 2013.
- Flatscher G (2017) Evaluation and approximation of timber connection properties for displacement-based simulation of CLT wall systems (working title),. Graz University of Technology
- Gavric I, Fragiaco M, Ceccotti A (2015) Cyclic behavior of typical screwed connections for cross-laminated ( CLT ) structures. Eur J Wood Wood Prod 179–191. <https://doi.org/10.1007/s00107-014-0877-6>
- Hossain A, Popovski M, Tannert T (2019) Group Effects for Shear Connections with Self-Tapping Screws in CLT. J Struct Eng 145:04019068. [https://doi.org/10.1061/\(asce\)st.1943-541x.0002357](https://doi.org/10.1061/(asce)st.1943-541x.0002357)
- Kode A, Amini MO, van de Lindt JW, Line P (2021) Lateral Load Testing of a Full-Scale Cross-Laminated Timber Diaphragm. Pract Period Struct Des Constr 26:04021001. [https://doi.org/10.1061/\(asce\)sc.1943-5576.0000566](https://doi.org/10.1061/(asce)sc.1943-5576.0000566)
- Line P, Nyseth S, Waltz N (2022) Full-Scale Cross-Laminated Timber Diaphragm Evaluation. I: Design and Full-Scale Diaphragm Testing. J Struct Eng 148:1–13. [https://doi.org/10.1061/\(asce\)st.1943-541x.0003308](https://doi.org/10.1061/(asce)st.1943-541x.0003308)
- Loss C, Frangi A (2017) Experimental investigation on in-plane stiffness and strength of innovative steel-timber hybrid floor diaphragms. Eng Struct 138:229–244. <https://doi.org/10.1016/j.engstruct.2017.02.032>
- Loss C, Hossain A, Tannert T (2018a) Simple cross-laminated timber shear connections with spatially arranged screws. Eng Struct 173:340–356. <https://doi.org/10.1016/j.engstruct.2018.07.004>
- Loss C, Rossi S, Tannert T (2018b) In-Plane Stiffness of Hybrid Steel–Cross-Laminated Timber Floor Diaphragms. J Struct Eng 144:04018128. [https://doi.org/10.1061/\(asce\)st.1943-541x.0002105](https://doi.org/10.1061/(asce)st.1943-541x.0002105)
- Moroder D (2016) Floor Diaphragms in multi-storey timber buildings
- Moroder D, Smith T, Pampanin S, et al (2015) Design of Floor Diaphragms in Multi-Storey Timber Buildings. Journal 23:
- Popovski M, Auclair SC, Chen Z (2023) Performance, analysis, and design of mass timber diaphragms
- Popovski M, Gavric I (2016) Performance of a 2-Story CLT House Subjected to Lateral Loads. J Struct Eng 142:1–12. [https://doi.org/10.1061/\(ASCE\)ST.1943-541X.0001315](https://doi.org/10.1061/(ASCE)ST.1943-541X.0001315)
- Xiong HB, Huynh A (2018) Mechanical behaviour of connections between CLT panels under monotonic and cyclic loading. IOP Conf Ser Earth Environ Sci 153:. <https://doi.org/10.1088/1755-1315/153/4/042014>
- Yin T, Zhang J, Wang Z, et al (2022) Shear performance of tongue-and-groove joints for CLT. Constr Build Mater 322:. <https://doi.org/10.1016/j.conbuildmat.2022.126449>

## DISCUSSION

**The paper was presented by G D'Arenzo**

*F Lam commented about complications in research on in-plane stiffness of CLT diaphragms including diaphragm aspect ratio, openings, supporting beams acting as tension ties, irregular diaphragm shape, and contribution of topping.*

*D Moroder received confirmation that different floor constructions and spacing of the fasteners were studied. He questioned how to define the stiffness of diaphragms in practice and how to quantify the influence of walls above the diaphragm.*

*G D'Arenzo agreed that these issues are complicated and confirmed that a maximum value in each story was calculated. D Moroder received confirmation that the analytical equations were used to estimate diaphragm stiffness.*

*G Doudak received confirmation that only one direction of the diaphragm was studied. G Doudak asked about the ratio of stiffness between wall and floor and received clarification of the value of  $k$  for single story structures. Also the diaphragm was considered rigid if  $k_{\text{floor}}/k_{\text{wall}} < 1$ .*

*A Frangi and G D'Arenzo discussed whether the diaphragm can be easily reached for conventional design of connections. A Frangi asked whether a differentiation between multi-storey and single-storey was necessary.*

*A Ceccotti and G D'Arenzo discussed where the two real cases were loaded. Also typical CLT building floors would usually be semi-rigid, whereas the results in this study showed closer to rigid diaphragm behaviour.*



# Design implications for Cross-Laminated Timber shear walls connected to perpendicular walls

Giuseppe D'Arenzo<sup>1</sup>, Elisabetta Maria Ruggeri<sup>2</sup>, Johannes Hummel<sup>3</sup>, Marinella Fossetti<sup>2</sup>, Werner Seim<sup>4</sup>

<sup>1</sup> Department of Civil and Architectural Engineering, Aarhus University, Denmark; <sup>2</sup> Faculty of Engineering and Architecture, University of Enna Kore, Italy; <sup>3</sup> EFG Beratende Ingenieure GmbH, Fuldaabrück, Germany; <sup>4</sup> Timber Structures and Building Rehabilitation, University of Kassel, Germany;

Keywords: Cross Laminated Timber, lateral load, seismic design, shear-wall

## 1. Introduction

In Cross-Laminated Timber (CLT) platform-type buildings, the CLT shear walls are interconnected through screws and metal brackets, forming vertical connections with other CLT wall elements and horizontal connections with CLT floor elements or foundations. Numerous studies in the last decade have investigated the lateral behaviour of CLT structures, primarily focusing on the role of the wall base connections, such as hold downs and angle brackets (Lukacs et al. 2019).

However, several experimental studies (Popovski and Gavric 2016; Yasumura et al. 2016) have demonstrated that, in addition to the wall base connections, the connections between CLT shear walls and surrounding structural elements influence the lateral behaviour of CLT buildings, contributing to the observed "box behaviour". Examples of these interactions are those between perpendicular walls and between walls and floors (Fragiacomo et al. 2011; Shahnewaz et al. 2020; Brown et al. 2021).

Despite the significant influence of these interactions on the lateral response of CLT buildings, no established methods currently exist to account for such contributions. Disregarding such interactions in structural analysis can lead to unreliable predictions and inaccuracies in the design process, particularly concerning lateral loads and seismic design considerations. This emphasises the need to establish a better understanding of the effects of these interactions on the lateral behaviour and structural design of CLT buildings.

This study focuses on the effect of the interaction between perpendicular walls in CLT platform-type buildings and discusses the design implications based on research conducted by the authors in the last three years. To quantify the effects of these interactions, the methodology adopted in the research involved the analysis of CLT shear walls in single wall and connected to perpendicular wall configurations. The investigation was conducted at wall level, by means of experimental tests, and at building level, by



means of numerical simulations. An analytical model for the prediction of the elastic stiffness and the load carrying capacity were proposed, representing a simplified tool to be used for structural design purposes.

## 2. Experimental tests

In the experimental tests, two configurations were analysed. The first configuration, called Single Shear Wall (SW), involved a single CLT shear wall subjected to lateral load (see Figure 1 (a)). The second configuration, called Shear Wall connected to a Perpendicular Wall (SW+PW), involved the same CLT shear wall subjected to lateral load but connected to a perpendicular wall positioned at the end of the shear wall (see Figure 1 (b)).

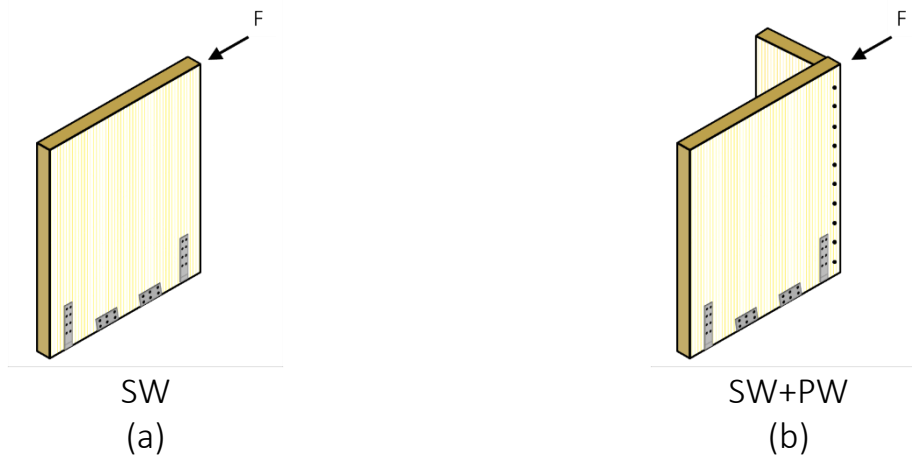


Figure 1: (a) Single shear wall; (b) shear wall connected to a perpendicular wall.

### 2.1. Materials

The experimental tests were conducted using CLT panels manufactured by Binderholz GmbH, as specified in their European Technical Assessment (ETA-Denmark 2017). Each panel was composed of five 20 mm thick wooden layers, resulting in a total thickness of 100 mm. The panels had an average modulus of elasticity ( $E_{\text{mean}}$ ) of 12,000 MPa and a shear modulus ( $G_{\text{mean}}$ ) of 690 MPa. To anchor the wall panels and resist overturning forces, WHT340 hold-downs (HDs) by Rothoblaas (ETA-Denmark 2015) were used, each fastened with twelve 4×60 mm annular ringed nails and anchored to the foundation with M16 bolts. For the shear forces, WBR90110 angle brackets (ABs) from Rothoblaas (ETA-Denmark 2015) were employed, fastened with thirteen 4×60 mm nails and connected to the foundation using M12 bolts. The perpendicular walls were connected to the shear walls using ten HBS 10×200 mm self-tapping screws by Rothoblaas (ETA-Denmark 2016).

### 2.2. Geometry Configuration and Test Set-Up

Three shear wall-perpendicular wall system geometries were explored in the study, all utilizing CLT panels with a height of 2.50 meters (Figure 2). The shear walls varied in

length to create height-to-length ( $h/b$ ) aspect ratios of 2.0, 1.0, and  $2/3$ , corresponding to lengths of 1.25 m, 2.50 m, and 3.75 m, respectively. The perpendicular walls were 0.50 m long. The shear walls were anchored to the foundation differently based on their length: the 1.25 m wall was anchored with two hold-downs and two angle brackets; the 2.50 m wall was anchored with two hold-downs and four angle brackets; the 3.75 m wall was anchored with two hold-downs and six angle brackets. The perpendicular walls were anchored with one hold-down close to the edge. Connections between shear walls and perpendicular walls were realized using self-tapping screws installed at 250 mm intervals, ensuring penetration into at least two layers of the perpendicular wall panel.

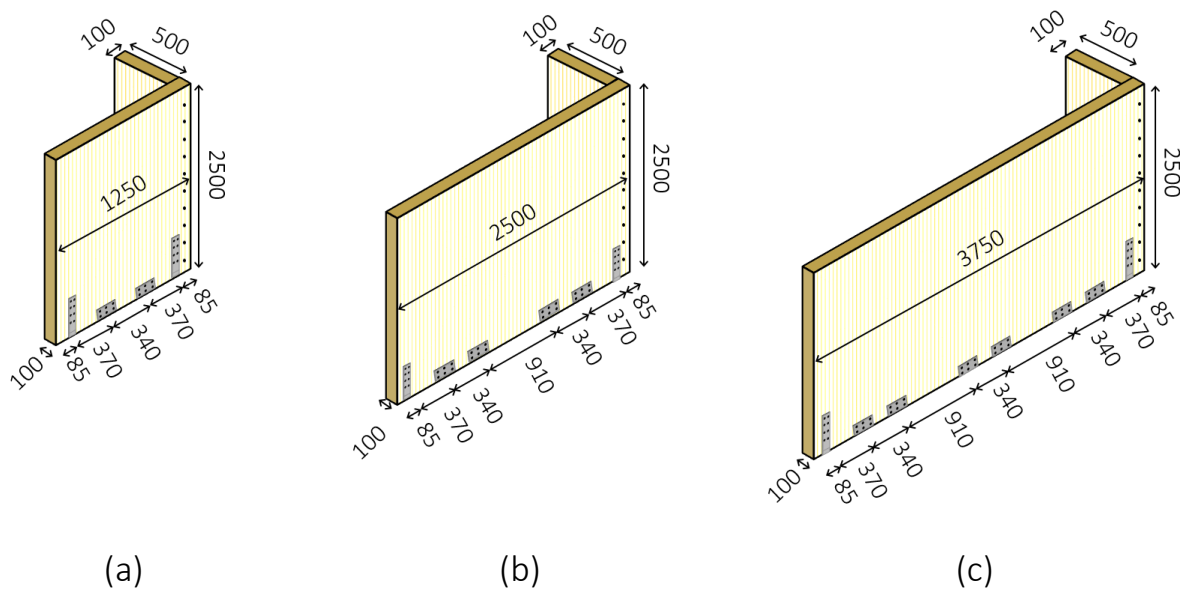


Figure 2: CLT wall systems geometries (dimensions in mm): (a)  $b=1.25$  m, (b)  $b=2.50$  m and (c)  $b=3.75$  m.

The experimental tests included twelve full-scale shear wall tests: six monotonic and six cyclic. Table 1 summarizes the ID test, the shear wall geometry, the number of connections, and the type of test for all analysed configurations.

Table 1 Test configurations: geometries size, number of connections and type of test.

ID test	Length [m]	Height [m]	N° HDs (12 nails)	N° ABs (13 nails)	Type of test
SW_1.25	1.25	2.50	2	2	Monotonic Cyclic
SW+PW_1.25	1.25	2.50	2+1	2	Monotonic Cyclic
SW_2.50	2.50	2.50	2	4	Monotonic Cyclic
SW+PW_2.50	2.50	2.50	2+1	4	Monotonic Cyclic
SW_3.75	3.75	2.50	2	6	Monotonic Cyclic
SW+PW_3.75	3.75	2.50	2+1	6	Monotonic Cyclic

### 2.3. Experimental Procedure

The tests were conducted at the L.E.D.A. Research Centre of the University of Enna “Kore” (Italy). Lateral loads were uniformly applied across the shear wall panels using a 300 kN hydraulic actuator connected to the top of the wall with HBS 10×200 mm self-tapping screws and an IPE 160 steel beam. Foundation conditions were simulated using HEB 220 steel beams drilled for hold-downs and angle brackets. Vertical and horizontal displacements were measured using linear variable displacement transducers (LVDTs). To measure uplift, three LVDTs were placed at the bottom corners of the shear wall and the perpendicular wall. An additional LVDT was positioned at the shear wall's bottom corner to measure horizontal base displacements. Another LVDT was placed on an external steel structure to measure the horizontal displacement at the top of the shear wall. The absolute horizontal displacement at the top of the shear wall was calculated by subtracting the horizontal displacement of the foundation beam from the top displacement of the shear wall. A robust steel frame system was utilized to prevent out-of-plane movements. No vertical load was applied.

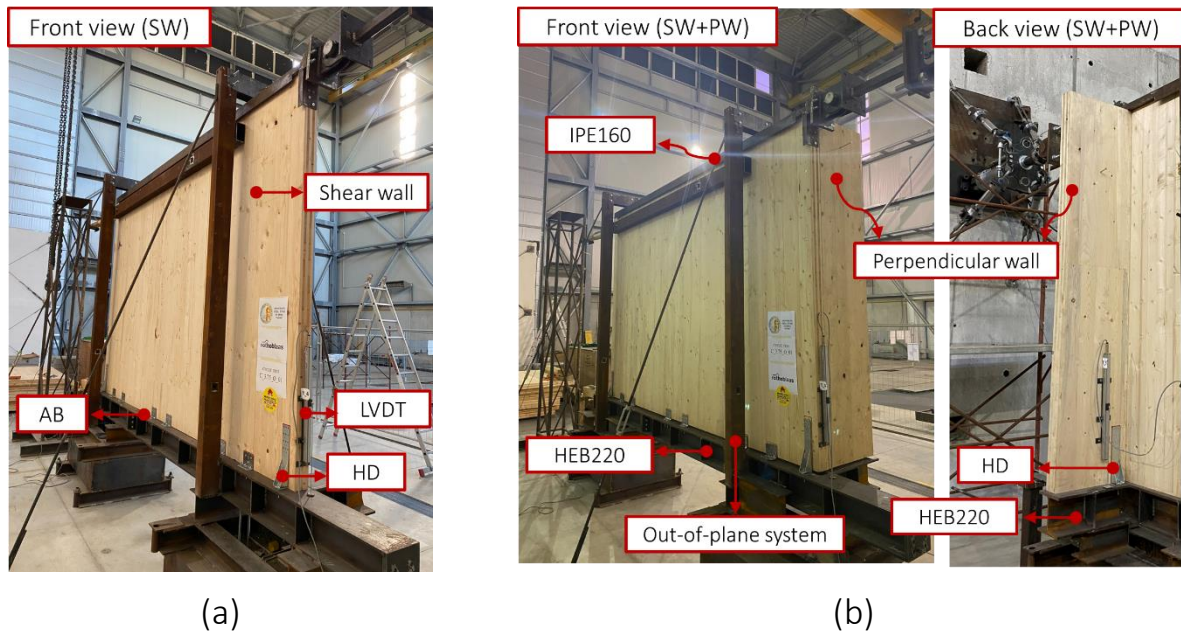


Figure 3: Test set-up: (a) SW configuration and (b) SW+PW configuration.

## 2.4. Load Protocols and Evaluation of Mechanical Parameters

The monotonic tests were conducted under displacement control, with a constant rate of 0.10 mm/sec, following EN594 (2011) provisions. Cyclic tests were performed at rates varying from 0.05 to 0.25 mm/sec, depending on displacement levels, according to EN12512 (2005). The cyclic load protocol was based on the expected yielding displacement and the aspect ratio of the shear walls. For shear walls with an aspect ratio of 2.0 ( $b = 1.25$  m), the yielding displacement was 10 mm, while for aspect ratios of 1.0 ( $b = 2.50$  m) and  $2/3$  ( $b = 3.75$  m), it was 5 mm, due to the lower expected yielding displacement in these cases.

The mechanical parameters of the CLT shear wall-perpendicular wall systems were evaluated according to EN12512 (2005) for both monotonic and cyclic tests. Parameters derived from the load-displacement curves of monotonic tests and the backbone curve of cyclic tests included elastic stiffness ( $K_{el}$ ), yielding load ( $F_y$ ), yielding displacement ( $d_y$ ), maximum load ( $F_{max}$ ), maximum displacement ( $d_{max}$ ), ultimate load ( $F_{ult}$ ), ultimate displacement ( $d_{ult}$ ), and ductility ( $\mu$ ).

## 2.5. Experimental Results

### 2.5.1. Deformation Mechanisms and Failure Modes

Different deformation mechanisms and failure modes were observed for the two configurations: SW and SW+PW. The state of the specimens at the end of the tests is shown in the photographic documentation in Figure 4. For shear walls with aspect ratios of 2.0 ( $b=1.25$  m) and 1.0 ( $b=2.50$  m), rocking was observed as the primary deformation mechanism. Conversely, for walls with an aspect ratio of  $2/3$  ( $b=3.75$  m), sliding

was predominant. The CLT panels exhibited a nearly rigid response, with deformations primarily occurring at the joints between the panels and wall base connections.

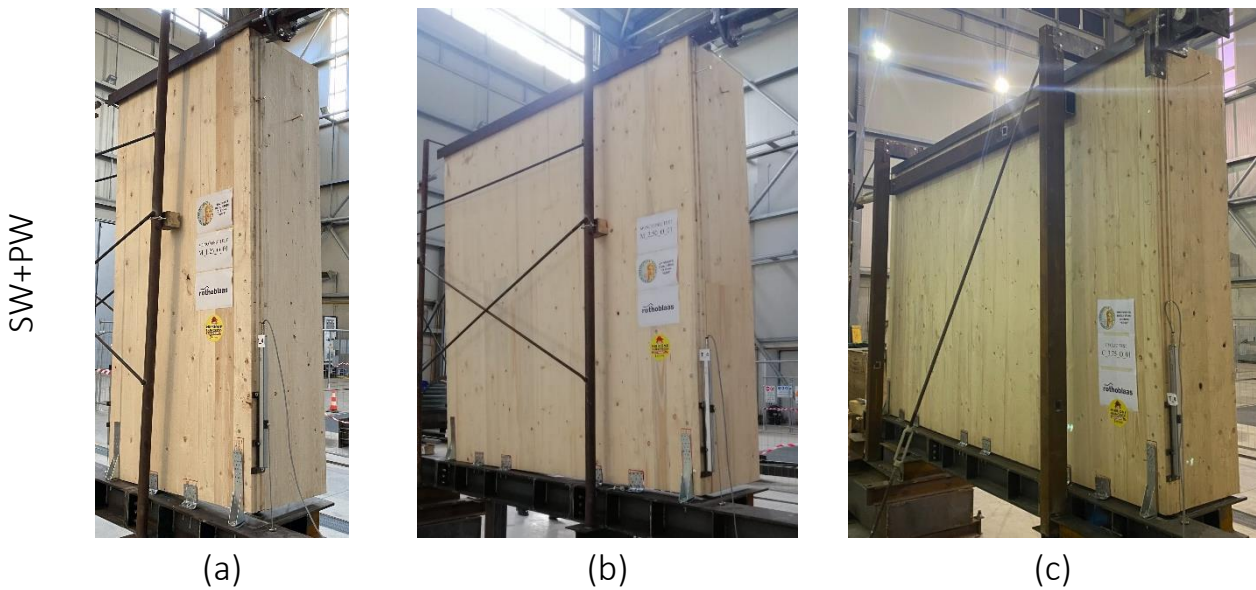


Figure 4: Photos of the specimens at the end of the tests: (a)  $b=1.25$  m, (b)  $b=2.50$  m and (c)  $b=3.75$  m.

Similar deformation and failure mechanisms at the base connections were exhibited by both configurations SW and SW+PW. Deformations in the hold-downs were observed, and failures were primarily attributed to the failure of nails. This failure involved the formation of plastic hinges in the nails and embedment of the wood (Figure 5 (a)). For angle brackets, failures occurred in the nails, causing plastic hinges, or in the bolts, leading to plastic deformation in the metal bracket (Figure 5 (c) and Figure 5 (d)).

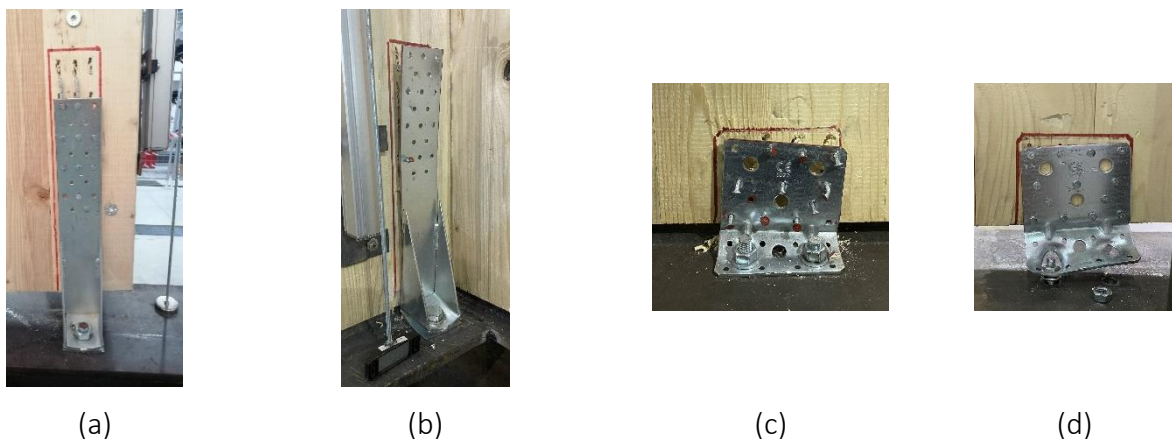


Figure 5: Photos of the connection failures: (a) HD of shear wall, (b) HD of perpendicular wall, (c) ABs of shear wall with failure in the nails and (d) in the horizontal flange.

The hold-downs of the perpendicular walls also engaged in the resisting mechanism of the SW+PW systems, exhibiting similar failure modes to those of the shear walls (Figure

5 (b)). No failure and limited deformation were shown by the wall-to-wall connections, allowing the perpendicular walls to fully engage and activate their hold-downs.

### ***2.5.2. Load-Displacement Curves and Mechanical Parameters***

The load-displacement curves from monotonic tests and hysteresis loops from cyclic tests for the SW and SW+PW configurations are presented in Figure 6. Close alignment can be observed between the cyclic test results and the monotonic test results. Symmetrical hysteresis loops, typical of CLT shear walls, are shown by the SW configuration, while asymmetric loops, indicating different behaviours for positive and negative displacements due to the non-uniform distribution of connections at the base, are exhibited by the SW+PW configuration.

Table 2 and Table 3 present the mechanical parameters from the monotonic and cyclic tests, respectively. The results show that the presence of a perpendicular wall improves the lateral performance of the shear wall in terms of strength.

Increased lateral stiffness ( $\Delta K_{el}$ ), load-bearing capacity ( $\Delta F_{max}$ ), and deformation capacity ( $d_{ult}$ ) were exhibited by the SW+PW configuration in comparison to the SW configuration. Specifically, the percentage increases in  $\Delta K_{el}$ , calculated considering both monotonic and cyclic tests in the positive displacement range, were +5%, +40%, and +29% for wall lengths of 1.25 m, 2.50 m, and 3.75 m, respectively. Similarly,  $\Delta F_{max}$  increased by +70%, +41%, and +30%, and  $d_{ult}$  by +59%, +25%, and +19%, for the respective wall lengths (Table 4).



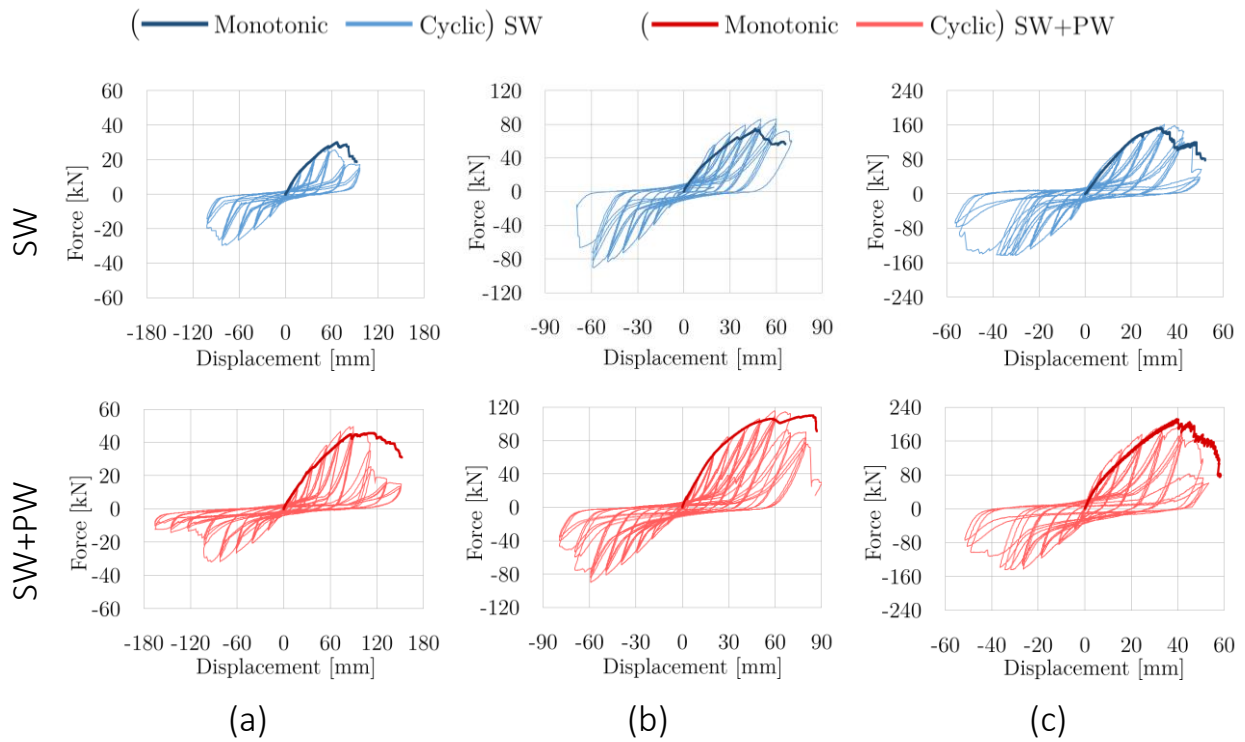


Figure 6: Comparison of the hysteresis loops and the load-displacement curves: (a)  $b=1.25$  m, (b)  $b=2.50$  m and (c)  $b=3.75$  m.

Table 2 Mechanical parameters evaluated from the load-displacement curves of monotonic tests.

ID test	$K_{el}$ [kN/mm]	$F_y$ [kN]	$d_y$ [mm]	$F_{max}$ [kN]	$d_{max}$ [mm]	$F_{ult}$ [kN]	$d_{ult}$ [mm]	$\mu$ [-]
SW_1.25	0.72	26.37	36.39	30.05	66.81	24.04	82.40	2.26
SW+PW_1.25	0.68	42.05	60.45	45.80	112.00	36.64	144.06	2.38
SW_2.50	2.28	67.67	28.03	74.46	46.41	59.57	64.0	2.38
SW+PW_2.50	3.19	91.69	27.66	110.19	83.84	88.16	86.81	3.14
SW_3.75	6.95	140.45	20.25	153.26	32.00	122.61	38.00	1.88
SW+PW_3.75	7.44	195.74	25.21	212.16	40.00	169.73	50.80	2.14

Table 3 Mechanical parameters evaluated from the backbone curves of the cyclic tests.

ID test	Displ	$K_{el}$	$F_y$	$d_y$	$F_{max}$	$d_{max}$	$F_{ult}$	$d_{ult}$	$\mu$
	.	[kN/mm]	[kN]	[mm]	[kN]	[mm]	[kN]	[mm]	[-]
SW_1.25	(+)	0.62	24.00	37.00	26.02	55.3	22.0	78.0	2.11
	(-)	0.49	-26.60	-50.30	-29.60	-82.0	-23.7	-94.5	1.88
SW+PW_1.25	(+)	0.73	46.60	63.90	49.50	85.2	39.6	111.0	1.73
	(-)	0.69	-26.90	-40.60	-32.00	-93.0	-29.0	-102.0	2.51
SW_2.50	(+)	2.46	79.60	33.20	85.90	49.9	69.9	69.9	2.10
	(-)	1.99	-85.10	-42.70	-90.00	-59.4	-72.0	-65.0	1.52
SW+PW_2.50	(+)	3.47	96.60	26.90	115.70	59.9	92.6	81.0	3.00
	(-)	1.99	-85.10	-42.73	-90.06	-59.36	-72.05	-75.0	1.76
SW_3.75	(+)	7.43	141.20	17.95	161.50	34.46	129.2	45.0	2.50
	(-)	9.43	-114.00	-12.00	-141.50	-31.4	-113.2	-52.0	4.33
SW+PW_3.75	(+)	11.09	160.80	13.44	195.90	33.25	156.7	48.00	3.57
	(-)	14.41	-100.00	-7.70	-144.10	-34.05	-115.3	-39.66	5.15

Table 4 Increments of the lateral performance.

b	$\Delta K_{el}$	$\Delta F_{max}$	$\Delta d_{ult}$
[m]	[%]	[%]	[%]
1.25	+5%	+70%	+59%
2.50	+40%	+41%	+25%
3.75	+29%	+30%	+19%

### 3. Analytical models

This section presents the analytical models used for calculating the lateral stiffness and load-bearing capacity of CLT shear walls connected to perpendicular walls and validates these models with experimental results. The mechanical models are enhancements of those proposed by Ruggeri et al. (2022), incorporating vertical reactions of the angle brackets ( $K_{AB,v}$ ) and panel deformations ( $\delta_{shear}$  and  $\delta_{bend}$ ) in stiffness calculations (elastic model), as well as the vertical reaction of the angle brackets ( $R_{AB,v}$ ) and horizontal reaction of the hold-downs of the shear wall ( $R_{HD,h,SW}$ ) in load capacity calculations (load capacity model). These models are applicable to CLT shear walls anchored with one hold-down per corner, angle brackets along the base, and perpendicular walls with one hold-down. The elastic model and the load capacity model are visually represented in Figure 7.



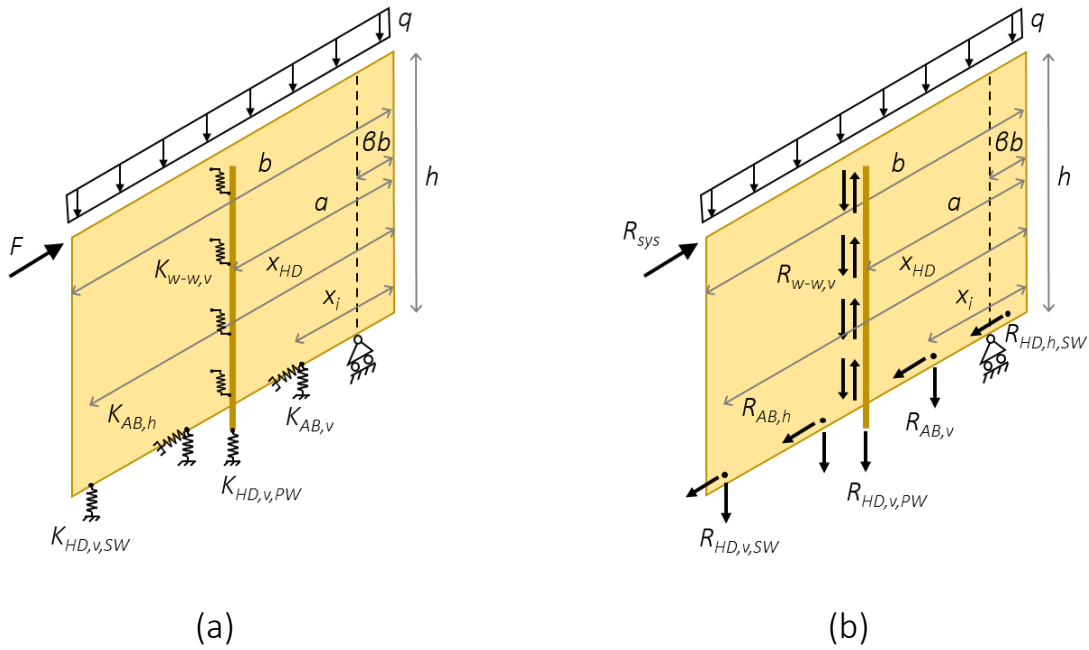


Figure 7: Mechanical system of CLT shear wall connected to a perpendicular wall: (a) elastic stiffness model and (b) plastic load capacity model.

### 3.1. Elastic model

The elastic model calculates the lateral stiffness of a one-story CLT shear wall-perpendicular wall system subjected to horizontal ( $F$ ) and vertical ( $q$ ) loads by considering four displacement contributions: rocking ( $\delta_{rock}$ ), sliding ( $\delta_{slid}$ ), bending ( $\delta_{bend}$ ), and shear ( $\delta_{shear}$ ), as shown in Equation (1). The rocking displacement depends on the vertical stiffness of the wall base connections and wall geometry, and can be calculated using Equation (2). Vertical stiffness contributions from the perpendicular wall ( $K_{PW}$ ) are considered in Equation (3), combining the hold-down of the perpendicular wall ( $K_{HD,v,PW}$ ) and wall-to-wall connections ( $K_{w-w,v}$ ) in an in-series configuration. Sliding displacement, governed by the number and horizontal stiffness of the angle brackets ( $K_{AB,h}$ ), is calculated using Equation (4). Panel deformations, involving bending ( $\delta_{bend}$ ) and shear ( $\delta_{shear}$ ), depend on the panel's elastic properties and internal structure, and can be calculated using Equations (5b). The lateral stiffness of the system ( $K_{sys}$ ) is determined as the ratio of the applied force ( $F$ ) to the total displacement ( $\delta_{sys}$ ) (Equation (6)).

$$\delta_{sys} = \delta_{rock} + \delta_{slid} + \delta_{bend} + \delta_{shear} \tag{1}$$

$$\delta_{rock} = \frac{\left[ Fh - qb^2 \left( \frac{1}{2} - \beta \right) \right] h}{\left[ K_{HD,v,SW} (x_{HD} - \beta b)^2 + K_{AB,v} \sum_{i=1}^{n_{AB}} (x_i - \beta b)^2 + K_{PW} (a - \beta b)^2 \right]} \tag{2}$$

$$K_{PW} = \left( \frac{1}{K_{HD,v,PW}} + \frac{1}{n_{w-w}K_{w-w,v}} \right)^{-1} \quad (3)$$

$$\delta_{slid} = \frac{F}{n_{AB}K_{AB,h}} \quad (4)$$

$$\delta_{bend} = \frac{Fh^3}{3E_{eff,v}I} \quad \delta_{shear} = 1.2 \frac{Fh}{G_{eff}A} \quad (5a) \quad (5b)$$

$$K_{sys} = \frac{F}{\delta_{sys}} \quad (6)$$

### 3.2. Load capacity model

The load capacity model determines the lateral load-bearing capacity of a CLT shear wall-perpendicular wall system subjected to horizontal (F) and vertical (q) loads as the minimum of the rocking capacity ( $R_{rock,sys}$ ) and sliding capacity ( $R_{slid,sys}$ ) (Equation (7)). Rocking capacity can be calculated using Equation (8), incorporating the vertical strength of the shear wall hold-down ( $R_{HD,v,SW}$ ), angle brackets ( $R_{AB,v}$ ), and perpendicular wall contributions ( $R_{PW}$ ) using Equation (9). Sliding capacity, derived from horizontal equilibrium, is calculated using Equation (10), considering the horizontal strength of the angle brackets ( $R_{AB,h}$ ) and hold-downs of the shear wall ( $R_{HD,h,SW}$ ).

$$R_{sys} = \min(R_{rock,sys}; R_{slid,sys}) \quad (7)$$

$$R_{rock,sys} = R_{HD,v,SW} \frac{x_{HD} - \beta b}{h} + \frac{qb^2}{h} \left( \frac{1}{2} - \beta \right) + R_{AB,v} \sum_{i=1}^{n_{AB}} \frac{x_i - \beta b}{h} + R_{PW} \frac{a - \beta b}{h} \quad (8)$$

$$R_{PW} = \min \left\{ \begin{array}{l} R_{HD,v,PW} \\ n_{w-w} R_{w-w,v} \end{array} \right. \quad (9)$$

$$R_{slid,sys} = n_{AB} R_{AB,h} + n_{HD,SW} R_{HD,h,SW} \quad (10)$$

### 3.3. Validation

The analytical models were validated against experimental results considering the mechanical properties of the wall base and the wall-to-wall connections investigated by Gavric et al. (2015a) and Gavric et al. (2015b). In these studies, hold-downs and angle

brackets under tension and shear loads, and wall-to-wall connections with self-tapping screws were tested. Stiffness values from European Technical Assessment (ETA-Denmark 2015) were used for the vertical stiffness of hold-downs, taking into account the different number of nails through a linear proportion factor based on the number of nails. In the elastic model validation, values of  $E_0$ ,  $E_{90}$ , and  $G_0$  equal to 12000 MPa, 370 MPa and 690 MPa, respectively, were used. These values were used for the calculation of the effective elastic and shear moduli. The system geometry and connector positions were according to Figure 2, with the factor  $\beta$  set to 10%. The values of stiffness and strength used for the analytical-experimental validation are given in Table 5 and Table 6, following the notation adopted in the current study.

Table 5 Stiffness properties of the connections and elastic properties of the CLT panels considered in the elastic model.

$K_{HD,v,SW}$	$K_{AB,v}$	$K_{AB,h}$	$K_{w-w,v}$	$K_{HD,v,PW}$	$E_{eff,v}$	$G_{eff}$
[kN/mm]	[kN/mm]	[kN/mm]	[kN/mm]	[kN/mm]	[MPa]	[MPa]
3.44	2.53	2.09	1.49	3.44	7348.0	596.2

Table 6 Strength properties of the connections considered in the capacity model.

$R_{HD,v,SW}$	$R_{HD,h,SW}$	$R_{AB,v}$	$R_{AB,h}$	$R_{w-w,v}$	$R_{HD,v,PW}$
[kN]	[kN]	[kN]	[kN]	[kN]	[kN]
48.33	9.98	23.47	31.73	7.54	48.33

The analytical-experimental comparison showed reasonable agreement in terms of lateral stiffness and load-bearing capacity. Figure 8 presents this comparison, with load-displacement curves from monotonic and cyclic tests, and analytical predictions. The analytical models showed higher accuracy for load capacity predictions, with an average error of 4.23%, and lower accuracy for stiffness predictions, with an average error of 16.50%. The discrepancies in stiffness predictions can be attributed to the higher variability of connection stiffness properties compared to their strength counterparts. Overestimations of lateral capacity may result from the assumption that all angle brackets are engaged at full capacity under tensile loads. The differences observed in stiffness and strength predictions are typical for comparisons between mechanical models and experimental tests of complex systems and are considered within reasonable bounds. Despite the complexities arising from timber heterogeneity, connection variability, non-linear connection responses, and localized timber plastic deformations, the analytical models provide a reliable estimation of the mechanical properties of CLT shear wall-perpendicular wall systems.

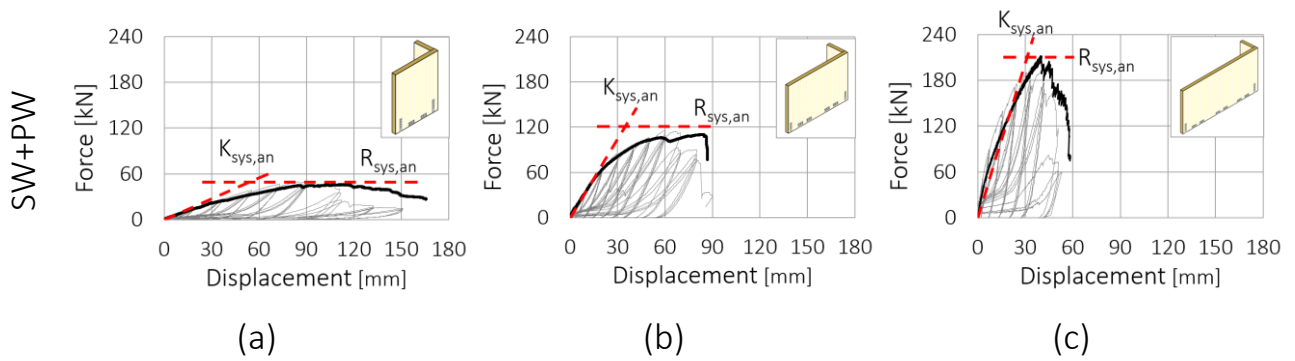


Figure 8: Analytical-experimental comparison in terms of stiffness and lateral capacity of the systems in case of SW+PW configuration: (a)  $b=1.25$  m, (b)  $b=2.50$  m, (c)  $b=3.75$  m.

## 4. Numerical simulations

### 4.1. Building description

Numerical simulations were conducted to investigate the effects of the interaction between perpendicular walls in CLT buildings. A CLT platform-type building with a rectangular plan and a shear wall and perpendicular wall configuration was considered for the analyses.

Figure 9 illustrates the floor plan of the one-storey CLT building considered for the analysis, including the distribution of its shear walls and base connections. Each shear wall measures 2.5 meters in length and 3.0 meters in height. The floor plan replicates that used in Hummel (2017), with the addition of two perpendicular walls connected to the central shear walls.

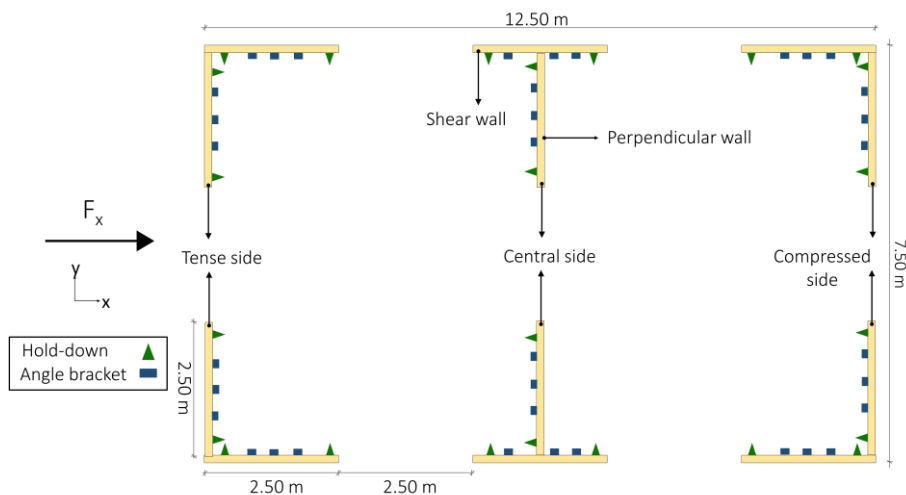


Figure 9: Floor plan of the one-storey CLT building and distribution of the wall base connections.

The CLT walls are anchored to the foundation using two hold-downs positioned at the wall ends and three angle brackets distributed along the wall lengths. These hold-

downs and angle brackets have the same mechanical properties as those of the hold downs and angle brackets tested by Gavric et al. (2015a). Wall-to-wall connections are spaced at 300 mm intervals, and have the same mechanical properties of the wall-to-wall connections tested by Gavric et al. (2015b). Floor-to-wall connections, with the same stiffness in the in-plane x and y directions and a spacing of 300 mm, are considered based on Gavric et al. (2015b).

As depicted in Figure 9, three distinct positions of the perpendicular walls relative to the shear walls are examined: perpendicular wall on the tense side of the shear wall, perpendicular wall at the centre of the shear wall, and perpendicular wall on the compressed side of the shear wall. To assess the effects of interactions between perpendicular walls, the reference one-storey CLT building is analysed in two configurations: the shear wall configuration (SW), where the perpendicular walls are not interconnected, and the shear wall plus perpendicular wall configuration (SW+PW), where the perpendicular walls are connected using wall-to-wall connections.

#### **4.2. Numerical model**

The three-dimensional numerical model, depicted in Figure 10, was developed to simulate the interaction between perpendicular walls and shear walls in a typical one-storey CLT building. This model incorporates shear walls and perpendicular walls complete with their respective base hold-downs and angle brackets, along with wall-to-wall connections and floor-to-wall connections. The CLT panels were modelled as shell elements with elastic behaviour taken from the SAP2000 library. Hold-downs were modelled as 1-joint links with multilinear elastic behaviour in the vertical direction, in order to simulate the elastic-plastic behaviour of the hold down for tensile loads and the rigid behaviour for compressive forces, due to the wall-to-foundation contact. Angle brackets were modelled as 1-joint links with multilinear elastic behaviour in the horizontal direction, in order to simulate the elastic-plastic behaviour of the angle brackets for shear loads. Wall-to-wall connections are represented by a series of 2-joint multilinear elastic links exhibiting elastic-plastic behaviour in the vertical direction, linking the nodes of the shear walls to those of the perpendicular walls. Conversely, floor-to-wall connections are modelled using a series of 2-joint linear elastic links characterized by elastic behaviour in the x and y directions of the floor plane. The floor was modelled as a rigid diaphragm to distribute horizontal loads to the walls. The lateral load was applied at floor level, and nonlinear static analyses were conducted to reproduce the elastic-plastic behaviour of the building. No vertical load was applied.

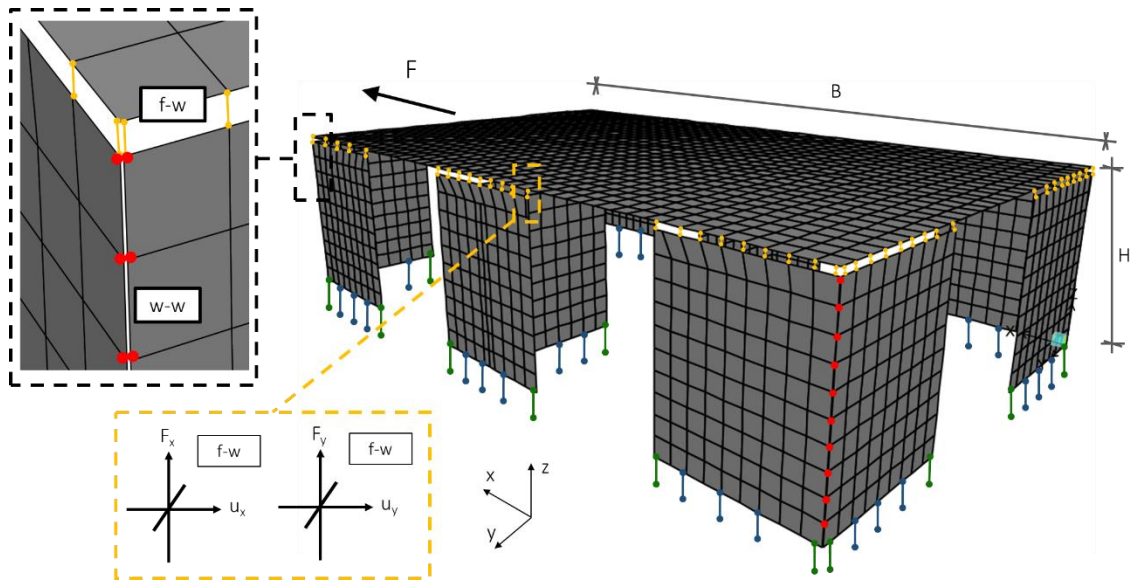


Figure 10: Three-dimensional numerical model of one-storey CLT building developed in SAP2000.

### 4.3. Numerical results

To assess the validity of the elastic and plastic models outlined in sections 3.1 and 3.2 in capturing the interactions between perpendicular walls in a building system, their results were compared with those obtained from the three-dimensional numerical model described in section 4.2.

This comparison involved evaluating the overall response of the reference building detailed in section 4.1, focusing on both lateral stiffness and lateral capacity. The shear wall-perpendicular wall systems within the reference building were considered to behave in parallel, allowing for the analytical calculation of the global lateral stiffness and capacity of the building as the sum of the individual systems' properties.

Table 7 presents the global lateral stiffness and capacity values for the shear wall (SW) and shear wall plus perpendicular wall (SW+PW) building configurations. The comparison between analytical and numerical models in Table 7 reveals minimal differences, below 2%, demonstrating the accuracy of the analytical models in predicting the effects of perpendicular wall interactions within a one-storey CLT building.

Table 7 Global Lateral Properties of the Reference CLT Building.

	SW		SW+PW	
	Analytical	Numerical	Analytical	Numerical
$K_{building}$ [kN/mm]	17.42	17.43	22.23	22.22
$R_{building}$ [kN]	202.30	203.62	303.45	301.41

Figure 11 illustrates the load-displacement curves obtained from the three-dimensional numerical model for the two building configurations analysed. The figure shows the increase in both lateral stiffness and capacity when perpendicular walls and wall-to-wall connections are considered in the numerical modelling. Specifically, the lateral stiffness increases by 28%, while the capacity increases by 48% in the SW+PW building

configuration. In this configuration, the system's capacity is primarily governed by the hold-downs of both the shear walls and perpendicular walls, whereas in the SW configuration, it is governed solely by the hold-downs of the shear walls.

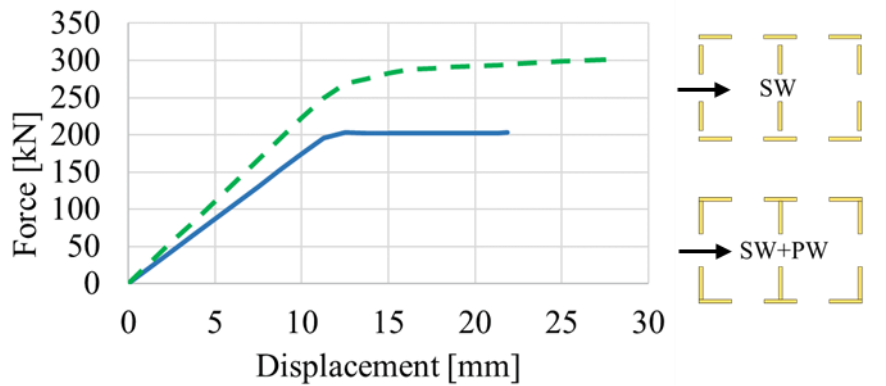


Figure 11: Load displacement curves obtained from the three-dimensional numerical model of the two CLT building configurations, SW and SW+PW.

## 5. Design implications and concluding remarks

The outcomes of the study can be summarized in three main design implications.

(I) When shear walls and perpendicular walls are interconnected, the lateral stiffness, and the load carrying capacity of CLT buildings increase due to the interaction between shear walls and perpendicular walls.

(II) The effects of the interactions between perpendicular walls should be considered in structural analyses, including numerical simulations and calculation models. This also applies to seismic design, for which overdesign of the connections between the perpendicular walls may be required. Disregarding this interaction when the perpendicular walls are interconnected can lead to inaccuracies in the design process and unforeseen failure mechanisms.

(III) If the connections between the perpendicular walls are properly designed, the interaction between perpendicular walls can be exploited to increase the overturning capacity of the walls, overcoming limitations related to the capacity of the hold down connections, which often represent a limiting factor in the design of multi-storey CLT buildings.

The significance of considering the impact of perpendicular walls on the lateral behaviour of CLT structures is underscored in this paper, along with the necessity of incorporating these interactions into the design process. Although the conclusions are specific to the conditions examined in this project, the insights gained from the study may prove valuable to engineers and architects in designing CLT structures that are more resilient and efficient in withstanding lateral loads and seismic events.

## 6. References

- Brown JR, Li M, Palermo A, et al (2021) Experimental Testing of a Low-Damage Post-Tensioned C-Shaped CLT Core-Wall. *J Struct Eng* 147:04020357. [https://doi.org/10.1061/\(asce\)st.1943-541x.0002926](https://doi.org/10.1061/(asce)st.1943-541x.0002926)
- EN12512 (2005) Timber structures. Test methods. Cyclic testing of joints made with mechanical fasteners. Brussels, Belgium: CEN
- EN594 (2011) Timber structures. Test methods. Racking strength and stiffness of timber frame wall panels, Brussels Belgium: CEN, European Committee for Standardization
- ETA-Denmark (2017) ETA-06/0009. European Technical Assessment. Solid wood slab element to be used as a structural element in buildings.
- ETA-Denmark (2015) ETA-11/0086. European Technical Assessment. Three-dimensional nailing plate (Angle brackets and hold-downs for timber-to-timber or timber-to-concrete or steel connections).
- ETA-Denmark (2016) ETA-11/0030. European Technical Assessment. Screws for use in timber construction
- Fragiacomo M, Dujic B, Sustersic I (2011) Elastic and ductile design of multi-storey crosslam massive wooden buildings under seismic actions. *Eng Struct* 33:3043–3053. <https://doi.org/10.1016/j.engstruct.2011.05.020>
- Gavric I, Fragiaco M, Ceccotti A (2015a) Cyclic behaviour of typical metal connectors for cross-laminated ( CLT ) structures. *Mater Struct* 48:1841–1857. <https://doi.org/10.1617/s11527-014-0278-7>
- Gavric I, Fragiaco M, Ceccotti A (2015b) Cyclic behavior of typical screwed connections for cross-laminated ( CLT ) structures. *Eur J Wood Wood Prod* 179–191. <https://doi.org/10.1007/s00107-014-0877-6>
- Hummel J (2017) Displacement-based seismic design for multi-storey cross laminated timber buildings. Doctoral Thesis, Kassel University Press GmbH
- Lukacs I, Björnfort A, Tomasi R (2019) Strength and stiffness of cross-laminated timber (CLT) shear walls: State-of-the-art of analytical approaches. *Eng Struct* 178:136–147. <https://doi.org/10.1016/j.engstruct.2018.05.126>
- Popovski M, Gavric I (2016) Performance of a 2-Story CLT House Subjected to Lateral Loads. *J Struct Eng* 142:1–12. [https://doi.org/10.1061/\(ASCE\)ST.1943-541X.0001315](https://doi.org/10.1061/(ASCE)ST.1943-541X.0001315)
- Ruggeri EM, D’Arenzo G, Fossetti M, Seim W (2022) Investigating the effect of perpendicular walls on the lateral behaviour of Cross-Laminated Timber shear walls. *Structures* 46:1679–1695. <https://doi.org/10.1016/j.istruc.2022.10.141>
- Shahnewaz M, Popovski M, Tannert T (2020) Deflection of cross-laminated timber shear walls for platform-type construction. *Eng Struct* 221:111091. <https://doi.org/10.1016/j.engstruct.2020.111091>
- Yasumura M, Kobayashi K, Okabe M, et al (2016) Full-Scale Tests and Numerical Analysis of Low-Rise CLT Structures under Lateral Loading. *J Struct Eng (United States)* 142:1–12. [https://doi.org/10.1061/\(ASCE\)ST.1943-541X.0001348](https://doi.org/10.1061/(ASCE)ST.1943-541X.0001348)



DISCUSSION

**The paper was presented by G D'Arenzo**

*F Lam commented that J Brown PhD thesis from University of Canterbury studied the contribution of end walls on CLT working as shear core and the work should be cited. G D'Arenzo responded that he was aware of the work but the work is different.*

*D Casagrande discussed the importance of hold down design in order to achieve optimal ductility, indicating the possibility of inverting loading direction. G D'Arenzo agreed that this would be an important and good approach. D Casagrande further commented that a nonuniform application of vertical loads could influence the assumed rocking behaviour.*

*A Ceccotti agreed that studying 3D effect would be important especially for tall buildings.*

*M Fragiaco commented that B Dujic's paper from ~ 10 years ago already addressed some of these issues including a long perpendicular wall with hold downs. Influence of perpendicular walls in tubular systems for taller building would be important. He commented that simplified approaches would be needed to make these situations applicable. Finally tubular systems would need floor stiffness to ensure system behaviour.*

*D Moroder discussed asymmetrical response and questioned the use of screws in connections as bolts are sometimes preferred.*

*G Doudak and G D'Arenzo discussed diaphragm actions.*

*P Dietsch commented that the 1<sup>st</sup> and 2<sup>nd</sup> conclusion should be reconsidered based on comments from discussions on past research.*





# Structural Means for Fire-Safe Green Façade Design on Multi-Storey Buildings

Thomas Engel<sup>1</sup>,

Stefan Winter<sup>1</sup>

Technical University of Munich; TUM School of Engineering and Design; Chair of Timber Structures and Building Construction

Keywords: fire safety, green façades, fire spread, flammability

## 1 Introduction

In recent years, green façades (also called vertical greenery systems) have become increasingly important. Although cities occupy only 2% of the global land area, more than half of the world's population lives in cities and urban agglomerations. Three-quarters of Europe's population live in urban areas, and this proportion is forecast to increase sharply (United Nations 2019). The resulting need for sustainable urban development requires a sufficient amount of green and recreational space. However, the increasing shortage of residential areas often stands in the way of the creation of new public green spaces and thus creates major challenges for the responsible authorities.

One possible solution would be the greening of the numerous existing horizontal and vertical building surfaces. Green façades offer multiple benefits, including improving air quality, minimising the heat island effect (or urban heat island=significantly warmer area in cities than surrounding rural areas), improving the thermal performance of the building, reducing noise through absorption and providing additional oxygen (Alexandri, E.& Jones, P. 2008), (Perini, K. et al. 2011).

However, the fire safety aspects of green façades have not yet been investigated in detail.

Figure 1 shows the various types of green façades. In principle, a differentiation can be made between direct greening on the exterior wall using climbing plants, indirect greening controlled by trellises and climbing aids set off from the exterior wall, or greenery wall systems using shrubs and bushes in boxes or substrate systems (living

wall). Mixed types are also possible, (Köhler, M.; Ansel, W. 2012), (Mahabadi, M.; et al. 2018), (Pfoser, N. 2018).

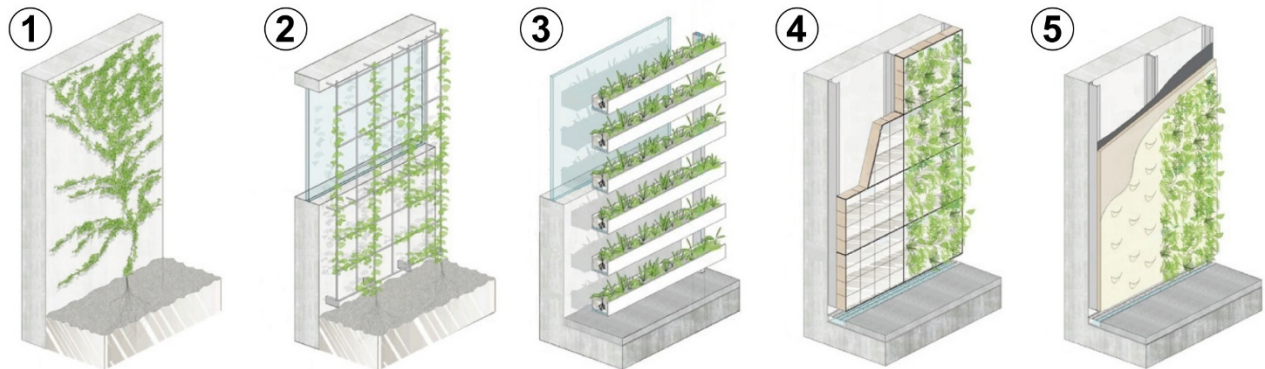


*Figure 1: Types of green façade design. 1 Direct growth with self-climbers, ground-based, 2 Growth on climbing aid/trellis, ground-based, 3 Plant boxes, horizontal vegetation surfaces, wall-based, 4 Modular system (living wall), vertical vegetation surfaces, wall-based, and 5 Planar system (living wall), vertical vegetation surfaces, wall-based; based on (Pfoser, N. 2018)*

For ground-based growth on climbing aid/trellis, wall distances of 50 to 200 mm to the climbing aid have become established, depending on the growth thickness (Köhler, M.; Ansel, W. 2012), (Mahabadi, M.; et al. 2018). In addition to the growth of the plant, a sufficient distance is also necessary due to the otherwise possible overheating of the climbing plant by the outer wall (Pfoser, N. 2018).

Wall-based green façades (living walls) are characterised by built-in irrigation systems, plants of various sizes and the interchangeability of plants. These enable an extensive greening of the façade from the moment the building is completed through module or shelf systems (Pfoser, N. 2018). Wall-based green façades as "living walls" are a complete rear-ventilated façade system. It consists of a rear-ventilated void cavity, supporting structure, cladding panels, substrate, fleece, irrigation system and the plant itself. The systems differ significantly between the manufacturers.

The use of climbing plants for green façades has many regional peculiarities (Köhler, M. & Ansel, W. 2012), (Mahabadi, M.; et al. 2018), (Pfoser, N. 2018). The species potential for climbing plants in the central European climate region consists of approx. 150 species and varieties (Köhler, M. & Ansel, W. 2012). The range of possible plant species for wall-based planting systems encounters only a few restrictions and is, therefore, much more extensive. For the central European climate region, approx. 100 species and varieties are listed in (Mahabadi, M.; et al. 2018). A differentiation is made between perennials, grasses and woody plants (Pfoser, N. 2018).

Figure 2 and Figure 3 show examples of realised green facades.



Figure 2 Ground-based growth on climbing aids (Swiss Re office building in Munich); (Source: Bundesverband GebäudeGrün)



Figure 3 Wall-based modular system (living wall) (Municipality of Venlo, Netherlands); (Source: Bundesverband GebäudeGrün)

## 2 Fire safety assessment of the various types of green façades

As described in the previous section, "living walls" are complex façade systems that differ significantly from manufacturer to manufacturer. The manufacturer-specific systems can only be analysed in a product-specific manner through full-scale fire tests on the respective overall system (Engel, T. 2023). The situation is different for climbing plants on climbing aids. These can be generally analysed and evaluated in terms of fire safety. General principles for fire safe use can be developed from these tests (Engel, T. 2023). (Bielawski J, et al. 2024) shows the critical fire behaviour of a corresponding living-wall-system based on fire tests.

## 3 State of the art

There is currently little international research available on the fire behaviour of green façades and the resulting fire spread along the façade. A detailed overview of the current state of research into the fire behaviour of green façades can be taken from (Engel, T. 2023) and (Engel, T. & Werther, N. 2024).

To summarise, it can be stated that medium and large-scale fire tests on green façades have so far been carried out primarily in Austria and Germany. However, these tests have mainly been carried out on standardised façade fire test stands, which were originally designed for a different application and do not correspond to the effects of real fire incidents (Engel, T. 2023). The current challenge for green façades is therefore that the results of scaled test methods, such as those according to (ÖNORM B 3800–5) or (DIN 4102-20), in conjunction with assessment criteria that were also designed for other building materials, are directly transferred to reality or measures are derived based on them. This approach can lead to unrealistic results and involves risks without a holistic view (Engel, T. 2023).

Analysing the state of research provides two key findings: Firstly, regular care and maintenance is an important basis for fire-safe green façades. Large areas of dead

plants must be recognised and removed quickly. Secondly, if the green façades are exposed to fire, the plants can be expected to dry out and, in the further course of the fire, an abrupt, short-term fire spread ("flare-up") can be expected in areas outside the primary fire (Engel, T. 2023), (Engel, T. & Werther, N. 2024).

## 4 Flammability of the plants

An initial part of the FireSafeGreen (FireSafeGreen 2024) research project investigated the fire behaviour of green façades. The focus here was on the flammability of the plants, which was determined in 43 calorimetric fire tests on a medium scale using the Single Burning Item (SBI) test method (EN 13823). The study focussed on a total of 25 climbing plant species. The main factor influencing the fire behaviour of plants is the moisture content of the plant (Engel, T. & Werther, N. 2024). A comparison of the heat release rate of vital plants (normal moisture content) shows similar behaviour, as shown in Figure 4.

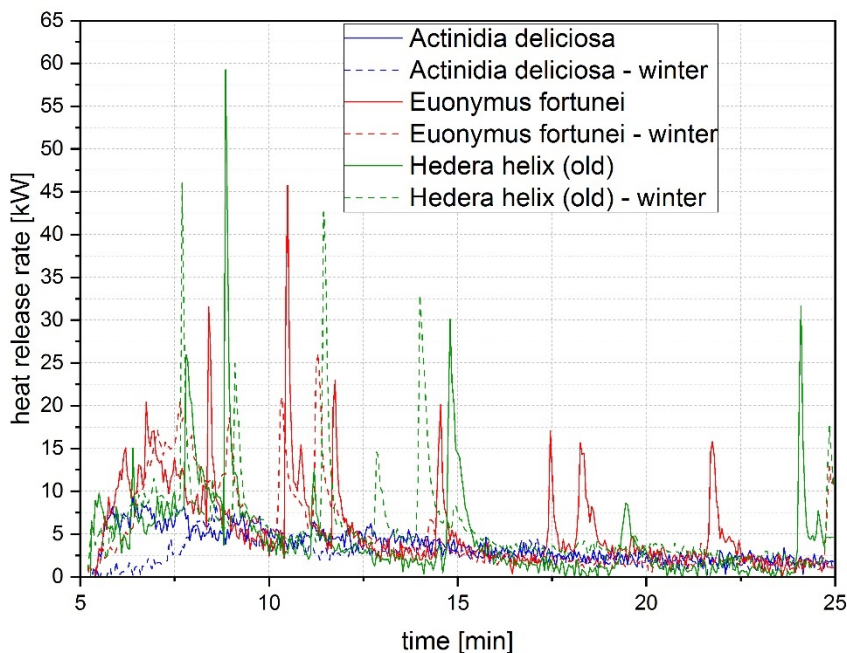


Figure 4: Comparison of the heat release rate of *Actinidia deliciosa*, *Euonymus fortunei* and *Hedera helix* in summer and winter

In the course of exposure, there are short peaks in the heat release rate. These peaks are the "flare-ups" known from previous studies. They occur when parts of the plants dry out due to the fire exposure and then ignite abruptly. The plant species itself has no significant influence on the fire behaviour. In all tests, only a very small amount of horizontal fire spread occurred with vital, maintained plants and self-extinguishing occurred after the burner was switched off. A direct comparison between young and old plants as well as a comparison of the seasonal influence between summer and winter also showed no significant difference for vital, well-tended plants (Engel, T. & Werther, N. 2024).



There was a significant difference for dried plants. Here, an abrupt heat release occurred at the beginning. Dead plants and unmaintained plants with a high content of dead wood therefore represent the most critical case. Figure 5 shows the heat release rate of a 42-day dried, a vital young and a vital old ivy (*Hedera helix*) in comparison to a 13 mm chipboard and a 9 mm plywood panel (Engel, T. & Werther, N. 2024).

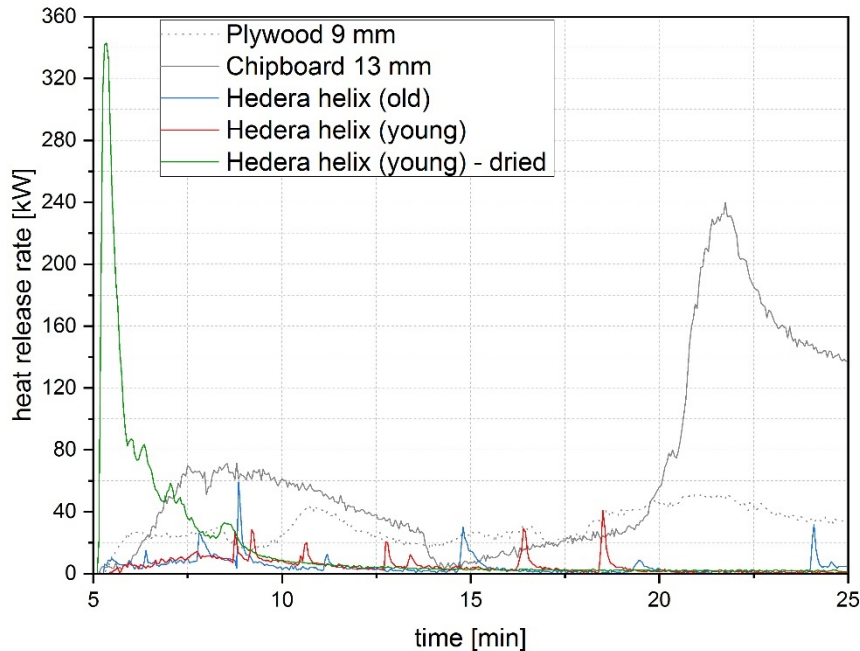


Figure 5: Heat release rate of a 42-day dried, a vital young and a vital old *Hedera helix* compared to a 13mm chipboard and a 9mm plywood panel

The care and maintenance of a green façade is therefore the most important factor for maintaining fire safety. Dead wood in the form of dead leaves, branches or bird nests must be removed regularly. It is also necessary to constantly check whether the plants are still vital and have a normal moisture content. The plants should also be cut back regularly. Uncontrolled growth can lead to a lot of deadwood - especially in the case of light-fleeing plants (Engel, T. & Werther, N. 2024).

In the next step, it is necessary to verify the findings from the medium-scale tests in full-scale tests; in particular, the vertical fire spread must be analysed in more detail (Engel, T. 2023), (Engel, T. & Werther, N. 2024).

## 5 Combination of wooden and green façades

A central question for the realisation of combined wooden and green façades are the resulting interactions in case of fire. The focus of the investigation was whether the heat flux of burning climbing plants is sufficient to ignite a wooden cladding and whether the burning climbing plants lead to fire spread on the wooden façade above the fire stops (Engel, T. & Werther, N. 2023).

Medium-scale fire tests were carried out to investigate this question (Engel, T. 2023), (Schoofs, N. 2023), as shown in Figure 6.





*Figure 6: Photo documentation of the fire test (Test 3) with wooden and green façade in the 3rd test minute*

As part of the tests, a distance of 110 mm was set between the trellis and the wooden cladding. This choice is intended to generate a critical fire impact of the green façade due to the small distance to the wooden cladding. It is known that wall distances of 50 mm to 200 mm from the climbing aids are common for ground-based climbing plants (Mahabadi, M.; et al. 2018), (Pfoser, N. 2018). These guide values are based on typical mineral external walls without fire stops. A sufficient minimum distance to the external wall is necessary, as plants with heavy leaf mass in particular can promote heat build-up and consequently die. To prevent overheating, air circulation on the façade must be possible without restriction due to sufficient distance between the trellis and the outer wall (Pfoser, N. 2018).

In many European countries, fire stops (Engel, T. & Werther, N. 2023) are required in each storey for wooden façades on multi-storey buildings. These fire stops define a minimum distance between the greenery and the external wall, as the plant cannot grow through the fire stop on one side and a sufficient minimum distance to the steel fire stop is required on the other side to prevent the plant from overheating in this area. As the projection of the fire stop increases, the distance between the trellis and the wooden cladding also increases; consequently, the effect of the burning plants reduces due to the greater distance. This is the reason why a tongue-and-groove wooden cladding with a relatively small projection of the fire stops was chosen for

the fire tests which were described in more detail in (Engel, T. 2023), (Schoofs, N. 2023).

In the tests, the greenery was placed directly in front of the 100 mm projecting fire stop. Furthermore, the area between the wooden cladding and the trellis was filled with plant shoots of an over 15-year-old ivy (*Hedera helix*) (Engel, T. 2023). Ivy was chosen as it has a high leaf mass and a relatively large shoot diameter. The test arrangement and the plant density were intended to simulate an unmaintained and therefore critical green façade in terms of fire exposure, which did not have large masses of dead wood, but was also not regularly cut back.

The medium-scale test setup is representative in this case, as the plant mass and arrangement determine the possible area-related fire load or maximum heat release of the green façade and not the size of the test stand or the size of the fire exposure (Engel, T. 2023).

In both tests with arranged greenery, there was no independent burning on the wooden cladding above the fire stop either during the test or during the following observation period (Engel, T. 2023). This can best be seen on the wooden cladding at the end of the fire tests, as shown in Figure 7.



*Figure 7: Photo documentation of the wooden cladding above the fire stop after completion of the test and the observation time for test 3*

Colouration and charring occurred in some areas of the wooden cladding due to the fire exposure from the greenery. The charring was most intense in the central, lower area of the façade directly above the fire stop. This is due to the fact that individual wooden shoots of the wire-fixed ivy fell off the trellis after the leaves and young shoots had burnt down and then burnt on the fire stop (Engel, T. 2023). Even this fire exposure did not lead to an independent burning of the wooden façade. The direct fire impact on the lower area of the wooden cladding caused by burning plant parts

on the fire stop would be more critical for open claddings than in the present case due to the three-sided fire exposure on the wooden cross-section. However, due to the greater distance between the greenery and the wooden cladding and the greater projection of the fire stops described above, a fire exposure directly on the wooden cladding is not to be expected with open cladding (Engel, T. 2023).

To summarise, it can be stated that the burning green façade in the tests [6] did not lead to ignition the wooden façade. Requirements for this are a minimum distance of 110 mm between the trellis and the wooden cladding and regular care and maintenance of the greenery, during which dead wood is removed.

## 6 Full-scale fire tests

The final full-scale fire tests serve as proof of the findings made during the FireSafeGreen (FireSafeGreen 2024) research project and as a basis for verifying the fire safety objectives.

The investigation focussed on evaluating the fire spread through the green façade under the influence of a representative fire exposure. In addition, the influence of a short-term heat flux of the burning green façade on the exterior walls, windows, balconies, roof overhangs and the areas behind them and the associated risk were analysed. Particular focus was placed on the influence of living and dead (dry) plants on the fire spread and fire behaviour along the façade. One specific question is, for example, whether the heat flux of a dry green façade (worst case) is sufficient to ignite the furnishings directly at the opening within the window is open. In addition, the vertical fire spread in particular is to be analysed in more detail.

Eight fire tests were carried out in total in three different test series (as shown in Figure 8). These three test-series included an wall test, an balcony test with central fire exposure and an balcony test with a fire exposure in the inner corner. A reference test without greenery (plants) was carried out for each test series in order to quantify the influence of the plants in more detail and to validate the results. In the test series, one test was also carried out with vital and one with dried (dead) plants, as shown in Figure 9 and Table 1.



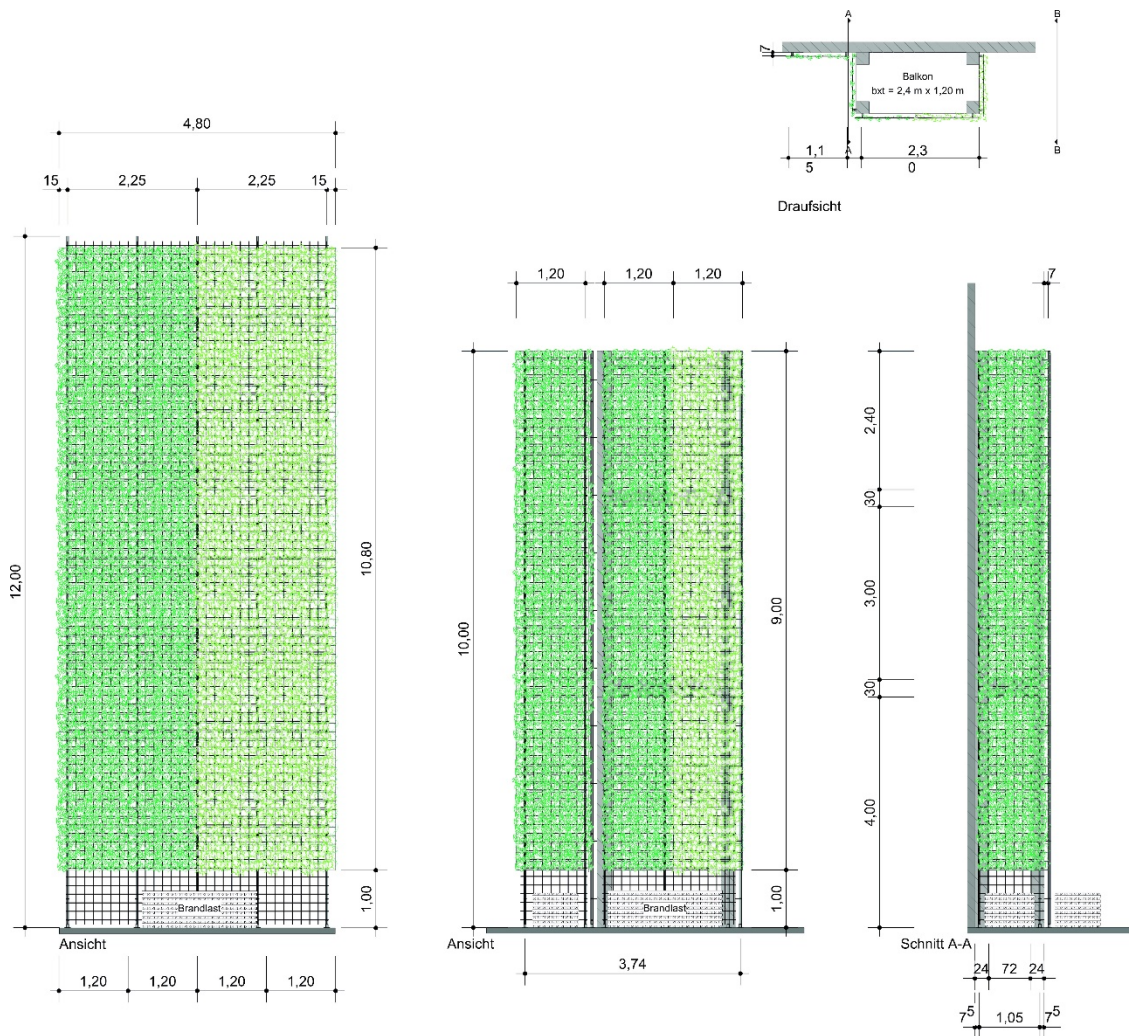


Figure 8: Left: Wall test stand (12m high) for tests V0, V1 and V2; right: balcony test stand (10m high) for tests V3, V4, V5, V6 and V7 [15]



Figure 9: a) Wall test with vital plants (V1); b) Wall test with dried (dead) plants (V2); c) Balcony test with fire exposure in the corner with vital plants (V6)

Table 1. Requirements to sound insulation.

Test	Test description	Fire load
V0	Wall test without plants (reference test)	
V1	Wall test with vital plants	4 × 35 kg (140 kg)
V2	Wall test with dried (dead) plants	
V3	Balcony test with central fire exposure without plants (reference test)	3 × 35 kg (105 kg)
V4	Balcony test with fire exposure in the corner without plants (reference test)	1 × 35 kg
V5	Balcony test with central fire exposure with vital plants	3 × 35 kg (105 kg)
V6	Balcony test with fire exposure in the corner with vital plants	1 × 35 kg
V7	Balcony test with central fire exposure with vital dried (dead) plants	3 × 35 kg (105 kg)

Hedera helix with a plant density (vital) of approx. 1.85 kg/m<sup>2</sup> (left side, in Figure 9) and Euonymus fortunei with a plant density (vital) of approx. 2.55 kg/m<sup>2</sup> (right side, in Figure 9) were arranged on the trellis of the test stand.

Figure 9 shows the wall test with vital plants (V1), the wall test with dried (dead) plants (V2) and the balcony test with fire exposure in the corner with vital plants (V4).

During the fire tests with plants, regardless of the plant species (Hedera helix or Euonymus fortunei) and their moisture content, vertical fire spread occurred in the form of "flare-ups". The moisture content had a significant influence on their intensity. The findings of (Engel, T. & Werther, N. 2023) could be confirmed in the full-scale test. In the case of vital plants directly in front of an external wall, a burn-off of the green façade in the ratio of approx. 2.5 times the actual primary flame (wooden crips) was observed. In an open arrangement in front of a balcony (external wall further away), the factor was approx. 1.5. In general, self-extinguishing of the greenery was observed. The detailed test evaluation is currently still being processed and can be found in (Engel, T. 2024).

## 7 Conclusion and outlook

Currently, there are only a few principles for a fire safety assessment of green façades. Medium-scale fire tests as part of the FireSafeGreen research project (FireSafeGreen 2024) showed that the main factor influencing the fire behaviour of plants is the moisture content. The plant species itself plays a subordinate role in terms of fire behaviour and, according to these findings, is of minor relevance - at least for the tested variants. The direct comparison of young and old plants and the comparison of the seasonal influence of summer and winter also showed no significant difference for vital, well-maintained plants. During fires on green facades, short heat release peaks occur. These peaks are known as "falre-ups". They occur when parts of the plants dry out due to the fire exposure and then ignite abruptly. For vital, well-maintained plants, horizontal fire spread occurs only to a very small area. Furthermore, vital green façades are self-extinguishing after the end of the primary fire (Engel, T. 2024), (Engel, T. & Werther, N. 2023).

For a combination of wooden and green façade, it can be stated that the burning green façade does not lead to the ignition of the wooden façade behind it. The requirement is a minimum distance of 110 mm between the trellis and the wooden cladding and regular care and maintenance of the green façade (Engel, T. 2024).

The final full-scale tests also showed that correct care and maintenance are the key factor for fire-safe green façades. The conclusions from the full-scale tests can therefore be summarised as follows.

- "Living walls" or wall-based systems can behave critically from a fire safety perspective. Full-scale fire tests and corresponding certificates of applicability are required here in the medium term. At the moment, it is important to carefully check which materials are used.
- Climbing plants on non-combustible climbing aids can be generally evaluated and represent a lower risk from a fire safety point of view.
- The decisive factor for a fire-safe green façade is care and maintenance. Standard green façades generally require one maintenance cycle per year.
- A distance of 50 cm should be maintained from components such as horizontally projecting wooden roof trusses (combustible building materials).
- If climbing plants are arranged across several storeys on non-combustible climbing aids on balconies, closed balustrades made of non-combustible building materials should be chosen.

## Acknowledgements

The research was funded by the Federal Institute for Research on Building, Urban Affairs and Spatial Development on behalf of the Federal Ministry for Housing, Urban Development and Building with funds from the Zukunft Bau Research Grant. For the support in providing the plants and the pre-selection, the research partner and staff of Weihenstephan-Triesdorf University of Applied Sciences are acknowledged.

## References

- United Nations: Department of Economic and Social Affairs Population Division (2019) World urbanization prospects the 2018 revision. United Nations, New York
- Alexandri, E.; Jones, P. (2008) Temperature decreases in an urban canyon due to green walls and green roofs in diverse climates. In: Building and Environment 43:480–493. <https://doi.org/10.1016/j.buildenv.2006.10.055>
- Perini, K.; et al. (2011) Vertical greening systems and the effect on air flow and temperature on the building envelope. In: Building and Environment 46:2287–2294. <https://doi.org/10.1016/j.buildenv.2011.05.009>
- Köhler, M.; Ansel, W. (2012) Handbuch Bauwerksbegrünung. Planung – Konstruktion – Ausführung. Köln: Rudolf Müller.



Mahabadi, M.; et al. (2018) Fassadenbegrünungsrichtlinien – Richtlinien für die Planung, Bau und Instandhaltung von Fassadenbegrünungen. Bonn: Forschungsgesellschaft Landschaftsentwicklung Landschaftsbau e.V. FLL.

Pfoser, N. (2018) Vertikale Begrünung. Bauweisen und Planungsgrundlagen zur Begrünung von Wänden und Fassaden mit oder ohne natürlichen Boden-/Bodenwasseranschluss. Stuttgart (Hohenheim): Ulmer, Fachbibliothek grün.

Engel, T. (2023) Brandschutz für biogene Fassaden – Experimentelle Untersuchungen als Grundlage brandschutztechnischer Prinzipien [Dissertation]. Technical University of Munich <https://mediatum.ub.tum.de/?id=1715368>

Bielawski J, et al. (2024) An exploratory investigation into moisture content and wind impact on the fire behaviour of modular living walls. Fire Safety Journal 142. <https://doi.org/10.1016/j.firesaf.2023.104024>

Engel, T.; Werther, N. (2024) Fire Safety for Green Façades: Part 1: Basics, State-of-the-Art Research and Experimental Investigation of Plant Flammability. Fire Technology <https://doi.org/10.1007/s10694-024-01566-0>

ÖNORM B 3800–5:2013 Brandverhalten von Baustoffen und Bauteilen – Teil 5: Brandverhalten von Fassaden – Anforderungen, Prüfungen und Beurteilungen

DIN 4102-20:2017-10 Brandverhalten von Baustoffen und Bauteilen – Teil 20: Ergänzender Nachweis für die Beurteilung des Brandverhaltens von Außenwandbekleidungen.

FireSafeGreen (2024) research project [online] <http://www.firesafegreen.de>

EN 13823:2020-09 Reaction to fire tests for building products - Building products excluding floorings exposed to the thermal attack by a single burning item

Engel, T., Werther, N. (2023) Structural Means for Fire-Safe Wooden Façade Design. Fire Technology 59:117–151. <https://doi.org/10.1007/s10694-021-01174-2>

Schoofs, N. (2023) Untersuchung des Einflusses von Fassadenbegrünung auf Holzaußenwandbekleidungen im Brandfall [Master Thesis]. Technical University of Munich.

Engel, T. (2024) Fire Safety for Green Façades: Part 2: Full-Scale Façade Fire Tests and Means for Fire-Safe Green Façade Design for Climbing Plants on Trellises. Fire Technology [Manuscript in preparation].

## DISCUSSION

**The paper was presented by T Engel**

*R Lemaitre asked about the effect of wind. T Engel mentioned that the issue of wind would be challenging to implement in testing requirements.*

*P. Vinco da Sesso commented that the difference between dried and living plant seemed to be limited.*

*S Aicher commented about the importance of risk associated with the mass of the wood, the mass of wood in the dried state as fuel load is important. Also burning of the leaves seemed to promote fire growth.*

*P Dietsch questioned that the distance of 50 cm was not supported and suggested that the author add information in the final paper.*

*T Ehrhart and T Engel agreed that the influence of wind may change the fire spread characteristics of such fires. T Ehrhart agreed that fire load considerations are important.*

*P Palma asked about the possibility of external fire leading to compartment fire. T Engel said this is possible but not likely unless open windows are available.*

*A Frangi commented that testing in an outdoor environment might not be appropriate as comparability with other tests are limited and stated that no consensus is given on European level for façade tests.*





# Comfort assessment of timber floor vibrations

Maria Felicita, Empa & ETH Zürich, Switzerland

Rudi Roijackers, Adviesbureau Lüning & Quake Innovation, Netherlands

Ruxandra Cojocaru, ABT Consulting Engineers & Quake Innovation, Netherlands

Dr. Geert Ravenshorst, TU Delft, Netherlands

Keywords: Floor vibrations, Serviceability, Human perception, Numerical simulation

## 1 Introduction

Due to their inherited light weight, the design of timber floors is in most cases governed by vibrations. There are different methods to assess the vibration response of floors. Some methods are based on achieving a minimum performance requirement, whereas other methods categorize the response into comfort classes. Additionally, while some methods use deterministic approaches to define representative loading cases, others use probabilistic approaches considering the probability of occurrence of the loading event. The most widely accepted method to assess the vibration response of timber floors in Europe is found in the current version of Eurocode 5 (EN 1995-1-1:2004). The EC5 method uses a deterministic minimum performance criteria approach with unit loading and minimum response levels defined in National Annexes. The three criteria assessed with this method are point load deflection, frequency and unit impulse velocity response. This method is only applicable for floors with a natural frequency larger than 8 Hz, thus additional methods to verify the performance of floors with lower natural frequencies are accepted. In the Netherlands, the vibration response of lightweight floors is currently assessed based on the 'SBR 539 – Trillingen van vloeren door lopen'. The SBR is based on a probabilistic comfort classification method presented by Feldmann et al 2007 on the Hivoss (Human induced vibrations of steel structures) guideline, currently used in practice in various countries across Europe. This method considers the probability distribution of users' mass and walking frequency to assess the effective velocity response of floors.

The draft version of Eurocode 5 (prEN 1995-1-1), provides a new method for assessing timber floor vibrations. The method proposed in the latest draft version of the document (CEN/TC 250/SC 5 N 2077), is based on a comfort classification assessment for a simplified deterministic definition of the loading. The simplified definition of the loading considers a representative user mass and walking frequency, for which larger safety margins are expected to account for the unknown distributions. This method defines the classification of the floor response based on four criteria, stiffness, frequency, acceleration and velocity, therefore considering floors where resonant build up may occur. The draft code provides an additional advanced deterministic assessment method presented in the Annex, which shall be applied using modal properties extracted from a numerical analysis. Due to its dependency on numerical analysis, this method has an additional computational expense. However, it might lead to a more accurate representation of the floor response and support an optimized design of the floor.

The simplified and advanced methods presented in the prEC5 lead to floor performance levels which are further divided into three comfort categories, namely premium, standard and base choice, with large ranges for each of the choices based on the use class of the structure. The relation between this new definition of comfort classes and the ones presented in design guidelines currently used in practice is unknown. Understanding the relation between new and existing codes and guidelines is of high importance, as the implementation of new codes should not lead to a significant impact in design outcome, unless problems within existing guidelines have been identified. Based on the different approaches, loading definitions and threshold limits, the implementation of the methods presented in prEC5 could have a significant economic impact on the design of timber floors. This paper evaluates the relation between the comfort classes provided in the prEC5, as a result of both the simplified and advanced methods, to the comfort classes presented on the Hivoss method, which is currently used in the Netherlands and other European countries. Additionally, this paper evaluates the correlation between the performance levels given by the two methods in the draft code.

## 2 Theoretical background

### 2.1 Footfall floor vibrations

Footfall vibrations are defined as vibrations caused by the dynamic loads induced by the walking of people. Such vibrations are often small and do not represent a hazard for structural integrity, but they can cause user discomfort. The response of the floor structures is dependent on the dynamic loads applied by the walker and the dynamic properties of the structure, such as mode shapes, natural frequencies, modal masses and damping. The magnitude of the dynamic load is defined by the weight and pace of the walker. Normal walking pace is approximately 1.5 - 2.5 Hz; however, due to the

large variability there is no universally correct force to apply to assess the response of floors, rather different methods focus on adopting statistically representative values with known probabilities of exceedance. Dynamic loads are also influenced by the structural response and thus the modal properties of the structure. When the natural frequency of the floor is much higher than the walking frequency, the floor response dies out in between footfalls, so the footfall loading can be idealized as an impulse load, this is known as transient response. On the other hand, when the natural frequency of the floor is low and corresponds with the frequency of one of the harmonics of the walking frequency, resonant build-up is likely to occur. For resonant response, the footfall loading is often idealised as a harmonic load with up to four relevant harmonics. It can be assumed that resonant response can occur on floors with a natural frequency of up to the fourth harmonic of the assumed walking pace (Willford 2007).

### **2.1.1 Human acceptance limits**

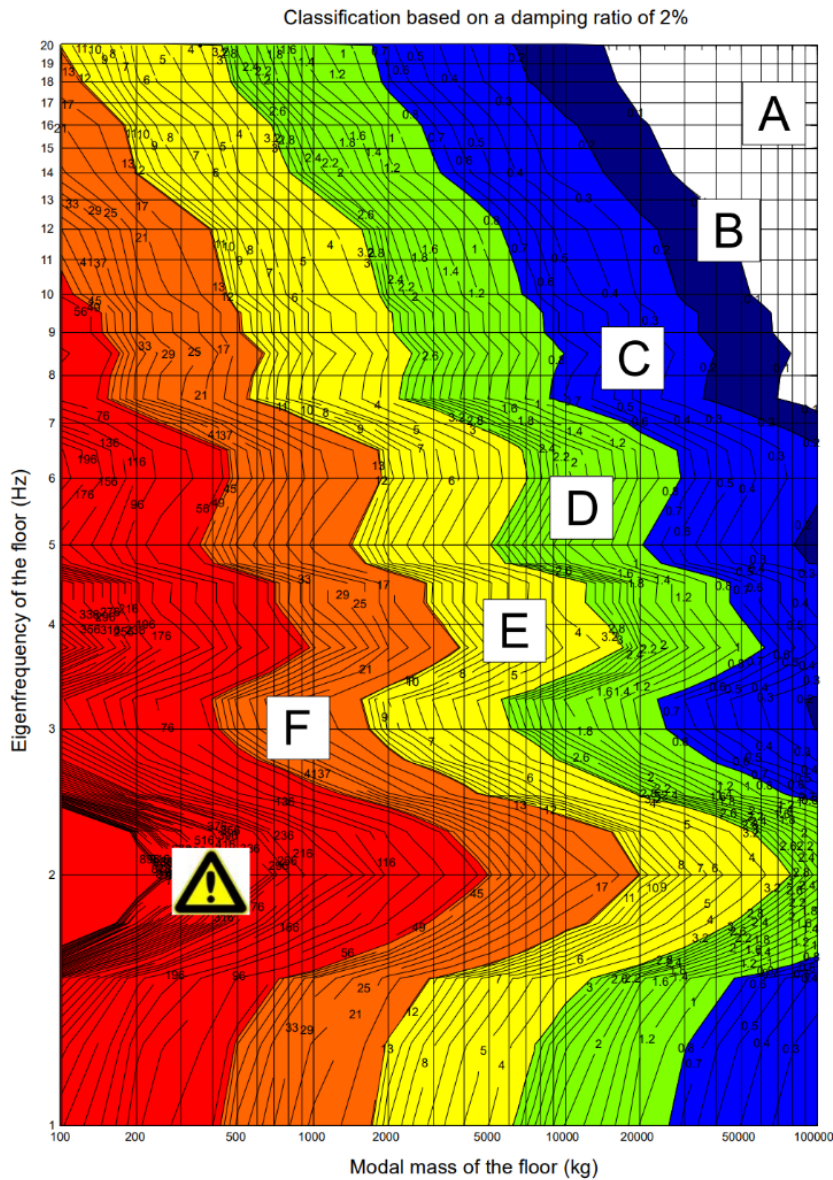
Human perception to floor vibrations is highly dependent on the characteristics of the structural response, but it is also related to non-structural parameters such as distance between walker and receiver. Due to the uncertainty in walker and receiver distance in practice, guidelines often take the conservative assumption that they are at the same location. Standards such as the ISO 10137, provide insight into frequency ranges where humans are more susceptible to vibrations and additionally provide limits to the structural response after which the response is perceptible to most people. On the other hand, human acceptance limits are more difficult to quantify as they must be defined on a societal context. The threshold for defining a perception as acceptable/unacceptable will vary from individual to individual and is highly influenced by habituation and thus to local traditional construction solutions (Toratti et al 2006). Based on the abstract nature of human acceptance limit definition, these are often defined on a national level, rather than based on a generalized code or standard.

## **2.2 Assessment methods**

### **2.2.1 SBR/Hivoss**

The method presented in the SBR 539 and Hivoss guidelines is based on a dynamic loading defined as time domain functions that represent the normalized contact force due to a single step for a given walker mass. The load functions combine coefficients of up to the eighth order, based on a walking frequency definition. Based on the load functions for a single step, the root-mean-squared velocity response (OS-RMS) can be determined. These guidelines provide simplified design charts based on the statistical outcome of numerous time-history calculations on single degree of freedom systems. The graphs were developed based on an experimental campaign conducted in the Netherlands, where the distributions of walker mass and walking frequency were measured for a random population of 700 persons. In the parametric study, all the produced time domain functions were used to calculate the 90% upper limit of a single step response for a given system and thus define the OS-RMS-value of the acceleration

response velocity for a significant single step that is larger than the 90% fractile of peoples' walking steps ( $OS-RMS_{90}$ ). This value was determined for large ranges of system eigenfrequencies and modal masses with a given damping ratio, to develop the simplified graphs presented in the guidelines. Separate graphs are presented for different definitions of damping ratio. An example of such a graph can be found in Figure 2.1. Additionally, Figure 2.1 presents the allocation of comfort classes to threshold values of  $OS-RMS_{90}$  – values and their relation to acceptance limits for office and residential buildings.



Class	A	B	C	D	E	F	
Lower limit	0.0	0.1	0.2	0.8	3.2	12.8	Recommended
Upper limit	0.1	0.2	0.8	3.2	12.8	51.2	Critical
							Not recommended

Figure 2.1. Hivoss  $OS-RMS_{90}$  design chart for floors with 2% damping ratio and allocation of comfort classes

The SBR/Hivoss design charts take as an input the modal properties of the floor in the form of eigenfrequency and modal mass, for which analytical definitions are presented based on the floor support conditions. For two-sided supported floors, the natural frequency is defined based on beam theory and the modal mass is defined as 50% of the mass acting on the floor. The modal properties of four-sided supported floors must account for load redistribution in the transverse direction, thus the orthotropic properties of the floor are considered in the natural frequency definition. The modal mass for four-sided supported floors is defined as 25% of the mass acting on the floor. Additionally, this method can be used with the output of numerical models to define the modal properties of the floors.

### 2.2.2 Draft Eurocode 5 – Simplified

The method described in this section refers clause 9.3 in the latest version of the draft Eurocode 5 at the moment of writing, presented in document CEN/TC 250/SC 5 N 2077. This method aims to classify the floor response into performance levels defined by different criteria based on the expected response of the floor. All floors must be checked against frequency, stiffness and velocity criteria, while floors with a natural frequency lower than the fourth harmonic of the expected walking frequency, must also be checked against acceleration criterion. The threshold value for each criterion is defined by the intended performance level of the floor, as presented in Table 2.1. Additionally, the draft code presents recommended floor performance levels for different comfort choices based on the use category of the building as presented in Table 2.2. The performance levels in each category do not correspond to the same limits for the different criteria, thus requiring designers to choose a specific performance level for verification. Premium floors are defined as acceptable and intended for high-quality choices, standard floors are defined as floors where vibrations are perceived, but regarded as acceptable, and base floors are defined as floors where vibrations are perceived. The table presented for recommended performance levels is included in the draft code as NDP (National Dependent Parameter).

Table 2.1. Floor vibration criteria according to floor performance level in draft Eurocode 5

Floor performance levels								
Criteria	I	II	III	IV	V	VI	VII	VII
Frequency criteria	$f_1 \geq 4.5 \text{ Hz}$			$f_1 \geq f_{1,lim}$				
Stiffness criteria	$w_{1kN} \leq w_{lim} \text{ mm}$							
Deflection limit $w_{lim}$	$w_{lim} = w_{lim,max}$			$w_{lim} = \max(w_{lim,max} \cdot 3.6 / L, 0.5) \leq w_{lim,max}$				
Upper deflection limit $w_{lim,max}$	0.25	0.5	1.0	1.25	1.5	1.75	2.0	
Velocity criteria	$v_{rms} \leq v_{rms,lim} \text{ m/s}$							
Limit rms velocity $v_{rms,lim}$	0.0004	0.0008	0.0012	0.0016	0.0024	0.0036	0.0042	0.0048
Acceleration criteria	$a_{rms} \leq a_{rms,lim} \text{ m/s}^2$				Not applicable			
Limit rms acceleration $a_{rms,lim}$	0.02	0.04	0.06	0.08				

Table 2.2. Recommended floor performance levels for use categories A and B draft Eurocode 5

Use category	Premium choice	Standard choice	Base choice
A (residential) - multi storey building	I - III	IV, V	VI, VII
- single family house	I - IV	V	VI - VIII
B (office)	I, II	III	IV, V

The velocity criterion aims to evaluate the transient response of the floors and thus defines the dynamic loading as a mean modal impulse based on the expected walking frequency and the natural frequency of the floor. On the other hand, the acceleration criterion aims to evaluate the resonant response for floor where resonant built-up can occur. The formulation presented in the simplified method, calculates the response for full resonant build up with a reduction factor to account for the low probability of occurrence based on walker pattern behaviour. In the simplified method, both velocity and acceleration criteria are assessed for a single governing vibration mode. However, factors that account for higher vibration modes are presented in both definitions and defined based on the orthotropic properties of the plates. The analytical definitions for the modal properties of the floors are in line with the formulations presented by the SBR/Hivoss method.

### 2.2.3 Draft Eurocode 5 – Advanced

The method described in this section refers to Annex G of the latest version of the draft Eurocode 5. Performance levels and assessment criteria for velocity and acceleration criteria refer to the definitions presented for the simplified method in Tables 2.1 and 2.2. This method aims to provide a more detailed definition of the floor response considering higher vibration modes and a more detailed definition of the dynamic loading. The modal properties of the floor for all significant vibration modes should be determined based on the output of a numerical analysis. The velocity criterion is assessed based on the same principle of modal impulse; however, it is described as an effective modal impulse defined for each mode of the floor with a frequency lower than 25 Hz. Additionally, the rms velocity is evaluated from the result of the time history response over the period of one footfall.

The acceleration criterion is assessed based on a harmonic force definition of the dynamic loading. Analytical formulations are presented to determine the harmonic force imposed by the first four harmonics of the walking frequency and assess the rms acceleration for all natural frequencies below 15 Hz. Additionally, it is stated that the rms acceleration of the floor must be verified for all possible walking frequencies, as resonant build-up may occur for any of them.

### 3 Materials and methods

#### 3.1 Simulation framework

For this study over fifty thousand CLT floors were simulated within various ranges of width, span, build-up and imposed loads, as presented in Table 3.1. These ranges were selected to represent the large variety of floor geometries and loading found in practice. The simulated parameter space was filtered using ULS (out-of-plane bending, shear and rolling shear) and SLS (permanent deformation) minimum requirement criteria. The mechanical properties of the CLT build-ups were taken from a database provided by CLT manufacturer Derix, and a damping ratio of 2.5% was assumed, as recommended for CLT floors (prEC5 9.3.1.1). Based on the influence of the boundary conditions on the response of the floors, two datasets were simulated, one representing the assumption of floors supported on two sides and another representing floors supported on all sides. All the variants in the simulated databases were run in a parametric numerical model developed in OpenSeespy to obtain the modal properties of the floors for the first five modes of vibration. The workflow for the data simulation is shown in Figure 3.1

Table 3.1. Ranges for variables in parameter space of numerical simulations

	units	lower limit	upper limit	step
Floor width	m	2.5	10.0	2.5
Floor span	m	3.0	8.0	0.5
Build-up height	mm	60	400	10
Permanent load	kg/m <sup>2</sup>	0	300	100
Variable load	kg/m <sup>2</sup>	0	500	100

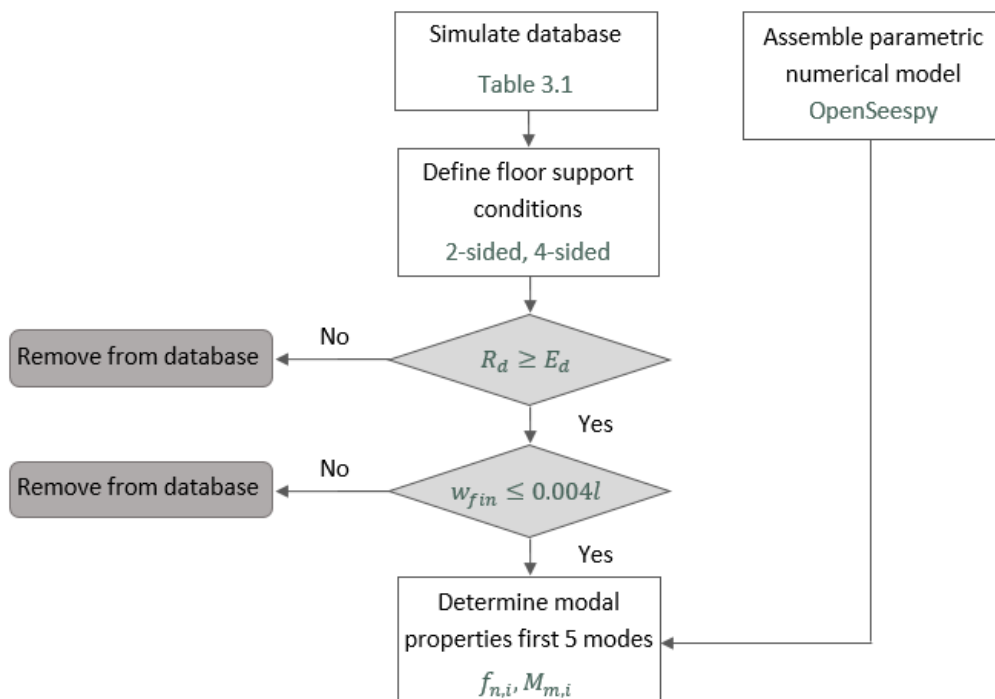


Figure 3.1. Database simulation workflow



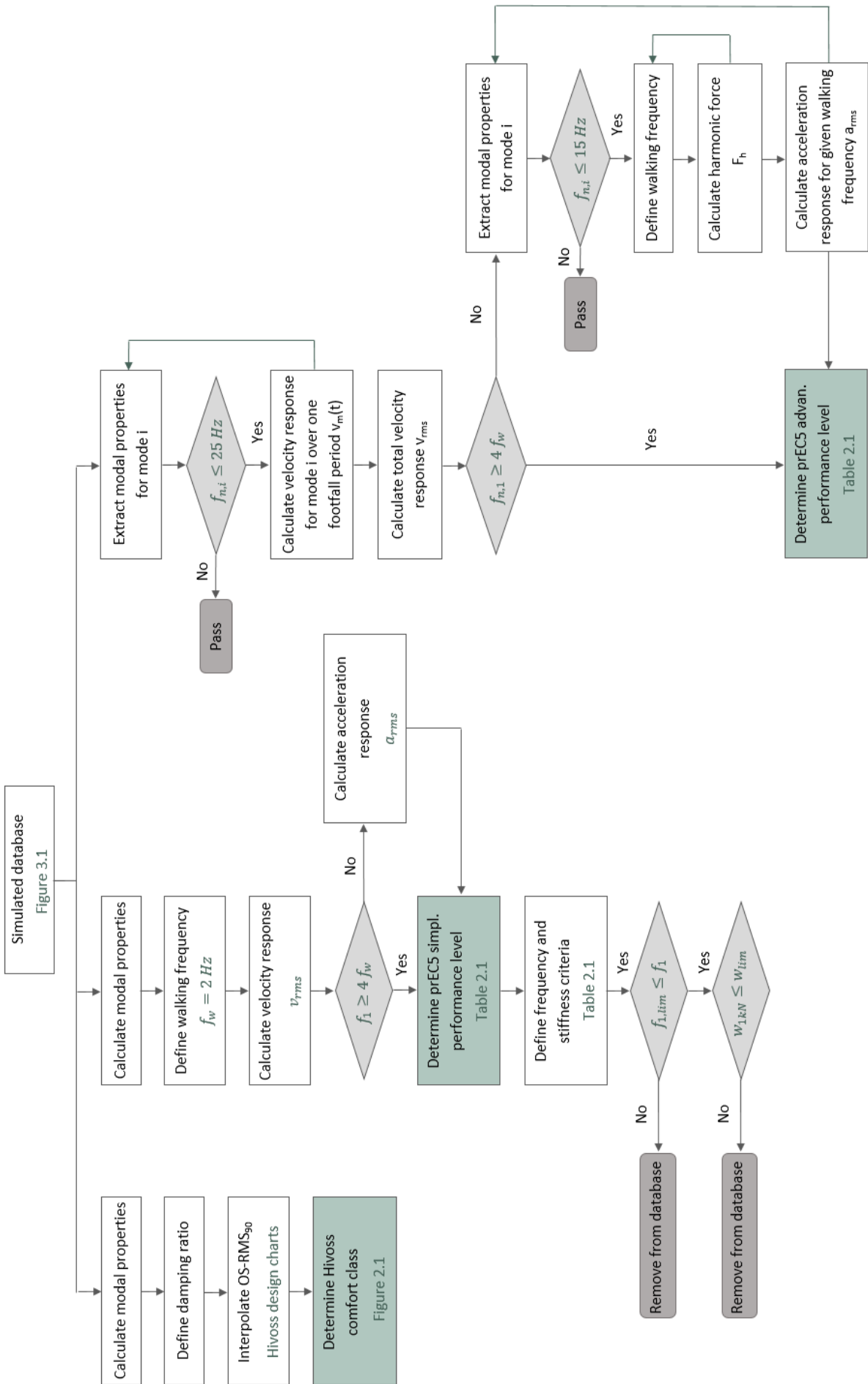


Figure 3.2. Performance level assessment framework for prEC5 and Hivoss methods

Based on the simulated data from Figure 3.1, the performance levels based on prEC5 simplified and advanced methods, and comfort class based on SBR/Hivoss method was determined for all variants as shown in Figure 3.2. As mentioned in section 2.2.2, the method presented in the prEC5 requires the selection of a performance level for verification, thus some adjustments were done on the proposed framework to match the framework of this study. Based on the governing performance level found from the velocity and acceleration criteria, the frequency and stiffness limits were defined to further filter the databases. Based on this adjusted framework, higher demands were imposed on better performing floors, which influenced the final number of variants in the databases. For the two-sided supported database 15% of the variants were removed, while for the four-sided supported database 22% of the variants were removed.

### 3.2 OpenSees model

The advanced method presented in the prEC5 takes as input the modal properties of the floor obtained from a numerical model. In order to efficiently model and analyse all the variants in the parameter space of this study, a parametric model was developed in OpenSeespy. All floor plates were simulated using 'ShellMITC4' elements with 'ElasticOrthotropic' material definition. Equivalent bending and shear stiffness properties were extracted from the cross-sectional stiffness matrix provided by the Derix database. From a short sensitivity study it was found that the mesh size had an influence in the deformed shape of the floors, and thus the modal properties. For the scope of this study a mesh of 0.5 m was found to provide an accurate representation of the floor behaviour. The supports of the system were defined as continuous hinges along either two or four sides of the plate, based on the boundary conditions definition. Additionally, pinned connections were added to represent panel-to-panel connections, for variants with widths larger than one panel. The panel width is defined as 2.5 m, thus all variants with larger width, incorporate the inter-panel connection. The assumption of pinned connections considers the expected behaviour of the connectors under SLS loading, as mentioned in prEC5 Clause G.3 (5). The output of the numerical model provides the modal properties of the floor for the first five modes of vibration.

#### 3.2.1 Model validation

Given the dependency of the advanced prEC5 method on the output from the numerical model, an example validation is done to compare the magnitude of the frequency of the first vibration mode against the analytical formulations presented in prEC5 Clause 9.3. Table 3.2 presents the geometry and build-up characteristics of the example floor taken as a reference from practice.

Table 3.2. Ranges for variables in parameter space of numerical simulations

Build-up	Span (m)	Width (m)	G* (kg/m <sup>2</sup> )	Q (kg/m <sup>2</sup> )	(EI) <sub>L</sub> (Nm <sup>2</sup> )	(EI) <sub>T</sub> (Nm <sup>2</sup> )
L-180/7s	5	5.4	181	300	4224000	1122000

\*including self-weight

$$m = G + 0.1 \cdot Q = 181 + 0.1 \cdot 300 = 211 \text{ kg/m}^2$$

Two-sided supported

$$f_1 = k_{e,1} k_{e,2} \frac{\pi}{2l^2} \sqrt{\frac{(EI)_L}{m}} = 1.0 \cdot 1.0 \cdot \frac{\pi}{2 \cdot 5^2} \sqrt{\frac{4224000}{211}} = 8.9 \text{ Hz}$$

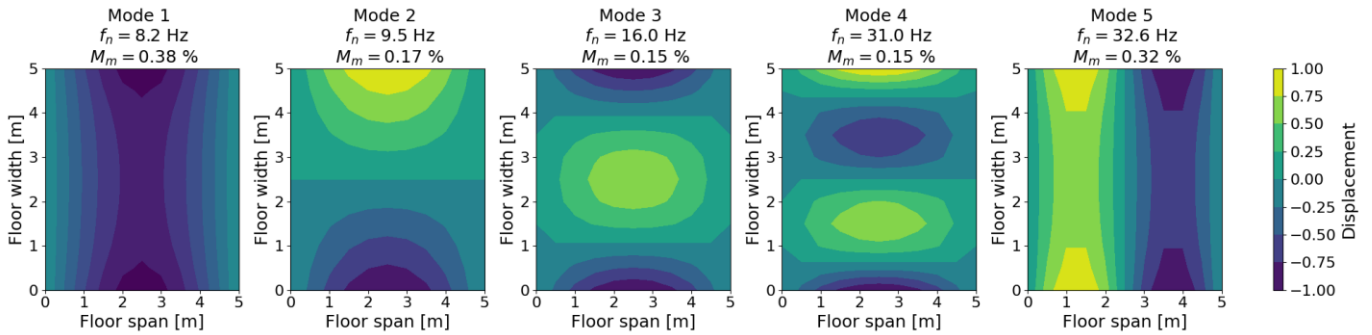


Figure 3.3. Modal properties example floor two-sided supported

Four-sided supported

$$k_{e,2} = \sqrt{1 + \left(\frac{l}{b}\right)^4 \frac{(EI)_T}{(EI)_L}} = \sqrt{1 + \left(\frac{5}{5.0}\right)^4 \cdot \frac{1122000}{4224000}} = 1.16$$

$$f_1 = k_{e,1} k_{e,2} \frac{\pi}{2l^2} \sqrt{\frac{(EI)_L}{m}} = 1.0 \cdot 1.16 \cdot \frac{\pi}{2 \cdot 5^2} \sqrt{\frac{4224000}{211}} = 10.4 \text{ Hz}$$

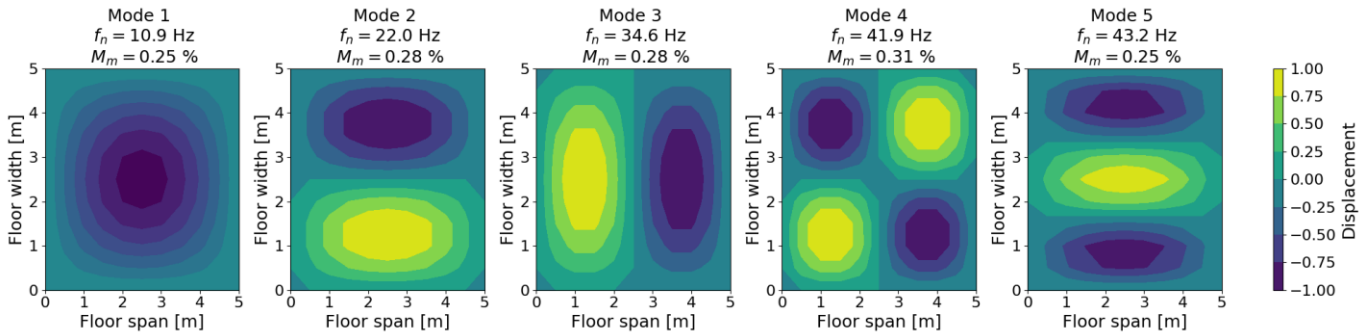


Figure 3.4. Modal properties example floor four-sided supported

Additionally, the frequency of the first mode obtained from the numerical model was compared to the analytical formulation for all floor variants, as presented in Figure 3.5. The correlation coefficient, *R*, was found to be 0.99 for the two-sided supported floors and 0.97 for the four-sided supported floors. These high correlation factors indicate that the numerical model is well validated against the analytical results. Small deviations between the methods could be attributed to the shear stiffness properties of the shell elements in the numerical model, which are not considered by the analytical formulation.

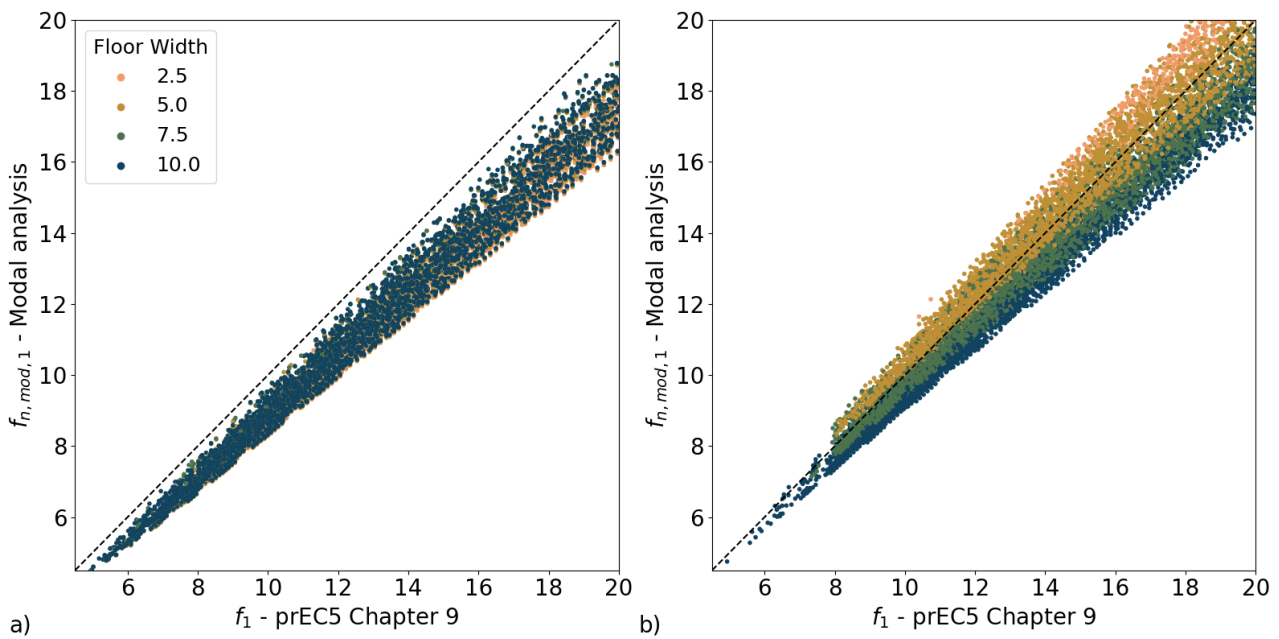


Figure 3.5. Correlation analytical vs. numerical natural frequency for floors supported on a) two-sides b) four-sides.

## 4 Results and discussion

### 4.1 Modal properties

Both the Hivoss and prEC5 methods can be applied based on the modal properties obtained from analytical formulations or numerical models for a more accurate representation of the floor behaviour. As shown in section 3.2.1, the natural frequency of the first mode is accurately represented by the analytical formulations. On the other hand, the modal mass activated by the first vibration mode obtained from the numerical model shows a deviation from the analytical formulations presented by both methods. Figure 4.1 a) shows that for floors supported on two sides, the percentage of the mass activated by the first mode decreases as the width of the floor increases, while the analytical formulation remains constant. It can be seen that the variability of the modal mass obtained from the numerical model also increases as the floor width increases, and this is related to the different ratios between longitudinal and transverse stiffness found in the floor variants. Floor variants with a lower transverse stiffness are found to have a higher correlation to the analytical formulation, while as the transverse stiffness increases, there are larger deviation. Figure 4.1 b) shows that for floors supported on four sides the output from the numerical models show a nearly constant definition of the modal mass with a low variability which aligns with the analytical formulation. It can be seen that floors with widths of 2.5 m show a small deviation from the analytical formulation; however, this was found to be caused by the roughness of the mesh in the numerical model, which influences the deformed shape for the floors with the smallest width.

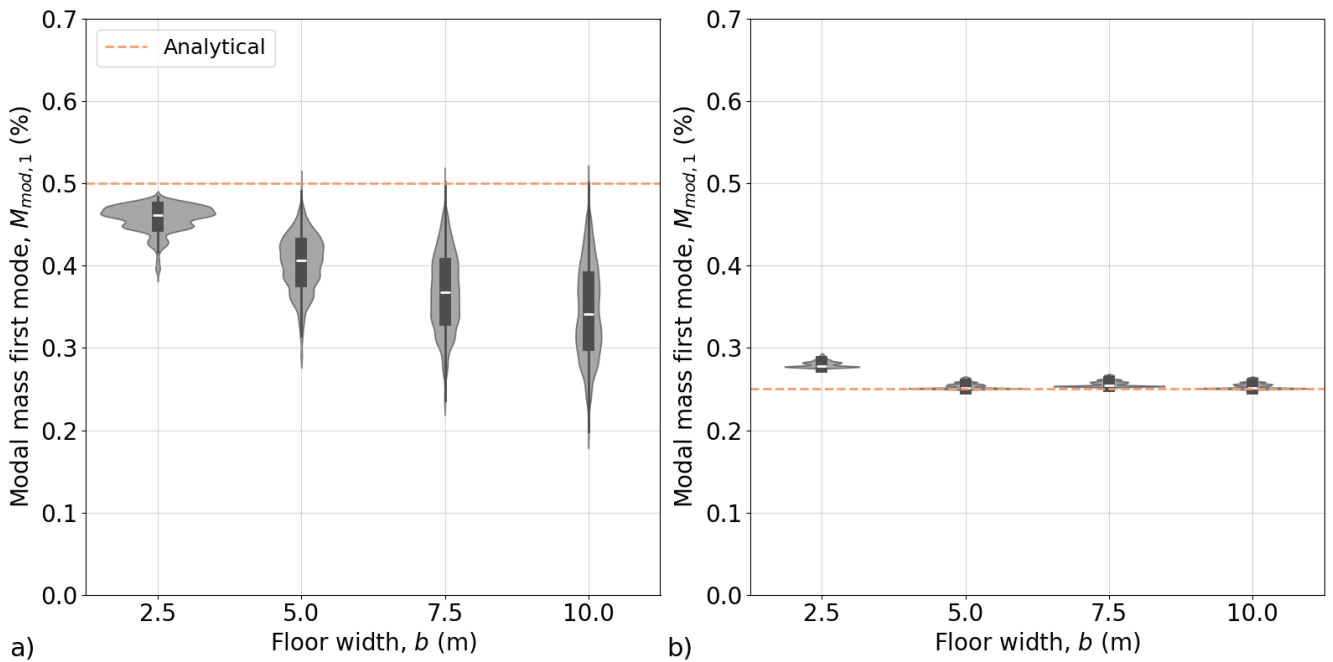


Figure 4.1. Modal mass first mode from numerical model for floors supported on a) two-sides b) four-sides.

#### 4.2 Correlation prEC5 simplified and advanced methods

Figure 4.2 presents the correlation between the performance levels given by prEC5 simplified and advanced methods for the two different boundary conditions definitions. Only floors with assigned performance levels by both simplified and advanced methods were considered to assess the correlation between the methods. The size of the dots in each graph represents the number of variants at a given location, while the colour indicates the governing criterion to determine the performance level. When the governing criterion is labelled as either 'velocity' or 'acceleration', this indicates that at least 80% of the variants at that location are governed by said criterion, while the label 'mixed' indicates that variants at that location have no clear governing criterion. In the figure it can be seen that for most variants where the velocity criterion is governing, the simplified method provides a good or conservative estimation of the response, compared to the advanced method. However, for a small number of floors, the advanced method shows a worst performance when velocity is governing. These variants are characterized by larger floor width, where as shown in Figure 4.1, the modal mass obtained from the numerical model is significantly lower than the analytical definitions, thus leading to higher velocity response. Additionally, the more critical response given by the advanced method could be caused by the definition of the modal impulse. While the simplified method provides mean modal impulse values, the advanced method assesses the effective design value of the modal impulse, which leads to higher loads. Lastly, it must be noted that in this investigation the integration of the time history velocity response of the floor during a footfall period presented by the advanced method, was assessed by discretizing the response into time steps. It was found that the response is sensitive to the time step definition, as smaller time steps provide a better representation of the response. For the scope of

this study, it was found that a minimum of fifty time steps provided an accurate representation of the response as recommended by the SBR/Hivoss method.

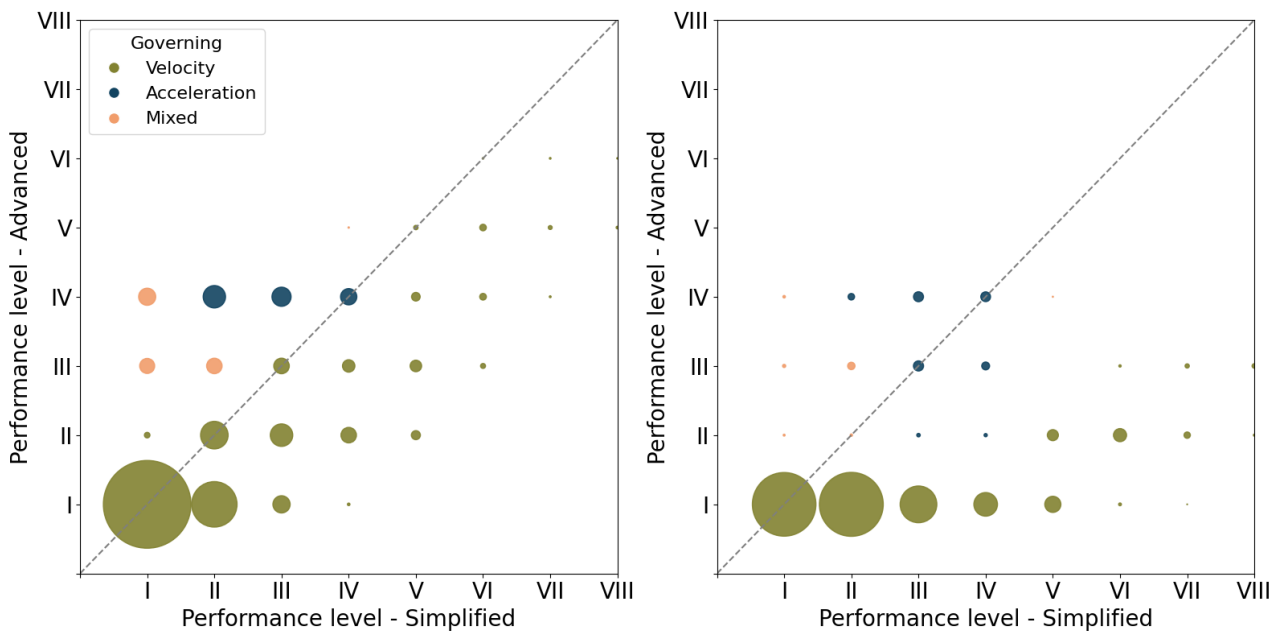


Figure 4.2. Correlation performance levels based on prEC5 Chapter 9 method and prEC5 Annex G method for a) 2-sided supported floors and b) 4-sided supported floors.

Figures 4.2 a) and b) show that for most variants where the acceleration criterion is governing, the advanced method provides a worst performance level than the simplified method. A sharp change on this trend can be seen at performance level IV, caused by the limits presented in Table 2.1, where it is mentioned that for higher performance level the acceleration criterion is not applicable. As explained for the velocity response, the deviation between the modal mass definitions for wider floors supported on two sides influences the discrepancy in performance level; however, larger deviations can be explained by fundamental differences between the two methods. The simplified method determines the rms acceleration for full resonance build up for a single governing mode, with a reduction factor that accounts for the low probability that the walker path aligns with the critical path that would cause resonant build up (Abeysekera et al 2018). This reduction factor is defined as 0.4, as presented in the Austrian National Annex, regardless of the floor modal properties and assumed walking frequency. On the other hand, the advanced method determines the rms acceleration for all combinations of floor modes and walking frequency harmonics, which increases the likelihood that full resonant build up might be captured for certain floor variants. A reduction factor to account for the low probability of full resonant build up occurring is also presented; however, this factor is defined based on the geometry of the floor and the harmonic loading. For the scope of this study it is found that this reduction factor is much larger than the one presented in the simplified method. Additionally, it is stated that the factor can be conservatively taken as 1.0, which would lead to considering full resonant build up in the response.

4.3 Correspondence Hivoss and prEN 1995-1-1

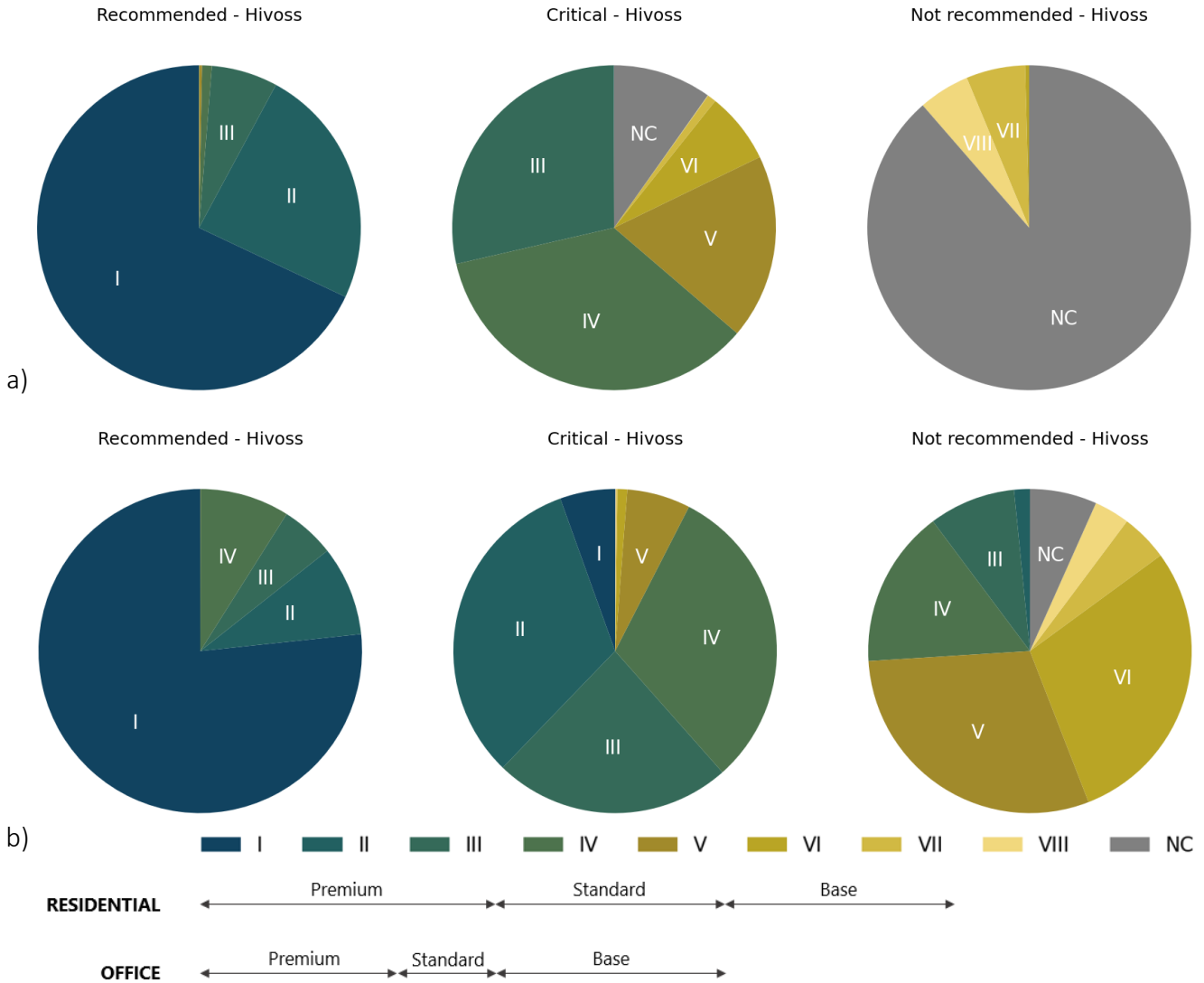


Figure 4.3. Correspondence SBR comfort criteria and prEC5 performance levels for a) simplified method and b) advanced method

Figure 4.3 shows the correspondence between the comfort acceptance levels defined by the Hivoss method (presented in Figure 2.1) and the performance levels from the prEC5 for two-sided supported floors according to a) simplified method and b) advanced method. Each chart presents the percentage of the floors within the Hivoss category that correspond to the different performance levels defined by the prEC5. An additional label 'NC' is added for all floors that would be assigned the given Hivoss comfort category, but are disregarded by the prEC5 methods due to the response being outside the acceptable limits or due to the stiffness and/or frequency criteria from the simplified method. Figure 4.3 a) shows that a large number of floors are labelled as 'NC' by the prEC5 for the Hivoss classes 'Critical' and 'Not recommended', this shows that the prEC5 provides a more strict assessment of more flexible floors than the Hivoss, which could potentially lead to an impact on current design practices.

When assessing the relation between the two comfort definitions, Figures 4.3 a) and b) show a high correspondence between prEC5 class 'Premium' and Hivoss class

'Recommended', for both residential and office use. On the other hand, Figure 4.3 b) shows the effect of the differentiation between comfort threshold levels for residential and office use presented by prEC5, which is not considered by the Hivoss. For residential use there is a good relation between the prEC5 class 'Standard' and the Hivoss class 'Critical', well as the prEC5 class 'Base' and the Hivoss class 'Not recommended'. However, for office use it can be noted that both prEC5 classes 'Standard' and 'Base' can be related to the Hivoss class 'Critical', which could potentially lead to a significant impact on current design practices.

## 5 Conclusions and recommendations

The main goal of this investigation was to study the correspondence between the Hivoss method currently used in practice to assess the vibration response of lightweight floors and the method proposed by the prEC5. Additionally, to study the correlation between the comfort assessment provided by the simplified and advanced methods within the prEC5. In terms of the correspondence between the methods, it was found that based on the prEC5 simplified method assessment criteria a large percentage of floors, which would have been accepted by the SBR/Hivoss method and labelled as either 'Critical' or 'Not recommended' are now discarded due to minimum frequency and stiffness criteria. Thus highlighting that the implementation of the suggested frequency and stiffness criteria for performance levels IV-VIII would have a large impact on the current design of timber lightweight floors. On the other hand, the performance level distribution found from the prEC5 advanced method over the Hivoss categories, showed a good correspondence to the comfort choice ranges presented by Table 2.2. However, the differentiation between comfort acceptance for office and residential buildings could lead to differences in design.

When comparing the assessment based on the simplified and advanced methods from the prEC5, it was found that the definition of the modal properties was of high influence on the outcome. The simplified method uses analytical definitions for the natural frequency and modal mass of the governing vibration mode, while the advanced method uses the output from numerical models. It was found that the modal mass of floors supported on two sides was significantly overestimated by the analytical formulations, especially for floors with larger widths, which influenced the response assessment. It is recommended that more guidance is provided for assessing the modal mass of floors supported on two sides, considering the geometry and orthotropic properties of the plate. Additionally, it was found that there are fundamental differences between the methods to assess the acceleration response. While the simplified method provides high reduction factors to account for the low probability of full resonant build up occurring, the advanced method presents more conservative factors which lead to significantly higher response, and thus a worst classification of the floor performance.



## 6 References

- Eurocode 5 (2004): Design of timber structures - Part 1-1: General and rules for buildings. CEN. (EN 1995-1-1).
- SBR 539 (2008): Trillingen van vloeren door lopen – Richtlijn voor het voorspellen, meten en beoordelen. SBR.
- Feldmann, M., Heinemeyer, C., Lukic, M., Caetano, E., Cunha, A., Goldack, A., Keil, A., Schlaich, M., Hicks, S., Smith, A., Hechler, O., Obiala, R., Galanti, F., Waarts, P. (2007): Human-induced vibration of steel structures (Hivoss). Research Fund for Coal and Steel.
- CEN/TC 250/SC 5 N 2077 (2024): Eurocode 5 – Design of timber structures – Part 1.1: General rules and rules for buildings.
- Willford, M.R., Young, P. (2007): A Design Guide for Footfall Induced Vibration of Structures. The Concrete Center.
- Toratti, T., Talja, A. (2006): Classification of Human Induced Floor Vibrations. Journal of Building Acoustics 2006 vol 13 no 3.
- Abeysekera, I.K., Hamm, P., Toratti, T., Lawrence, A. (2018): Development of a floor vibration design method for Eurocode 5. International Network on Timber Engineering Research 2018, Tallinn Estonia.

## DISCUSSION

**The paper was presented by M Felicita**

*F Lam asked, how was the continuity between adjacent panels considered? Also, the boundary conditions suggest the floors were supported by walls and what about floors supported by beams? M Felicita responded that pin-pin connectors were used to connect adjacent panels in the model. Results were not sensitive to the type of connection. The beam supported case was not studied and can be considered in future.*

*P. Vinco da Sesso commented that concrete topped CLT floors are commonly used and pinned connections between adjacent panels may not be appropriate. M Felicita responded that model results indicated low impact whether pin connections or other fasteners were considered.*

*A Frangi and M Felicita discussed about the fact that the simplified method assumed resonance occurred whereas the advanced model had factors that considered low probability occurrence of resonance, discussing which one is more suitable for codes. E Serrano and M Felicita discussed details of the difference between the simplified and advanced model.*

*P Dietsch asked whether the CLT layup was adapted to the different sizes and spans of floors. M Felicita said this was not done. P Dietsch asked whether there are plans to consider the influence of non-load bearing walls. M Felicita agreed that this is an important topic and will be studied in future.*

*E Serrano asked whether point loads were applied in the FEM. M Felicita said that the model did not consider modelling loading from a walker but only consider the dynamic properties of the floor.*

*D Casagrande questioned the ratios between longitudinal versus transverse properties. M Felicita responded that manufacturer's publication data was used.*



## 4 INTER Notes, Padova 2024



# Beech LVL and moisture – a known challenge

Carmen Sandhaas, Karlsruhe Institute of Technology

## 1 Introduction

Laminated veneer lumber made of beech (beech LVL) is a versatile and popular building product in Europe. Due to its higher mechanical properties in comparison to products made of spruce, beech LVL is often used for high load-bearing purposes, e.g. as columns. This increase in use, however, comes hand in hand with an increase in observed issues with moisture uptake, see example shown in Figure 1, where it is important to realise that beech LVL is produced and delivered with moisture contents between 5% and 10% (ETA-14/0354, 2021).

The effects of moisture content changes on beech LVL (resp. *Fagus sylvatica* in general) are well known. Lower mechanical properties of beech LVL at higher moisture contents for instance are reflected in different characteristic compressive strength values for different service classes (ETA-14/0354, 2021). Also shrinkage and swelling of beech LVL were investigated, for instance by Wenker and Welling (2017) who stated that the reaction of beech LVL to changes in relative humidity is slow, but that uptake of moisture can lead to severe damage or even complete failure of beech LVL elements. Wenker and Welling stated that beech LVL must be protected from water e.g. during transport, that erection works should be stopped during rainfall and they recommend to monitor finalised buildings for leakages. Recent publications provide methods for monitoring of moisture in beech LVL (Schiere et al., 2022; Grönquist et al., 2021). Finally, producers state clearly that beech LVL should be coated to prevent damage due to absorption of moisture (Pollmeier, n.d.; Koch & Schulte and Pollmeier, 2018). It can be assumed that coated beech LVL could suffer damage during CNC machining, transport or erection.

Despite all this knowledge, Figure 1 shows how difficult implementation of protective measures is on site, and this note wants to emphasise just how severe moisture uptake of beech LVL via the end grain can be.



Figure 1. Detail on site of observed moisture uptake of a column made of beech LVL (photo taken in February 2024).

## 2 Test programme, results and conclusions

Triggered by observed moisture uptakes, see Figure 1, a simple test programme was carried out, simulating beech LVL columns subject to rainfall. For this, specimens were placed with their end grain onto a plane basin, which was filled with water up to a certain water level. After a certain time span, the specimens were sawn into 10 mm thick slices along the specimen length  $L$ , and the moisture content of the slices was determined with the oven-dry method in order to obtain the moisture gradient along the length  $L$ . Figure 2 shows the specimen geometry and the sawing pattern after soaking. Table 1 lists the different series, where all specimens were stored at 20/65 prior to testing. Before soaking, a reference slice was cut from each specimen, and the moisture content (m.c.) of the reference slice was determined with the oven-dry method (initial m.c. in Table 1, only Series 1 to 4). On un-cut dry and soaked specimens, Series 5, the compressive strength parallel-to-grain was determined by putting the complete specimens with a length of 272 mm in a testing machine.

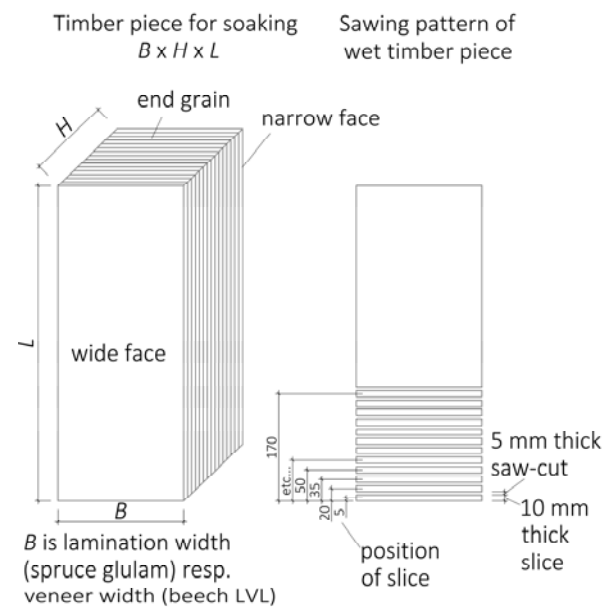


Figure 2. Test specimens and sawing pattern after soaking

Table 1. Test series. Weight in g.

Series	Material	$B \times H \times L$ in mm	Test	Initial m.c.	Initial % weight	Weight after 10 min wet	Weight after 2 days	Final weight
1	a	Spruce GLT 100x100x287	Water level 5 mm:	11.6	1208	1216	1252	1286
	b	Beech LVL 100x100x287	7 days wet (large specs 8 days wet)	7.4	2186	2208	2400	2544
	c	Beech LVL 198x198x487		7.7	15002	15114	15794	16370
2	a	Spruce GLT 100x100x287	Water level 10 mm:	11.8	1234	1282	1282	1316
	b	Beech LVL 100x100x287	7 days wet (large specs 8 days wet)	7.7	2192	2406	2406	2554
	c	Beech LVL 198x198x487		7.6	15190	15924	15924	16538
3	a	Spruce GLT 100x100x272	Water level 5 mm:	11.9	1142	1148	1192	
	d	Spruce LVL 100x100x300	4 days wet, 2 days dry, 1 day wet	9.6	1468	1484	1652	
	b	Beech LVL 100x100x272		8.5	2084	2100	2312	
4	a	Spruce GLT 100x100x272	Water level 2 mm: 2 days wet	12.0	1156	1162		1208
	d	Spruce LVL 100x100x300		9.4	1492	1506		1640
	b	Beech LVL 100x100x272		8.0	2070	2088		2288
5			Dry		2112	2112	2116	2116
			Dry		2102	2102	2104	2106
			6 days wet (5 mm water)		2088	2104	2342	2484
			6 days wet (water)		2080	2098	2324	2456

Figure 3 shows the m.c. profiles along the specimen length (Series 1 to 4), where the position of the slices starts from the end grain, see also Figure 2. Obviously, the water level does not influence the m.c. profile of timber, whereas the timber product and the duration of soaking matters, which does not come as a surprise. However, the speed with which moisture penetrates LVL products and to which “height” it reaches is astonishing. For LVL products, the m.c. is back to its initial values only after about 140 mm, whereas for spruce, the initial m.c. is reached already after about 80 mm. Already after 2 days of exposure to liquid water at the end grain, Series 4, the fibre saturation point of LVL products is reached at 50 mm distance from the end grain, leading to significantly reduced compressive strength parallel-to-grain. However, the severity of moisture uptake is less strong at shorter exposition times to liquid water. The swelling deformation in particular of beech LVL is permanent, also if the specimens are re-dried.

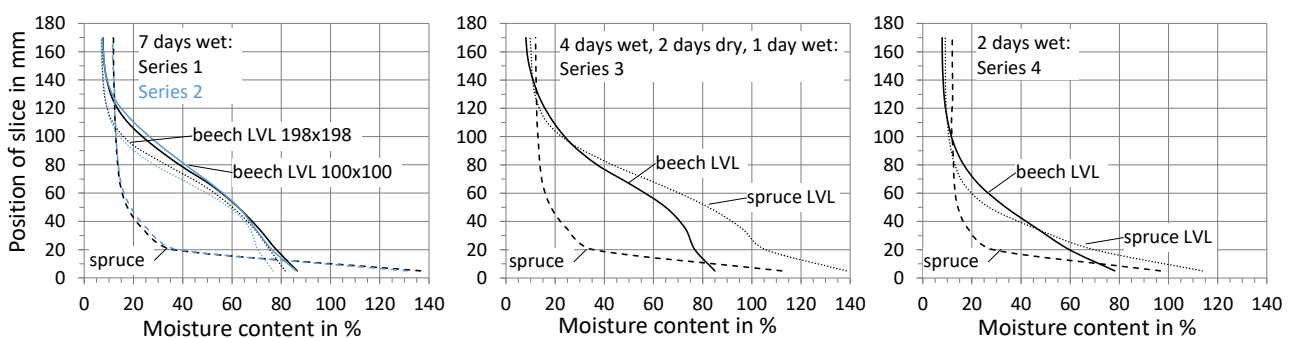


Figure 3. Moisture content versus position of slice from “bottom” for Series 1 to 4.

Table 2. Results Series 5.

Specimen	$f_{c,0}$ in MPa
Dry	61.8
Dry	62.4
Wet	24.3
Wet	23.8

Table 2 gives the compressive strength (Series 5), where the maximum measured force was divided by an area of 100x100 mm<sup>2</sup> and where the m.c. profiles of the wet specimens will correspond to those of Series 1b and 2b. If the rule from EN 384 of 3% change of compressive strength parallel-to-grain for every percentage point difference in m.c. is considered, a compressive strength of 62 MPa at 8% m.c. results in 11.8 MPa for a m.c. of 35%, which is the fibre saturation point of beech.

The known issues of rapid moisture uptake and significantly reduced strength at higher m.c. could again be underlined and clearly illustrated with the simple test programme. In order to develop recommendations for building practise (in case of exposition of uncoated products to moisture), further, more systematic tests could derive feasible time limitations (e.g. max 12h of exposure to liquid water at end grain) and the reduction of compressive strength parallel-to-grain of re-dried specimens could be assessed.

ETA-14/0354 (2021): Beam BauBuche GL75. European Technical Assessment.

Grönquist P, Weibel G, Leyder C, Frangi A (2021): Calibration of electrical resistance to moisture content for beech laminated veneer lumber “BauBuche S” and “BauBuche Q”. *Forests* **12**:635. DOI: 10.3390/f12050635.

Koch & Schulte, Pollmeier (2018): Beschichtungssysteme für BauBuche - Lasst es regnen. Advertisement in *Mikado* (1–2):56–57.

Pollmeier (n.d.): BauBuche - Wood preservation and surface treatment. Available at <https://www.pollmeier.com/wp-content/uploads/2023/03/Section-09-Wood-preservation-surface-treatment.pdf>. Accessed 03.07.2024.

Schiere M, Franke B, Franke S, Müller A (2022): Calibration and comparison of two moisture content measurement methods for in situ monitoring of beech laminated veneer lumber. *Wood Material Science and Engineering* **17**(6):790–801. DOI: 10.1080/17480272.2021.1958918.

Wenker JL, Welling J (2017): Klimaversuche für den Baustelleneinsatz. *Bauen mit Holz* (11):28–32.





# Withdrawal Capacity of Coated Ring Shank Nails

Aygül Ceylan, Faculty of Architecture, Yildiz Technical University, Istanbul, Turkiye

Z.Canan Girgin, Faculty of Architecture, Yildiz Technical University, Istanbul, Turkiye

Keywords: Withdrawal capacity  $F_{ax}$ , Ring shank nails, Coating.

## 1 Introduction

The equations for the withdrawal capacity ( $F_{ax}$ ) of nailed joints are based on the allowable design values in current standards and regression analyses from test results. Although the withdrawal capacity of screws has been addressed in numerous studies so far, the studies on ring shank nails and their coatings are less prevalent (Görlacher, 1995; Skulteti et al., 1997; Rammer et al., 2001; Franke et al., 2018), and there are no consistent rules for ring shank nails in the current version of EC5. Skulteti et al. (1997) and Rammer et al. (2001) indicated  $F_{ax}$  to 34-50% higher capacity than National Design Specification. Kevarinmaki (2005) tested five types of gun-driven nails on spruce samples and recommended for EC5 to reduce the withdrawal parameter  $f_{ax}$  by a factor of 0.4 for plain nails and at least 0.7 for profiled nails by noting hot-dip galvanized nails to have the highest pull-out strength. Sandhaas & Görlacher (2017) emphasized quite similar results of stainless steel nails and hot-dip galvanized nails.

Coatings can be used not only to resist corrosion in damp conditions but also to improve driving resistance for nails. The properties of the grade and thickness for stainless steel as well as *Fe-Zn* coatings are defined in EN 14592. However, current standards lack information about alternative corrosion-resistant coatings of threaded nails. Phosphate coating is used in the metalworking industry, and Ceylan & Girgin (2020) is the first experimental study about that coating of ring shank nails. In this paper, findings from withdrawal tests on three kinds (galvanized, galvanised+resin, phosphate) of coated ring shank nails are evaluated. The other aim of this paper is to discuss common models from current literature for proper engineering design.

## 2 Material, Method, and Findings

First, the mechanical characteristics (yield/ultimate strength, hardness) of nails were experimentally determined before the tests. Three kinds, and six series of ring shank nails were used in withdrawal tests ( $d= 2.95-3.38$  mm). The symbols are galvanized (RN-G), galvanized+resin (RN-RG), and phosphate coated nails (RN-P) (Figure 1). The

nails were applied to total 200 European spruce CLT samples (C24,  $\rho=0.46$ , perpendicular to grain) of 50mmx50mmx100mm as gun (G) and manual (M) driven in a universal test machine.  $P-\Delta$  curves under pull-out were drawn and withdrawal energy ( $E$ ) beyond the elastic limit was computed.

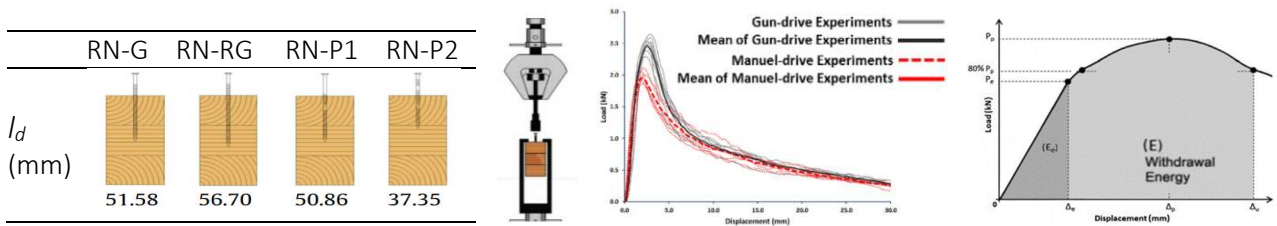


Figure 1. CLT samples with penetration depths ( $l_d$ ), test set-up, the mean  $P-\Delta$  curves, and  $E$  graph.

$F_{ax}$  (EN 14592) is described by excluding smooth nails, and the other characteristics are the penetration depth of fastener  $l_d$ , and the nominal diameter of nail  $d$  (EN 1382). Common models to predict  $F_{ax}$  are given in Table 1.

Table 1. Common models of  $F_{ax}$  (N/mm) for ring shank nails from current literature.

Model	Equations	Source
1	$F_{ax} = 36 \cdot 10^{-6} \rho_k^2 d$	Ehlbeck and Siebert, 1988
2	$F_{ax} = 42.8 \rho^{1.38} d$	Rammer et al., 2001
3	$F_{ax} = 0.117 d^{0.6} l_d \rho_k^{0.8}$	Blaß and Uibel, 2006
4	$F_{ax} = 73.11 \rho^2 d l_d$	FLP-GTR-190:2010
5	$F_{ax} = 77.51 \rho^2 d$	Rammer and Zelinka, 2015
6	$F_{ax} = f_{ax} d l_d$ , $\begin{cases} f_{ax} = 6.125 \left(1 + \frac{1.5 d}{l_d}\right) \left(\frac{\rho_k}{350}\right) \\ f_{ax} = (10.92 - 0.0158 d - 0.0968 l_d) \left(\frac{\rho_k}{320}\right)^2 \end{cases}$	Izzi et al., 2016

$\rho_k$ =characteristic density (kg/m<sup>3</sup>);  $\rho$ =specific gravity;  $l_d$ =penetration depth;  $d$ = nominal diameter of nail (mm).

According to test results, the mean  $F_{ax}$  of RN-P1-M nails is 42% higher than reference RN-G-M, and RN-P1-G nails is also 27% higher than RN-P1-M (Table 2). Those results are also discussed with common models through Mean Percentage Error (MPE). Model 1 underestimates the experimental results; Models 2 and 4 well predict gun driven phosphate coated nails; Model 3 gives good estimation only for RN-RG-M. Finally, Model 6 adopted by EC5 and ETA-04/0013 presents a good prediction for RN-G-M however underestimates other ones, gun/hand drive.

Table 2. Comparisons of observed withdrawal capacity with predicted ones.

Series	Experimental (N/mm)	Predicted from models (N/mm)					
		1	2	3	4	5	6
RN-P1-M	39.06	24.38 (+37.47%)	46.90 (-20.3%)	31.73 (+18.6%)	49.50 (-27.0%)	52.48 (-34.62)	28.19 (+27.7%)
RN-P1-G	49.53	24.38 (+50.0%)	46.90 (+6.3%)	31.73 (+35.9%)	49.50 (+2.6, -2.7%)	52.48 (-4.9%)	28.19 (+42.2%)
RN-P2-G	41.58	21.71 (+47.8%)	41.77 (+1, -1.2%)	29.61 (+28.8%)	44.09 (-6.06%)	46.74 (-12.4%)	25.57 (+38.5%)
RN-RG-M	30.37	22.47 (+26.0%)	43.24 (-42.5%)	30.22 (+1.5, -3.8%)	45.64 (-50.4%)	48.38 (-59.4%)	25.60 (+15.6%)
RN-RG-G	34.62	22.47 (+35.0%)	43.24 (-25.0%)	30.22 (+12.6)	45.64 (-31.9%)	48.38 (-39.9%)	25.60 (+26.0%)
RN-G-M (Reference)	27.40	22.5 (+16.2%)	43.24 (-61.2%)	30.22 (-10.7%)	45.64 (-67.3%)	48.38 (-80.4%)	25.78 (+3.9%)

### 3 Conclusions

The following conclusions from this study can be drawn:

- The phosphate coated ring nails have the highest pull-out strength due to the mechanical friction of rough crystalline coating as well as outdoor damp resistance.
- Models 2 and 4 successfully estimate gun driven phosphate coated nails (RN-P-G), Model 3 is the best one for manual-driven resin coating (RN-RG-M).
- Model 6 (EC5, ETA-04/0013) only predicts manual-driven galvanized ring nails (RN-G-M) quite well, there is a need to reveal a reliable model for other coatings.
- Higher withdrawal capacity of phosphate coated ring nails may lead to more economical and high-performance solutions of CLT connections in future applications.

### 4 Acknowledgements

This study was financially supported with Project Number FDK2018-3367 by Research Fund of the Yildiz Technical University.

### 5 References

- Ceylan A, Girgin ZC (2020) Comparisons on withdrawal resistance of resin and phosphate coated annular ring nails in CLT specimens. *Constr. Build. Mater.*, 238.
- Ehlbeck J, Siebert W (1988) Axially loaded nails: Proposals for supplement to the CIB code, Int. Council Build. Res. Studies Docum. Working Commis. W18A-Timber Struct. CIB-W18A/21-7-5, Universitat Karlsruhe, Germany.
- EN 1995-1-1:2004 (Eurocode 5). Design of timber structures - Part 1-1: General - Common rules and rules for buildings. CEN.
- EN 1382. 2016. Timber Structures - Test methods - Withdrawal capacity of timber fasteners. CEN.
- EN 14592. 2008. Timber structures. Dowel-type fasteners. Requirements. CEN
- Franke S, Schiere M, Franke B (2018) Press glued connections-Research results for discussion and standardization. INTER Confer. Proc., Estonia, paper 51-18-2.
- Görlacher, R (1995) Load-carrying capacity of steel-to-timber joints with annular ringed shank nails- A comparison with the EC5 design method. CIB/W18 Confer. Proc. 1995, Copenhagen, Denmark, paper 28-7-3.
- Izzi M, Flatscher G, Fragiaco M, Schickhofer G (2016) Experimental investigations and design provisions of steel-to-timber joints with annular-ring shank nails for cross-laminated timber structures, *Constr. Build. Mater.* 122 446–457.
- Kevarinmaki, A (2005) Nails in spruce splitting sensitivity, end grain joints and withdrawal strength. CIB/W18 Conf. Proc., Karlsruhe, Germany, paper 38-7-6.
- Rammer DR, Winistorfer SG, Bender DA (2001) Withdrawal strength of threaded nails. *J. Struct. Eng.* 127 (4), 442–449.
- Rammer DR, Zelinka SL (2015) Withdrawal strength and bending yield strength of stainless steel nails. *J. Struct. Eng.* 141 (5), 04014134.
- Sandhaas C, Görlacher R. (2017) Nailed joints: Investigation on parameters for Johansen model. INTER Conf. Proc., Kyoto, Japan, paper 50-7-3.
- Skulteti MJ, Bender DA, Winistorfer SG, Pollock DG (1997) Withdrawal strength of ring-shank nails embedded in southern pine lumber. *Trans. ASAE*, 40(2), 451-456.



# An Ecologic Lightweight Suggestion for Concrete Layer of CLT-Composite Floors

Z.Canan Girgin

Yildiz Technical University, Faculty of Architecture, Structural Technologies Research Group, Istanbul, Turkiye; [zcgirgin@yildiz.edu.tr](mailto:zcgirgin@yildiz.edu.tr)

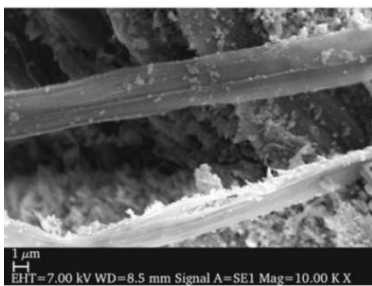
Keywords: CLT, concrete layer, cellulosic fibers, lightweight aggregates (LWA), compressive strength, flexural strength, aging

## 1 Introduction

Numerous studies have been conducted on timber-concrete composite floors for several years. Concrete slab, or topping layer, is almost normal-strength concrete (NC), and is used for in-plane/out-of-plane rigidity, to increase load carrying capacity, fire resistance as well as to decrease vibration and acoustics sensitivity. The concrete slab where coarse lightweight aggregates (LWA) were used in mix design is the least studied topic. For similar compressive strength ( $f_{ck}$ ) levels, structural lightweight concrete (LC) has significant advantages compared with NC, e.g. 25-30% less dead load and less earthquake loads, superior shock absorption (Raman&Bhuvaneshwari, 2022), fire resistance, less human step based vibration (Kozaric et al.,2022), thermal and acoustics benefits. Despite those advantages, the articles structural LC with coarse LWA are very limited even for steel composite decks. The biggest question is about the possible necessity of more connectors due to lower shear strength/rigidity, and higher slip concerns as a result of about 40% lower Young modulus of structural LC. Ollgaard et al. (1971) indicated that shear strength of connector is not directly related with density or compressive/tensile strength of NC/LC concrete. Kan et al. (2013) implied ultimate load-slip levels in concrete-steel composite not to be different for LC and NC. In TCC slabs, Fragiaco et al. (2007) noted LC9/11 affected neither shear force-slip behaviour nor creep compared with NC (C20/25, EN 1992-1-1). Stiffness of those composite floors was detailed in COST WG4 report (2018), nothing exists on LC layers. Another issue for NC top layer, Holschemacher et al. (2002) suggested traditional steel mesh, which increases dead weight not effective for bending, to change with steel fiber and usage of LC slab. This study, based on those literature survey, presents an ecological concrete layer with volcanic coarse LWAs and cellulosic fibers from recent test results (Tuncer&Girgin, 2023). No other study is available on natural fiber reinforced lightweight concrete (NFRLC) with coarse LWA according to author's knowledge. This study may contribute more lightweight, ecological and cost-effective design of CLT-concrete composite or other timber-concrete composite types.

## 2 Materials, Method and Evaluations

The target of this study is to provide ductility in NFRLC by satisfying durability as well. An easily applicable water to binder ratio (0.45) and economical mix design was chosen to achieve C25/30 (EN 1992-1-1:2023) in 100 mm cubes with air dry density of 1700-1800 kg/m<sup>3</sup> and low water absorption (4-5%). Coarse LWA (volcanic based *pumice*) from Nevsehir were provided; bulk density is 650 kg/m<sup>3</sup>,  $D_{max}=8$  mm (ASTM C 173), 1-hour water absorption is 13.6% (EN 1097-6:2013). LWAs were stirred to the mixture in saturated surface dry form. As cellulosic fiber, hemp (H) (*Cannabis Sativa*, elastic modulus 40-60 GPa, tensile strength 590-890 MPa, elongation 1.6%) was used as  $V_f=1\%$ . For cellulosic fibers, degradation due to alkaline environment of concrete is a very critical issue (Juradin et al.,2021), hence cement was partially replaced with metakaolin (calcined clay, MK) economically and practically to satisfy the durability of cellulosic fibers without chemical pre-treatment of fibers. After first reference trials (e.g. LC,LC-H), cement (60%) and MK (40%), total binder 350 kg/m<sup>3</sup>, were decided with 13-15 cm slump (S3) for workability. Three-point flexure tests (40x40x160 mm, EN 12390-5) and water absorption tests (EN 12390-7) were executed after 28 days. Aging tests were also conducted to accelerate Ca(OH)<sub>2</sub> attack in 50°C during 10 days. 28-day and aging test results (Fig.1) indicate ten times higher energy dissipation than without MK (LC-H), 30% decrease in unit weight (compared with reinforced with steel mesh), only 4.8% water absorption (LCMK-H). 28-day splitting tensile strengths ( $f_{st}$ ) are about 3.0 MPa ( $V_f=0$ ), 4.3 MPa ( $V_f=1\%$ ); those values are higher than min. 2.1 MPa (1760 kg/m<sup>3</sup>, ASTM C330) for structural LC.



Series	Density $\rho_{air}$ kg/m <sup>3</sup>	$f_{ck,cube}$ MPa	$f_{cf}$ MPa	$\Delta_u$ mm	$E$ Nmm	$w$ mm	Water absorb. %
LC	1868	35.5	7.91	0.40	509.6	0.01	4.3
LC-H	1861	29.3	5.39	0.42 <sup>a</sup>	238.5 <sup>a</sup>	0.01 <sup>a</sup>	5.4
LCMK-H	1774	29.5	6.99	2.38 <sup>a</sup>	2159.7 <sup>a</sup>	7.10 <sup>a</sup>	4.8

<sup>a</sup> After 10-day aging in 50°C water

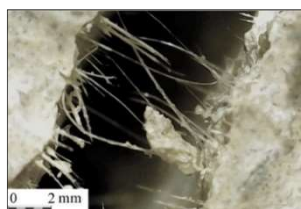


Figure 1 Bending test, no degradation in hemp fibers  
 $\Delta_u$ : deflection at failure,  $w$ : crack mouth opening at failure  
 $E$ : Energy absorption up to failure

It would be appropriate to mention other aspects from the literature. Duration of fire resistance is 65% higher (10 cm depth, 1600 kg/m<sup>3</sup>, ACI 213R-14) compared with NC. Brittleness ( $\eta_{cc}$ ) of LC is enhanced with cellulosic fibers. 28-day creep coefficient  $\varphi(t, t_0)$  is proposed as  $1.0 \eta_{w, Ec}$  ( $f_{ck} \geq 20$  MPa, EN 1992-1-1:2023). Fragiaco et al. (2007) predicted  $\varphi(50y, t_0)$  about 0.5 (1<sup>st</sup> service class) for plain LC9/11 concrete. Internal water reservoir of LWAs contributes internal curing and proper adherence as well as less drying shrinkage ( $\epsilon_{cds}$ ). For final total shrinkage,  $\epsilon_{cs,50y}$  is defined as multiplying NC with 1.2 ( $f_{ck} \geq 20$  MPa). However, EN 1992-1-1:2004 notes autogenous shrinkage decreases

with internal water content of LWA as well. ACI 213R-14 expresses drying shrinkage of LC with normal sand to be less than all LWA-LC. Jorge et al. (2010) state higher autogenous strains can be reduced with less creep coefficient and reduced dead load, and denoting advantages for time dependent behaviour. In COST Action WG4 Report (2018), there is no knowledge about creep/shrinkage of LC concrete layer of timber-concrete composites.

### 3 Conclusions

In this study the following results can be defined;

- o Test results of MK modified hemp fiber reinforced concrete indicate to proper bonding with C-S-H and ten times higher energy absorption than LC-H. There is no disintegration, 30% decrease in unit weight is available only 4.8% water absorption.

- o While creep strains in LC decreases, drying and autogenous shrinkages may be less than anticipated one due to water saturation of LWAs and fiber usage. Cellulosic fibers, instead of steel mesh, may also increase ductility, enhance energy saving, and enable lightweight/sustainable production. From an ecological stand point, in addition to the superiority of CLT deck, top concrete layer with LWA and cellulosic fibers will carry these advantages to a higher level.

Regarding EN 1992-1-1:2023, further research on creep and shrinkage characteristics of plain LC and fiber reinforced structural LC are necessary.

### 4 References

- ACI 213R-14 (2014): Guide for Structural Lightweight-Aggregate Concrete.
- ASTM C330/330M-23: Standard specification for lightweight aggregates for structural concrete, American Society for Testing and Materials.
- COST Action FP1402/WG4. A state-of-the-art report (2018) Design of timber-concrete composite structures Ed. A.Dias, J. Schänzlin, P.Dietsch.
- Eurocode 2 (2023): Design of concrete structures - Part 1-1: General rules and rules for buildings, bridges and civil engineering structures (EN 1992-1-1:2023)
- Eurocode 5 (2021) Design of timber structures - Part 1-1: General - Common rules and rules for buildings. CEN. (EN 1995-1-1).
- Fragiacomo M, Amadio C, Macorini L (2007) Short- and long-term performance of the “Tecnaria” stud connector for timber-concrete composite beams, *Mater. and Struc.* 40:1013–1026.
- Jorge LF, Schänzlin J, Lopes SMR, Cruzd H, Kuhlmann U. (2010) Time-dependent behaviour of timber lightweight concrete composite floors. *Engin. Struc.* 32:3966–3973.
- Holschemacher K, Klotz S, Weibe D (2002) Application of steel fibre reinforced concrete for timber-concrete composite constructions. *Lacer*, 7, 161-170.
- Juradin S, Boko I, Grubeša IN, Jozić D, Mrakovčić S (2021) Influence of different treatment and amount of Spanish broom and hemp fibres on the mechanical properties of reinforced cement mortars. *Constr. and Build. Mater.* 273, 121702.
- Kan YC, Chen LH, Yen T (2013). Mechanical behavior of lightweight concrete steel deck, *Constr. and Build. Mater.* 42, 78-86.
- Ollgaard JG, Slutter RG, Fisher JW (1971) Shear strength of stud connectors in lightweight and normal weight concrete, *AISC Engin. J*, Fritz Laboratory Reports.
- Raman KS, Bhuvaneshwari P (2022) Performance of semi lightweight concrete composite deck slabs under falling mass. *Struct.*, 42, 502-514.
- Tuncer HM, Girgin ZC (2023) Hemp fiber reinforced lightweight concrete (HRLWC) with coarse pumice aggregate and mitigation of degradation. *Mater. and Struc.* 56(3), 59.





# Structural Design Method for CLT Drift Pinned Joint

Shoichi Nakashima, Building Research Institute, Japan

Keywords: CLT, Connection, Dowel, Drift-pin, Japanese Standard

## 1 Introduction

The material strength and structural design method of CLT structure in Japan is defined by the building code in 2016. Detailed design methods are described in the CLT Panel Construction Method Design and Construction Manual that published by the Japan Housing and Wood Technology Center. It is important in the structural design of CLT structures to express the stiffness and strength of the joint, as well as their deformation performance up to the failure. Therefore, in the 2024 revision, a design method for drift pin joints will be added to this manual, which is presented in this paper.

## 2 Structural Design Method of Connection

### 2.1 Materials and Regulation

The following (a) to (f) are specification on materials. (a) Diameter  $d$ :  $12 \leq d \leq 30$ . (b) Slenderness ratio  $L/d$ :  $4 \leq L/d \leq 14$  where  $L$  is the length of the joint and  $d$  is the diameter of the joint. (c) Hole diameter of CLT shall be the same diameter as that of the joint. (d) The standard hole diameter for steel inserts is +1mm up to  $d=16$ , and +1.5mm for  $d=20$ mm and larger. (e) The standard thickness of the insertion steel plate is 6 mm or more for  $d=12$ , 9 mm or more for  $d=16$ , and 12 mm or more for  $d=20$ . (f) the edge distance, edge distance, and joint spacing shall be  $4d$  or more in principle.

### 2.2 Bi-linear Model

Figure 1. shows the bi-linear model of the joint. Each value on this figure will be calculated as follows.

#### 2.2.1 Allowable load, Yield load and Ultimate load

Short-term allowable load  ${}_sP_a$  and long-term allowable load  ${}_lP_a$ , are expressed by ultimate load  $P_u$  as follows;  ${}_sP_a = 2/3 \cdot P_u$ ,  ${}_lP_a = 1.1/3 \cdot P_u$ . Ultimate load  $P_u$  and yield load  $P_y$  is as follows;

$$P_u = \min(r_u \cdot P_y, P_{ug}, P_{u\delta})$$

here,  $r_u$  is Ultimate load – Yield load ratio,  $r_u = 1.5$ .  $P_y$ , is yield load and expressed as  $P_y = n \cdot p_y$ .  $n$  is number of drift pins. Single yield load  $p_y$  is determined with reference to Table1.,  $P_{ug}$  is failure load of CLT. Failure load of CLT is determined by the minimum value after calculating effective cross-sectional area and multiplying by the material strength to calculate the failure load, referring to Fig.2.  $P_{u\delta}$  is failure load determined by the bending of drift pin.

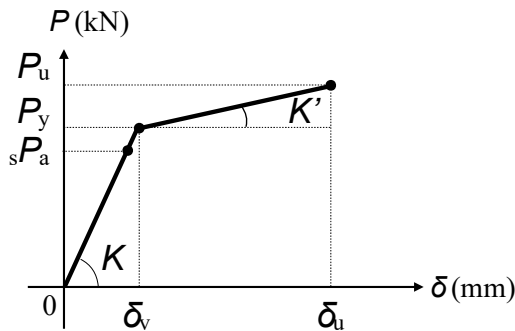


Figure 1. Bi-linear curve

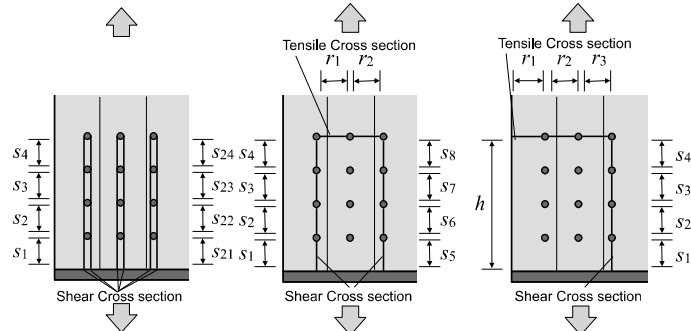


Figure2. Group Shear Failure

Table 1. Yield load and initial stiffness of single joint.

layer	l	d	Yield Load $p_y$ (kN) **						Initial Stiffness $k$ (kN/mm) **					
			Strong Axis ***			Weak Axis			Strong Axis			Weak Axis		
			J3	J2	J1	J3	J2	J1	S60	S90	S120	S60	S90	S120
3-3	90	12	13.3	14.7	16.1	13.7	15.2	16.7	22.4	30.5	37.5	16.6	24.4	31.8
3-3	90	16	21.6	23.4	25.3	20.8	22.8	24.6	27.9	40.1	51.5	16.8	25.0	33.0
3-4	120	12	13.8	15.4	16.6	17.7	19.9	22.1	17.1	22.1	26.5	25.7	36.3	46.2
3-4	120	16	20.3	22.4	24.4	25.9	28.8	31.7	25.8	34.8	42.5	29.1	42.4	55.1
5-5	150	12	17.3	18.8	20.2	16.5	17.6	18.5	20.4	27.9	35.1	22.9	30.8	38.0
5-5	150	16	24.3	27.2	30.0	25.9	28.8	31.8	27.9	37.6	46.4	31.1	43.4	54.4
5-7	210	16	28.4	30.7	32.8	30.3	32.4	34.3	28.5	38.4	47.9	31.5	43.6	54.7
5-7	210	20	40.8	45.6	48.5	41.4	46.5	51.6	37.4	49.4	60.4	38.3	53.8	68.1
7-7	210	16	30.3	32.4	34.3	28.4	30.7	32.8	31.9	43.9	55.2	28.2	38.0	47.1
7-7	210	20	43.0	48.5	53.4	37.0	41.2	45.4	40.9	55.7	69.6	35.9	48.5	59.8

\* Layer 3-3 means 3 layers 3 ply. All laminae are same thickness. \*\* Single yield load  $p_y$  calculated based on European Yield Theory and single initial stiffness  $k$  calculated based on Beams on Elastic Foundation Theory. \*\*\* Strong and Weak axis are parallel and perpendicular to the CLT Panel strong axis. J1, J2 and J3 are species group, S60, S90 and S120 are CLT grade in Japanese Standard.

### 2.2.2 Initial Stiffness, Secondary Stiffness and Plasticity Ratio $\mu$

Initial stiffness  $K$  is expressed as follows;

$$K = n \cdot \alpha \cdot \beta \cdot k$$

Here,  $n$  is numbers of drift pins. Single initial stiffness  $k$  is also determined with reference to Table 1.  $\alpha$  is reduction factor of Steel hole diameter clearance.  $\alpha = k'/k$ ,  $k' = p_v / (d_0/2 + p_v/k)$ .  $\beta$  is reduction factor of non-linearity and  $\beta$  is 0.8. Secondary stiffness  $K_2$  is  $K_2 = 0.08K$ . Plasticity ratio  $\mu$  is  $\delta_u / \delta_v$ , here,  $\delta_v$  is yield displacement;  $\delta_v = P_y / K$ .  $\delta_u$  is ultimate displacement;  $\delta_u = \min (\delta_v + (P_u - P_y) / K_2, \delta_{u2})$ .  $\delta_{u2}$  is the displacement at the drift pin fails due to repeated deformation, and the diameter  $d$  at present.

### 2.3 Beam and Spring Model

In addition to the bilinear modelling described above, the load-displacement relationship can be directly determined using beam on plasto-elastic foundation model as shown in Figure 3. The drift pin modelled as the beam. The parallel and perpendicular layers of CLT are assumed to be independent, and each is modelled as axis spring. Slit thickness, steel plate thickness, and taper of drift pin should be considered in the model.

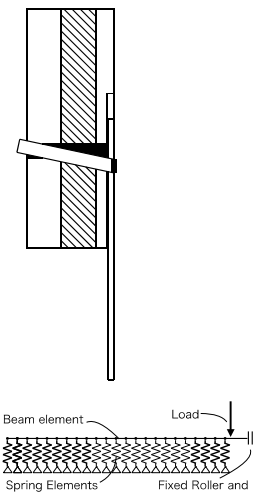


Figure 3. Beam and Spring model of joint

### 2.4 Comparison of calculated and experimental values

Figure 4 shows the relationship between the values obtained in past experiments performed in Japan and the values obtained by calculation described in 2.2. It is seen that evaluated yield loads and ultimate loads are approximately the lower limits, and the evaluated initial and secondary stiffness are approximately the average value.

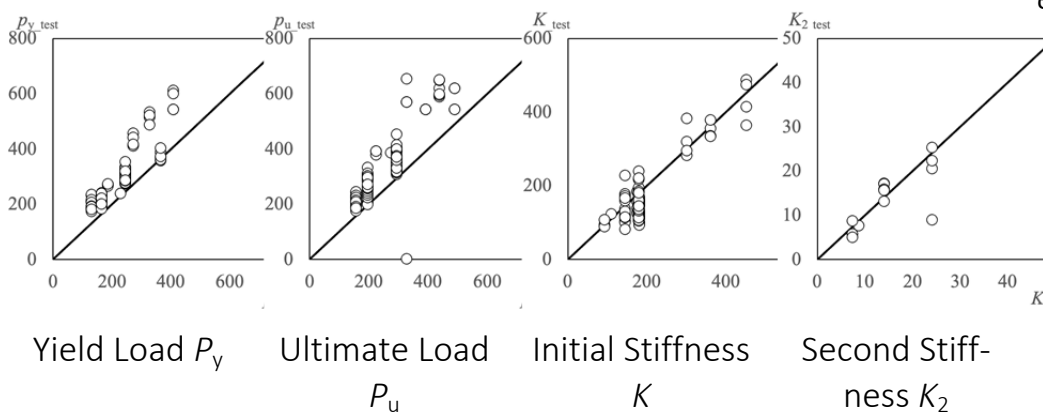


Fig. 4 Comparison of calculated and experimental values (kN)

## 3 References

Nakashima, S (2021) Ultimate load with shear failure of CLT Drift Pinned Connection, Proceedings of World Conference on Timber Engineering 2021

Nakashima, S (2019) Evaluation of Initial Stiffness and Yield Strength of CLT Drift Pinned Connection, PTEC2019



# 5 Peer review of papers for the INTER Proceedings

Experts involved:

The reviews are undertaken by long standing members of the INTER group which is a community of experts in the field of timber engineering.

Procedure of peer review

- Submission of manuscripts: all members of the INTER group attending the meeting receive the manuscripts of the papers at least four weeks before the meeting. Everyone is invited to read and review the manuscripts especially in their respective fields of competence and interest.
- Presentation of the paper during the meeting by the author
- Comments and recommendations of the experts, discussion of the paper
- Comments, discussion and recommendations of the experts are documented in the minutes of the meeting and are printed on the front page of each paper.
- Final acceptance of the paper for the proceedings with
  - no changes
  - minor changes
  - major changes
  - or reject
- Revised papers are to be sent to the editor of the proceedings and the chairman of the INTER group
- Editor and chairman check, whether the requested changes have been carried out.



# 6 Meetings and list of all CIB W18 and INTER Papers

## CIB Meetings:

- 1 Princes Risborough, England; March 1973
- 2 Copenhagen, Denmark; October 1973
- 3 Delft, Netherlands; June 1974
- 4 Paris, France; February 1975
- 5 Karlsruhe, Federal Republic of Germany; October 1975
- 6 Aalborg, Denmark; June 1976
- 7 Stockholm, Sweden; February/March 1977
- 8 Brussels, Belgium; October 1977
- 9 Perth, Scotland; June 1978
- 10 Vancouver, Canada; August 1978
- 11 Vienna, Austria; March 1979
- 12 Bordeaux, France; October 1979
- 13 Otaniemi, Finland; June 1980
- 14 Warsaw, Poland; May 1981
- 15 Karlsruhe, Federal Republic of Germany; June 1982
- 16 Lillehammer, Norway; May/June 1983
- 17 Rapperswil, Switzerland; May 1984
- 18 Beit Oren, Israel; June 1985
- 19 Florence, Italy; September 1986
- 20 Dublin, Ireland; September 1987
- 21 Parksville, Canada; September 1988
- 22 Berlin, German Democratic Republic; September 1989
- 23 Lisbon, Portugal; September 1990
- 24 Oxford, United Kingdom; September 1991
- 25 Åhus, Sweden; August 1992
- 26 Athens, USA; August 1993
- 27 Sydney, Australia; July 1994
- 28 Copenhagen, Denmark; April 1995
- 29 Bordeaux, France; August 1996
- 30 Vancouver, Canada; August 1997
- 31 Savonlinna, Finland; August 1998
- 32 Graz, Austria; August 1999



- 33 Delft, The Netherlands; August 2000
- 34 Venice, Italy; August 2001
- 35 Kyoto, Japan; September 2002
- 36 Colorado, USA; August 2003
- 37 Edinburgh, Scotland; August 2004
- 38 Karlsruhe, Germany; August 2005
- 39 Florence, Italy; August 2006
- 40 Bled, Slovenia; August 2007
- 41 St. Andrews, Canada; August 2008
- 42 Dübendorf, Switzerland; August 2009
- 43 Nelson, New Zealand; August 2010
- 44 Alghero, Italy; August 2011
- 45 Växjö, Sweden; August 2012
- 46 Vancouver, Canada; August 2013

**INTER Meetings:**

- 47 Bath, United Kingdom; August 2014
- 48 Šibenik, Croatia; August 2015
- 49 Graz, Austria; August 2016
- 50 Kyoto, Japan; August 2017
- 51 Tallinn, Estonia; August 2018
- 52 Tacoma WA, USA; August 2019
- 53 Online Meeting; August 2020
- 54 Online Meeting; August 2021
- 55 Bad Aibling, Germany; August 2022
- 56 Biel/Bienne, Switzerland; August 2023
- 57 Padova, Italy; August 2024

The titles of the CIB W 18 and INTER papers (starting from 2014) are included in the complete list of CIB/INTER papers: <http://holz.vaka.kit.edu/741.php>